

# REPORT DOCUMENTATION PAGE

Form Approved  
OMB No. 0704-0188

Public reporting burden for this collection of information is estimated to average 1 hour per response, including the time for reviewing instructions, searching existing data sources, gathering and maintaining the data needed, and completing and reviewing the collection of information. Send comments regarding this burden estimate or any other aspect of this collection of information, including suggestions for reducing this burden, to Washington Headquarters Services, Directorate for Information Operations and Reports, 1215 Jefferson Davis Highway, Suite 1204, Arlington, VA 22202-4302, and to the Office of Management and Budget, Paperwork Reduction Project (0704-0188), Washington, DC 20503.

1. AGENCY USE ONLY (Leave blank)		2. REPORT DATE June 28, 2005	3. REPORT TYPE AND DATES COVERED Technical 01/04/99 to 06/15/05
4. TITLE AND SUBTITLE : <b>Structure of 2-D and 3-D Turbulent Boundary Layers with Sparsely Distributed Roughness Elements</b>			4. FUNDING NUMBERS N00014-99-1-0228 N00014-01-1-0421
5. AUTHORS Jacob George and Roger L. Simpson			
6. PERFORMING ORGANIZATION NAME(S) AND ADDRESS(ES) Department of Aerospace and Ocean Engineering Virginia Polytechnic Institute and State University Blacksburg, Virginia 24061-0203			7. PERFORMING ORGANIZATION REPORT NUMBER  VPI-AOE-302
8. SPONSORING/MONITORING AGENCY NAME(S) AND ADDRESS(ES) Office of Naval Research, 800 N. Quincy Street Arlington, Virginia 22217			10. SPONSORING/MONITORING AGENCY REPORT NUMBER
11. SUPPLEMENTARY NOTES			
12a. DISTRIBUTION/AVAILABILITY STATEMENT Unlimited			12b. DISTRIBUTION CODE
<p>13. ABSTRACT (Maximum 200 words)</p> <p>The present study deals with the effects of sparsely distributed three-dimensional elements on two-dimensional (2-D) and three-dimensional (3-D) turbulent boundary layers (TBL) in three parts: Part 1 with isolated cylinders in the turbulent boundary layers, thus considering the effect of a single perturbation on the TBL; Part 2 when the same individual elements were placed in a sparse and regular distribution, thus showing the response of the flow to a sequence of perturbations; and Part 3, with the distributions subjected to 3-D turbulent boundary layers, thus examining the effects of streamwise and spanwise pressure gradients on the same perturbed flows as considered in Part 2. The 3-D turbulent boundary layers were generated by an idealized wing-body junction flow.</p> <p>Detailed 3-velocity-component Laser-Doppler Velocimetry (LDV) and other measurements were carried out to understand and describe the rough-wall flow structure around the elements. The measurements include mean velocities, turbulence quantities (Reynolds stresses and triple products), skin friction, surface pressure and oil flow visualizations in 2-D and 3-D rough-wall flows for Reynolds numbers, based on momentum thickness, greater than 7000. For the 2-D rough-wall flows, the roughness Reynolds numbers, <math>k^+</math>, based on the element height (<math>k</math>) and the friction velocity (<math>U_\tau</math>), range from 26 to 131. When these elements are placed in a distribution, the roughness elements create a large region of back flow behind them which is continuously replenished by faster moving fluid flowing through the gaps in the rough-wall. The fluid in the back flow region moves upward as low speed ejections where it collides with the intruding high speed flow, thus, leading to a strong mixing of shear layers. This is responsible for the generation of large levels of turbulent kinetic energy (TKE) in the vicinity of the element height which is transported, primarily, by turbulent diffusion. As regards the 3-D rough-wall TBL, the effect of flow three-dimensionality is seen in the large skewing of the distributions of mean velocities, Reynolds stresses and TKE, aft of the elements.</p>			
14. SUBJECT TERMS Rough wall turbulent boundary layers, laser-Doppler velocimetry			15. NUMBER OF PAGES 261
			16. PRICE CODE
17. SECURITY CLASSIFICATION OF REPORT UNCLASSIFIED	18. SECURITY CLASSIFICATION OF THIS PAGE UNCLASSIFIED	19. SECURITY CLASSIFICATION OF ABSTRACT UNCLASSIFIED	20. LIMITATION OF ABSTRACT UNLIMITED



# Structure of 2-D and 3-D Turbulent Boundary Layers with Sparsely Distributed Roughness Elements

Jacob George

## ABSTRACT

The present study deals with the effects of sparsely distributed three-dimensional elements on two-dimensional (2-D) and three-dimensional (3-D) turbulent boundary layers (TBL) such as those that occur on submarines, ship hulls, etc. This study was achieved in three parts: Part 1 dealt with the cylinders when placed individually in the turbulent boundary layers, thereby considering the effect of a single perturbation on the TBL; Part 2 considered the effects when the same individual elements were placed in a sparse and regular distribution, thus studying the response of the flow to a sequence of perturbations; and in Part 3, the distributions were subjected to 3-D turbulent boundary layers, thus examining the effects of streamwise and spanwise pressure gradients on the same perturbed flows as considered in Part 2. The 3-D turbulent boundary layers were generated by an idealized wing-body junction flow.

Detailed 3-velocity-component Laser-Doppler Velocimetry (LDV) and other measurements were carried out to understand and describe the rough-wall flow structure. The measurements include mean velocities, turbulence quantities (Reynolds stresses and triple products), skin friction, surface pressure and oil flow visualizations in 2-D and 3-D rough-wall flows for Reynolds numbers, based on momentum thickness, greater than 7000. Very uniform circular cylindrical roughness elements of 0.38mm, 0.76mm and 1.52mm height ( $k$ ) were used in square and diagonal patterns, yielding six different roughness geometries of rough-wall surface. For the 2-D rough-wall flows, the roughness Reynolds numbers,  $k^+$ , based on the element height ( $k$ ) and the friction velocity ( $U_\tau$ ), range from 26 to 131. Results for the 2-D rough-wall flows reveal that the velocity-defect law is similar for both smooth and rough surfaces, and the semi-logarithmic velocity-distribution curve is shifted by an amount  $\Delta U/U_\tau$  depending on the height of the roughness element, showing that  $\Delta U/U_\tau$  is a function of  $k^+$  and the geometry. For the 3-D flows, the data show that the surface pressure gradient is not strongly influenced by the roughness elements. Higher roughness elements cause greater turbulence intensities near the wall, which cause the pressure-driven mean flow three-dimensionality to propagate or diffuse more rapidly from the wall region. In general, for both 2-D and 3-D rough-wall TBL, the differences between the two roughness patterns (straight and diagonal), as regards the mean velocities and the Reynolds stresses, are limited to about 3 roughness element heights from the wall.

For the single elements, the values of  $k^+$  range from 23 to 92. The study on single elements revealed that the separated shear layers emanating from the top of the elements form a pair of counter rotating vortices that dominate the downstream flow structure. These vortices, termed as the roughness top vortex structure (RTVS), in conjunction with the mean flow, forced over and around the elements, are responsible for the production of large Reynolds stresses in the neighborhood of the element height aft of the elements. The motions associated with the RTVS are responsible for the transport and diffusion of these large stress levels away from the regions where it is produced. Further, large downwash velocities in the common flow region of the vortex pair leads to increased wall shear. When these elements are placed in a distribution, the effects of RTVS are not apparent. The roughness elements create a large region of back flow behind them which is continuously replenished by faster moving fluid flowing through the gaps in the rough-wall. The fluid in the back flow region moves upward as low speed ejections where it collides with the intruding high speed flow, thus, leading to a strong mixing of shear layers. This is responsible for the generation of large levels of turbulent kinetic energy (TKE) in the vicinity of the element height which is transported, primarily, by turbulent diffusion. As regards the 3-D rough-wall TBL, the effect of flow three-dimensionality is seen in the large skewing of the distributions of mean velocities, Reynolds stresses and TKE, aft of the elements. In general, the regions of large TKE production-rates seem to propagate in the direction of the local velocity vector at the element height. The data-sets also enable the extraction of the turbulent flow structure to better describe the flow physics of these rough-wall turbulent boundary layers.



# Table of Contents

ACKNOWLEDGEMENTS .....	IV
TABLE OF CONTENTS .....	V
LIST OF FIGURES .....	VII
NOMENCLATURE .....	XVI
CHAPTER 1 INTRODUCTION .....	1
1.1 PART 1: SINGLE ELEMENTS .....	2
1.1.1 <i>Laminar flow past isolated protuberances leading to transition to turbulence</i> .....	3
1.1.2 <i>Turbulent flow past isolated protuberances</i> .....	4
1.1.3 <i>Turbulent flow past surface-mounted obstacles</i> .....	5
1.1.4 <i>Embedded vortex flows</i> .....	6
1.2 PART 2: TWO-DIMENSIONAL ROUGH-WALL TURBULENT BOUNDARY LAYERS .....	8
1.2.1 <i>Mean flow structure</i> .....	9
1.2.2 <i>Turbulence structure</i> .....	12
1.2.3 <i>Determination of wall shear</i> .....	14
1.3 PART 3: THREE-DIMENSIONAL ROUGH-WALL TURBULENT BOUNDARY LAYERS .....	15
1.4 ORGANIZATION OF THE DISSERTATION .....	16
FIGURES .....	20
CHAPTER 2 EXPERIMENTAL APPARATUS AND MEASUREMENT TECHNIQUE .....	21
2.1 INTRODUCTION .....	21
2.2 WIND TUNNEL .....	21
2.3 MANUFACTURE OF ROUGH SURFACE .....	21
2.4 OIL-FLOW VISUALIZATION .....	21
2.5 ROUGH-WALL GEOMETRY .....	22
2.6 THREE-VELOCITY-COMPONENT FIBER-OPTIC LDV (3CLDV) .....	22
2.7 MEASUREMENT OF PRESSURE GRADIENTS IN 3-D ROUGH-WALL TBL .....	24
2.8 MEASUREMENT LOCATIONS .....	24
2.8.1 <i>Measurement locations: Single Elements</i> .....	24
2.8.2 <i>Measurement locations – 2-D rough-wall turbulent boundary layers</i> .....	25
2.8.3 <i>Measurement locations – 3-D rough-wall turbulent boundary layers</i> .....	25
2.9 FREE-STREAM VELOCITY DISTRIBUTION IN THE WIND TUNNEL .....	26
2.10 UNCERTAINTIES IN THE MEASURED QUANTITIES .....	26
FIGURES .....	28
CHAPTER 3 SINGLE ELEMENTS .....	40
3.1 RESULTS AND DISCUSSION .....	40
3.1.1 <i>Oil flow visualizations</i> .....	40
3.1.2 <i>Mean quantities – mean velocities</i> .....	40
3.1.3 <i>Derived quantities from the mean flow structure</i> .....	42
3.1.4 <i>Turbulence structure</i> .....	49
3.2 CONCLUSIONS .....	57
FIGURES .....	62
CHAPTER 4 TWO-DIMENSIONAL ROUGH-WALL TURBULENT BOUNDARY LAYERS .....	130
4.1 RESULTS AND DISCUSSION .....	130
4.1.1 <i>Mean quantities – mean velocities</i> .....	130
4.1.2 <i>Vorticity</i> .....	134
4.1.3 <i>Turbulent stresses</i> .....	134
4.1.4 <i>Turbulent kinetic energy (TKE)</i> .....	136
4.1.5 <i>Structural parameters</i> .....	138
4.2 CONCLUSIONS .....	138
FIGURES .....	142



<b>CHAPTER 5</b>	<b>THREE-DIMENSIONAL ROUGH-WALL TURBULENT BOUNDARY LAYERS..</b>	<b>190</b>
5.1	RESULTS AND DISCUSSIONS .....	190
5.1.1	<i>Surface pressure gradients</i> .....	190
5.1.2	<i>Mean velocities</i> .....	191
5.1.3	<i>Reynolds stresses</i> .....	191
5.1.4	<i>Turbulent kinetic energy (TKE)</i> .....	192
5.1.5	<i>Check of “flow symmetry” in 3-D rough-wall TBL</i> .....	194
5.2	CONCLUSIONS .....	195
	FIGURES .....	198
<b>CHAPTER 6</b>	<b>COMPARISON OF THE THREE FLOW CASES: SINGLE ELEMENTS, 2-D TBL AND 3-D TBL .....</b>	<b>221</b>
<b>CHAPTER 7</b>	<b>CONCLUSIONS.....</b>	<b>223</b>
	FIGURES .....	225
	REFERENCES .....	226
<b>APPENDIX A</b>	<b>METHOD TO APPROXIMATE THE VORTEX STREAMWISE WAVELENGTH</b>	<b>232</b>
<b>APPENDIX B</b>	<b>COMPUTING THE TOTAL DRAG DUE TO THE SINGLE ELEMENT.....</b>	<b>233</b>
B.1	FORM DRAG .....	233
B.2	SKIN FRICTION DRAG .....	236
<b>APPENDIX C</b>	<b>UNCERTAINTY ANALYSIS ON THE DATA .....</b>	<b>238</b>
C.1	CORRECTIONS APPLICABLE TO THE ACQUIRED LDV DATA .....	238
C.1.1	<i>Velocity bias effects</i> .....	238
C.1.2	<i>Angular bias effects</i> .....	239
C.1.3	<i>Fringe bias and geometric bias effects</i> .....	239
C.1.4	<i>Broadening effects</i> .....	239
C.2	FRICTION/SCALE VELOCITY .....	241
C.3	MEASUREMENT LOCATION, MEAN VELOCITIES AND TURBULENCE QUANTITIES.....	241
C.4	DRAG DUE TO SINGLE ELEMENTS .....	242
C.5	CIRCULATION .....	243
C.6	MEAN VORTICITY .....	243
	GLOSSARY .....	244
	VITA .....	245



# List of Figures

Figure 1.1. Pictorial representation of the three-part study .....	20
Figure 2.1. Side-view schematic of the wind tunnel set-up: (a) Part 1 (Single Elements), (b) Part 2 (2-D Rough-wall TBL) and (c) Part 3 (3-D Rough-wall TBL). .....	28
Figure 2.2. A picture of a sample roughness pattern. ....	29
Figure 2.3. Roughness geometry and flow orientation. ....	30
Figure 2.4. Optical table (BC: Bragg cell; BSC: beam splitter cube; LTFC: laser to fibre coupler; M: mirror; PR: polarization rotator). ....	31
Figure 2.5. Short range, original configuration (right side) and long range, modified configuration (left side) transmitting lens configuration for the three component LDV (3CLDV). Complete optical systems not shown for either short or long range systems. The receiving lens configuration is for the long range design. ....	32
Figure 2.6. Appendage Junction: Laser beams passing through transparent floor through the spacing between the cylindrical roughness elements. ....	33
Figure 2.7 (a). Measurement locations downstream of the isolated cylinder along the centerline at $x/d = 1.36, 2.75, 5, 10, 20$ and $40$ and at off-center locations along $z/d$ . ....	34
Figure 2.7 (b). Measurement locations downstream of the Gaussian spike along the centerline at $x/d = 2.75, 5, 10, 20$ and $40$ and at off-center locations along $z/d$ . ....	34
Figure 2.8 (a). Measurement in the 2-D rough-wall boundary layers ( <i>straight</i> orientation). Each plane consists of 9 measurement locations totaling 45 measuring stations. ....	35
Figure 2.8 (b). Measurement in the 2-D rough-wall boundary layers ( <i>staggered</i> orientation). Each plane consists of 5 measurement locations totaling 40 measuring stations. ....	35
Figure 2.9 (a). Schematic of the wing-body junction and the seven measurement stations. ....	36
Figure 2.9 (b). Measurements in the 3-D rough-wall boundary layers at the seven stations around the wing-body junction. $\alpha$ is the angle the velocity vector makes with the tunnel axis at $3k$ height. ....	36
Figure 2.10. Measurements in the 3-D rough-wall boundary layers (straight orientation) at station 5. ....	37
Figure 2.11. Streamwise variation of the free-stream velocity, $[U_e(x)/U_{ref}]$ , in the wind tunnel. ....	38
Figure 2.12. Streamwise variation of the pressure gradient, $[(dp/dx)/(\frac{1}{2}\rho U_e^2)]$ , in the wind tunnel. ....	39
Figure 3.1. Top-view of surface oil flow over isolated elements; from top, Gaussian spike, $k = 1.52mm$ , circular cylinders, $k = 1.52mm, 0.76mm, 0.38mm$ . ....	62
Figure 3.2. $U/U_\tau$ versus $yU_\tau/\nu$ , streamwise mean velocity profiles along the centerline. ....	63
Figure 3.3 (a). Semi-log contours of $U/U_\tau$ in the $y^+ - z/d$ plane at $x/d = 2.75$ . ....	64
Figure 3.3 (b). Semi-log contours of $U/U_\tau$ in the $y^+ - z/d$ plane at $x/d = 10$ . ....	65
Figure 3.4 (a). $V/U_\tau$ versus $yU_\tau/\nu$ , wall-normal mean velocity profiles along the centerline. ....	66
Figure 3.4 (b). Semi-log contours of $V/U_\tau$ in the $y^+ - z/d$ plane along $z/d = 0$ . ....	67
Figure 3.5 (a). Semi-log contours of $V/U_\tau$ in the $y^+ - z/d$ plane at $x/d = 2.75$ . ....	68
Figure 3.5 (b). Semi-log contours of $V/U_\tau$ in the $y^+ - z/d$ plane at $x/d = 10$ . ....	69
Figure 3.6 (a). Semi-log contours of $W/U_\tau$ in the $y^+ - z/d$ plane at $x/d = 2.75$ . ....	70
Figure 3.6 (b). Semi-log contours of $W/U_\tau$ in the $y^+ - z/d$ plane at $x/d = 10$ . ....	71



Figure 3.7 (a). Semi-log contours of streamwise vorticity, $\Omega_x \sqrt{A}/U_\tau$ , with secondary velocity vectors, $V/U_\tau$ and $W/U_\tau$ , in the $y^+ - z/d$ plane at $x/d=2.75$ . + denotes the center of rotation, $\times$ denotes the location of $\Omega_{x_{max}}$ , and $L'$ denotes the line of flow separation. ....	72
Figure 3.7 (b). Semi-log contours of streamwise vorticity, $\Omega_x \sqrt{A}/U_\tau$ , with secondary velocity vectors, $V/U_\tau$ and $W/U_\tau$ , in the $y^+ - z/d$ plane at $x/d=10$ . + denotes the center of rotation, $\times$ denotes the location of $\Omega_{x_{max}}$ , and $L'$ denotes the line of flow separation. ....	73
Figure 3.8 (a). A perspective of the flow structure downstream of the cylinder at $x/d = 2.75$ . ....	74
Figure 3.8 (b). A perspective of the flow structure downstream of the cylinder at $x/d = 10$ . ....	74
Figure 3.9 (a). Variation of Circulation, $\Gamma/(U_\tau \sqrt{A})$ , with normalized length scale, $U_\tau \sqrt{A}/\nu$ at $x/d=2.75$ . ....	75
Figure 3.9 (b). Variation of $\Gamma/\nu$ , with $(\sqrt{A}^+)^3$ at $x/d=2.75$ . ....	75
Figure 3.9 (c). Variation of Circulation, $\Gamma/(U_\tau \sqrt{A})$ , with streamwise distance, $x/d$ ....	76
Figure 3.10 (a). Semi-log contours of mean-flow helicity density, $h\sqrt{A}/U_\tau^2$ , in the $y^+ - z/d$ plane at $x/d=2.75$ . ....	77
Figure 3.10 (b). Semi-log contours of mean-flow helicity density, $h\sqrt{A}/U_\tau^2$ , in the $y^+ - z/d$ plane at $x/d=10$ . ....	78
Figure 3.11 (a). Normalized wall shear ( $\tau_w/\tau_o$ ): Spanwise variation at $x/d=2.75$ and 10. ....	79
Figure 3.11 (b). Normalized wall shear ( $\tau_w/\tau_o$ ): Centerline streamwise variation ....	80
Figure 3.12. Normalized drag coefficient, $C_d/C_f$ , of the cylinders and the Gaussian spike. ....	80
Figure 3.13 (a). Semi-log contours of streamwise normal stress, $\overline{u^2}/U_\tau^2$ , in the $y^+ - z/d$ plane at $x/d=2.75$ . ....	81
Figure 3.13 (b). Semi-log contours of streamwise normal stress, $\overline{u^2}/U_\tau^2$ , in the $y^+ - z/d$ plane at $x/d=10$ . ....	82
Figure 3.14. $\overline{u^2}/U_\tau^2$ versus $yU_\tau/\nu$ , streamwise Reynolds normal stress profiles along the centerline. ....	83
Figure 3.15 (a). Semi-log contours of wall-normal Reynolds normal stress, $\overline{v^2}/U_\tau^2$ in the $y^+ - z/d$ plane at $x/d = 2.75$ . ....	84
Figure 3.15 (b). Semi-log contours of wall-normal Reynolds normal stress, $\overline{v^2}/U_\tau^2$ in the $y^+ - z/d$ plane at $x/d = 10$ . ....	85
Figure 3.16. $\overline{v^2}/U_\tau^2$ versus $yU_\tau/\nu$ , wall-normal Reynolds normal stress profiles along the centerline. ....	86
Figure 3.17 (a). Semi-log contours of spanwise Reynolds normal stress, $\overline{w^2}/U_\tau^2$ in the $y^+ - z/d$ plane at $x/d = 2.75$ . ....	87



Figure 3.17 (b). Semi-log contours of spanwise Reynolds normal stress, $\overline{w^2}/U_\tau^2$ in the $y^+ - z/d$ plane at $x/d = 10$ .	88
Figure 3.18. $\overline{w^2}/U_\tau^2$ versus $yU_\tau/\nu$ , spanwise Reynolds normal stress profiles along the centerline.	89
Figure 3.19 (a). Semi-log contours of Reynolds streamwise shearing stress, $-\overline{uv}/U_\tau^2$ in the $y^+ - z/d$ plane at $x/d = 2.75$ .	90
Figure 3.19 (b). Semi-log contours of Reynolds streamwise shearing stress, $-\overline{uv}/U_\tau^2$ in the $y^+ - z/d$ plane at $x/d = 10$ .	91
Figure 3.20. $-\overline{uv}/U_\tau^2$ versus $yU_\tau/\nu$ , streamwise Reynolds shear stress profiles along the centerline.	92
Figure 3.21 (a). Quadrant contributions to streamwise Reynolds shear stress, $-\overline{uv}$ : profiles, normalized by $-\overline{uv}_{\text{smooth}}$ , varying with $yU_\tau/\nu$ at $x/d = 1.36$ .	93
Figure 3.21 (b). Quadrant contributions to streamwise Reynolds shear stress, $-\overline{uv}$ : profiles, normalized by $-\overline{uv}_{\text{smooth}}$ , varying with $yU_\tau/\nu$ at $x/d = 2.75$ .	94
Figure 3.21 (c). Quadrant contributions to streamwise Reynolds shear stress, $-\overline{uv}$ : profiles, normalized by $-\overline{uv}_{\text{smooth}}$ , varying with $yU_\tau/\nu$ at $x/d = 5$ .	95
Figure 3.21 (d). Quadrant contributions to streamwise Reynolds shear stress, profiles, normalized by $-\overline{uv}_{\text{smooth}}$ , varying with $yU_\tau/\nu$ at $x/d = 10$ .	96
Figure 3.21 (e). Quadrant contributions to streamwise Reynolds shear stress, $-\overline{uv}$ : profiles, normalized by $-\overline{uv}_{\text{smooth}}$ , varying with $yU_\tau/\nu$ at $x/d = 20$ .	97
Figure 3.21 (f). Quadrant contributions to streamwise Reynolds shear stress, profiles, normalized by $-\overline{uv}_{\text{smooth}}$ , varying with $yU_\tau/\nu$ at $x/d = 40$ .	98
Figure 3.21 (g). Ratio of sweep to ejection contributions varying with $yU_\tau/\nu$ at the six streamwise locations.	99
Figure 3.21 (h). Quadrant contributions to streamwise Reynolds shear stress, $-\overline{uv}$ : profiles, normalized by $U_\tau^2$ , varying with $yU_\tau/\nu$ at $x/d = 1.36$ .	100
Figure 3.21 (i). Quadrant contributions to streamwise Reynolds shear stress, $-\overline{uv}$ : profiles, normalized by $U_\tau^2$ , varying with $yU_\tau/\nu$ at $x/d = 2.75$ .	101
Figure 3.21 (j). Quadrant contributions to streamwise Reynolds shear stress, $-\overline{uv}$ : profiles, normalized by $U_\tau^2$ , varying with $yU_\tau/\nu$ at $x/d = 5$ .	102
Figure 3.21 (k). Quadrant contributions to streamwise Reynolds shear stress, $-\overline{uv}$ : profiles, normalized by $U_\tau^2$ , varying with $yU_\tau/\nu$ at $x/d = 10$ .	103
Figure 3.21 (l). Quadrant contributions to streamwise Reynolds shear stress, $-\overline{uv}$ : profiles, normalized by $U_\tau^2$ , varying with $yU_\tau/\nu$ at $x/d = 20$ .	104
Figure 3.21 (m). Quadrant contributions to streamwise Reynolds shear stress, $-\overline{uv}$ : profiles, normalized by $U_\tau^2$ , varying with $yU_\tau/\nu$ at $x/d = 40$ .	105



Figure 3.22. $-\overline{uw}/U_\tau^2$ versus $yU_\tau/\nu$ , streamwise Reynolds shear stress profiles along the centerline at $x/d = 20$ and $40$ . .....	106
Figure 3.23. Reynolds streamwise shearing stress coefficient, $R_w$ , varying with $yU_\tau/\nu$ at the six streamwise locations. ....	107
Figure 3.24 (a). Semi-log contours of Reynolds shearing stress, $-\overline{uw}/U_\tau^2$ in the $y^+ - z/d$ plane at $x/d = 2.75$ . ....	108
Figure 3.24 (b). Semi-log contours of Reynolds shearing stress, $-\overline{uw}/U_\tau^2$ in the $y^+ - z/d$ plane at $x/d = 10$ . ....	109
Figure 3.25 (a). Semi-log contours of Reynolds shearing stress, $-\overline{vw}/U_\tau^2$ in the $y^+ - z/d$ plane at $x/d = 2.75$ . ....	110
Figure 3.25 (b). Semi-log contours of Reynolds shearing stress, $-\overline{vw}/U_\tau^2$ in the $y^+ - z/d$ plane at $x/d = 10$ . ....	111
Figure 3.26 (a). Semi-log contours of turbulent kinetic energy (TKE), $\frac{1}{2}\overline{q^2}/U_\tau^2$ , along with diffusion velocity vectors, $V_q$ and $W_q$ , in the $y^+ - z/d$ plane at $x/d = 2.75$ . ....	112
Figure 3.26 (b). Semi-log contours of turbulent kinetic energy (TKE), $\frac{1}{2}\overline{q^2}/U_\tau^2$ , along with diffusion velocity vectors, $V_q$ and $W_q$ , in the $y^+ - z/d$ plane at $x/d = 10$ . ....	113
Figure 3.27 (a). $\frac{1}{2}\overline{q^2}/U_\tau^2$ versus $yU_\tau/\nu$ , turbulent kinetic energy (TKE) profiles along the centerline. ....	114
Figure 3.27 (b). Semi-log contours of turbulent kinetic energy (TKE), $\frac{1}{2}\overline{q^2}/U_\tau^2$ , along with diffusion velocity vectors, $U_q$ and $V_q$ , in the $x/d - y^+$ plane along the centerline. ....	115
Figure 3.28 (a). Semi-log contours of production (PR) of TKE, normalized by $\nu/U_\tau^4$ , in the $y^+ - z/d$ plane at $x/d = 2.75$ . ....	116
Figure 3.28 (b). Semi-log contours of production (PR) of TKE, normalized by $\nu/U_\tau^4$ , in the $y^+ - z/d$ plane at $x/d = 10$ . ....	117
Figure 3.28 (c). Semi-log contours of production (PR) of TKE, normalized by $\nu/U_\tau^4$ , in the $y^+ - z/d$ plane along the centerline. ....	118
Figure 3.29. Variation of transport-rate budget of TKE, $\overline{q^2}/2$ , normalized by $U_\tau^4/\nu$ , with $yU_\tau/\nu$ (2-D smooth wall BL). ....	119
Figure 3.30 (a). Variation of transport-rate budget of TKE, $\overline{q^2}/2$ , normalized by $U_\tau^4/\nu$ , with $yU_\tau/\nu$ at $x/d = 1.36$ . ....	120
Figure 3.30 (b). Variation of transport-rate budget of TKE, $\overline{q^2}/2$ , normalized by $U_\tau^4/\nu$ , with $yU_\tau/\nu$ at $x/d = 2.75$ . ....	121
Figure 3.30 (c). Variation of transport-rate budget of TKE, $\overline{q^2}/2$ , normalized by $U_\tau^4/\nu$ , with $yU_\tau/\nu$ at $x/d = 5$ . ....	122



Figure 3.30 (d). Variation of transport-rate budget of TKE, $\overline{q^2}/2$ , normalized by $U_\tau^4/\nu$ , with $yU_\tau/\nu$ at $x/d = 10$ .	123
Figure 3.30 (e). Variation of transport-rate budget of TKE, $\overline{q^2}/2$ , normalized by $U_\tau^4/\nu$ , with $yU_\tau/\nu$ at $x/d = 20$ .	124
Figure 3.30 (f). Variation of transport-rate budget of TKE, $\overline{q^2}/2$ , normalized by $U_\tau^4/\nu$ , with $yU_\tau/\nu$ at $x/d = 40$ .	125
Figure 3.31. Variation of the Kolmogorov scale, $\eta$ , normalized by $\nu/U_\tau$ , with streamwise distance at the wall and at $y^+ = 3$ .	126
Figure 3.32 (a). Structural parameter, $A_1$ , versus $yU_\tau/\nu$ , profiles along the centerline.	127
Figure 3.32 (b). Structural parameter, $1/S$ , versus $yU_\tau/\nu$ , profiles along the centerline.	128
Figure 3.33. Schematic of the flow past the single cylinder.	129
Figure 4.1 (a). Semi-log contours of $U/\sqrt{-\overline{uv}_{\max}}$ in the $y/k - z/d$ plane at $x/D = 0.295$ with secondary flow vectors, $V/\sqrt{-\overline{uv}_{\max}}$ and $W/\sqrt{-\overline{uv}_{\max}}$ [ $k = 0.38mm$ (top row), $k = 0.76mm$ (middle), $k = 1.52mm$ (bottom)].	142
Figure 4.1 (b). Semi-log contours of $U/\sqrt{-\overline{uv}_{\max}}$ in the $y/k - z/d$ plane at $x/D = 0.398$ with secondary flow vectors, $V/\sqrt{-\overline{uv}_{\max}}$ and $W/\sqrt{-\overline{uv}_{\max}}$ [ $k = 0.38mm$ (top row), $k = 0.76mm$ (middle), $k = 1.52mm$ (bottom)].	143
Figure 4.1 (c). Semi-log contours of $U/\sqrt{-\overline{uv}_{\max}}$ in the $y/k - z/d$ plane at $x/D = 0.5$ with secondary flow vectors, $V/\sqrt{-\overline{uv}_{\max}}$ and $W/\sqrt{-\overline{uv}_{\max}}$ [ $k = 0.38mm$ (top row), $k = 0.76mm$ (middle), $k = 1.52mm$ (bottom)].	144
Figure 4.1 (d). Semi-log contours of $U/\sqrt{-\overline{uv}_{\max}}$ in the $y/k - z/d$ plane at $x/D = 0.625$ with secondary flow vectors, $V/\sqrt{-\overline{uv}_{\max}}$ and $W/\sqrt{-\overline{uv}_{\max}}$ [ $k = 0.38mm$ (top row), $k = 0.76mm$ (middle), $k = 1.52mm$ (bottom)].	145
Figure 4.1 (e). Semi-log contours of $U/\sqrt{-\overline{uv}_{\max}}$ in the $y/k - z/d$ plane at $x/D = 0.75$ with secondary flow vectors, $V/\sqrt{-\overline{uv}_{\max}}$ and $W/\sqrt{-\overline{uv}_{\max}}$ [ $k = 0.38mm$ (top row), $k = 0.76mm$ (middle), $k = 1.52mm$ (bottom)].	146
Figure 4.1 (f). Semi-log contours of $U/\sqrt{-\overline{uv}_{\max}}$ in the $y/k - z/d$ plane at $x/D = 0.879, 1.008$ and $1.137$ with secondary flow vectors, $V/\sqrt{-\overline{uv}_{\max}}$ and $W/\sqrt{-\overline{uv}_{\max}}$ [staggered cases only: $k = 0.38mm$ (top row), $k = 0.76mm$ (middle), $k = 1.52mm$ (bottom)].	147
Figure 4.2. Semi-log contours of $U/\sqrt{-\overline{uv}_{\max}}$ in the $y/k - x/D$ plane along center line ( $z/d = 0$ ) [ $k = 0.38mm$ (top row), $k = 0.76mm$ (middle), $k = 1.52mm$ (bottom)].	148
Figure 4.3. Variation of the ratio, $A_{sep}/A$ , with streamwise distance, $x/D$ . Values denoting 1 are due to the element itself by virtue of its location.	149



Figure 4.4. $U/\sqrt{-\overline{uv}_{\max}}$ versus $y\sqrt{-\overline{uv}_{\max}}/\nu$ , streamwise mean velocity profile at $x/D=0.5$ , $z/d=0$ .	150
Figure 4.5. Velocity defect profiles, $(U_e - U)/\sqrt{-\overline{uv}_{\max}}$ versus $y/\delta$ , at $x/D=0.5$ , $z/d=0$ .	151
Figure 4.6. $U/\sqrt{-\overline{uv}_{\max}}$ versus $(y - \varepsilon)\sqrt{-\overline{uv}_{\max}}/\nu$ , streamwise mean velocity profile at $x/D=0.5$ , $z/d=0$ . Corrected for displacement of origin and excludes locations in the viscous sublayer and buffer layer.	152
Figure 4.7 (a). Effects of roughness density, $\lambda$ , on law of the wall intercept, $f(\lambda)$ .	153
Figure 4.7 (b). Effects of roughness density, $\Lambda_s$ , on law of the wall intercept, $f(\Lambda_s)$ .	154
Figure 4.8 (a). Semi-log contours of $V/\sqrt{-\overline{uv}_{\max}}$ in the $y/k - z/d$ plane at $x/D = 0.5$ [ $k = 0.38mm$ (top row), $k = 0.76mm$ (middle), $k = 1.52mm$ (bottom)].	155
Figure 4.8 (b). Semi-log contours of $V/\sqrt{-\overline{uv}_{\max}}$ in the $y/k - x/D$ plane along center line ( $z/d = 0$ ) [ $k = 0.38mm$ (top row), $k = 0.76mm$ (middle), $k = 1.52mm$ (bottom)].	156
Figure 4.9 (a). Semi-log contours of streamwise vorticity, $\Omega_x \sqrt{A}/\sqrt{-\overline{uv}_{\max}}$ , with secondary velocity vectors, $V/\sqrt{-\overline{uv}_{\max}}$ and $W/\sqrt{-\overline{uv}_{\max}}$ in the $y/k - z/d$ plane at $x/D = 0.295$ [ $k = 0.38mm$ (top row), $k = 0.76mm$ (middle), $k = 1.52mm$ (bottom)].	157
Figure 4.9 (b). Semi-log contours of streamwise vorticity, $\Omega_x \sqrt{A}/\sqrt{-\overline{uv}_{\max}}$ , with secondary velocity vectors, $V/\sqrt{-\overline{uv}_{\max}}$ and $W/\sqrt{-\overline{uv}_{\max}}$ in the $y/k - z/d$ plane at $x/D = 0.5$ [ $k = 0.38mm$ (top row), $k = 0.76mm$ (middle), $k = 1.52mm$ (bottom)].	158
Figure 4.9 (c). Semi-log contours of streamwise vorticity, $\Omega_x \sqrt{A}/\sqrt{-\overline{uv}_{\max}}$ , with secondary velocity vectors, $V/\sqrt{-\overline{uv}_{\max}}$ and $W/\sqrt{-\overline{uv}_{\max}}$ in the $y/k - z/d$ plane at $x/D = 0.75$ [ $k = 0.38mm$ (top row), $k = 0.76mm$ (middle), $k = 1.52mm$ (bottom)].	159
Figure 4.10 (a). Semi-log contours of wall-normal vorticity, $\Omega_y \sqrt{A}/\sqrt{-\overline{uv}_{\max}}$ , with velocity vectors, $U/\sqrt{-\overline{uv}_{\max}}$ and $W/\sqrt{-\overline{uv}_{\max}}$ in the $x/D - z/d$ plane at $y/k = 0.3$ (left) and $y/k = 0.5$ (right), [ $k = 0.38mm$ (top row), $k = 0.76mm$ (middle), $k = 1.52mm$ (bottom)], straight orientations only.	160
Figure 4.10 (b). Semi-log contours of wall-normal vorticity, $\Omega_y \sqrt{A}/\sqrt{-\overline{uv}_{\max}}$ , with velocity vectors, $U/\sqrt{-\overline{uv}_{\max}}$ and $W/\sqrt{-\overline{uv}_{\max}}$ in the $x/D - z/d$ plane at $y/k = 0.8$ (left) and $y/k = 1.1$ (right), [ $k = 0.38mm$ (top row), $k = 0.76mm$ (middle), $k = 1.52mm$ (bottom)], straight orientations only.	161
Figure 4.11. Semi-log contours of spanwise vorticity, $\Omega_z \sqrt{A}/\sqrt{-\overline{uv}_{\max}}$ , with velocity vectors, $U/\sqrt{-\overline{uv}_{\max}}$ and $V/\sqrt{-\overline{uv}_{\max}}$ in the $y/k - x/D$ plane along center line ( $z/d = 0$ ) [ $k = 0.38mm$ (top row), $k = 0.76mm$ (middle), $k = 1.52mm$ (bottom)].	162
Figure 4.12 (a). Semi-log contours of $\overline{u^2}/\overline{uv}_{\max}$ in the $y/k - z/d$ plane at $x/D = 0.5$	163
Figure 4.12 (b). Semi-log contours of $\overline{u^2}/\overline{uv}_{\max}$ in the $y/k - x/D$ plane along the centerline.	164



Figure 4.13 (a). Quadrant fraction to the Reynolds normal stress, $\overline{u^2}$ , along the centerline, varying with $y/\delta$ , at $x/D=0.5$ .....	165
Figure 4.13 (b). Ratio of sweeps to ejections from quadrant contribution to the Reynolds normal stress, $\overline{u^2}$ , along the centerline, varying with $y/k$ , at various streamwise locations, $x/D$ .....	166
Figure 4.14. Variation of the streamwise Reynolds normal stresses, $\overline{u^2}/-\overline{uv}_{\max}$ , with $y/\delta$ at $x/D = 0.5$ , $z = 0$ .....	167
Figure 4.15 (a). Semi-log contours of $\overline{v^2}/-\overline{uv}_{\max}$ in the $y/k - z/d$ plane at $x/D = 0.5$ .....	168
Figure 4.15 (b). Semi-log contours of $\overline{v^2}/-\overline{uv}_{\max}$ in the $y/k - x/D$ plane along the centerline.....	169
Figure 4.16 (a). Quadrant fraction to the Reynolds normal stress, $\overline{v^2}$ , along the centerline, varying with $y/\delta$ , at $x/D=0.5$ .....	170
Figure 4.16 (b). Ratio of sweeps to ejections from quadrant contribution to the Reynolds normal stress, $\overline{v^2}$ , along the centerline, varying with $y/k$ , at various streamwise locations, $x/D$ .....	171
Figure 4.17. Variation of the wall-normal Reynolds normal stresses, $\overline{v^2}/-\overline{uv}_{\max}$ , with $y/\delta$ at $x/D = 0.5$ , $z = 0$ .....	172
Figure 4.18 (a). Semi-log contours of $\overline{w^2}/-\overline{uv}_{\max}$ in the $y/k - z/d$ plane at $x/D = 0.5$ .....	173
Figure 4.18 (b). Semi-log contours of $\overline{w^2}/-\overline{uv}_{\max}$ in the $y/k - x/D$ plane along the centerline. ...	174
Figure 4.19. Variation of the spanwise Reynolds normal stresses, $\overline{w^2}/-\overline{uv}_{\max}$ , with $y/\delta$ at $x/D = 0.5$ , $z = 0$ .....	175
Figure 4.20 (a). Semi-log contours of $-\overline{uv}/-\overline{uv}_{\max}$ in the $y/k - z/d$ plane at $x/D = 0.5$ .....	176
Figure 4.20 (b). Semi-log contours of $-\overline{uv}/-\overline{uv}_{\max}$ in the $y/k - x/D$ plane along the centerline..	177
Figure 4.21. Ratio of sweeps to ejections from quadrant contribution to the Reynolds shear stress, $-\overline{uv}$ , along the centerline, varying with $y/k$ , at various streamwise locations, $x/D$ .....	178
Figure 4.22. Variation of the streamwise Reynolds shear stresses, $-\overline{uv}/-\overline{uv}_{\max}$ , with $y/\delta$ at $x/D = 0.5$ , $z = 0$ .....	179
Figure 4.23 (a). Semi-log contours of turbulent kinetic energy (TKE), $(\overline{q^2}/2)/-\overline{uv}_{\max}$ , along with diffusion velocity vectors, $V_q/\sqrt{-\overline{uv}_{\max}}$ and $W_q/\sqrt{-\overline{uv}_{\max}}$ , in the $y/k - z/d$ plane at $x/D = 0.5$ .....	180
Figure 4.23 (b). Semi-log contours of turbulent kinetic energy (TKE), $(\overline{q^2}/2)/-\overline{uv}_{\max}$ , along with diffusion velocity vectors, $U_q/\sqrt{-\overline{uv}_{\max}}$ and $V_q/\sqrt{-\overline{uv}_{\max}}$ , in the $y/k - x/D$ plane along the centerline. ....	181
Figure 4.24. Variation of the turbulent kinetic energy, $(\overline{q^2}/2)/-\overline{uv}_{\max}$ , with $y/\delta$ at $x/D = 0.5$ , $z = 0$ .....	182
Figure 4.25 (a). Semi-log contours of production of TKE, $(TKE \text{ Prod})\sqrt{A}/(\sqrt{-\overline{uv}_{\max}})^3$ , in the $y/k - z/d$ plane at $x/D = 0.5$ .....	183



Figure 4.25 (b). Semi-log contours of production of TKE, $(TKE \text{ Prod}) \sqrt{A} / (\sqrt{-uv_{\max}})^3$ , in the $y/k - x/D$ plane along the centerline. ....	184
Figure 4.26. Variation of transport-rate budget of TKE, $\overline{q^2}/2$ , normalized by $(\sqrt{-uv_{\max}})^4/\nu$ , with $y\sqrt{-uv_{\max}}/\nu$ (2-D smooth wall BL). ....	185
Figure 4.27. Variation of transport-rate budget of TKE, $\overline{q^2}/2$ , normalized by $(\sqrt{-uv_{\max}})^4/\nu$ , with $y\sqrt{-uv_{\max}}/\nu$ at $x/D = 0.5$ at the centerline. ....	186
Figure 4.28 (a). Structural parameter, $A_1$ , versus $yU_\tau/\nu$ , profiles along the centerline. ....	187
Figure 4.28 (b). Structural parameter, $1/S$ , versus $yU_\tau/\nu$ , profiles along the centerline. ....	188
Figure 4.29. Schematic of the flow in a 2-D rough-wall (straight orientation). Similar structures are seen upstream and aft of each element. ....	189
Fig. 5.1 (a). Pressure gradients in the $x$ -direction as calculated at each station and in between adjacent stations. Also plotted are smooth wall data (From Ölçmen and Simpson, 1995). ....	198
Figure 5.1 (b). Pressure gradients in the $z$ -direction as calculated at each station and in between adjacent stations. Also plotted are smooth wall data (From Ölçmen and Simpson, 1995b). ....	199
Figure 5.2. $U/U_w$ versus $yU_w/\nu$ , streamwise mean velocity profiles. ....	200
Figure 5.3. $W/U_e$ versus $y/\delta$ , spanwise mean velocity profiles. ....	201
Figure 5.4. $\overline{u^2}/U_w^2$ versus $y/\delta$ , streamwise Reynolds normal stress profiles. ....	202
Figure 5.5. $\overline{v^2}/U_w^2$ versus $y/\delta$ , wall-normal Reynolds normal stress profiles. ....	203
Figure 5.6. $\overline{w^2}/U_w^2$ versus $y/\delta$ , spanwise Reynolds normal stress profiles. ....	204
Figure 5.7. $-\overline{uv}/U_w^2$ versus $y/\delta$ , streamwise Reynolds shear stress profiles. ....	205
Figure 5.8. $-\overline{vw}/U_w^2$ versus $y/\delta$ , spanwise Reynolds shear stress profiles. ....	206
Figure 5.9. Structural parameter: $1/S$ versus $y/\delta$ . ....	207
Figure 5.10. Semi-log contours of $U/U_w$ in the $y/k - z/d$ plane at $x/D = 0.5$ with secondary flow vectors, $V/U_w$ and $W/U_w$ [ $k = 0.38mm$ (top row), $k = 0.76mm$ (middle), $k = 1.52mm$ (bottom)], (LHS: 2-D BL, RHS: Station 5, 3-D BL). ....	208
Figure 5.11 (a). Semi-log contours of $\overline{u^2}/U_w^2$ in the $y/k - z/d$ plane at $x/D = 0.5$ [ $k = 0.38mm$ (top row), $k = 0.76mm$ (middle), $k = 1.52mm$ (bottom)], (LHS: 2-D BL, RHS: Station 5, 3-D BL). ....	209
Figure 5.11 (b). Semi-log contours of $\overline{v^2}/U_w^2$ in the $y/k - z/d$ plane at $x/D = 0.5$ [ $k = 0.38mm$ (top row), $k = 0.76mm$ (middle), $k = 1.52mm$ (bottom)], (LHS: 2-D BL, RHS: Station 5, 3-D BL). ....	210
Figure 5.11 (c). Semi-log contours of $\overline{w^2}/U_w^2$ in the $y/k - z/d$ plane at $x/D = 0.5$ [ $k = 0.38mm$ (top row), $k = 0.76mm$ (middle), $k = 1.52mm$ (bottom)], (LHS: 2-D BL, RHS: Station 5, 3-D BL). ....	211

Figure 5.11 (d). Semi-log contours of $-\overline{uv}/U_w^2$ in the $y/k - z/d$ plane at $x/D = 0.5$ [ $k = 0.38mm$ (top row), $k = 0.76mm$ (middle), $k = 1.52mm$ (bottom)], (LHS: 2-D BL, RHS: Station 5, 3-D BL).	212
Figure 5.11 (e). Semi-log contours of $-\overline{vw}/U_w^2$ in the $y/k - z/d$ plane at $x/D = 0.5$ [ $k = 0.38mm$ (top row), $k = 0.76mm$ (middle), $k = 1.52mm$ (bottom)], (LHS: 2-D BL, RHS: Station 5, 3-D BL).	213
Figure 5.12. Semi-log contours of $(\overline{q^2}/2)U_w^2$ in the $y/k - z/d$ plane at $x/D = 0.5$ with diffusion velocities, $V_q/U_w$ and $W_q/U_w$ [ $k = 0.38mm$ (top row), $k = 0.76mm$ (middle), $k = 1.52mm$ (bottom)], (LHS: 2-D BL, RHS: Station 5, 3-D BL).	214
Figure 5.13. $(\overline{q^2}/2)U_w^2$ versus $y/\delta$ , TKE profiles.	215
Figure 5.14. Variation of transport-rate budget of TKE, $\overline{q^2}/2$ , normalized by $U_{\tau o}^4/\nu$ , with $yU_{\tau o}/\nu$ .	216
Figure 5.15 (a). Contours of TKE production rate normalized by $U_{\tau o}^4/\nu$ : in the $y - z$ plane along $x/D=0.5$ for the 2-D rough-wall, and in the $y - z'$ plane along $x'/D=0.5$ for the 3-D rough-wall. Dashed lines show the outline of the cylinder. $\alpha = 28^\circ$ .	216
Figure 5.15 (b). Contours of TKE production rate normalized by $U_{\tau o}^4/\nu$ : in the $x - y$ plane along $z=0$ for the 2-D rough-wall, and in the $x' - y$ plane along $z'=0$ for the 3-D rough-wall. $\alpha = 28^\circ$ .	217
Figure 5.16 (a). Contours of TKE $[(\overline{q^2}/2)/U_{\tau o}^2]$ with diffusion velocity vectors, $V_q/U_{\tau o} = [\overline{vq^2}/\overline{q^2}]/U_{\tau o}$ and $W_q/U_{\tau o} = [\overline{wq^2}/\overline{q^2}]/U_{\tau o}$ : in the $y - z$ plane along $x/D=0.5$ for the 2-D rough-wall, and in the $y - z'$ plane along $x'/D=0.5$ for the 3-D rough-wall. $\alpha = 28^\circ$ .	217
Figure 5.16 (b). Contours of TKE $[(\overline{q^2}/2)/U_{\tau o}^2]$ with diffusion velocity vectors, $U_q/U_{\tau o} = [\overline{uq^2}/\overline{q^2}]/U_{\tau o}$ and $V_q/U_{\tau o} = [\overline{vq^2}/\overline{q^2}]/U_{\tau o}$ : in the $x - y$ plane along $z=0$ for the 2-D rough-wall, and in the $x' - y$ plane along $z'=0$ for the 3-D rough-wall. $\alpha = 28^\circ$ .	217
Figure 5.17. Semi-log contours of $(\overline{q^2}/2)U_w^2$ in the $y/k - z''/d$ plane at $x''/D = 0.5$ with diffusion velocities, $V_q''/U_w$ and $W_q''/U_w$ [ $k = 0.38mm, \beta = 25^\circ$ (top row), $k = 0.76mm, \beta = 17^\circ$ (middle), $k = 1.52mm, \beta = 19^\circ$ (bottom)], (LHS: 2-D BL, RHS: Station 5, 3-D BL).	218
Figure 5.18. Semi-log contours of $-\overline{uv''}/U_w^2$ in the $y/k - z''/d$ plane at $x''/D = 0.5$ [ $k = 0.38mm, \beta = 25^\circ$ (top row), $k = 0.76mm, \beta = 17^\circ$ (middle), $k = 1.52mm, \beta = 19^\circ$ (bottom)], (LHS: 2-D BL, RHS: Station 5, 3-D BL).	219
Figure 5.19. Schematic of the flow in a 3-D rough-wall turbulent boundary layer (straight orientation).	220
Figure 7.1. A conceptualized view of an arbitrary rough-wall.	225
Figure B.1: Views of the element with the control volume enclosing one-half of the flow domain.	237



# Nomenclature

## Roman

2-D TBL	Two-Dimensional Turbulent Boundary Layers
3-D TBL	Three-Dimensional Turbulent Boundary Layers
3CLDV	Three component Laser Doppler Velocimeter
$A, A_f$	Projected frontal area of the roughness element
$A_1$	Structural parameter, $\frac{\sqrt{(-\overline{uv}) + (-\overline{vw})}}{u^2 + v^2 + w^2}$
$A_{inner}$	Projected wall area downstream of the single element: Inner wake region
$A_{outer}$	Projected wall area downstream of the single element: Outer regions where there is no wake influence
$A_w$	Windward wetted surface area of the roughness element
BL	Boundary Layers
$C$	Correlation coefficient between the data rate fluctuations and the fluctuations in the magnitudes of velocity Also, Convection, of TKE or Reynolds stresses Also, intercept in the log-law of the wall for smooth-wall TBL, has a value of 5.1
$C_1, C_2$	Coefficients for curve fit of skin friction velocity
$C_d$	Drag coefficient defined as $\Delta D / (1/2)\rho U_e^2 A$ , where, $\Delta D$ is the total drag due to the single element
$C_{d,form}$	Form drag coefficient
$C_{d,skin}$	Skin friction component of drag coefficient
$C_f$	Skin friction coefficient
$C_{f,outer}, C_{f,inner}$	Average skin friction coefficients in the outer region and inner regions (wake) within the control volume (Single elements)
$C_p$	Coefficient of pressure, $\frac{P - P_{ref}}{P_{oref} - P_{ref}}$
CV	Control volume used in the calculation of form drag due to single elements
CV1	Control volume used in the calculation of the skin friction component of drag due to single elements. The width (along spanwise direction) of CV1 is twice as much as that of CV with rest of the dimensions remaining unchanged.
$d$	Diameter of the cylinder, or the base diameter of the Gaussian spike
$d_{max}$	Maximum acceptable deviation in the measured data
$D$	Center to center spacing between the elements

$k$	Element height
$k^+$	Non-dimensional roughness height: $k^+ = \frac{kU_\tau}{\nu}$ (single elements) or $k^+ = \frac{k\sqrt{-\overline{uv}_{\max}}}{\nu}$ (2-D BL) or $k^+ = \frac{kU_w}{\nu}$ (3-D BL)
$k_s$	Equivalent sandgrain roughness
LDV	Laser Doppler Velocimeter, also Laser Doppler Velocimetry
PIV	Particle Image Velocimetry
$P$	Static pressure
$P_{ref}$	Static pressure at the reference station
$P_{oref}$	Stagnation pressure at the reference station
$PD$	Rate of pressure diffusion of TKE
$PR$	Production-rate of TKE
$S_f$	Frontal area of rough surface normal to the flow, also denoted as $A$ or $A_f$
$ref$	reference station which is 1.524m from the entrance to the test section
TKE	Turbulent kinetic energy, $\overline{q^2}/2$ , where $\overline{q^2}$ is the sum of normal Reynolds stresses and is equal to $(\overline{u^2} + \overline{v^2} + \overline{w^2})$
$u, v, w$	Velocity fluctuations in $x, y$ , and $z$ axes
$TD$	Turbulent diffusion of TKE or Reynolds stresses
$U, V, W$	Mean velocities in $x, y$ , and $z$ axes
$U_c$	Streamwise velocity at location of maximum stream wise vorticity
$U_\infty$	Free-stream velocity
$U_{ref}$	Velocity at reference station (about 27.5 m/s)
$\overline{u^2}, \overline{v^2}, \overline{w^2}$	Reynolds normal stresses
$-\overline{uv}, -\overline{uw}, -\overline{vw}$	Reynolds shear stresses
$\sqrt{-\overline{uv}_{\max}}$	Friction velocity, velocity scale for 2-D rough-wall BL
$-\overline{uv}_{\text{smooth}}$	Streamwise Reynolds shear stress at a given $y^+$ in the 2-D smooth wall TBL
$U_\tau = \sqrt{\frac{\tau_w}{\rho}}$	Wall-shear-stress velocity, friction velocity
$U_w$	Friction velocity or velocity scale for 3-D rough-wall TBL



$U^+$	Non-dimensional streamwise velocity, $U^+ = U/U_\tau$
$V^+$	Non-dimensional wall-normal velocity, $V^+ = V/U_\tau$
$\vec{V}$	Velocity vector
$V_q/U_\tau$	Non-dimensional diffusion velocity vector in wall-normal direction: where $V_q/U_\tau = (\sqrt{v}q^2/\sqrt{q^2})U_\tau$
$VD$	Viscous diffusion of TKE or Reynolds stresses
$W_q/U_\tau$	Non-dimensional diffusion velocity vector in spanwise direction: where $W_q/U_\tau = (\sqrt{w}q^2/\sqrt{q^2})U_\tau$
$W^+$	Non-dimensional spanwise velocity, $W^+ = W/U_\tau$
$x, y$ , and $z$ axes	Coordinate system for wind tunnel
$y^+$	Non-dimensional distance from the wall : $y^+ = \frac{yU_\tau}{\nu}$ (single elements) or $y^+ = \frac{y\sqrt{-uv_{\max}}}{\nu}$ (2-D BL) or $y^+ = \frac{yU_w}{\nu}$ (3-D BL)
$y_c^+, z_c^+$	Locations of maximum streamwise vorticity, normalized by $\nu/U_\tau$

### Greek

$\alpha$	Angle that the velocity vector makes with tunnel axis at three element heights in the 3-D rough-wall TBL
$\beta$	Angle, about the tunnel axis, through which the coordinate system needs to be rotated for quantities to display a “form of symmetry” in 3-D rough-wall TBL
$\delta$	Streamwise boundary layer thickness defined as the distance from the wall where the local velocity is 99.5% of $U_e$
$\delta^*$	Streamwise displacement thickness, $\delta^* = \int_0^\delta \left(1 - \frac{U}{U_e}\right) dy$
$\delta( )$	Uncertainty in a given quantity
$\Delta U^+$	Roughness function, $\Delta U^+ = \Delta U/U_\tau$ or $\Delta U/\sqrt{-uv_{\max}}$
$\theta$	Streamwise momentum thickness, $\theta = \int_0^\delta \frac{U}{U_e} \left(1 - \frac{U}{U_e}\right) dy$
$\varepsilon$	Displacement surface due to the rough-wall, = 0 for smooth wall Also, the dissipation rate of TKE
$\Gamma$	Circulation in $y - z$ plane: $\Gamma = \oint_C \vec{V} \cdot d\vec{s}$
$\lambda$	Roughness density, Ratio of: (projected frontal area normal to flow)/(total surface area), i.e., $\lambda = S_f/S$ , = $kd/D^2$ for the cylinders. Also, streamwise wavelength of the RTVS
$\lambda_c$	Roughness concentration, Ratio of: (projected roughness area)/(total surface area)

$N_\sigma$	Number of fringes in the probe volume
$\tilde{\Omega}$	Mean vorticity vector
$\Omega_x$	Streamwise vorticity
$\Omega_y$	Wall-normal vorticity
$\Omega_z$	Spanwise vorticity
$\sigma$	Standard deviation of the measured data
$\sigma_1$	LDV measurement probe volume

### **Superscript**

+	Denotes quantities normalized by $v/U_\tau$ (single elements), $v/\sqrt{-\overline{uv}_{\max}}$ (2-D rough-wall boundary layers), $v/U_{\tau o}$ (3-D rough-wall boundary layers)
'	Denotes quantities in the transformed coordinates, coordinates rotated by angle, $\alpha$ , which is the angle the velocity vector makes with tunnel axis at three element heights
“	Denotes quantities in a transformed coordinate system obtained by rotating through angle, $\beta$ , about the tunnel axis



# Chapter 1 Introduction

## Motivation and Background

Even with the existence of a wealth of knowledge as regards smooth wall boundary layers, there exists differing interpretations of the physical mechanisms behind its sustenance and generation – especially as to the relative importance of the inner regions and the outer regions of the layers (Kline *et al.*, 1967, Corino and Brodkey, 1969). It is more likely that an interactive process between these two regions governs the maintenance of the smooth wall boundary layers (Robinson, 1990). This controversy exists despite the fact the flow is dictated primarily by two length scales:  $\nu/U_\tau$  (where,  $\nu$  is the kinematic viscosity and  $U_\tau$  is the friction velocity) for the inner region and  $\delta$  (the boundary layer thickness) for the outer region. Now, add to it the rough nature of the wall and this makes the interaction even more complex, since the roughness elements also become sources of instability, shear and turbulence production. Further, the rough-wall introduces several length scales that characterize its surface which can be construed as a measure of even greater complexity that the roughness problem poses.

There are several practical engineering and meteorological motivations for research in rough-wall turbulent boundary layers (TBL). In the atmospheric boundary layer flow, the underlying surface is almost rough, leading micrometeorologists to study the flow above and within vegetation canopies (like rough walls in a fluid mechanical sense). Examples of some engineering situations are flow past airplanes, turbomachinery blades and flows through piping ducts, heat exchangers, etc. In most of these cases, surface roughness alters the flow resistance and heat transfer characteristics primarily by altering the near-wall velocity and temperature fields. Some examples of 3-D rough-wall turbulent layers are flows past ship hulls and submarines (especially on the ‘walk way’).

While there exists a body of literature on rough-wall boundary layers, most deal with 2-D roughness elements such as bars, grooves, rods and meshes that are easy to reproduce under laboratory conditions. However, in most flows in nature, the roughness elements constituting a surface are essentially 3-D, and their effects on flow structure are not well understood, especially the turbulence structure (Jimenez, 2004). Further, there are no studies where the effects of roughness heights, shapes and the wall geometry have been systematically and thoroughly documented. Hence a systematic study as regards the effect of 3-D roughness elements on turbulent boundary layers is of considerable interest to both engineers and scientists.

This is a study geared towards a better understanding of turbulent boundary layers (2-D as well as 3-D) that have developed over rough surfaces containing distributions of 3-D roughness elements. The present study makes measurements of mean and fluctuating quantities using the Laser Doppler Velocimetry (LDV) technique in these boundary layers. The few studies on 3-D roughness, available in the literature, do not probe the structure of the flow within the rough-wall and hence this study is unique in that aspect too. To the author’s best knowledge, this is the first time an attempt is made to measure near-wall regions of the rough-wall boundary layers using a three-velocity component LDV (3CLDV). The high turbulence intensities encountered near the roughness elements cause many standard measurement techniques (X-wire anemometry, in particular) to suffer from errors that have often proved difficult to diagnose and correct (Raupach *et al.*, 1991). The use of a three component orthogonal LDV system with a 30 micron measurement volume (hence a small spatial resolution) facilitates the capture of all the finer scales of turbulence that occur in the rough-wall turbulent boundary layers, especially the kind that occur close to the tops of the roughness elements.

Measurements in the 2-D rough-wall turbulent boundary layers are made in the regions of the flow that have been fully developed over long streamwise lengths roughened with elements of the same kind and distribution as that present in the measurement regions. The use of LDV also permits a non-intrusive way of making measurements. The 3-D rough-wall boundary layers is generated by a wing/body junction flow similar to the well documented smooth wall 3-D boundary layers around the



wing/body junction (Ölçmen and Simpson, 1995), the difference being that the body surface around the wing has a distribution of roughness elements. The distributions are the same as those tested in the 2-D rough-wall TBL. As previously mentioned, though considerable data are available as regards 2-D rough-wall boundary layers, those regarding 3-D boundary layers have been very few. To be specific, only one study (Krogstad and Fannelop, 1983) has come to the author's attention where mean flow measurements were carried out; however, no study towards the understanding of the turbulence structure was made. The 3-D boundary layer is naturally expected to be different from the 2-D case on account of significant mean and fluctuation flow skewing near the wall. Further, these experiments yield valuable cases with which to extract the flow physics behind the generation and maintenance of rough-wall TBL, both 2-D as well as 3-D.

One of the primary objectives of this study is to understand the structure of the rough-wall layers – in the regions close to the wall, around the elements and further away in the outer layers. It is imperative to understand how the flow structures created by the roughness elements in a distribution affect the rest of the boundary layer. It is important to know the mechanism behind the generation and diffusion of turbulent kinetic energy and shear that occur adjacent to the roughness elements. As regards the constitution of the rough-wall, cylindrical posts were chosen as representative roughness elements since they are simple in shape and 3-D in geometry and also because an issue of its orientation to the flow does not arise due to its axisymmetric shape. The need for avoidance of this issue eliminated the choice of rectangular or square prisms, etc. Since the roughness elements needed to be spread over a large area to constitute the rough-wall, the choice of cylindrical posts made the task of manufacturing easier than would be the case had the choice been objects like cones, conical frustums, hemispheres.

The present study is carried out in three parts: Part 1 deals with the cylinders when placed individually in the turbulent boundary layers, Part 2 considers the effects when the same individual elements are placed in a sparse and regular distribution and in Part 3 the distributions are subjected to a 3-D turbulent boundary layer. In the first part, the objective was to study the effect of an individual perturbation on the TBL. In the second part, the effects of a distribution of such discrete perturbations on the flow structure are measured and studied and in the final part, the same distributions are subjected to flow three-dimensionality and the effects analyzed.

In the first part, the individual elements used are three cylinders of heights,  $k = 0.38mm$ ,  $0.76mm$  and  $1.52mm$ , and a Gaussian shaped spike of height,  $k = 1.52mm$ , each with a base diameter of  $1.98mm$ . For the 2-D rough-wall boundary layers which constitute the second part, the fetch for the rough-wall is generated by using the three cylinders (same as the ones in part 1) in *square* and *diagonal* patterns to yield six different roughness geometries, thus six cases of 2-D rough-wall boundary layers, with each distribution using cylinders of same height. The choice of the element heights and distribution was motivated by the requirement that the roughness Reynolds number  $[k^+, \text{height of the elements } (k) \text{ normalized by the viscous length scale } (\nu/U_\tau)]$  of the flow regimes fall in the transitionally rough and fully rough regimes. In the transitionally rough flow regime, both viscous and form drag effects matter, while in the fully rough regime flow the form drag effects dominate and the viscous effects can be considered negligible. Also, the distributions of the roughness elements were such that they were discretely and sparsely placed so as to avoid the complexity of large effects of wake interactions that would be the case had they been closely packed elements. In the third part, the effect of mean flow three dimensionality on roughness is studied by subjecting the six cases of rough surfaces to a wing/body junction flow. This three-part study is pictorially depicted in Fig. 1.1. This introductory chapter is sub-divided into three main sections, with each section dealing with their respective studies performed thus far, along with key contributions made by them.

## 1.1 Part 1: Single Elements

This is the first part of the larger study dealing with the effect of sparse distributions of cylindrical roughness elements on two-dimensional and three-dimensional turbulent boundary layers.



In this part, isolated single elements, having heights ( $k$ ) less than 4% of the boundary layer thickness ( $\delta$ ), are submerged in a two-dimensional turbulent boundary layer and their effects on the mean and turbulence structure are measured, in considerable detail, and analyzed. Four isolated elements are used, three of them being cylinders of heights,  $k=0.38mm$ ,  $0.76mm$  and  $1.52mm$ , and the remaining one being a Gaussian shaped spike of  $k=1.52mm$ , each with a base diameter of  $1.98mm$ . The information garnered is important since the rough-wall used in this study is essentially a sparse and uniform distribution of these individual roughness elements. Thus, the rough-wall boundary layers perhaps can be construed as a cumulative response of these discrete disturbances. The present study is also unique in the sense that while one of the single elements studied here – the smallest cylinder, is submerged in the very viscous regions of the turbulent boundary layer, i.e., within the buffer layer, the other elements are within the log law region. The former element is expected to generate structures of the order of the quasi-streamwise vortices that occur very close to the wall in smooth-wall turbulent boundary layers – structures that are important to the generation and maintenance of turbulence (Kline *et al.*, 1967, Corino and Brodkey, 1969, and Robinson, 1990). The literature study has revealed a dearth of studies on the effects of small  $k/\delta$  elements on high Reynolds number boundary layers, a fact also attested to by Tomkins (2001), and this study would also satisfy such a requirement.

Most such flows available in the literature are laminar flows past single elements or 3-D protuberances. The object of these studies was to examine the effect of the disturbances caused by these elements on transition to turbulent flows and are reviewed in section 1.1.1. Turbulent approach flows are discussed in section 1.1.2. Flows with protuberances greater than or equal to 10 percent of the boundary layer thickness are discussed in section 1.1.3. Since protuberances or obstacles cause the formation of a system of vortices that interact with the boundary layer, studies pertaining to embedded vortices and their interaction with the boundary layer are reviewed in section 1.1.4. The reviewed literature is by no means exhaustive and only those with some relevance to the present study are discussed, with a view to include different aspects pertaining to the qualitative features of the flows and quantitative features such as the mean velocity, circulation, streamwise vorticity, drag coefficient, Reynolds stresses and the triple products.

### **1.1.1 Laminar flow past isolated protuberances leading to transition to turbulence**

The earlier experiments on isolated roughness or protuberances were conducted in laminar boundary layers to determine whether the disturbances caused by them would be sufficient to cause the flow to transition to turbulence. The accent of these efforts has been to define critical values of Reynolds number, based on the height of the roughness element and velocity in the laminar boundary layer at the height of the element, that would affect transition. An excellent treatise on this aspect is available in Tani (1961). For a low speed flow, it can be concluded that if the roughness height is small compared to the boundary layer thickness and the free-stream velocity is small enough, transition does not occur, but the disturbance persists for a few hundred roughness heights. Even though the present set of experiments were conducted in a turbulent boundary layer, the inclusion of this section was considered relevant for the sake of discussion. Both laminar and turbulent flows past protuberances display similar mean flow features in the wake and in the formation of a vortex system. This system, formed at the upstream junction of the element, gets wrapped around the element in a horseshoe fashion with trailing legs that convect downstream of it. It is important to note that the horseshoe vortex structure is formed only when the pressure gradient at the upstream junction of the protuberance or obstacle is sufficiently adverse to produce a 3-D flow separation. This causes the near-wall shear layers to roll up. More information on the formation and structure of these vortices is available in a recent review of juncture flows by Simpson (2001).

Sedney (1973) has reviewed several results on laminar flow past protuberances having shapes of cylinders, hemispheres and cones and has discussed mostly the qualitative features of the flow fields. Included in this review are the experiments conducted by Gregory and Walker (1955) who



observed the flow in the wake of isolated elements and gave a systematic account of transition due to these 3-D roughness elements. The tests were conducted in a wind tunnel with speeds up to  $37\text{ m/s}$  using the china-clay surface flow visualization technique, and in a smoke tunnel with speeds up to  $5\text{ m/s}$ . The isolated elements were (a) cylinders with height equal to diameter, which varied from  $0.18\text{ mm}$  to  $5.1\text{ mm}$ , (b)  $60^\circ$  cone with different heights similar to those of the cylinder, and (c) some short cylinders with the height less than the diameter. Note that the dimensions of the cylinders are close to those used in this current study. They were apparently the first to observe the horseshoe vortex structure formed at the nose of the cylindrical element at moderate Reynolds numbers, with trailing legs that persist downstream of the element as streamwise vortices, and also to observe the qualitative effect of the Reynolds number on the structure of this horseshoe vortex system. Their flow visualizations show a wake behind the element that spreads like a small angle wedge with an apex close to it. With the aid of the china-clay technique, they have also determined the critical heights at which the wakes exhibit turbulence. The conical elements also reveal similar turbulent wakes downstream of the element at moderate to high Reynolds numbers. The review article by Sedney (1973) also contains pictures of smoke visualization on flow past hemispherical roughness elements that reveal a similar horseshoe vortex pattern. Recent experiments by Ichimaya (1999) in the turbulent wedge region downstream of a single roughness element, a  $2\text{ mm}$  high cylinder with height equal to diameter, placed in a  $2.2\text{ mm}$  thick laminar boundary layer also show many streamwise vortices. Their measurements also show marked increases in the turbulence stresses downstream of the element when compared to the rest of the fully developed turbulent boundary layer.

Investigations on the evolution of a turbulent boundary layer by a hemisphere on a flat plate conducted by Klebanoff *et al.* (1992) also reveal the presence of streamwise vortices similar to those generated by the cylinders. They have postulated a two region model for this transitional boundary layer: an inner region generated by the complex interaction of hairpin like eddies, shed by the roughness element, with the near-surface horseshoe vortices and an outer region where these eddies deform and generate turbulent vortex rings. Barrett *et al.* (1993) have made measurements, at several cross sectional planes, in the wake of a  $0.8\text{ mm}$  sphere mounted on a flat plate in a  $1.4\text{ mm}$  thick laminar boundary layer and have shown the development of the streamwise vorticity at successive downstream locations. The plots reveal a sharp decline in the levels of the vorticity immediately behind the sphere followed by a gradual decline at further downstream locations. Several vortical structures are seen in the wake of the sphere which spreads like a turbulent wedge behind it.

### 1.1.2 Turbulent flow past isolated protuberances

The existing literature is surfeit with studies on flow behind protuberances in laminar boundary layers dealing mainly with transition, with few studies as regards turbulent boundary layers. The primary aim of these studies was to determine the drag of these protuberances since they exist in practical flows as aircraft excrescences. The earliest studies on three-dimensional protruding cylinders in turbulent boundary layers were conducted by Wiegardt (1946) primarily to measure the drag due to these elements. Different cylinders, of varying height-to-diameter ratios, were tested in a  $67\text{ mm}$  thick turbulent boundary layer at a Reynolds number of  $7.2 \times 10^6$ , based on the distance. These results are available in Young and Paterson (1981) as plots of drag coefficients, normalized by undisturbed flow skin friction coefficient, versus the roughness Reynolds number, based on the undisturbed flow friction velocity and the element height. Functional representation of the curve fits for the plotted data is given in Gaudet (1987) who also presents the results of Wiegardt (1946) and results of additional experiments (Gaudet and Winter, 1973) which were performed to investigate the role of Reynolds number on the drag of similar elements.

Little literature is available on the details on the turbulence structure behind protuberances that are submerged in fully developed turbulent boundary layers. Fontaine and Deutsch (1996) have investigated the near-wall region downstream of a “Gaussian” shaped spike mounted in a pipe, of height and diameter of 16.4 and 13 wall units respectively, that generated a pair of counter rotating



vortices of approximately 15 wall units in diameter. They concluded that the converging downstream flow behind the element leads to a decoupling of the inner region and the outer region where the low speed fluid is unable to cross into the buffer region and likewise the outer region high speed fluid is unable to penetrate the inner region. This caused the sweeps and ejections, the events that generate turbulence, to be retarded in the near-wall region leading to a lower near-wall  $-\overline{uv}$  Reynolds stress and local wall shear. This implied that the production of turbulence can be influenced by locally manipulating these events. However, in the present experiments, a reduction in wall shear is seen only in the lowest cylindrical element; and that too only in the far downstream locations.

Recently, a set of experiments in a similar Reynolds number flow facility were carried out by Bennington (2004). His study complements the present one with experiments on protuberances such as cones (both smooth and concentrically ridged), pyramids, cubes (different orientations) and Gaussian shaped bumps that were submerged in turbulent boundary layers. These elements were larger and higher than those considered in the present study, albeit still less than 7% of the boundary layer thickness. Similar findings of larger Reynolds stresses, turbulent kinetic energy (TKE) and wall shear were found downstream of the elements which were attributed mainly to the presence of the horseshoe vortex that formed at their upstream junctions. However, the smaller elements considered in the present study have many differences as regards the structure, one of them being that the downstream effects are attributed primarily to the vortex system emanating from the top of the elements rather than that formed at the junction. Considering the present study, also of significance was the aforementioned presence of lower wall shear in the far downstream locations behind the smallest cylindrical element. Bennington (2004) has also developed a model equation to correlate the drag of the different protuberances.

### 1.1.3 Turbulent flow past surface-mounted obstacles

Under this classification are studies pertaining to obstacles that display significant bluff-body aerodynamics – those associated with strongly separated shear layers that emanate from the sharp edges. These flow features can be more clearly seen and quantified than those past mere protuberances. Moreover, these obstacles have heights comparable to the boundary layer thickness. Flows past 3-D obstacles are more complex than those past 2-D obstacles due to the horseshoe vortex structure that forms upstream of it and the sets of streamwise vortices that trail downstream, structures that radically change the flow field. These vortices alter the downstream flow by influencing both the immediate separated flow region and the further downstream recovery region. A couple of notable differences between flows past 2-D and 3-D obstacles are that – (a) there are no closed separation bubbles behind a 3-D obstacle (Hunt *et al.*, 1977) as is seen behind a 2-D one, and (b) flow reattaches earlier behind a 3-D obstacle when compared with a similar 2-D obstacle of the same relative height (Martinuzzi and Tropea, 1993), since a large proportion of the flow goes around the 3-D object than over it. Flow past protuberances (previous category) exhibits most features of flows included in this section albeit to a smaller scale since they do not perturb the flow as much.

There have been a few studies on flow past bluff bodies with reference to wind engineering applications geared towards the estimation of wind load on man-made structures. The focus of these studies was to measure the form drag and pressure distributions due to these obstacles (Arie *et al.*, 1975a and 1975b, Taniguchi *et al.*, 1981, Sakamoto *et al.*, 1982, Sakamoto, 1985). Their efforts have yielded a large amount of experimental data on flow past obstacles such as rectangular cylinders, cubes and circular cylinders. Their data include the effects of various parameters on the form drag, parameters such as the ratio of height of the obstacle to the boundary layer thickness, ratio of friction velocity of the undisturbed flow to the free-stream velocity and aspect ratio (ratio of width to height of the obstacle). The form drag is usually calculated from the surface pressure distribution measured on the obstacles. Most of the tested obstacles are contained within the turbulent boundary layer and have heights close to the boundary layer thickness.



The results of these and other prior studies demonstrate that flow is mainly influenced by the dimensions of the obstacle, the approach flow boundary layer thickness and the wall shear. The mean features of the flow around obstacles such as three-dimensional prisms have been the subject of several studies (Hunt *et al.*, 1977, Castro and Robins, 1977, Schofield and Logan, 1990, Martinuzzi and Tropea, 1993, and Chou and Chao, 2000, to name a few). As mentioned earlier, there are no closed separation bubbles around the 3-D obstacle and the separated regions have fluid passing through them and are origins of vortices that are shed into the flow. Based on flow visualizations and from surface pressure measurements from previous studies, Schofield and Logan (1990) have presented a schematic of the vortices in the upstream and downstream vicinities of the prismatic obstacle and the induced flow due to these vortices. The number and locations of these vortices is strongly dependent on the flow Reynolds number and the aspect ratio of the obstacle. The horseshoe vortex structure branches itself into smaller regular vortices when the aspect ratio is increased (Chou and Chao, 2000). Please note that the aspect ratios of all the circular cylinders tested in the present study are less than one and hence only one horseshoe vortex structure is formed at the upstream junction.

Martinuzzi and Tropea (1993) have also made surface pressure measurements and flow visualizations around surface-mounted rectangular obstacles in a turbulent channel flow. They have documented the influence of aspect ratio on major features of the flow – the upstream separation location, the reattachment length, the location of the vortices (the upstream horseshoe vortex and the downstream vortices) and the surface pressure distributions both upstream and downstream of the obstacle. Also, for rectangular obstacles, vortex pairs occur at the free corners, i.e., at the roof. Continuing on the effects of aspect ratio, an earlier study by Logan and Lin (1982) contains centerline wall shear recovery for 3-D prisms of different aspect ratios. When compared with the results of the 2-D obstacle of the same relative height, they showed a quicker recovery in the 3-D case which was attributed to the additional mixing due to the streamwise vortices. They also show that a decrease in the aspect ratio leads to an increase in the rate of decay of maximum deficit in the mean velocity.

As regards the turbulence structure of the flow field downstream of an obstacle, Castro and Robins (1977) have made measurements of turbulent intensities and mean velocities in the wake of a surface-mounted cube in turbulent boundary layers, along with the body surface mean pressures. Two different orientations of the cube to the flow direction were tested: the vortices from the cube when orientated at 45° to the flow were stronger than those when the cube is set square on to the flow. This vorticity primarily affects the streamwise mean velocity and decays rapidly so much so that, at six cube heights downstream, all three velocity components are similar to those for the cube set normal to the flow. Further, for both orientations, the velocity deficits in the wake are present only up to about eight heights in the streamwise direction. Hussein and Martinuzzi (1996) have made LDV measurements in the flow field of a surface-mounted cube in a turbulent channel and have calculated the different terms in the transport equation for the turbulent kinetic energy along the cube centerline, excluding the pressure velocity correlation terms (which was modeled) and the dissipation term which was determined as the closing term needed to balance the equation. These results give a better interpretation of the turbulence structure of the different flow regimes, beginning with the upstream separation zone to the downstream recirculating region behind the obstacle and finally to the far-wake region, by providing, quantitatively, the contributions of the production, diffusion and the dissipation of turbulence. They also determined the appropriate length and velocity scales for these different regions. Results also revealed that the area of maximum production and the largest turbulent stresses coincided with the regions of maximum vorticity present along the shear layer enveloping recirculation region.

#### **1.1.4 Embedded vortex flows**

The vortex system formed at the upstream of an obstacle leading to counter-rotating streamwise vortices is one of the most common cases of embedded vortex flows and the study of this class of flows is relevant to the present study. The role of arrays of embedded vortices in preventing



boundary layer separation and the effects of the interaction of the streamwise vortices from a junction (e.g., wing/body, blade/hub, etc.) with the main boundary layers are a couple of examples cited as motivation behind these studies.

Many studies available in the literature concerning longitudinal embedded vortices in turbulent boundary layers have used the half delta wing or vanes as vortex generators and in most cases these wall-mounted generators have heights beyond the boundary layer thickness. Hence, the vortices generated in these cases are much stronger than the vortices generated by the protruding cylinders in the present study which have heights of a few percent of the boundary layer thickness. Based on a non-dimensional vortex circulation parameter defined as  $\Gamma/(U_e \delta)$ , where  $\Gamma$  is the vortex circulation,  $U_e$  is the free-stream velocity and  $\delta$  is the boundary layer thickness, Cutler and Bradshaw (1986) have loosely classified vortices as *weak* when the parameter was in the range 0.08-0.2 and *strong* when the parameter was 7 or greater. By this token, the value for this parameter, considering only one of the pair of vortex legs, was never more than 0.006 even for the largest cylinder in the present study and hence the vortices in the present cases are considered as *very weak* vortices. Additionally, vortex pairs have also been classified as “common flow down” when the common flow between them is directed towards the wall and “common flow up” when it is directed away from the wall (Mehta *et al.*, 1983).

There have been several investigations into the interaction of relatively *weak* vortices, generated by half-delta wings on a flat plate, with turbulent boundary layers (Shabaka *et al.*, 1985, Westphal *et al.*, 1985, 1987, and Pauley and Eaton, 1988). Measurements of Shabaka *et al.* (1985) show that circulation around the embedded vortex is nearly conserved, with a slight streamwise decay due to the spanwise component of the wall shear which opposes the rotation of the vortex. Westphal *et al.* (1985, 1987) examined the effects of an interaction between a single streamwise vortex and a turbulent boundary layer in both zero and adverse pressure gradients, the vortex generator being a half delta wing of height greater than the boundary layer thickness. From the examination of streamwise vorticity contours at successive streamwise locations, they observed significant vortex core growth as compared to that for a similar free vortex, which was accentuated by the presence of adverse pressure gradient along with a stronger distortion of the core shape. Their work also shows that circulation and the point of maximum vorticity in the vortex can be used to quantitatively describe the strength and location of the vortex structure. One of the major effects of vortex interaction with the boundary layer is the thinning of the boundary layer region between the vortices (downwash region) and thickening of the boundary layer where secondary flow is away from the wall (upwash region). See Westphal *et al.* 1985, 1987 and Pauley and Eaton, 1988. The magnitude of this boundary layer distortion is strongly dependent on the vortex strength which is also evident from the large eddy simulation of the experiments (Pauley and Eaton, 1988) by Esmaili and Piomelli (1992). The results of Pauley and Eaton (1988) also show that the decay of vortex circulation is governed by the proximity of the vortex to the wall. The decay of the vortices themselves is governed by the manner and rate in which the boundary layer fluid is entrained as well as by the near-wall viscous effects. In general, the different studies show that vortices first move towards the wall as a result of the self-induced velocity and then apart from each other due to the presence of the “image” vortex pair beneath the wall surface.

On the basis of the earlier classification, studies by Cutler and Bradshaw (1986, 1993a and b) and Pauley and Eaton (1989) would be termed as those on *strong* vortex/boundary layer interactions since the non-dimensional vortex circulation parameter  $[\Gamma/(U_e \delta)]$  is of the order 10 or greater. The flow behavior in all aspects is very similar to those seen in the *weak* vortex/boundary layer interactions’ case except that the region of influence of the vortices is much larger. Also, high levels of turbulent kinetic energy and Reynolds shear stresses are seen in the vicinity of the vortex core. Further, the vortices convect highly turbulent, low momentum boundary layer fluid away from the wall thus exhibiting high turbulence levels in the upwash region.

While the above-referenced studies have vortex generators that have profiles projecting out of the boundary layers, there have been a few studies that have used low-profile vortex generators (VG) which are submerged within the boundary layers (Ashill *et al.*, 2002 and Yao *et al.*, 2002). These low



profile vortex generators improve the ability of the boundary layer to resist flow separation with relatively low drag penalty since they are immersed in flows of low dynamic pressure. Yao *et al.* (2002) have measured and compared the streamwise evolution of a low-profile VG with a conventional VG. The low-profile VG shows a higher rate of vorticity decay when compared to the conventional VG.

## 1.2 Part 2: Two-Dimensional Rough-Wall Turbulent Boundary Layers

This part focuses on the effect of the roughness elements on 2-D turbulent boundary layers and is the second part of the three-pronged approach towards understanding roughness effects. While the previous part focused on the condition when the roughness element was placed individually, the present one considers when they are uniformly and sparsely distributed. This study should help lead to a better understanding of fully developed rough-wall turbulent boundary layers. In the past, much attention has been focused on smooth wall boundary layers leading to a satisfactory knowledge pertaining to its turbulence structure. Many studies have led to characterizing roughness elements as "equivalent sand-grain roughness" along the lines of Nikuradse (1933). The effects of 2-D roughness elements such as ribs and grooves on turbulent boundary layers have also been well researched (e.g., Perry *et al.*, 1969, Perry *et al.*, 1987, Bandyopadhyay, 1988, Krogstad and Antonia, 1992). However, in nature, viz., flow past submarines (especially on the 'walk way') and ship hulls, the roughness elements are essentially 3-D, and hence a systematic study as regards the effect of 3-D roughness elements on turbulent boundary layers would be of considerable interest (as a study in basic turbulence research too). In addition to these considerations, there are several practical engineering and meteorological situations where turbulent boundary layers develop over rough surfaces. In the atmosphere boundary layer flow, the underlying surface is almost rough, leading micrometeorologists to study the flow above and within vegetation canopies (like rough walls in a fluid mechanical sense). In engineering applications, roughness affects the transport of heat and mass by changing the surface resistance. In a basic sense, it thoroughly alters the velocity and turbulence fields adjacent to the surface and in applications involving heat transfer, the temperature field is altered as well.

Raupach *et al.* (1991) have summarized the known behavior of such flows for three-dimensional "sandgrain" or protuberance-type of surface elements and for spanwise rib types of surface elements. Many of the studies have used the spanwise type of roughness element because these elements are relatively easy to reproduce and modify for parametric studies of the effects of the rib roughness on the flow. However, surface roughness on practical surfaces is thought to be usually of the sandgrain type of three-dimensional elements and is more difficult to reproduce reliably because of the complex roughness geometry. Correlations of data from various experiments show relatively large scatter because of the complex geometry. This has led to the common opinion among turbulent boundary layer workers that one cannot know *a priori* how a rough surface affects a flow without making measurements for that particular flow. However, for low roughness densities  $\lambda < 0.1$  [ $\lambda = (\text{projected frontal area to flow})/(\text{projected surface area})$ ], the ability to describe the important surface features is not so bleak with discrete roughness elements such as "deck" roughness. This type of geometry is simpler than for sandgrain roughness and the roughness geometries, sizes, and distributions can be used to calculate the effect of individual isolated elements on the flow. Raupach *et al.* (1991) point out that for this type of roughness, the additive constant of the semi-logarithmic "law-of-the-wall" velocity profile varies exponentially with  $\lambda$ , both from experimental data and theoretical arguments. This leads the author to believe that future research results on the 3-D flow over "deck type" roughness can also be reliably used in calculating the effect of "deck type" roughness in practical cases.

In the literature, there are few studies that deal with flow physics in the very near wall regions of rough-wall turbulent boundary layers. The high turbulence intensities encountered near the roughness elements cause many standard measurement techniques (X-wire anemometry in particular)



to suffer from errors that have often proved difficult to diagnose and correct. The present study uses precise low uncertainty near-wall measurements of mean and fluctuating quantities to characterize the roughness effects. To the author's best knowledge, this is the first time measurements of rough-wall boundary layers have been made using a 3-orthogonal velocity component LDV, including near-wall flow regions around the cylinders. Further, these experiments yield valuable test cases with which to compare and adjust turbulence models for rough-wall flows. The main objective is to understand the structure of the rough-wall layers, regions close to the wall, around the elements and further away in the outer layers. It is imperative to understand how the structures created by the roughness elements in a distribution affect the rest of the boundary layer. It is important to know the mechanism behind the generation and diffusion of energy and shear stresses that occur adjacent to the roughness elements.

In this part of the study, a rough-wall fetch is created from a sparse distribution of the very same cylinders that were used in the study on single elements. Each distribution (pattern) uses the cylinders of the same height. To generate the fetch, cylindrical roughness elements of  $0.38\text{ mm}$ ,  $0.76\text{ mm}$  and  $1.52\text{ mm}$  height ( $k$ ) were used in *square* and *diagonal* patterns to yield six different roughness geometries, thus six cases of 2-D rough-wall boundary layers. Circular cylinders were chosen as roughness elements to avoid the issue of the individual element 'flow orientation' which would be the case if elements such as prisms, pyramids etc are selected.

Measurements of mean velocities, turbulence stresses and triple products, using LDV, were made around the cylinders very close to the wall to within a few tens of microns and extending to regions beyond the boundary layer edge, thus encompassing the entire boundary layer and some potential flow regions. In each case, profiles were made at 40-50 locations around the cylinders. This enabled the author to analyze in detail the transfer of momentum and turbulence from the wall to the adjacent regions. While the rough-wall with  $k = 0.38\text{ mm}$  and  $0.76\text{ mm}$  elements (both square and diagonal patterns) yield rough-wall boundary layers in the transitionally rough regime, the other two cases of  $1.52\text{ mm}$  height cylinders fall in the fully rough regime. In the transitionally rough wall boundary layers, both bluff-body-form drag and viscosity affect the near-wall flows, while in the fully rough BL, the form drag effects dominate and the viscosity effects are negligible.

The accent of this part of literature review is on studies that deal with the effects of 3-D roughness elements such as cylinders, cones, cubes, pebbles, hemispheres and spheres in sparse distributions. Section 1.2.1 deals with the mean flow structure while section 1.2.2 deals with the turbulent structure and section 1.2.3 presents the different schemes available in the literature to calculate the wall shear.

## 1.2.1 Mean flow structure

It is known that the mean velocity distribution  $U$  in both smooth-wall and rough-wall boundary layers are derivable by a classical asymptotic matching process (e.g., see Wooding *et al.*, 1973). Let  $\delta$  be the boundary layer thickness and  $U_\tau$  the friction velocity  $[= \sqrt{(\tau_w/\rho)}]$ , where  $\tau_w$  is the wall shear stress and  $\rho$  the fluid density]. The asymptotic matching analysis postulates that the boundary layer consists of two overlapping regions: an outer layer scaling with  $U_\tau$  and  $\delta$ , and an inner scaling with  $U_\tau$  and a set  $S_L$  of length scales characterizing the surface. For a smooth surface,  $S_L$  consists only of the viscous length scale,  $\nu/U_\tau$ , whereas, for a rough surface,  $S_L$  consists of  $\nu/U_\tau$  together with the roughness height  $k$  and all additional lengths  $L_i$  needed to completely characterize the roughness. Typically,  $L_i$  includes the roughness element dimensions along the  $x$  and  $y$  directions, and the mean element separation distance,  $D$  (defined by  $D = (A/n)^{1/2}$ ) where  $n$  is the number of elements in a horizontal area  $A$ . For bringing simplicity into the present analysis, the additional length scales are represented by a single parameter,  $\lambda$ . Simpson (1973) defined  $\lambda$  as the ratio of total projected surface area ( $S$ ) parallel to the flow to the projected frontal area normal to the



flow ( $S_f$ ). However, in our discussion  $\lambda$  will be defined as the ratio of frontal area normal to the flow to the total surface area, i.e.,  $\lambda = S_f/S$ , reciprocal to Simpson's definition.

Thus, in the outer layer, the velocity profile is given by the velocity-defect law, which is

$$\frac{U_e - U}{U_\tau} = G\left(\frac{y}{\delta}\right) \quad (1.1)$$

where,  $U_e$  is the free-stream velocity. In the inner layer, the law of the wall is given by

$$\frac{U}{U_\tau} = F\left(\frac{yU_\tau}{\nu}, \frac{kU_\tau}{\nu}, \lambda, \frac{k}{\delta}\right) \quad (1.2)$$

For the present study,  $k/\delta$  is very small and hence it is not considered. In the overlap region between the two layers, equations (1) and (2) must be valid simultaneously leading to the logarithmic law of the wall. In this region of constant shear stress, it is accepted that away from the wall the flow pattern is independent of roughness and viscosity. The rough surface law of the wall (see Betterman, 1965 and Dvorak, 1969) becomes

$$\frac{U}{U_\tau} = \frac{1}{\kappa} \ln \left| \frac{yU_\tau}{\nu} \right| + C - \frac{\Delta U}{U_\tau} (k^+, \lambda) \quad (1.3)$$

where,  $\kappa$  and  $C$  are the smooth wall constants and are equal to 0.40 and 5.1 respectively. A “+” superscript denotes lengths normalized by  $\nu/U_\tau$ , and  $\Delta U/U_\tau$  is the roughness function. Following Nikuradse (1933), it is well accepted that  $\Delta U/U_\tau = 0$  for  $kU_\tau/\nu \leq 5$  (aerodynamically smooth surface). For transition or intermediate roughness ( $5 \leq kU_\tau/\nu \leq 70$ ), Dvorak (1969) has presented a family of curves for  $\Delta U/U_\tau$  as a function of  $kU_\tau/\nu$  and  $\lambda$ . The values for  $k^+$  demarcating the transitional flow regime and fully rough regime are a function of  $\lambda$  (Dvorak, 1969). Different researchers give different values – Nikuradse's data give a value of 70 while Hama's data (1954) give 30. For the completely rough regime ( $k^+ \geq 70$ ), the right hand side of equation (1.3) is independent of viscosity, i.e., the tangential stress exerted on the wall is entirely due to form drag produced by the pressure distribution on the roughness elements. For the completely rough regime, this equation can be further written in terms of relative roughness ( $y/k$ )

$$\frac{U}{U_\tau} = \frac{1}{\kappa} \ln \left| \frac{y}{k} \right| + C - \left( \frac{\Delta U}{U_\tau} - \frac{1}{\kappa} \ln \left| \frac{kU_\tau}{\nu} \right| \right) \quad (1.4)$$

where,

$$\frac{\Delta U}{U_\tau} - \frac{1}{\kappa} \ln \left| \frac{kU_\tau}{\nu} \right| = f(\lambda)$$

For a fully rough-wall BL, Schlichting (1936), also recast equation (1.3) in terms of the equivalent sand grain roughness ( $k_s$ ) along the lines of Nikuradse which is given by

$$\frac{U}{U_\tau} = \frac{1}{\kappa} \ln \frac{y}{k_s} + B$$

where,  $B = 8.5$  for a completely rough-wall.

### 1.2.1.1 Roughness density correlations

Dvorak (1969) also presents data correlations for  $f(\lambda)$  for several roughness geometries: 2-D elements (square or round rods), sand, screens, and staggered rows of spheres. For  $0.214 \leq \lambda \leq 1$ , Betterman and Dvorak presented the correlation

$$f(\lambda) = 17.35 [1.625 \log(1/\lambda) - 1] \quad (1.5)$$

while for  $\lambda < 0.214$ , Dvorak proposed



$$f(\lambda) = -5.95 [1.103 \log(1/\lambda) - 1] \quad (1.6)$$

Note that in the correlations proposed in Betterman and Dvorak,  $1/\lambda$  was taken as the ratio of the total surface area to the roughness area as compared to Simpson's use of the frontal area normal to the flow instead of the roughness area in his definition of  $1/\lambda$ . Their use of this parameter can be better interpreted as a measure of the roughness concentration. When the correlation results of  $f(\lambda)$  [equations (1.5) and (1.6)] are applied, Simpson's interpretation of the parameter yields a better agreement when compared to Betterman and Dvorak's as regards the data for roughness elements such as spherical segments, cones, and short angles.

Sigal and Danberg (1990) decided to modify these correlations to include a shape factor to account the shape of the individual elements. They proposed a roughness density factor,  $\Lambda_s$ , as a modification to  $1/\lambda$  and is given by  $\Lambda_s = (S/S_f)(A_f/A_w)^{1.6}$ . This expression can be rewritten as  $\Lambda_s = (1/\lambda)(A_f/A_w)^{1.6}$ , where  $A_f$  is the frontal area of a single element and  $A_w$  is the windward wetted surface area of the roughness element. In their approach,  $f(\lambda)$  is replaced as  $f(\Lambda_s)$  and rewritten as

$$\frac{\Delta U}{U_\tau} - \frac{1}{\kappa} \ln \left| \frac{kU_\tau}{v} \right| = f(\Lambda_s) \quad (1.7)$$

and the modified correlation becomes

$$f(\Lambda_s) = \begin{cases} 17.35 [1.634 \log \Lambda_s - 1] & 1.4 \leq \Lambda_s \leq 4.89 \\ 2.2 & 4.89 \leq \Lambda_s \leq 13.25 \\ 9.55 [1 - 0.686 \log \Lambda_s] & 13.25 \leq \Lambda_s \leq 100 \end{cases} \quad (1.8)$$

As shown by Raupach *et al.* (1991), equation (1.4) can be further re-written in terms of a roughness length  $y_o$

$$\frac{U}{U_\tau} = \frac{1}{\kappa} \ln \frac{y}{y_o}, \text{ where, } \ln \frac{y_o}{k} = -\kappa \left( C - \frac{\Delta U}{U_\tau} \right) - \ln \left( \frac{kU_\tau}{v} \right) \quad (1.9)$$

According to an extensive study on the effect of roughness density  $\lambda$  on  $y_o/k$  carried out by Koloseus and Davidian (1966), the data for 3-D roughness elements show that  $y_o/k$  increases with increasing  $\lambda$  to a maximum value, say  $\lambda_{\max}$ . For the distribution of circular cylinders,  $\lambda_{\max}$  is about 0.2. For the present study, the values of  $\lambda$  are restricted to 0.1.

As regards the rough-wall turbulent boundary layers, a composite profile that includes the log-law region and the outer region is given by

$$\frac{U}{U_\tau} = \frac{1}{\kappa} \ln \left| \frac{yU_\tau}{v} \right| + C - \frac{\Delta U}{U_\tau} (k^+, \lambda) + \frac{\Pi}{\kappa} w \left( \frac{y}{\delta} \right) \quad (1.10)$$

where, the wake function,  $w(y/\delta)$ , represents the outer layer dynamics and  $\Pi$  is denoted the wake parameter, and for a smooth wall, this parameter has a suggested value of 0.55 (Coles, 1956).

Most of the literature dealing with the mean flow aspect of rough-wall BL have focused on the effect of roughness on the roughness function,  $\Delta U/U_\tau$ . Some of the earliest experiments were conducted by Schlichting (1936) who determined the equivalent sandgrain roughness for a large number of roughness elements such as spheres, spherical segments, cones and short angles that were distributed in a regular pattern. A later investigation by Perry *et al.* (1969) has classified roughness into two classes called "k" type and "d" type based on the scaling of the roughness function,  $\Delta U^+$ . In "k" type roughness,  $\Delta U^+$  is a function of  $k$ , and hence is given by  $\Delta U^+ = (1/\kappa) \ln(k^+) + \text{constant}$ , while in "d" type, the roughness function scales on the pipe diameter ( $d$ ) or the boundary layer



thickness ( $\delta$ ) and is given by  $\Delta U^+ = (1/\kappa) \ln(d^+) + \text{constant}$ , as the case maybe. The usual bar roughness or the groove roughness is considered “ $d$ ” type when the cavities are narrowly spaced and “ $k$ ” type when widely spaced. The sandgrain type of roughness and most 3-D roughness come under the category of “ $k$ ” type and so does the present study.

Table 1.1 presents a summary of previous two-dimensional mean turbulent flow experiments on sparse distributed roughness with cylinders, cones, cubes, pebbles, hemispheres and spheres. They primarily deal with the effects of roughness height on the roughness function.

## 1.2.2 Turbulence structure

Roughness elements cause the generation of near-wall structures that produce turbulence which is diffused throughout the boundary layers. Most of the literature that deal with the turbulence structure consider 2-D roughness elements such as bars and grooves and few are available that consider 3-D roughness elements.

Grass (1971) conducted experiments in a water channel with Reynolds number, based on the depth, ranging from 6620 to 6740 in three different flow regimes: smooth, transitionally rough and fully rough. For the transitionally rough case ( $k^+ = 21$ ), 2mm pebbles were used as roughness elements and for the full rough case ( $k^+ = 85$ ), 9mm pebbles were used. The hydrogen bubble technique was employed for flow visualization and quantitative velocity measurements. He demonstrated the existence of both violent ejection and inrush events over the rough wall and concluded that these were common features of boundary layer turbulence irrespective of wall roughness condition. There were differences, he noted, in that in the smooth-wall flows, the ejection sequence draws on the viscous sublayer fluid leading to streak formation while for the rough flows, the source of the ejection is the low speed fluid trapped between the interstices. Grass also noted that the ejection process was “violent” with almost vertical motions outwards into the BL and giving rise to very large contributions to the Reynolds stresses.

Antonia and Luxton (1971) conducted experiments in a boundary layer formed downstream of a sudden change from a smooth to a rough surface that was roughened with “ $k$ ” type grooves with crests aligned with the smooth surface. They found large near-wall fluctuation levels due to enhanced production of energy. They also found that the growth rate of the shear layer was governed by the diffusion of turbulent energy away from the wall and that the mixing length was reduced relative to the smooth wall

Andreopoulos and Bradshaw (1981) measured mean velocities, double and triple products on a sand paper roughened boundary layer yielding a roughness Reynolds number,  $k^+$ , of 310 thus indicating a fully rough flow regime. The behavior of the triple products indicated that turbulent energy and shear stress were transported from the inner layers to the immediate vicinity of the roughness elements and that sweeps were more frequent than ejection motions. They regarded the roughness region as a turbulent energy sink.

To investigate the relative importance of sweeps and ejections to the Reynolds shear stress production, Raupach (1981) performed a quadrant analysis in boundary layers roughened with different arrays of cylinders of 6mm height and diameter. The roughness density parameter ( $\lambda$ ) ranged from 0.011 to 0.189. He found that sweeps were the dominant contributor to the Reynolds shear stress close to the surface and that their relative magnitudes, compared to ejections, increases with surface roughness and also with the proximity to the surface. He also found that profiles of the triple products, normalized with friction velocity, were the same away from the wall.

Ligrani and Moffat (1986) conducted several experiments mainly in the transitionally rough regime on rough-wall boundary layers, with  $Re_\theta$  ranging from 3310 to 18700. The surface was roughened using uniform spheres and had a equivalent sandgrain roughness ( $k_s$ ) of 0.79mm. The different Reynolds numbers were obtained by varying the free-stream velocity. The roughness



Reynolds number ( $k^+$ ) ranged from 21 to 63. In the transitionally rough regime, distributions of streamwise normal stresses, normalized with friction velocity, vary significantly with  $k^+$  in the inner regions of BL while for the fully rough boundary layers they do not. Further, for the fully rough cases, the same normalized stresses are invariant with  $k^+$  in outer regions of the BL. For a rough-wall of  $k^+ = 21$ , the production to the TKE peaks at  $y^+ = 20$  indicating that it occurs very close to the element height.

Bandyopadhyay and Watson (1988) made measurements on surfaces laid with grooves to investigate the effects of spanwise aspect ratio,  $\lambda_z$  (span/height), on the flow structure. The different aspect ratios reflect different flow regimes: when  $\lambda_z \gg 1$ , the flow is considered over grooves; when  $\lambda_z \ll 1$ , it is considered a plant canopy flow; and when the aspect ratio is in-between, i.e.,  $\lambda_z = O(1)$ , then the roughness is considered sandgrain roughness. The measurements of triple products reveal that the signs of the vertical and streamwise flux of shear stress change depending on whether the roughness element is 2-D or 3-D. The two cases behave in an opposite manner although the 2-D case behaves similar to the smooth wall case. In the 2-D case, shear stress is transported outward and is associated with streamwise deceleration while in the 3-D case the shear stress is transported wallward and is associated with a streamwise acceleration. Behavior similar to the 3-D case was also seen in the cases of sandgrain (Andreopoulos and Bradshaw, 1981) and gravel (Mulhearn and Finnigan, 1978). Bandyopadhyay and Watson (1988) also found the Townsend structural parameter ( $A_1 = -\overline{uv}/q^2$ ) to be a constant between  $y/\delta$  of 0.1 and 0.8 thereby implying that the turbulence structure is independent of wall condition.

Measurements on a mesh screen rough-wall in a  $Re_\theta = 12800$  turbulent boundary layer were carried out by Krogstad *et al.* (1992). The rough-wall yielded a  $k^+$  of 104 thereby indicating that flow was in the fully rough regime. Streamwise stresses, normalized by local friction velocity, show only small differences when the smooth wall results are compared with those for the rough-wall. However, the rough-wall distributions of both normalized wall-normal Reynolds stress and the Reynolds shear stress show significantly large increases over those for the smooth wall. These enhancements were attributed to the sweeping motions near the roughness, motions that were made possible by the less severe boundary condition for the  $v$  motion. In the outer regions of the rough wall BL, contributions from both sweeps and ejections are larger relative to the smooth wall. In a sequel to their investigation, Krogstad and Antonia (1999) performed a similar experiment by replacing the mesh screen with lateral rods. In this case, the roughness function,  $\Delta U^+$ , is the same as in the previous experiment although the boundary layer has  $Re_\theta$  of 4806, a value lower than the previous experiment. For the same roughness function, there seems to be differences in the turbulent structure indicating flow sensitivity to the roughness geometry. While ejection motion contributions are significantly less than those for either the mesh wall or the smooth wall and with lesser frequency of occurrence, the sweeping motions show a large increase in their contributions. Also, there is a significant increase in the interaction events.

Tomkins (2001) carried out an investigation, using PIV, on walls roughened with uniform distributions of hemispheres. Two distributions were tested, one had a  $k^+$  of 100 and  $k/\delta$  of 0.045 in a  $Re_\theta = 7700$  turbulent boundary layer while the other had a  $k^+$  of 200 and  $k/\delta$  of 0.09 in a  $Re_\theta = 8700$  turbulent boundary layer. In the former case the boundary layer thickens by 3.28 % over that for the smooth wall BL while maintaining the same momentum thickness, and in the latter case, the thickening is 4.5 %. The smaller elements yielded a transitionally rough flow with a  $\Delta U^+$  of 3 and the larger elements cause a fully rough wall flow with a  $\Delta U^+$  of 11. Using a quadrant analysis, he found that the contributions from sweeps to Reynolds stress is greatly increased relative to the smooth wall case in the regions where  $y/\delta < 0.1$  and the contributions by ejections are reduced in the regions



where  $y/\delta > 0.2$ . Several vortex signatures are noted that are associated with sweep/ejection events and he attributed the signatures to those left behind by hairpin vortex structures. He also found that sweeps dominate the near-wall regions of the flow. Further, at the element height, he found that ejection events were large compared to those for the smooth wall case and this increase was due to the vortices shed from the roughness elements. He also suggested universality in the behavior of ejection events further away from the wall as the ejections for both rough and smooth wall were found to be similar.

### 1.2.3 Determination of wall shear

Several methods have been used by researchers to calculate the wall shear stress ( $\tau_w$ ). Specifically one needs the friction velocity ( $U_\tau = \sqrt{\tau_w/\rho}$ ) to scale the mean velocities and turbulence quantities. One method is to determine the drag force that the elements exert on the flow. The total drag force when divided by the area that the elements occupy would yield the wall shear stress. A popular way of measuring the drag force is the floating element method (Acharya *et al.*, 1986). However, in this method, large areas are needed to get accurate answers. Hence, this method is unsuitable for applications where large variations of wall shear occur over small distances. An indirect determination of the skin friction can be determined from the von Karman momentum integral equation. However, this method is fraught with large uncertainties (Tomkins, 2001).

Another scheme is the Clauser method which involves matching of a measured mean velocity profile to the law of the wall. This method is rather inaccurate in the case of the rough-wall BL because there is a large range of possible combinations of wall parameters. The log law of the wall is assumed to be valid for the rough case and is given by

$$\frac{U}{U_\tau} = \frac{1}{\kappa} \ln \left| \frac{(y - \varepsilon) U_\tau}{\nu} \right| + C - \frac{\Delta U}{U_\tau} \quad (1.11)$$

which is a modified form of equation 1.3. The three unknowns in Eq. 1.11 are the displacement of origin ( $\varepsilon$ ), the friction velocity ( $U_\tau$ ), and the roughness function ( $\Delta U^+$ ). As mentioned earlier, iterating all these three values simultaneously would lead to multiple solutions (Perry *et al.*, 1969). This system does, however, become accurate if, of the three, only two are unknown. Hence, if an approximate answer is obtained using a drag balance or from the momentum integral approach and then the above equation is iterated, a satisfactory answer can then be obtained. This approach can be termed as a displacement of origin method. A more accurate answer is obtained when the above equation also includes the wake function to account for the outer layers since the wake function is also affected by roughness (Krogstad *et al.*, 1992), and this equation is given by

$$\frac{U}{U_\tau} = \frac{1}{\kappa} \ln \left| \frac{(y - \varepsilon) U_\tau}{\nu} \right| + C - \frac{\Delta U}{U_\tau} + \frac{\Pi}{\kappa} w \left( \frac{y - \varepsilon}{\delta} \right) \quad (1.12)$$

Most authors (Raupach, 1981, Mulhearn and Finnigan, 1978, and Tomkins, 2001) simply set the wall shear stress by choosing  $U_\tau^2 = -\overline{uv}$  in the constant shear stress layer in each profile. The author is also confident in the determination of wall shear stress from this method. It is in this region where the log law is satisfied, thus indicating that this is also a region of overlap between the inner layers and the outer region. It appears as if the role of the wall is to set an average shear stress thus yielding the friction velocity ( $U_\tau$ ) that scales the outer regions.

It is also possible to integrate the boundary layer equation from the wall to some height,  $Y$ , above the crests of the elements (Ligrani and Moffat, 1986), which is given by

$$\frac{C_f}{2} = \frac{(-\overline{uv})}{U_e^2} + \frac{\nu}{U_e^2} \frac{\partial U}{\partial y} \bigg|_y + \frac{U(Y)}{U_e^2} \frac{\partial}{\partial x} \int_0^y U dy - \frac{1}{U_e^2} \frac{\partial}{\partial x} \int_0^y U^2 dy \quad (1.13)$$



where,  $C_f/2 = U_\tau^2/U_e^2$ . In all their cases,  $(-\overline{uv})/U_e^2$  was 96-98% of  $C_f/2$ .

### 1.3 Part 3: Three-Dimensional Rough-Wall Turbulent Boundary Layers

While the previous two parts dealt with the effects of individual elements (Part 1) and effects of these elements when placed as a distribution in a 2-D turbulent boundary layer (Part 2), the present part (Part 3) deals with the same rough-wall when subjected to a 3-D turbulent boundary layer. The 3-D turbulent boundary layers are characterized by varying directions of the velocity vectors within the boundary layers which are, in general, not aligned with the direction of the free-stream velocity vector, although they remain nearly parallel to the wall. Most prior studies on rough-wall turbulent boundary layers pertain mainly to two-dimensional boundary layers with two-dimensional elements such as ribs and grooves used as roughness elements (e.g., Perry *et al.*, 1969, Perry *et al.*, 1987, Krogstad and Antonia, 1994). However, in nature, the roughness elements are randomly distributed and are three-dimensional in shape and flows subjected to these obstacles are essentially three-dimensional in the mean-flow sense, e.g., in the case of flow past submarines (especially on the deck) and ship hulls. As regards 3-D rough-wall turbulent boundary layers, only one study (Krogstad and Fanneløp, 1983) has come to the attention of the author where mean flow measurements were carried out; however, no study towards the understanding of the turbulent structure was made.

About 10% of the drag on a submarine is due to roughness. The upper fifth of the curved submarine hull is a rough surface that is used as a deck by the crew when in port. At sea, the flow over this roughened surface passes downstream into the propulsor. Grit is also used on rotating-arm and remote-control submarine models to modify the maneuvering performance. The effect of distributed 3-D roughness on the structure of a 3-D turbulent boundary layer has not been previously examined and is important in modeling such flows. It is interesting to note that Prof. V.C. Patel of the Univ. of Iowa entitled his 1997 ASME Fluids Engineering Award lecture: "Flow at High Reynolds Number and Over Rough Surfaces – Achilles Heel of CFD." There is also no other study available on the flow structure and behavior of rough-wall 3-D flows. This basic research is examining the fundamental way in which roughness affects the near-wall behavior of 3-D turbulent boundary layers. This is somewhat different than for 2-D cases because of significant mean and fluctuation flow skewing nearest the wall (Anderson and Eaton, 1989, Schwarz and Bradshaw, 1994, and Ölçmen and Simpson, 1995b). One of the key differences between 2-D and 3-D TBL is the presence of the cross-stream velocity gradient ( $\partial W/\partial y$ ) which is the main contributor to the streamwise vorticity.

Measurements carried out in the rough-wall 3-D turbulent boundary layers are at the same locations where Ölçmen and Simpson (1995b) performed their smooth wall measurements. An idealized wing/body junction was used to generate a 3-D pressure driven TBL in its vicinity and measurements were made at seven stations around it. Each of the measurement locations exist outside the strong chaotic horseshoe vortex system that is formed at the nose of this junction. Further, each station is subjected to a different surface pressure gradient. At the locations where the cross flow pressure gradient effects are prominent, the shear stress angle lags behind the flow gradient angle in the inner regions. In other words, the direction of the turbulent shear stress and the directions for the mean flow and the mean velocity gradient direction are much different. Hence, the presence of the roughness elements is expected to complicate this flow behavior nearest the wall. Further, at these very same locations, the parameter,  $1/S = \overline{v^2}/|\tau/\rho|$ , displays higher values in 3-D flows when compared to those for the 2-D flows. This parameter is the correlation between the momentum-transporting velocity scale and the resulting magnitude of the shear stress. Hence, higher values in the case of 3-D flows is due to less correlation between the  $u$  and  $v$  velocity fluctuation components.



The present study is performed by making measurements at seven stations (same locations as in Ölçmen and Simpson, 1995b). The same six distributions of cylinders used to generate the 2-D rough-wall flows were placed around the wing-body junction. The objective of the experiments is to obtain a better understanding of the effect of roughness on a mean 3-D flow field and towards improved predictions using the Reynolds stress transport models by providing a detailed data set of double and triple products of the fluctuating quantities in addition to the mean quantities. Further, the data set is used to extract valuable flow physics behind the mechanisms that govern these 3-D rough-wall layers.

## **1.4 Organization of the Dissertation**

The organization of the dissertation is as follows. Chapter 1 presents the introduction to this experimental investigation. Chapter 2 contains details on the experimental apparatus and measurement. Chapter 3 deals with the effects of the single elements in 2-D turbulent boundary layers, while Chapter 4 deals with the same when the elements are in a distribution and is entitled “2-D rough-wall boundary layers.” The effects of flow three-dimensionality on the same sets of distributions, as in the previous chapter, are considered in Chapter 5. A comparison of the three parts that form this entire study is considered in Chapter 6. This chapter thus affords a direct comparison between the three effects: those of the individual elements on 2-D turbulent boundary layers, the distributions of the same elements on the 2-D turbulent boundary layers and thirdly, the same distributions on the 3-D turbulent boundary layers. Chapter 7 contains the conclusions which are a compendium of the concluding remarks made in the preceding four chapters. Appendix A consists of a simple scheme to estimate the streamwise wavelength of the roughness top vortex structure. Appendix B presents the derivation of total drag due to the single elements. Appendix C contains an uncertainty analysis performed on the measured data and the uncertainties associated with it.



Table 1.1. Summary of previous two-dimensional mean turbulent flow experiments on sparse distributed roughness with cylinders, cones, cubes, pebbles, hemispheres and spheres

Reference	Roughness geometry and flow conditions	Measurements and results
Schlichting (1936)	Measurements were conducted in a water channel with average velocity of $8\text{ m/s}$ . Surfaces were roughened with spheres, spherical segments, cones and short angles that were distributed in a regular pattern. Schlichting proposed the concept of 'equivalent sandgrain roughness', $k_s$ , which is the size of sand grain in Nikuradse's experiment which would give the same resistance as the particular roughness being investigated. He determined the value of $k_s$ for each of the surfaces in his measurement.	From the measurements of the velocity distribution, the shearing stress on the rough wall is determined with the aid of the logarithmic formula and the sandgrain roughness. However, a recent reevaluation of these experiments by Coleman <i>et al.</i> (1984) reveals that the skin friction coefficients are higher than the actual values by amounts ranging from 0.5% to 73% and the equivalent sand roughness values are higher than the actual ones by 26% to 555%.
Koloseus and Davidian (1966)	A channel flow experiment was conducted with wall roughened with $4.76\text{ mm}$ cubes uniformly distributed with different spacing and yielding $\lambda$ of 0.00195, 0.0078, 0.03125 and 0.125	They found a linear relationship between $f(\lambda)$ and $\log \lambda$ .
Marshall (1971)	Measurements were carried out in a wind tunnel with a free-stream velocity of $20.3\text{ m/s}$ . Roughness elements were cylinders of $25.4\text{ mm}$ heights. Elements of varying density were set in two patterns-regular and random. The diameter ( $d$ )/height ratios are 0.5, 1, 2, 3 and 5. The values of $\lambda$ range from 0.0004 to 0.102.	Velocity profiles are measured using a Pitot-static tube. The profiles are sampled at various distances from the leading edge of the roughness field on a line displaced by $y = 77.5\text{ mm}$ . The drag force is measured using a special drag 'balance'. For closely spaced elements, a linear relationship between the elements drag coefficient and $1/\sqrt{\lambda}$ is shown.
Grass (1971)	Measurements were carried out in a water channel with Reynolds number, based on the depth, ranging from 6620 to 6740 in three different flow regimes: smooth, transitionally rough and fully rough. For the transitionally rough case ( $k^+ = 21$ ), $2\text{ mm}$ pebbles were used and for the full rough case ( $k^+ = 85$ ), $9\text{ mm}$ pebbles. The hydrogen bubble technique was used for flow visualization and quantitative velocity measurements.	He demonstrated the existence of both violent ejection and inrush events over the rough wall. He, however, concluded that these were common features of boundary layer turbulence irrespective of wall roughness condition.



Reference	Roughness geometry and flow conditions	Measurements and results
Counihan (1971)	Measurements in the wind tunnel yield a test Reynolds number of 6000 based on the free-stream velocity and the roughness element height. "Lego" bricks of 9.5mm height and 15.9mm square were used as roughness elements.	He obtained a variation of the roughness length $y_o$ as a function of both fetch and roughness concentration and derived a semi-empirical expression for $y_o$ . He also deduced that a distance of 1000 $k$ is needed to achieve near equilibrium boundary layer flow.
Chen and Roberson (1974)	Tests were conducted in a circular pipe roughened with hemispheres. The roughness concentrations ( $\lambda_c$ ) used in this study are 0.0046, 0.0138 and 0.039, which correspond to hemispheres having a radii ( $k$ ) of 5.486mm, 9.525mm, and 15.875mm, respectively. Flow velocity was varied to obtain different values of the roughness Reynolds number ( $k^+$ ) ranging from 110.8 to 1165.5.	In the region above the tops of the roughness elements the distribution of the normalized intensities of turbulence, $\sqrt{\overline{u^2}}/U_\tau$ , $\sqrt{\overline{v^2}}/U_\tau$ and Reynolds shear stress $-\overline{uv}/U_\tau^2$ , and the macroscale of turbulence, $L_x/R$ , in roughened pipe are about the same as in smooth pipe. The profiles of $U/U_\tau$ vs. $y/k$ for a given $\lambda_c$ with varying $k^+$ show that the distributions follow the semi-logarithmic relations very well both above and below the tops of the elements. The velocity distributions depend on the values of $k^+$ and $\lambda_c$ . Relative viscous shear stress (shear stress produced by smooth part of the pipe) is plotted against the roughness Reynolds number for different roughness concentration. The relative resistance produced by the smooth boundaries decreases (resistance by element increases) as the roughness Reynolds number increases.
Lee and Soliman (1977)	Roughness elements are cubes of 20mm size. The flow velocity measurements are made using an X-configuration hot wire probe. Pressure measurements are obtained using a multi-tube inclined manometer. The lowest probe position is at about $y^+$ of 200. Following parameters are varied: 1. Element layout pattern: normal, staggered and random. 2. Roughness density ( $\lambda_c$ ), defined by plan area, varies from 0.03125 to 0.5 3. Different incident flow directions 4. Roughness Reynolds numbers ( $HU_\tau/\nu$ ) are around 2000.	Three different regimes of flow are seen. They are characterized by different rates of change of drag coefficient with increasing layout density where the elements were normal to the flow. A linear relationship is shown to exist between the element density and zero plane displacement. Relationship between the roughness function and roughness Reynolds number, based on the origin error, yields a good correlation for the experimental results.



Reference	Roughness geometry and flow conditions	Measurements and results
Raupach <i>et al.</i> (1980)	<p>Circular cylinders, 6mm in both height and diameter, were used as roughness elements in the wind tunnel experiment. Parameters describing the roughness distribution are:</p> <ol style="list-style-type: none"> <li>1. Roughness parameter, <math>\lambda</math>, the values of which are 0.011, 0.023, 0.045, 0.091 and 0.179.</li> <li>2. Roughness length, <math>y_o</math>. Their values are 0.054, 0.144, 0.214, 0.346, and 0.395.</li> <li>3. Friction velocity, <math>U_\tau</math>. Their values are 0.843, 0.938, 1.000, 1.025, and 1.068. There is a one to one correspondence in the values of <math>\lambda</math>, <math>z_o</math> and <math>U_\tau</math> presented above.</li> </ol>	Measurements of mean and turbulence quantities were carried out with the help of an X-configuration hot wire probe. The lowest probe position was about 3.2 mm ( $y^+ \approx 180$ ) above the working surface. It is shown that below a layer in which the velocity profile is semi-logarithmic, two surface influences upon the mean velocity field can be distinguished.
Tomkins (2001)	Experiments using PIV on walls roughened with uniform distributions of hemispheres were carried out. Two sizes of hemispheres were used: one with $k^+$ of 100 and $k/\delta$ of 0.045 in a $Re_\theta = 7700$ turbulent boundary layer while the other had a $k^+$ of 200 and $k/\delta$ of 0.09 in a $Re_\theta = 8700$ turbulent boundary layer.	Measured instantaneous velocity vectors, mean velocity and turbulent fluctuations. He also identified motions that contribute to the Reynolds stresses and their locations within the BL. He also used an iterative approach called the “error-in-origin” method to determine the zero plane displacement which is the correction needed to make the rough-wall mean velocity distribution fit the log-law with a von Karman constant ( $\kappa$ ) of 0.41. This method is similar to the displacement of origin method used by the author.
Van Rij <i>et al.</i> (2002)	Measurements were made in a channel flow with walls roughened with randomly placed, non-uniform 3-D roughness elements. The Reynolds number based on the hydraulic diameter ranged from 10,000 to 25,000.	They tested their new relationships that correlated roughness function with roughness density ( $\lambda$ ).



## Figures

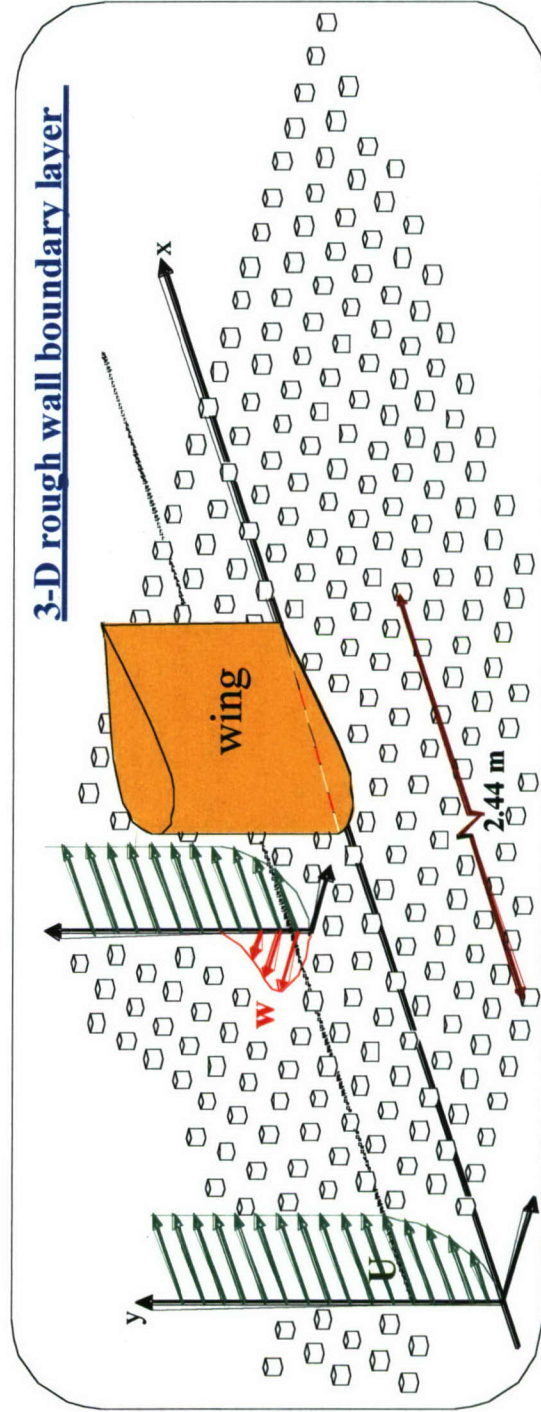
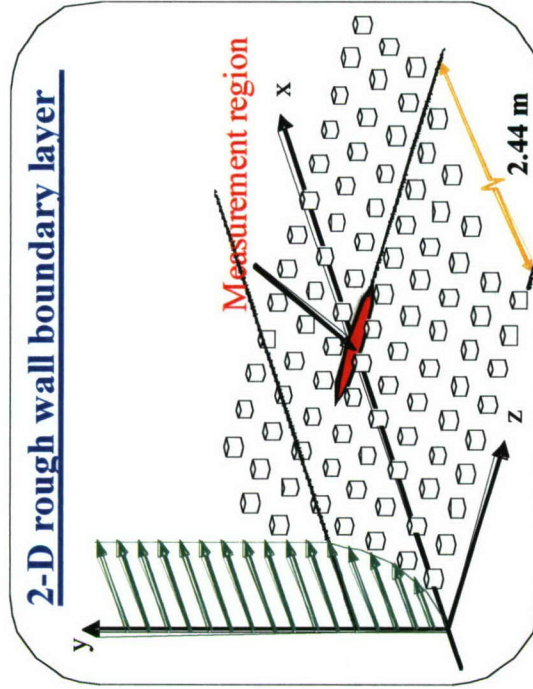
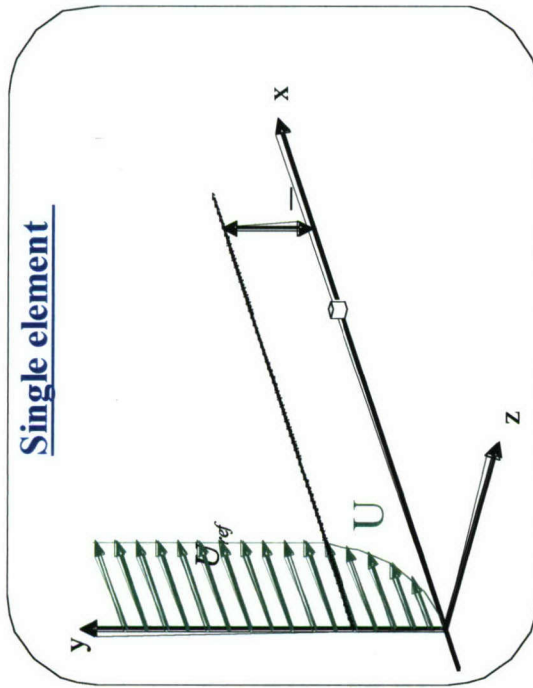


Figure 1.1. Pictorial representation of the three-part study.



## Chapter 2 Experimental Apparatus and Measurement Technique

### 2.1 Introduction

This chapter contains details about the rough wall geometry and the processes involved in creating such a rough surface. This chapter also discusses the three-component LDV (3CLDV) which is used to measure the mean velocities and the turbulence quantities. Also included in this chapter are details concerning the oil flow visualization, the measurement of surface pressure in the 3-D turbulent boundary layers. The measurement locations for the three-part study are presented in this chapter.

### 2.2 Wind Tunnel

The measurements were carried out in the Virginia Tech Aerospace and Ocean Engineering Department Low Speed Boundary Layer Tunnel. The inlet flow is tripped by the 0.63cm blunt leading edge of the tunnel floor to ensure that the boundary layer is turbulent. The test section is 0.91m wide and 8m long. Inserts for the wind tunnel sidewalls were used to minimize blockage-induced pressure gradients around the vertical wing. The experiments were run at a nominal speed ( $U_{ref}$ ) of 27.5 m/s, at a “reference” location of around 1.524m from the beginning of the tunnel test section. For the case of the single elements, the individual element is located about 2.90m from the beginning of the tunnel test section [Fig. 2.1 (a)] and measurements are made aft of it. In the cases of 2-D rough-wall TBL, flow is allowed to develop over a roughness fetch of 2.44m length and 0.91m wide which is also the width of the tunnel wall [Fig. 2.1 (b)]. The measurement locations for the 2-D rough-wall TBL are also at a distance of about 2.90m from the beginning of the tunnel test section. For the 3-D rough-wall TBL cases, the three-dimensional boundary layer is generated by a 3:2 elliptical nose NACA 0020 tail cylinder protruding from a flat plate [Fig. 2.1 (c)]. The model has the dimensions of 22.86cm in height, a chord length of 30.48cm, and a maximum thickness ( $t$ ) of 7.163cm.

### 2.3 Manufacture of rough surface

The construction of the roughness patterns is as follows. For each distribution/pattern of a particular roughness height, a mold is used. The mold was typically a teflon sheet with punched holes of 1.98mm diameter, spaced 5.486mm apart in a square pattern same as that desired in the distribution of elements. Each pattern of roughness element height ( $k$ ) required a teflon sheet of the same thickness,  $k$ . For the purpose of manufacturing of the rough-wall (fetch), a mixture of epoxy resin and hardener is poured on long aluminum sheets, and the teflon mold sheet is laid on top. Then the teflon sheet is pressed against the aluminum sheet by the process of *vacuum bagging* which removes all air between the epoxy resin and a clear plastic cover and forces the epoxy resin into the holes in the mold. Once the epoxy resin settles down, it is allowed to cure and the vacuum bag is removed. After the curing process, where the epoxy resin just hardens, the top of the teflon sheet is sanded to remove excess epoxy material and the teflon sheet is then peeled off revealing cylindrical pegs of hardened epoxy sticking out on the aluminum sheet. The aluminum sheet is then fastened along the tunnel floor to yield the fetch of roughness elements. A picture of a roughness pattern is presented in Fig. 2.2.

### 2.4 Oil-Flow visualization

The mixture for flow visualization contained 20 ml Titanium dioxide and 9 ml of oleic acid and kerosene was added until the mixture reached a volume of 55 ml. The single elements were glued on a glossy sheet of paper and the mixture was applied on the glossy surface. Then the tunnel was run until the mixture was dried, after which a lacquer fixer was applied to preserve the picture. This



visualization procedure was primarily done in the case of the single elements. The same procedure without the glossy sheet of paper was carried out in the cases of the 2-D and 3-D rough-wall TBL.

## 2.5 Rough-wall geometry

The quantities that define the geometrical details of the rough-wall are the roughness height  $k$  which is the height of the individual roughness element and  $\lambda$ , a parameter that is assumed to include all the additional lengths  $L_i$  needed to completely characterize the roughness. Typically,  $L_i$  includes the roughness element dimensions in the  $x$  and  $z$  spanwise directions (the cylinder diameter,  $d$ , for our case) and the mean element separation distance  $D$ , which in the case of the square pattern is the center to center distance between the elements. The values of  $d$  and  $D$  are the same in each of the six cases and are equal to  $1.98\text{mm}$  and  $5.486\text{mm}$ , respectively (See Fig. 2.3). The roughness density parameter,  $\lambda$ , is defined as the ratio of frontal area normal to the flow to the total surface area, and is given by  $\lambda = kd/D^2$ . Six cases of rough-wall (fetch) were manufactured with roughness heights ( $k$ ) of  $0.38\text{mm}$ ,  $0.76\text{mm}$  and  $1.52\text{mm}$ , each in straight and staggered configurations. The fetch of roughness elements oriented such that the rows/columns of the pattern are parallel/perpendicular to the tunnel axis are called straight patterns and those that are at an angle of 45 degrees to the flow are termed staggered (Fig. 2.3). Please note that the orientations do not change the value of  $\lambda$ . The values of  $\lambda$  for the element heights ( $k$ ) of  $0.38\text{mm}$ ,  $0.76\text{mm}$  and  $1.52\text{mm}$  are 0.025, 0.050 and 0.10 respectively.

## 2.6 Three-velocity-component fiber-optic LDV (3CLDV)

In the current study a three-velocity-component fibre-optic LDV (3CLDV) system was used, which is a sub-system of a five-velocity-component fibre-optic LDV system (Ölçmen and Simpson 1995a). The three component system consists of two main sub-systems: an optical table [Fig. 2.4] and a probe head [Fig. 2.5]. The components on the optical table are lasers and the optical equipment necessary to generate and couple the laser beams into polarization-preserving single-mode fibres that terminate in the probe. The optical equipment on the table include Bragg cells (BC), beam splitter cube (BSC), Laser to fiber couplers (LTFC), mirrors (M) and polarization rotators (PR). Laser beams from the probe pass through a glass window in the wind tunnel floor and form three coincident probe volumes to measure three simultaneous orthogonal velocity components at the  $U$ ,  $V$ ,  $W$  measurement point. The probe head consists of two transmitting optic trains and a receiving optics train with a fibre to a photomultiplier (PM) tube that forms a unit that can be translated and adjusted independent of each other.

The present setup uses two lasers. Two beams ( $488\text{nm}$ , blue, and  $514.5\text{nm}$ , green) from two lasers (INNOVA 90-5 for blue and INNOVA 90-6 for green, both with etalons) were used to generate the five beams (two blue, and three green) that intersected to produce the three probe volumes. The frequencies of the laser beams were shifted acousto-optically by Bragg cells. The purpose was to resolve the directional ambiguity, i.e, to determine the direction of the fringe movement within the measurement volume. The frequency shifts for green beams are 0,  $-50$ , and  $+30$  and for the blue beams 0,  $+40$ . These frequency shifts are large enough to eliminate cross-talk between the signals. Final dimensions for the intersecting volumes of each of two beams are  $60\text{ }\mu\text{m}$  in diameter and  $690\text{ }\mu\text{m}$  in length. The included angles between the two couples of green beams used in the measurements are both  $6.31^\circ$ , which result in a  $4.67\text{ }\mu\text{m}$  fringe spacing. The included angle between the blue beams is  $5.91^\circ$  which lead to a fringe spacing of  $4.99\text{ }\mu\text{m}$ . As mentioned previously, the five transmitted beams result in three probe volumes which at their coincident intersection formed a nearly spherical measurement probe volume of a diameter of  $30\text{ }\mu\text{m}$ .

The light scattering particles with an approximate diameter of  $1\text{ }\mu\text{m}$  were generated from Dioctal Phthalate by an aerosol generator originally. The smoke was injected into the flow at the



entrance of the tunnel test section. The scattered light (Doppler burst) was acquired by an optical arrangement located at the base of the probe head and fed through an optical fibre to a PM tube. The PM tube voltage output signals which contain the Doppler frequency information were processed by three Macrodyne Frequency Domain Analyzers (FDP 3100). In order to accommodate the signals into the appropriate Macrodyne bandwidth with the highest resolution, the signals from the PM tube are down mixed with RF signals which were generated using a RF generator. The analog signal from the PM tube was amplified and wide band-pass filtered (using Mini-Circuits BLP models) to obtain clean signals rather than depending only on the Macrodyne processor band-pass filters. These steps enabled acquisition of signals with minimal noise and hence, resulted in signal validation ratios of at least 95% and, in general, 98% to 100%. The  $U$ ,  $V$ ,  $W$  velocities are measured in a coincidence mode with the FDP's. Due to the lack of memory storage in the Macrodyne units, a computer board from Dostek (1400A Laser Velocimeter Interface with TCEM daughterboard option) and software were used in a personal computer. With this board, the data acquired from each of the three processors are accepted as valid data if all the data values occurred within a time coincidence window of  $10\ \mu\text{s}$ .

At every measurement point 30000 samples were acquired. The sampling rate varied from 100 samples per second very near the wall to 300 to 500 samples per second away from the wall. The  $U$ ,  $V$ ,  $W$  system data were systematically reduced in the following manner:

- (i). The acquired Doppler burst frequencies were converted into velocities in the optical axes (a coordinate system defined by three directly measured orthogonal directions) and the histograms of these velocities were obtained. The absolute arrival time for each velocity value was recorded too.
- (ii). A parabola was fit to each side of the logarithm of the histogram ordinate between the ranges of 1% and 80 % of the peak value. The data lying outside the intersection of the parabolas with the ordinate value of one occurrence of a velocity signal were discarded. For noisier histograms, the edges of the histograms were interactively located and the data lying outside the skirts were again discarded. The clean velocity information was transformed into tunnel coordinates and saved.
- (iii). In the tunnel coordinates too, the velocity data were cleaned using the same parabola fitting and data discard routine described above.
- (iv). The time-dependent clean velocity data in tunnel coordinates were then used to calculate the flow variables. No weighting factor was applied since there was no correlation between data rate fluctuations and velocity fluctuations (see Appendix C.1.1). Hence, velocity component histograms over 512 bins ranging from the minimum to maximum were calculated without weighting. The mean value of these histograms results in mean velocities. The mean velocities were then subtracted from the time-dependent data to obtain the time-dependent fluctuating velocities. Histograms were calculated for all second- and third-order cross-products of the fluctuating velocities, and the mean values of these histograms resulted in Reynolds stresses and triple products, respectively.

The above LDV probe head was only used to measure up to a distance of  $42500\ \mu\text{m}$  from the wall. The rough-wall TBL had boundary layer thicknesses of a few tenths of a millimeter more than those for the smooth-wall TBL. Hence, at heights beyond  $42500\ \mu\text{m}$ , a modified version of the LDV head was used (Ölçmen *et al.*, 2001). The modified system has 56 degrees between the bisectors of the beams emerging from the two transmitting probe heads, as opposed to 90 degrees obtained with the original LDV system (Fig. 2.5, LHS). This was accomplished by inserting  $17^\circ$  apex angled aluminum wedges between the transmitting optics heads and the translators that hold the heads in their place. In the modified system the velocities are thus not measured in an orthogonal frame, however the three components measured could easily be transformed into an orthogonal frame. The fringe spacing in this case was different and was determined to be  $11.3\ \mu\text{m}$ . The light collection probe volume for the system is defined by the overlapping portions of the individual probe volumes which were three in number, same as in the original LDV probe head. Thus the long interference region of individual probe volumes does not reduce the spatial resolution. However the probe volume of the system in the modified system is larger than the original 3CLDV due to the larger size of the focused beam diameters. Since the modified system is intended to be used only in regions of the flow away from the wall, where the velocity



gradients are not large, the reduced spatial resolution, therefore, does not affect the overall quality of the measured velocities. Also, the differences between the quantities from the two systems are within the uncertainty bounds prescribed in them.

No corrections were made to the data set as the corrections made were within the uncertainty bounds. However, the suggested corrections to LDV are included in Appendix C.

## 2.7 Measurement of pressure gradients in 3-D rough-wall TBL

To measure the wall static pressure, pressure taps of approximately  $0.5\text{mm}$  in diameter were placed centered between the roughness elements and formed a square grid of 16 taps, at each of the seven measurement stations. The pressure measurements were made with a J-type scanivalve and Setra 239 pressure transducers. The pressure coefficients are calculated using the following equation:

$$C_p = \frac{P - P_{ref}}{P_{oref} - P_{ref}}$$

The subscript *ref* denotes values at the reference station which is  $1.524\text{m}$  from the entrance to the test section.  $P_{ref}$  is the static pressure,  $P_{oref}$  is the stagnation pressure, and  $P$  is the static pressure at each location [see Fig. 2.1 (c)]. The pressure gradients along  $x$  and  $z$  directions at the seven stations are then interpolated from the gradients calculated from the measured pressures

## 2.8 Measurement locations

For the cases of the rough-wall boundary layers (both 2-D and 3-D), measurements were made without disturbing the roughness elements. The gaps between the elements act as slits for the laser beams to go through to make the measurements. A view of this is presented in Fig. 2.6 where the laser beams are passing through the tunnel floor between the gaps in the rough-wall. The depicted view, in this case, is that of a 3-D rough-wall TBL.

### 2.8.1 Measurement locations: Single Elements

As briefly mentioned earlier, the isolated roughness elements are circular cylinders of heights ( $k$ ) of  $0.38\text{mm}$  (also, sometimes designated smallest cylinder),  $0.76\text{mm}$  (intermediate cylinder), and  $1.52\text{mm}$  (highest cylinder), each having a diameter ( $d$ ) of  $1.98\text{mm}$ . For the fourth element, the Gaussian spike, the equation in  $\text{mm}$  defining its contour is given by:  $y = 1.52 \exp[-4.692(x^2 + z^2)]$ ; hence, ' $d/2$ ' for the Gaussian spike is the distance from its axis to the location where the height is 1% of the peak height, i.e., at  $y/k = 0.01$ . By design,  $d/2$  is half of  $1.98\text{mm}$ , which is also the diameter of each of the cylinders.

Single point measurements are made using the LDV at the locations downstream of the three isolated cylinders and the Gaussian spike. The measurement profiles, along the centerline ( $z/d = 0$ ), are at six streamwise locations,  $x/d = 1.36, 2.75, 5, 10, 20$  and  $40$  for the cylinders [Figs. 2.7 (a)], and at five streamwise locations,  $x/d = 2.75, 5, 10, 20$  and  $40$  for the Gaussian spike [Figs. 2.7 (b)]. The right-hand coordinate system is fixed on the wall at the axis of symmetry of the single element. Further, for all four cases, off-centerline measurements are made at several locations (12-15 in number) ranging from  $z/d$  of  $0.14$  to  $-3.05$  at two streamwise locations,  $x/d = 2.75$  and  $10$ , yielding several hundred grid points of data in a  $y-z$  plane. This helps in determining contours of the measured and derived quantities in a plane. In the case of each of the three cylinders, off-center profile measurements were also made at  $z/d$  locations of  $-0.69$  and  $-1.39$  at the  $x/d$  location of  $1.36$ . Preliminary investigations in the downstream flow field have shown statistics involving ' $u$ ' and ' $v$ '



velocities to be symmetric and ‘ $w$ ’ velocity to be anti-symmetric about the centerline/plane and hence detailed measurements were made mainly in the negative  $z$ -axis (at two,  $x/d$ , streamwise locations) and along the centerline ( $z = 0$ ). The displayed results also include the results of the undisturbed smooth wall boundary layer (also called reference smooth wall) at the exact location where the isolated elements are mounted later for measurements. In order to establish a common base for the purpose of analysis, the velocity scale used in the plots is the skin friction velocity,  $U_\tau$ , of the reference smooth wall boundary layer. The length scale used to non-dimensionalize distance from the wall,  $y$ , is  $y/U_\tau$  and for the spanwise and streamwise distances, the length scale is the element diameter,  $d$ . Dashed lines are also shown in the plots to denote the height of the individual elements:  $k^+ = 23$  indicates the smallest cylinder ( $k = 0.38mm$ ),  $k^+ = 46$  indicates the intermediate cylinder ( $k = 0.76mm$ ) and  $k^+ = 92$  represents the highest cylinder and Gaussian spike, both of which have  $k$  of  $1.52mm$ . In the contour plots, the dashed lines are the outlines of the individual elements’ shape. Discussions of the plots are based on the behavior shown by the various quantities in the negative  $z$ -axis only. Measurements carried out in the few off center locations in positive  $z$ -axis, along the streamwise distance, are used to locate the center of the downstream flow system and to calculate spatial derivatives of the measured quantities.

## 2.8.2 Measurement locations – 2-D rough-wall turbulent boundary layers

Measurements are made at locations as shown in Figs 2.8 (a) and (b) for two orientations containing distributions of cylinders of height,  $k$ , of  $0.38mm$ ,  $0.76mm$  and  $1.52mm$ , each having a diameter ( $d$ ) of  $1.98mm$ . This yields a total of six cases of rough-wall boundary layers. Please note that each of the geometrical pattern/orientations use the same distribution of the uniform roughness elements of equal heights. The fetch of roughness elements oriented such that the rows/columns of the pattern are parallel/perpendicular to the tunnel axis are called straight orientations or patterns and those that are at an angle of 45 degrees to the flow are termed staggered [Figs. 2.8 (a) and (b)]. For each of the six cases, 40-45 profiles were made at the indicated locations.

Results are presented as contours of the quantity in most cases and locations selected for presentation are usually two orthogonal planes at ( $x/D=0.5$ ,  $z = 0$ ). The line plots are, in general, mainly presented for the measurements made at the intersection of these two planes, ie., at  $x/D=0.5$  on the  $x$ -axis ( $z = 0$ ). The choice of this location and the two orthogonal planes was made to provide a representative case. Results at other planes and locations will be presented as and when needed to complete the description of the mean and turbulence structure. Please note that when the mid plane is mentioned in the discussions it refers to the  $y-z$  streamwise mid plane at  $x/D=0.5$ . Spanwise mid plane would be the  $x-y$  plane located equi-distant to elements.

## 2.8.3 Measurement locations – 3-D rough-wall turbulent boundary layers

The three-dimensional boundary layer is generated by a 3:2 elliptical nose NACA 0020 tail cylinder protruding from a flat plate. The model has the dimensions of 9 inches in height, a chord length of 12 inches, and a maximum thickness ( $t$ ) of 2.82 inches. Measurements are carried out at seven stations around the wing-body junction and a schematic of it is shown in Fig. 2.9 (a). The coordinate system is chosen with  $x$ -axis parallel to the tunnel centerline pointing downstream,  $y$ -axis perpendicular to the tunnel floor and  $z$ -axis completing a right handed coordinate system. The measurement locations and the flow details for smooth-wall 3-D TBL are presented in Table 2.1. The measurement locations are such that they are outside the strong horseshoe vortex system formed at the wing-body junction. At stations 1 to 3, strong streamwise pressure gradients are present and at subsequent stations significant spanwise gradients are present. At station 7, the flow shows signs of relaxation.



All profiles are taken at a distance of  $D/2$  from the center of the post (closest to the particular station) at a direction given by the mean velocity vector at 3 element heights, i.e.,  $3k$  [Fig. 2.9 (b)].  $\alpha$  is the angle the velocity vector makes with the tunnel axis at  $3k$  height. Each measurement location (Loc.) was usually within  $2.5\text{cm}$  of the stations' locations of the smooth wall experiments (Ölçmen and Simpson, 1995b). Profiles were made at each of the seven stations for both straight and staggered orientations for each of the element heights ( $k = 0.38\text{mm}$ ,  $0.76\text{mm}$  and  $1.52\text{mm}$ ).

Detailed profile measurements in a  $x$ - $z$  grid were also made at station 5 at the same  $x/D$  locations as in the 2-D straight pattern, viz.,  $x/D = 0.295, 0.398, 0.5, 0.625$  and  $0.75$ . Each  $x/D$  plane consists of 10 measurement locations totaling 50 measuring stations (Fig. 2.10) and was made for each of the element heights in the straight orientation. These detailed measurements were made only in the straight patterns of element heights,  $k = 0.38\text{mm}$ ,  $0.76\text{mm}$  and  $1.52\text{mm}$ .

## 2.9 Free-stream velocity distribution in the wind tunnel

The distribution of streamwise velocity was obtained from the streamwise traverse of a Pitot-static tube located  $15.24\text{cm}$  above the tunnel floor. The presence of the rough-wall introduced minimal changes in the free-stream velocity,  $[U_e(x)]$ , distribution when compared with the smooth-wall case. The variations of the normalized free-stream velocity,  $[U_e(x)/U_{ref}]$ , along the streamwise distance,  $x$ , with origin at the beginning of the test section/end of the contraction are presented in Fig. 2.11. A very mild adverse pressure gradient is noticed which is confirmed in the presentation of the ratio of streamwise pressure gradient to the free-stream dynamic pressure along the streamwise distance in Fig. 2.12. However, at the measurement locations, for the different cases, this ratio,  $[(dp/dx)/(\frac{1}{2}\rho U_e^2)]$ , has very low values and as such the flows can be considered as occurring under nominally zero pressure gradient conditions. The values of this ratio for the four cases are:  $-0.077$  (smooth-wall),  $-0.021$  ( $k = 0.38\text{mm}$ ),  $-0.025$  ( $k = 0.76\text{mm}$ ), and  $-0.030$  ( $k = 1.52\text{mm}$ ). The three cases of rough-wall presented are for straight patterns in the 2-D TBL.

## 2.10 Uncertainties in the measured quantities

An uncertainty analysis was performed on the measured and calculated data and the uncertainties in the quantities are presented in Appendix C.



Table 2.1. Measurement locations and flow details for smooth-wall 3-D TBL.

Stations	$X$ (in.)	$Z$ (in.)	$U_e$	$\delta$ , mm	$\delta^*$ , mm	$\theta$ , mm	$Re_\theta$
1	-3.50	-1.45	25.73	40.25	7.08	4.93	7666
2	-2.29	-1.75	25.46	39.96	7.14	4.93	7578
3	-1.33	-2.04	25.88	39.57	6.93	4.81	7523
4	-0.47	-2.58	28.13	39.82	6.12	4.48	7613
5	0.26	-2.94	29.75	39.98	5.58	4.24	7615
6	1.19	-3.30	31.06	40.16	5.10	3.99	7487
7	2.17	-3.53	31.67	39.92	4.95	3.92	7504

Note that only for these locations, the  $X - Z$  coordinate system is located at the nose of the wing-body along the tunnel centerline.



## Figures

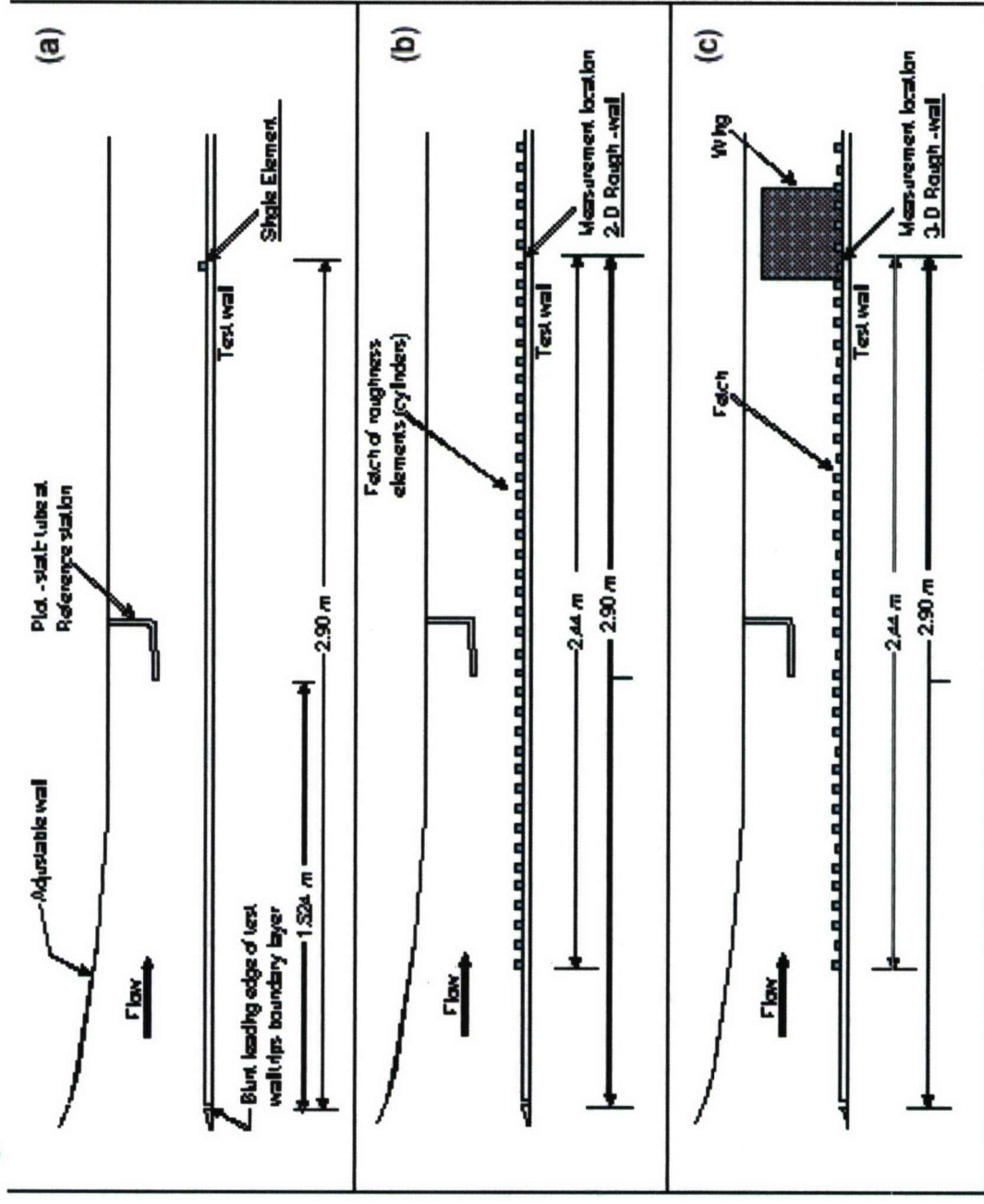


Figure 2.1. Side-view schematic of the wind tunnel set-up: (a) Part 1 (Single Elements), (b) Part 2 (2-D Rough-wall TBL) and (c) Part 3 (3-D Rough-wall TBL).



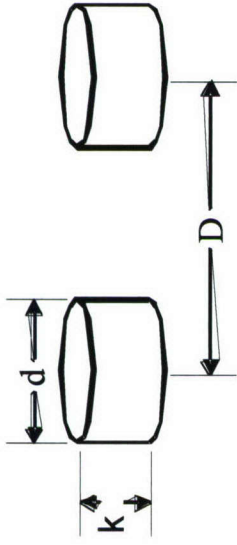


Figure 2.2. A picture of a sample roughness pattern.

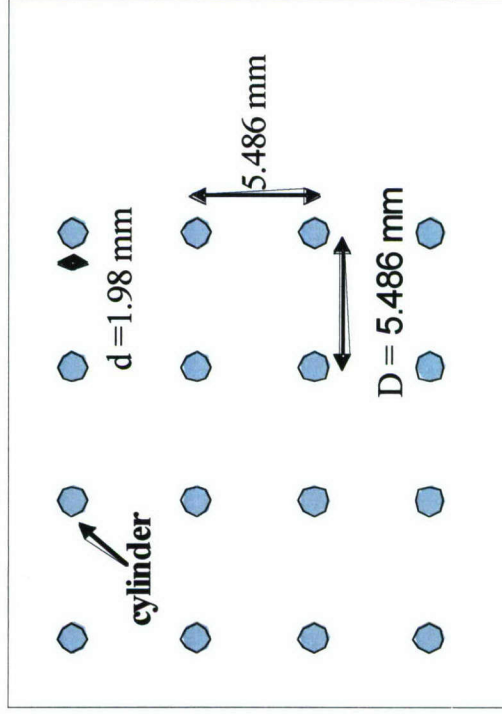


## Roughness Geometry

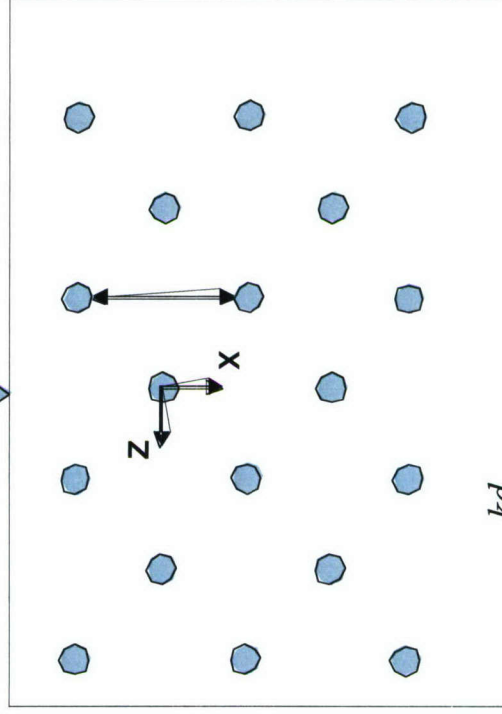
8' Fetch of roughness upstream  
of measurement zone



*Flow, Straight orientation*



*Flow, Staggered*



$$\lambda = \frac{kd}{n^2}$$

Figure 2.3. Roughness geometry and flow orientation.

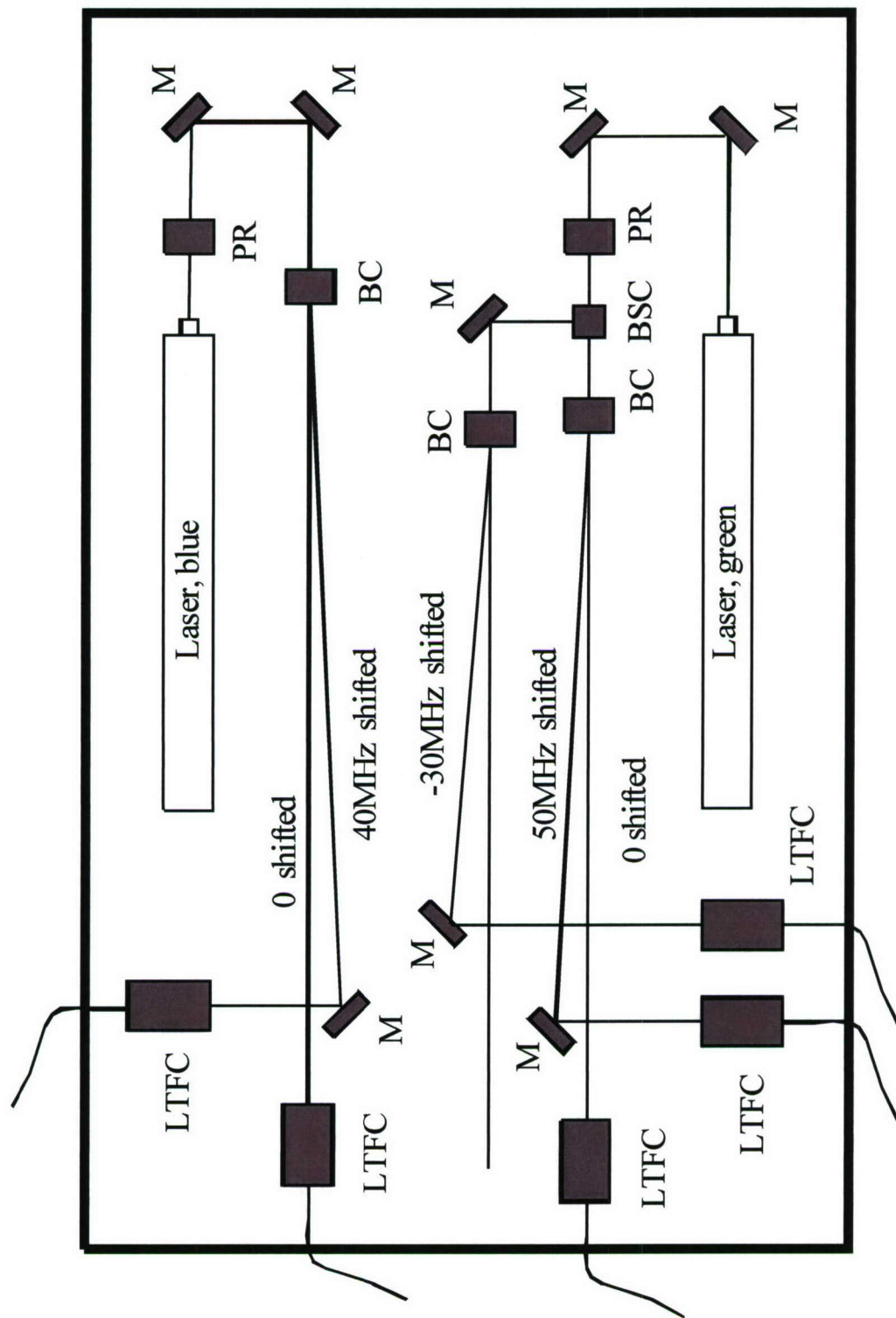


Figure 2.4. Optical table (BC: Bragg cell; BSC: beam splitter cube; LTFC: laser to fibre coupler; M: mirror; PR: polarization rotator).



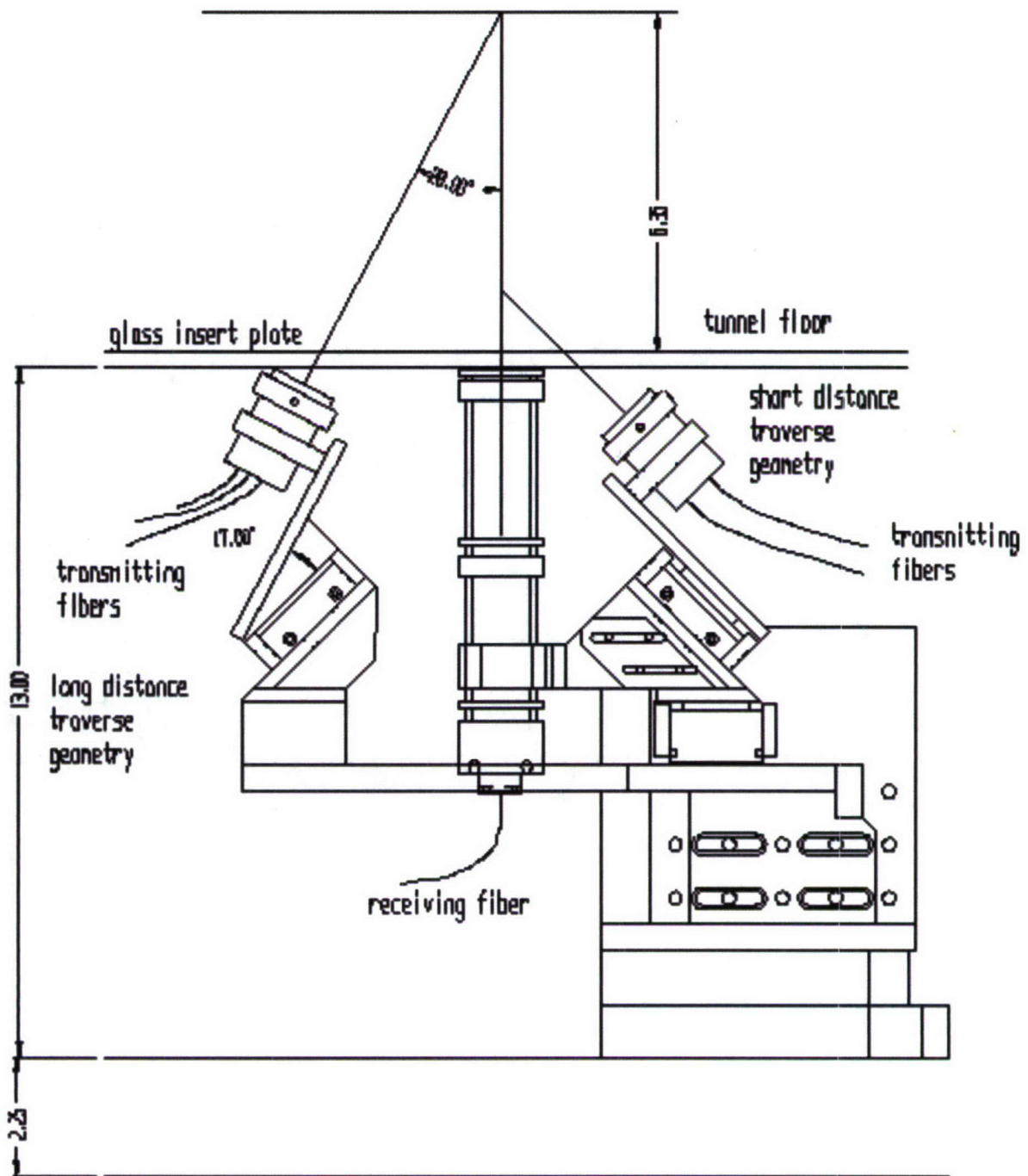


Figure 2.5. Short range, original configuration (right side) and long range, modified configuration (left side) transmitting lens configuration for the three component LDV (3CLDV). Complete optical systems not shown for either short or long range systems. The receiving lens configuration is for the long range design.

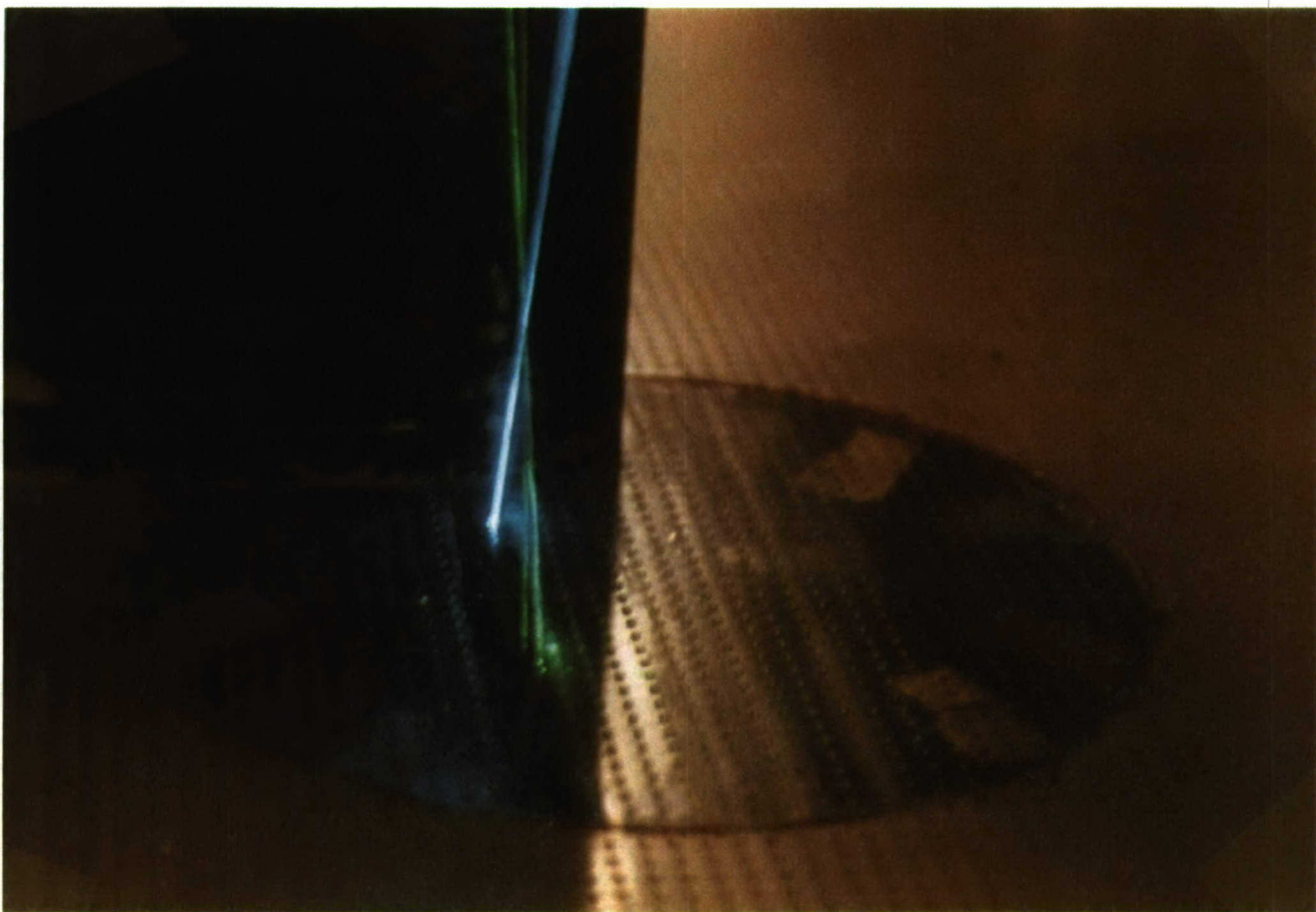


Figure 2.6. Appendage Junction: Laser beams passing through transparent floor through the spacing between the cylindrical roughness elements.



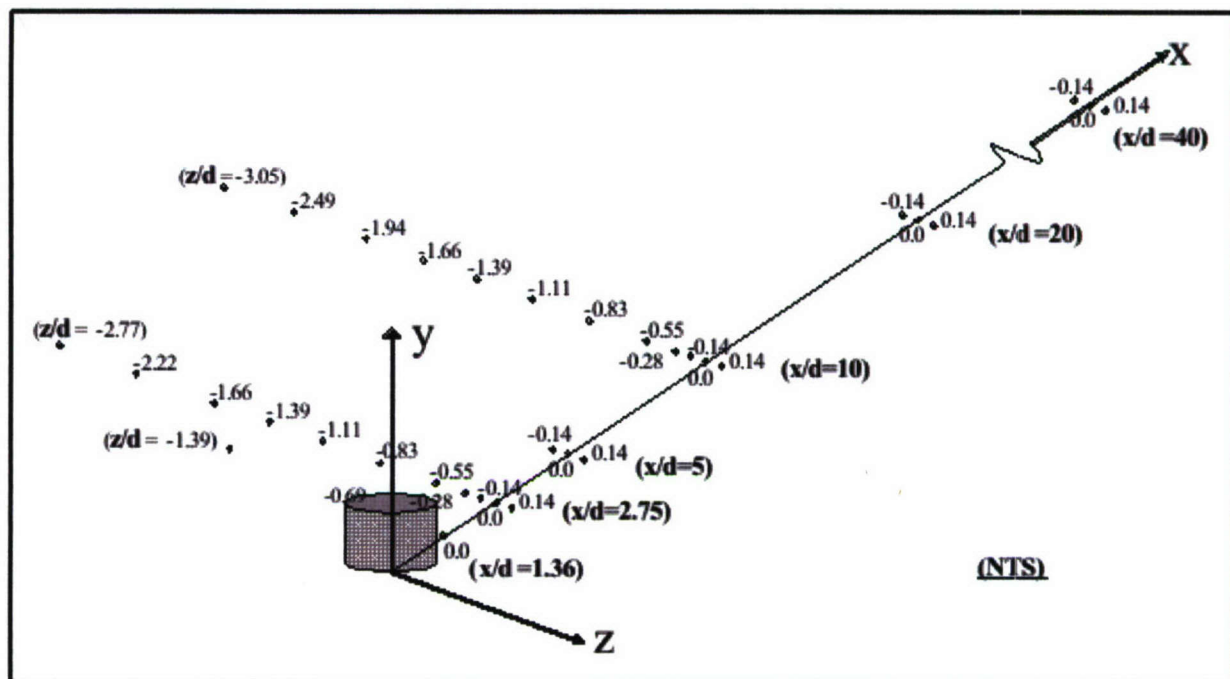


Figure 2.7 (a). Measurement locations downstream of the isolated cylinder along the centerline at  $x/d = 1.36, 2.75, 5, 10, 20$  and  $40$  and at off-center locations along  $z/d$ .

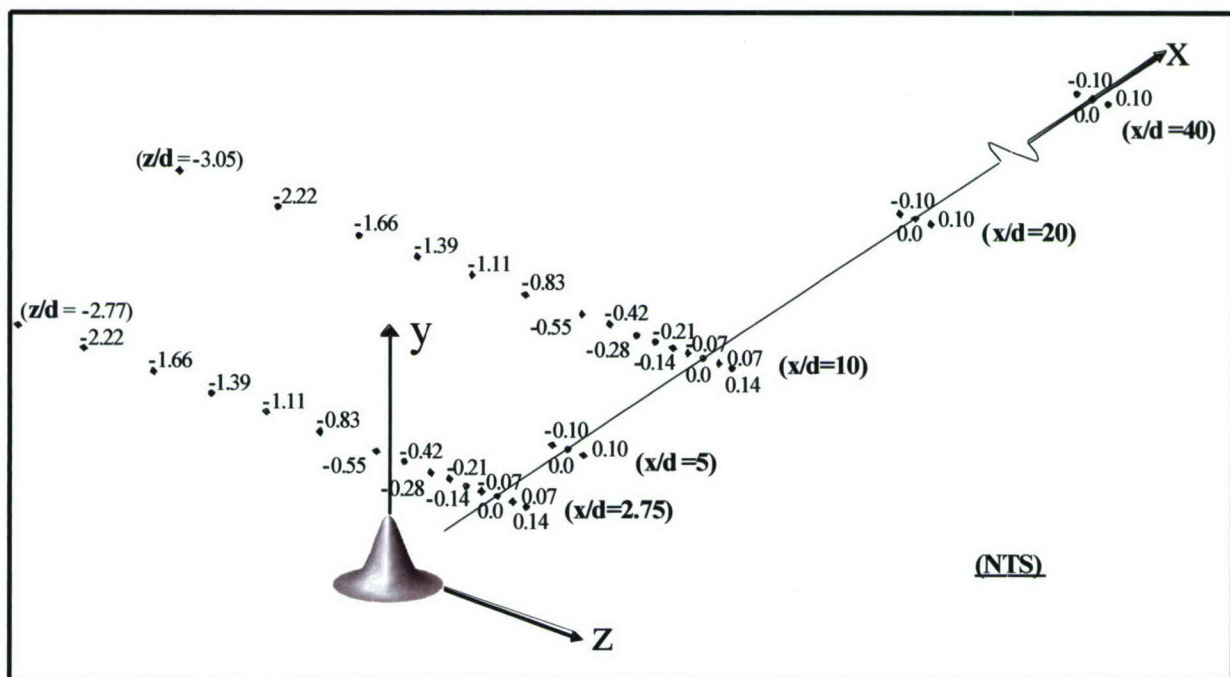


Figure 2.7 (b). Measurement locations downstream of the Gaussian spike along the centerline at  $x/d = 2.75, 5, 10, 20$  and  $40$  and at off-center locations along  $z/d$ .

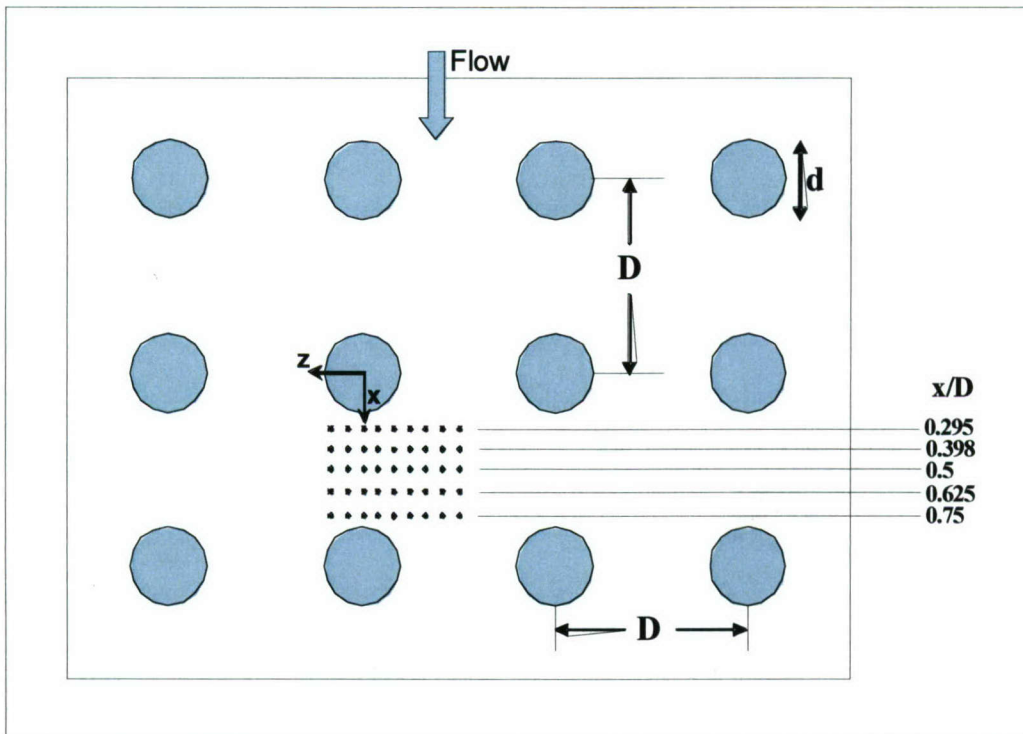


Figure 2.8 (a). Measurement in the 2-D rough-wall boundary layers (*straight* orientation). Each plane consists of 9 measurement locations totaling 45 measuring stations.

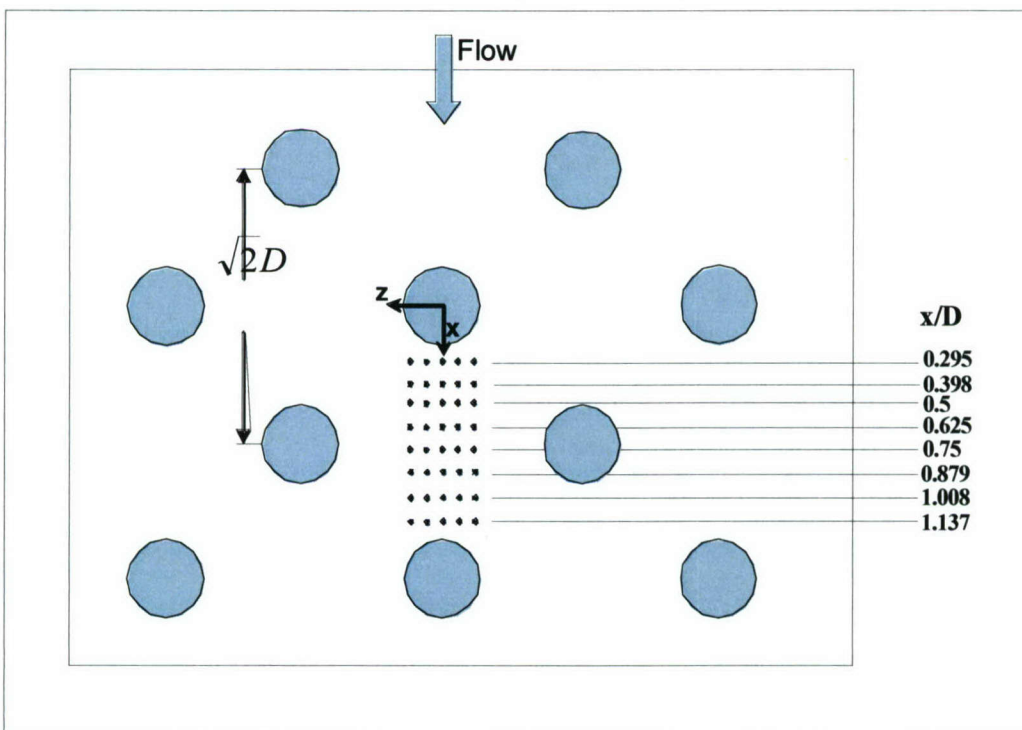


Figure 2.8 (b). Measurement in the 2-D rough-wall boundary layers (*staggered* orientation). Each plane consists of 5 measurement locations totaling 40 measuring stations.



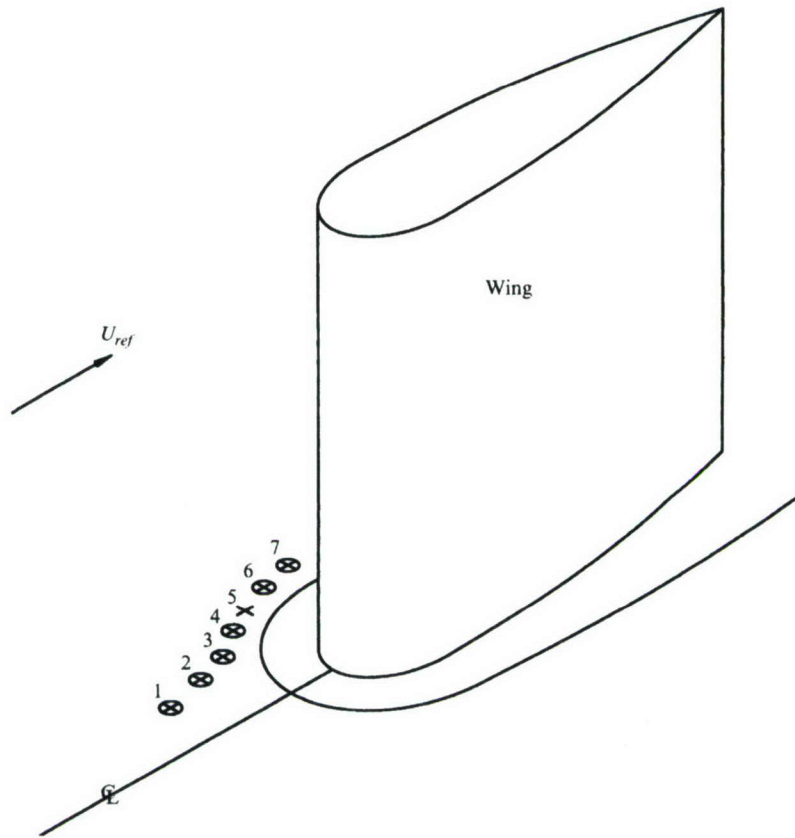


Figure 2.9 (a). Schematic of the wing-body junction and the seven measurement stations.

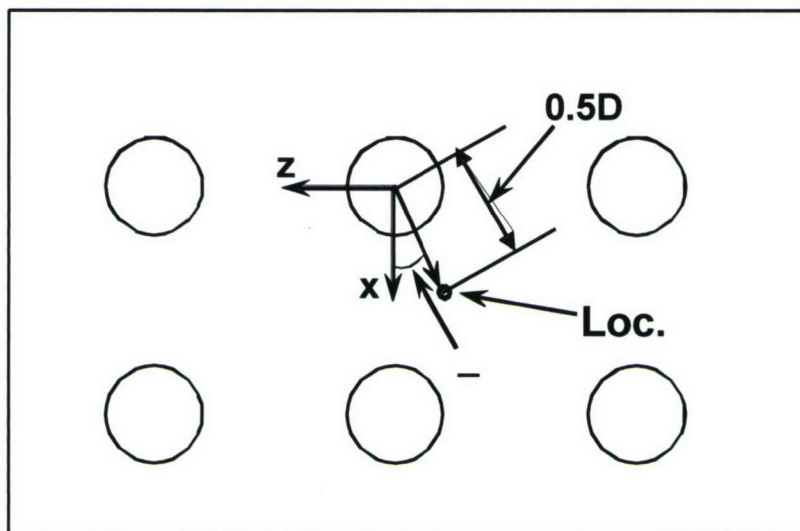


Figure 2.9 (b). Measurements in the 3-D rough-wall boundary layers at the seven stations around the wing-body junction.  $\alpha$  is the angle the velocity vector makes with the tunnel axis at  $3k$  height.

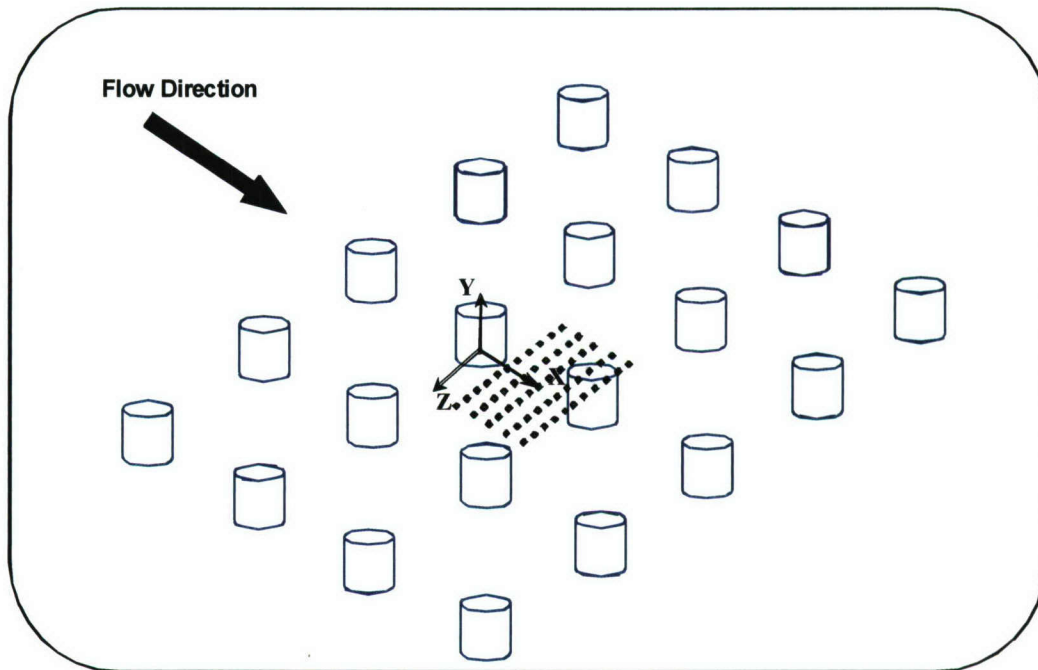


Figure 2.10. Measurements in the 3-D rough-wall boundary layers (straight orientation) at station 5. Each  $x/D$  plane consists of 10 measurement locations totaling 50 measuring stations.



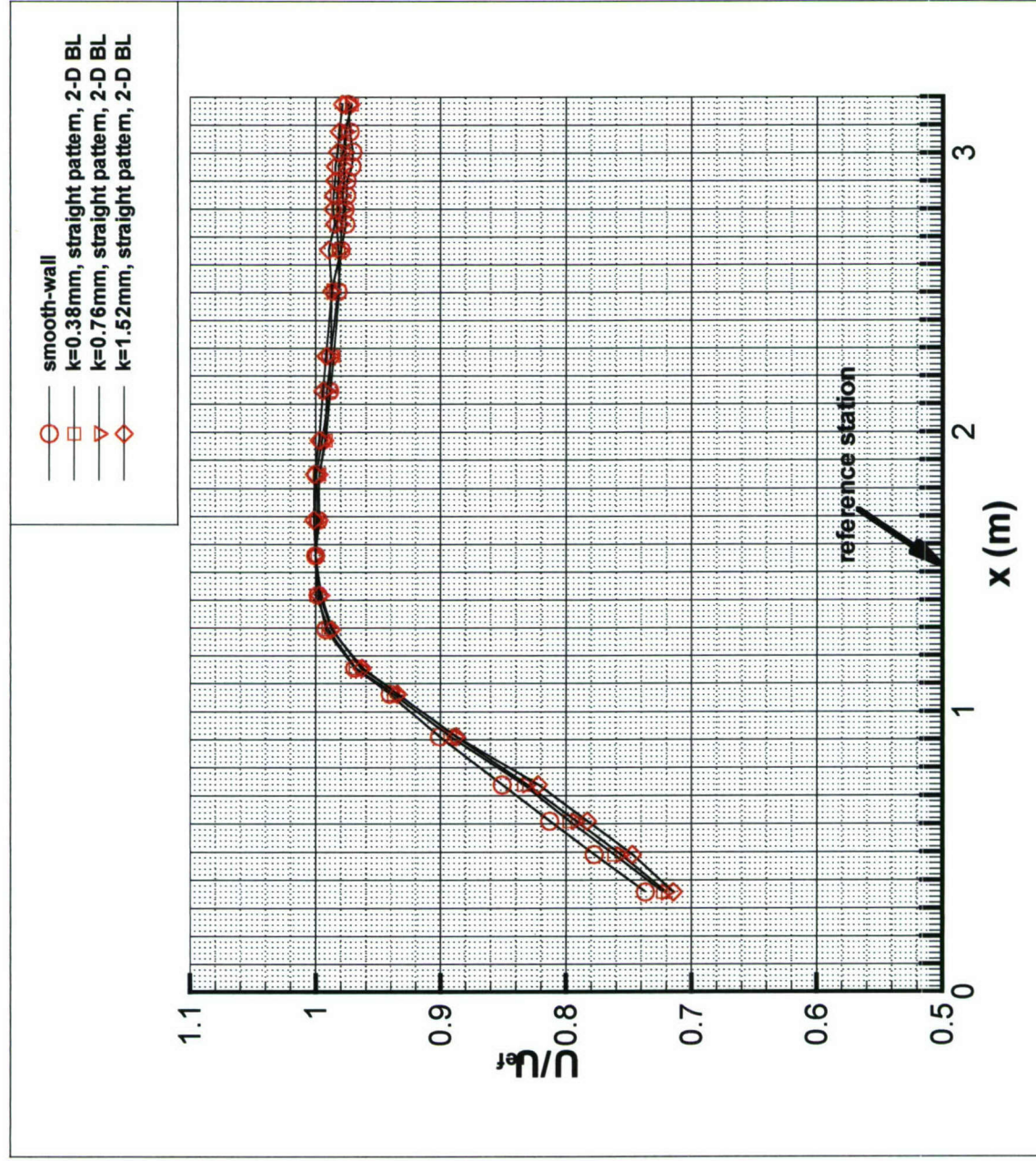


Figure 2.11. Streamwise variation of the free-stream velocity,  $\left[ \frac{U_e(x)}{U_{ref}} \right]$  in the wind tunnel.

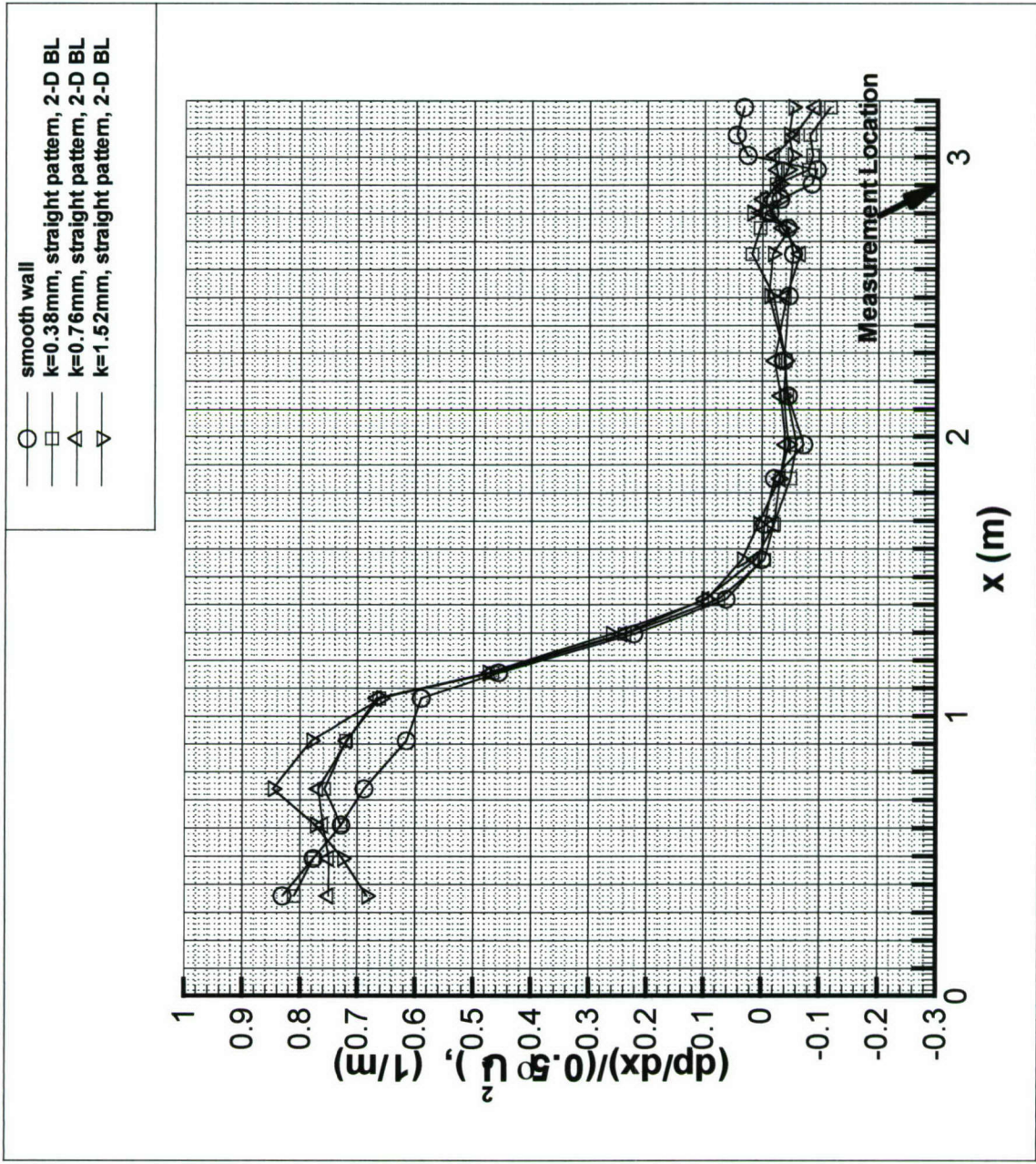


Figure 2.12. Streamwise variation of the pressure gradient,  $[(dp/dx)/(\frac{1}{2} \rho U^2)]$ , in the wind tunnel.



## Chapter 3 Single Elements

### 3.1 Results and Discussion

#### 3.1.1 Oil flow visualizations

Figure 3.1 shows the top view of the flow pattern using the oil flow visualization technique. In all four cases, an oil build-up is seen upstream of the element and subsequently curving beside it, indicating a flow separation which is due to the formation of a horseshoe vortex structure. Immediately behind the elements too, there is a strong downwash leading to back flow as evidenced by the scoured region which then is followed by a small region of tracer particle deposit; the end of this whitish region signifies flow reattachment as the shear layers from the top of the elements and the flow around the side of the element converge towards the centerline. The picture also demonstrates that flow has attached prior to 2.25 diameters downstream of the element, i.e., at  $x/d = 2.75$ , the significance being that this is the first location where the first  $y-z$  planar measurements are made and the data gathered is used for calculating the form drag of the individual elements. Approximate locations for re-attachments are  $x/d$  of 2.0, 2.1, 2.4 and 2.4 for the cylinders of heights,  $k = 0.38mm$ ,  $0.76mm$ ,  $1.52mm$  and the Gaussian bump, respectively. These values are based on locations that are just aft of the oil build-up. These pictures seem to indicate that the junction horseshoe vortex wraps itself around the element but does not seem to persist beyond 3 to 5 diameters downstream of the elements.

Downstream of the reattached region, all four cases show significant scouring along the centerline downstream of the element as shown by the dark region. The scoured region along and about the centerline is due to the downwash behind the element – an inrush of high momentum fluid from the outer layers towards the wall that leads to a higher wall shear when compared to that in the adjacent areas. This downwash is primarily induced by the vortex structure emanating from the top of the elements rather than the junction horseshoe vortex structure. Considering the flow downstream of the cylinders, the lowest element shows the least scouring which is an indication of weaker wallward motions as compared with those in the wakes of the other two cylinders. The smallness of the lowest element also permits low speed flow over and around the element. The wake behind the Gaussian spike shows more of a wedge-shaped wake as compared to the almost “constant width” wake flow behind the cylinders. In all the cases, the wake flow extends (as seen by the scoured region) tens of diameters downstream. At several diameters downstream of the elements, the flow visualization pictures also reveal deposits (of suspended particles) away from the immediate region about the centerline along the spanwise direction, thus indicating lower wall shear in these areas of “upwash” as compared to areas of “downwash” in the neighborhood of the centerline. The oil flow visualization pictures in conjunction with the measurements serve as a useful tool in explaining the complex flow field surrounding the isolated elements.

#### 3.1.2 Mean quantities – mean velocities

Profiles of the streamwise mean velocity, along the centerline, are presented as  $U/U_\tau$  versus  $yU_\tau/\nu$  in Fig. 3.2. At the very first measurement location,  $x/d = 1.36$ , flow has reattached only for the smallest cylinder, with the other two cylinders showing reverse flow regions. Significant velocity defects are seen in the wakes of all the three cylinders with the magnitude of the defects increasing with the cylinder height. The effect of the separated shear layers from elements on the velocity profiles is confined within three element heights in the three cylinder cases. At the subsequent station,  $x/d = 2.75$ , which is also the first measurement location for the Gaussian spike, flow has already reattached behind the elements for all four cases, as also evidenced in the flow visualization pictures.



These profiles show lesser magnitudes of velocity defects as compared to those at the previous location and no defect above three element heights. Further, no wake effect is seen in the velocity profiles at  $x/d$  of 10. At  $x/d = 5$ , while the smallest cylinder shows mild flow acceleration close to the wall, the other elements show considerable flow acceleration as revealed by higher velocities relative to the smooth wall values. The higher speed flow, close to the wall, along the centerline is due to the wallward rush of high momentum fluid, as also shown by the dark scoured out region in the flow visualization pictures. This wallward rush towards the center plane is attributed to – (1) the approach boundary layer deflected over and by the sides of the element converging towards the center plane, and (2) entrained fluid directed towards the wall by the counter-rotating vortices emanating from the top of the roughness elements. All cases show very mild near-wall flow accelerations at  $x/d = 10$  with the exception of the highest cylinder which still shows considerable higher near-wall velocities thus indicating that the vortices generated by this element are stronger than those of the other elements. At further downstream locations, though the profiles tend towards recovery to smooth wall values, the effects of flow acceleration seems to persist even at  $x/d = 40$  as seen in the near-wall regions in the flow past the intermediate and highest cylinders. In all the cases considered, the profiles are seen to be same as that of the undisturbed smooth wall boundary layer in most of the log-law region and into the outer regions.

To gauge the distortion of the streamwise velocity field due to the elements, contours of  $U/U_\tau$  in the  $y^+ - z/d$  plane at  $x/d = 2.75$  and 10 are presented in Figs. 3.3 (a) and 3.3 (b), respectively. At  $x/d = 2.75$ , the disturbances are confined within two diameters in the spanwise direction for all cases except the largest cylinder where its extent is about 2.5 diameters. Further, the contours reveal least perturbations in the case of the smallest cylinder with their extent increasing with the cylinder height. In case of the Gaussian spike, the perturbations are not as spread out as in case of the cylinders but rather the contours show a very narrow region about the centerline where most of the perturbations are seen. At the next downstream location where the  $y - z$  planar data are available,  $x/d = 10$ , the perturbations have waned drastically and only the highest cylinder shows perturbations of some significance and are seen to extend to about 3 diameters in the spanwise direction.

Figure 3.4 (a) shows profiles of wall-normal mean velocity, plotted as  $V/U_\tau$  versus  $yU_\tau/\nu$ . At the first measurement location for the cylinders, peaks of negative velocities are seen in the profiles at or below the element height, with peak values increasing with element height. These high velocities indicate a strong rush of high speed fluid towards the wall in this region of reverse flow. For the Gaussian spike, at its first measurement location, a peak is seen close to the element height at  $x/d = 2.75$ . A same interpretation is made when presenting  $V/U_\tau$  in the form of contours in a  $y^+ - x/d$  plane along the centerline and accompanied by velocity vectors,  $U/U_\tau$  and  $V/U_\tau$ , in Fig. 3.4 (b). For a different view of this transport of fluid towards the wall, contours of  $V/U_\tau$  in the  $y^+ - z/d$  plane are presented for two downstream locations – at  $x/d = 2.75$  [Fig. 3.5 (a)] and  $x/d = 10$  [Fig. 3.5 (b)]. At  $x/d = 2.75$ , the contour plots reveal a convergence of flow towards the center plane with wallward flow velocities decreasing in magnitude with increase in spanwise distance from the center plane. Here too, the highest cylinder shows the largest region of flow convergence followed by the intermediate cylinder, and then by the Gaussian spike with a lesser region of flow convergence albeit similar values of wall-normal velocities and finally, the smallest cylinder showing the least values. In each case, the highest magnitude in the velocities is seen at locations slightly below the element height. Further downstream at  $x/d = 10$ , while the wallward normal component of velocity shows significant values only in the flow behind the highest cylinder and hardly any in that behind the lowest cylinder, while the other cases show only small remnants of fluid flowing towards the wall. Considering the streamwise evolution [Figs. 3.4 (a) and (b)], for all cases, the peaks in the  $V$  profiles become gentler as the flow proceeds downstream. At the penultimate measurement location,  $x/d =$



20, the remnants of fluid onrush towards the wall has all but vanished, except for small values in case of the highest cylinder. At the last measurement location, all flows seem to have nearly recovered to smooth wall values.

Figures 3.6 (a) and (b) depict the spanwise velocities generated in the wake at the streamwise locations of  $x/d = 2.75$  and 10, respectively, as contours of  $W/U_\tau$  in the  $y^+ - z/d$  plane. All four cases show velocities directed towards the center plane in the vicinity of the cylinder's corners or the Gaussian spike's corner, as the case maybe, and as the wall are approached, significant velocities (negative sign) are seen directed away from the center plane. The center plane is also the plane of flow symmetry and hence  $W = 0$ . While the highest cylinder generates the highest magnitudes of negative spanwise velocities and the smallest cylinder the least, the other two cases show in-between peak negative velocities. The intermediate and the highest cylinders show distinct regions of spanwise velocities directed towards the center plane (and hence, velocities of positive sign) that display a maxima located about their corners. These spanwise positive velocities are indicative of the motion of the vortices, emanating from the upstream top corners of the elements, that have induced flow towards the center plane. Still smaller magnitudes of spanwise velocities are seen close to the corners in case of the smallest cylinder and the Gaussian spike indicating vortices of relatively weaker strength. These spanwise velocities are indicative of the mean flow three-dimensionality away from the center plane, with the highest cylinder displaying relatively the largest flow three-dimensionality and the smallest cylinder the least. At the next downstream location where the next planar data are available, i.e., at  $x/d = 10$  [Fig. 3.6 (b)], large regions of negative spanwise velocities are seen up to the element height and across 1.5 to 2 diameters from the center plane. These velocities have diminished in magnitude and can be attributed to the weakened streamwise vortices. Here too, at this location, the highest cylinder shows the strongest evidence of the streamwise vortices, albeit weakened, with higher magnitudes of negative spanwise velocities than the other cases. In the case of the smallest cylinder, considering both  $V$  and  $W$  velocities, very little mean-flow three dimensionality is seen.

### 3.1.3 Derived quantities from the mean flow structure

#### 3.1.3.1 Streamwise vorticity

Since these protuberances generate vortices, each with trailing legs that form a pair of counter-rotating vortices, one can analyze them by means of contours of streamwise mean vorticity,  $\Omega_x (= \partial W / \partial y - \partial V / \partial z)$ . Figures 3.7 (a) and (b) present the contours of the streamwise vorticity,  $\Omega_x$ , normalized by  $U_\tau / \sqrt{A}$  (where  $A$  is the element frontal projected area) along with the secondary velocity vectors,  $V/U_\tau$  and  $W/U_\tau$ , in the  $y^+ - z/d$  plane at  $x/d = 2.75$  and  $x/d = 10$ , respectively.  $\sqrt{A}$  was found to be more appropriate than the diameter ( $d$ ) or height ( $k$ ) or even the frontal wetted area of the element ( $\sqrt{A_w}$ ) as a length scale for the purpose of non-dimensionalizing streamwise vorticity.

In all cases, the vector plots of secondary flow [Fig. 3.7 (a)] reveal a strong wallward rush of fluid curving first towards the center plane and then turning away from it as the wall is approached with the flow being almost parallel to the wall as the flow recedes from the center plane. The secondary flow is attributed to that induced by the vortex pair emanating from the upstream edges of the top of the cylinders or the spike, as the case maybe – the pair being aptly named the roughness top vortex structure (RTVS). At the center plane, the secondary flow is directed normal to the wall indicating symmetry of the secondary flow about this plane. At this location, the center plane convergence is seen mainly in regions in the neighborhood of the cylinder corners (looking axially) or the spike's top sides. Considering the elements individually, the highest magnitudes of secondary flow are seen in the case of the highest cylinder and the lowest magnitudes in the smallest cylinder with the other two cases showing intermediate magnitudes. The spike shows narrower regions of



strong secondary flow at the top sides when compared with the same while considering the cylinder corners. A “+” sign denotes the center of rotation of the secondary flow consider this  $y-z$  plane slice. As flow proceeds downstream,  $x/d = 10$  [Fig. 3.7 (b)], the lowest cylinder does not show any secondary flow directed towards the wall. However, in the case of other elements, flow is directed towards the wall only in the neighborhood of the element height at the center plane and at off-center plane regions. Away from these regions, most of the near-wall regions show secondary flow directed mostly parallel and slightly away from the wall. Also, the magnitudes of the secondary flow decrease, for each of the cases, at this location as compared to the previous location ( $x/d = 2.75$ ).

At the first measurement location,  $x/d = 2.75$ , where the streamwise vorticity values are available, the cases of the cylinders ( $k = 0.38mm$  and  $k = 0.76mm$ ) and the Gaussian spike show clearly demarcated large elliptically shaped regions of positive vorticity. The highest cylinder shows a distortion of the near-wall regions as seen by an even larger area of influence, though with non-elliptical contours. These large regions of positive vorticity extend from a little above the element height to  $y^+ \approx 7$ , and are seen to extend from the center plane to about a diameter in the case of the smallest cylinder, about 1.6 diameters in the case of the highest cylinder, and about 1.3 diameters in the other two cases. Further along the spanwise direction, in each of the cases there exist small near-wall regions ( $y^+ \leq 10$ ) of positive vorticity that display magnitudes comparable to the peak values that are displayed in the large regions. This small near-wall region of positive vorticity is due to the junction horseshoe vortex structure that has formed so close to the wall. Between the large and small regions of positive vorticity is a line of flow separation that extends all the way up to the nose of the elements. Also, at this first location,  $x/d = 2.75$ , very small regions of high negative vorticity are seen close to the wall directly below the large regions of positive vorticity that is associated with the roughness top vortex structure. This negative vorticity is generated by the secondary flow to satisfy the no-slip condition at the wall. Further, all cases reveal small pockets of relatively very weak vorticity of negative sign in the upwash region which can be attributed to the convection of the induced negative vorticity at the wall as the roughness top vortex pair convects downstream. A perspective of the flow structure downstream of the cylinder at  $x/d = 2.75$  is shown in Fig. 3.8 (a) and a similar view holds good for the Gaussian spike too.

Although a true center of the vortex structures has not been determined since the planes of measurements are not perpendicular to their axes, some measure of the vortex position is provided by identifying a center of rotation of the secondary flow induced by the vortex structure and another, a location of the maximum streamwise vorticity ( $\Omega_{x_{max}}$ ). The former location is denoted by a subscript “0”, and the latter by a subscript “c.” Table 3.1 contains the details of the location and magnitude of maximum streamwise vorticity,  $\Omega_{x_{max}}$ , associated with the very near-wall junction horseshoe vortex structure in the measurement plane at  $x/d = 2.75$ . The Gaussian spike does not show a local maximum while displaying the small region of positive vorticity. Table 3.2 provides the location and magnitude of maximum streamwise vorticity,  $\Omega_{x_{max}}$ , associated with the roughness top vortex structure (RTVS), in the measurement planes at  $x/d = 2.75$  and 10. Table 3.3 presents the details of the secondary flow associated with the roughness top vortex structure at  $x/d = 2.75$  and 10. Two new attributes of the roughness top vortex structure (RTVS) are introduced, viz., the streamwise wavelength ( $\lambda$ ) and the circumferential velocity ( $V_\theta$ ), and Appendix A contains the scheme to calculate these values. The information of  $\lambda$ , in conjunction with the details of location and magnitude of  $\Omega_{x_{max}}$  and the details of the secondary flow and its center, are one of the means by which the streamwise progress of the roughness top vortex structure is analyzed.

At the streamwise location of  $x/d = 2.75$ , while the streamwise vorticity contours associated with the RTVS display a maxima at about 12-17 wall units from the wall, the secondary flow



associated with it are centered at about 16-29 units [Fig. 3.7 (a), Tables 3.2 and 3.3]. Both the circumferential velocity,  $V_\theta$ , and the maximum values of the streamwise vorticity,  $(\Omega_x \sqrt{A}/U_\tau)_{\max}$ , increase with the element height in case of the cylinders, while the Gaussian spike displays values in-between those of the smallest and the intermediate cylinder. Also, the streamwise wavelength of this structure indicates that this structure is several tens of diameters long, about 20 to 200 diameters (Table 3.3). As the flow proceeds downstream, at  $x/d = 10$ , in all cases, a drastic decrease in the magnitude of maximum streamwise vorticity occurs [Fig. 3.7 (b) and Table 3.2], and the vortex structure diffuses and is transported away from the wall in both wall-normal and spanwise directions. Table 3.4 provides the wall-normal and spanwise movements of locations of  $\Omega_{x\max}$  and the center of rotation with progress in the streamwise distance. This rapid decay and diffusion of the vortex structure is primarily governed by the gradients of the differences in the normal stresses,  $\frac{\partial^2}{\partial y \partial z}(\overline{v^2} - \overline{w^2})$ , and the gradients of the shear stresses,  $\left(\frac{\partial^2}{\partial y^2} - \frac{\partial^2}{\partial z^2}\right)(-\overline{vw})$  as given by the equation governing the transport of streamwise vorticity (Cutler and Bradshaw, 1993b) which is

$$U \frac{\partial \Omega_x}{\partial x} + V \frac{\partial \Omega_x}{\partial y} + W \frac{\partial \Omega_x}{\partial z} = \Omega_x \frac{\partial U}{\partial x} + \Omega_y \frac{\partial U}{\partial y} + \Omega_z \frac{\partial U}{\partial z} + \left(\frac{\partial^2}{\partial y^2} - \frac{\partial^2}{\partial z^2}\right)(-\overline{vw}) + \frac{\partial^2}{\partial y \partial z}(\overline{v^2} - \overline{w^2}) + \nabla^2 \Omega_x \quad (3.1).$$

The other factors that contribute to the decay of the vortices are the entrainment of the boundary layer fluid and its proximity to the wall where viscous effects dominate. At the downstream location,  $x/d = 10$ , in the case of the lowest cylinder, only remnants of the RTVS is seen, with the structure having almost completely diffused outward into the turbulent boundary layer. Even so, it has a persisting influence as seen by the scoured region along the flow centerline in flow visualization pictures. All cases reveal areas of negative vorticity directly below the RTVS primary vortex with peak values much higher than the peak values of positive vorticity. Also, the peak values of negative vorticity occur very close to the wall. The extent of these regions of negative vorticity is up to  $y^+ \approx 5$  in the case of the smallest cylinder while in the other three cases the extent is up to  $y^+ \approx 15$ . As mentioned previously, the negative vorticity is due to the presence of the secondary flow (mainly the  $W$  velocity component) and the requirement of no-slip condition at the wall leading to significant wall-normal gradients of the  $W$  velocity, i.e.,  $\partial W / \partial y$ . The RTVS in case of the highest cylinder generates the strongest secondary flow which is also reflected in the much higher magnitudes and extent of negative vorticity when compared with the other cases. A perspective of the flow structure downstream of the cylinder at  $x/d = 10$  is shown in Fig. 3.8 (b).

Considering the movement of the RTVS, the vertical transport of the location of  $\Omega_{x\max}$  ( $\Delta y_c^+$ ) and the center of rotation ( $\Delta y_0^+$ ), are about 22-32 wall units and 40-55 wall units, respectively (see Table 3.4). This movement is much more than that afforded by the growth of the turbulent boundary layers and can only be attributed to the diffusion of the vortex structure as governed by equation 3.1. The spanwise movements can be explained using the inviscid theory in that by replacing the wall by an image vortex, the RTVS should move away from the center plane due to velocity induced on it by the image vortex.

### 3.1.3.2 Circulation

The circulation ( $\Gamma$ ) is calculated by integrating the velocity vector along a closed rectangular circuit in the  $y-z$  plane, with the center plane ( $z = 0$ ) and the wall ( $y = 0$ ) as two of the sides, the other sides formed by  $z = \text{constant}$  and  $y = \text{constant}$  lines such that these two sides forming the circuit show no effect of the protuberance in the velocity profiles. To be exact, this rectangular circuit



had a height of 15 mm and 20 mm with the origin at the centerline and the outer edges being  $y = 15 \text{ mm}$  and  $z = -20 \text{ mm}$  (where the velocity profiles were same as the smooth wall profiles). Since along this path of integration  $W$  is essentially zero (zero at the center plane owing to flow symmetry, zero at the wall and nominally zero at the other two paths/edges since the mean flow is two-dimensional), the circulation is essentially dependent on the  $V$ -velocity distribution in the center plane. At the initial locations,  $x/d = 1.36$  and  $2.75$ , the flow field is dominated by the RTVS, with very little secondary flow induced vorticity of opposite sign occurring near the wall and with the presence of a relatively small region of positive vorticity associated with the junction horseshoe vortex structure [Fig. 3.7 (a)]. Hence, the circulation calculated from the path integration is nearly the same as the circulation that drives the RTVS and so the circulation can be termed the vortex circulation too. At further downstream locations, where the RTVS induces vorticity of opposite sign close to the wall [Fig. 3.7 (b)] along with a transport of this negative vorticity to the upwash region, the calculated circulation is still a measure of the circulation around the primary vortex since the wallward velocity, i.e.,  $V$ -velocity distribution in the center plane, is mainly due to the presence of the primary vortex, and also because the region of negative vorticity is relatively small compared to the region of positive vorticity.

The variations of the non-dimensional circulation,  $\Gamma/U_\tau\sqrt{A}$ , enclosing one-half of the flow domain with the length scale,  $U_\tau\sqrt{A}/\nu$ , at a streamwise location,  $x/d = 2.75$ , are presented in Fig. 3.9 (a). The choice of  $\sqrt{A}$  instead of the diameter ( $d$ ) or height ( $k$ ) or  $\sqrt{A_w}$  of the element as a length scale leads to a trend in the variation of circulation. Any of these four scales lead to a trend when only the cylinders are considered; however, the length scales,  $d$ ,  $k$  or  $\sqrt{A_w}$ , do not perform well when the Gaussian spike is included. Considering the individual elements, the creation of circulation, in the one-half domain, is due to the protuberances that generate vorticity under the action of induced pressure gradients. For an incompressible flow over stationary surfaces with a unit vector normal to the surface,  $\vec{e}_n$ , all vorticity ( $\vec{\Omega}$ ) arises at the surface due to the pressure gradients as indicated by the following relationship:

$$\nu \left( \frac{\partial \vec{\Omega}}{\partial n} \right) = -\frac{1}{\rho} (\vec{e}_n \times \nabla p), \quad (3.2)$$

where,  $p$  is the static pressure and  $\vec{\Omega}$  is the vorticity vector. From the values of circulation and vorticity generated by the elements (considering one half of the flow domain), one can imply that the highest cylinder generates the most upstream junction pressure gradients followed by the intermediate cylinder, the Gaussian spike and finally, the lowest cylinder, as corroborated by the magnitude of circulation [Fig. 3.9 (a)] and the extent and magnitude of the streamwise vorticity generated in their wakes [Fig. 3.7 (a) and Table 3.2]. The vortex circulation, since it is the circulation at  $x/d = 2.75$ , when presented as a ratio of circulation to kinematic viscosity,  $\Gamma/\nu$ , almost varies linearly with  $(\sqrt{A})^3$  as shown in Fig. 3.9 (b).

Figure 3.9 (c) presents the streamwise decay of the circulation around one half of the flow domain, as a plot of  $\Gamma/(U_\tau\sqrt{A})$  varying with  $x/d$ . While the intermediate cylinder, the highest cylinder and the Gaussian spike show a sharp decay up to  $x/d = 10$ , for the lowest cylinder, it is only up to  $x/d = 5$ , with all cases displaying a gradual decay at subsequent downstream locations. Curve fits using power functions or exponential functions proved to be unsuccessful in unifying the data on the decay exhibited by the four elements. While the lowest and the intermediate cylinders display negligible circulation at  $x/d = 20$ , the other two cases show circulation persisting even up to  $x/d = 40$ , thus confirming the presence of the RTVS this far downstream. The decay of circulation is primarily due to the near-wall viscous forces – the spanwise component of the wall shear which retards the rotation of the vortices. Another factor contributing to the loss in circulation is due to



viscous diffusion within the vortices since they are present very near the wall where the viscous effects dominate.

It may be borne in mind that the vortices occurring in this study are extremely weak in strength, based on the vortex circulation parameter,  $[\Gamma/(U_e \delta)]$ , (Cutler and Bradshaw, 1986)] and consequently, any assignment of terms of “weak” or “strong” to these vortices would be solely to distinguish them from one another in a relative sense. This parameter, based on their definition, for the present study is presented in Table 3.5. It should be noted that this parameter is a function of the streamwise distance. The values clearly indicate that even the strongest vortex (as in the wake of the highest cylinder), which shows a value of 0.006, is an order of magnitude weaker than the *weak* vortices considered in their study and by this token, the present vortices should fall under the category of *extremely weak* vortices. This also implies that the perturbations, due to these protuberances, that modify the turbulent boundary layer under consideration should then be characterized as *extremely weak* perturbations. It is interesting to note that even vortices having as low a parameter value as 0.0011 (in the case of the lowest cylinder) significantly alter the near-wall structure of the turbulent boundary layers. Another interesting aspect is that the vortex structures generated have dimensions that are of the same order as the quasi streamwise vortices that dominate the near-wall regions of smooth wall boundary layers and hence this study should provide some insight into the near-wall mechanics of the smooth turbulent boundary layers too.

### 3.1.3.3 Helicity

From topological considerations, one can also analyze these flows using the inviscid concept of helicity which has been used in the past to study coherent structures (Hussein, 1986). Moffat (1969) first introduced the concept of helicity ( $H$ ) which is defined as  $H = \iiint_V h d\sigma = \iiint_V \vec{V} \cdot \vec{\Omega} d\sigma$ ,

where  $h$  is the helicity density. The total amount of helicity density remains conserved so long as there are no viscous effects and when there is neither helicity supply nor loss across the flow boundary. Hence, in inviscid flows,  $H$  is an invariant when the helicity density is integrated over a flow domain.

Contours of non-dimensionalized total mean-flow helicity density,  $h$ , at  $x/d = 2.75$  [Fig. 3.10 (a)] show nearly circular regions of positive helicity in all the cases except in the case of the highest cylinder where the contours are distorted, though with a nearly circular inner core. The regions of positive helicity extend from the centerline to about 1.5 diameters in the spanwise direction with the exception of the smallest cylinder where the extent is seen to about 1 diameter only. All cases show maximum levels of positive helicity occurring more or less in the neighborhood of where the maximum level of the streamwise vorticity occurs which is understandable since helicity is a measure of the swirl due to the RTVS. All cases show small regions of negative helicity in the upwash regions due to the convection of induced helicity which was generated to satisfy the no-slip condition at the wall. Here too, the maximum levels of positive helicity are generated by the highest cylinder followed by the intermediate cylinder, the Gaussian spike and finally by the smallest cylinder. As the flow proceeds downstream, at  $x/d = 10$  [Fig. 3.10 (b)], all cases display large areas of positive helicity away from the wall (in the neighborhood of the element height) but with much lower values as compared to the previous station, thus indicating the events of diffusion and dissipation of helicity. Dissipation can only occur by the action of viscosity, the effect of which is considerable as the helical structures generated by the vortices are present so close to the wall. Diffusion of helicity, as mentioned earlier, must be occurring under the action of effects similar to that governing the transport and diffusion of the streamwise vortices (Eq. 3.1).

### 3.1.3.4 Wall shear

To determine wall shear, the friction velocity ( $U_\tau$ ) was calculated from a refined determination of the measurement volume location relative to the wall, obtained by a least squares fit



of the viscous sublayer mean velocity profile,  $Q = C_1 y + C_2 y^4$ , with  $Q = \sqrt{U^2 + W^2}$ , and  $C_1, C_2$  as coefficients. The curve was fit through  $(y, Q)$  of  $(0, 0)$ . Using only the data up to  $y^+ = 9$ , an iterative process was used to maximize the curve fit correlation coefficient by shifting the  $y$  values by  $\Delta y$ . At least 4 points were used to obtain the curve fits. Using the curve fit, the wall shearing stress is given by the following relation:

$$\frac{\tau_w}{\rho} = \nu \left. \frac{\partial Q}{\partial y} \right|_{\text{wall}} = U_\tau^2 = C_1 \nu. \quad (3.3)$$

The wall shear values thus obtained are presented as ratios of local wall shear ( $\tau_w$ ) to the reference BL wall shear ( $\tau_o$ ), along the spanwise directions for the two streamwise locations of  $x/d = 2.75$  and 10 [Fig. 3.11 (a)]. At  $x/d = 2.75$ , the mean streamwise velocity profiles (Fig. 3.2) reveal that the flow has reattached upstream of this location. Due to the mean flow convergence towards the center plane and the ability of the RTVS in entraining outer layer fluid towards the wall [as evidenced by the  $V$  profiles [Figs. 3.4 (a) and (b)], and the secondary flow patterns [Fig. 3.7 (a)], the regions directly downstream of the element up to  $z/d \approx -0.55$  show an increased wall shear relative to the smooth wall value. However, this is not so in the cases of the lowest cylinder and the Gaussian spike at the centerline where lower wall shear relative to the reference BL value is seen. At the centerline, tracer particle deposits in wakes of the lowest cylinder and the Gaussian spike at  $x/d = 2.75$  support the findings of lower wall shear. Away from the centerline and beyond  $z/d \approx -0.55$ , in all cases this ratio reaches a minimum and then gradually increases to a value of 1 as the edge of the wake is approached where the wall shear attains to smooth wall values. The lowering of wall shear relative to the reference BL value is a consequence of the secondary flow, due to the RTVS, being directed away from the wall, and the decrease in the wall shear is proportional to the magnitude of the secondary flow. As the effect of the secondary flow (which is dependant on the strength of the RTVS) relaxes, the wall shear gradually approaches smooth wall values towards the wake edge.

The flows gain near-wall momentum with downstream distance with the continual dumping of high-speed fluid towards the wall by the streamwise vortices. Proceeding downstream, at  $x/d = 10$ , even though the strength of the RTVS is waning with distance, the wallward rush of fluid due to it results in higher wall shear relative to the reference BL values [Fig. 3.11 (a)]. In general, each flow case shows a dip in the wall shear profile at the centerline, a peak at slightly off-center locations, and then a tapering off towards smooth wall values at the edge of the wake. The regions close to the center where the wall shear values increase from the “dip” are locations where the secondary flow, of some magnitude, is almost parallel to the wall. At span-wise distances further away from the centerline where the wall shear approaches smooth wall values, the secondary flow has decreased even further in magnitude due to the movement of the RTVS away from the wall as well as away from the centerline. The “dip” at the centerline can be attributed to the fact that this is also the center plane or the plane of flow symmetry and wallward flow diverges away from the center plane, especially as the wall is approached. In the neighborhood of the centerline, considering the four cases, the Gaussian spike shows least wall shear as compared to those for the other cases. This result is also supported by the oil flow visualization pictures where the wake of the Gaussian spike shows the least scoured region.

Considering the streamwise development of wall shear, Fig. 3.11 (b) presents the centerline variation of this ratio,  $\tau_w/\tau_o$ , with  $x/d$ . The location of  $x/d = 2.75$  is the first location where the wall shear for all the cases is available and this location is just aft of the flow reattachment. As the flow proceeds downstream, higher velocities occur close to the wall relative to the smooth wall values as this region is the “common flow down” region between the two counter-rotating primary vortices. The wall shear increases from that of the previous location to a maximum at  $x/d = 5$  (intermediate cylinder and Gaussian spike) and at  $x/d = 10$  (lowest and highest cylinder). Again, the increase in wall shear is a measure of the strength of the streamwise vortices in entraining the high speed outer



layer fluid towards the wall. As the flow proceeds, all cases show increased wall shear relative to the reference BL. However, there is an exception in the case of the lowest cylinder at the downstream locations ( $x/d=20$  and  $40$ ). For added confidence, values of this ratio ( $\tau_w/\tau_o$ ) at locations slightly off-center at these two  $x/d$  locations are shown in Table 3.6. The occurrence of lower wall shear warrants comparison of the present set of experiments with those conducted by Fontaine and Deutsch (1996) in the flow field downstream of the Gaussian spike, approximately  $k^+=16$ . They obtained reduced skin friction downstream of the reattachment point which extended up to 180 wall units which is markedly different from that in the present study where lower skin friction is seen just at one location ( $x/d=2.75$ ) aft of reattachment, as seen in the cases of the lowest and the highest cylinder and the Gaussian spike, and in the aforementioned case of the lowest cylinder at far downstream locations ( $x/d=20$  and  $40$ ). This indicates a de-correlation of the near-wall structure at these downstream locations. Please note that  $d$  has been used to normalize  $x$  and  $z$  distances only to bring a commonality in locations for the purpose of discussion and should not be construed as the only form of scaling.

### 3.1.3.5 Drag

The total drag for these four protuberances was calculated by considering the undisturbed boundary layer upstream of the element and the wake boundary layers at various locations spanning from the centerline up to and beyond the wake edge at the constant streamwise location of  $x/d = 2.75$ . Appendix B contains a complete derivation of the expression for the drag coefficient. The drag is presented as a drag coefficient and is composed of a form drag component and a skin friction component, i.e.,

$$C_d = C_{d,form} + C_{d,skin} \quad (3.4)$$

where,

$$C_{d,form} = \frac{2\rho \int_0^{y_{top}} \int_{-z_u}^{-z_u} \left\{ \left( U(y) \Big|_{z=-z_u} - U(y,z) \right) \left( U(y) \Big|_{z=-z_u} + U(y,z) - U(y_{top}) \Big|_{z=-z_u} \right) \left( \overline{u_2^2}(y) \Big|_{z=-z_u} - \overline{u_2^2}(y) \right) \right\} dy dz}{\frac{1}{2} \rho U_e^2 A}$$

$$\text{and } C_{d,skin} = \frac{-[C_{f,outer} (\frac{1}{2} \rho U_e^2) A_{outer} + C_{f,inner} (\frac{1}{2} \rho U_e^2) A_{inner}]}{\frac{1}{2} \rho U_e^2 A}.$$

The expression for  $C_{d,form}$  was evaluated at the streamwise location of  $x/d = 2.75$ .  $C_{f,inner}$  is the average skin friction coefficient in a triangular section aft of the element such that base of this section is the element diameter and the apex is at  $x/d = 2.75$ . Further,  $A_{inner}$  is the area of this triangular section which is directly influenced by the element wake.  $A_{outer}$  is the area of rest of the control volume (CV1) floor, aft of the element axis, where the wake effects are not present. See Appendix section B.2.  $\frac{1}{2} \rho U_e^2$  is the free-stream dynamic pressure and  $A$  is the projected frontal area of the element.

In the evaluation of the expression for  $C_{d,form}$ ,  $y_{top} = 7k$  for the smallest cylinder,  $4.5k$  for the intermediate cylinder and  $3k$  for the highest cylinder and the Gaussian spike, and  $z_u = 4d$  for all the four elements. This expression ignores the contribution by the pressure term to the form drag, which is assumed to be negligible for the control volume used in the analysis. The oil flow visualization pictures seem to indicate a pressure recovery prior to this streamwise location for all the cases, and therefore, support this assumption. For the flow field downstream of a cube, Martinuzzi and Tropea (1993) presented plots of pressure coefficient along the centerline that reveal a full recovery at  $x/H$  ( $x/w$ )  $\approx 2.25$ . Thus, if a cube with similar aspect ratio as the present cylinders, though with pointed edges, shows pressure recovery within a certain distance, then the pressure around the cylinders should



recover at a shorter distance. This conclusion supports the validity for neglecting the pressure term contribution for the selected control volume.

Figure 3.12 presents the drag coefficients normalized by the reference BL skin friction coefficient,  $C_d/C_f$ , as a variation with  $U_\tau \sqrt{A}/\nu$  for the three cylinders and the Gaussian spike. When the drag coefficient was plotted considering the four non-dimensionalized lengths ( $\sqrt{A}^+$ ,  $\sqrt{A_w}^+$ ,  $k^+$ , and  $d^+$ ) separately as abscissa, only the plot using  $\sqrt{A}^+$  showed a trend when all the four elements were considered together. The plots reveal that the form drag is dependent on the area facing the flow with the highest cylinder creating the most drag and the lowest cylinder the least drag, results that are rather obvious. This data set is the first reported experiment on drag due to such small protuberances (the lowest cylinder of height even submerged within the buffer layer). If the drag coefficient is defined by substituting the denominator with the frontal dynamic pressure facing the element, as was done by Wieghardt (1946), instead of the free-stream dynamic pressure, then the coefficients obtained are in the neighborhood of those obtained in the experiments conducted on short circular cylinders by Wieghardt (1946). However, his  $k/\delta$  values were much larger than the ones used in the present study.

### 3.1.4 Turbulence structure

#### 3.1.4.1 Streamwise Reynolds normal stress, $\overline{u^2}$

One of the ways to study the turbulence structure is by examining the Reynolds stress field downstream of the elements. Figure 3.13 (a) shows the contour plots of the streamwise Reynolds normal stresses,  $\overline{u^2}/U_\tau^2$ , in the  $y^+ - z/d$  plane at the streamwise location,  $x/d = 2.75$ . All the four flows reveal a region of high magnitudes in the neighborhood of the element height connected to a clear core, of still higher magnitude of stresses, centered beyond the edge of the elements (as seen in this elevated view). This core of high stresses is due to the flow past the top and sides of the elements that has been reorganized by the roughness top vortex structure (RTVS). Here too, the magnitude of the stresses in the core is directly dependent on the strength and extent of the RTVS in these flows which is in turn related to the size of the element. Further downstream, at  $x/d = 10$  [Fig. 3.13 (b)], the effect of the streamwise vortices has drastically reduced and the profiles closely resemble smooth wall profiles, though with slightly elevated levels, except for the center plane where a reduction in the magnitude of the normal stresses is seen in region,  $y^+ \sim 10-20$ , relative to those in the neighborhood at the same  $y^+$  locations. The reduction is attributed to the near-wall flow acceleration along the center plane that leads to the suppression of the axial turbulence levels. It may be noted that there is not much augmentation in the peak levels at either plane over that which is seen in the near-wall regions in a smooth-wall TBL.

Considering the streamwise development of the normal stresses along the centerline, profiles of the normal stress,  $\overline{u^2}/U_\tau^2$ , are shown varying with  $yU_\tau/\nu$  at various streamwise locations,  $x/d$ , in Fig. 3.14. The peak stress levels are considerably enhanced by the confluence of the flow past the tops of the elements in the neighborhood of the center plane at the very first location,  $x/d=1.36$ , with peaks occurring at or below the element height. The peaks at or below the element height decay with streamwise distance so much so that by  $x/d=40$  there is no perceptible trace of roughness element effects.



### 3.1.4.2 Wall-normal Reynolds normal stress, $\overline{v^2}$

Contours of wall-normal Reynolds normal stresses,  $\overline{v^2}/U_\tau^2$ , in the  $y^+ - z/d$  plane at the streamwise location,  $x/d = 2.75$ , are shown in Fig. 3.15 (a). A clear core of high stresses is seen about the center plane with its maxima located below the element height in all the cases except the smallest cylinder where the maximum is centered slightly above the element height. The high stresses are due to the intense mixing of the shear layers – forced from the sides and the top of the elements – converging towards the center plane. It is well known that separated shear layers are sources of high turbulence and large-scale flow unsteadiness (Simpson, 1996). Further, the center plane convergence is accentuated by the counter-rotating roughness top vortex pair. As regards the magnitude of  $\overline{v^2}$  stresses and its extent, most effects are seen in the wake of the highest cylinder and the least effects in the case of the smallest cylinder with the other two cases displaying intermediate effects. The peak values seen, at the center plane, in all the cases seem to correlate with the location of the maximum velocity gradient ( $\partial V/\partial y$ ) since the term  $\overline{v^2}(\partial V/\partial y)$  is a dominant term in the contribution towards the production of  $\overline{v^2}$ . At the downstream station,  $x/d = 10$  [Fig. 3.15 (b)], as the RTVS moves away from the center plane and the wall, the secondary flow induced by it wraps the shear layers containing high stresses away from the center plane, slightly upwards where a core of high stress levels is seen, relative to adjacent locations. The peak stress levels are, however, considerably lower than those at the previous location,  $x/d = 2.75$  but the extent of the stresses is larger. There are also regions of high stresses in the neighborhood of the element height (except in the case of smallest cylinder) which are maintained by the transport of turbulence towards the center plane by the RTVS, even as it is convected away from the center plane and wall (Tables 3.2 and 3.3). As regards the new core, the reduction in the magnitude of stresses can be attributed to the diffusion of turbulence by the vortices so much so that in the case of the smallest element there is hardly any trace stress levels higher than that seen in smooth wall BL, although the stress levels in this case were already quite small to begin with (at  $x/d = 2.75$ , when compared to the other cases).

Considering the streamwise development of the normal stresses, profiles of  $\overline{v^2}/U_\tau^2$  are shown varying with  $yU_\tau/\nu$  at various streamwise locations,  $x/d$ , in Fig. 3.16. At the first measurement location of  $x/d = 1.36$ , peaks are seen slightly below the element height in case of the cylinders. The peak levels in the cases of the intermediate and the highest cylinders are, respectively, about 4 and 5 times of that seen in the case of the smallest cylinder. In the case of the former cylinders, the peaks are located where the back flow meets the separated shear layers that have emanated from the top, while in the latter case of the smallest cylinder the peak is at the forward flow region where the shear layers over the top and sides of it converge. At  $x/d = 2.75$ , the peaks become smaller and are located further below the element height (when compared to that for the previous location) as the streamwise vortices (RTVS) transport turbulence away from the center plane through turbulent diffusion. As flow proceeds downstream, the peak levels decay rapidly although these levels are still much higher than those for the smooth wall BL ( $x/d = 5$ ). At  $x/d = 10$ , some detectable enhanced stress levels (relative to those for the smooth wall) are still seen in the neighborhood of the element height in all cases except that of the smallest cylinder. At further downstream locations of  $x/d = 20$  and 40, no roughness effect is seen in the  $\overline{v^2}$  profiles, indicating a complete diffusion of the high stresses that were generated far upstream, and also to some extent demonstrating the absence of turbulent transport towards the center plane by the already weakened streamwise vortices.



### 3.1.4.3 Spanwise Reynolds normal stress, $\overline{w^2}$

The behavior of the spanwise normal stresses,  $\overline{w^2}$ , is very similar to that of the  $\overline{v^2}$  stresses. A core of high stresses is also seen with maximum levels located below the element heights at  $x/d = 2.75$  as seen in the contour plots of  $\overline{w^2}/U_\tau^2$ , in the  $y^+ - z/d$  plane [Fig. 3.17 (a)]. These high stresses  $\overline{w^2}$  are generated by the same mechanisms that are responsible for the generation of high  $\overline{v^2}$  stresses – the confluence of shear layers, forced over and around the elements, that was induced towards center plane by the RTVS. Discussions pertaining to the behavior of the  $\overline{v^2}$  stresses hold good in this case too. At the next downstream location of  $x/d = 10$  [Fig. 3.17 (b)], the secondary flow due to the RTVS transports turbulent fluctuations away from the center plane similar to the behavior exhibited by the  $\overline{v^2}$  stresses. The maximum stress levels are much smaller than those at the previous station ( $x/d = 2.75$ ) owing to diffusion and dissipation. Although, both  $\overline{v^2}$  and  $\overline{w^2}$  stresses are influenced by the same mechanisms, the extent and magnitude of  $\overline{w^2}$  are slightly more than that for the  $\overline{v^2}$ , as spanwise fluctuations are uninhibited by the wall.

To examine the streamwise development along the center plane, profiles of  $\overline{w^2}/U_\tau^2$  are shown varying with  $yU_\tau/\nu$  at various streamwise locations,  $x/d$ , in Fig. 3.18. In the case of cylinders, at the very first measurement location ( $x/d = 1.36$ ), peak levels showing large enhancement (over those of smooth wall BL) are seen below the element heights. The highest cylinder shows an almost constant region of high stresses in the near-wall region ( $y^+ < 40$ ) which is a region that shows reverse flow (Fig. 3.2). Similar to the streamwise development of the  $\overline{v^2}$  stresses, at  $x/d = 2.75$ , the peaks in  $\overline{w^2}$  stresses become gentler and decrease in magnitude. Also, the intermediate cylinder and the Gaussian spike exhibit about the same peak levels. The peak intensities decay with distance and only small enhanced levels are seen in all cases at the element heights. A full recovery to smooth wall BL values is seen by  $x/d = 20$ .

Comparing the effects of the elements on the normal stresses flow field – the perturbation effects of the elements were more pronounced on the  $\overline{v^2}$  and  $\overline{w^2}$  stresses when compared with those on the  $\overline{u^2}$  stresses as regards the enhancement and extent of the stress levels – the reason being that the secondary flow induced by the streamwise vortices are more efficient in the transport of the wall-normal and the spanwise fluctuations than the streamwise fluctuations. Also, wall-normal and spanwise fluctuations are directly created by the rotational motion of the roughness top vortex pair.

### 3.1.4.4 Streamwise Reynolds shear stress, $-\overline{uv}$

Figures 3.19 (a) and (b) depict the streamwise Reynolds shear stresses in the wake at the streamwise locations of  $x/d = 2.75$  and 10, respectively, as contours of  $-\overline{uv}/U_\tau^2$  in the  $y^+ - z/d$  plane. The combinations of converging mean flow and the secondary flow (induced by the roughness top vortex pair) cause high  $v$  fluctuations that correlate with  $u$  fluctuations to generate large shearing stresses. In each case, a core of high shear stress levels are seen in the neighborhood of the element height formed by the merging of the separated shear layers emanated from the top of the elements and also to some extent by the transport of turbulence by the vortex induced cross flow. This is the same mechanism that is responsible for the generation of high magnitudes of  $\overline{v^2}$  and  $\overline{w^2}$  stresses at the same location. The core of high shear stresses can also be attributed to the elevated values of  $\overline{v^2}$  and



large streamwise velocity gradients leading to enhanced  $\overline{v^2} \frac{\partial U}{\partial y}$  and to a much smaller extent to

another production term,  $-\overline{uv} \frac{\partial V}{\partial y}$ . The spanwise regions of stress levels away from the center plane,

of relatively higher levels than rest of the BL, are maintained primarily by the turbulence transported by the secondary flow. Here too, the highest cylinder exhibits the largest extent and magnitude of stress levels and the smallest cylinder the least, with the other two cases exhibiting intermediate effects. With the advance in streamwise distance, at  $x/d = 10$  [Fig. 3.19 (b)], some of the high shear stress carrying fluid behind the element are convected in the spanwise direction (away from the center plane and slightly upwards) by the cross flow. These shear layers form a new core containing high levels of shear stresses with the core centered about a diameter to a diameter and a half from the center plane. Further, the center of the core is located above the element height in case of the smallest and the intermediate cylinder and for the other two cases the center is located slightly below the element height. In each of the four cases, the location of the centers can be attributed to the mobility of the RTVS (Tables 3.2 and 3.3) as it convects downstream while inducing cross flow that transports turbulence in all directions. The large scale unsteadiness of the RTVS itself is a minor factor in this transport. The growth of this core of shear layers, albeit with reduced levels, can also be attributed to the diffusion and re-distribution of shear stresses as the vortices entrain fluid. At this location too, the largest extent and the highest magnitudes are observed downstream of the highest cylinder and the least extent and magnitude by the smallest cylinder, with the other two cases displaying intermediate behavior.

The streamwise development of these stresses is examined by considering the variations of  $-\overline{uv}/U_\tau^2$  with  $yU_\tau/\nu$  along the centerline at various streamwise locations,  $x/d$ , which are presented in Fig. 3.20. In order to obtain a better understanding of the motions that contribute to the shear stresses,  $-\overline{uv}$ , a quadrant analysis was performed. Details on motions that contribute to its generation are presented in Figs. 3.21 (a)-(f) for the six streamwise locations,  $x/d = 1.36, 2.75, 5, 10, 20$  and  $40$ , respectively, as profiles varying with  $yU_\tau/\nu$ . The values obtained in each of the four quadrants are normalized using the 2-D smooth wall BL total shear stress,  $-\overline{uv}_{\text{smooth}}$ , at the corresponding  $y^+$ . This permits a direct comparison between the different cases.

Large stress levels are generated downstream of the element at the very first measurement location,  $x/d = 1.36$ , as seen by the large peaks located below the element height in the case of cylinders. The quadrant contributions [Fig. 3.21 (a)] reveal that they are severely affected by the presence of the elements which is seen up to 3 times the element height in each of the cases. Contributions to quadrant-2 and quadrant-4 are termed “ejection” and “sweep” motions, while the other two quadrant motions are termed interactions. Further, ejection motions have negative  $u$  and positive  $v$  events while sweep motions have positive  $u$  and negative  $v$  events. Results at  $x/d = 1.36$  also indicate that ejection and sweep events have been much enhanced in each of the cases when compared with those for the 2-D smooth wall BL. Interaction events are enhanced too, but not to the same extent. In order to compare the relative magnitudes of the sweep and ejection events, a ratio of sweep to ejections is plotted as varying with  $yU_\tau/\nu$  for each of the elements at the six streamwise locations and is presented in Fig. 3.21 (g). While both of these events overwhelm the interaction events in the production of the shear stress, it is the sweeping motions that dominate ejection events in the near wall regions all the way up to the neighborhood of the element height whence the roles are reversed in that the ejection events occur more frequently than the sweeping events. This continues through the boundary layers and into the outer region as well. These motions are attributed to the RTVS as it convects downstream. Similar behavior is seen at the downstream locations of  $x/d = 2.75$ , though the peak levels in both sweep and ejections are much reduced [Fig. 3.21 (b)], leading to



lower total shear stresses (Fig. 3.20). There is an exception, however, in the case of the highest cylinder at the very near-wall region where the sweeping motions peak since this happens to be the location immediately aft of flow reattachment. Further downstream at  $x/d = 5$ , in all cases, both contributions by sweeps and ejections decrease [Fig. 3.21 (c)] leading to gentler peaks in the total shear stress' levels (Fig. 3.20) with less enhancement over those for the smooth wall BL. Again the peaks in the total shear stresses occur below the element heights. Also, the regions where sweeps dominate ejections are limited to lesser distances from the wall. This statement holds good for further downstream stations too. Similar behavior is noted when the contributions, normalized by  $U_\tau^2$ , are presented [Fig. 3.21 (h)-(m)].

In all cases, the shear stress levels continue to decay with streamwise distance and at  $x/d = 10$ ; only slight enhanced levels (over those for the smooth wall BL) are seen in the case of the Gaussian spike, the intermediate and the highest cylinders. At further downstream stations,  $x/d = 20$  and 40, flow seems to have recovered to 2-D smooth wall values. The decay of stress levels seems to indicate a weakening of the streamwise vortices. A closer examination of the quadrant contributions reveal that at  $x/d = 10$  and beyond [Figs. 3.21 (d)-(f)], both sweeps and ejections seem to be suppressed when compared to the 2-D smooth wall levels at regions very close to the wall,  $y^+ < 7$ . In case of the smallest cylinder this decrement is seen even upstream at  $x/d = 5$ . However, only in the case of the smallest cylinder is there a net reduction in shear stress levels is seen very close to the wall at  $x/d = 20$  and 40 (Fig. 3.22). One of the motivations to conduct a quadrant analysis was to investigate the unusual phenomena of lower wall shear at the far downstream locations of  $x/d$  of 20 and 40, in the case of the smallest element [Fig. 3.11 (b)]. Fontaine and Deutsch (1996) found lower shear stresses and lower wall shear, relative to the smooth wall BL values, in the near downstream flow behind a Gaussian spike. They attributed this behavior to the suppression of the ejection and sweep events. This also seems to be the only plausible explanation in the case of the smallest cylinder.

To examine further the correlation between the  $u$  and  $v$  fluctuations, Fig. 3.23 presents the Reynolds streamwise shearing stress coefficient,  $R_{uv}$ , varying with  $yU_\tau/\nu$  at the six streamwise

locations, where,  $R_{uv} = \frac{-\overline{uv}}{\sqrt{\overline{u^2}}\sqrt{\overline{v^2}}}$ . In general, in the outer layers, this correlation shows a constant

value of 0.36. However, at regions in the neighborhood of the element height, high correlation coefficients are obtained at the first two streamwise locations. This indicates a strong correlation between the  $u$  and  $v$  fluctuations which, again, is attributed to the turbulent motions generated by the elements. At the next station,  $x/d = 5$ , a decay in peak values is observed. At subsequent downstream stations, the correlation coefficients relax to those exhibited by the smooth-wall TBL.

### 3.1.4.5 Reynolds shear stresses, $-\overline{uw}$ and $-\overline{vw}$

Figures 3.24 (a) and (b) present the contours of Reynolds shear stresses,  $-\overline{uw}/U_\tau^2$ , in the  $y^+ - z/d$  plane at the two streamwise locations of  $x/d = 2.75$  and 10, respectively. At  $x/d = 2.75$ , a clear core of negative values are seen off the center plane in all the cases with maxima located off-center in the cases of the lowest and intermediate cylinder and off the sides (in the elevated view) for the other two elements. The maximum values generated are comparable to those generated in the  $-\overline{uv}$  stresses. These stresses generated are in the downwash regions where the RTVS induces spanwise fluctuations ( $w$ ) that correlate strongly with the streamwise fluctuations ( $u$ ). A very small portion of these stresses can also be attributed to the meandering of the vortices off the center plane. The extent and magnitude of  $-\overline{uw}$  is also a measure of the flow three-dimensionality, with the largest three-dimensionality seen in the case of the highest cylinder, followed by the Gaussian spike. As flow



proceeds downstream, at  $x/d = 10$ , the effect of the vortex wanes and as it convects downstream, the regions of negative stresses move away from the center plane and flow becomes less three-dimensional [Fig. 3.24 (b)]. Closer to the center plane, a core of positive stresses is seen.

Figures 3.25 (a) and (b) present the contours of Reynolds shear stresses,  $-\overline{vw}/U_\tau^2$ , in the  $y^+ - z/d$  plane at the two streamwise locations of  $x/d = 2.75$  and 10, respectively. The cross flow gradients of this stress appear in the streamwise vorticity transport equation and control the diffusion of the vorticity. At  $x/d = 2.75$ , significant stresses are seen away from the center plane caused by the motions induced by the RTVS. The maximum values are lower than that for both  $-\overline{uv}$  and  $-\overline{uw}$  stresses. With progress in the downstream distance,  $x/d = 10$ , only the highest cylinder shows tangible levels of this stress away from the center plane and at the element height, further confirming the weakening of the RTVS as it convects downstream [Fig. 3.25 (b)].

In general, the relative magnitudes exhibited by the normal stresses are in the hierarchy of  $\overline{u^2} > \overline{w^2} > \overline{v^2}$  which is same as that observed in smooth-wall TBL. As regards the location of their peak values, all three stresses display their maximum magnitudes just below the element heights and along the centerline. Similar behavior is observed in the case of  $-\overline{uv}$  too. However, in the cases of  $-\overline{uw}$  and  $-\overline{vw}$ , these values are zero at the centerline due to flow symmetry. Significant amounts of these stresses, of the same order as the  $-\overline{uv}$  stress, are generated at slightly off-center locations as the vortex pair transports turbulent fluctuations from the center plane as it convects downstream.

### 3.1.4.6 Turbulent kinetic energy (TKE)

The study has shown that the separated shear layers emanating from the top of the elements convect downstream as a vortex pair that increases the turbulence levels in the downwash region by perpetually bringing  $v$  and  $w$  fluctuations. Hence, it is worthwhile to analyze the downstream field further by looking at the behavior of the turbulent kinetic energy (TKE),  $\frac{1}{2}\overline{q^2}$ , which is equal to  $\frac{1}{2}(\overline{u^2} + \overline{v^2} + \overline{w^2})$ . Contours of TKE are presented in the same two planes as in the cases of the Reynolds stresses. Figures 3.26 (a) and (b) present the contours of TKE,  $\frac{1}{2}\overline{q^2}/U_\tau^2$ , along with diffusion velocity vectors  $V_q/U_\tau$  and  $W_q/U_\tau$  in the  $y^+ - z/d$  plane at the two streamwise locations of  $x/d = 2.75$  and 10, respectively, where,  $V_q = \overline{vq^2}/\overline{q^2}$  and  $W_q = \overline{wq^2}/\overline{q^2}$ . At the first measurement plane, very high energy levels are generated at and below the element heights, in the downwash regions due to the motions induced by the RTVS. The merging of shear layers, forced over and around the elements, at the center plane also contributes to the generation of high TKE levels. Clear cores of high levels are located in the center plane with a maxima at  $y^+$  of about 28, 36, 44 and 56 for the cases of the cylinders,  $k^+ = 23, 46, 92$  and the Gaussian spike,  $k^+ = 92$ , respectively [Fig. 3.26 (a)]. The corresponding peak TKE  $(\frac{1}{2}\overline{q^2}/U_\tau^2)$  levels for the four cases are 7.5, 10.7, 15.6, and 11.3. In the case of the smallest cylinder ( $k^+ = 23$ ), the peak is above the element height due to the merging of the shear layers that were forced over the top rather than that forced around the sides. In general, the TKE diffuses outwards, in a radial manner, from locations of the maxima down its gradients. Although the vectors are not normal to the contours, the gradient diffusion models could still roughly give the direction of the diffusion of TKE. Close to a distance of about half the element width from the center plane, as regards the highest cylinder and the Gaussian spike, and to a lesser distance as regards the other two elements, large transport velocities are seen that indicate the outer edges of the RTVS which is responsible for it. Here, the “bluntness” factor of the cylindrical elements is seen in the even spread of diffusion as opposed to the “clustered” diffusion in the neighborhood of the spike top as seen in a more “peaky” element, factors that relate to the shape of the element. This “peaky” nature of the



Gaussian spike is also responsible for diffusion velocities that surpasses even those created by the highest cylinder although the region of influence is smaller.

With the progress in streamwise distance (at  $x/d = 10$ ), the RTVS diffuses the core of high TKE levels away from the center plane and a larger region of elevated levels is seen when compared with that for the previous location although with much lower magnitudes. These large regions of elevated levels (when compared to the surrounding boundary layer fluid) extend from  $y^+ \approx 10$  to beyond the element heights. The diffusion still does take place from regions of maximum TKE and directed outward although their rates are drastically reduced as seen by the very low diffusion velocities. The streamwise development of TKE is also presented in Fig 3.27 (a) as variations of  $(\overline{u^2}/U_\tau^2)$  with  $yU_\tau/\nu$  along the centerline at various streamwise locations,  $x/d$ . The same development is also presented by means of contours in the  $y^+ - x/d$  plane along the centerline and accompanied by diffusion velocity vectors,  $U_q/U_\tau$  and  $V_q/U_\tau$  [Fig 3.27 (b)], where  $U_q = \overline{uq^2}/\overline{q^2}$ . At the first measurement location of  $x/d = 1.36$ , peaks of TKE are seen at the element height in the case of the smallest cylinder and below the element heights in the cases of the other two cylinders [Fig 3.27 (a)]. At this location, large diffusion of TKE takes place from this peak location in the outward direction, with large diffusion velocities directed downward below this location and directed upward, even towards the element top, above it [Fig 3.27 (b)]. This behavior is consistent with the sweeping motions below the element height and ejection motions in the neighborhood of the element height – motions that are induced by the RTVS. With increase in distance [Fig 3.27 (a)], the peaks are located further below the element heights and the peak TKE levels decay so much so that by  $x/d = 10$ , very slight elevated levels over that for the smooth wall BL is only seen in the cases of the highest cylinder and the Gaussian spike. Further downstream, the levels show a recovery towards those for the smooth wall BL. Meanwhile, the diffusion velocities decay severely with distance and at further downstream locations, only the near-wall regions exhibit significant diffusion velocities which of course is expected from the near-wall regions of a boundary layer and is not due to the RTVS.

For a better understanding of the mechanisms that contribute to the generation of the high TKE levels and its locations thereof, the production rate term ( $PR$ ) of TKE is evaluated from the measured data. The  $-\overline{uv}(\partial U/\partial y)$  is the dominant term in the contribution to the production ( $PR$ ). Contours of  $PR$ , normalized by  $\nu/U_\tau^4$ , along the  $y^+ - z/d$  at the two streamwise locations,  $x/d = 2.75$  and 10, and along the  $y^+ - x/d$  plane at the centerline are presented in Figs. 3.28 (a), (b) and (c), respectively. At the first  $y - z$  plane at  $x/d = 2.75$ , high levels of  $PR$  are seen at and below the element heights for all the cases. These regions coincide with regions where high TKE levels are seen and also high  $PR$  regions translate to high TKE levels downstream. Again, the highest cylinder shows the largest  $PR$  levels leading to the most TKE levels as well. With the progress in streamwise distance [Figs. 3.28 (b)], the  $PR$  levels decay leading to lower TKE levels and here too there is a one to one correspondence as to where significant  $PR$  is seen, it has led to significant TKE levels. A better understanding of the relative distance between peak  $PR$  location and the peak TKE locations can be had from Fig. 3.28 (c) where peak TKE levels are seen just aft of peak  $PR$  regions. This indicates the turbulent diffusion occurs that leads to the distribution of TKE from regions where it is produced. For a detailed understanding of the production and redistribution of TKE, a term by term evaluation of the various terms in the transport-rate equations for the TKE was carried out, for the different streamwise locations, and is described in the next section



### 3.1.4.6.1 Transport-rate budget of turbulent kinetic energy (TKE)

The transport-rate equation for the TKE is as follows:

$$\begin{aligned}
 \underbrace{U \frac{\partial (\frac{1}{2} \overline{q^2})}{\partial x} + V \frac{\partial (\frac{1}{2} \overline{q^2})}{\partial y} + W \frac{\partial (\frac{1}{2} \overline{q^2})}{\partial z}}_{\text{Convection (C)}} = & \underbrace{- \left[ \overline{u^2} \frac{\partial U}{\partial x} + \overline{v^2} \frac{\partial V}{\partial y} + \overline{w^2} \frac{\partial W}{\partial z} + \overline{uv} \left( \frac{\partial V}{\partial x} + \frac{\partial U}{\partial y} \right) + \overline{uw} \left( \frac{\partial W}{\partial x} + \frac{\partial U}{\partial z} \right) + \overline{vw} \left( \frac{\partial W}{\partial y} + \frac{\partial V}{\partial z} \right) \right]}_{\text{Production (PR)}} \\
 & - \underbrace{\left[ \frac{\partial}{\partial x} \left( \frac{\overline{uq^2}}{2} \right) + \frac{\partial}{\partial y} \left( \frac{\overline{vq^2}}{2} \right) + \frac{\partial}{\partial z} \left( \frac{\overline{wq^2}}{2} \right) \right]}_{\text{Turbulent Diffusion (TD)}} - \underbrace{\left( \frac{\partial}{\partial x} \frac{\overline{up'}}{\rho} + \frac{\partial}{\partial y} \frac{\overline{vp'}}{\rho} + \frac{\partial}{\partial z} \frac{\overline{wp'}}{\rho} \right)}_{\text{Pressure Diffusion (PD)}} \\
 & + \underbrace{\nu \nabla^2 \left( \frac{1}{2} \overline{q^2} \right)}_{\text{Viscous Diffusion (VD)}} - \underbrace{\nu \frac{\partial u_i}{\partial x_i} \frac{\partial u_i}{\partial x_i}}_{\text{Dissipation } (\epsilon)}
 \end{aligned} \tag{3.5}$$

All the velocity fluctuation terms are point dependent except pressure diffusion (PD) which is a function of space. From the measurements, calculations of the convection (C), production (PR), turbulent diffusion (TD) and the viscous diffusion (VD) terms are straightforward. The pressure-diffusion term is estimated using Lumley's approximation (Lumley, 1978). Then the dissipation rate ( $\epsilon$ ) of TKE is extracted by balancing the TKE equation. More details on the calculation of various terms are presented in section 4.1.4.1.1.

For the sake of comparison, the transport-rate budget carried out by Ölçmen and Simpson (1996) for the same 2-D smooth wall is shown in Fig. 3.29 which presents the variation of transport-rate budget of TKE,  $\overline{q^2}/2$ , normalized by  $U_\tau^4/\nu$ , with  $yU_\tau/\nu$ . The same variation is presented for the cases of the cylinders in Fig. 3.30 (a). At the first streamwise location of  $x/d = 1.36$ , the flow has reattached only in the case of the smallest cylinder. In this case, production and dissipation are in equilibrium throughout the boundary layer, with peaks very close to the element height. The levels are much higher than those in the smooth wall BL (Fig. 3.29), by about 10 times. Turbulent diffusion is important too, from the wall to about 2 element heights [Fig. 3.30 (a)]. In the other two cases of the cylinder, production and dissipation are close to each other in magnitudes except in neighborhood of the location where the values display a peak which is at  $y^+ \approx 35$  in the case of the intermediate cylinder and at  $y^+ \approx 57$  in the case of the highest cylinder. At this peak location, dissipation trails production in magnitude. Convection is important throughout the BL and reaches maximum values close to the element heights. The turbulent diffusion also reach a maximum close to the locations where PR peaks indicating a diffusion of turbulence away from it. Again these two elements produce about 30 times TKE of that which is produced in a 2-D smooth wall BL. Among the individual terms that contribute significantly to PR are  $-\overline{uv}(\partial U/\partial y)$ ,  $-\overline{v^2} \partial V/\partial y$ ,  $-\overline{u^2}(\partial U/\partial x)$  and  $-\overline{w^2}(\partial W/\partial z)$ . However, their influences are not in the same regions along the boundary layer although at the peak PR location, all four terms contribute significantly to PR. While the former two make large positive contributions to PR, the latter two make smaller negative contributions. As mentioned previously,  $-\overline{uv}(\partial U/\partial y)$  is the dominant term thereby indicating the significance of the distortion of the turbulence field by the mean velocity gradient ( $\partial U/\partial y$ ) which has lead to a large generation of TKE. Also of significance is the large downwash due to the RTVS that is responsible for the large ( $\partial V/\partial y$ )



gradients. Flow acceleration immediately downstream of the element is a reason behind the negative contribution by the  $-\overline{u^2}(\partial U/\partial x)$  term.

As the flow proceeds downstream,  $x/d = 2.75$  [Fig. 3.30 (b)], each of the terms decrease in magnitudes, although still substantially higher than those generated in the 2-D smooth wall BL. The *PR* peaks occur at the element heights in the cases of the smallest and the intermediate cylinders and below the element heights as regards the other two cases. Significant turbulent diffusion occurs that transports fluctuations away from the peak *PR* locations. Substantial levels of negative *C* occur in the near-wall regions so much so that dissipation exceeds production as regards the intermediate and the highest cylinder. For the case of the Gaussian spike, the largest term close to the element height is the *TD* and not the *PR* or the  $\epsilon$ . This is consistent with the large diffusion velocities that are seen near the spike top that are seen to diffuse TKE away from regions of high TKE. In the case of the smallest cylinder, the peak values of the *PR*, *TD* and the  $\epsilon$  are seen above the element heights and throughout the boundary layers, *PR* is seen to be in local equilibrium with  $\epsilon$ . With the progress in streamwise distance, the magnitudes of each term decay with distance and tend towards smooth wall behavior [Figs. 3.30 (c)-(f)]. However, the magnitudes of the significant terms are still higher than those for the 2-D smooth wall.

The elements considered in this study are small so much so that the smallest element does not protrude beyond the buffer layer. Hence, the structures generated in the flow field are expected to be of the order of the Kolmogorov scales. The profiles of  $\epsilon$ , estimated from the transport rate budget, permitted the data to be extrapolated to yield the values of the  $\epsilon$  at the wall. This obtained value in conjunction with that obtained at the closest measurement point, which is at  $y^+ = 3$ , is used in the calculation of the Kolmogorov scale which is given by  $\eta = (\nu^3/\epsilon)^{1/4}$ . The values of  $\eta$ , normalized by  $\nu/U_\tau$ , at the wall and at  $y^+ = 3$  is plotted in Fig. 3.31 for the various streamwise distances. The values of  $\eta^+$ , at the wall, range from 1.5 to 3, in general. The scale of the structures that the smallest elements generate is a few times the Kolmogorov scale.

### 3.1.4.7 Structural parameters

The Townsend's structure parameter,  $A_1$ , defined as equal to  $-\overline{uv}/q^2$  (for 2-D flows) is a measure of the correlation between the magnitude of the kinematic shear stress and the TKE. Figure 3.32 (a) shows the variation of  $A_1$  with  $yU_\tau/\nu$  along the centerline, for the four cases. A fairly constant value is not seen in the outer layers and the values seem to plateau at about 0.12 in the outer region of the flow. A better constancy in the outer regions is seen when the variation of  $1/S = -\overline{uv}/v^2$  with  $yU_\tau/\nu$  is presented [Fig. 3.32 (b)]. This parameter reaches a constancy of 0.6 in the outer layers indicating that the roughness element does not affect this parameter. The constancy also implies that similar motions contribute to both the shear stress,  $-\overline{uv}$ , and the normal stress,  $\overline{v^2}$ .

## 3.2 Conclusions

A study has been carried out to examine the mean flow and turbulence structure downstream of three cylinders and a "Gaussian" shaped spike that were individually submerged in a 2-D turbulent boundary layer. The three cylinders were of heights,  $k=0.38mm$ ,  $0.76mm$  and  $1.52mm$ , and the Gaussian shaped spike was of height,  $k=1.52mm$ , each with a base diameter of  $1.98mm$ . All four elements were within 4% of the boundary layer thickness, and the smallest cylinder ( $k=0.38mm$ ) was even confined within the buffer layers. Based on the results and its analysis, a schematic of the flow past the cylinder is presented in Fig. 3.33. The schematic should be similar for the Gaussian spike too.

As the fully developed turbulent flow approaches the protuberance, the flow separates at the top of the elements and the separated shear layers convect downstream as a pair of counter rotating



vortices which is termed the roughness top vortex structure (RTVS). A vortex is also formed upstream at the nose of the element, termed the junction horseshoe vortex structure (JHTS), which is, however, short lived and does not seem to persist beyond 3-5 diameters. This behavior is attributed to the wall proximity of the JHTS as it is seen to exist in the very near-wall region of the boundary layer. Hence, most of the behavior of the mean flow and the turbulence structure in the downstream flow field is attributed to the presence of the RTVS. The flow separates immediately aft of the elements too and the RTVS induces large downwash velocities as it moves downstream. The convergence of mean flow, forced over and around the elements, at the center plane in conjunction with the downwash induced by the RTVS causes higher momentum fluid to be impinged on the wall leading to increased wall shear that persists several tens of diameters downstream of the elements. The increased wall shear was also confirmed using oil flow visualization as seen by the dark scoured out regions along the center line which is also the downwash region of the vortex structure. This also demonstrated the longevity of the RTVS in the downstream flow field. However, further away from the centerline, wall shear decreases beneath the upwash regions as the vortex transports fluid away from the wall.

The downstream flow field was studied primarily from the data gathered along the streamwise axis (with its origin at the element axis) and at two measurement planes (2.75 and 10 diameters downstream) normal to the streamwise axis. The distortion of the mean flow field by the roughness top vortex structure (RTVS) was examined from the magnitudes and extent of the streamwise vorticity and the secondary flow due to the vortex. The movement of the vortices was determined from the tabulations of the locations denoting the centers of rotation of the secondary flow and also from the locations where the streamwise vorticity is the maximum. However, neither of these locations are the true centers of the vortex. Immediately downstream of the elements, the circulation, around one half of the flow domain, decays drastically. With the increase in streamwise distance, this decay becomes gradual. The size of the elements determines the persistence and extent of the streamwise vorticity as seen by the largest extent and magnitude of streamwise vorticity that was generated in the case of the highest cylinder. An expression for the form drag due to the individual elements was derived. The drag evaluated by this expression from the measured data showed that it is dependant on the projected frontal area of the element. The vortex circulation was also dependent on the size of the element. Of all the length scales considered, the square root of the projected frontal area of the elements was the best in normalizing these quantities and hence, it is the most suitable candidate to quantify the “size” of the element.

As regards the turbulence structure, the merging of the shear layers at the downstream center plane, just aft of the element, in conjunction with the sweeping motions induced by the RTVS leads to large enhancement in the levels of the Reynolds normal stresses,  $\overline{v^2}$  and  $\overline{w^2}$ , and the Reynolds shear stresses,  $-\overline{uv}$ . The transport of wall-normal fluctuations and spanwise fluctuations by the RTVS is also responsible for creating large levels of shear stresses,  $-\overline{uw}$  and  $-\overline{vw}$ , that were comparable in magnitude to the Reynolds shear stresses,  $-\overline{uv}$ . Again the magnitudes and extent of the stresses were dependent on the size of the elements. A large generation and transport of TKE also occurred just aft of the elements, and for a better understanding of the source and redistribution of TKE, a transport-rate budget was performed. This also enabled in determining the individual terms that contribute to the production of TKE. The presence of the element severely distorts the mean velocity field in that large streamwise velocity gradients are generated, and the presence of the RTVS by its downwash generates large gradients in wall-normal velocity component as well. These gradients in conjunction with the Reynolds stresses lead to large production of TKE just aft of the element which is diffused away in a radial manner by the roughness top vortices which then lead to large TKE levels. One of the key differences between the cylinders and the Gaussian spike is seen as regards the large magnitudes of the diffusion velocities generated aft of the latter and this behavior is attributed to the latter’s “peaky” shape.

The information garnered from the present study is useful in conceptualizing rough-wall boundary layers where individual elements such as these are distributed in a discrete manner.

Table 3.1. Location and magnitude of maximum streamwise vorticity associated with the junction vortex structure at  $x/d = 2.75$ .

Flow Case	$k^+$	$x/d = 2.75$					
		$z_c/d$	$z_c^+$	$y_c^+$	$U_c^+$	$\left(\frac{\Omega_x \sqrt{A}}{U_\tau}\right)_{\max}$	$\left(\frac{\Omega_x d}{U_\tau}\right)_{\max}$
Single cylinder, $k = 0.38mm$	23	-1.94	-226.6	4.8	4.9	0.86	1.96
Single cylinder, $k = 0.76mm$	46	-1.67	-194.4	6.2	6.3	3.34	5.38
Single cylinder, $k = 1.52mm$	92	-2.21	-258.3	4.9	4.5	6.33	7.22
Gaussian spike, $k = 1.52mm$	92	-	-	-	-	-	-

Table 3.2. Location and magnitude of maximum streamwise vorticity associated with the roughness top vortex structure (RTVS) at  $x/d = 2.75$  and 10.

Flow Case	$k^+$	$x/d = 2.75$						$x/d = 10$					
		$z_c/d$	$z_c^+$	$y_c^+$	$U_c^+$	$\left(\frac{\Omega_x \sqrt{A}}{U_\tau}\right)_{\max}$	$\left(\frac{\Omega_x d}{U_\tau}\right)_{\max}$	$z_c/d$	$z_c^+$	$y_c^+$	$U_c^+$	$\left(\frac{\Omega_x \sqrt{A}}{U_\tau}\right)_{\max}$	$\left(\frac{\Omega_x d}{U_\tau}\right)_{\max}$
Single cylinder, $k = 0.38mm$	23	-0.54	-63.6	12.6	9.0	2.52	5.76	-	-	-	-	-	-
Single cylinder, $k = 0.76mm$	46	-0.56	-64.9	16.6	9.4	7.33	11.83	-0.84	-97.5	44.5	14.2	0.82	1.31
Single cylinder, $k = 1.52mm$	92	-0.83	-97.1	13.0	8.3	10.08	11.49	-1.10	-128.8	45.2	13.5	2.13	2.43
Gaussian spike, $k = 1.52mm$	92	-0.55	-64.0	13.0	9.7	5.34	9.48	-0.84	-97.5	35.0	13.7	0.67	1.19



Table 3.3. Details of the secondary flow associated with the roughness top vortex structure (RTVS) at  $x/d = 2.75$  and 10.

Flow Case	$k^+$	$x/d = 2.75$						$x/d = 10$				
		$z_0/d$	$z_0^+$	$y_0^+$	$U_0^+$	$V_\theta^+$	$\lambda/d$	$z_0/d$	$z_0^+$	$y_0^+$	$U_0^+$	$V_\theta^+$
Single cylinder, $k = 0.38mm$	23	-0.54	-62.9	16.7	10.1	0.16	210.4	-	-	-	-	-
Single cylinder, $k = 0.76mm$	46	-0.62	-72.6	24.4	10.4	0.80	51.0	-0.81	-94.5	65.1	15.1	0.08
Single cylinder, $k = 1.52mm$	92	-0.74	-86.2	28.8	10.1	1.96	24.0	-1.04	-121.3	79.6	14.9	0.49
Gaussian spike, $k = 1.52mm$	92	-0.75	-87.9	22.0	11.6	0.24	163.8	-1.03	-120.3	76.6	15.7	0.17

Table 3.4. Movement of the locations of  $\Omega_{x_{max}}$  and center of rotation with the streamwise distance.

Flow Case	Location of $\Omega_{x_{max}}$		Center of rotation	
	$\Delta z_c^+$	$\Delta y_c^+$	$\Delta z_0^+$	$\Delta y_0^+$
Single cylinder, $k = 0.76mm$	32.6	27.9	21.9	40.7
Single cylinder, $k = 1.52mm$	31.7	32.2	35.1	50.8
Gaussian spike, $k = 1.52mm$	33.5	22.0	32.4	54.6

Table 3.5. Vortex circulation parameter,  $\Gamma/(U_e \delta)$ .

Flow Case	Vortex circulation parameter	
	$x/d = 1.36$	$x/d = 2.75$
Single cylinder, $k = 0.38mm$	0.0011	0.0005
Single cylinder, $k = 0.76mm$	0.0040	0.0016
Single cylinder, $k = 1.52mm$	0.0060	0.0056
Gaussian spike, $k = 1.52mm$	<i>n/a</i>	0.0014

Table 3.6. Off-center values of  $\tau_w/\tau_o$  at  $x/d=20$  and  $40$ , for  $k = 0.38mm$  cylinder.

Locations	$z/d = -0.14$	$z/d = 0$	$z/d = 0.14$
$x/d = 20$	0.99	0.95	1.01
$x/d = 40$	0.97	0.95	0.99



## Figures

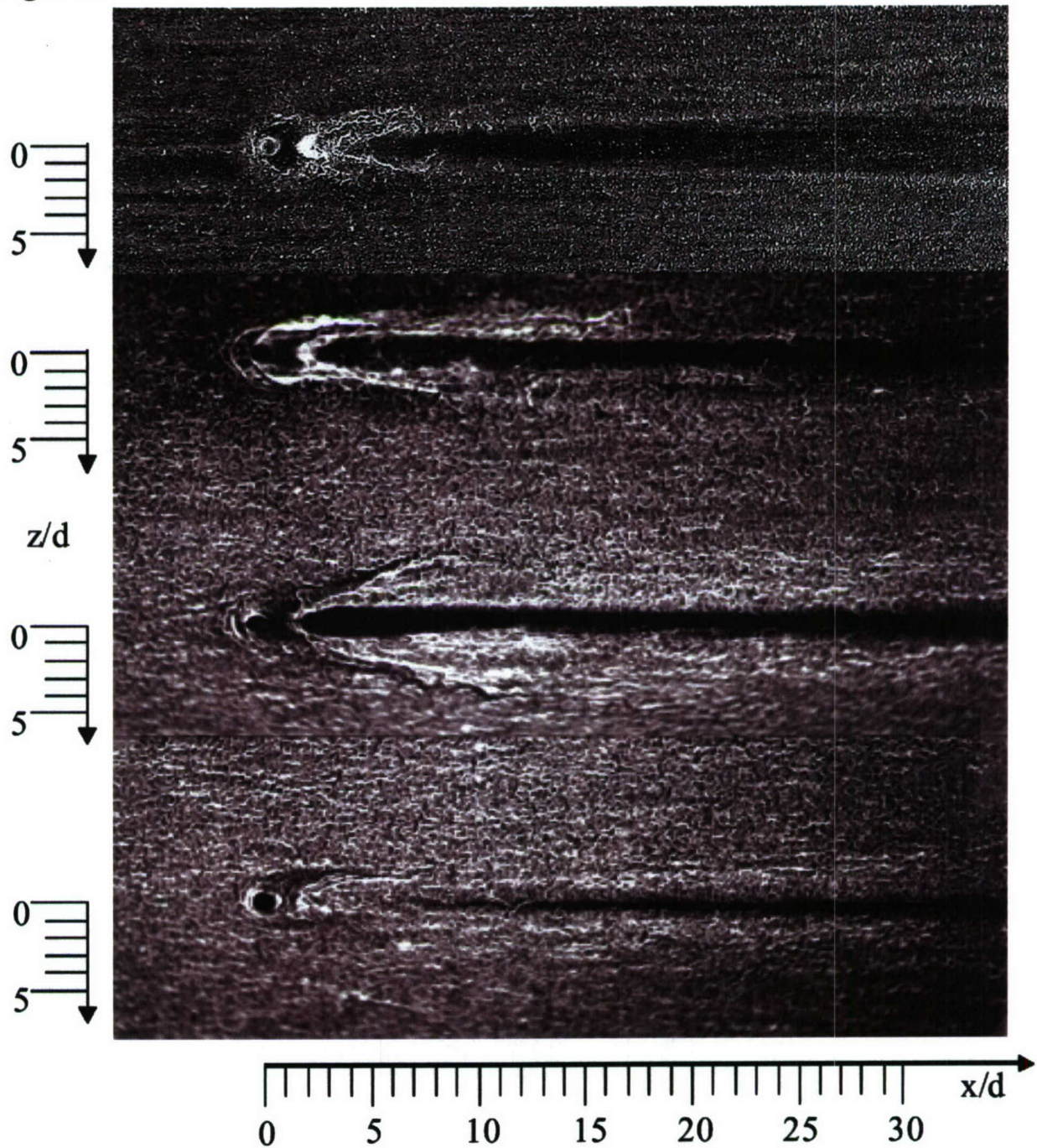


Figure 3.1. Top-view of surface oil flow over isolated elements; from top, Gaussian spike ,  $k = 1.52mm$ , circular cylinders,  $k = 1.52mm$ ,  $0.76mm$ ,  $0.38mm$ .

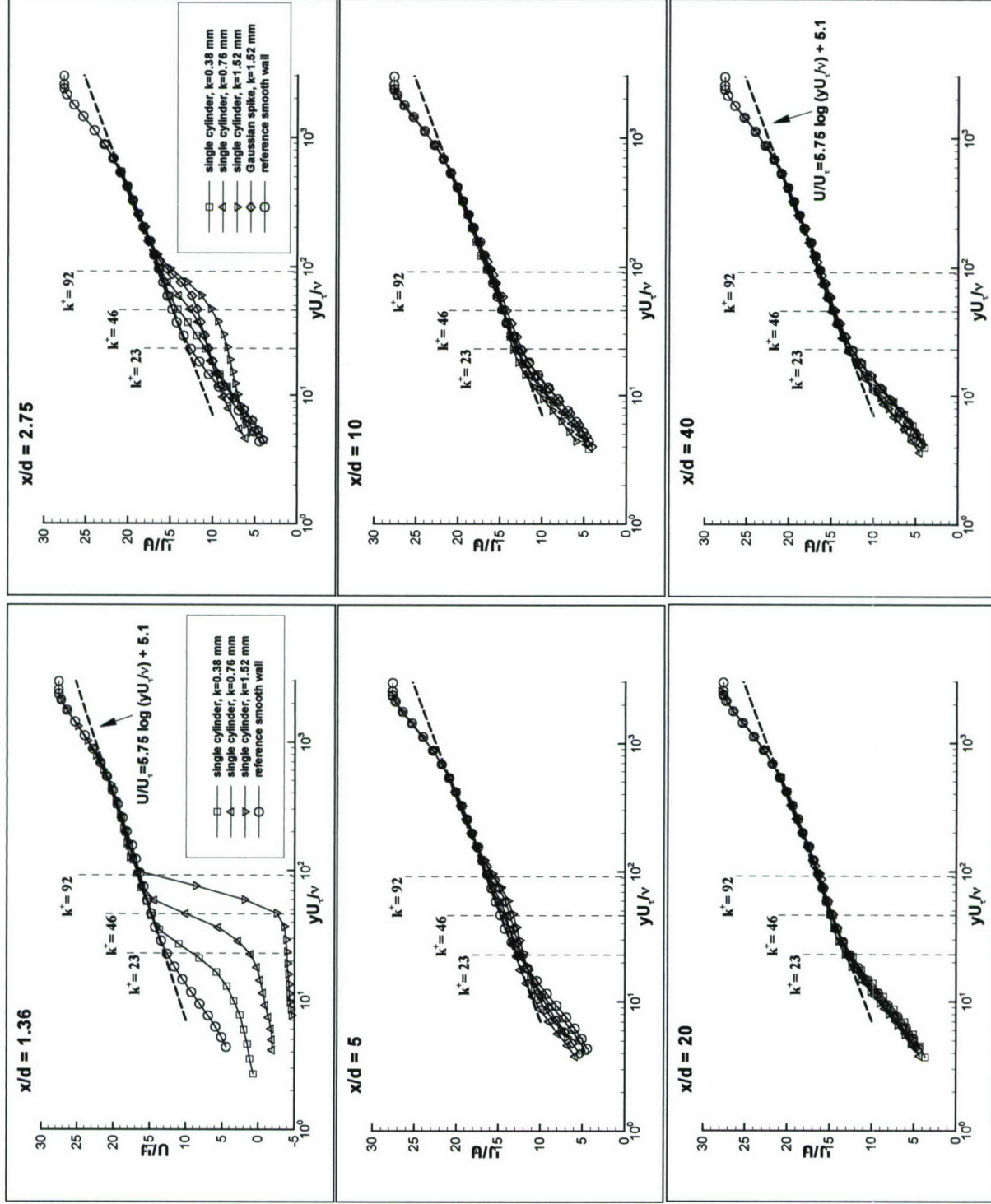


Figure 3.2.  $U/U_\tau$  versus  $yU_\tau/\nu$ , streamwise mean velocity profiles along the centerline.



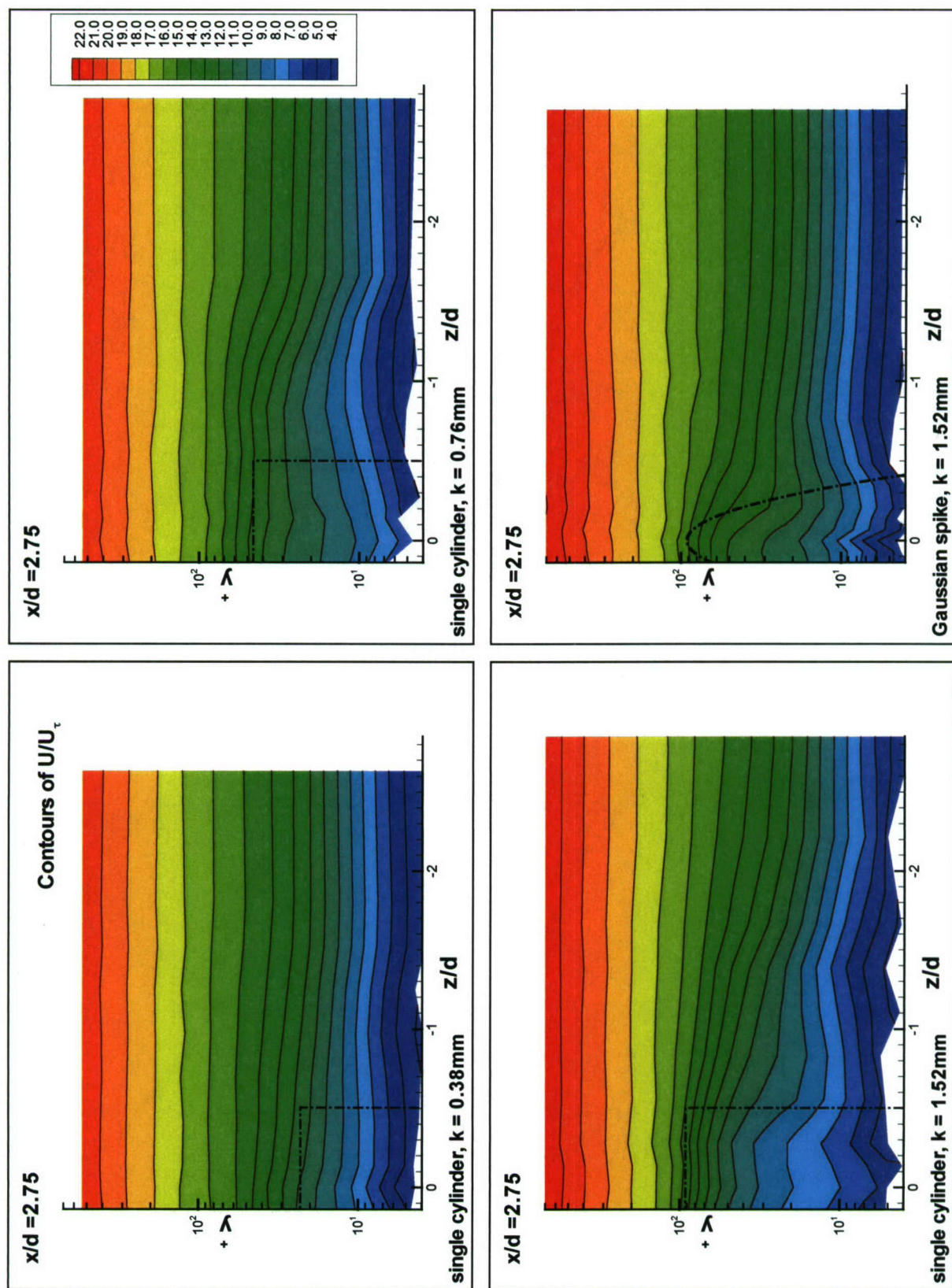


Figure 3.3 (a). Semi-log contours of  $U/U_\tau$  in the  $y^* - z/d$  plane at  $x/d = 2.75$ .

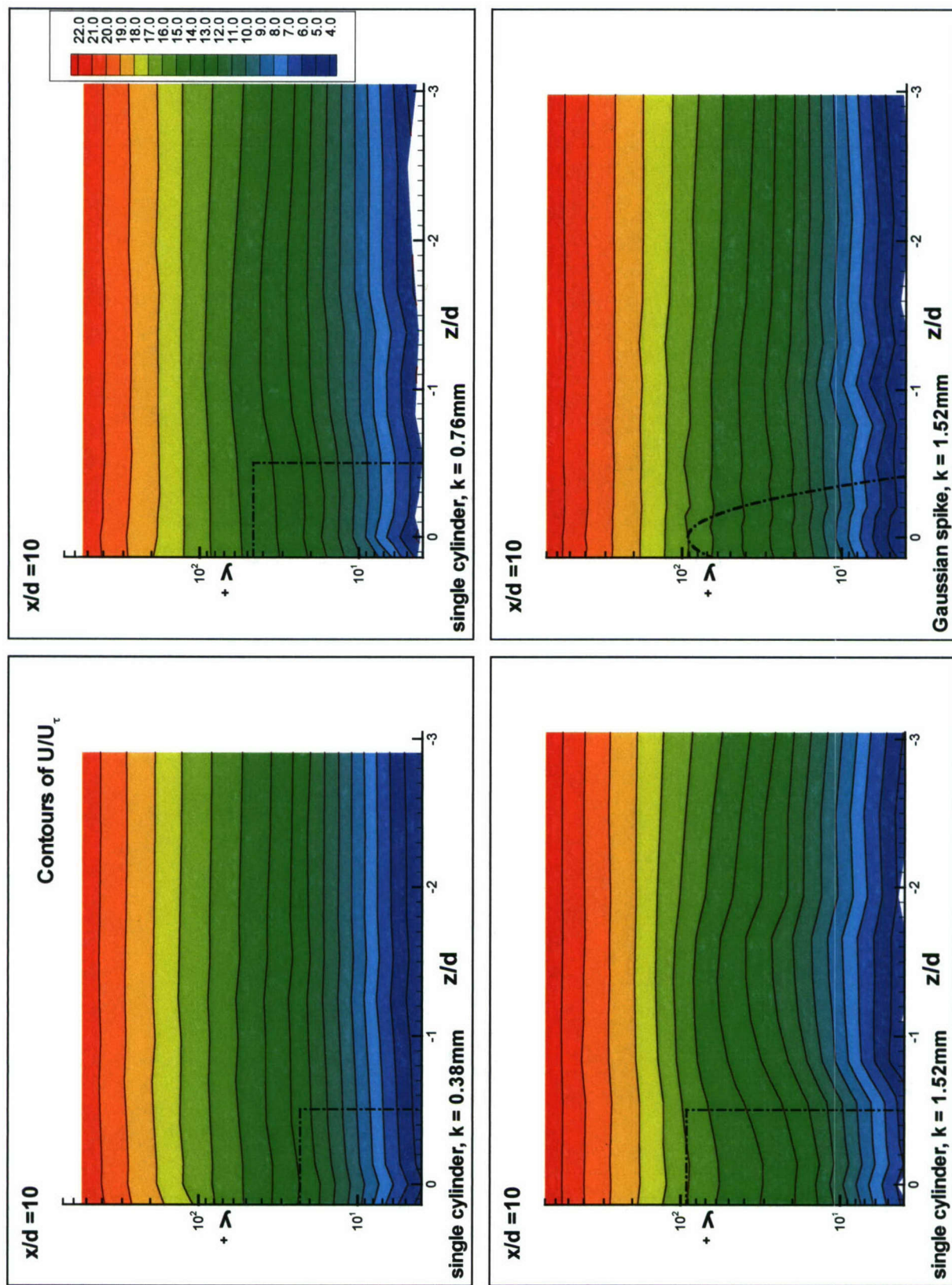


Figure 3. 3 (b). Semi-log contours of  $U/U_\tau$  in the  $y^* - z/d$  plane at  $x/d = 10$ .



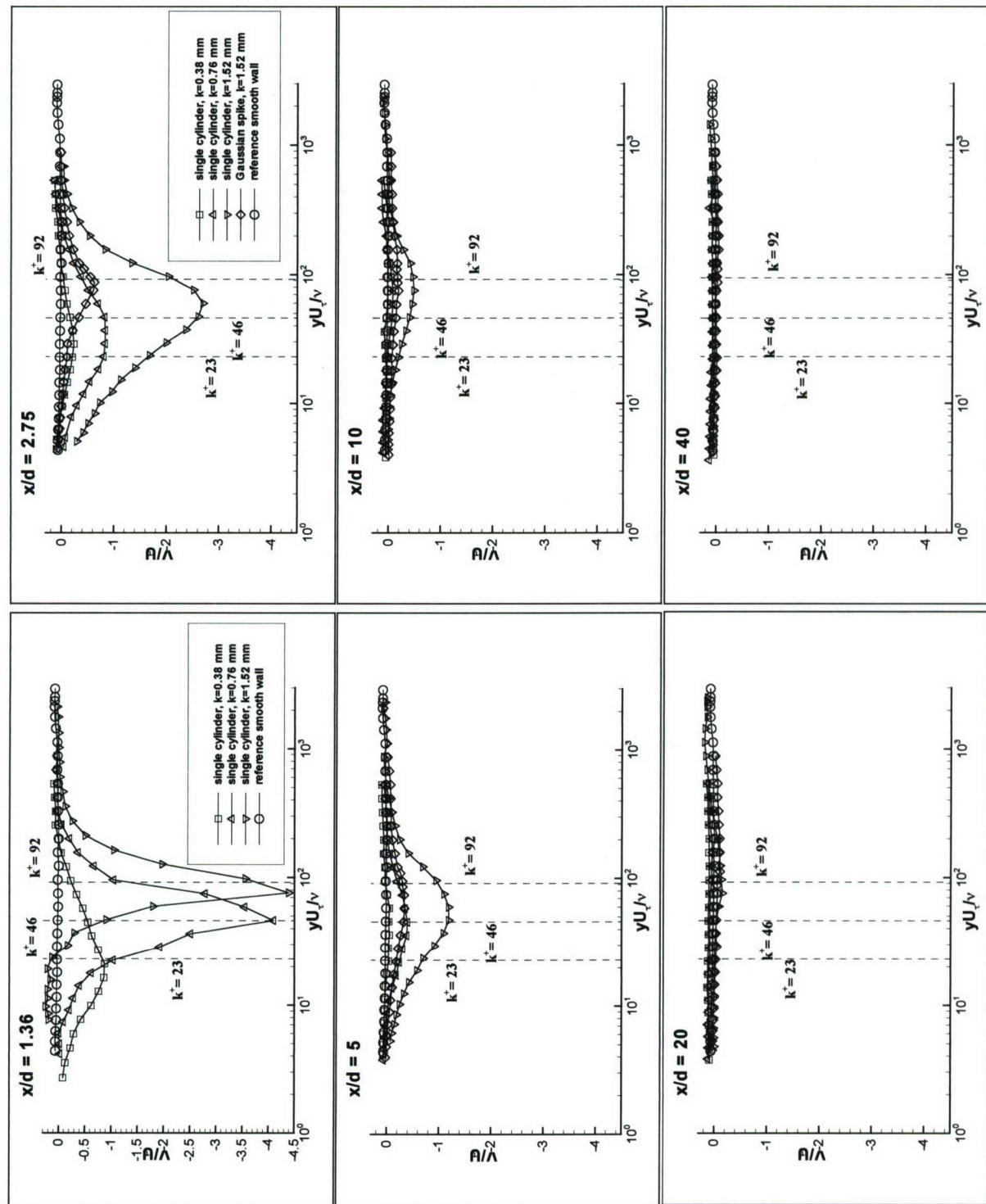


Figure 3.4 (a).  $V/U_\tau$  versus  $yU_\tau/v$ , wall-normal mean velocity profiles along the centerline.

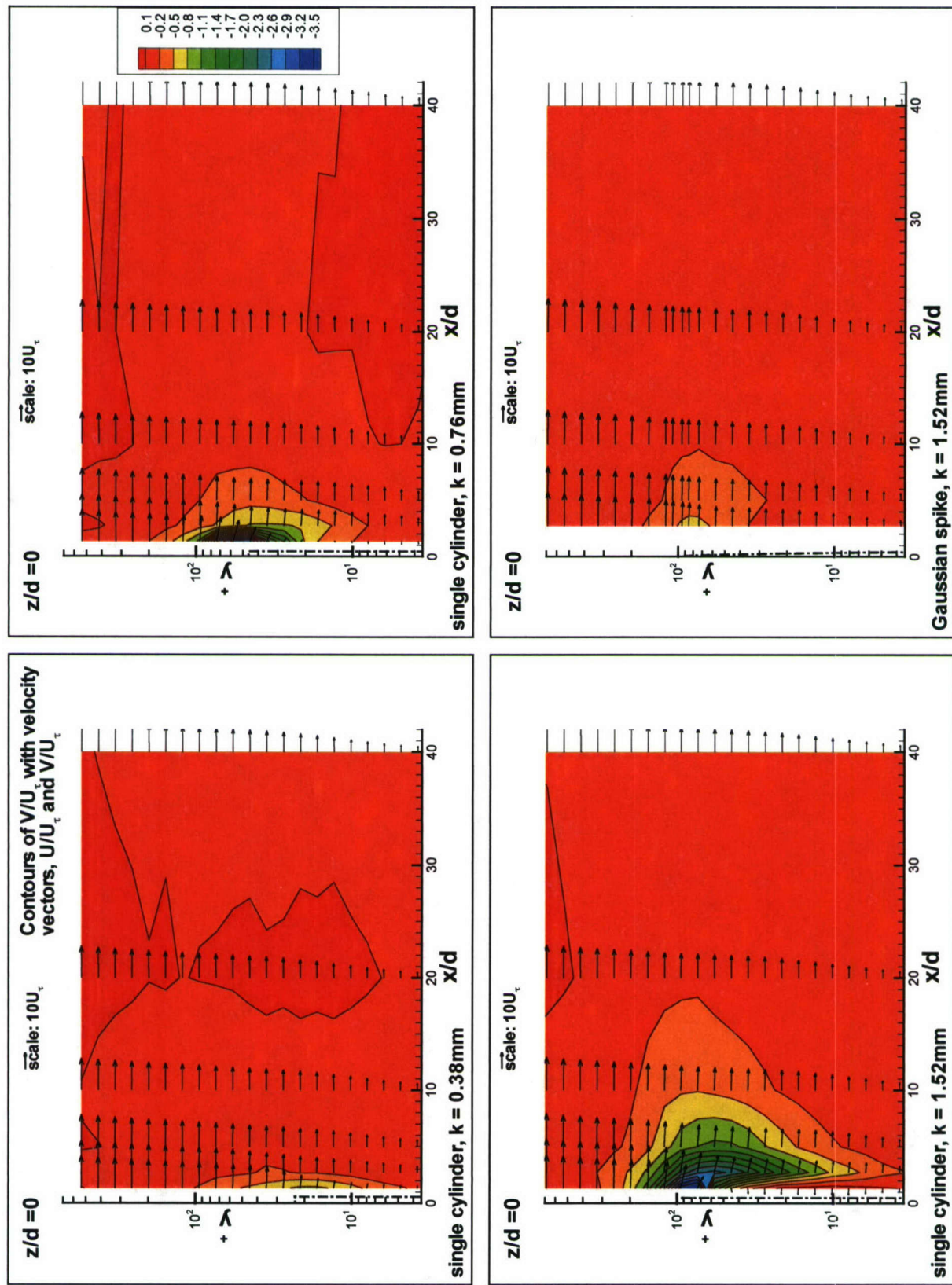


Figure 3.4 (b). Semi-log contours of  $V/U_\tau$  in the  $y^* - z/d$  plane along  $z/d = 0$ .



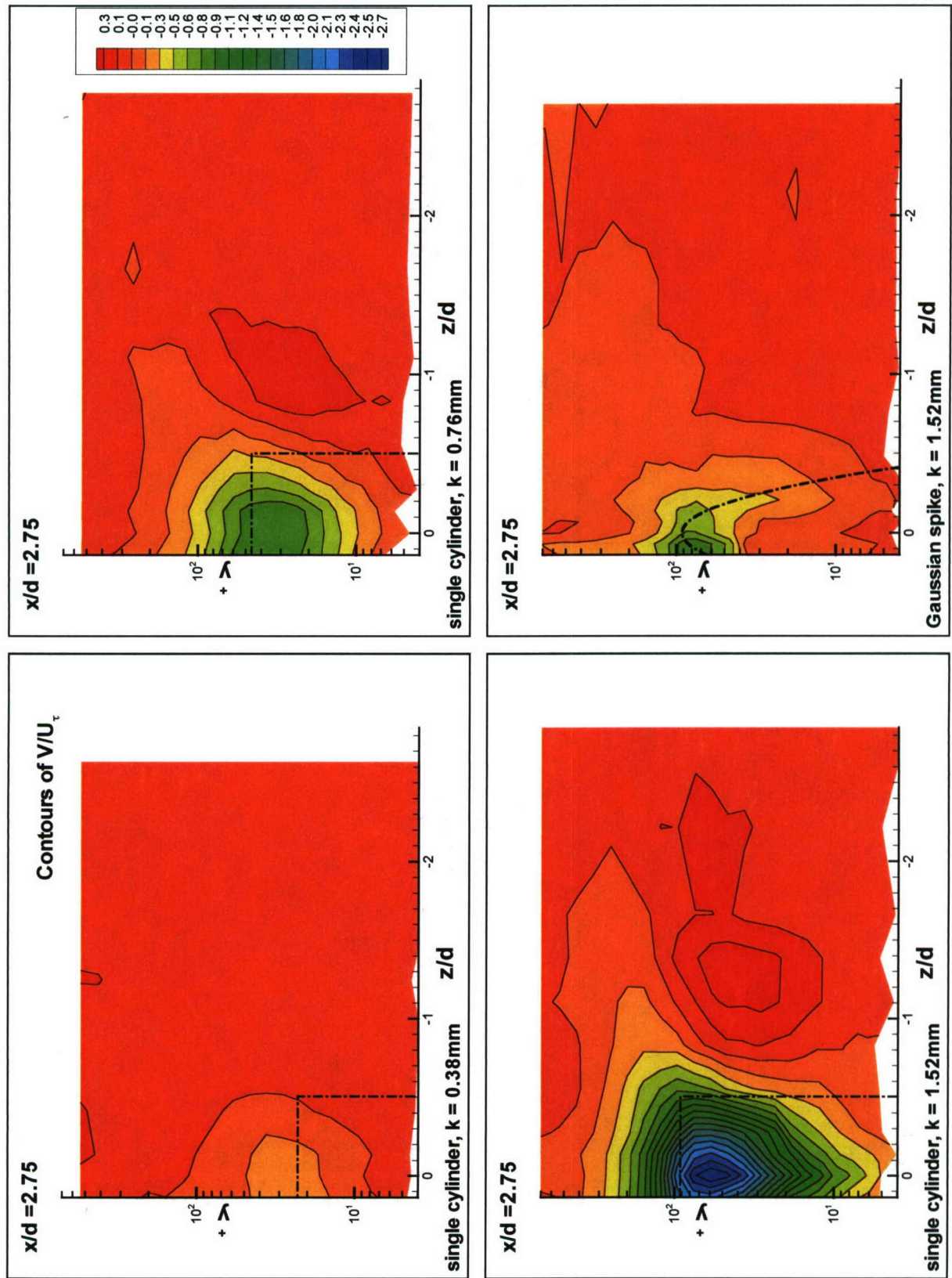


Figure 3.5 (a). Semi-log contours of  $V/U_\tau$  in the  $y^+ - z/d$  plane at  $x/d = 2.75$ .

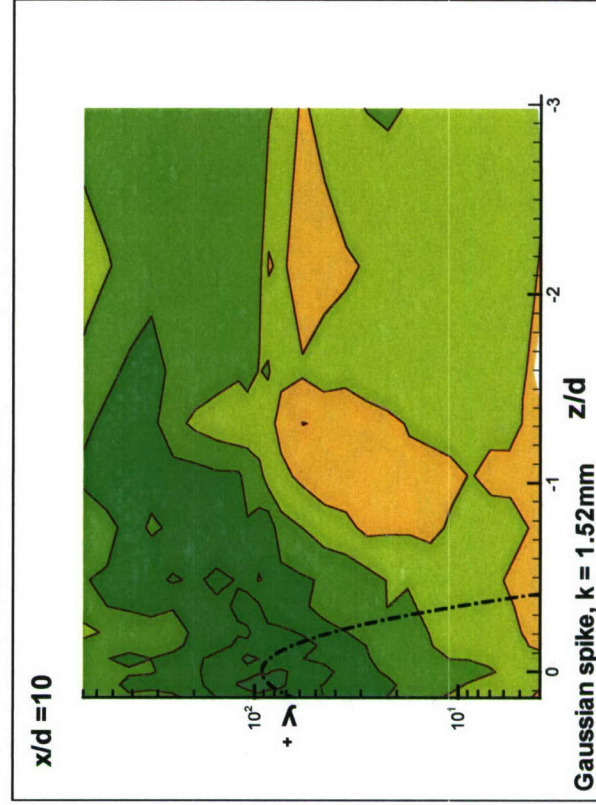
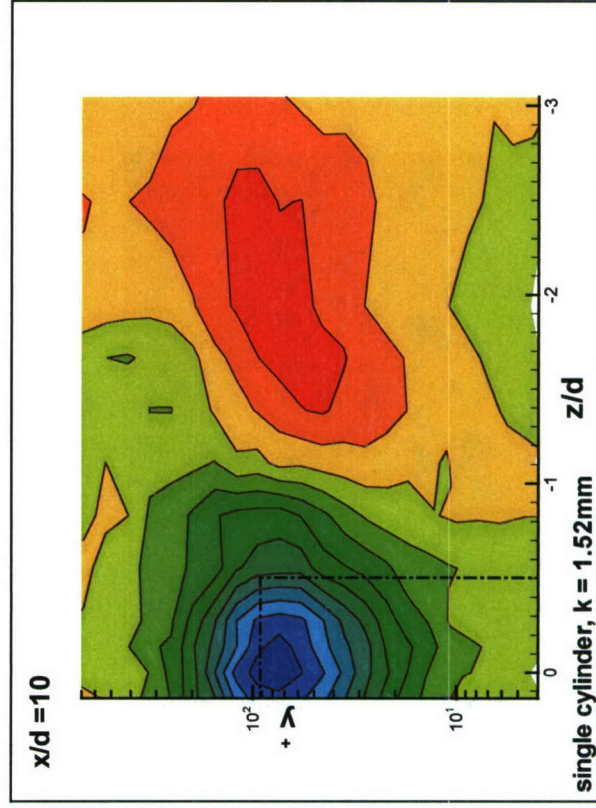
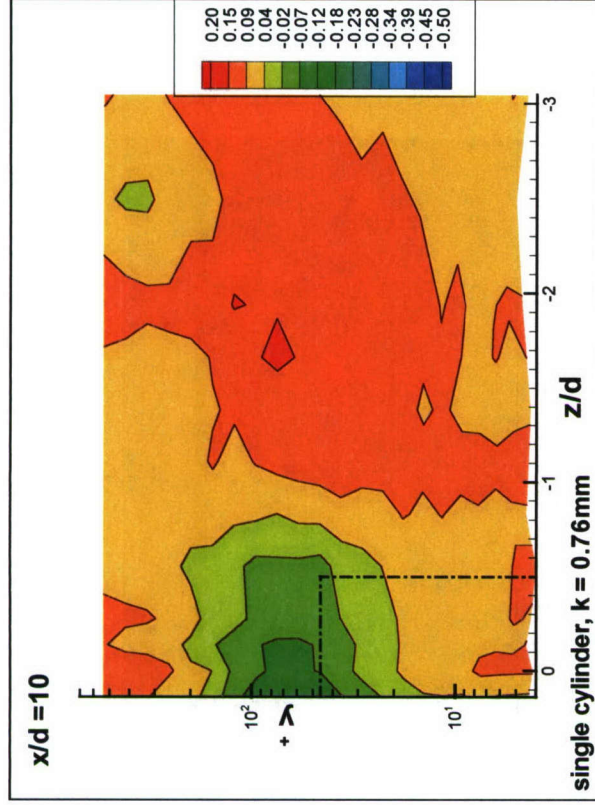
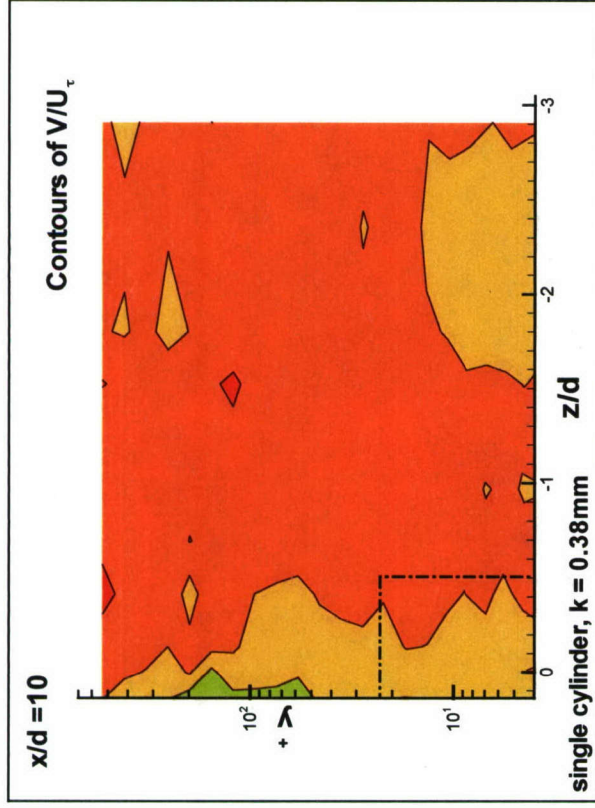


Figure 3.5 (b). Semi-log contours of  $V/U_\tau$  in the  $y^+ - z/d$  plane at  $x/d = 10$ .



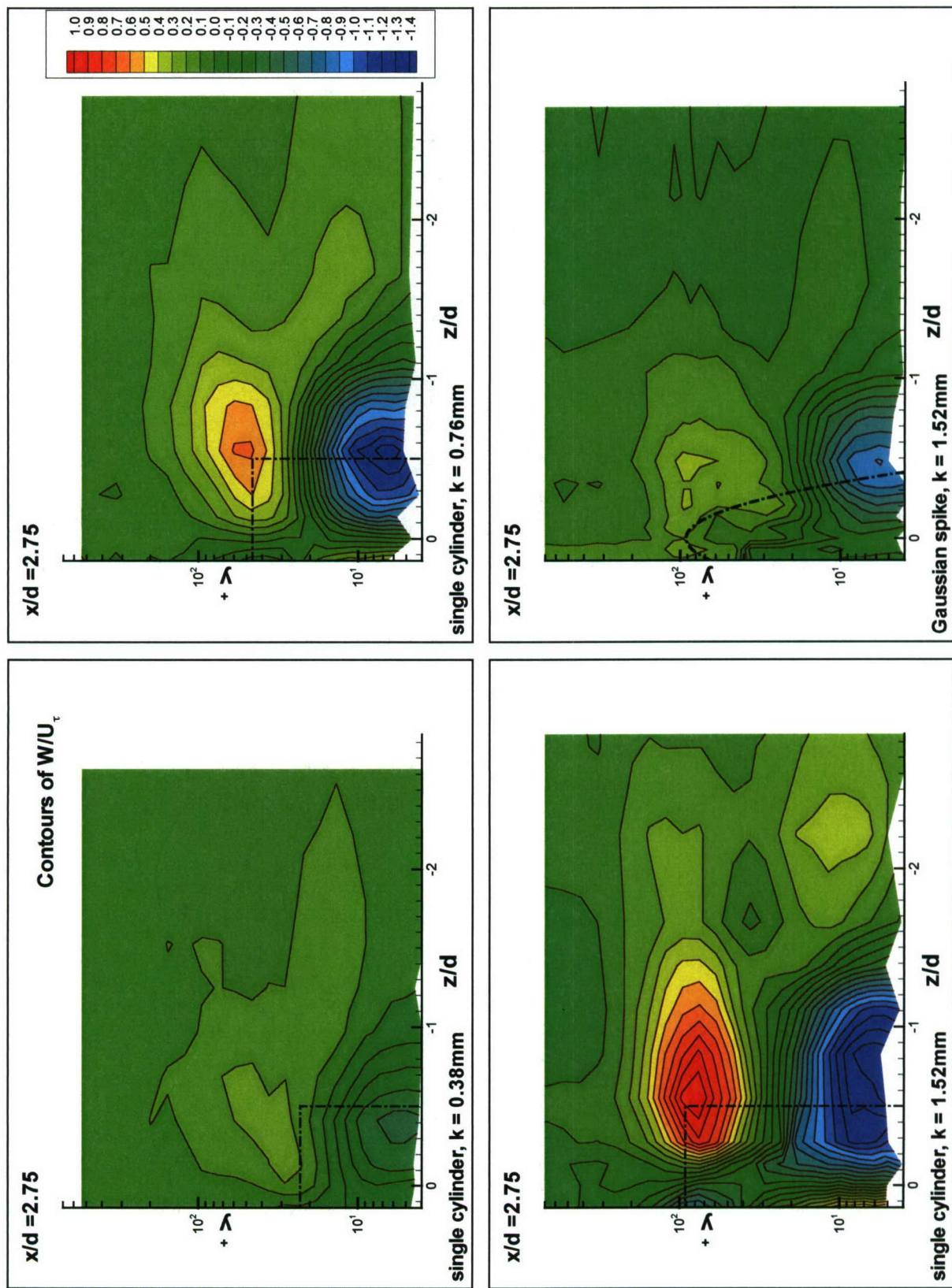


Figure 3.6 (a). Semi-log contours of  $W/U_\tau$  in the  $y^* - z/d$  plane at  $x/d = 2.75$ .

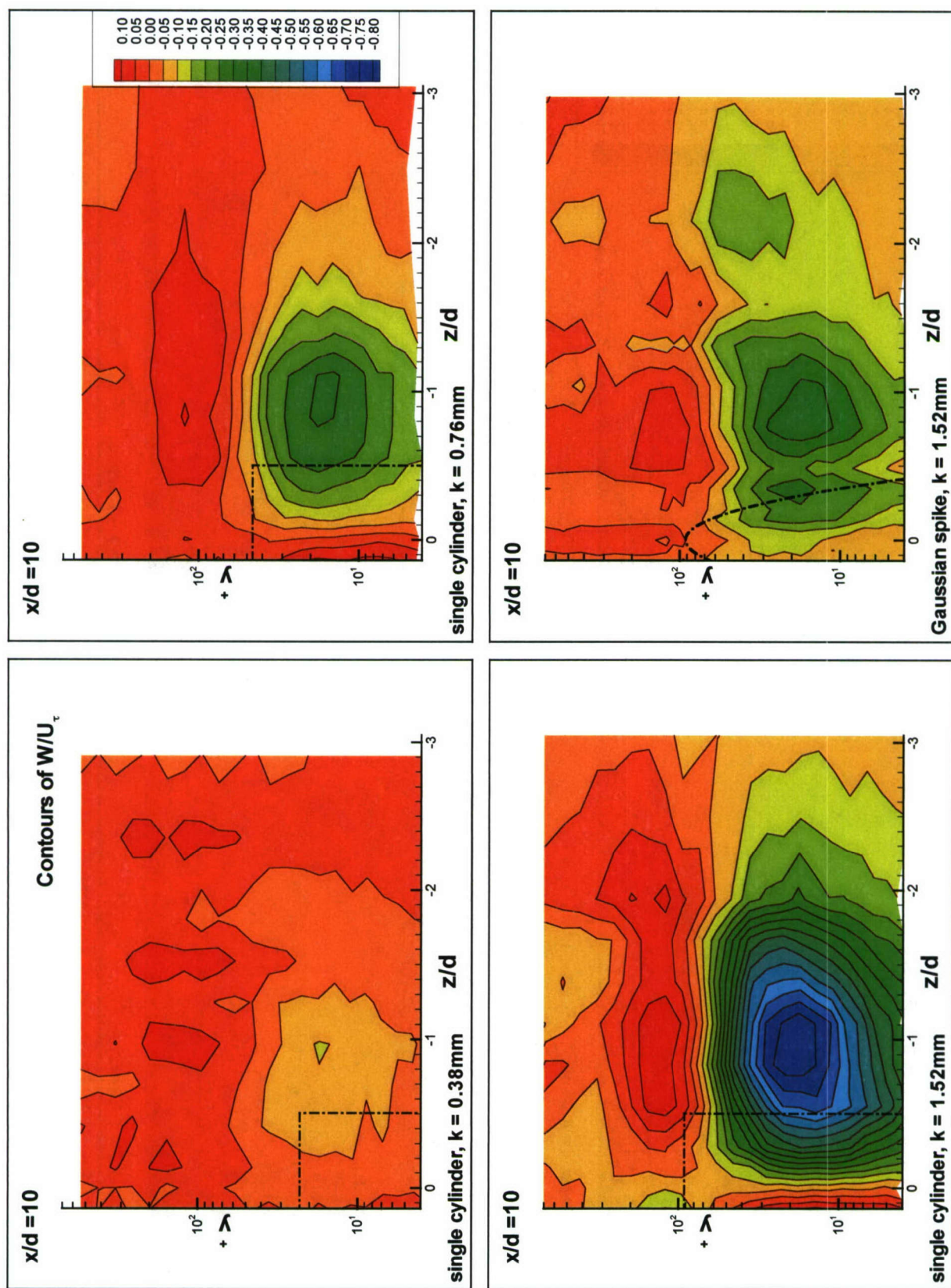


Figure 3.6 (b). Semi-log contours of  $W/U_\tau$  in the  $y^* - z/d$  plane at  $x/d = 10$ .



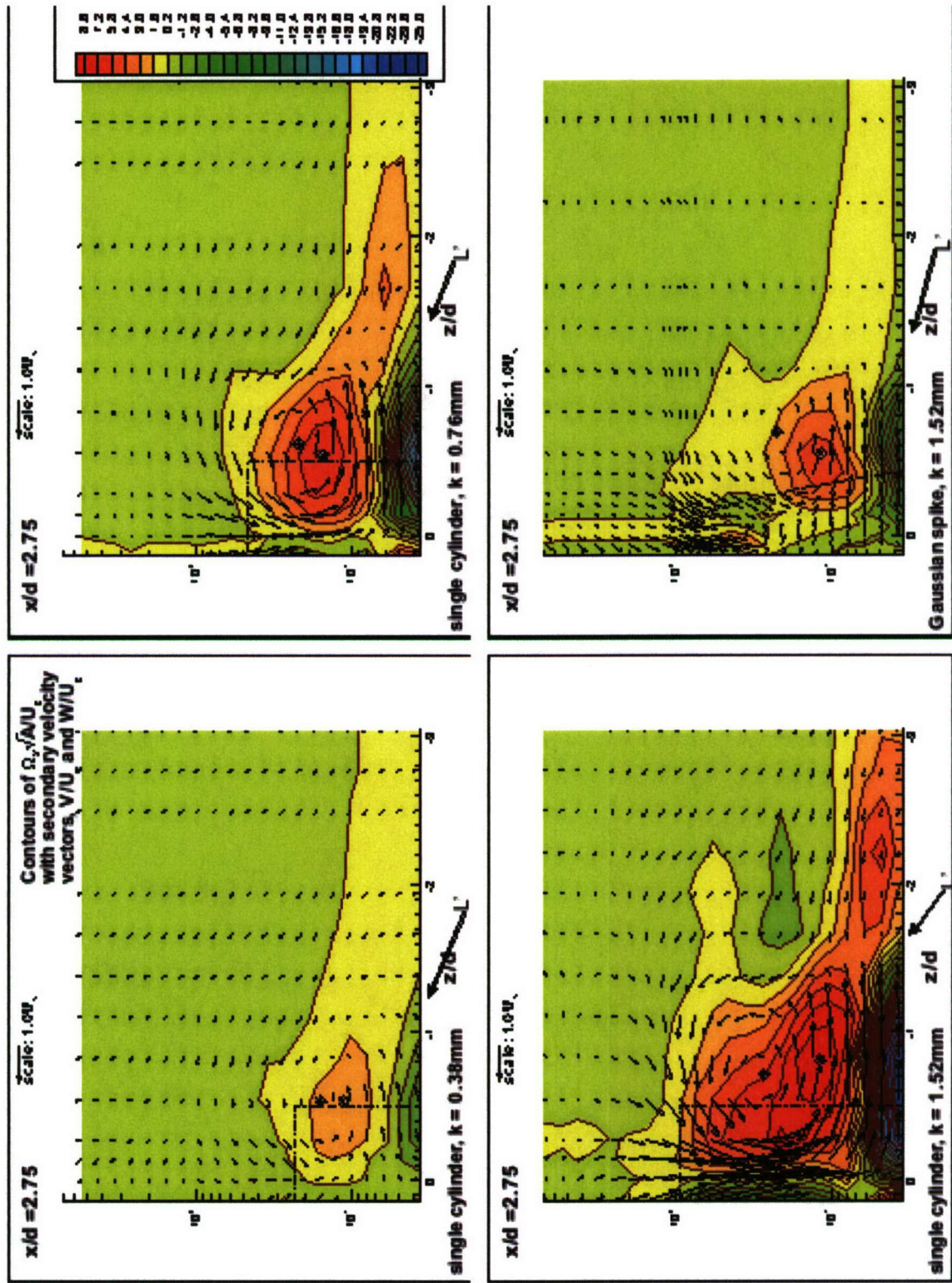


Figure 3.7 (a). Semi-log contours of streamwise vorticity,  $\Omega_x \sqrt{A}/U_\tau$ , with secondary velocity vectors,  $V/U_\tau$  and  $W/U_\tau$ , in the  $y^* - z/d$  plane at  $x/d = 2.75$ . + denotes the center of rotation,  $\times$  denotes the location of  $\Omega_{x_{\max}}$ , and  $L'$  denotes the line of flow separation.





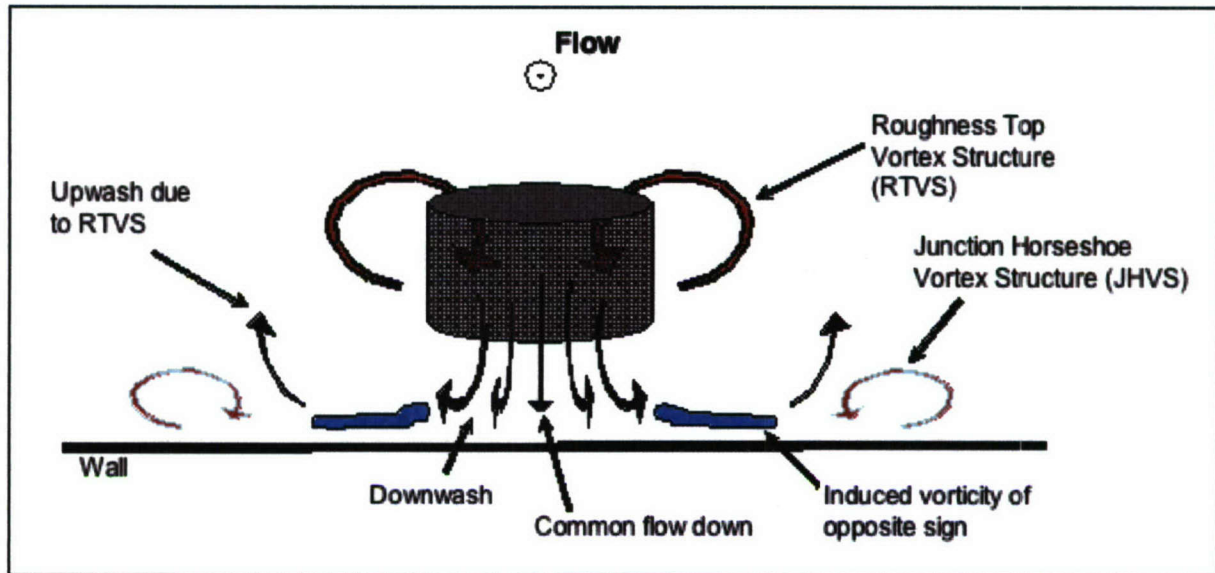


Figure 3.8 (a). A perspective of the flow structure downstream of the cylinder at  $x/d = 2.75$ .

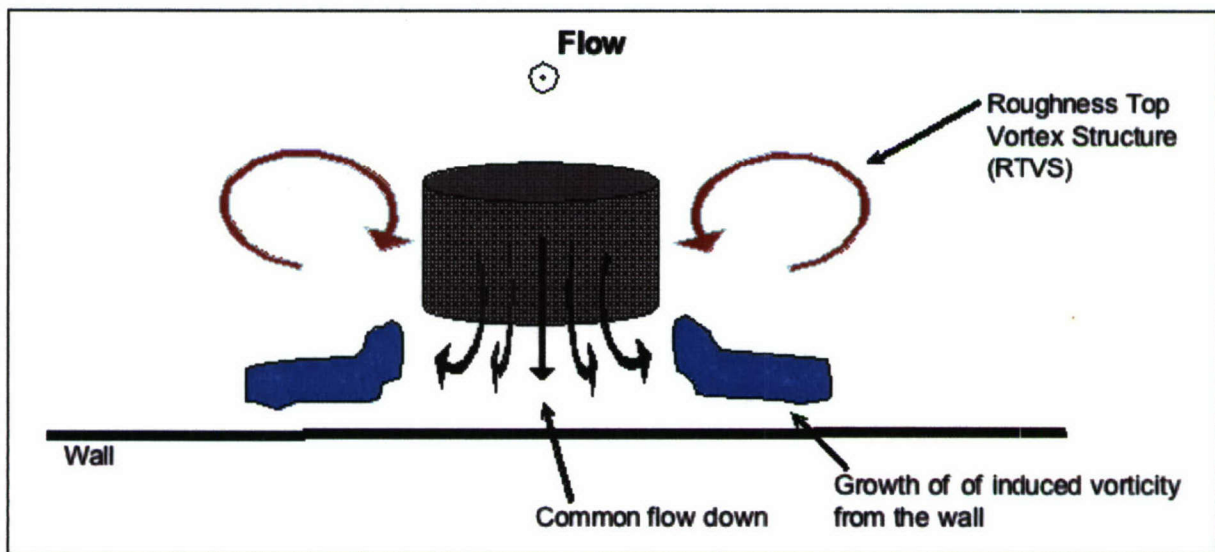


Figure 3.8 (b). A perspective of the flow structure downstream of the cylinder at  $x/d = 10$ .

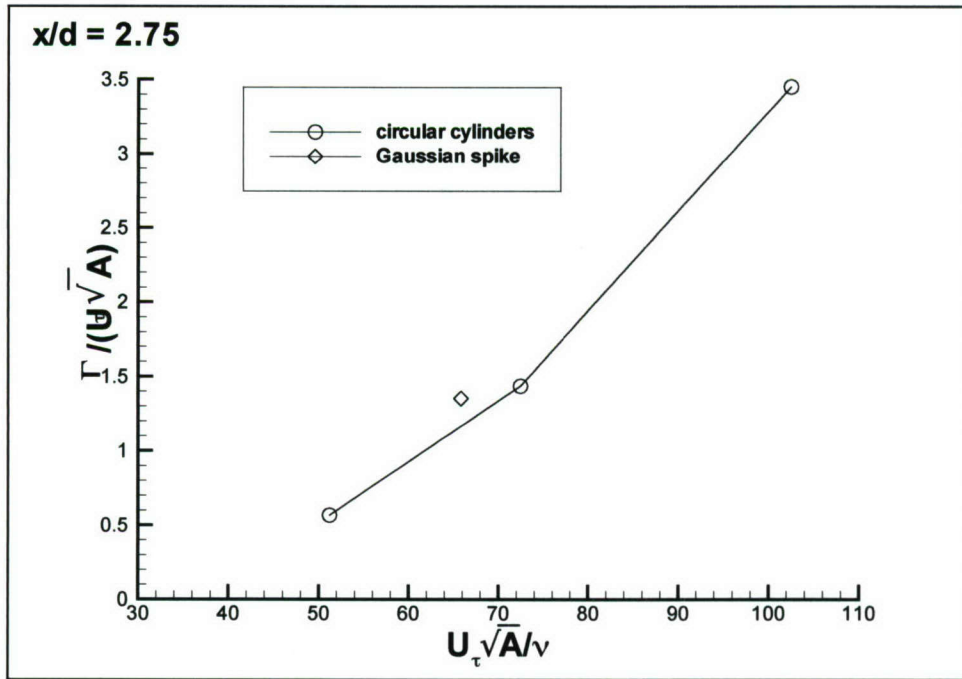


Figure 3.9 (a). Variation of Circulation,  $\Gamma/(U_\tau \sqrt{A})$ , with normalized length scale,  $U_\tau \sqrt{A}/\nu$  at  $x/d=2.75$ .

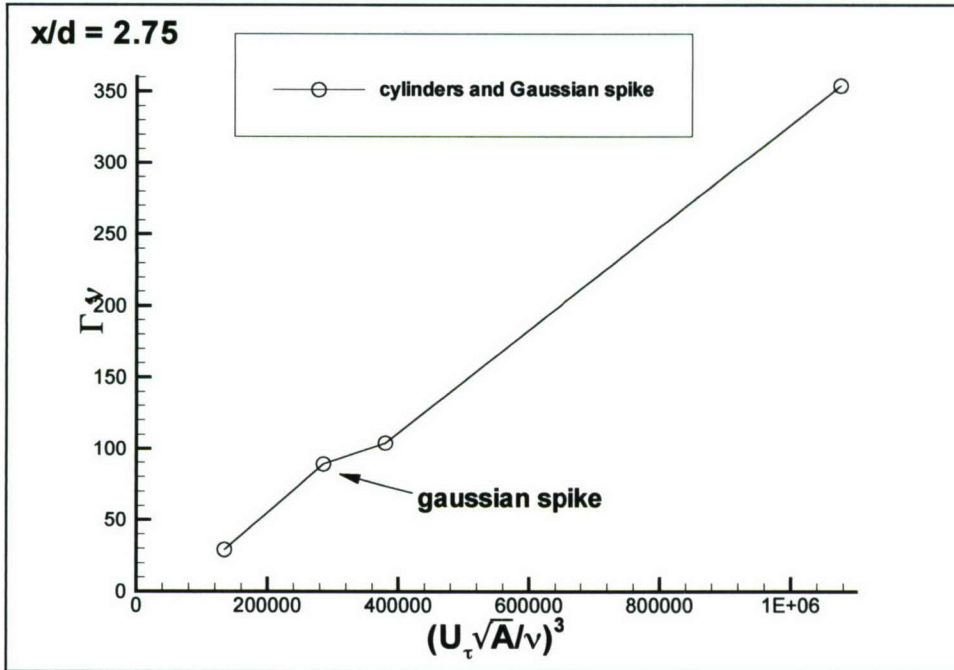


Figure 3.9 (b). Variation of  $\Gamma/\nu$ , with  $(\sqrt{A}^+)^3$  at  $x/d=2.75$ .



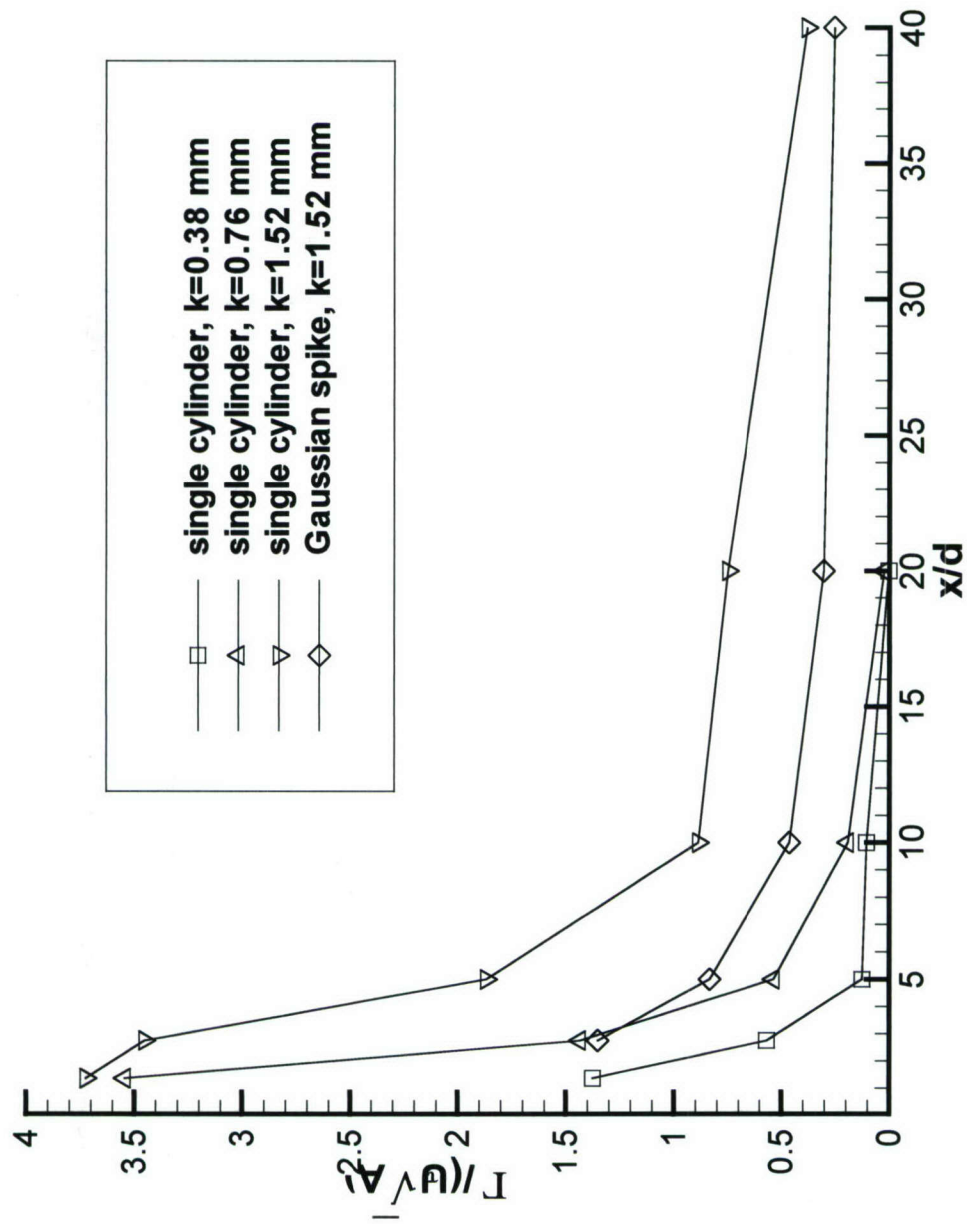


Figure 3.9 (c). Variation of Circulation,  $\Gamma/(U_\infty \sqrt{A})$ , with streamwise distance,  $x/d$ .

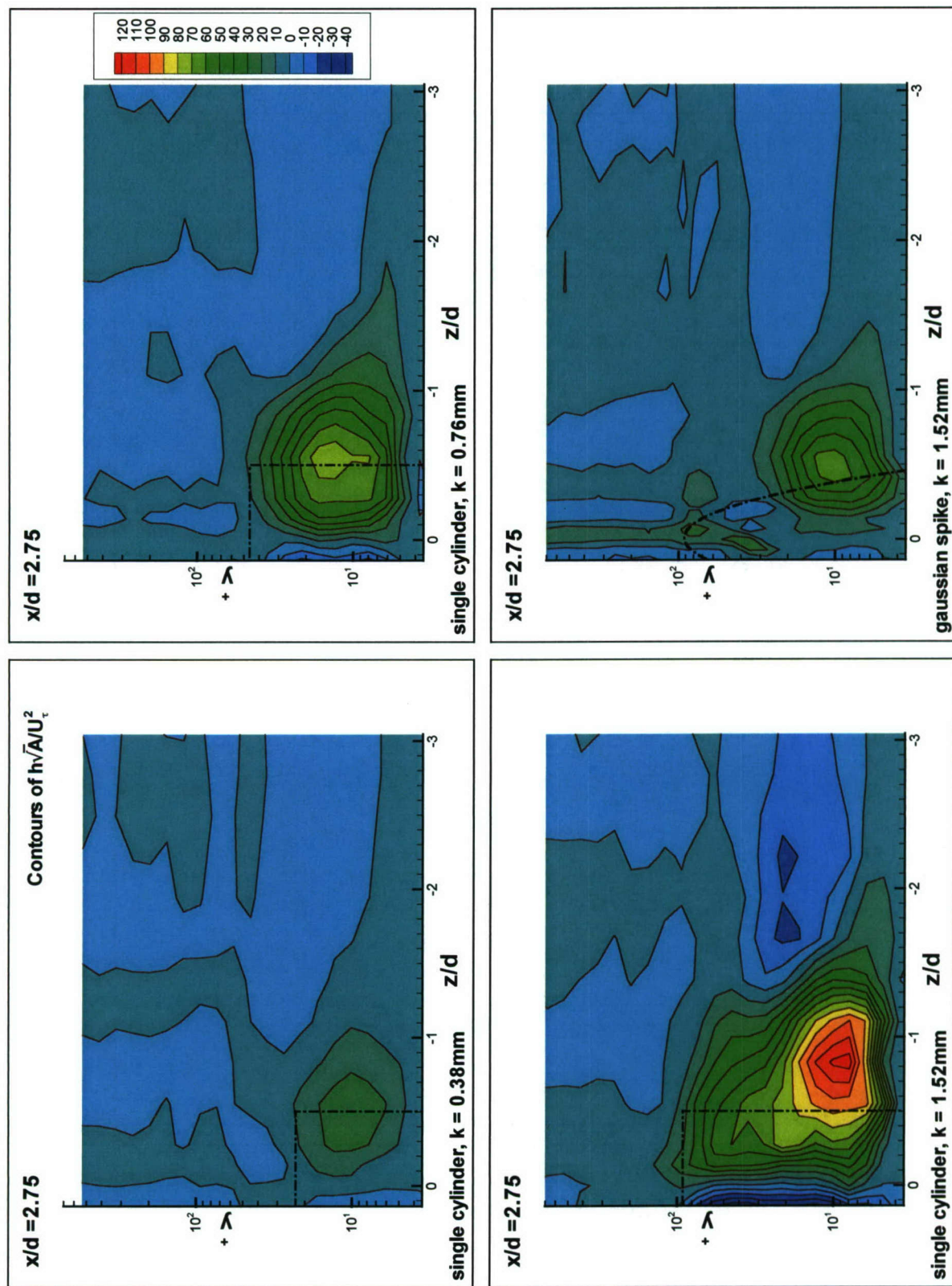


Figure 3.10 (a). Semi-log contours of mean-flow helicity density,  $h\sqrt{A}/U_\tau^2$ , in the  $y^* - z/d$  plane at  $x/d = 2.75$ .



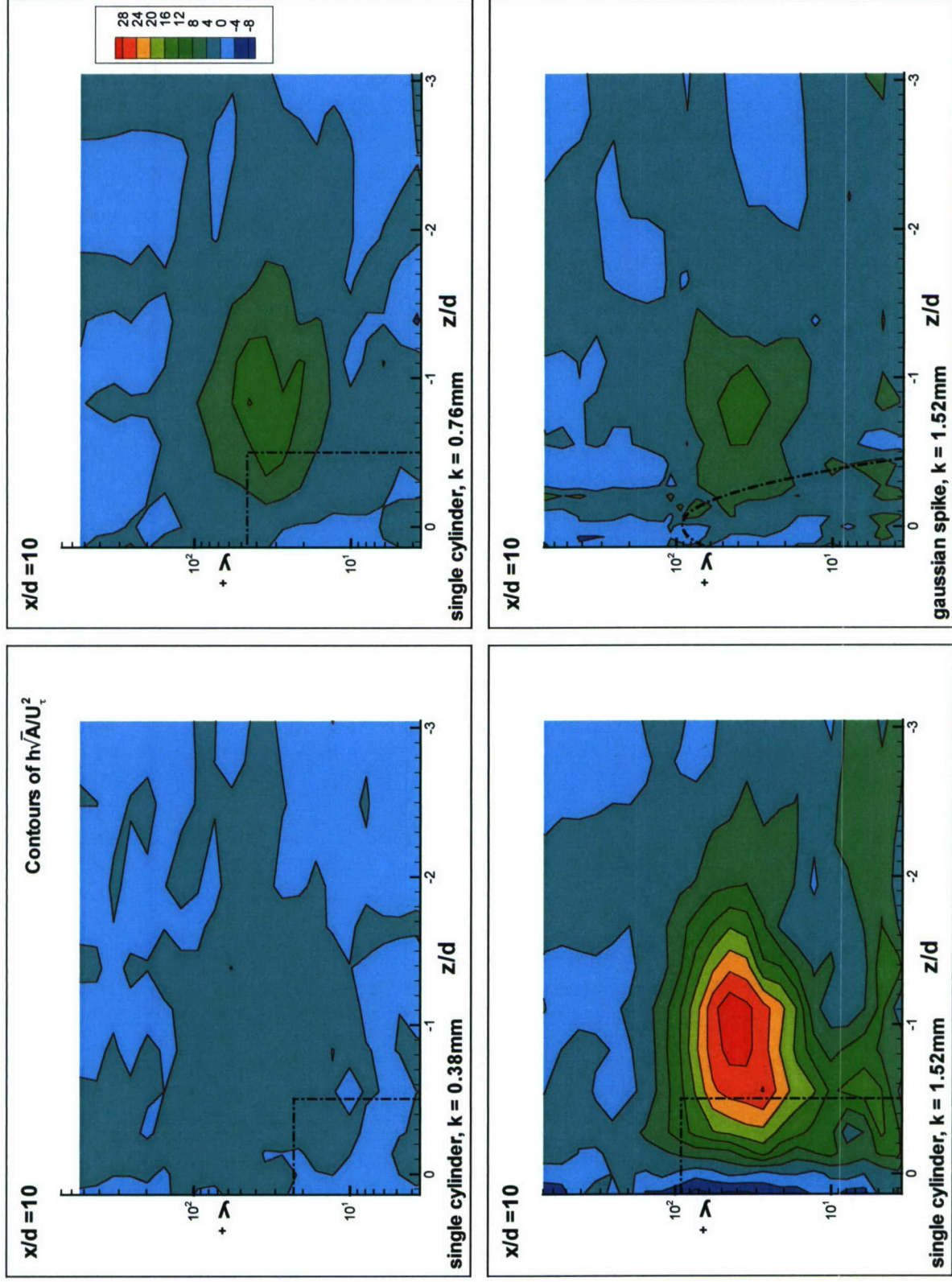


Figure 3.10 (b). Semi-log contours of mean-flow helicity density,  $h\sqrt{A}/U_\tau^2$ , in the  $y^* - z/d$  plane at  $x/d=10$ .

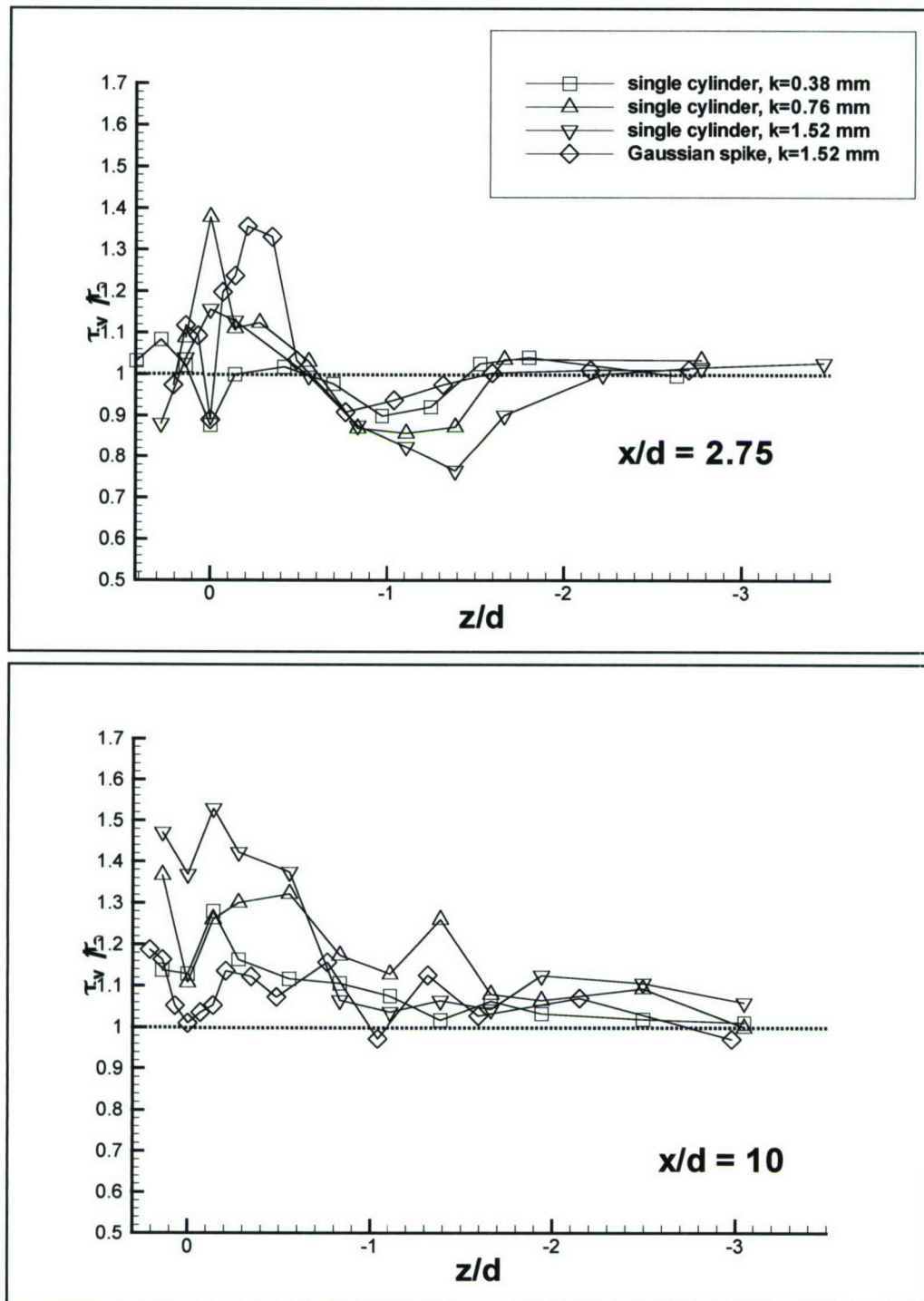


Figure 3.11 (a). Normalized wall shear ( $\tau_w/\tau_o$ ): Spanwise variation at  $x/d=2.75$  and 10.



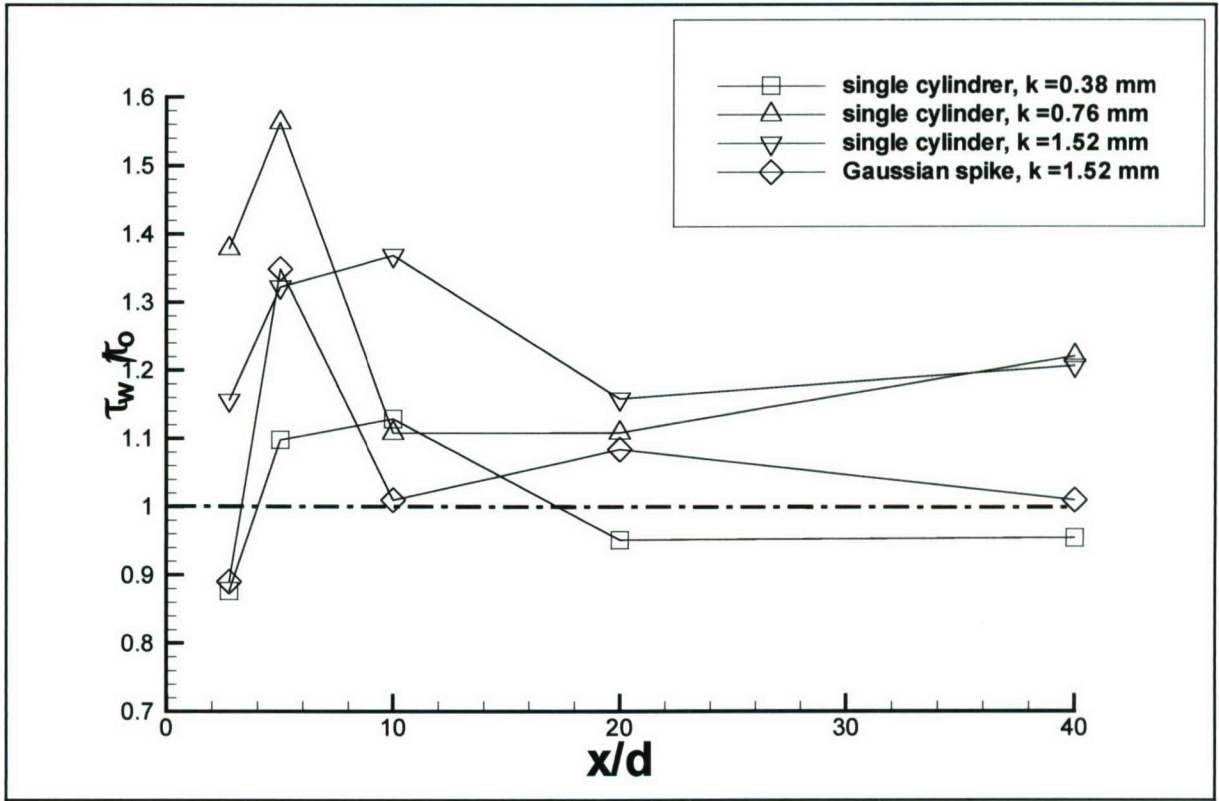


Figure 3.11 (b). Normalized wall shear ( $\tau_w/\tau_o$ ): Centerline streamwise variation

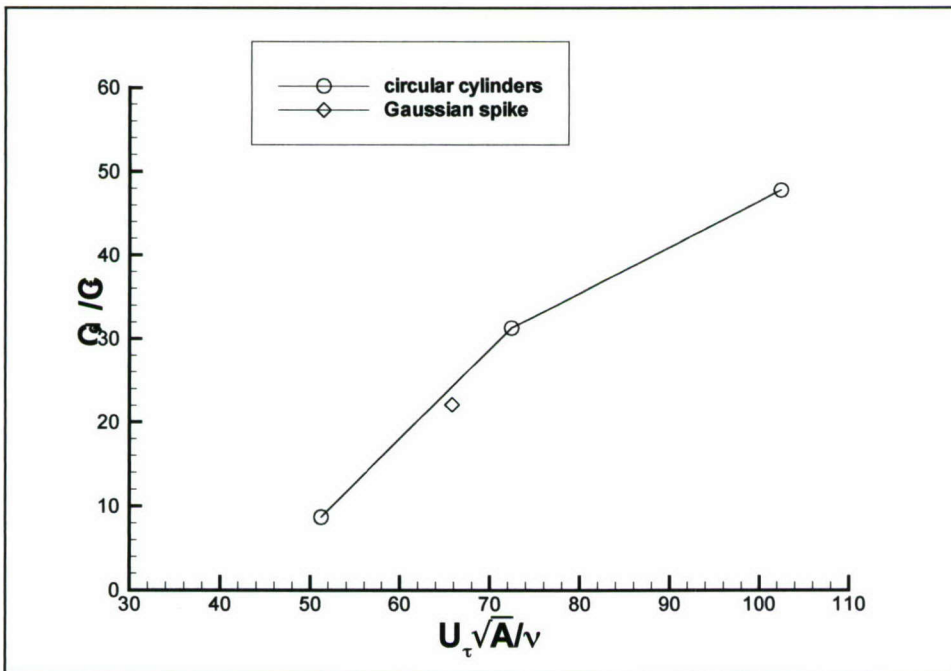


Figure 3.12. Normalized drag coefficient,  $C_d/C_f$ , of the cylinders and the Gaussian spike

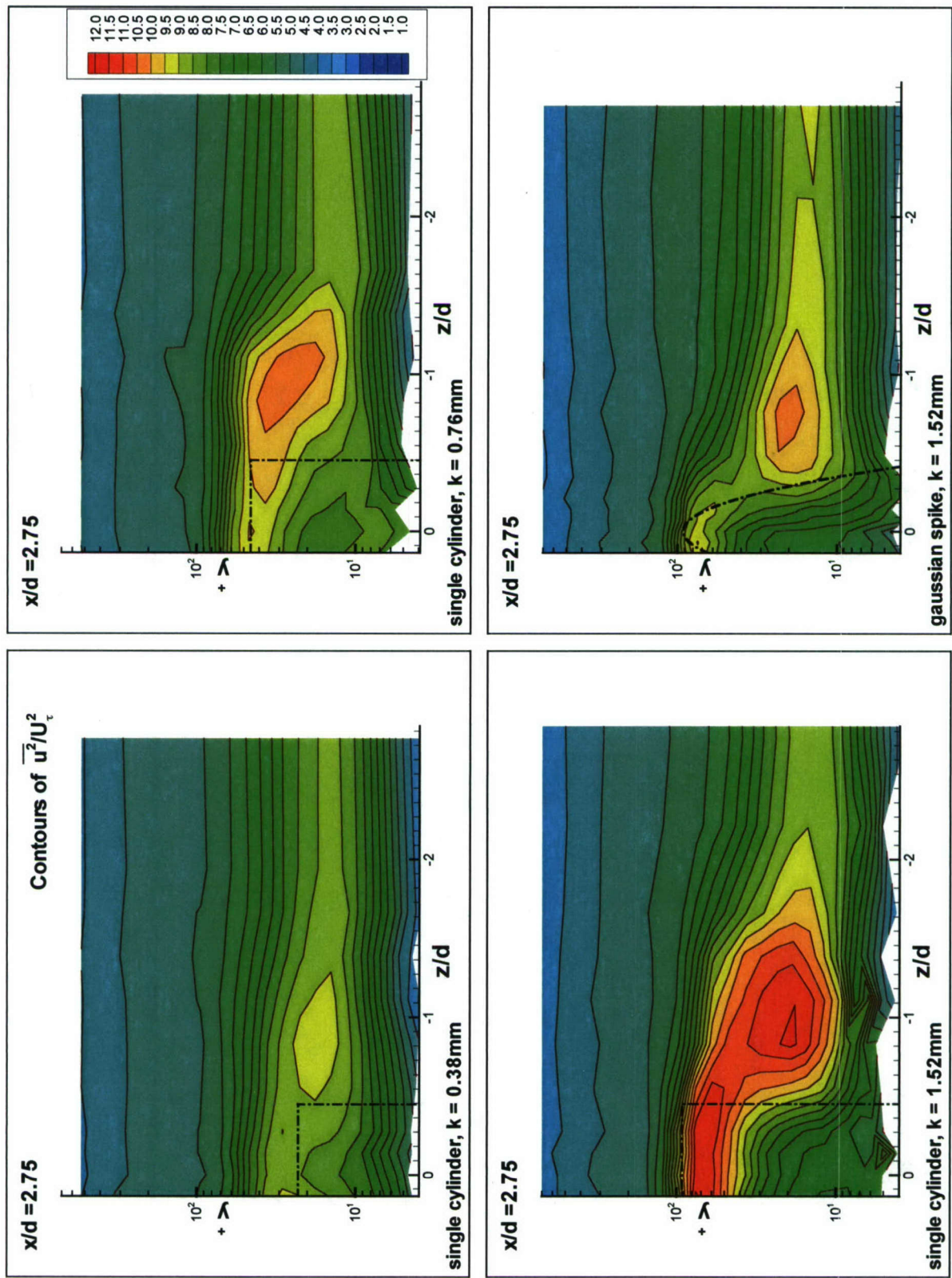


Figure 3.13 (a). Semi-log contours of streamwise normal stress,  $\overline{u^2}/U_\tau^2$ , in the  $y^*-z/d$  plane at  $x/d=2.75$ .



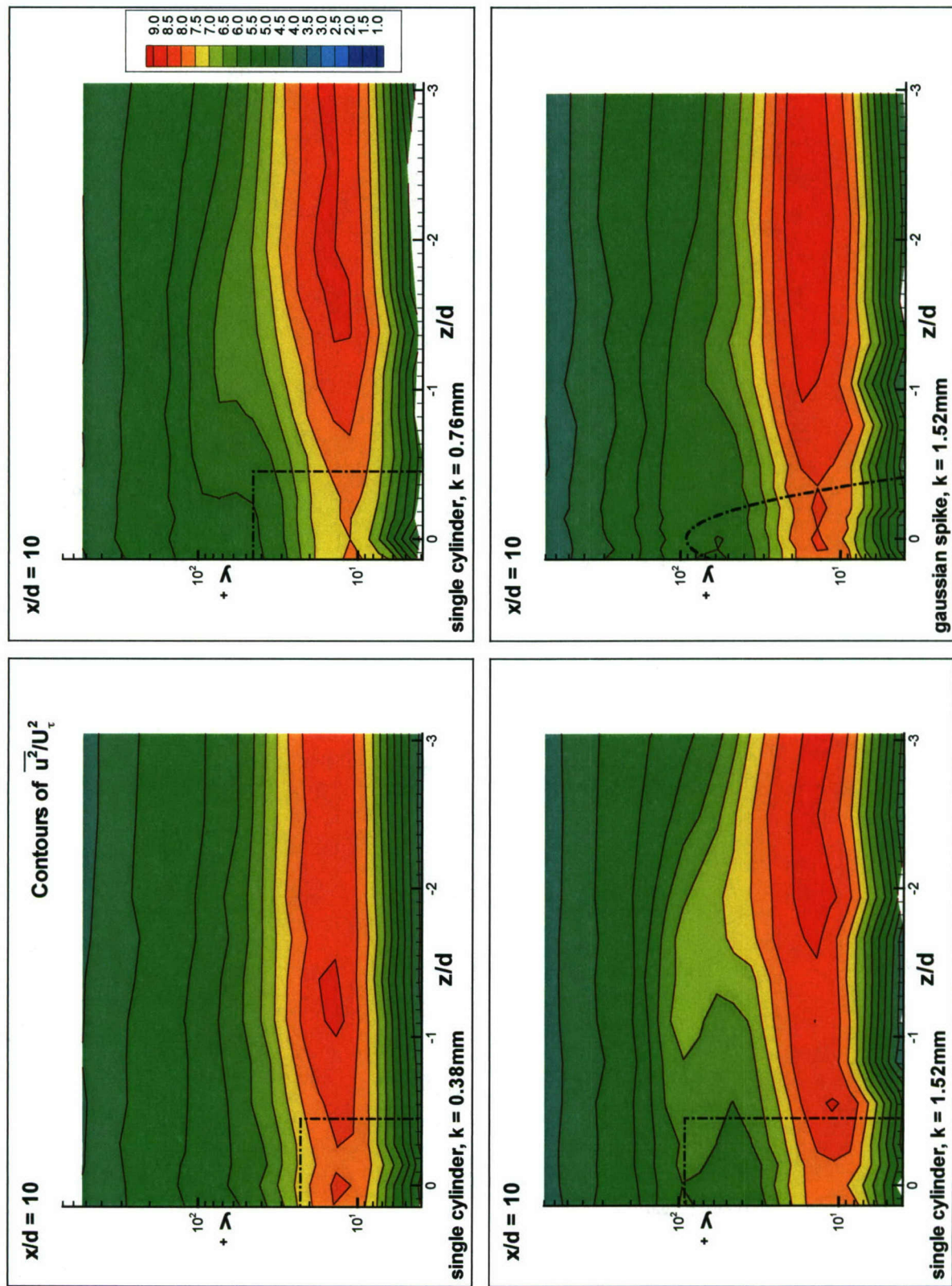


Figure 3.13 (b). Semi-log contours of streamwise normal stress,  $\overline{u^2}/U_\tau^2$ , in the  $y^* - z/d$  plane at  $x/d = 10$ .

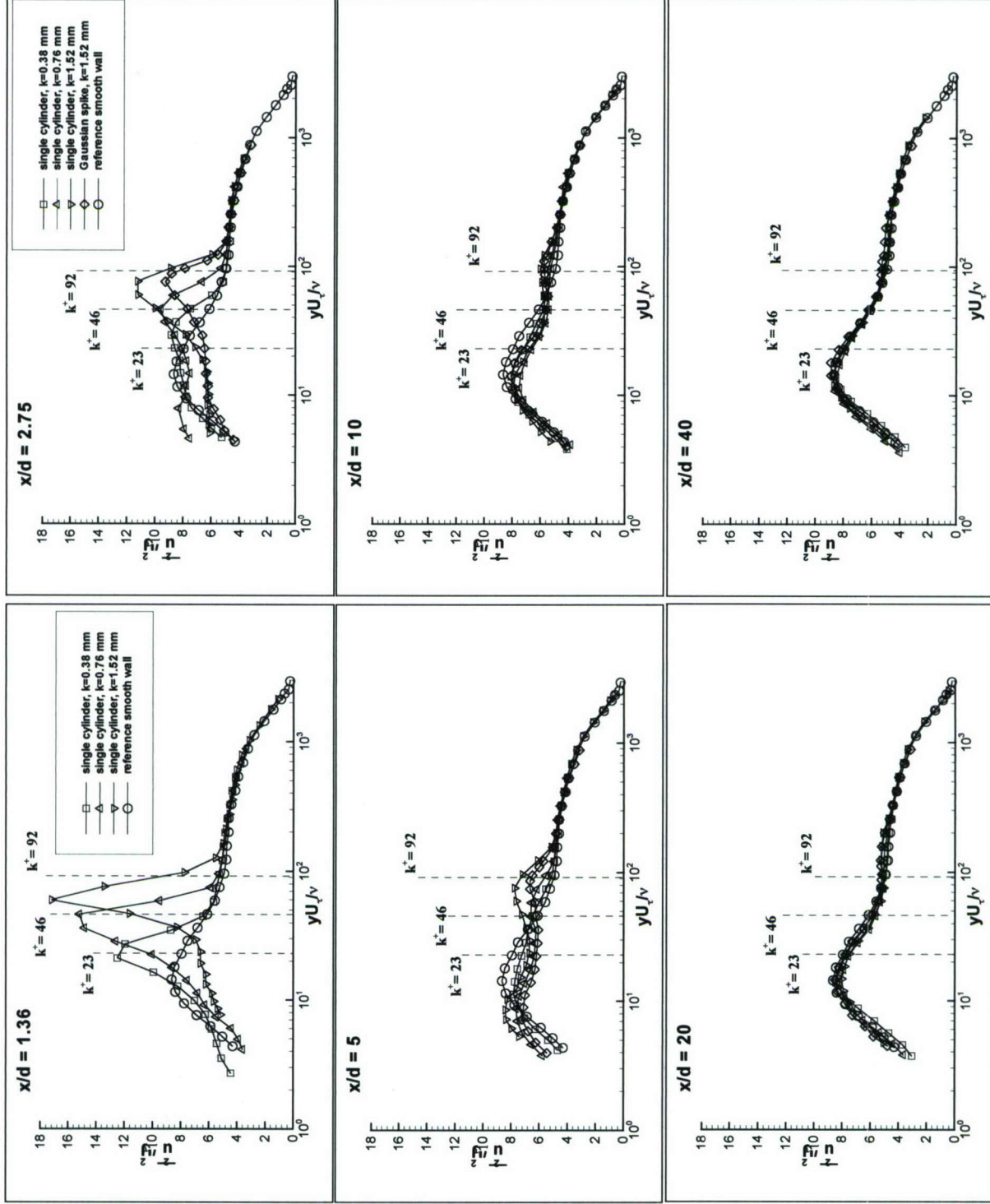


Figure 3.14.  $\overline{u'^2}/U_\tau^2$  versus  $yU_\tau/\nu$ , streamwise Reynolds normal stress profiles along the centerline.



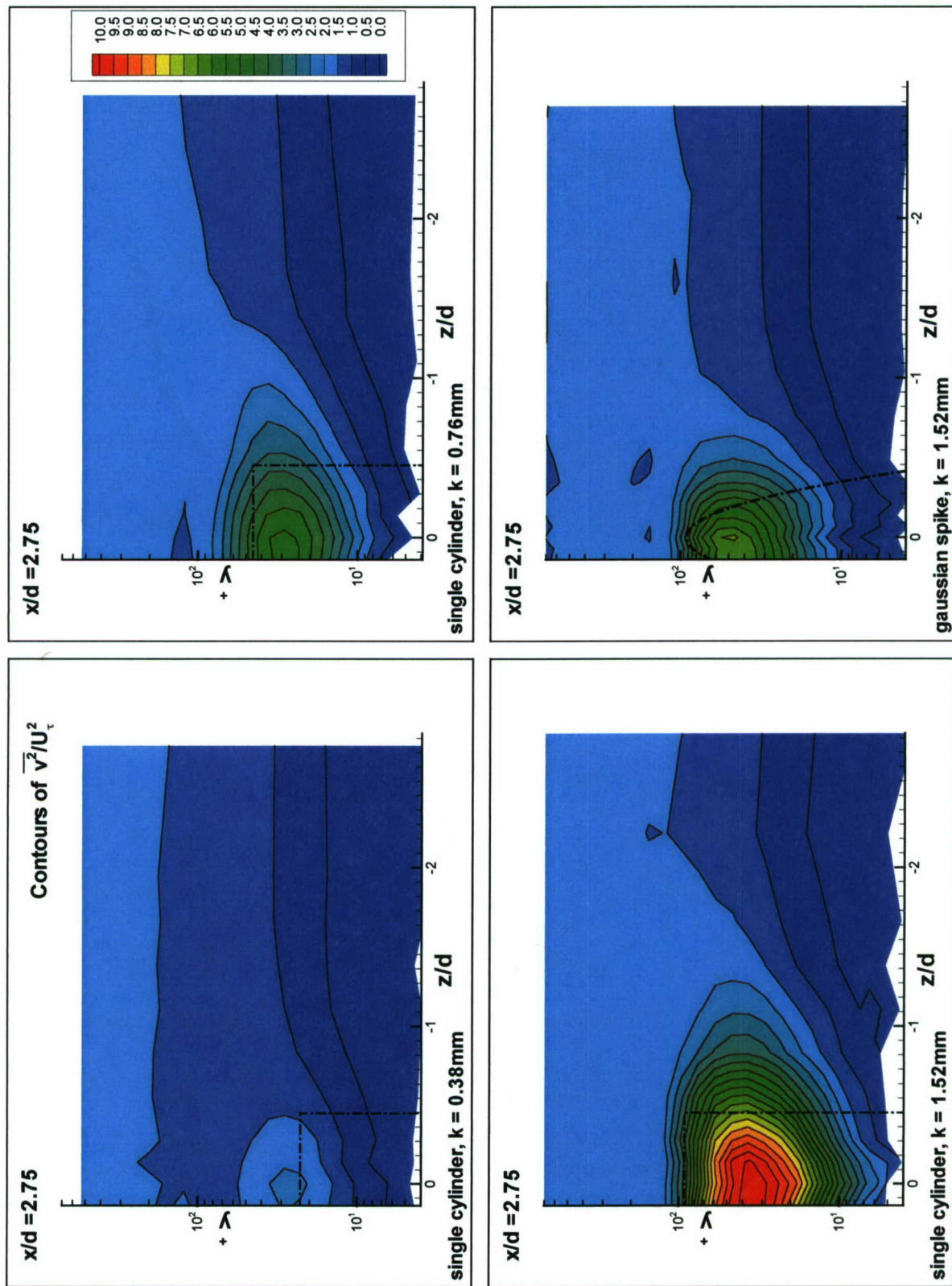


Figure 3.15 (a). Semi-log contours of wall-normal Reynolds normal stress,  $\overline{v^2}/U_\tau^2$  in the  $y^+ - z/d$  plane at  $x/d = 2.75$ .

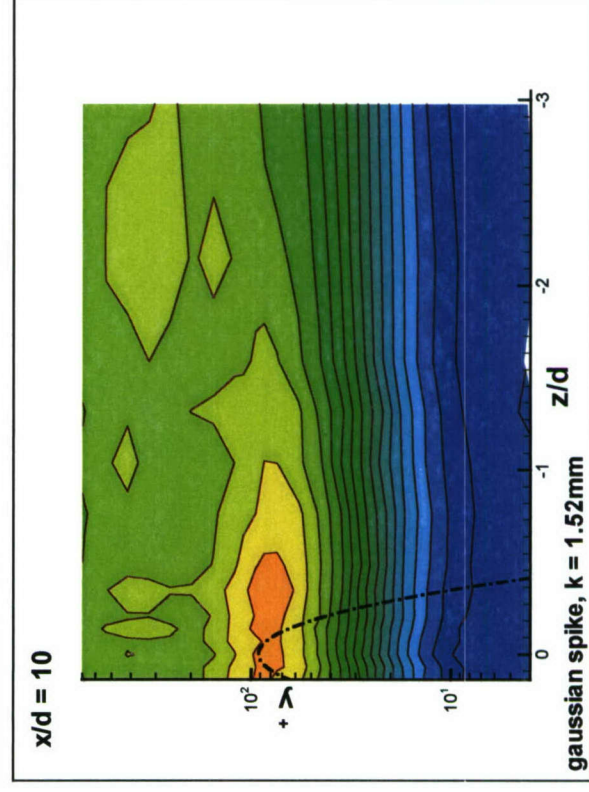
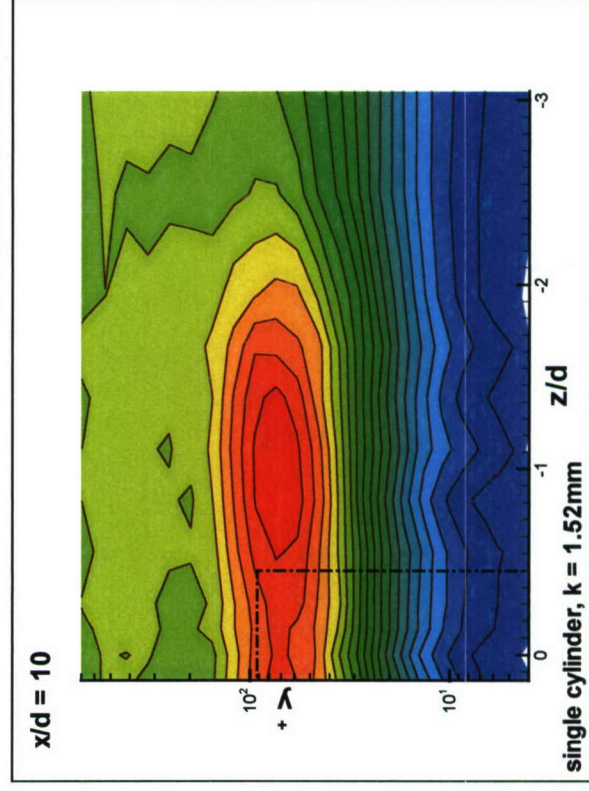
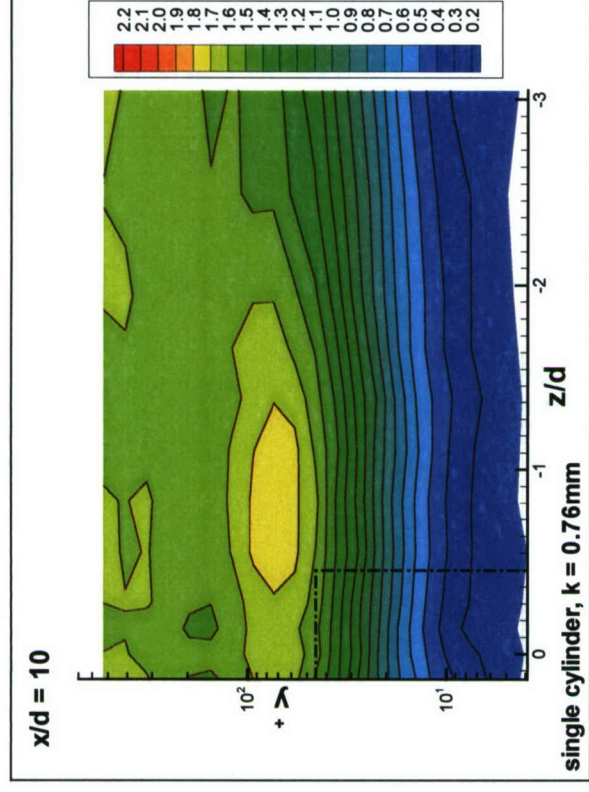
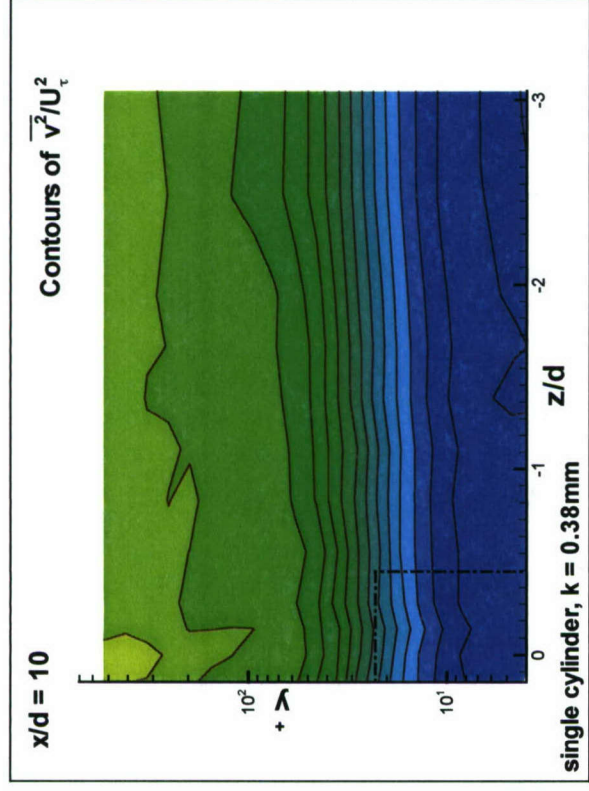


Figure 3.15 (b). Semi-log contours of wall-normal Reynolds normal stress,  $\overline{v^2}/U_\tau^2$  in the  $y^+ - z/d$  plane at  $x/d = 10$ .



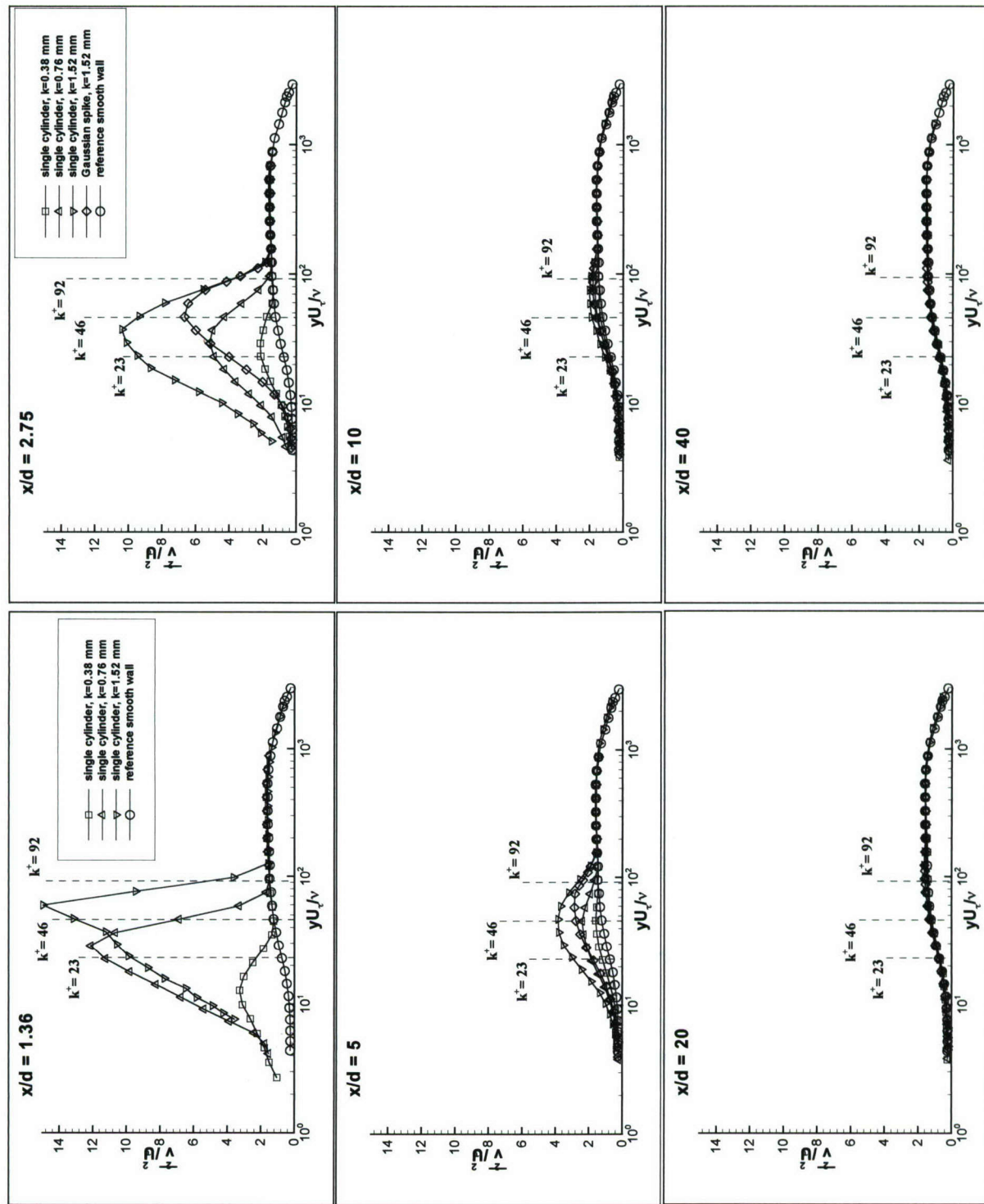


Figure 3.16.  $\overline{v^2}/U_\tau^2$  versus  $yU_\tau/\nu$ , wall-normal Reynolds normal stress profiles along the centerline.

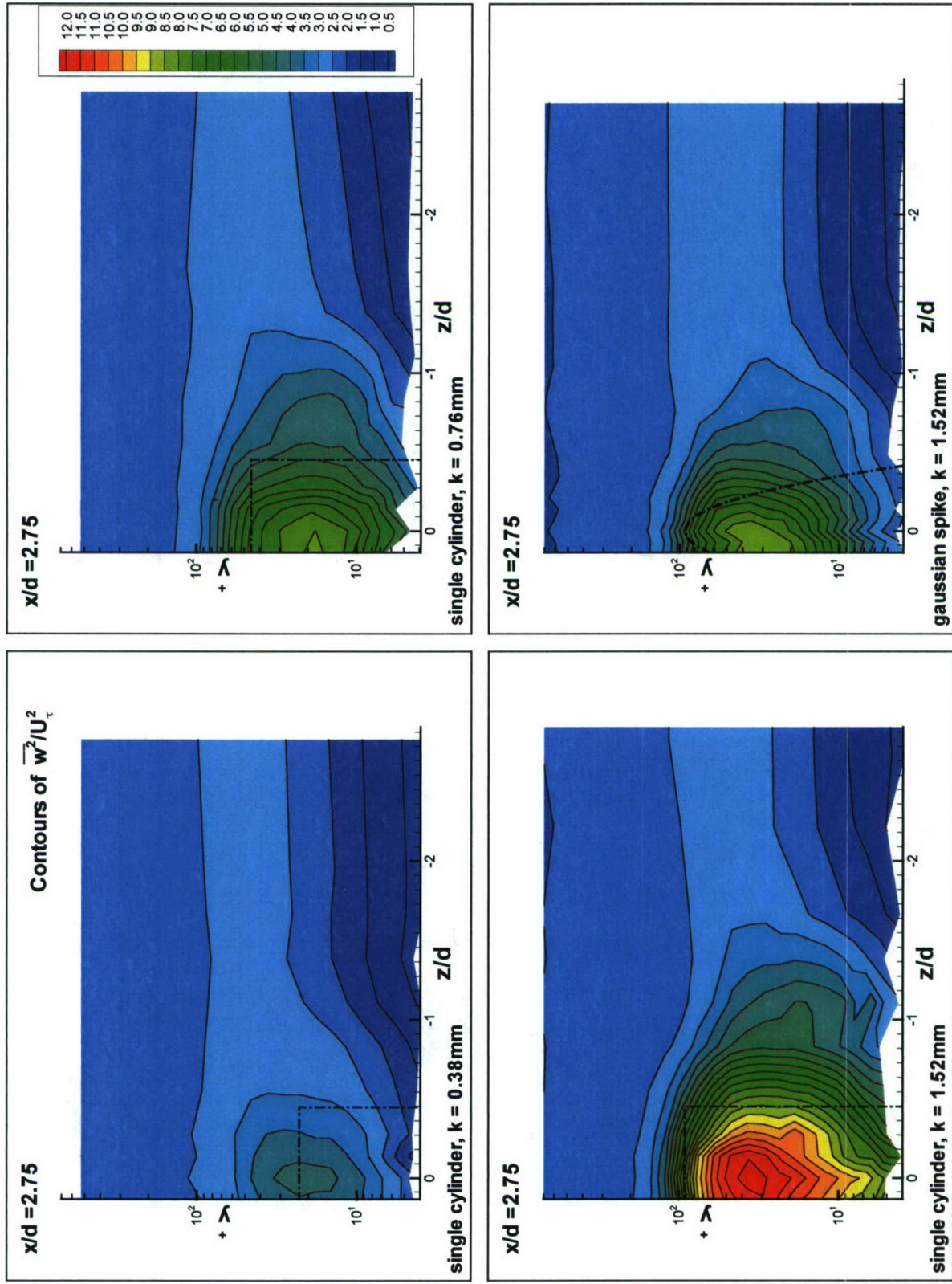


Figure 3.17 (a). Semi-log contours of spanwise Reynolds normal stress,  $\overline{w^2}/U_\tau^2$  in the  $y^* - z/d$  plane at  $x/d = 2.75$ .



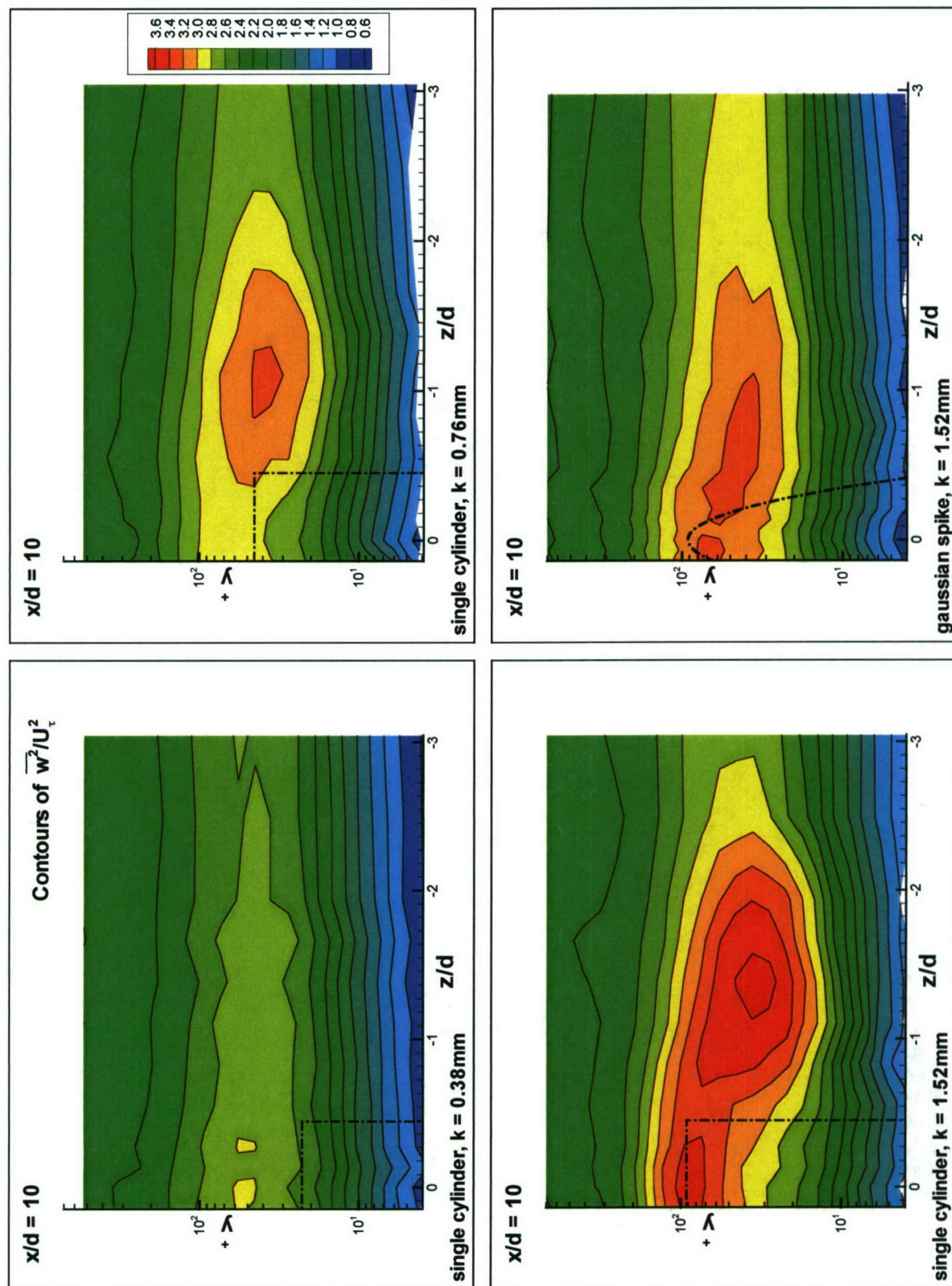


Figure 3.17 (b). Semi-log contours of spanwise Reynolds normal stress,  $\overline{w^2}/U_\tau^2$  in the  $y^* - z/d$  plane at  $x/d = 10$ .

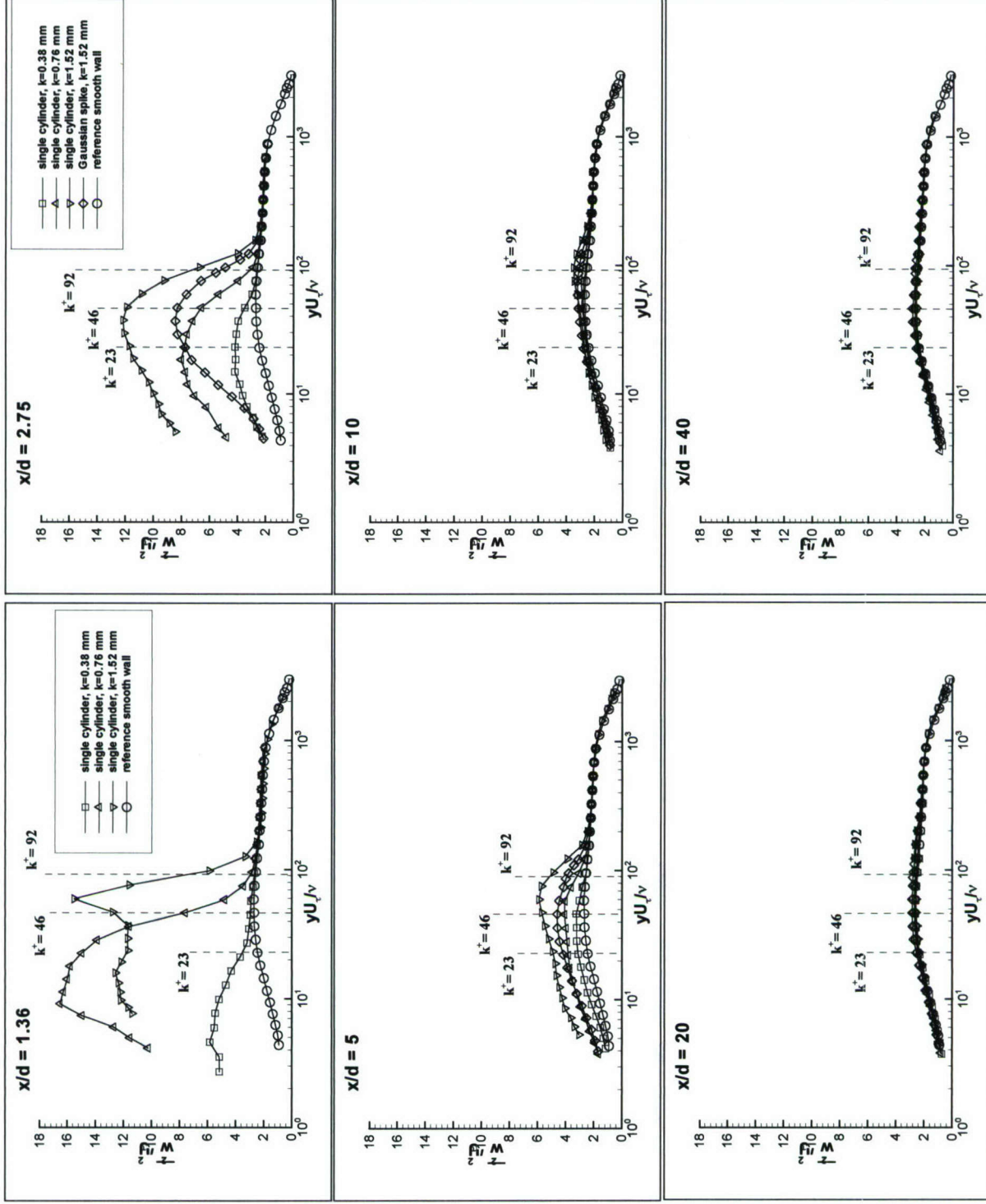


Figure 3.18.  $\overline{w^2}/U_\tau^2$  versus  $yU_\tau/\nu$ , spanwise Reynolds normal stress profiles along the centerline.



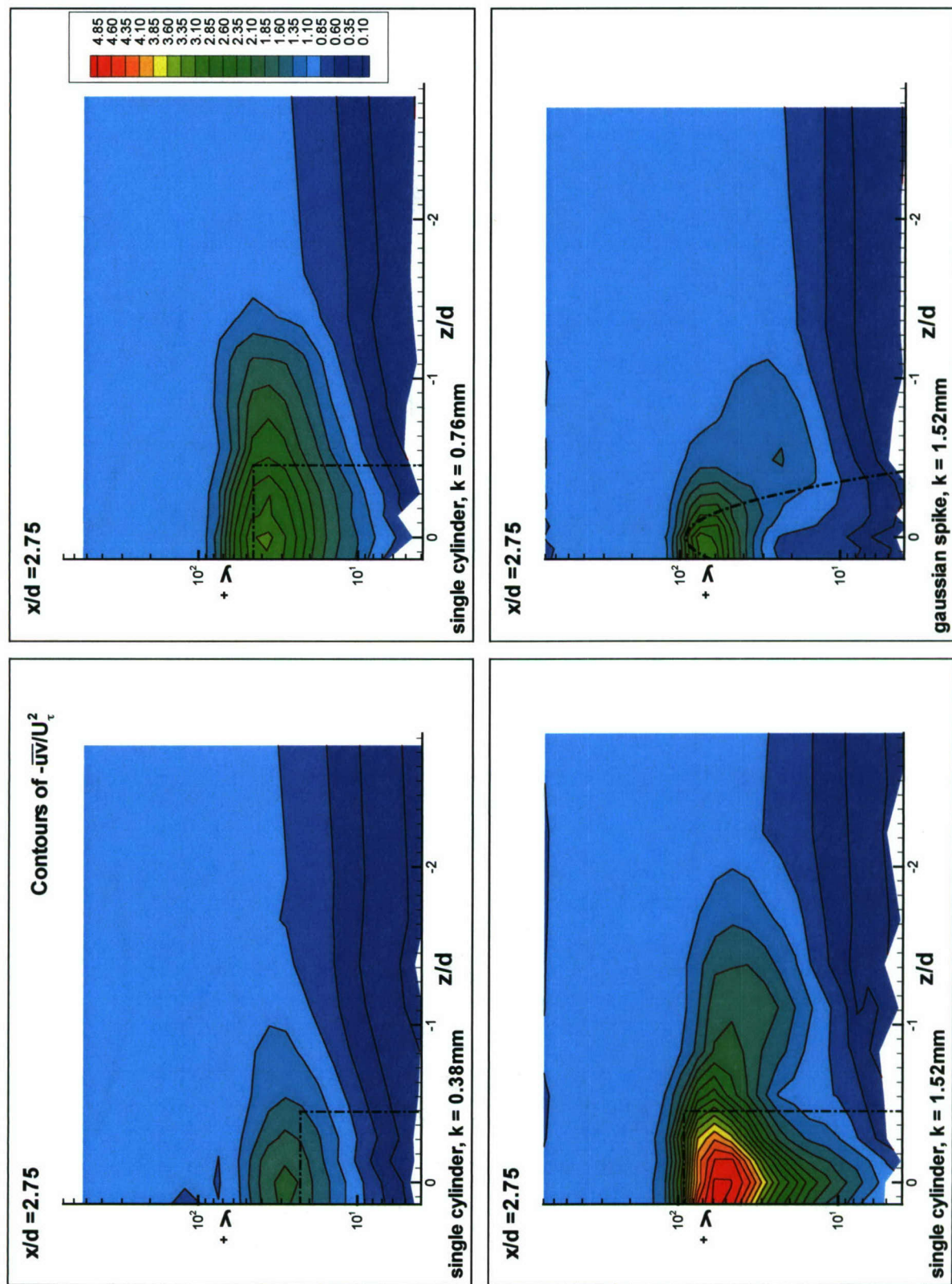


Figure 3.19 (a). Semi-log contours of Reynolds streamwise shearing stress,  $-\overline{uv}/U_\tau^2$  in the  $y^+ - z/d$  plane at  $x/d = 2.75$ .

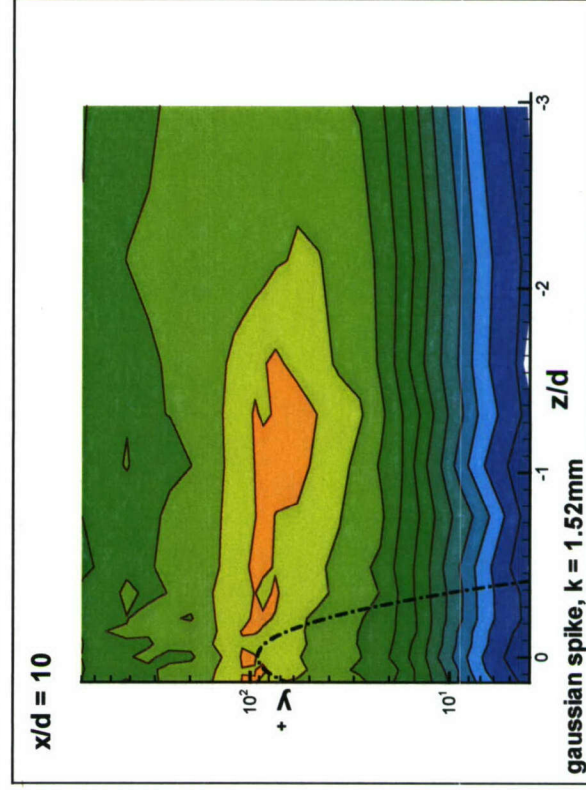
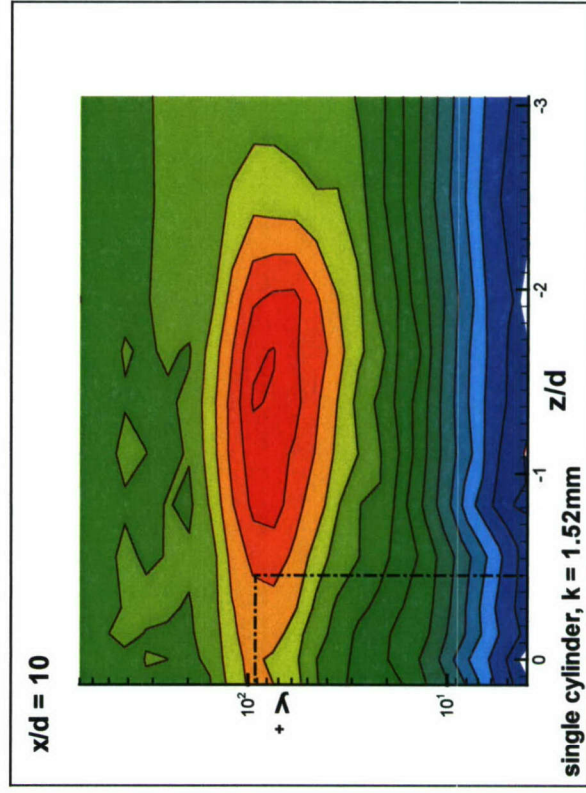
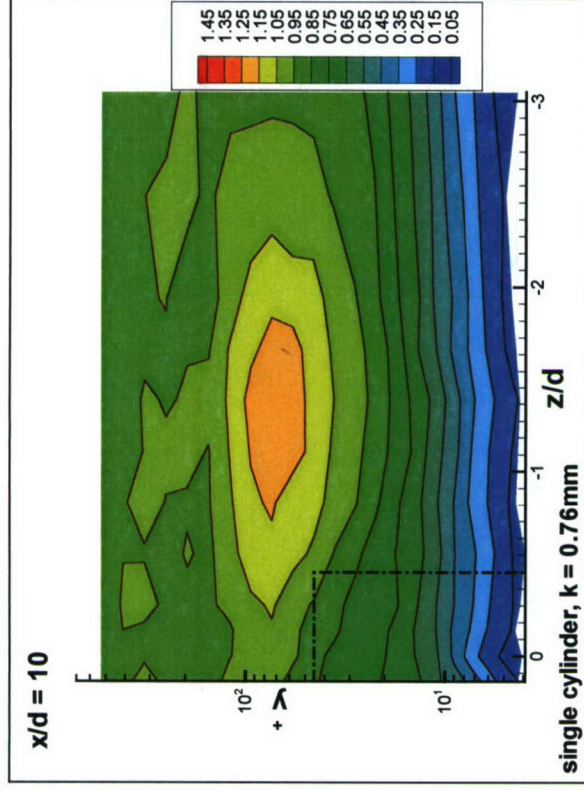
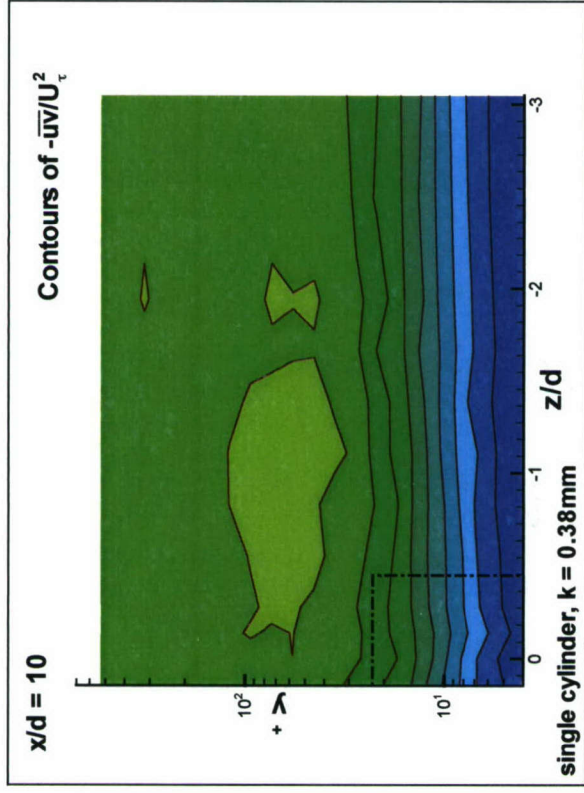


Figure 3.19 (b). Semi-log contours of Reynolds streamwise shearing stress,  $-\overline{uv}/U_\tau^2$  in the  $y^+ - z/d$  plane at  $x/d = 10$ .



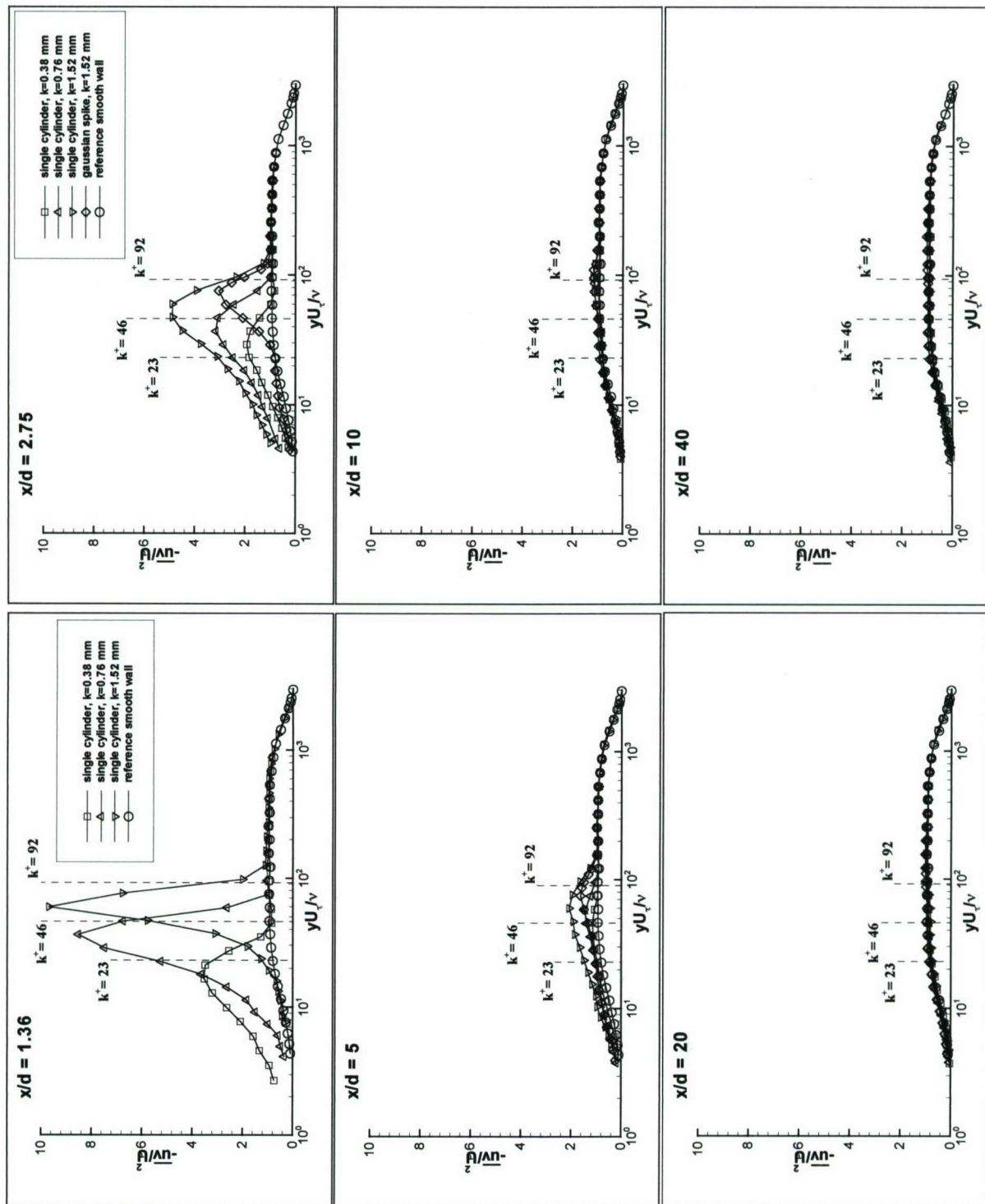
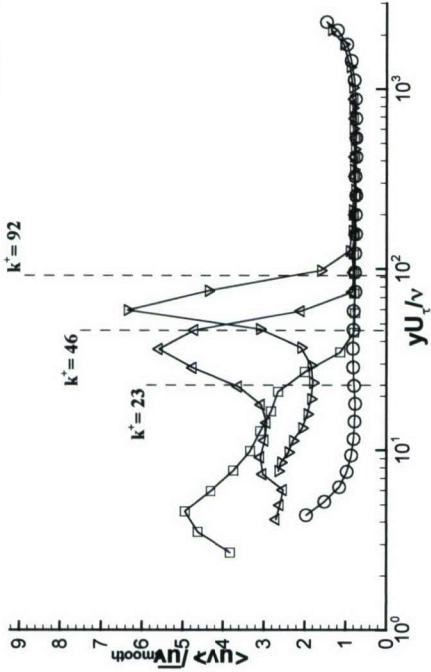


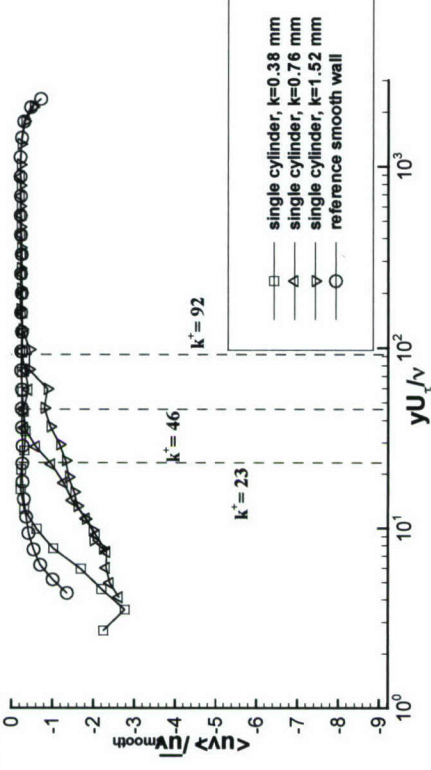
Figure 3.20.  $-\overline{uv}/U_\tau^2$  versus  $yU_\tau/\nu$ , streamwise Reynolds shear stress profiles along the centerline.

$x/d = 1.36$

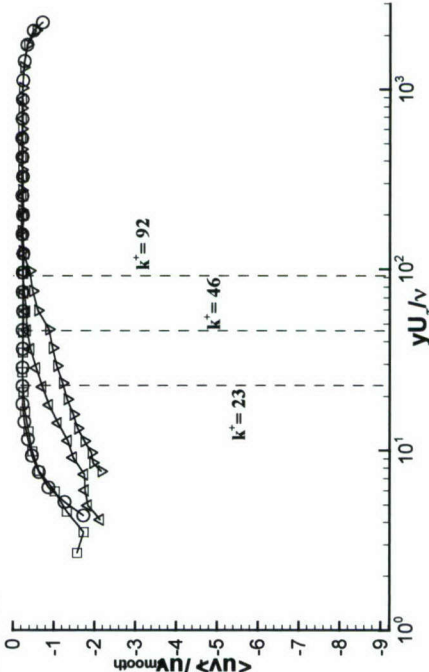
Quadrant-2



Quadrant-1



Quadrant-3



Quadrant-4

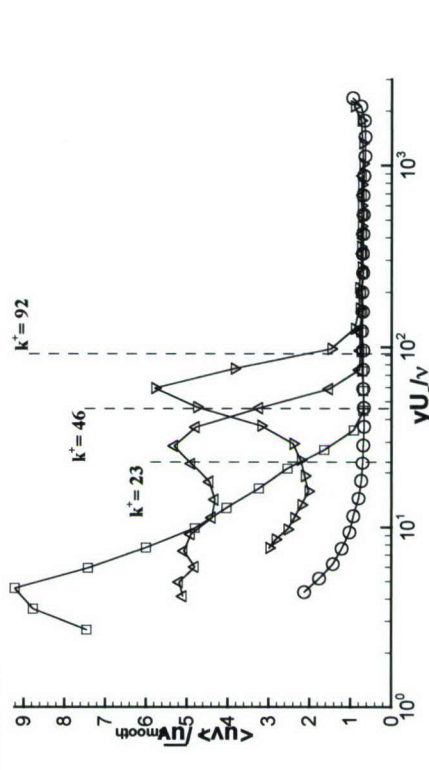


Figure 3.21 (a). Quadrant contributions to streamwise Reynolds shear stress,  $-\overline{uv}$  : profiles, normalized by  $\sqrt{\overline{u^2}\overline{v^2}}$ , varying with  $yU_\tau/\nu$  at  $x/d = 1.36$ .



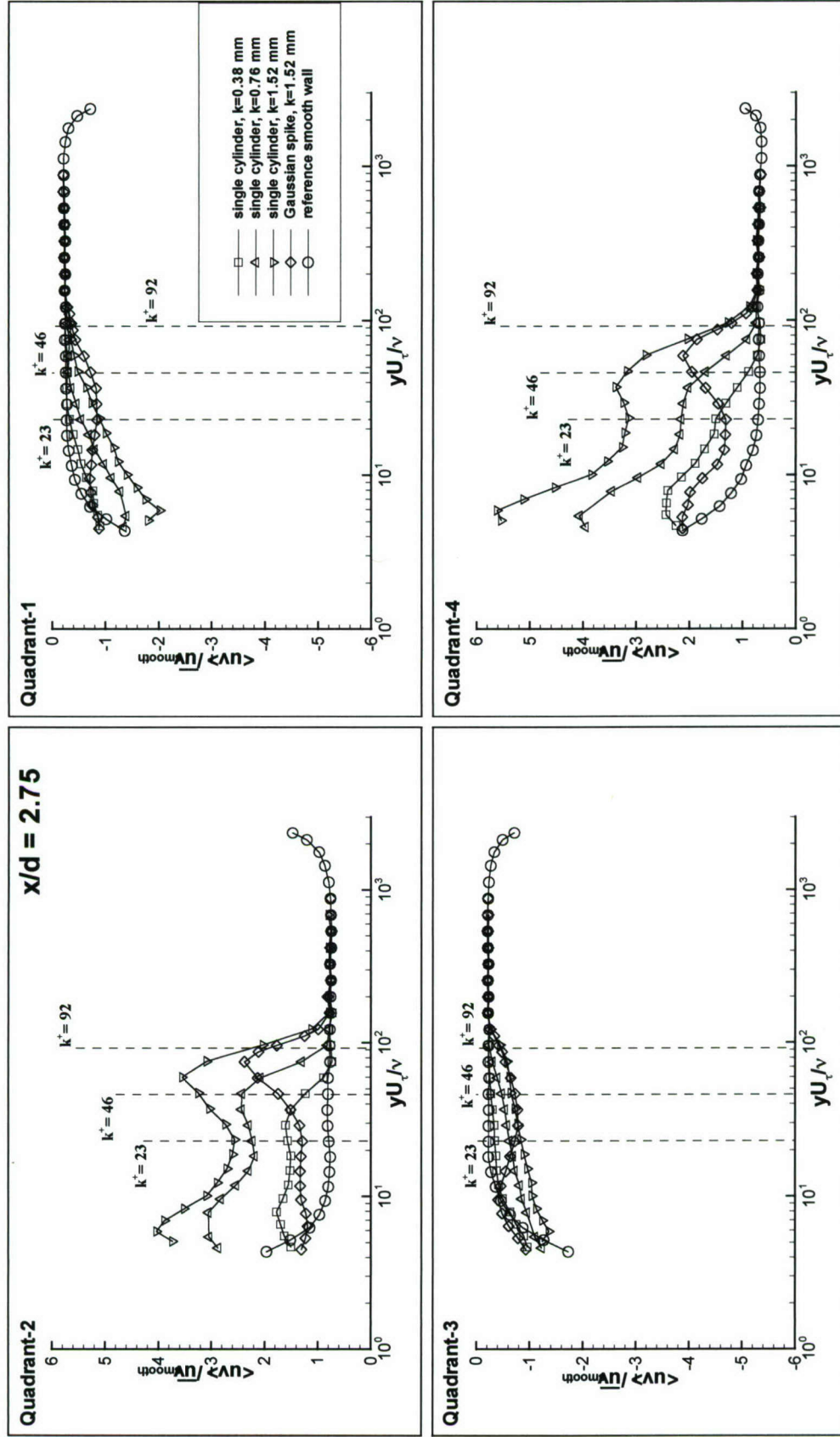


Figure 3.21 (b). Quadrant contributions to streamwise Reynolds shear stress,  $-\overline{u'v'}$  : profiles, normalized by  $U_\tau^2$ , varying with  $yU_\tau/\nu$  at  $x/d = 2.75$ .

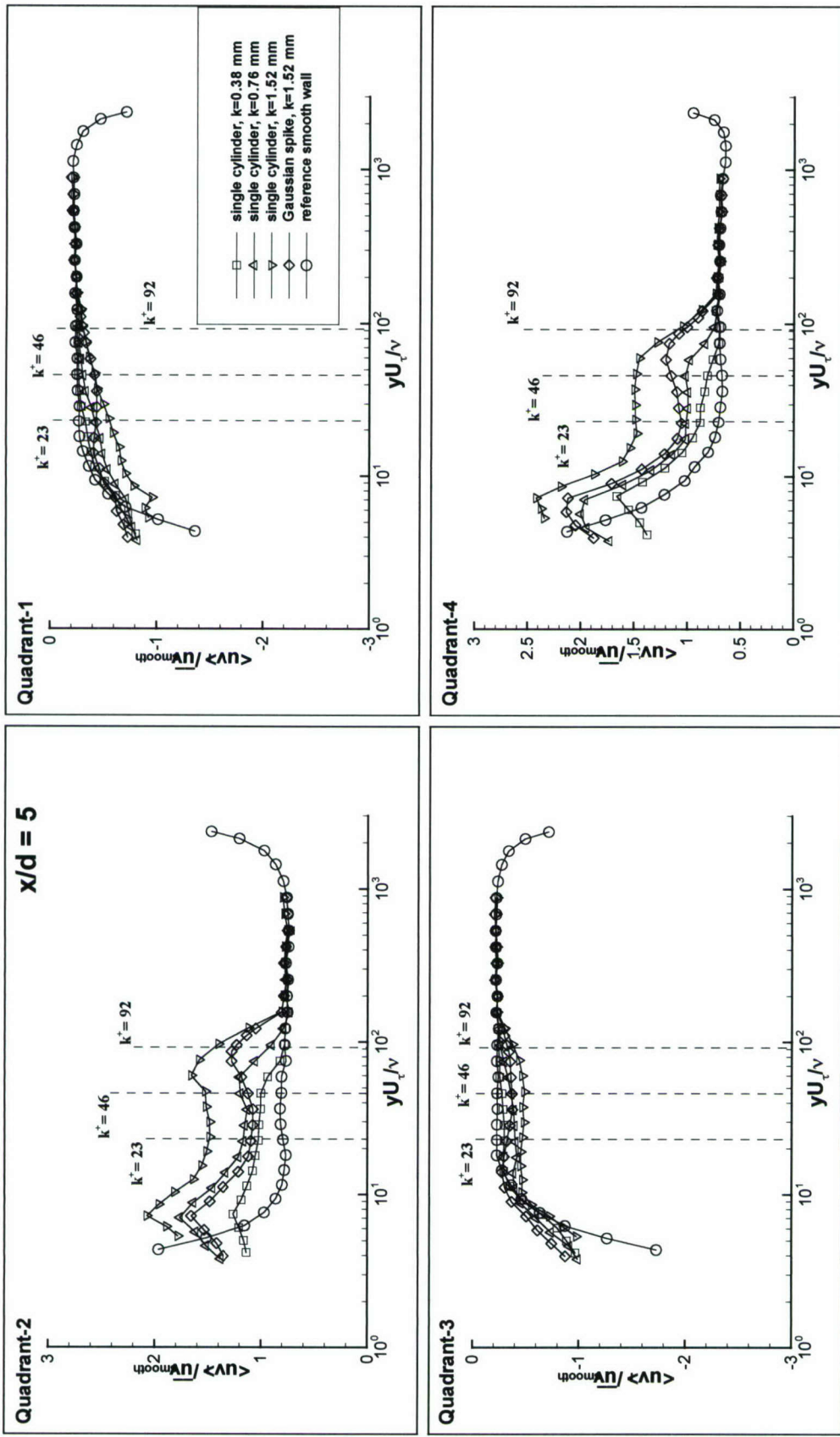


Figure 3.21 (c). Quadrant contributions to streamwise Reynolds shear stress,  $-\overline{uv}$ : profiles, normalized by  $\overline{uv}_{smooth}$ , varying with  $yU_\tau/\nu$  at  $x/d = 5$ .



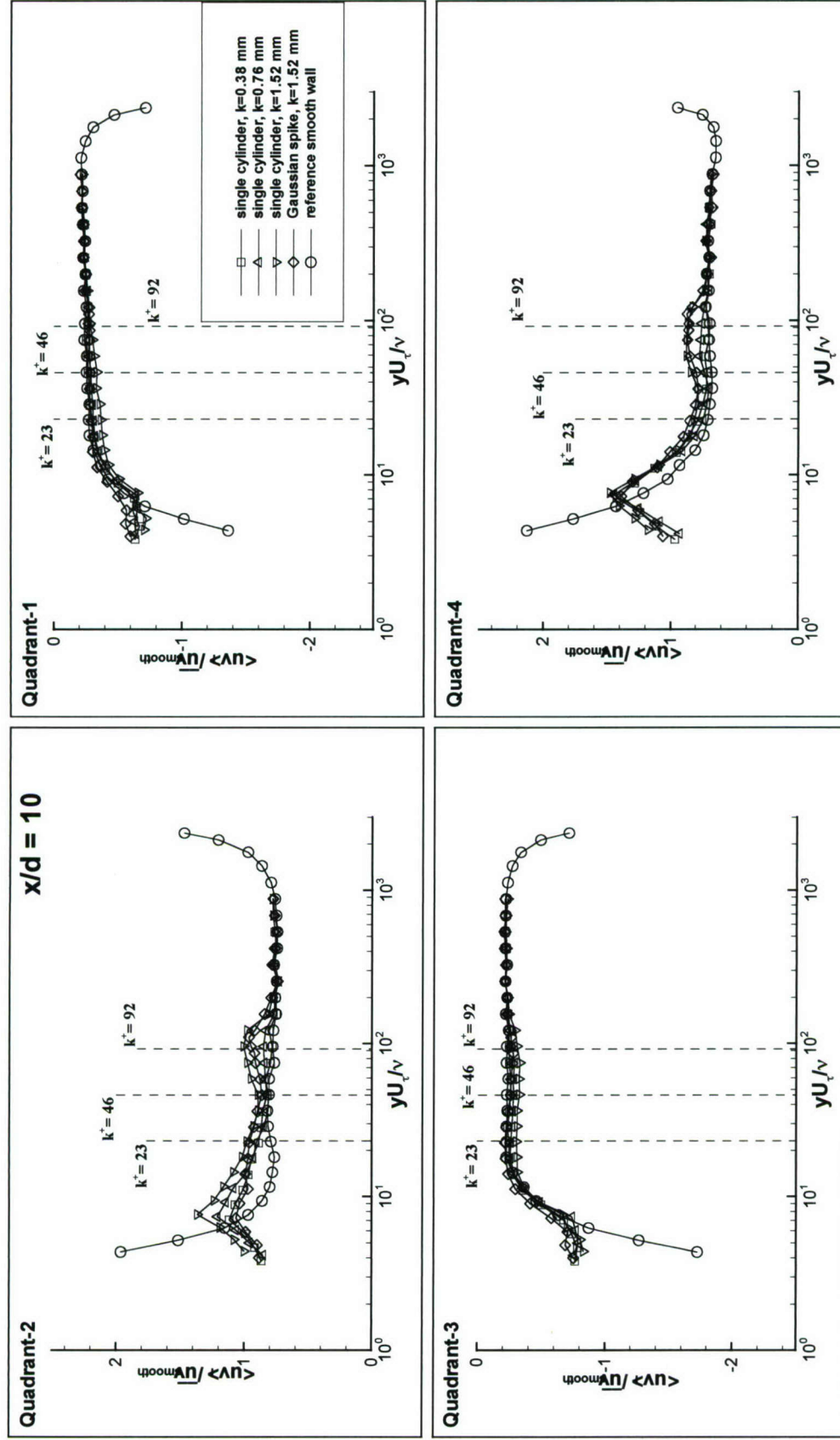


Figure 3.21 (d). Quadrant contributions to streamwise Reynolds shear stress, profiles, normalized by  $\overline{u'v'_{smooth}}$ , varying with  $yU_\tau/\nu$  at  $x/d = 10$ .

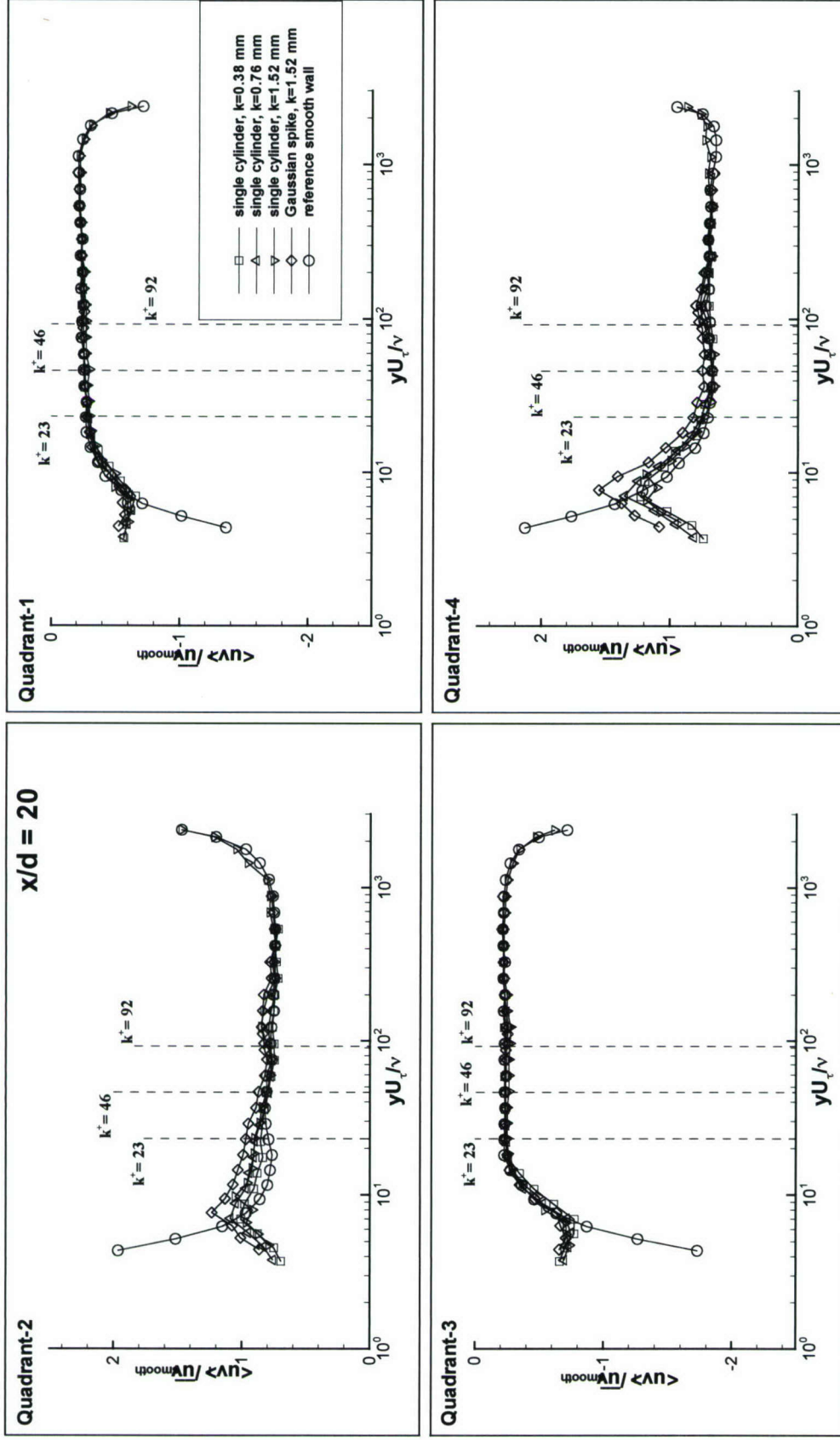


Figure 3.21 (e). Quadrant contributions to streamwise Reynolds shear stress,  $-\overline{uv}$  : profiles, normalized by  $\overline{uv}^{\text{smooth}}$ , varying with  $yU_{\tau}/\nu$  at  $x/d = 20$ .



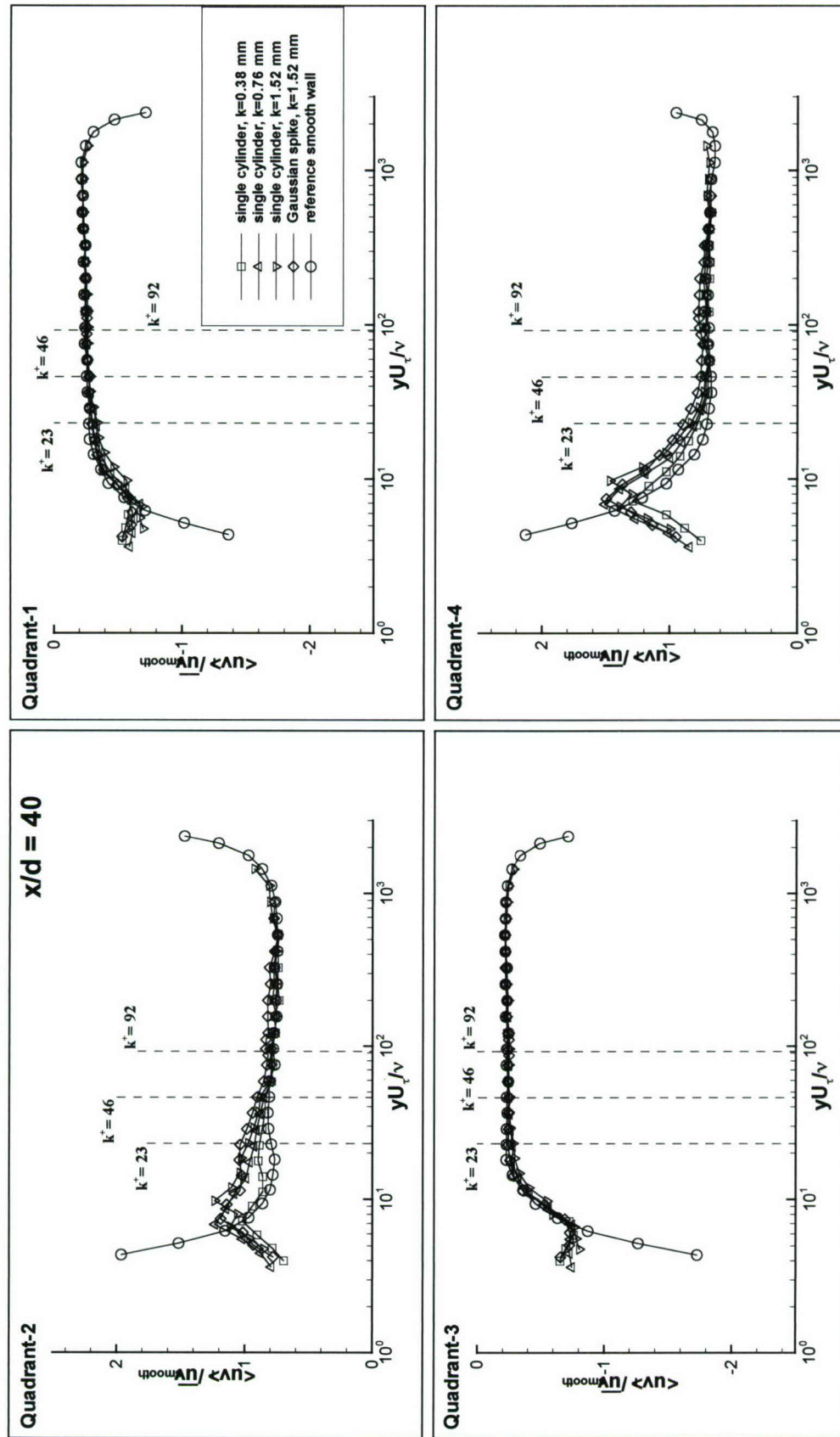


Figure 3.21 (f). Quadrant contributions to streamwise Reynolds shear stress, profiles, normalized by  $-\overline{uv}_{smooth}$ , varying with  $yU_\tau/\nu$  at  $x/d = 40$ .

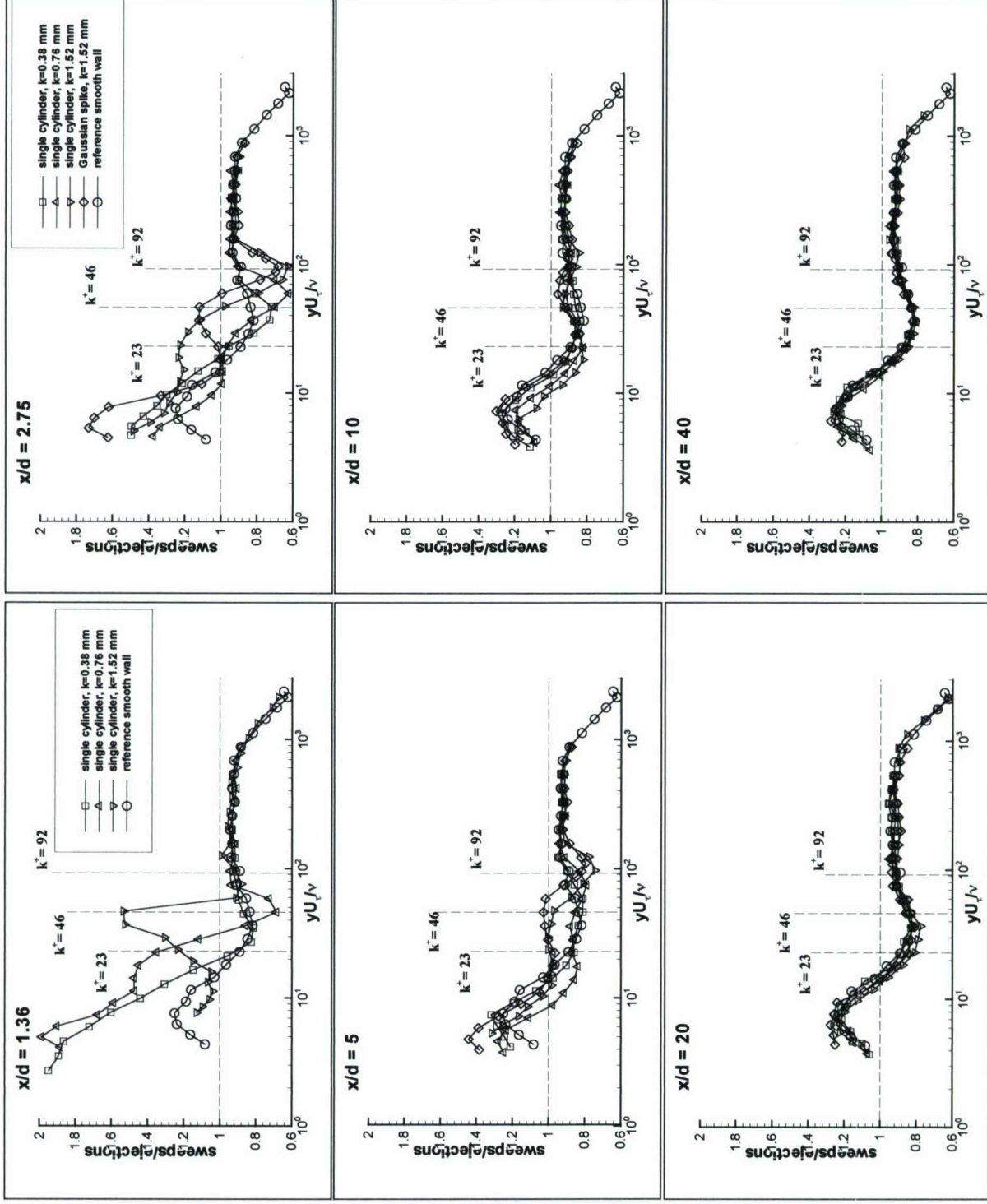


Figure 3.21 (g). Ratio of sweep to ejection contributions varying with  $yU_i/v$  at the six streamwise locations.



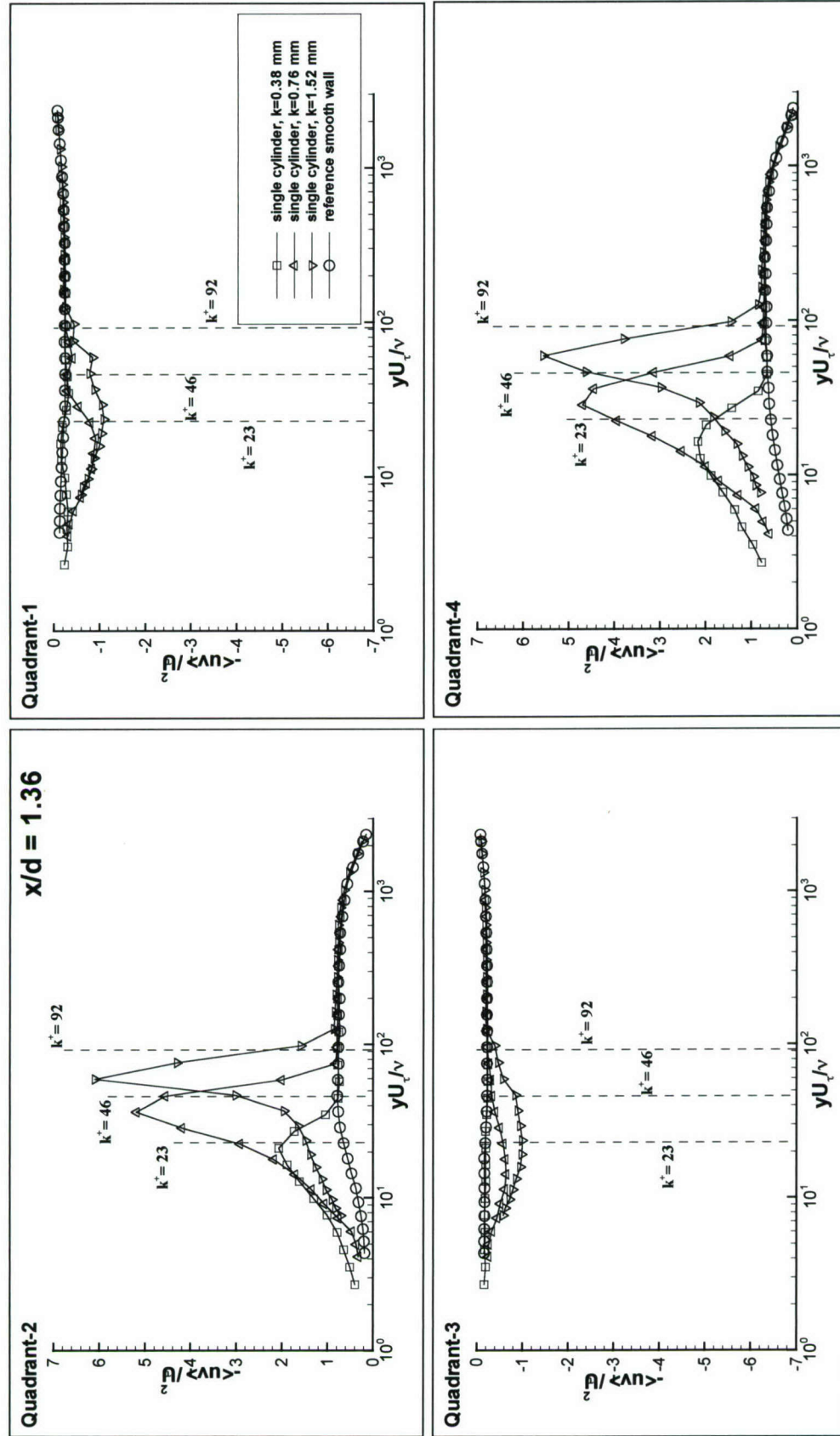


Figure 3.21 (h). Quadrant contributions to streamwise Reynolds shear stress,  $-\overline{uv}'$  : profiles, normalized by  $U_\tau^2$ , varying with  $yU_\tau/\nu$  at  $x/d = 1.36$ .

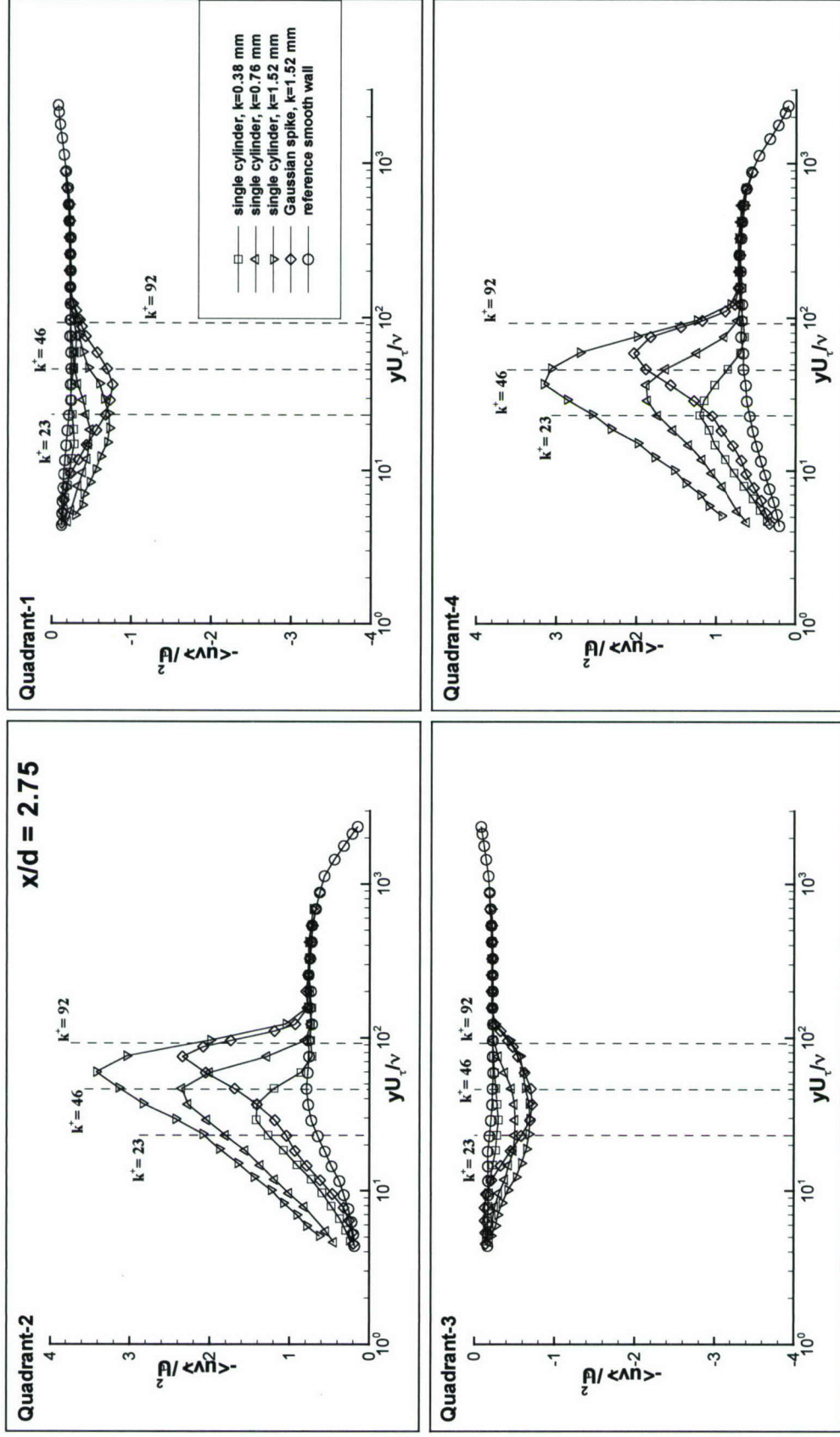


Figure 3.21 (i). Quadrant contributions to streamwise Reynolds shear stress,  $-\overline{uv}$  : profiles, normalized by  $U_\tau^2$ , varying with  $yU_\tau/\nu$  at  $x/d = 2.75$ .



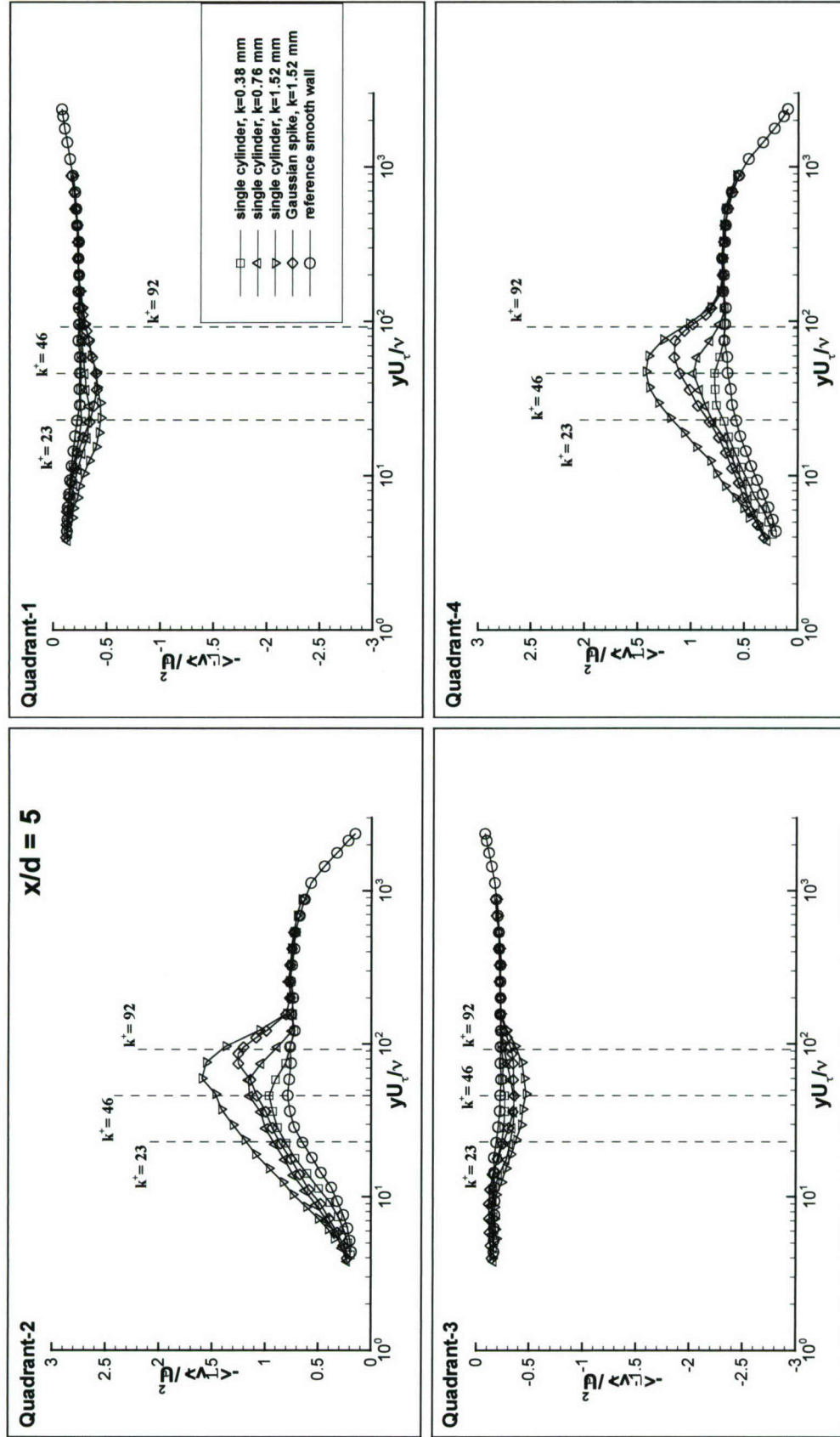


Figure 3.21 (j). Quadrant contributions to streamwise Reynolds shear stress,  $\overline{-uv}$  profiles, normalized by  $U_\tau^2$ , varying with  $yU_\tau/\nu$  at  $x/d = 5$ .

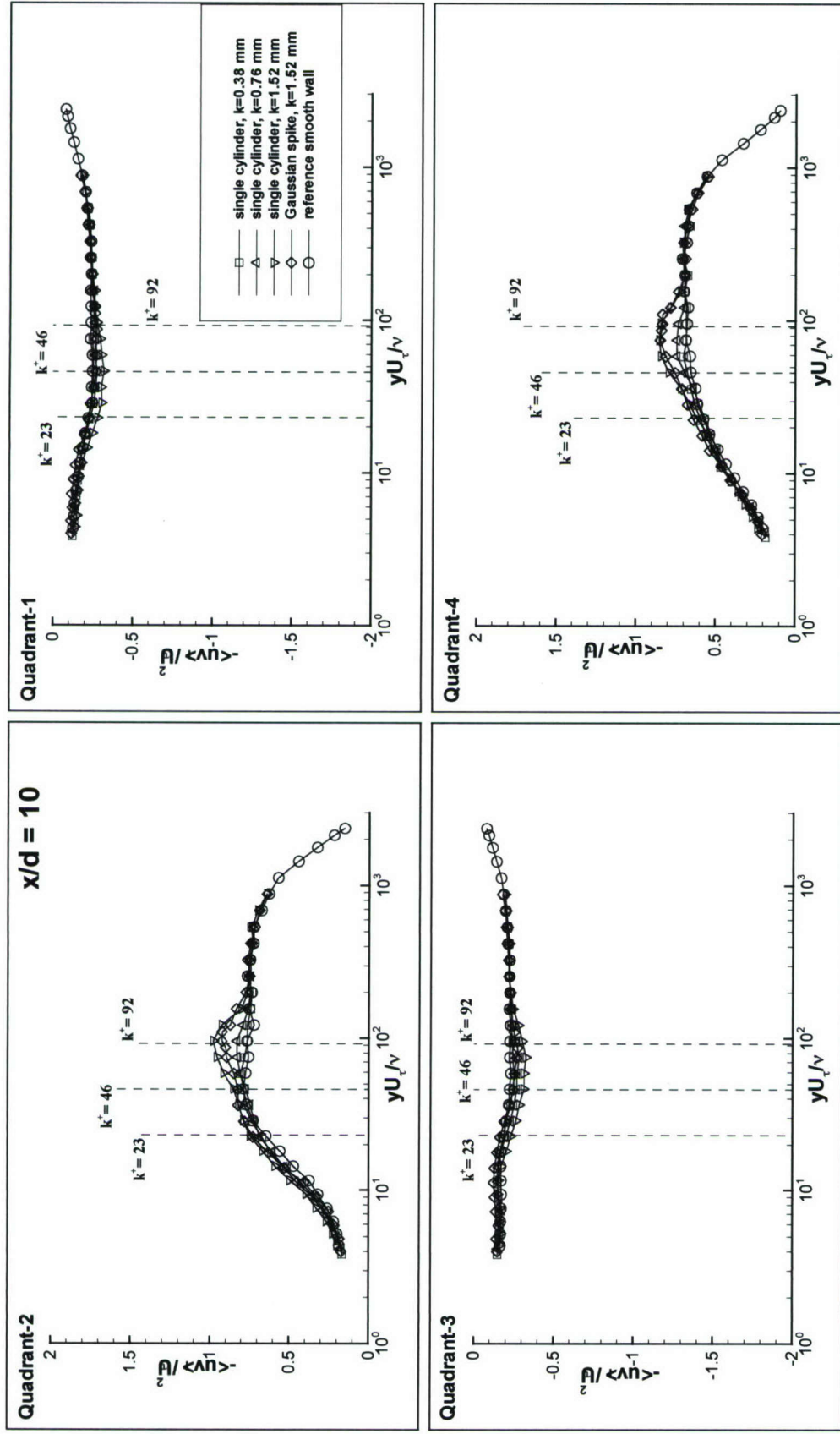


Figure 3.21 (k). Quadrant contributions to streamwise Reynolds shear stress,  $-\overline{uv}$  : profiles, normalized by  $U_\tau^2$ , varying with  $yU_\tau/\nu$  at  $x/d = 10$ .



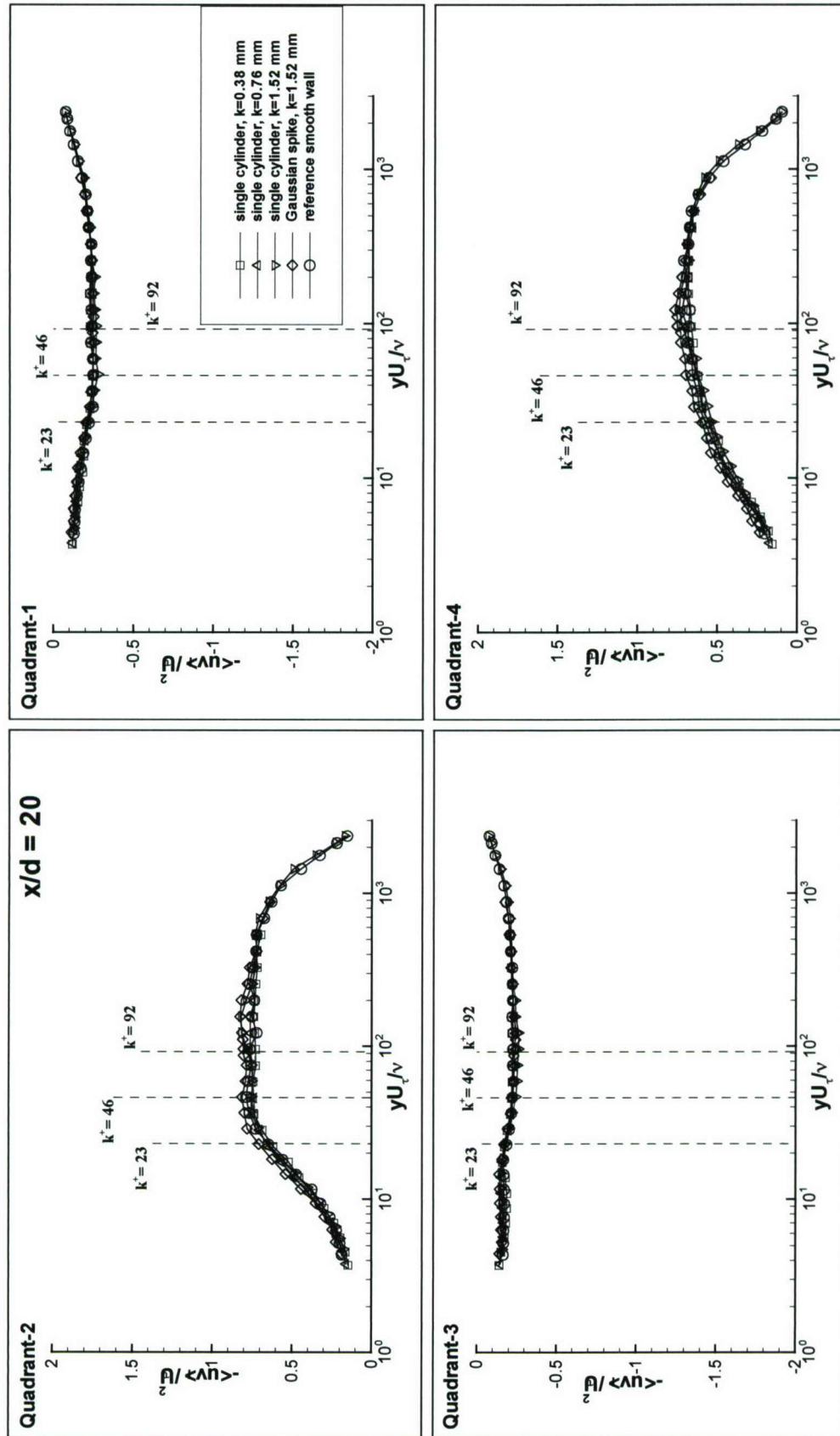


Figure 3.21 (I). Quadrant contributions to streamwise Reynolds shear stress,  $-\overline{uv}$ : profiles, normalized by  $U_{\tau}^2$ , varying with  $yU_{\tau}/\nu$  at  $x/d = 20$ .

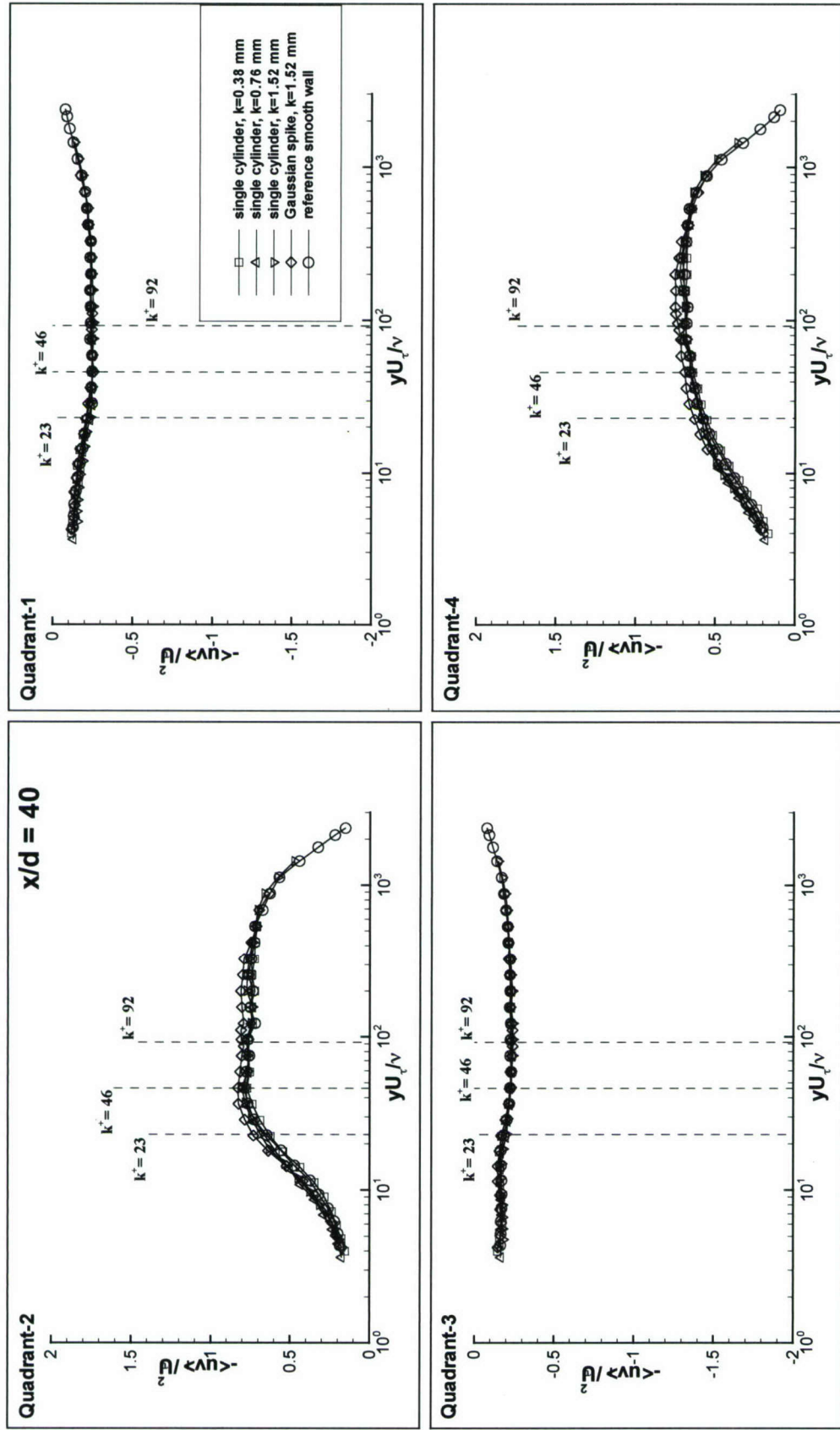


Figure 3.21 (m). Quadrant contributions to streamwise Reynolds shear stress,  $-\overline{uv}$  : profiles, normalized by  $U_\tau^2$ , varying with  $yU_\tau/\nu$  at  $x/d = 40$ .



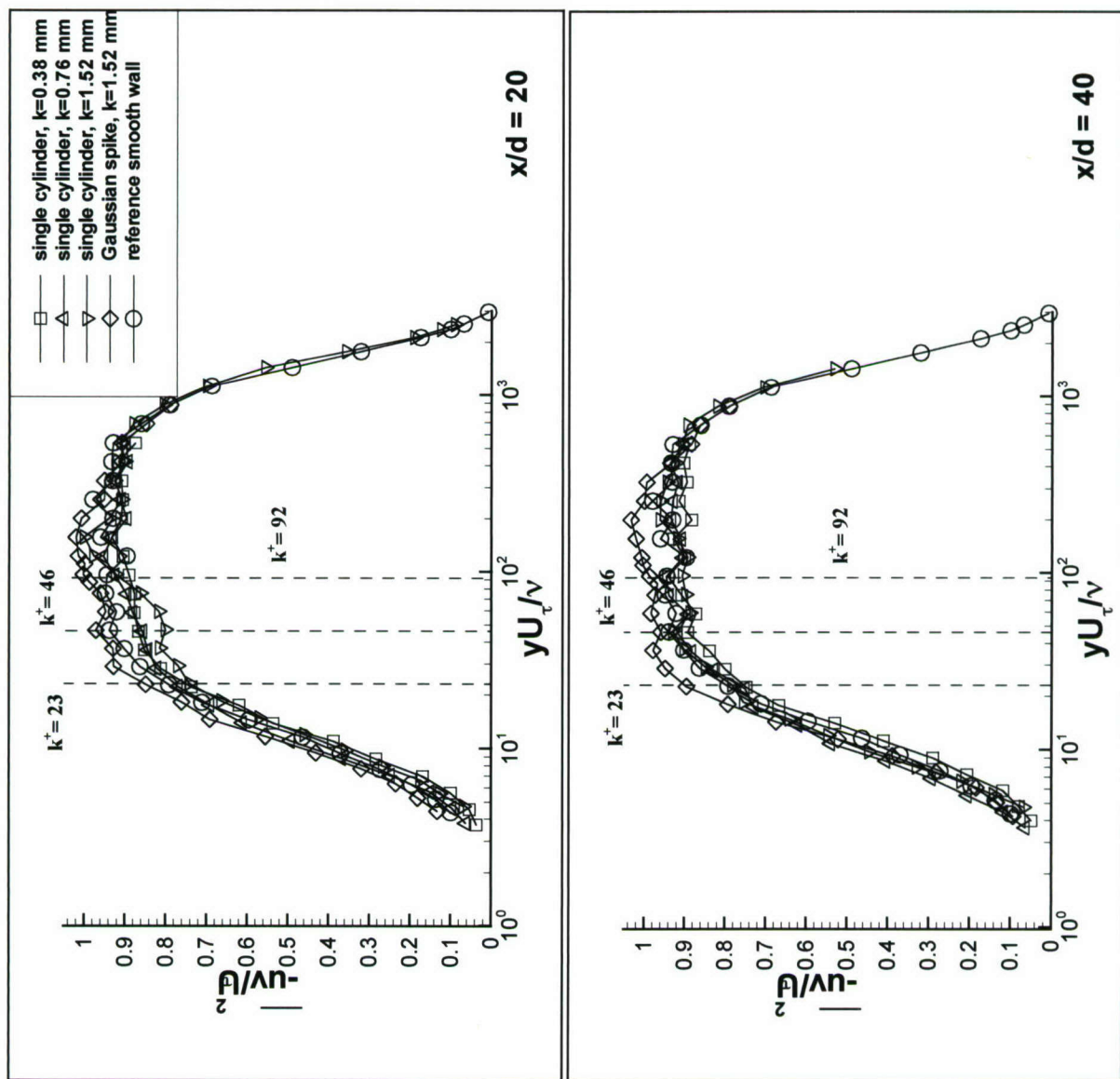


Figure 3.22.  $-\overline{w'w'}/U_\tau^2$  versus  $yU_\tau/\nu$ , streamwise Reynolds shear stress profiles along the centerline at  $x/d = 20$  and  $40$ .

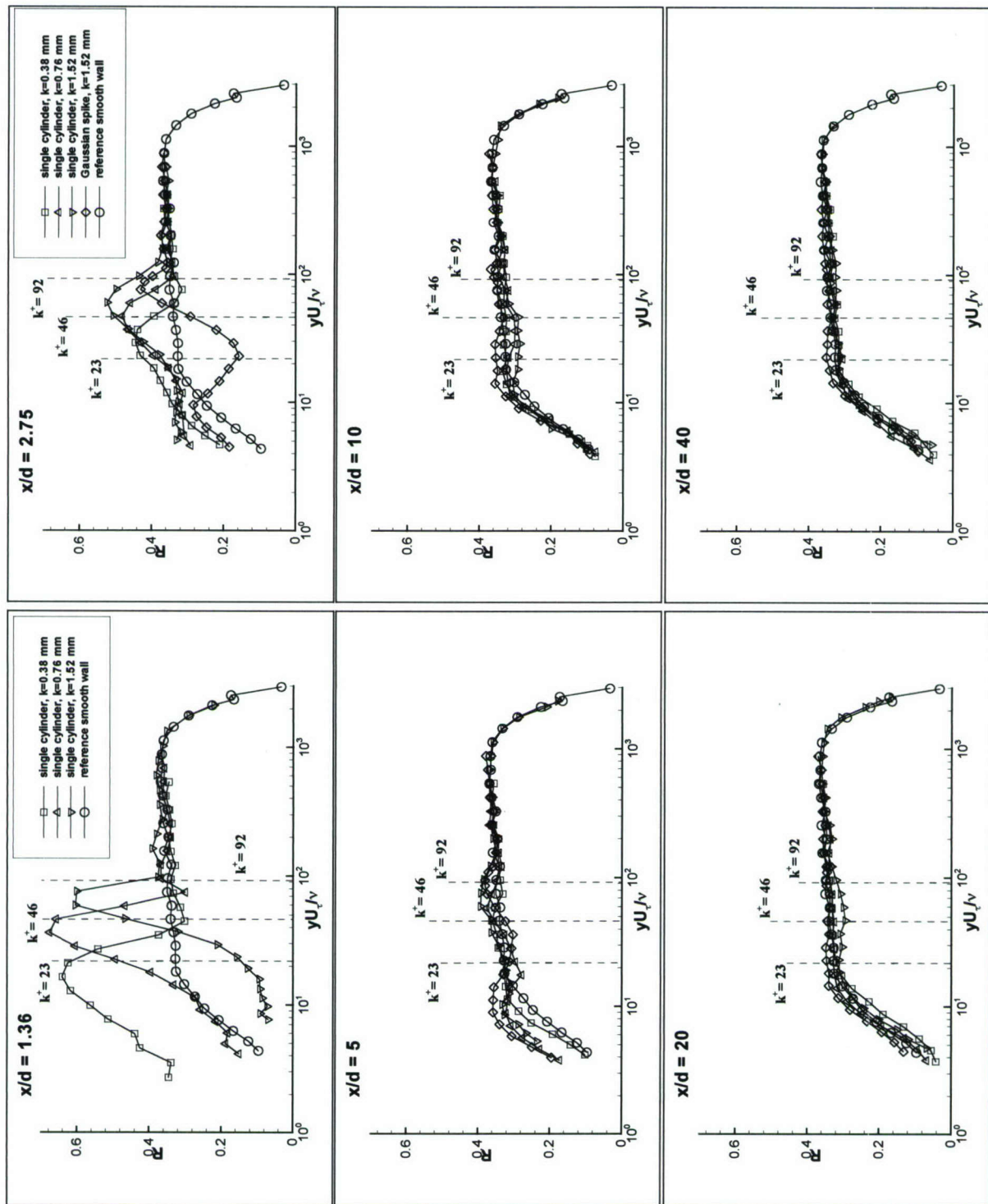


Figure 3.23. Reynolds streamwise shearing stress coefficient,  $R_{\tau}$ , varying with  $yU_{\tau}/\nu$  at the six streamwise locations.



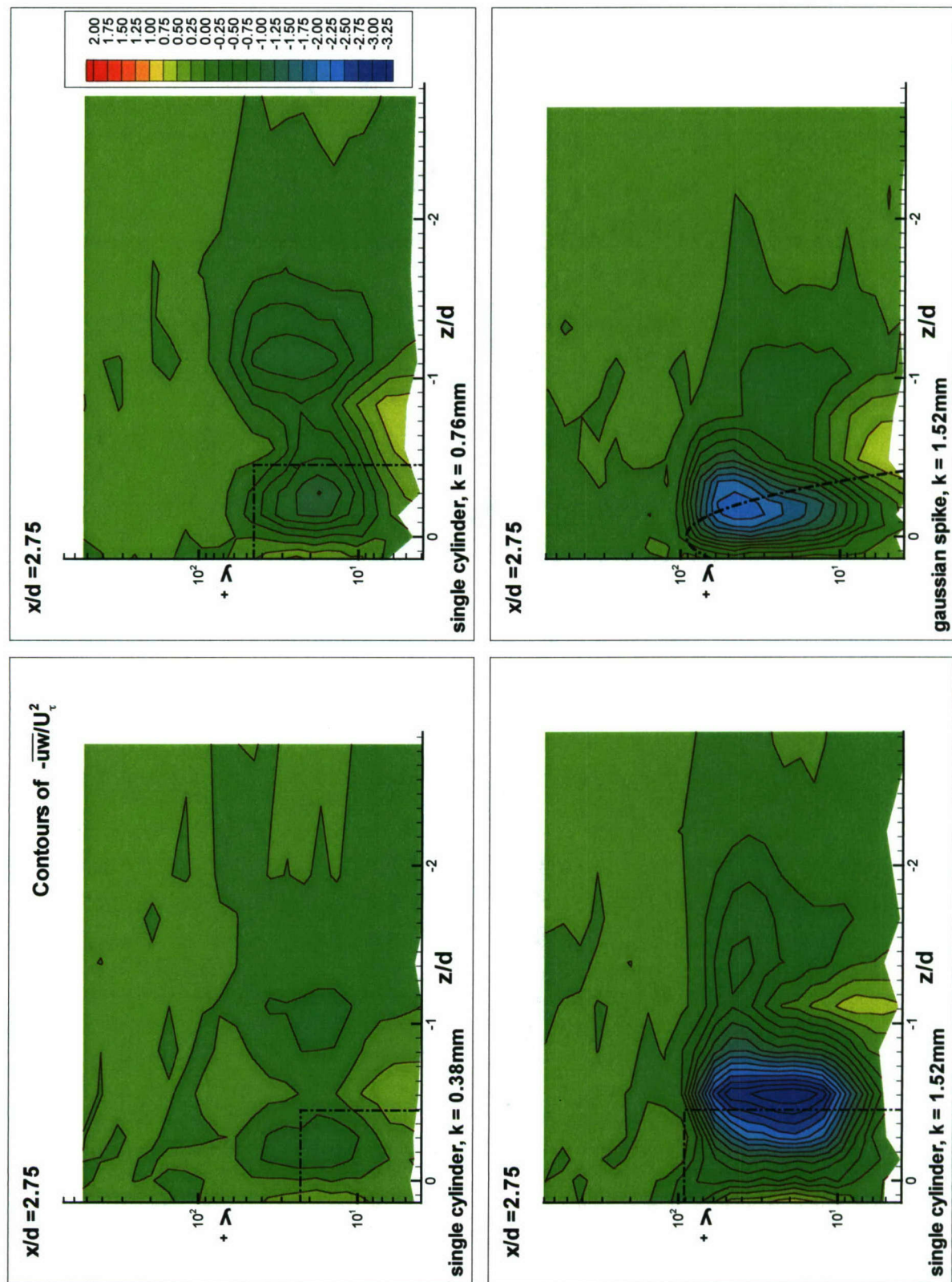


Figure 3.24 (a). Semi-log contours of Reynolds shearing stress,  $-\overline{uw}/U_\tau^2$  in the  $y^+ - z/d$  plane at  $x/d = 2.75$ .

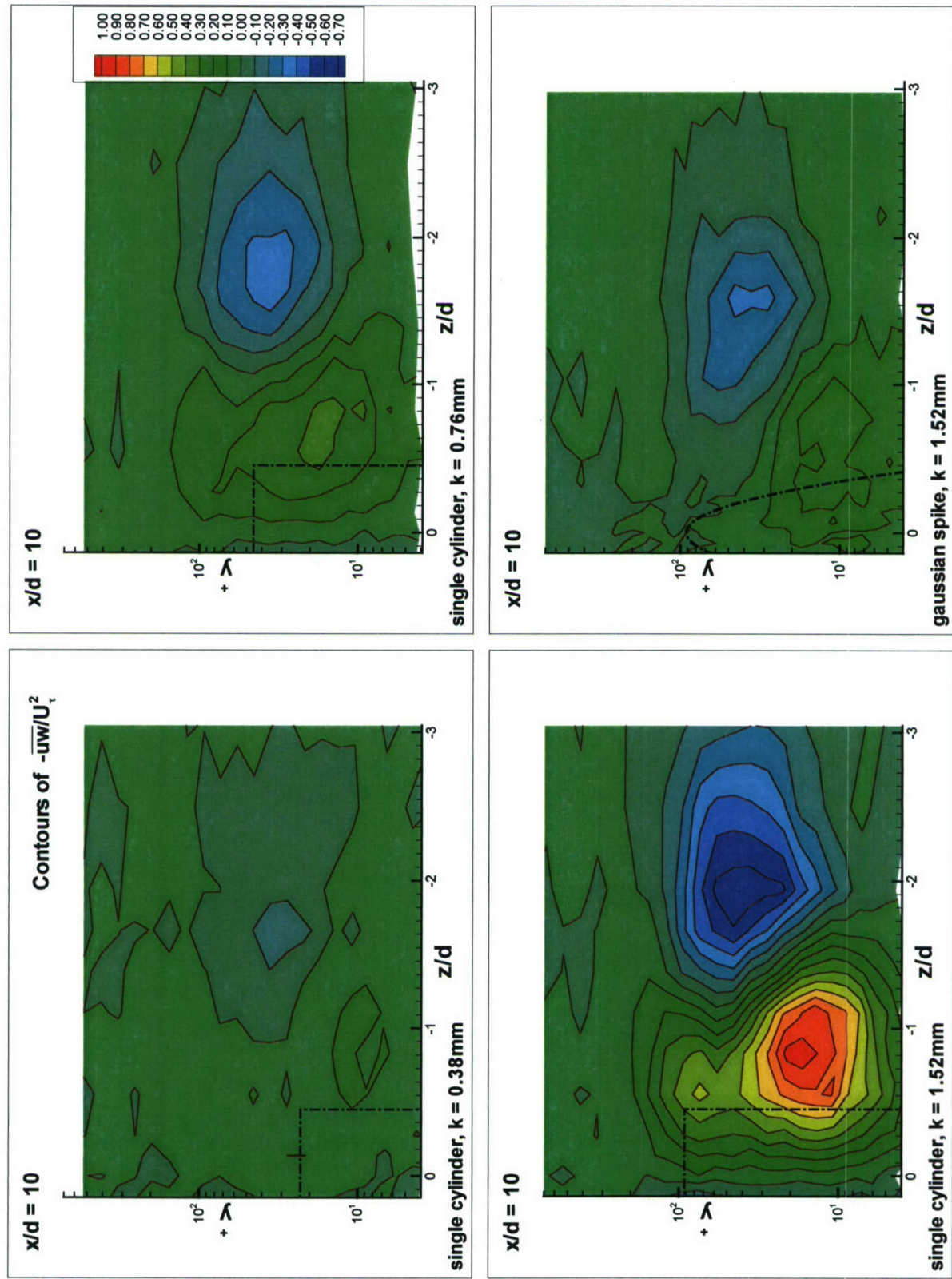


Figure 3.24 (b). Semi-log contours of Reynolds shearing stress,  $-\overline{uw}/U_\tau^2$  in the  $y^+ - z/d$  plane at  $x/d = 10$ .



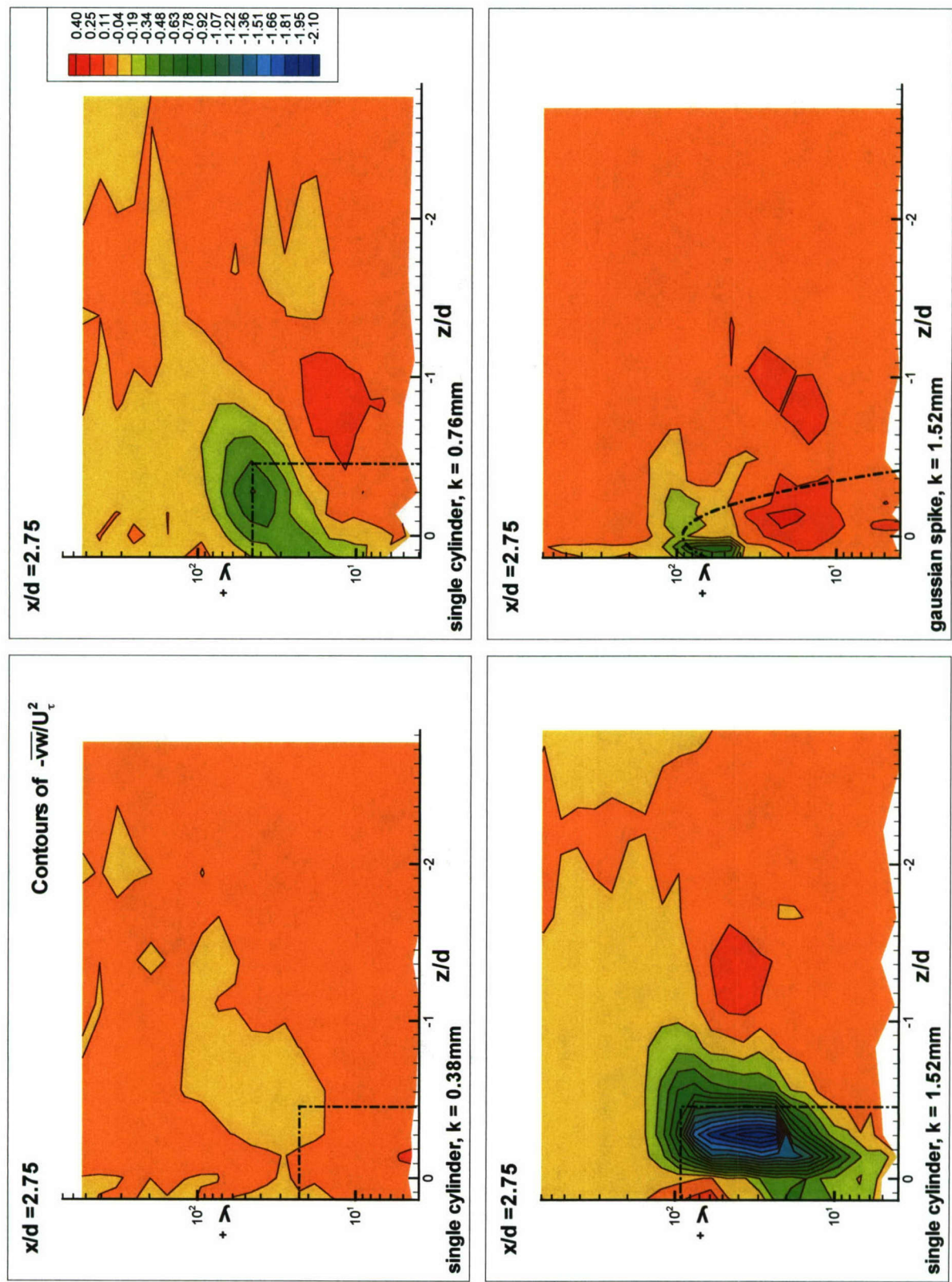


Figure 3.25 (a). Semi-log contours of Reynolds shearing stress,  $-\overline{vw}/U_t^2$  in the  $y^* - z/d$  plane at  $x/d = 2.75$ .

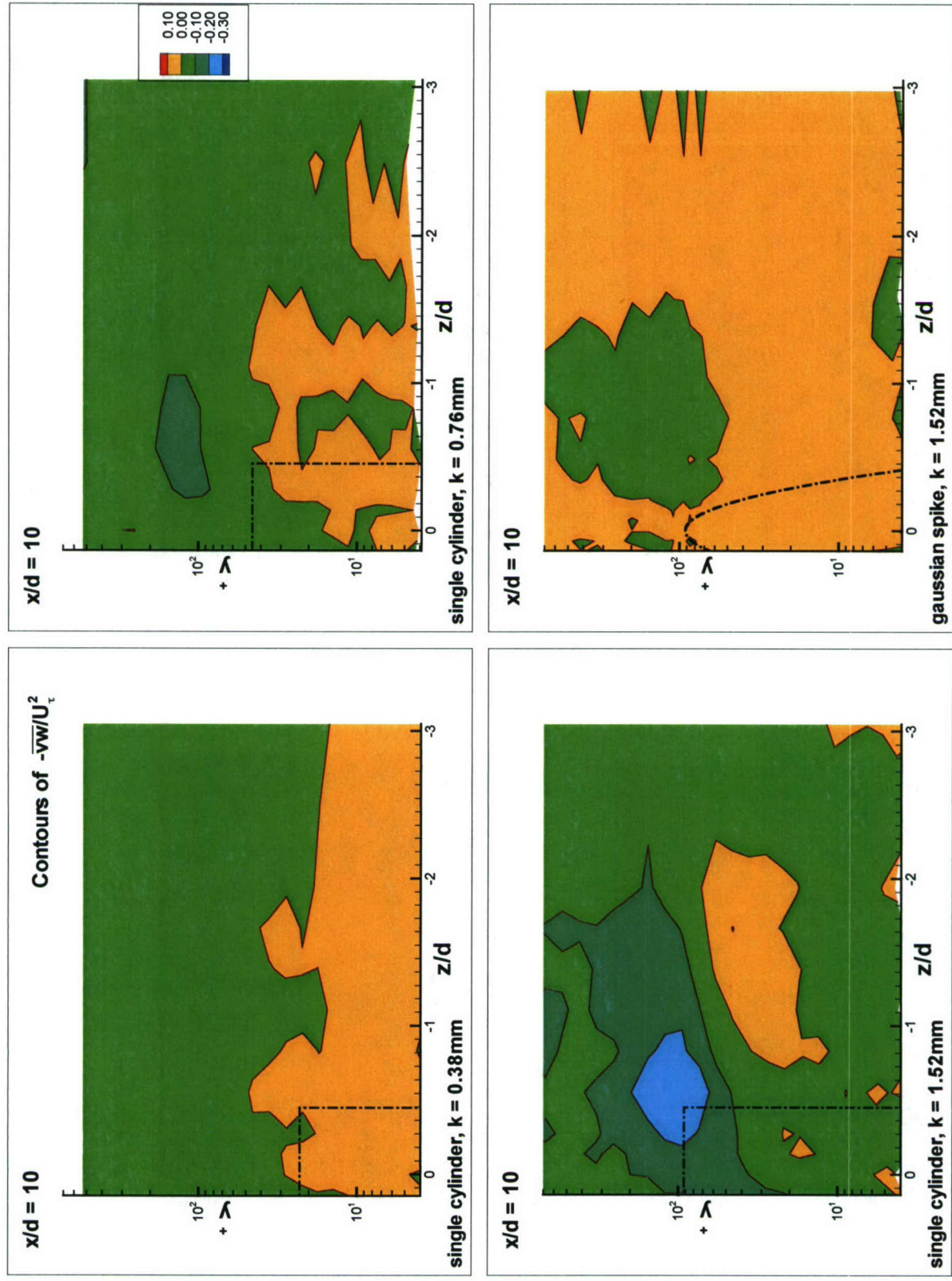


Figure 3.25 (b). Semi-log contours of Reynolds shearing stress,  $-\overline{vw}/U_\tau^2$  in the  $y^+ - z/d$  plane at  $x/d = 10$ .



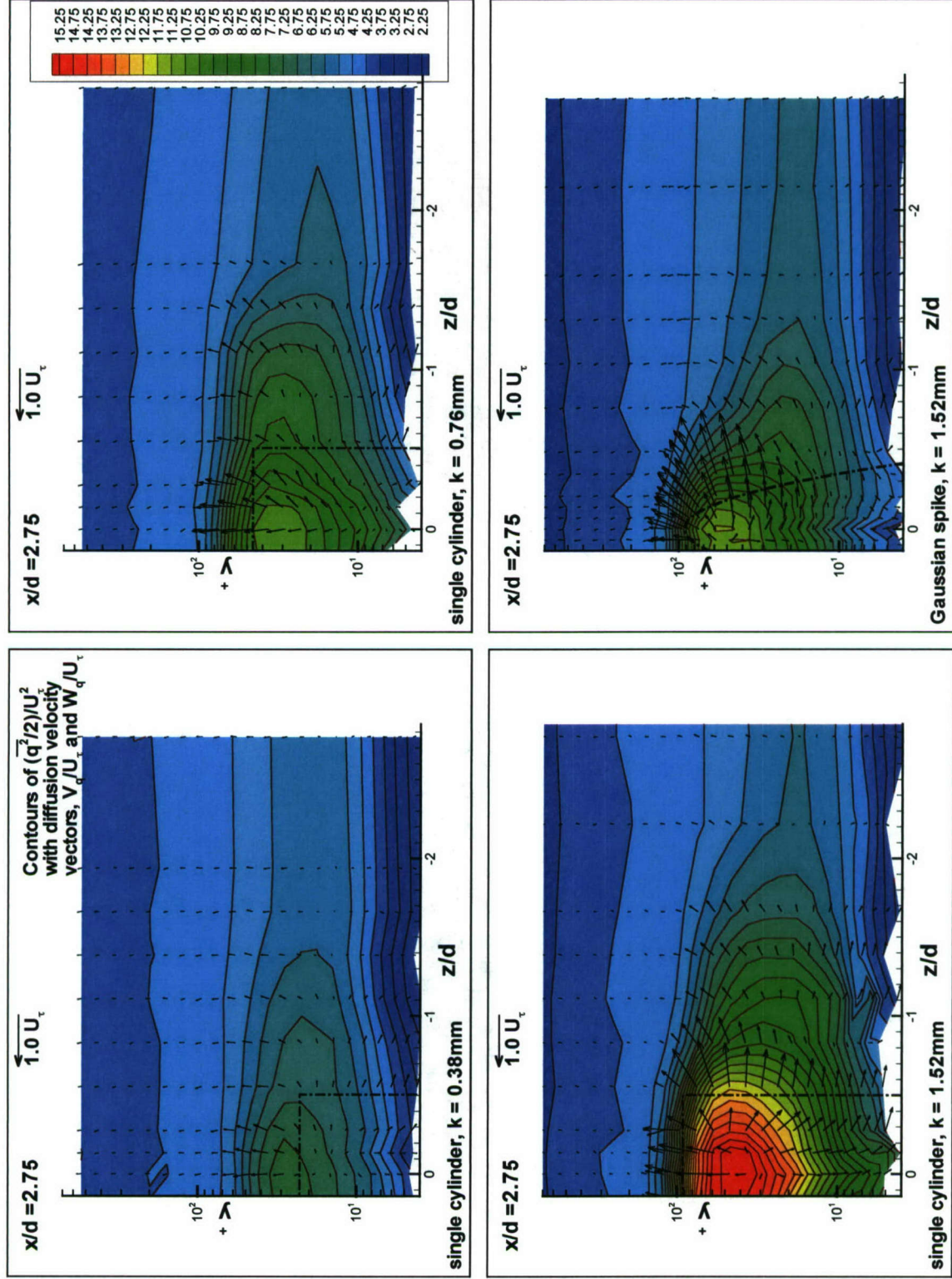


Figure 3.26 (a). Semi-log contours of turbulent kinetic energy (TKE),  $\frac{1}{2} \overline{q^2} / U_\tau^2$ , along with diffusion velocity vectors,  $V_q$  and  $W_q$ , in the  $y^+ - z/d$  plane at  $x/d = 2.75$ .

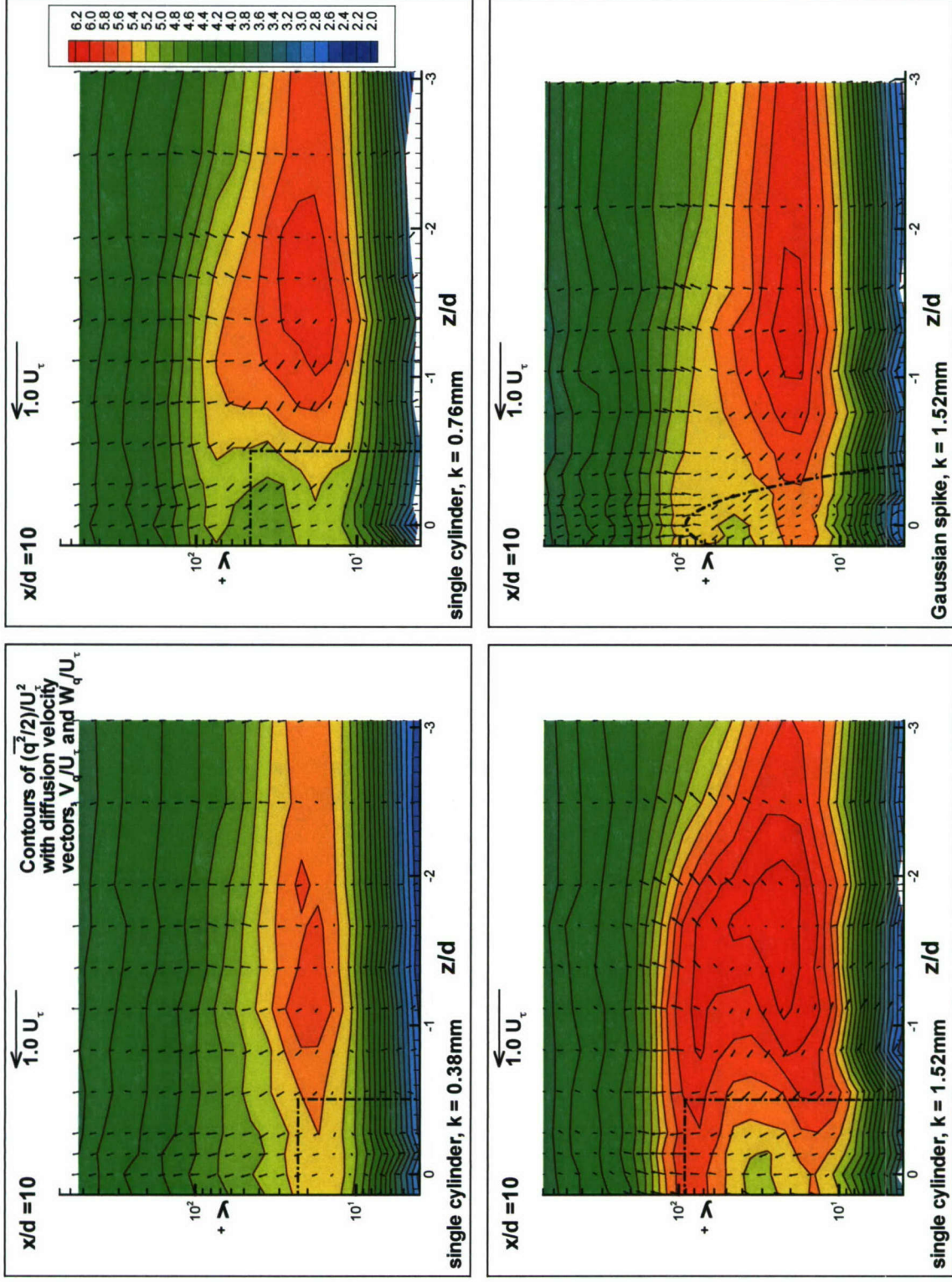


Figure 3.26 (b). Semi-log contours of turbulent kinetic energy (TKE),  $\frac{1}{2}\overline{q^2}/U_\tau^2$ , along with diffusion velocity vectors,  $V_q$  and  $W_q$ , in the  $y^*-z/d$  plane at  $x/d = 10$ .



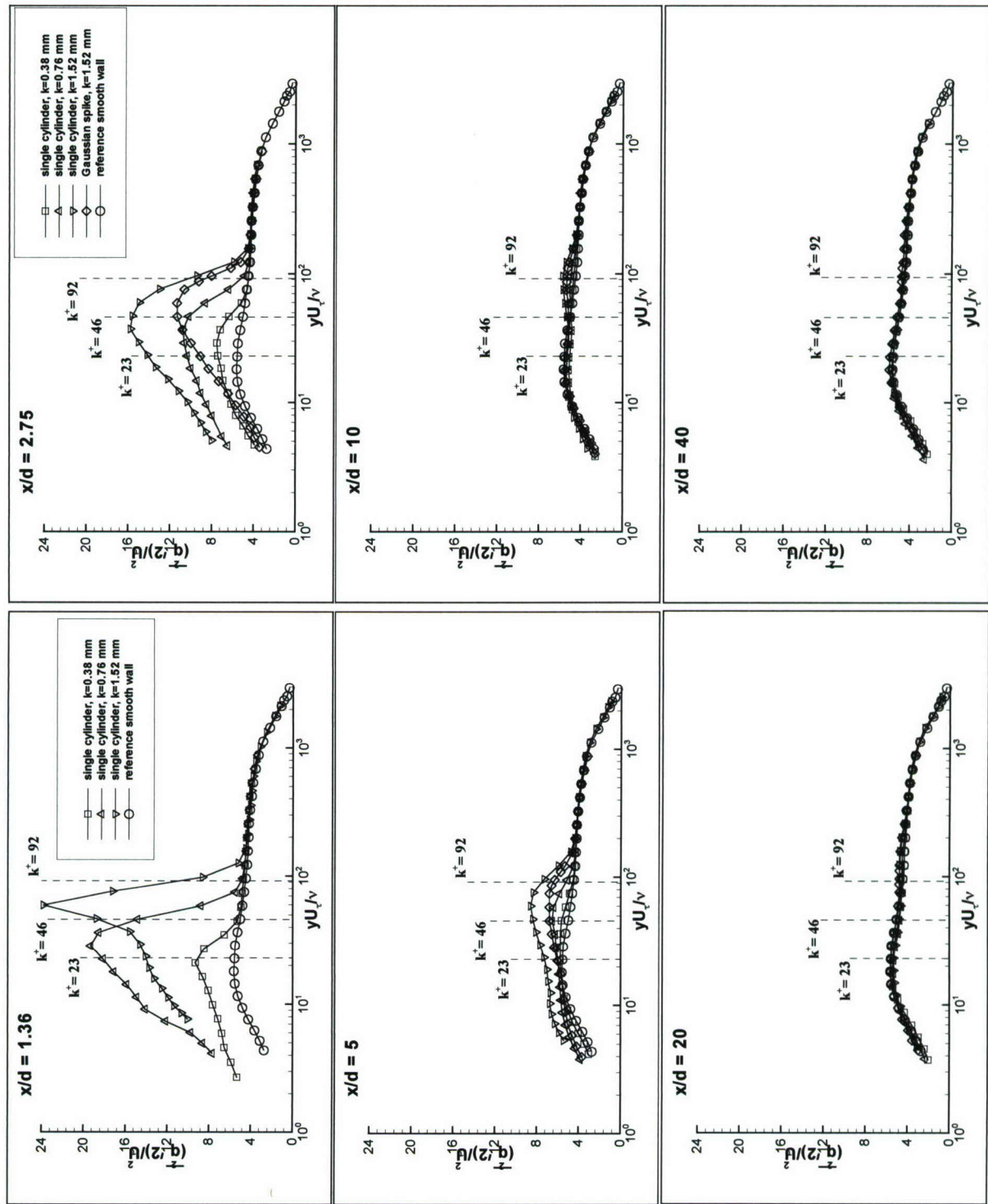


Figure 3.27 (a).  $\frac{1}{2} \overline{q^2} / U_\tau^2$  versus  $yU_\tau/\nu$ , turbulent kinetic energy (TKE) profiles along the centerline.

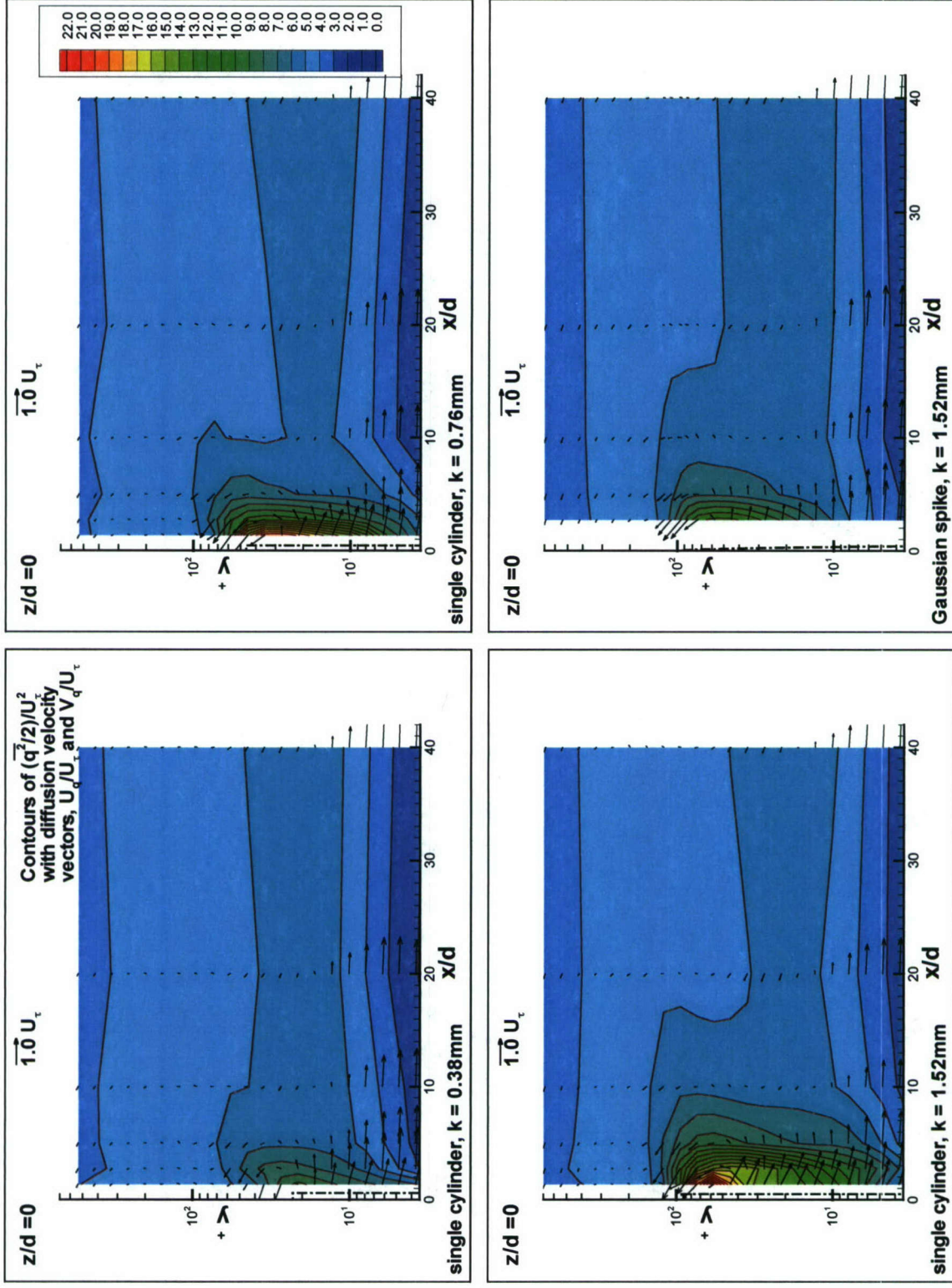


Figure 3.27 (b). Semi-log contours of turbulent kinetic energy (TKE),  $\overline{(q^2/2)}/U_\tau^2$ , along with diffusion velocity vectors,  $U_q$  and  $V_q$ , in the  $x/d - y^+$  plane along the centerline.



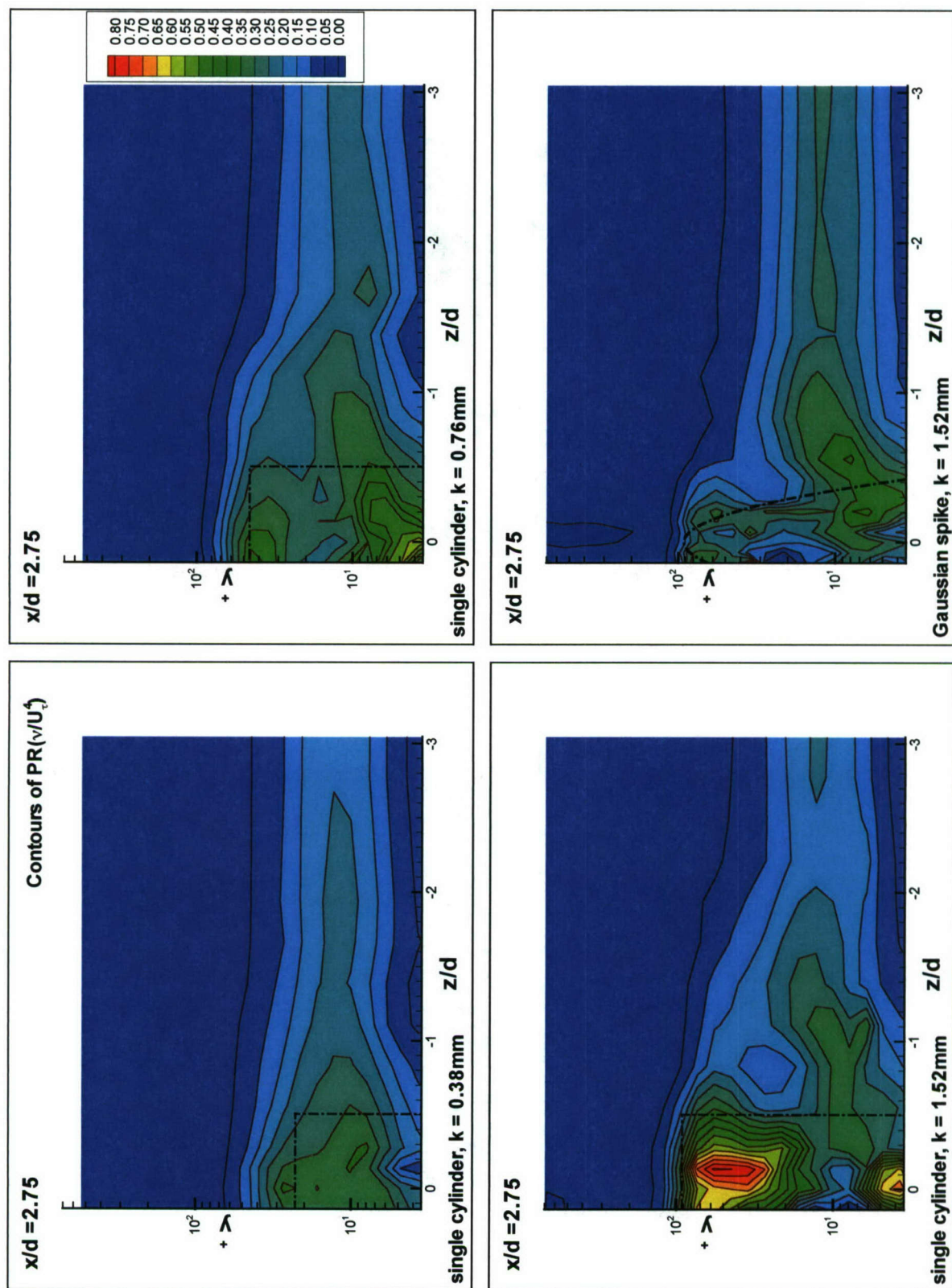


Figure 3.28 (a). Semi-log contours of production ( $PR$ ) of TKE, normalized by  $v/U_t^4$ , in the  $y^* - z/d$  plane at  $x/d = 2.75$ .

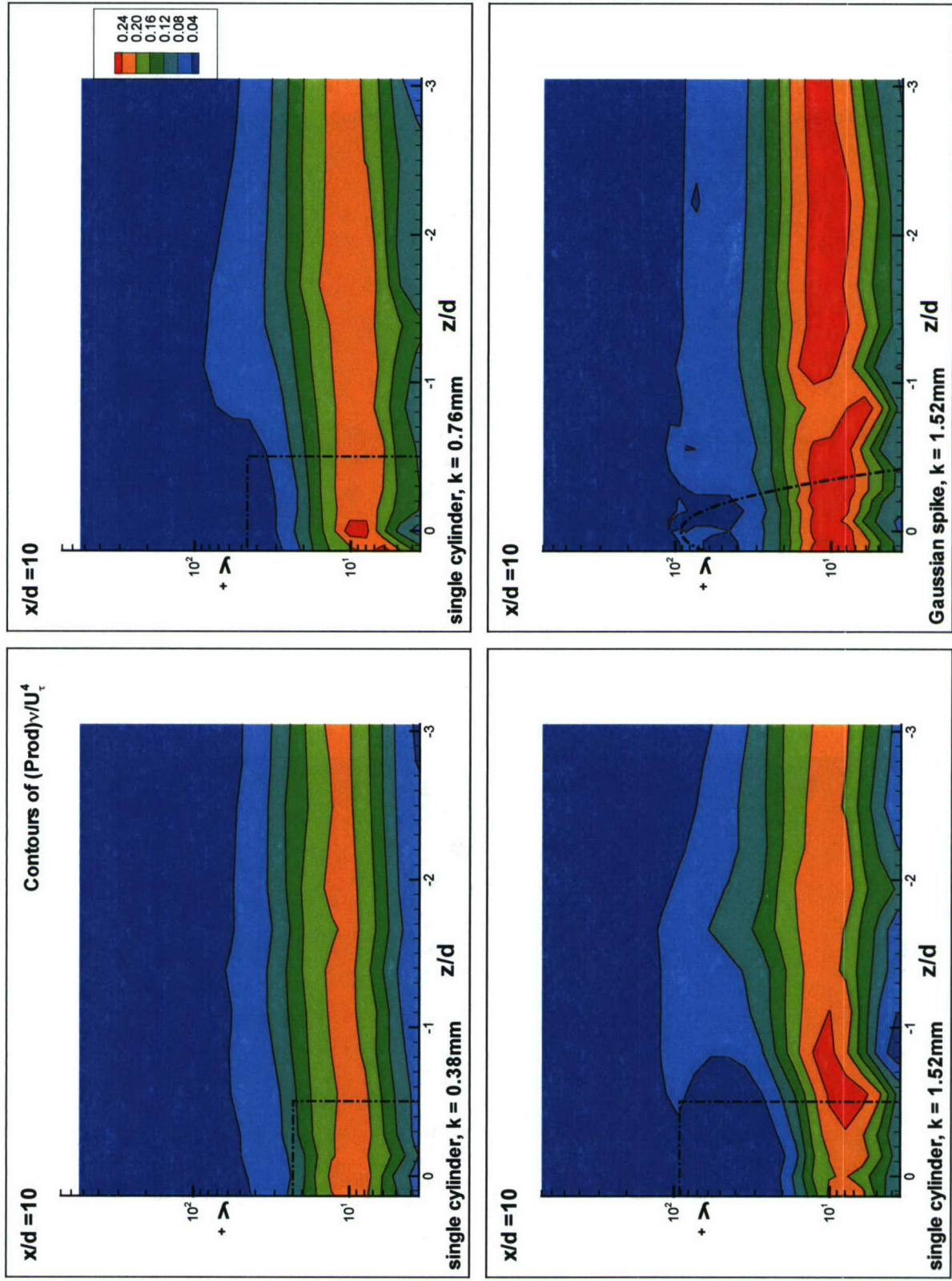


Figure 3.28 (b). Semi-log contours of production (PR) of TKE, normalized by  $v/U_t^4$ , in the  $y^* - z/d$  plane at  $x/d = 10$ .



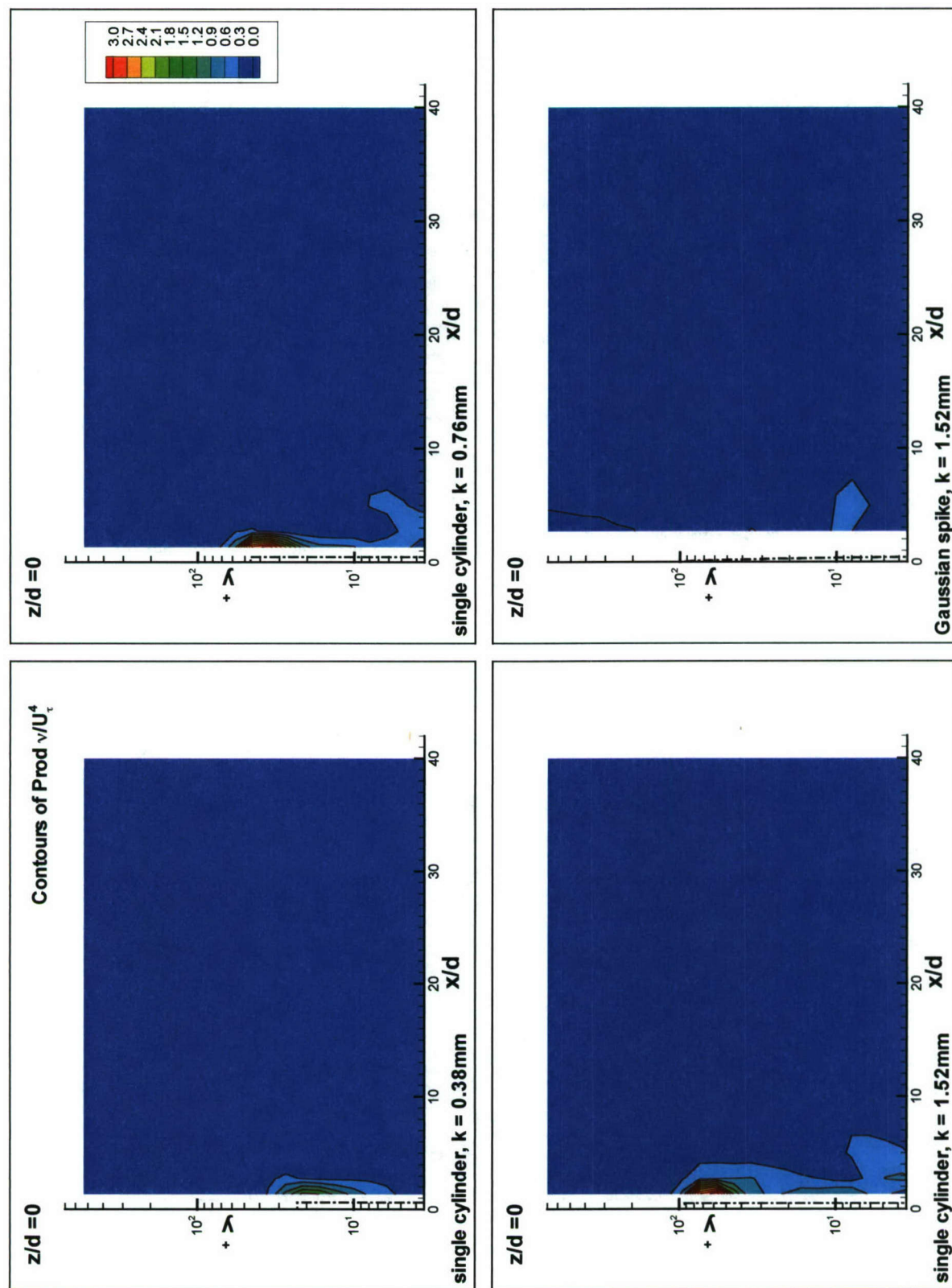


Figure 3.28 (c). Semi-log contours of production ( $PR$ ) of TKE, normalized by  $v/U_t^4$ , in the  $y^* - x/d$  plane along the centerline.

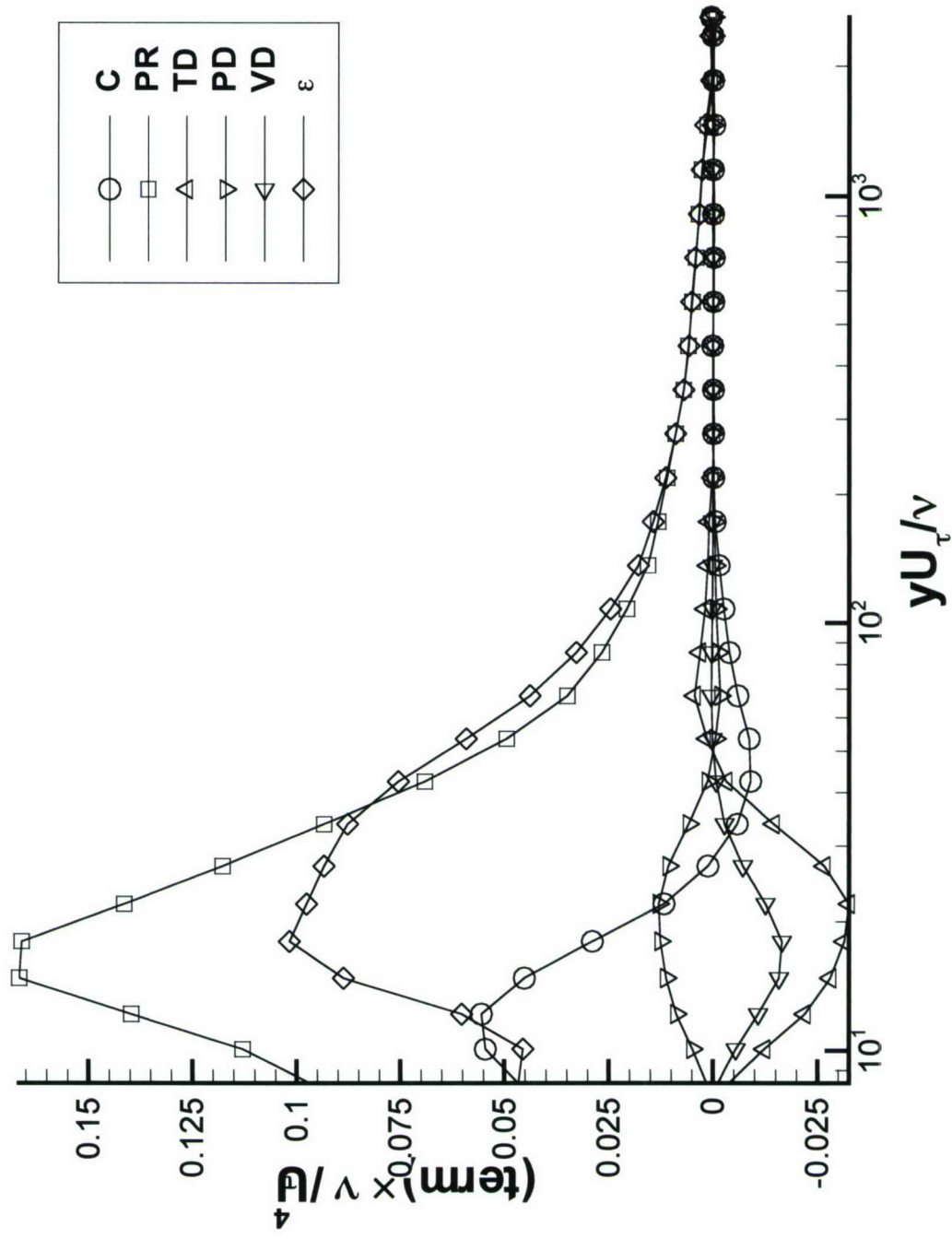


Figure 3.29. Variation of transport-rate budget of TKE,  $\overline{q^2}/2$ , normalized by  $U_\tau^4/\nu$ , with  $yU_\tau/\nu$  (2-D smooth wall BL).



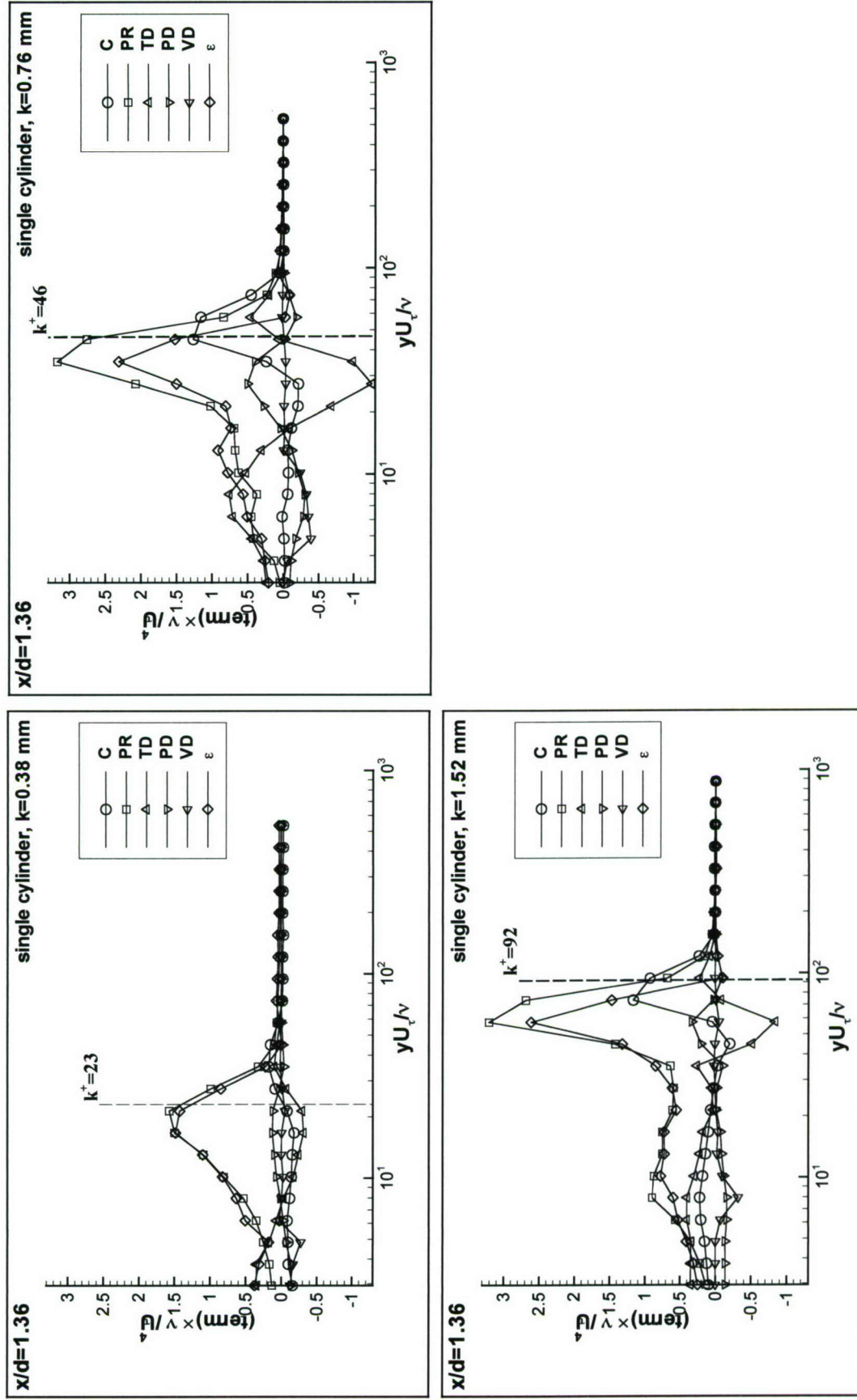


Figure 3.30 (a). Variation of transport-rate budget of TKE,  $\overline{q^2}/2$ , normalized by  $U_\tau^4/\nu$ , with  $yU_\tau/\nu$  at  $x/d = 1.36$ .

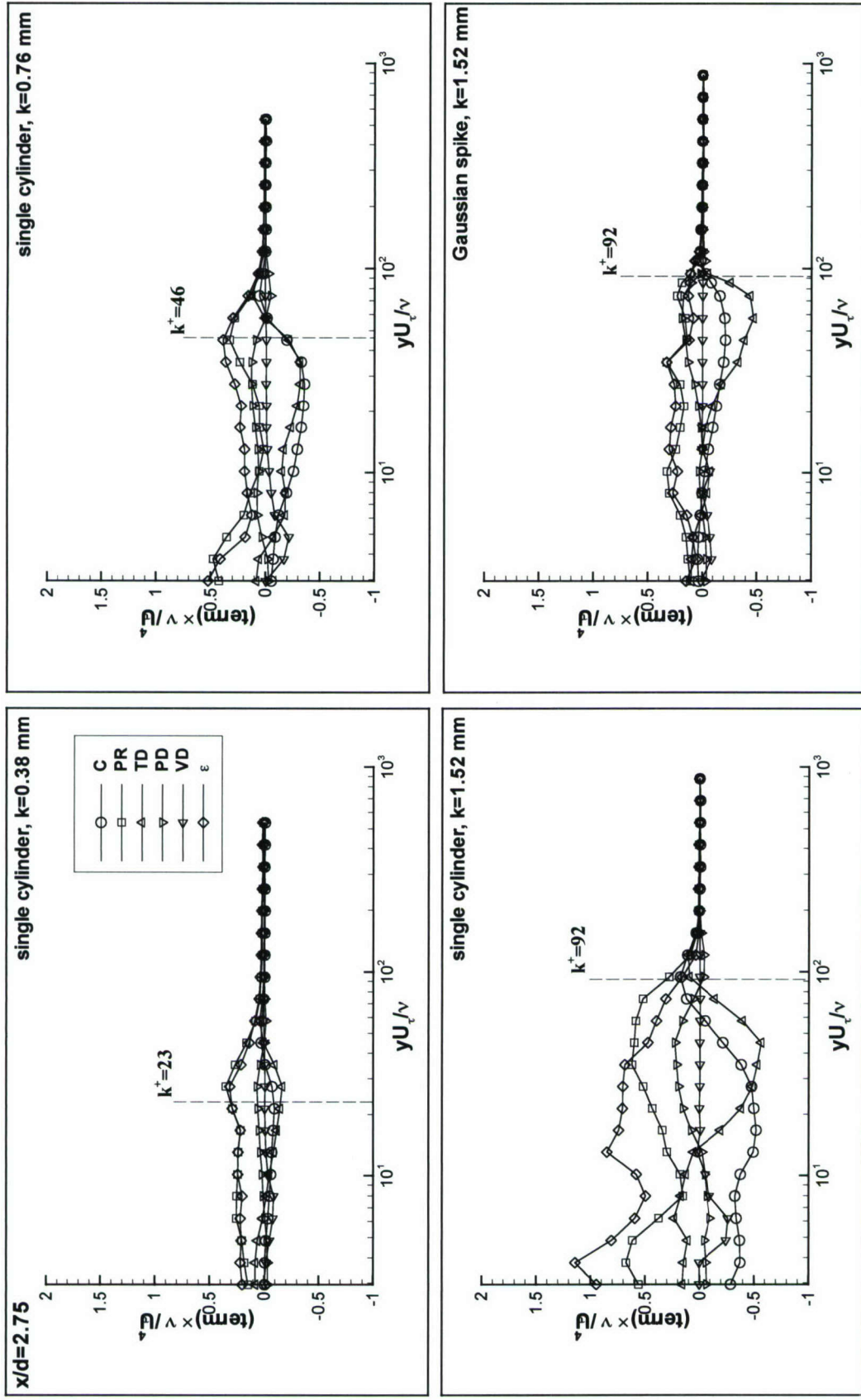


Figure 3.30 (b). Variation of transport-rate budget of TKE,  $\overline{q^2}/2$ , normalized by  $U_\tau^4/\nu$ , with  $yU_\tau/\nu$  at  $x/d = 2.75$ .



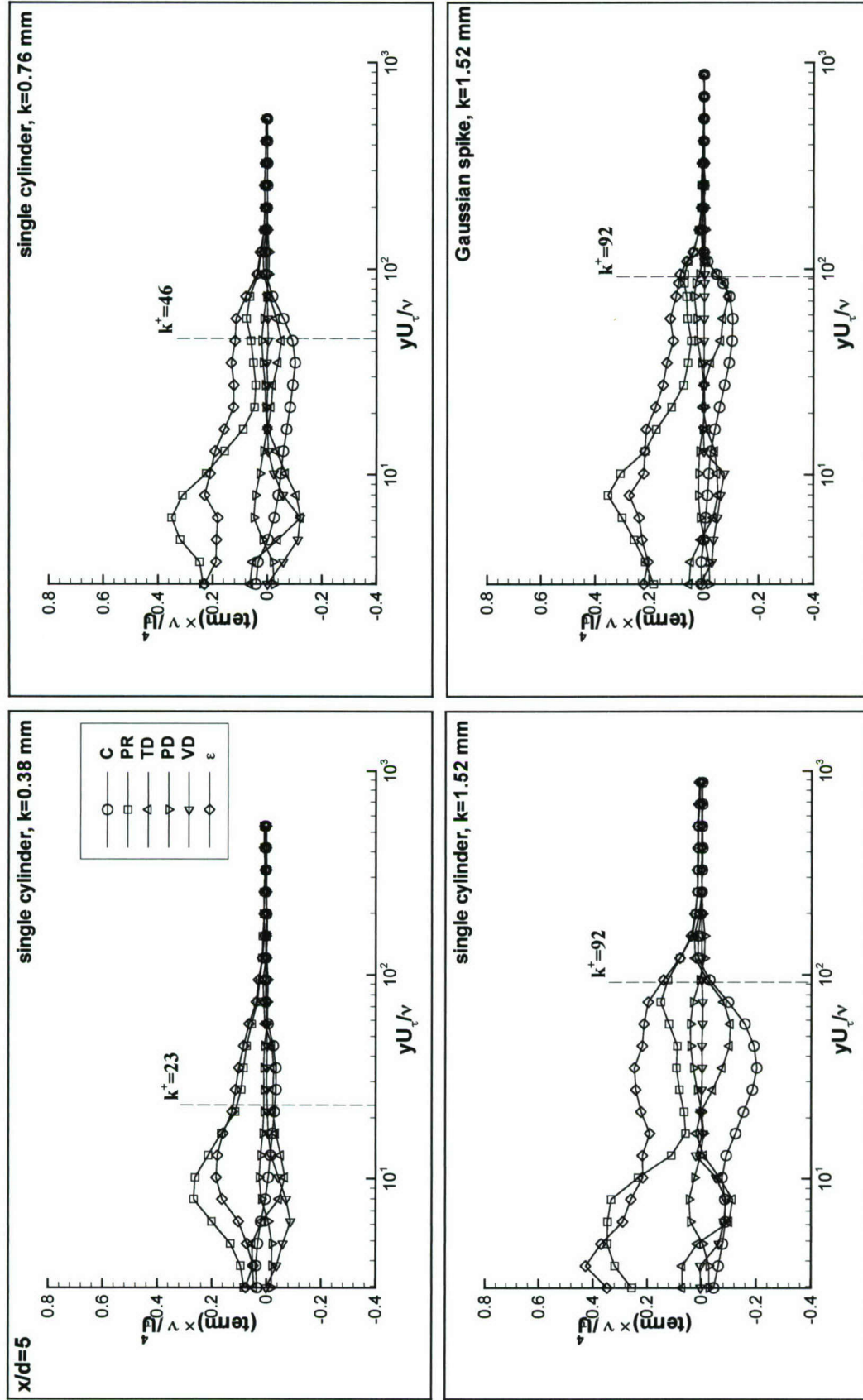


Figure 3.30 (c). Variation of transport-rate budget of TKE,  $\overline{q^2}/2$ , normalized by  $U_\tau^4/\nu$ , with  $yU_\tau/\nu$  at  $x/d = 5$ .

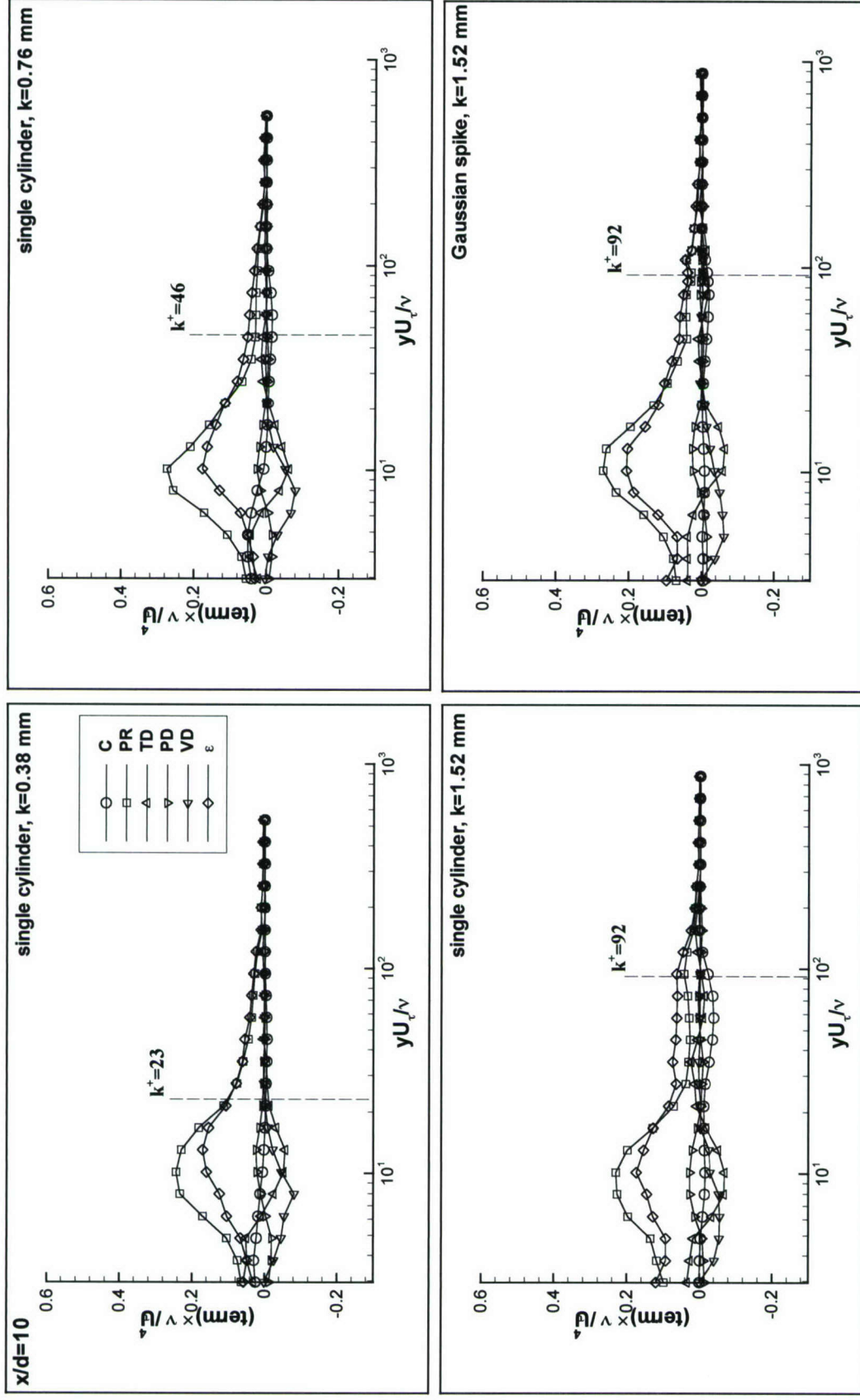


Figure 3.30 (d). Variation of transport-rate budget of TKE,  $\overline{q^2}/2$ , normalized by  $U_\tau^4/\nu$ , with  $yU_\tau/\nu$  at  $x/d = 10$ .



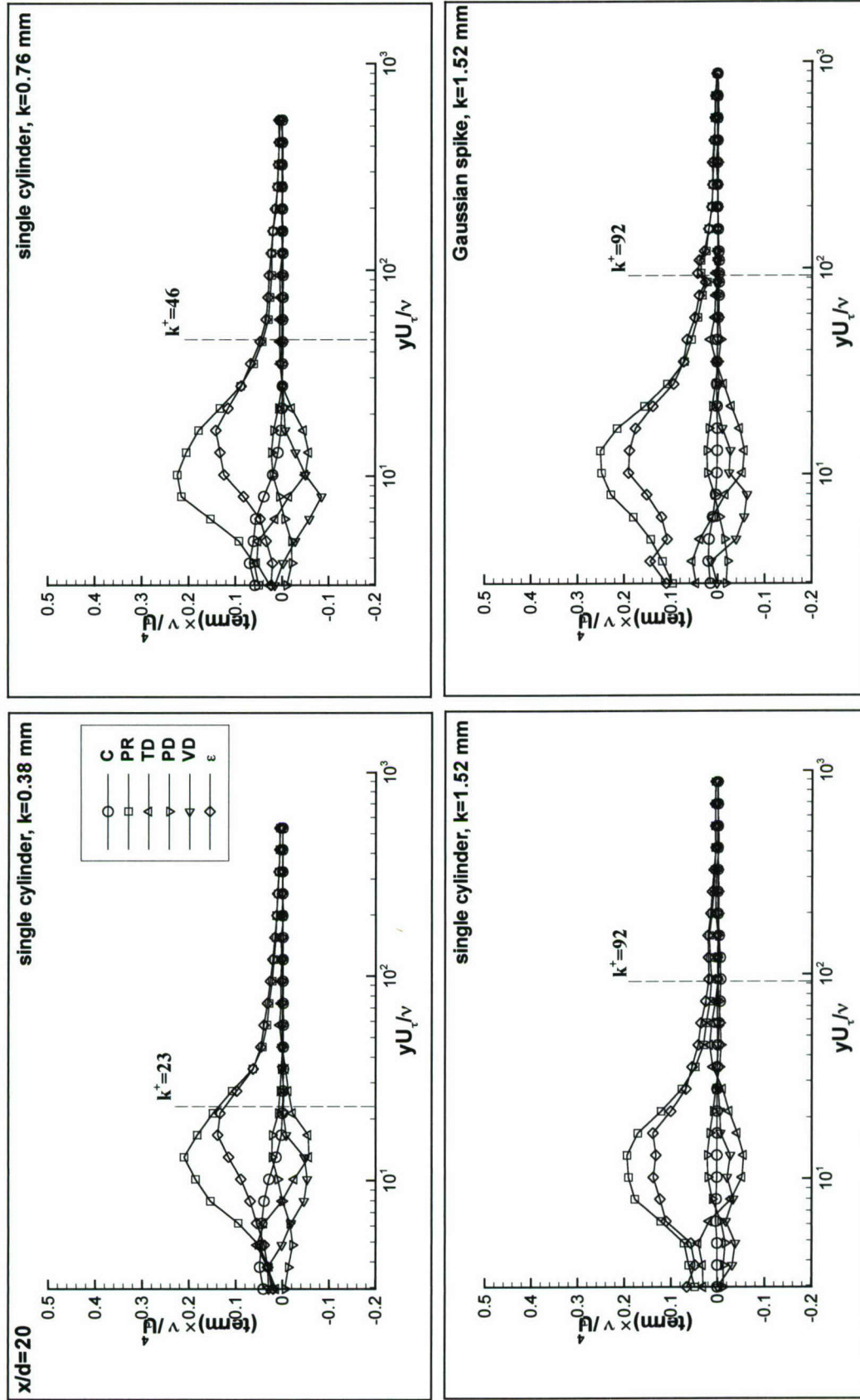


Figure 3.30 (e). Variation of transport-rate budget of TKE,  $\overline{q^2}/2$ , normalized by  $U_\tau^4/\nu$ , with  $yU_\tau/\nu$  at  $x/d = 20$ .

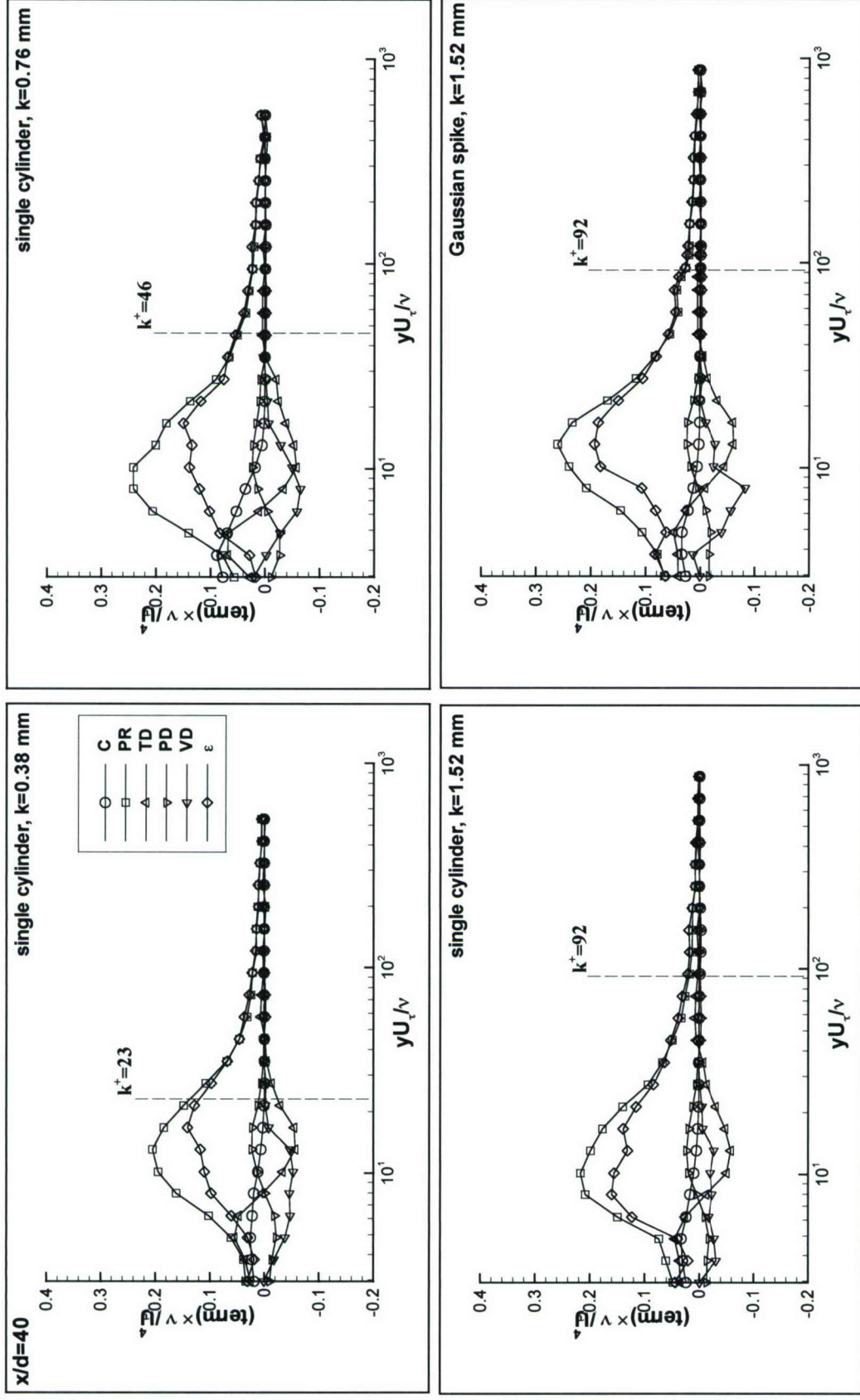


Figure 3.30 (f). Variation of transport-rate budget of TKE,  $\overline{q^2}/2$ , normalized by  $U_\tau^4/\nu$ , with  $yU_\tau/\nu$  at  $x/d = 40$ .



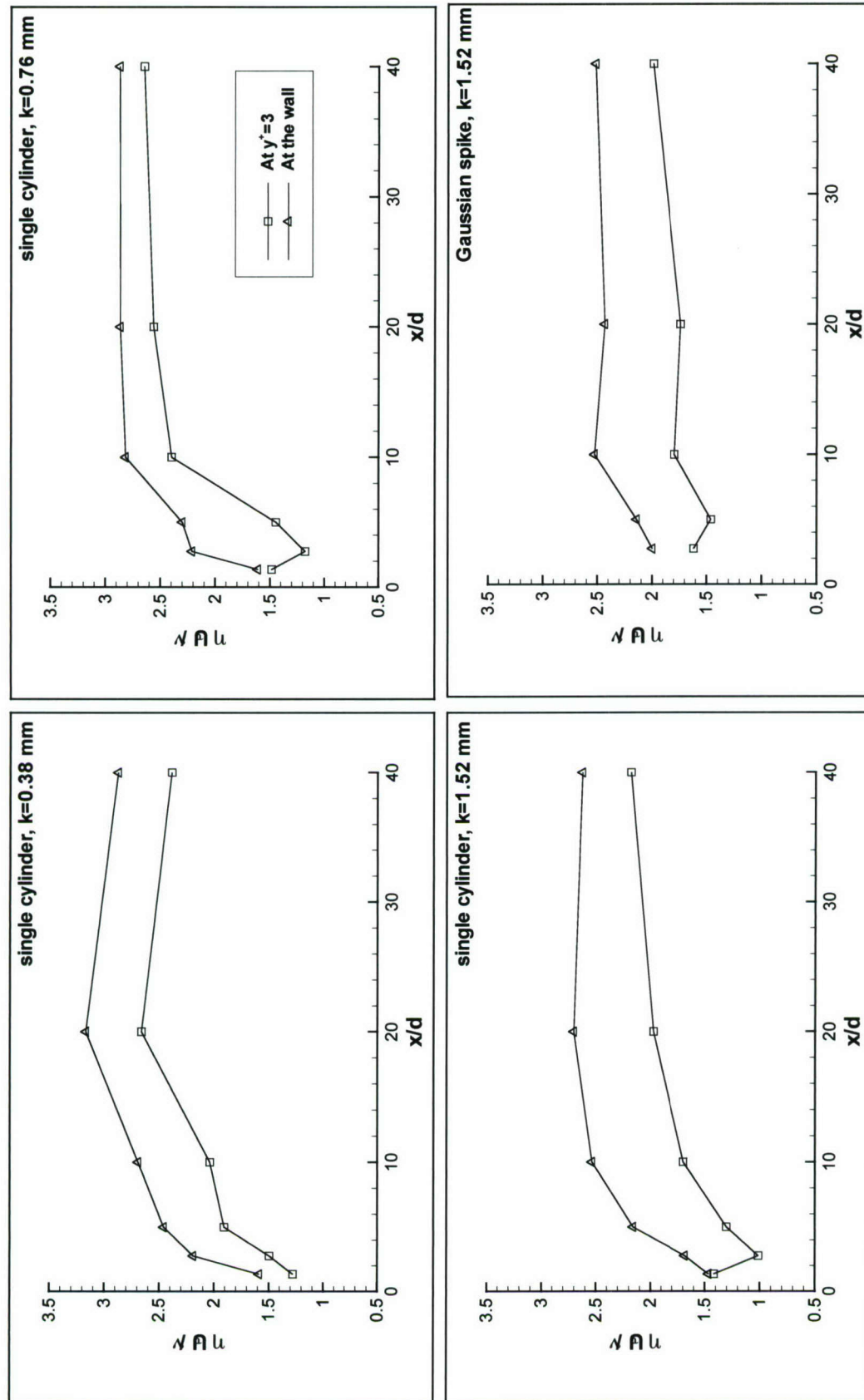


Figure 3.31. Variation of the Kolmogorov scale,  $\eta$ , normalized by  $\nu/U_\tau$ , with streamwise distance at the wall and at  $y^* = 3$ .

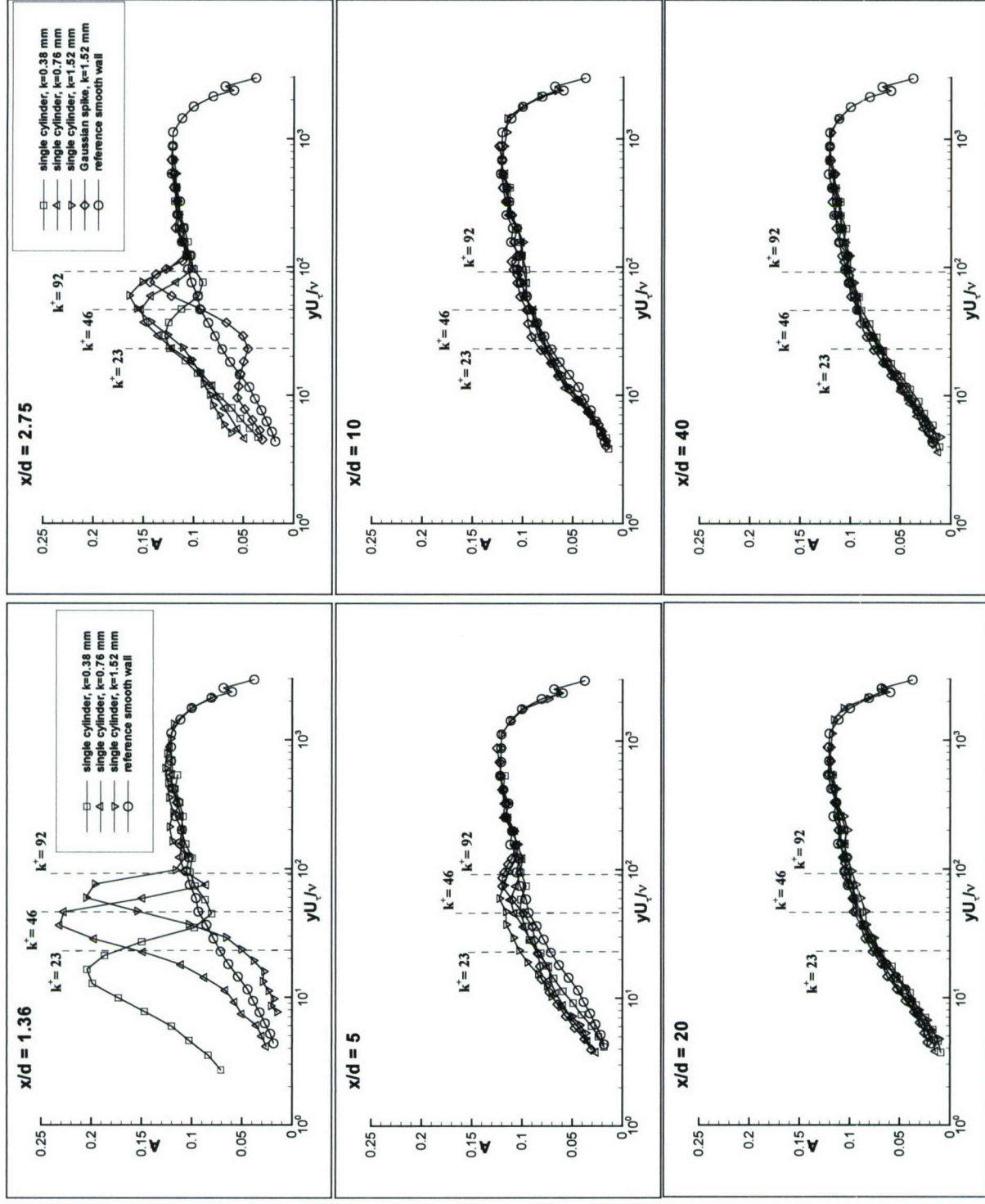


Figure 3.32 (a). Structural parameter,  $A_1$ , versus  $yU_\tau/\nu$ , profiles along the centerline.



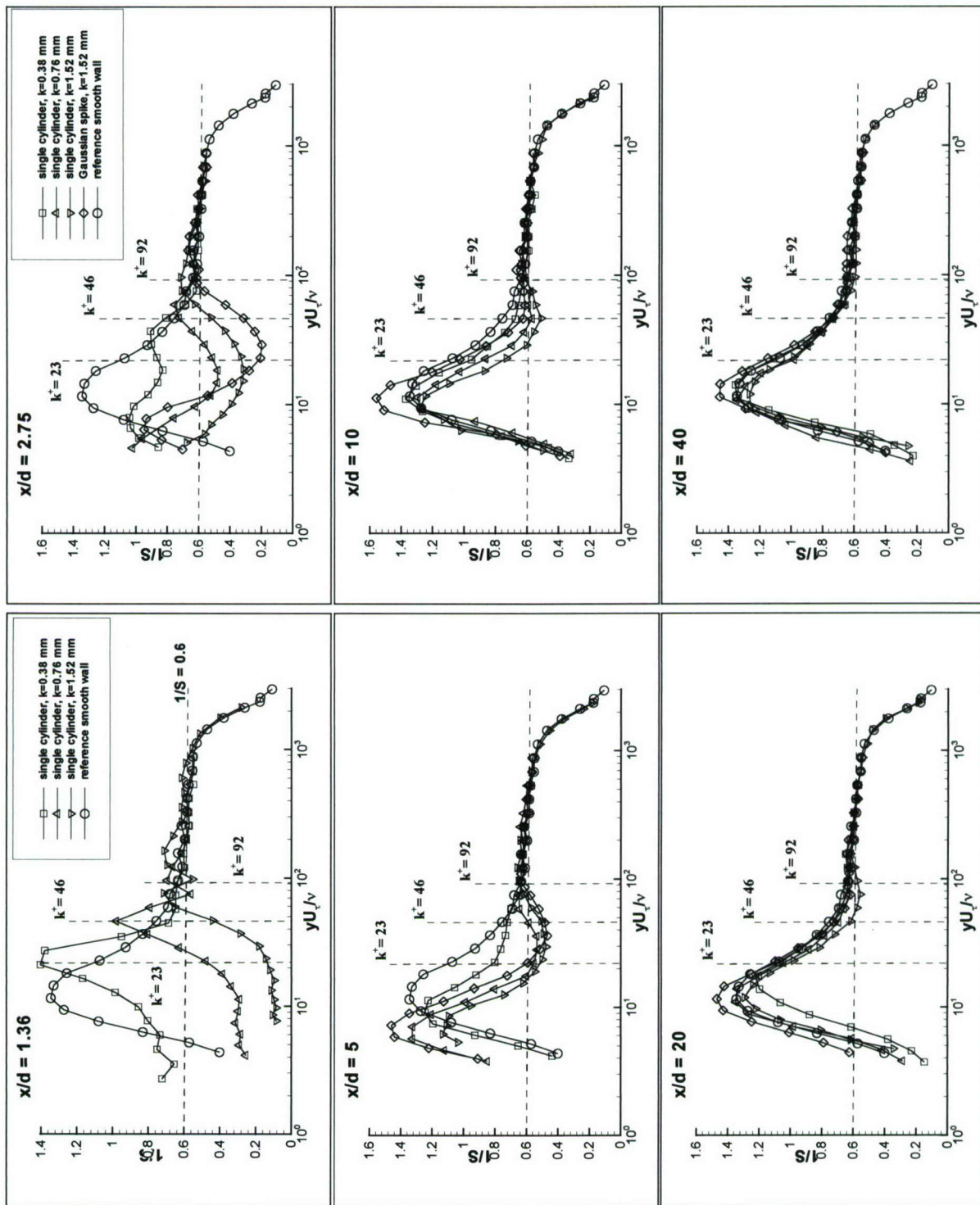


Figure 3.32 (b). Structural parameter,  $1/S$ , versus  $yU_{\tau}/\nu$ , profiles along the centerline.

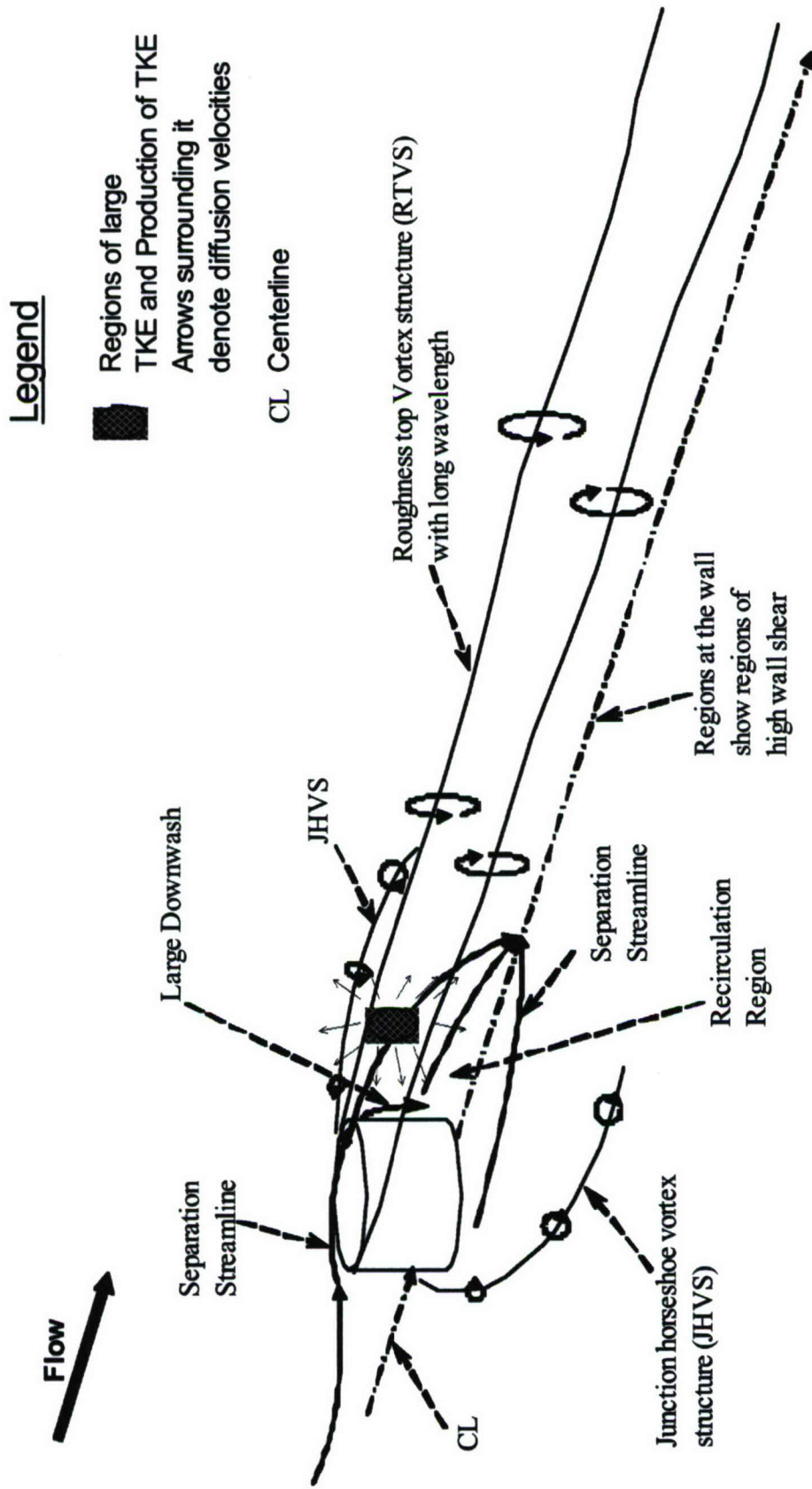


Figure 3.33. Schematic of the flow past the single cylinder.



## Chapter 4 Two-Dimensional Rough-Wall Turbulent Boundary Layers

### 4.1 Results and Discussion

The data-set showed that the Reynolds streamwise shearing stress,  $-\overline{uv}$ , are constant in the “constant shear stress” layer which is also the semi-logarithmic region in the streamwise velocity distribution. In each of the six 2-D rough-wall cases, profiles were made at 40-45 locations [Figs. 2.8 (a) and (b)], and for each case, the maximum of the spatial averages in the “constant shear stress” regions of the 40-45 profiles was determined. This maximum was denoted as  $-\overline{uv}_{\max}$  and the square root of this quantity was chosen to be the velocity scale ( $U_s$ ) or friction velocity ( $U_\tau$ ), i.e.,  $U_\tau = \sqrt{-\overline{uv}_{\max}}$ . The values of this scaling velocity in conjunction with other boundary layer parameters are presented in Table 4.1. The details of the smooth-wall boundary layer are also provided for the sake of comparison. Please note that when mid plane is mentioned in the discussions it refers to the streamwise mid plane. Spanwise mid plane would be the  $x-y$  plane located equidistant to elements.

#### 4.1.1 Mean quantities – mean velocities

From the extensive measurements around the elements in the rough-wall layers, in different planes normal to the streamwise direction, contours of various quantities can be plotted. Figures 4.1 (a)-(f) present contours of  $U/\sqrt{-\overline{uv}_{\max}}$  in the  $y/k-z/d$  plane with secondary flow vectors,  $V/\sqrt{-\overline{uv}_{\max}}$  and  $W/\sqrt{-\overline{uv}_{\max}}$  at  $x/D = 0.295, 0.398, 0.5, 0.625, 0.75, 0.879, 1.008$  and  $1.137$ , respectively. The latter three  $x/D$  are applicable to staggered cases only. At the very first measurement location,  $x/D = 0.295$ , all three cases of straight orientation show that the flow is separated at this location, with large regions of reverse flow that extend spanwise to about 0.3 to 0.4 diameters off the center plane and at about the element height in the vertical direction [Fig. 4.1 (a)]. There is a strong secondary flow directed spanwise towards the center plane from regions beyond the element width and this flow curves upwards as the center plane is approached. At the center plane, which is also the plane of symmetry, the flow is directed vertically upwards. Above the element height, the secondary flow comes over the top of the element and is directed towards the wall and away from the center plane. This indicates a nodal point close to the element height where the secondary flow convergence is seen. The magnitude of the secondary flow in the separated flow region is much higher than that above the element height. In the case of the staggered orientation, a similar behavior is observed although with smaller regions of separated flow. However, the magnitudes of the secondary flow are greater over those for the corresponding straight cases.

At the next measurement plane,  $x/D = 0.398$ , a similar behavior to that at the previous location is observed [Fig. 4.1 (b)], although there is a reduction in area where the flow is separated. There still exists a strong onrush of fluid from the sides of the element towards the separated flow regions and the center plane which converges at the center plane forming an updraft where it meets the faster moving fluid that has been forced over the upstream element. Also, the nodal point, where the secondary flow converges, is located at a distance below the element, though further below than at the previous location. At this measurement plane too, the separated flow regions in the staggered cases are lower than those in the straight cases albeit with higher magnitudes of secondary flow.

As the flow proceeds downstream, at  $x/D = 0.5$  [Fig. 4.1 (c)], only a weak updraft of secondary flow is seen at the center plane in the four cases of  $k=0.38\text{mm}$  and  $0.76\text{mm}$  height elements



(straight and staggered) due to a strong center plane convergence of flow from the top as well as from the sides. The regions of separation shrink and are present in the near-wall locations only. The distribution of highest cylinders still shows sizable reverse flow regions with strong secondary flow in the spanwise direction directed towards the center plane (which is also the plane of symmetry) where the flow converges and moves up. This upward draft of flow meets the fast moving shear layers rushing over the top and sides of the element. In general, the roughness elements create large back flow regions which are continuously fed with the fluid from the gaps where faster fluid is available since flow there is unimpeded. In the gaps the faster fluid impinging towards the wall branches towards the downstream separated flow regions behind the elements and rises upward at the center plane and meets the faster flow rushing over the top and sides of the element. While a symmetric branching of the flow occurs at the spanwise mid plane, between the elements, as regards the straight orientation, it is asymmetric as regards the staggered as the elements are placed in an alternate manner. This is reflected in a slightly stronger secondary flow aft of the elements in the case of the staggered elements.

With the progress in streamwise distance, at  $x/D = 0.625$ , in the cases with straight orientation, the effects of the next downstream element becomes apparent as the faster fluid directed towards the wall diverges upstream of it [Fig. 4.1 (d)]. Small regions of separated flow in the near-wall regions in the cases of  $k = 0.76mm$  and  $1.52mm$  height elements are seen as the nose of the downstream element approaches. Flow has reattached in the case of the  $k = 0.38mm$  height elements. As regards the staggered pattern flow, the flow has reattached in all the cases. This is so because the next downstream element is located further away in the staggered orientation when compared to the straight orientation, the distance of separation in the former case being  $\sqrt{2}$  times the latter. Also a simultaneous convergence of fluid towards the wall and the center plane is observed at this location which is also aft of the separated flow regions. At the next measurement location,  $x/D = 0.75$  [Fig. 4.1 (e)], the straight orientation shows strong diverging secondary flow away from the center plane, an indication of the faster wallward fluid going around the sides of the downstream element due to the pressure field imposed by it. In the staggered cases, the presence of the downstream element is not felt by the flow and the flow field still shows a simultaneous center plane and wallward convergence of higher momentum fluid.

The presence of the downstream element in the staggered cases is only apparent at about  $x/D = 1.008$  where the diverging secondary flow is observed [Fig. 4.1 (f)]. At the last measurement,  $x/D = 1.137$ , the flow separates ( $k = 0.76mm$  and  $1.52mm$  height elements) in the near-wall regions. Away from the wall, flow shows an upward trajectory as it is being forced over and around the next element. A different view of the flow reattachment and subsequent separation ahead of the next upstream element is observed in Fig. 4.2 which presents contours of  $U/\sqrt{-\overline{uv}_{max}}$  in the  $y/k - x/D$  plane along center line ( $z/d = 0$ ). Large flow gradients are seen in the neighborhood of the element height, directly behind the elements and above the backflow regions. Each case shows large regions of reverse flow aft of the elements. From this plot, locations of flow reattachment, on centerline, aft of the element and subsequent separation ahead of the next element were determined are presented in Table 4.3. In general, flow reattaches earlier for the staggered cases as faster fluid over and around the elements constricts the regions of separated flow. This also leads to smaller separated regions aft of the element as revealed from the examination of Figs. 4.1 (a)-(f). Similar analysis can also be made from the determination of the areas occupied by the separated flow which is presented as a variation of the ratio,  $A_{sep}/A$ , with streamwise distance,  $x/D$  in Fig. 4.3, where  $A_{sep}$  is separated flow area and  $A$  is projected frontal area of the element.

Figure 4.4 presents the mean velocity profiles  $U$  plotted in wall variables. In all cases, large differences are seen between the two orientations in the very near-wall locations, and these differences are confined within two element heights as regards the distribution with the  $k = 0.38mm$  elements and



within the element height in the other elements. However, in the log-law region, slight differences are observed between the two orientations as regards the distributions of the higher two elements which is due to the slightly larger Reynolds shear stresses in the staggered cases. A large log law region is seen in all cases which are due to low  $k/\delta$  values. The effect of roughness is seen in the decrement of the log law intercept,  $\Delta U^+$ , which is also the roughness function, as dictated by Eq. 1.1. The magnitude of this intercept increases with the increase in the height of the roughness elements. Mean velocity plotted in the defect law coordinates seems to indicate that the outer part of the mean velocity  $U$  profile is not directly affected by roughness. This supports conclusions drawn by Hama (1954) who showed that the defect law is independent of roughness condition (Fig. 4.5).

#### 4.1.1.2 Determination of roughness function and displacement of origin

The determination of  $\Delta U^+$  is done in conjunction with the determination of  $\varepsilon$ . It may be reiterated that  $\varepsilon$ , the displacement surface, also referred to as zero-plane displacement, is the displacement from the wall ( $y=0$ ) to the effective origin. The values of  $\varepsilon$  and the roughness function,  $\Delta U^+$  are determined the following way. Equation 1.12 is considered as a function to be minimized while function variables,  $\varepsilon$ ,  $\Pi$ , and  $\Delta U^+$  are iterated,  $\kappa$  and  $C$  are kept as constants and have values of 0.40 and 5.1, respectively. The values of  $\varepsilon$ ,  $\Pi$  and  $\Delta U^+$  thus obtained are included in Table 4.2. Figure 4.4 has been redrawn with the corrected displaced surface and uses data only from the apparent log layer and is presented in Fig. 4.6. The high values of wake parameter,  $\Pi$ , tends to increase due to roughness, a behavior also observed by Krogstad *et al.* (1992) in their case of mesh roughness where this parameter had a value as high as 0.70.

The detailed measurements made within the rough-wall, in and around 3-D roughness elements such as cylinders, also made possible the determination of the displacement of origin in an alternate way, for the first time.  $\varepsilon$  can also be considered as the average height of the displacement surface due to the presence of the roughness elements and the separated flow volume. It can be defined as:  $\varepsilon = d_{vol}/f_{area}$ , where  $d_{vol}$  is the sum of the volume of the roughness elements plus the volume of separated flow and  $f_{area}$  is the projected area. From this definition,  $\varepsilon/k = d_{vol}/f_{vol}$  where  $f_{vol}$  is the flow volume without the roughness. From the measurements of separated flow regions (Fig. 4.3), the numerator is calculated and the ratio,  $\varepsilon/k$ , from the displacement volume analysis is presented in Table 4.4. The values presented are within 18% of each other thereby confirming that  $\varepsilon$  is indeed the displaced wall surface that the flow “sees,” and satisfies the continuity equation.

#### 4.1.1.3 Effects of height and roughness density on roughness function

This section examines the effects of the element height ( $k$ ) and roughness density ( $\lambda$ ) on the roughness function,  $\Delta U^+$ . This is an important as it is a measure of the wall shear and it would be very useful if one can determine this just from the roughness height and density. Several correlations have been proposed and tested by various researchers to determine the roughness function,  $\Delta U^+$ , or the equivalent sand grain roughness,  $k_s$ . For a general case, after estimating  $\lambda$  or  $\Lambda_s$  from surface geometry,  $f(\lambda)$  or  $f(\Lambda_s)$  can be determined from the correlations and then one can use Eq. 1.4 to determine the roughness function. Several correlations are listed in section 1.2.1.1 and several of the correlations were tested using the present data-set. The six cases of rough-wall boundary layers yield six data points. Other data sets pertaining to two-dimensional rough-wall BL on sparsely distributed roughness elements such as cylinders, cones, cubes, pebbles, hemispheres and spheres are included for the sake of comparison and the validity of the existing correlations.

The different correlations tested are those attributed to Simpson (1973), Sigal and Danberg (1990) and van Rij *et al.* (2002). Sigal and Danberg (1990) modified Simpson's version of roughness density ( $\lambda$ ) to account for the shape of the individual element to define a new roughness density



parameter ( $\Lambda_s$ ), while van Rij *et al.* (2002) introduced a new correlation with the same definition of roughness density,  $\Lambda_s$ , as Sigal and Danberg (1990). Their definitions are listed in the same section. While Simpson's correlation is presented in Fig. 4.7 (a) and the latter two are presented in Fig. 4.7 (b). It appears that Simpson's correlation is a better fit for the current data-set than the newer correlations even though the newer ones were designed to be an improvement as it included a shape factor to account for the element shape.

Implicit in all these correlations is the assumption that the flow is fully rough. As mentioned previously, for fully rough cases, the RHS of Eq. 1.3 becomes independent of viscosity. Hence, the correlations for  $f(\lambda)$  or  $f(\Lambda_s)$  are not valid for transitional rough-wall cases. For transitional rough-wall flows, a novel modification for  $f(\lambda)$  is introduced here. For a smooth-wall TBL, Spalding (1961) derived a continuous closed form of "law of the wall" that described the three parts of the inner regions of the TBL, viz., the viscous sublayer, the buffer layer and the semi-logarithmic layer. This equation is given by

$$y^+ = U^+ + \frac{1}{e^{\kappa C}} \left\{ e^{\kappa C} - \left[ 1 + \kappa U^+ + \frac{(\kappa U^+)^2}{2!} + \frac{(\kappa U^+)^3}{3!} \right] \right\}, \quad (4.1)$$

where,  $\kappa$  and  $C$  are the smooth wall constants and are equal to 0.40 and 5.1, respectively. The same functional form of an equation is needed to describe the smooth, transitionally rough and fully rough  $\Delta U^+ = f(\lambda, k^+)$  in Eq. 1.3. The modified expression for  $f(\lambda)$  to describe transitional roughness is then given by

$$k^+ - k_0^+ = \Delta U^+ + \frac{1}{e^{\kappa f(\lambda)}} \left\{ e^{\kappa \Delta U^+} - \left[ 1 + \kappa \Delta U^+ + \frac{(\kappa \Delta U^+)^2}{2!} + \frac{(\kappa \Delta U^+)^3}{3!} \right] \right\}, \quad (4.2)$$

where,  $k_0^+$  is the thickness of the viscous sublayer which is 5. For a given roughness function,  $\Delta U^+$ , the only unknown in the above equation is  $f(\lambda)$ . This equation was applied to both orientations of 2-D rough-wall TBL involving the smallest elements,  $k=0.38\text{mm}$  ( $k^+=26$ ,  $\lambda=0.025$ ). The results, thus obtained, are presented in Fig. 4.7 (a) and they provide excellent agreement with Simpson's correlation.

In the subsequent sections, results are presented mostly for the  $y-z$  plane at  $x/D = 0.5$  and the plane along the  $x$ -axis ( $z = 0$ ). Profiles would be restricted to the location at  $x/D = 0.5$ ,  $z = 0$ .

#### 4.1.1.4 Wall-normal velocity

One of the main differences between the single elements and the 2-D rough-wall BL as regards mean flow structure is the region below the element height downstream of it. As regards the single element, there is a strong downwash induced by the RTVS that is felt all the way to wall, whereas in the distributed case the downwash is limited by the upward moving fluid in the back flow region. This is seen in the distribution of the wall-normal component of the velocity depicted as contours of  $V/\sqrt{-uv_{\max}}$  in the  $y/k - z/d$  plane at  $x/D = 0.5$  in Fig. 4.8 (a). Flow is directed towards the wall as the faster fluid is forced over the element where it meets the upwash due to the strong secondary flow which is attributed to the faster fluid that has moved through the gaps and feeds this region of backflow. The wallward motion of fluid over the top of the elements is also seen in the contours of  $V/\sqrt{-uv_{\max}}$  in the  $x/D - y/k$  plane along the centerline [Fig. 4.8 (b)]. In the straight orientation, flow is seen to impinge at the junction of the subsequent element while in the staggered case flow is directed over the top of the subsequent element. This also contributes to the lesser separated areas seen aft of the downstream elements in the cases with staggered orientation.



## 4.1.2 Vorticity

One of the key features in the flow downstream of the individual elements (Fig. 3.33) was the generation of RTVS that was associated with large magnitudes of streamwise vorticity. As regards a distribution of such elements the important feature is its ability to generate significant magnitudes of wall-normal vorticity,  $\Omega_y$ . Hence all components of the mean vorticity vector were calculated. The streamwise mean vorticity plotted as contours of streamwise vorticity,  $\Omega_x \sqrt{A} / \sqrt{-uv_{\max}}$ , along with secondary velocity vectors,  $V / \sqrt{-uv_{\max}}$  and  $W / \sqrt{-uv_{\max}}$ , are presented for the  $y/k - z/d$  plane at  $x/D = 0.295, 0.5$  and  $0.75$  in Figs. 4.9 (a)-(c). At the first measurements plane, a distinct region of negative vorticity is seen at the element height which is the location where the back flow meets the faster fluid directed towards the wall. The merging of the back flow with the faster fluid overwhelms the separated shear layers emanating from the top of the elements as seen in the absence of positive vorticity that would be due to the RTVS. At  $x/D = 0.5$ , the regions of negative vorticity, due to the backflow, diffuses to yield larger regions with lower magnitudes. At  $x/D = 0.75$ , as the nose region of the subsequent element (straight orientation), the faster fluid impinging towards the wall curves around this region and regions of positive vorticity are seen which is attributed to that generated by the secondary flow. A similar feature is seen in the staggered cases at  $x/D = 1.137$  which is the location close to the subsequent element in that case. The faster fluid moving in the gaps of the rough-wall constantly feed the back flow regions creating a recirculation motion in the  $x - z$  plane too as seen on the presentation of the flow vectors,  $U / \sqrt{-uv_{\max}}$  and  $W / \sqrt{-uv_{\max}}$ , along with  $\Omega_y$  at constant vertical heights, viz., at  $y/k = 0.3$  and  $0.5$  [Fig. 4.10 (a)], and  $0.8$  and  $1.1$  [Fig. 4.10 (b)]. Significant magnitudes are seen below the element heights. As regards the spanwise vorticity,  $\Omega_z$ , large magnitudes are generated aft of the element, in the neighborhood of the element heights, where large streamwise velocity gradients are generated, as seen in Fig. 4.11 where it is presented in conjunction with velocity vectors,  $U / \sqrt{-uv_{\max}}$  and  $V / \sqrt{-uv_{\max}}$ . Fluid separating at the nose of the subsequent element (staggered cases) also generates large spanwise vorticity. One of the key differences between the straight and the staggered case is the magnitude of the velocity and its gradient hitting the top of the subsequent element. The latter has larger magnitudes of both as it offers a longer distance for flow to reattach.

## 4.1.3 Turbulent stresses

Modification to the turbulence structure by the roughness elements is analyzed by examining the behavior of the Reynolds stresses. While measurements have been made at different planes, only a few representative cases are presented.

Contours of streamwise Reynolds normal stress,  $\overline{u^2} / -\overline{uv_{\max}}$ , in the  $y/k - z/d$  plane at  $x/D = 0.5$  are presented in Fig. 4.12 (a). Large magnitudes are seen at the element height above the element height where large velocity gradients are present. This is also the region where the higher speed fluid is moving towards the wall and entrains the low momentum fluid from the back flow region. The merging of these layers results in high stresses. Contours of the same quantity in the  $y/k - z/d$  plane [Fig. 4.12 (b)] shows high magnitudes above the element height being diffused in the streamwise direction by ejections motions above the element height seen at locations of  $x/D = 0.5$  and beyond. Quadrant contributions to the Reynolds normal stress,  $\overline{u^2}$ , along the centerline is shown in Fig. 4. 13 (a) as a variation streamwise distance,  $x/D$ . The figure clearly reveals that ejection/sweep mechanisms are disrupted by the roughness elements with the sweeping motion dominating ejection



motions below the element height as the effects of the inrush of faster fluid is felt closer to the wall than at previous locations. At the very first measurement location, it is the ejection motions emanating from the backflow regions that dominate the near wall regions while sweeps dominate the regions in the neighborhood of the element height, as revealed in Fig. 4.13 (b) where the ratio of sweeps to ejections as a variation with  $y/k$ , at various streamwise locations,  $x/D$ , is presented. The profiles of  $\overline{u^2}/-\overline{uv}_{\max}$  collapse in the outer regions of the boundary layers as observed in the variation of the streamwise Reynolds normal stresses,  $\overline{u^2}/-\overline{uv}_{\max}$ , with  $y/\delta$  at  $x/D = 0.5$  along the centerline (Fig. 4.14). Also the peak  $\overline{u^2}/-\overline{uv}_{\max}$  levels decrease with increase in roughness height owing to increased wall shear which decreases this normalized quantity.

The effect of roughness is most prominent on the stresses involving the  $v$  fluctuations with one of them being the Reynolds wall-normal stress,  $\overline{v^2}/-\overline{uv}_{\max}$ , which is presented as in the  $y/k - z/d$  plane at  $x/D = 0.5$  [Fig. 4.15 (a)]. Very large magnitudes are seen at and slightly below the element heights. This is again due to the interaction of low momentum fluid, ejected from the back flow regions, with the faster flow rushing over the elements directed in the wallward direction. Contours presented along the centerline [Fig. 4.15 (b)] indicate a diffusion of stresses away from the maxima locations. The examination of quadrant contributions and the sweep to ejection ratio [Fig. 4.16 (a) and (b)] show that sweeps dominate in regions close to the element height and below where the peak levels in the stresses are seen. Also these peak levels are seen along the centerline where the ejected fluid from the back flow regions rises vertically to meet with inrushing faster flow. The presentation of  $\overline{v^2}/-\overline{uv}_{\max}$  as a variation with  $y/\delta$  for the  $x/D = 0.5$  location (Fig. 4.17) shows that roughness has a pronounced effect on this quantity. While the outer regions show a collapse, much enhanced levels over those for the smooth wall are seen in all cases.

While the previous two stresses show peak levels at or slightly below the element height, it is not so in the case of the spanwise Reynolds normal stresses. Contours of spanwise Reynolds normal stresses,  $\overline{w^2}/-\overline{uv}_{\max}$ , in the  $y/k - z/d$  plane at  $x/D = 0.5$  are presented in Fig. 4.18 (a). At this location, high magnitude of stresses seen much below the element heights is mainly due to the confluence at the center plane of fluid rushing from the sides of the elements and the gaps which carry with it strong spanwise fluctuations. On the examination of the contours in  $x/D - y/k$  plane [Fig. 4.18 (b)], the regions where high magnitudes are generated seem to differ as regards the straight and staggered orientation. In the staggered case, the peak levels seem to be generated just as described, whereas in the straight case, high magnitudes are seen in the nose region of the subsequent element where the faster fluid directed towards the wall diverges. The variation of  $\overline{w^2}/-\overline{uv}_{\max}$  with  $y/\delta$  at the  $x/D = 0.5$  location (Fig. 4.19) does not show a collapse in the profiles at the outer regions of the BL. Further, the peak levels, located below the element height, increase with roughness height as opposed to the behavior seen in the  $\overline{u^2}/-\overline{uv}_{\max}$  stresses.

The behavior of the streamwise Reynolds shearing stress,  $-\overline{uv}/-\overline{uv}_{\max}$ , is very similar to that exhibited by the  $\overline{v^2}/-\overline{uv}_{\max}$  stresses. Contours of the streamwise Reynolds shearing stresses,  $-\overline{uv}/-\overline{uv}_{\max}$ , in the  $y/k - z/d$  plane at  $x/D = 0.5$  are presented in Fig. 4.20 (a) and for the  $x/D - y/k$  plane in Fig 4.20 (b). The similarity in the flow structure indicates that similar motions govern the behavior of these two stresses. Both stresses are dominated by the sweeping motions below the element height and ejection motions above it (Fig. 4.21). The sweeping motions are due to the faster fluid rushing over the elements in the wall direction and the ejection motions are due to the low speed fluid that have been pushed away from the wall. With the progress in distance the mixing of these fluids take place further away from the wall and is spread over larger regions in the BL.



Similar to the  $\overline{v^2}/-\overline{uv}_{\max}$  stresses, much elevated peak values over those for the smooth wall are seen in the neighborhood of the roughness height. The profiles of  $-\overline{uv}/-\overline{uv}_{\max}$  versus  $y/\delta$  at  $x/D = 0.5$ ,  $z = 0$  (Fig. 4.22) show a distinctly constant stress region which is also the over lap region between the inner layers and the outer layers as seen in the semi-logarithmic region in the streamwise mean velocity profile (Fig. 4.4). Further, a clear collapse in the profiles is seen in the outer layer regions. It should also be noted that, as regards the streamwise mean velocity and the Reynolds stresses, the effect of the roughness is limited to about 3 roughness heights. Except in the case of the spanwise Reynolds normal stresses, all other stresses seem to collapse in the outer regions.

#### 4.1.4 Turbulent kinetic energy (TKE)

The interaction of shear stresses with the large velocity gradients aft of the elements lead to large levels of turbulent kinetic energy (TKE). Figure 4.23 (a) presents the contours of turbulent kinetic energy,  $(\overline{q^2}/2)/-\overline{uv}_{\max}$ , along with diffusion velocity vectors,  $V_q/\sqrt{-\overline{uv}_{\max}}$  and  $W_q/\sqrt{-\overline{uv}_{\max}}$ , in the  $y/k - z/d$  plane at  $x/D = 0.5$ . Large levels of TKE are generated at regions about the element height for the  $k=0.38mm$  elements (both cases) and at regions about the element height and below as regards the other four cases. These high levels are generated at regions where the low speed ejected fluid from the back flow regions meet with strong wallward rush of high speed fluid. There is a strong entrainment at these locations leading large mixing of shear layers and sweep/ejection motions carry TKE levels away from the regions where it is produced in a direction as indicated by the diffusion velocity vectors. In general, TKE flows down the gradients of TKE. In the straight cases, large diffusion of TKE is seen about half a diameter from the center plane due to large values of  $\overline{w^3}$  which is the transport of  $\overline{w^2}$  by the  $w$  fluctuations. Much of the spanwise fluctuations are due to the strong draft of flow from the gaps of the elements into the regions of back flow aft of the elements. For the development of TKE along the streamwise direction, contours are presented in the plane along the centerline in conjunction with the diffusion velocity vectors,  $U_q/\sqrt{-\overline{uv}_{\max}}$  and  $V_q/\sqrt{-\overline{uv}_{\max}}$ , and is shown in Fig. 4.23 (b). Here too, the peak levels are seen in the neighborhood of the element height from where it is convected and diffused away from it. The variation of TKE with  $y/\delta$  for the  $x/D = 0.5$  location is shown in Fig. 4.24. The effect of the roughness is seen in enhanced peak levels, compared to the smooth wall case, in the neighborhood of the element heights. A collapse of the profiles is not seen in the outer regions similar to that seen in the  $\overline{w^2}$  stresses.

The transport equation for TKE shows that all of the production of TKE is due to the interaction of the Reynolds stresses with the mean flow gradients. The term that contributes to the production of TKE is plotted normalized as  $(TKE \text{ Prod})\sqrt{A}/\left(\sqrt{-\overline{uv}_{\max}}\right)^3$  in the  $y/k - z/d$  plane at  $x/D = 0.5$  [Fig. 4.25 (a)] and along the  $x/D - y/k$  plane [Fig. 4.25 (b)]. The major contributors to the production of TKE are for the 2-D rough-wall layers are  $-\overline{uv}\partial U/\partial y$ ,  $-\overline{u^2}\partial U/\partial x$ ,  $-\overline{v^2}\partial V/\partial y$ , and  $-\overline{w^2}\partial W/\partial z$ . Among them the most dominant term is the  $-\overline{uv}\partial U/\partial y$  term. This term in conjunction with  $-\overline{v^2}\partial V/\partial y$  are important in the vicinity of the element heights while the influences of the other two terms are felt in regions much below the element height. Figure 4.25 (a) shows that same regions that show high TKE also show high production rates which is of course obvious. The differences between the respective regions are perceptible only when seen in the contours presented in the  $x/D - y/k$  plane. The plots reveal a maxima in the TKE which is seen aft of that seen in the



production rates. This implies that the convection and diffusion processes are responsible for the transport of TKE.

#### 4.1.4.1 Transport-rate budget of turbulent kinetic energy (TKE)

In order to further examine the relative importance of the different terms that contribute to the transport of TKE (Eq. 3.5), an energy balance was carried out. The transport-rate equation for the TKE is presented again and is as follows:

$$\begin{aligned}
 \underbrace{U \frac{\partial (\frac{1}{2} \overline{q^2})}{\partial x} + V \frac{\partial (\frac{1}{2} \overline{q^2})}{\partial y} + W \frac{\partial (\frac{1}{2} \overline{q^2})}{\partial z}}_{\text{Convection (C)}} = & \underbrace{- \left[ \overline{u^2} \frac{\partial U}{\partial x} + \overline{v^2} \frac{\partial V}{\partial y} + \overline{w^2} \frac{\partial W}{\partial z} + \overline{uv} \left( \frac{\partial V}{\partial x} + \frac{\partial U}{\partial y} \right) + \overline{uw} \left( \frac{\partial W}{\partial x} + \frac{\partial U}{\partial z} \right) + \overline{vw} \left( \frac{\partial W}{\partial y} + \frac{\partial V}{\partial z} \right) \right]}_{\text{Production (PR)}} \\
 & - \underbrace{\left[ \frac{\partial}{\partial x} \left( \frac{\overline{uq^2}}{2} \right) + \frac{\partial}{\partial y} \left( \frac{\overline{vq^2}}{2} \right) + \frac{\partial}{\partial z} \left( \frac{\overline{wq^2}}{2} \right) \right]}_{\text{Turbulent Diffusion (TD)}} - \underbrace{\left( \frac{\partial}{\partial x} \frac{\overline{up'}}{\rho} + \frac{\partial}{\partial y} \frac{\overline{vp'}}{\rho} + \frac{\partial}{\partial z} \frac{\overline{wp'}}{\rho} \right)}_{\text{Pressure Diffusion (PD)}} \\
 & + \underbrace{\overline{v \nabla^2 \left( \frac{1}{2} \overline{q^2} \right)}}_{\text{Viscous Diffusion (VD)}} - \underbrace{\overline{v \frac{\partial u_i}{\partial x_i} \frac{\partial u_j}{\partial x_j}}}_{\text{Dissipation } (\epsilon)}
 \end{aligned}$$

(4.1)

##### 4.1.4.1.1 General strategy for estimating the various terms in the transport-rate budget of turbulent kinetic energy (TKE)

From the experimental point of view, derivatives of any quantity cannot be measured directly. Approximations are made by using either a Taylor series expansion or fitting a function to the data and calculating the derivatives of this function at the point of interest. The fine grid of measurement locations permits the calculation of  $x$ ,  $y$  and  $z$  derivatives and they are calculated either with a second or first order accurate in space finite difference approximation using the data. Thus, calculations of the “convection”, “production”, “turbulent diffusion” and the “viscous diffusion” terms are straightforward. A substantial list of uncertainties for the various terms is provided by Ölçmen and Simpson, (1996).

The pressure-diffusion term for each of the transport rate budgets in all the four cases is estimated using Lumley’s approximation (Lumley, 1978). Considering the TKE balance, since the pressure-strain term in the TKE equation equals zero due to continuity, the dissipation of TKE is extracted by balancing the TKE equation. For the rough-wall cases, as regards the individual stresses, a balance is not carried out and instead, four of the major terms in transport rate budgets are evaluated – terms that are point dependent, viz.,  $C$ ,  $PR$ ,  $TD$  and  $VD$ .

##### 4.1.4.1.2 Transport-rate budget of turbulent kinetic energy (TKE)

Figure 4.26 presents the variation of transport-rate budget of TKE,  $\overline{q^2}/2$ , normalized by  $\left( \sqrt{-\overline{uv_{\max}}} \right)^4 / \nu$ , with  $y \sqrt{-\overline{uv_{\max}}} / \nu$  for the 2-D smooth wall BL as performed by Ölçmen and Simpson (1996). This is presented for the sake of comparison. For the six cases of rough-wall BL, Fig. 4.27 presents the variation of transport-rate budget of TKE,  $\overline{q^2}/2$ , normalized by  $\left( \sqrt{-\overline{uv_{\max}}} \right)^4 / \nu$ , with  $y \sqrt{-\overline{uv_{\max}}} / \nu$  at  $x/D = 0.5$  at the centerline. Throughout the region, from



near-wall to about 2 element heights, a large amount of TKE is produced. Since a large amount is produced, there needs to be a transport of TKE. This transport is carried out by the velocity fluctuations and consequently large values of turbulent diffusion occur that transport TKE from regions of high TKE regions to lower TKE regions. The dissipation of TKE is important in the near-wall regions and in regions close to the element height. Further, the dissipation rates are comparable in magnitudes with that for the  $TD$  albeit with an opposite sign. Also, the distribution for dissipation is similar to that for the production ( $PR$ ) to the TKE, indicating that portions of TKE dissipated is proportional to that being generated. The pressure diffusion term,  $PD$ , is small in magnitude and is of significance in regions slightly below the element height in the 2-D rough-wall layers. The behavior of production and dissipation are similar in 2-D rough-wall BL and the smooth wall BL but with much higher levels in the former case. Also the effects of roughness on the transport processes are confined within 3 roughness heights.

### 4.1.5 Structural parameters

Figures 4.28 (a) and (b) show the variations of the structure parameter  $A_1$  ( $= -\overline{uv}/q^2$ , where  $q^2 = \overline{u^2} + \overline{v^2} + \overline{w^2}$ ) and  $1/S$  ( $= -\overline{uv}/\overline{v^2}$ ) respectively with  $y/\delta$ . The different rough boundary layers show no variation of  $k^+$  on either of these parameters in the outer region of the boundary layer. The structure parameter  $A_1$  shows a value of 0.12 in the outer regions close to the accepted values of 0.15 for the smooth wall boundary layers. At the outer part of the boundary layers in all cases, the values of the structure parameter are very close to each other indicating that the shear stresses and the turbulent kinetic energy change in the same manner. Further, this also implies that the turbulence structure in all these cases is similar and independent of the wall condition. Similar statement can be applied to the  $1/S$  parameter too which does not come as a surprise, since both  $-\overline{uv}$  and  $\overline{v^2}$  had shown strong sensitivity to roughness and also affected by the similar motions.

## 4.2 Conclusions

The present study has provided a detailed analysis on the effects of a sparse and uniform distribution of three-dimensional roughness elements on two-dimensional boundary layers. Six cases of rough-wall were studied: cylindrical elements of 0.38mm, 0.76mm and 1.52mm height ( $k$ ) were used in *square* and *diagonal* patterns to yield six different roughness geometries, thus six cases of 2-D rough-wall boundary layers. Each wall uses the roughness of same height.

These studies were performed by the measurements of mean velocities and fluctuating quantities (Reynolds stresses and the triple products) using a special fine-measurement-volume (30 microns diameter) three-velocity-component fiber-optic Laser Doppler Velocimeter (LDV) system, which views the flow through the transparent glass wall. Measurements of mean velocity  $U$  confirm the well-known fact that the velocity-defect law is similar for both smooth and rough surfaces, and the semi-logarithmic velocity-distribution curve is shifted by an amount  $\Delta U^+$  depending on the height of the roughness element showing that  $\Delta U^+$  is a function of  $k^+$ . The magnitude of this intercept,  $\Delta U^+$ , also known as the roughness function, increases with the increase in the roughness.  $\Delta U^+$  was determined iteratively using the “displacement of origin” method which fits the data in the apparent log-law regions of the boundary layer. The error of origin,  $\epsilon$ , is the distance from the wall to effective wall origin as seen by the flow. That it is also a displacement surface is verified by a simple analysis which takes into account the volume of fluid displaced due to flow separation by the elements and the volume occupied by the elements themselves. The values of  $\epsilon$  determined by the two methods were within 18% of each other. The values of the roughness function,  $\Delta U^+$ , were compared



with other data sets and different correlations that are used to correlate roughness density effects on it. The correlations of Simpson (1973) were found to fit the experimental data better than the newer correlations.

As regards the mean flow structure, the roughness elements in the distribution create regions of large back flow behind them that is continuously fed by the fast moving fluid moving through the gaps in the rough-wall. The fluid moves up within the back flow regions where it meets the high speed fluid forced over the elements that is rushing towards the wall. This collision of in-rushing high speed flow with the low speed ejections leads to a mixing of shear layers that contribute to large magnitudes of stresses, which is also seen in the generation of large levels of TKE in the vicinity of the element height. The sweeps of fluid are sources of large momentum and quadrant analysis reveals that the sweeps penetrate all the way to the wall. Figure 4.29 presents a schematic of the flow features gleaned from the measured results. One of the key differences between the flow aft of the single elements and the distributed elements is the lack of persistence of the roughness top vortex structure in the latter case. Surely flow does separate at the roughness top whose shear layers convect as vortical pair. However, in this case, these structures are overwhelmed by the intense mixing that occurs at the confluence of the high speed fluid with the ejecting fluid from the back flow regions. Also, the ejecting fluid is seen as an upwash of fluid as opposed to the strong downwash due to the RTVS as seen in the case of the single elements. Further, the upwash of fluid in the case of the distributed roughness is seen to generate regions of negative streamwise vorticity aft of the elements contrary to the positive streamwise seen in the case of the single elements that were attributed to the RTVS. Also, significant amounts of wall-normal vorticity are generated within the rough wall.

As regards the orientation effects, slightly higher averaged Reynolds stresses occur in the staggered cases when compared with the straight cases. This leads to lower mean velocities, greater displacement and momentum thicknesses in the former case which also implies a greater exchange of momentum between the flow down in the roughness elements and the flow above them. Further, staggered cases also offer a longer streamwise length for the flow to re-attach and consequently higher velocities are seen to hit the top of the elements.

As regards the turbulence structure, the effects of roughness are more pronounced on the  $\overline{v^2}$ ,  $\overline{w^2}$  and  $-\overline{uv}$  stresses than on  $\overline{u^2}$  stresses, with significant enhancement in the peak levels over those for the smooth wall BL. The sweeping motions associated with the high speed fluid and the ejection motions due to the low speed fluid ejected from the back flow regions are responsible for the high levels of stresses as regards the  $\overline{v^2}$  and  $-\overline{uv}$  stresses. A quadrant analysis of the different stresses revealed that, in general, sweeps dominate the near-wall regions below the element heights and ejections dominate region at the element height and above. The enhancement in the  $\overline{w^2}$  stresses is due to the large spanwise fluctuations associated with the fast moving spanwise fluid that is seen to rush from the sides of the elements and from the gaps in the rough-wall towards the regions of back flow. The distributions of  $\overline{u^2}$ ,  $\overline{v^2}$  and  $-\overline{uv}$  stresses in both the smooth wall BL and the rough-wall boundary layers collapse in the outer regions thereby implying that the outer regions are independent of wall conditions. Further the effects of roughness are limited to three roughness heights as regards both the mean velocities and the Reynolds stresses. An energy balance of the TKE was carried out in all the six rough-wall cases. It showed considerable levels of production and dissipation right from the near-wall regions to about 3 element heights with the peak levels in the vicinity of the element height. At distances below the element height, the only other quantity that is of importance is the turbulent diffusion. Convection is negligible except for regions in the neighborhood of the element heights and slightly below it. Above 3 element heights, the normalized terms behave similar to the smooth wall BL.



Table 4.1. Boundary layer parameters for the smooth wall and the six cases of 2-D rough-wall turbulent boundary layers.

Cases	Element height ( $k$ ), $mm$	Orientation	Free-stream velocity ( $U_e$ ), $m/s$	Boundary layer thickness ( $\delta$ ), $mm$	Displacement thickness ( $\delta^+$ ), $mm$	Momentum thickness ( $\theta$ ), $mm$	$Re_\theta$	$k/\delta$	Friction velocity, ( $\sqrt{-uv_{max}}$ ), $m/s$	$k^+$	$\lambda$	$\frac{\Delta U}{U_e}$	$\varepsilon^+$	$\Pi$
0	Smooth wall		26.97	39.00	6.09	4.47	7300	-	0.966	-	-	-	-	0.55
1	0.38	straight	27.19	51.89	8.68	5.92	9719	0.0073	1.131	26	0.025	4.4	14	0.60
2	0.38	staggered	27.34	51.20	8.72	6.02	9945	0.0074	1.144	26	0.025	4.6	9	0.60
3	0.76	straight	27.56	58.51	11.28	7.25	12067	0.013	1.272	59	0.050	7.6	27	0.62
4	0.76	staggered	27.37	58.70	11.38	7.40	12231	0.013	1.295	60	0.050	8.1	19	0.62
5	1.52	straight	27.51	63.07	13.94	8.30	13789	0.024	1.394	128	0.100	10.2	60	0.68
6	1.52	staggered	27.20	70.41	14.77	9.03	14828	0.022	1.420	131	0.100	10.7	44	0.65

Kinematic viscosity,  $\nu$ , is  $1.65576 \times 10^{-5} \text{ m}^2/s$ .

Table 4.2. Locations of flow reattachment, on centerline, aft of the element and subsequent separation ahead of the next element.

Cases	Element height ( $k$ ), $mm$	Orientation	Downstream of the element			Ahead of the subsequent element		
			$x/D$	$x/d$	$x/k$	$x/D$	$x/d$	$x/k$
1	0.38	straight	0.60	1.65	8.55	0.64	1.74	9.0
2	0.38	staggered	0.46	1.24	6.44	0.82*	2.27*	11.82*
3	0.76	straight	0.70	1.93	5.01	Not available		
4	0.76	staggered	0.49	1.34	3.48	1.10	3.00	7.8
5	1.52	straight	Flow does not reattach			Flow does not reattach		
6	1.52	staggered	0.50	1.39	1.8	1.04	2.85	3.70

“\*\*” denotes measurements from the flow visualization pictures.

Note that the streamwise distance between the elements in staggered orientation is  $\sqrt{2}D$ .

Table 4.3. Ratios of  $\varepsilon/k$  and  $d_{vol}/f_{vol}$  in 2-D rough-wall turbulent boundary layers.

Cases	Element height ( $k$ )	Orientation	$\varepsilon/k$ , from fitting the mean velocity data	$\varepsilon/k$ , from the displaced volume analysis
1	0.38mm	straight	0.538	0.519
2	0.38mm	staggered	0.346	0.285
3	0.76mm	straight	0.458	0.456
4	0.76mm	staggered	0.317	0.291
5	1.52mm	straight	0.469	0.420
6	1.52mm	staggered	0.336	0.287



## Figures

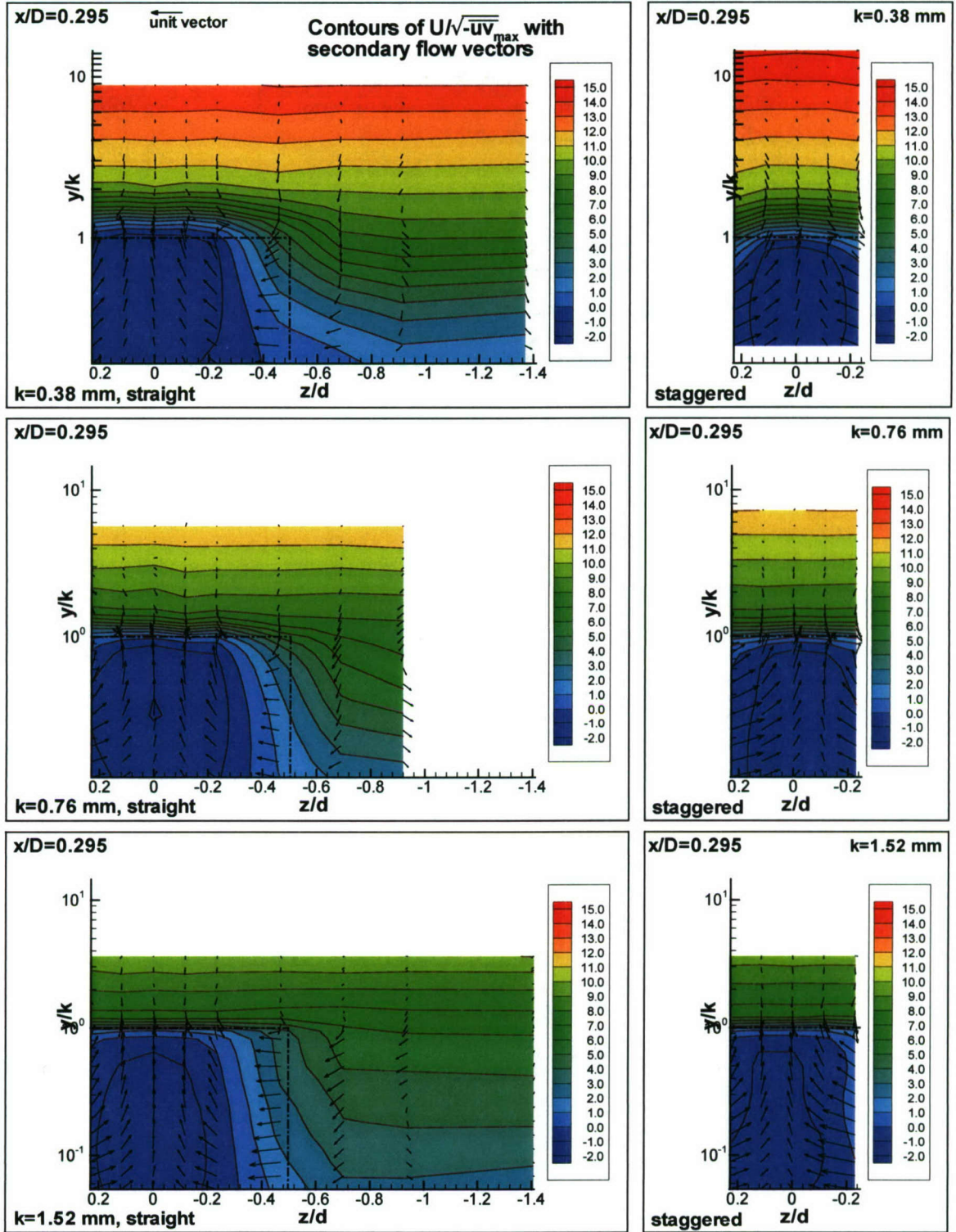


Figure 4.1 (a). Semi-log contours of  $U/\sqrt{-\overline{uv}_{\max}}$  in the  $y/k - z/d$  plane at  $x/D = 0.295$  with secondary flow vectors,  $V/\sqrt{-\overline{uv}_{\max}}$  and  $W/\sqrt{-\overline{uv}_{\max}}$  [ $k = 0.38$  mm (top row),  $k = 0.76$  mm (middle),  $k = 1.52$  mm (bottom)].

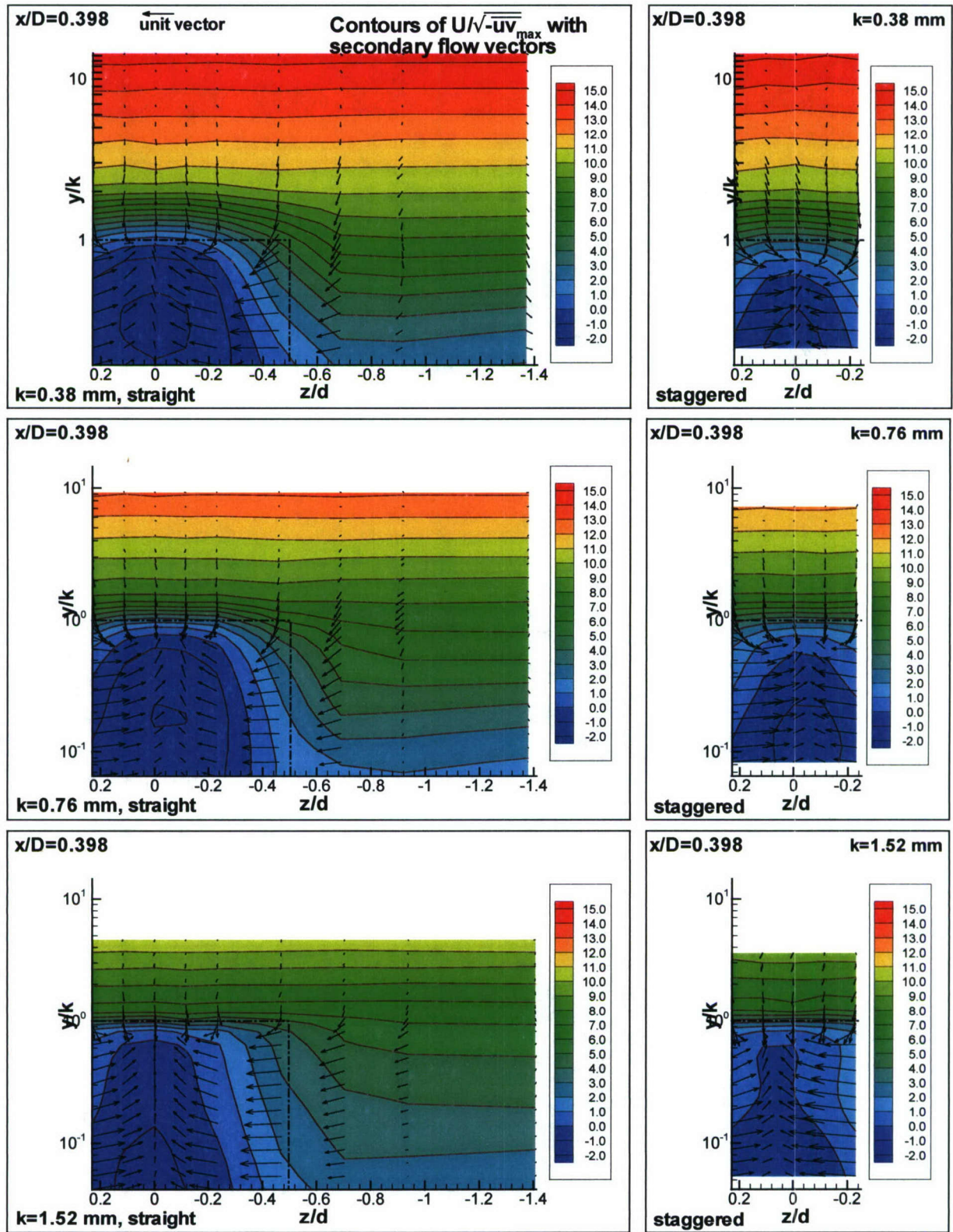


Figure 4.1 (b). Semi-log contours of  $U/\sqrt{-uv_{\max}}$  in the  $y/k - z/d$  plane at  $x/D = 0.398$  with secondary flow vectors,  $V/\sqrt{-uv_{\max}}$  and  $W/\sqrt{-uv_{\max}}$  [ $k = 0.38 \text{ mm}$  (top row),  $k = 0.76 \text{ mm}$  (middle),  $k = 1.52 \text{ mm}$  (bottom)].



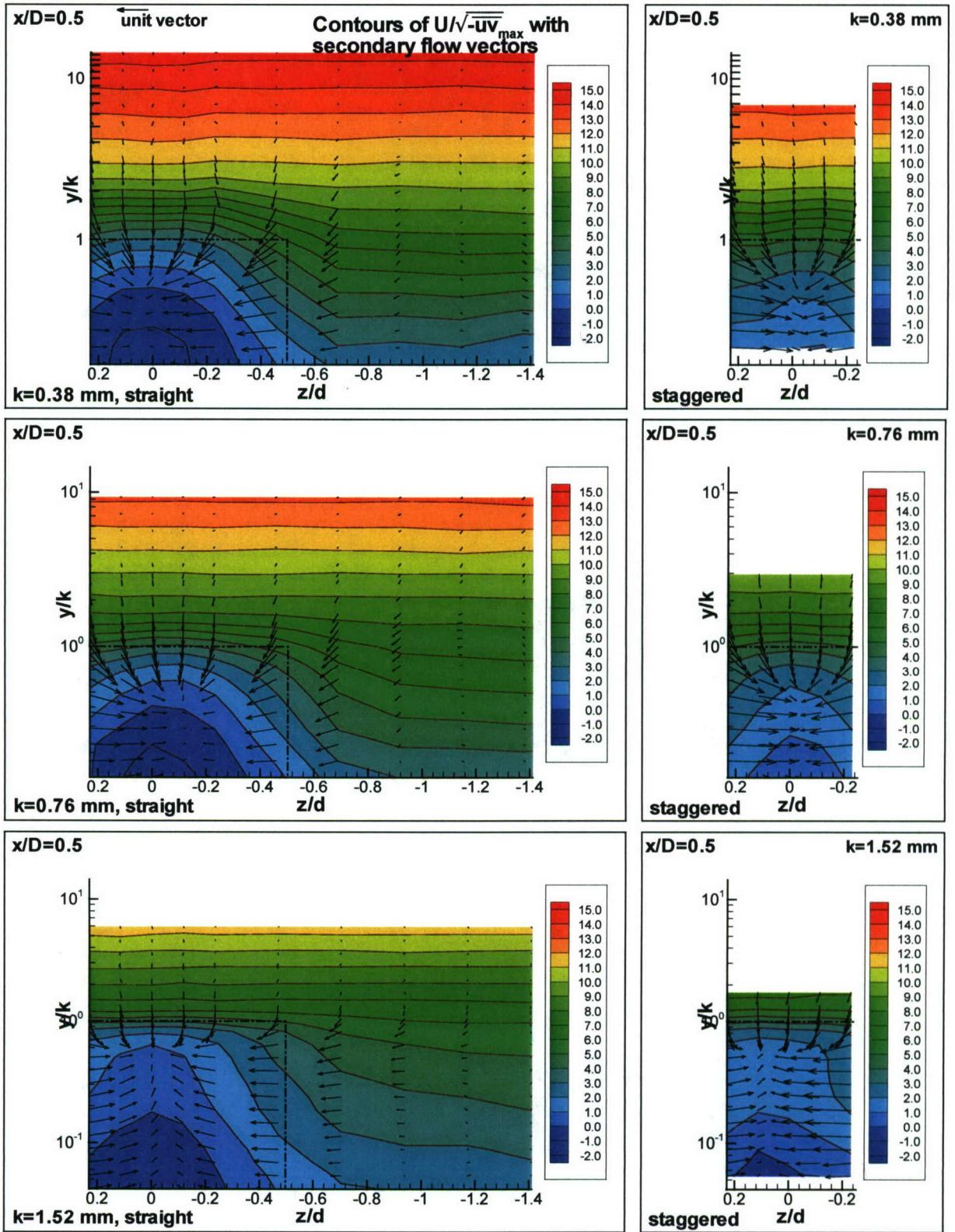


Figure 4.1 (c). Semi-log contours of  $U/\sqrt{-uv_{\max}}$  in the  $y/k - z/d$  plane at  $x/D = 0.5$  with secondary flow vectors,  $V/\sqrt{-uv_{\max}}$  and  $W/\sqrt{-uv_{\max}}$  [ $k = 0.38\text{mm}$  (top row),  $k = 0.76\text{mm}$  (middle),  $k = 1.52\text{mm}$  (bottom)].

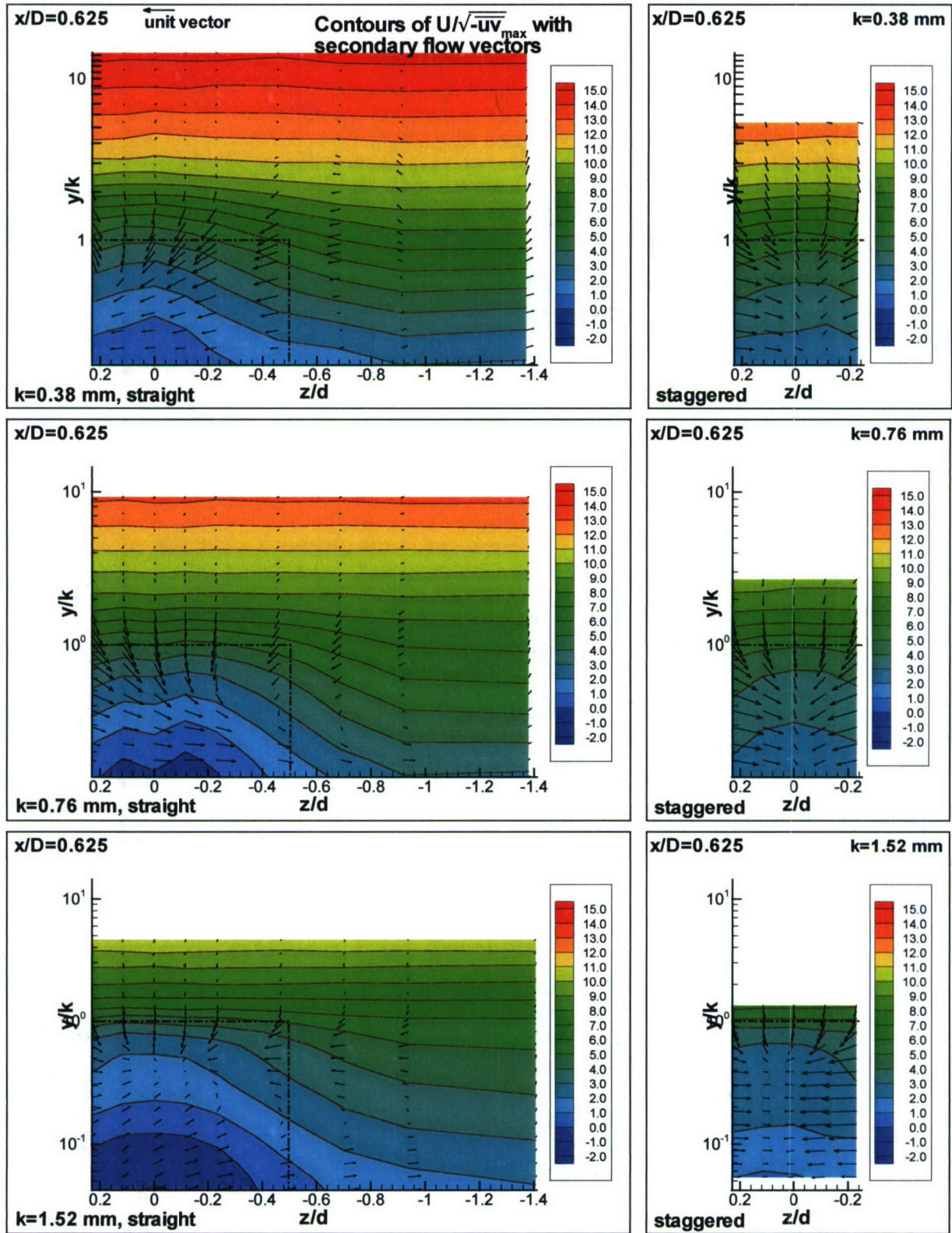


Figure 4.1 (d). Semi-log contours of  $U/\sqrt{-uv_{\max}}$  in the  $y/k - z/d$  plane at  $x/D = 0.625$  with secondary flow vectors,  $V/\sqrt{-uv_{\max}}$  and  $W/\sqrt{-uv_{\max}}$  [ $k = 0.38 \text{ mm}$  (top row),  $k = 0.76 \text{ mm}$  (middle),  $k = 1.52 \text{ mm}$  (bottom)].



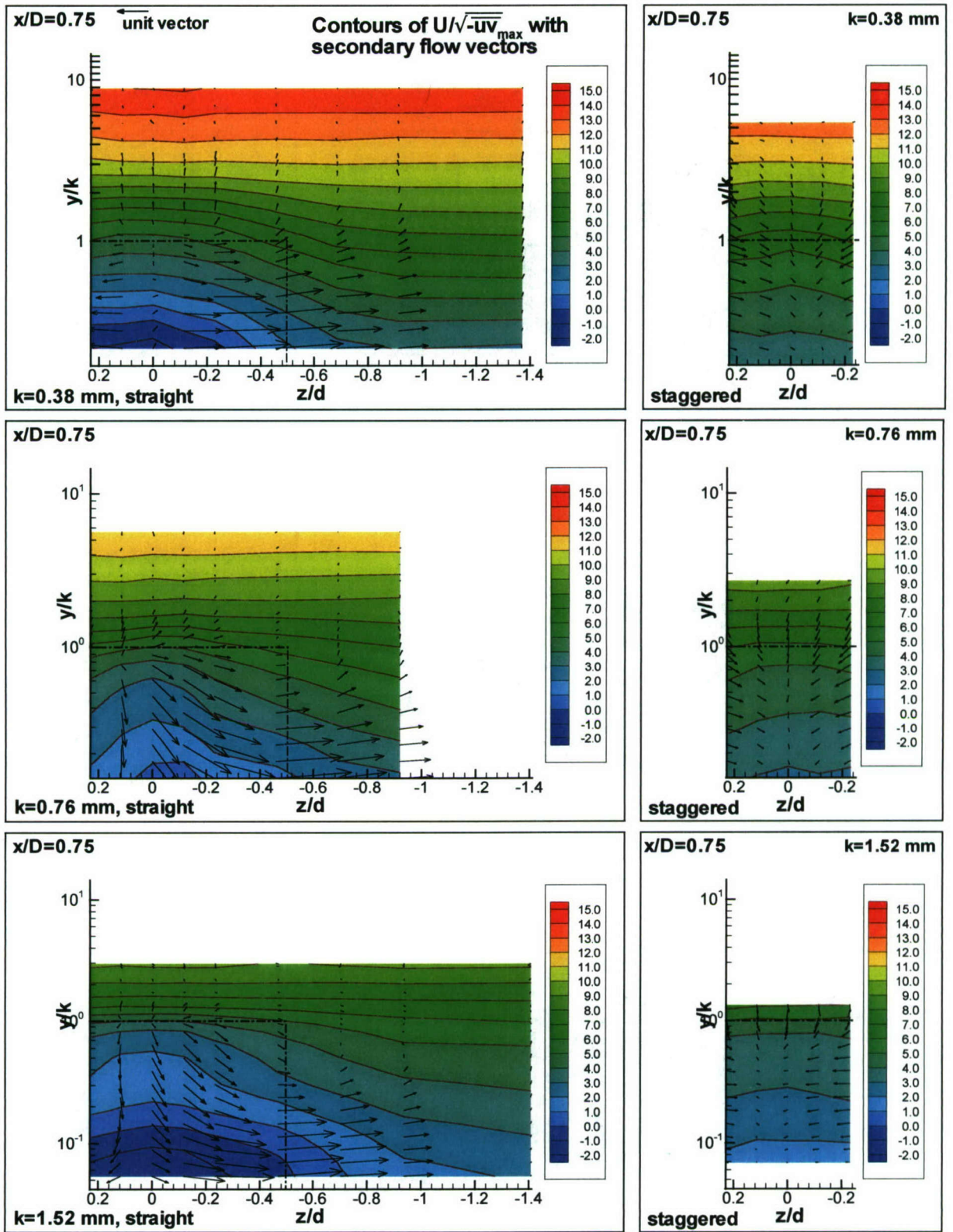


Figure 4.1 (e). Semi-log contours of  $U/\sqrt{-uv_{\max}}$  in the  $y/k - z/d$  plane at  $x/D = 0.75$  with secondary flow vectors,  $V/\sqrt{-uv_{\max}}$  and  $W/\sqrt{-uv_{\max}}$  [ $k = 0.38$  mm (top row),  $k = 0.76$  mm (middle),  $k = 1.52$  mm (bottom)].

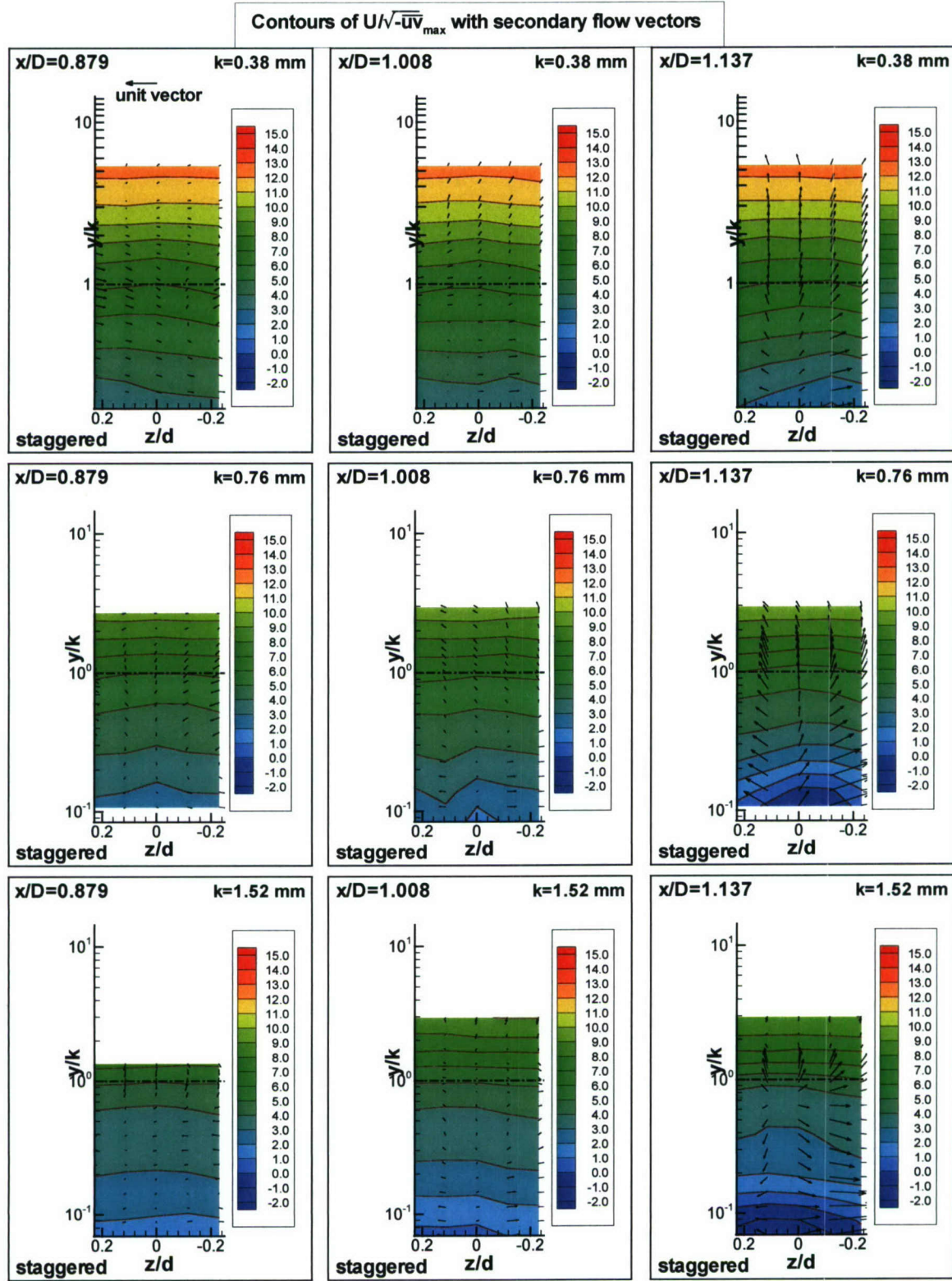


Figure 4.1 (f). Semi-log contours of  $U/\sqrt{-\overline{uv}}_{\max}$  in the  $y/k - z/d$  plane at  $x/D = 0.879, 1.008$  and  $1.137$  with secondary flow vectors,  $V/\sqrt{-\overline{uv}}_{\max}$  and  $W/\sqrt{-\overline{uv}}_{\max}$  [staggered cases only:  $k = 0.38\text{mm}$  (top row),  $k = 0.76\text{mm}$  (middle),  $k = 1.52\text{mm}$  (bottom)].



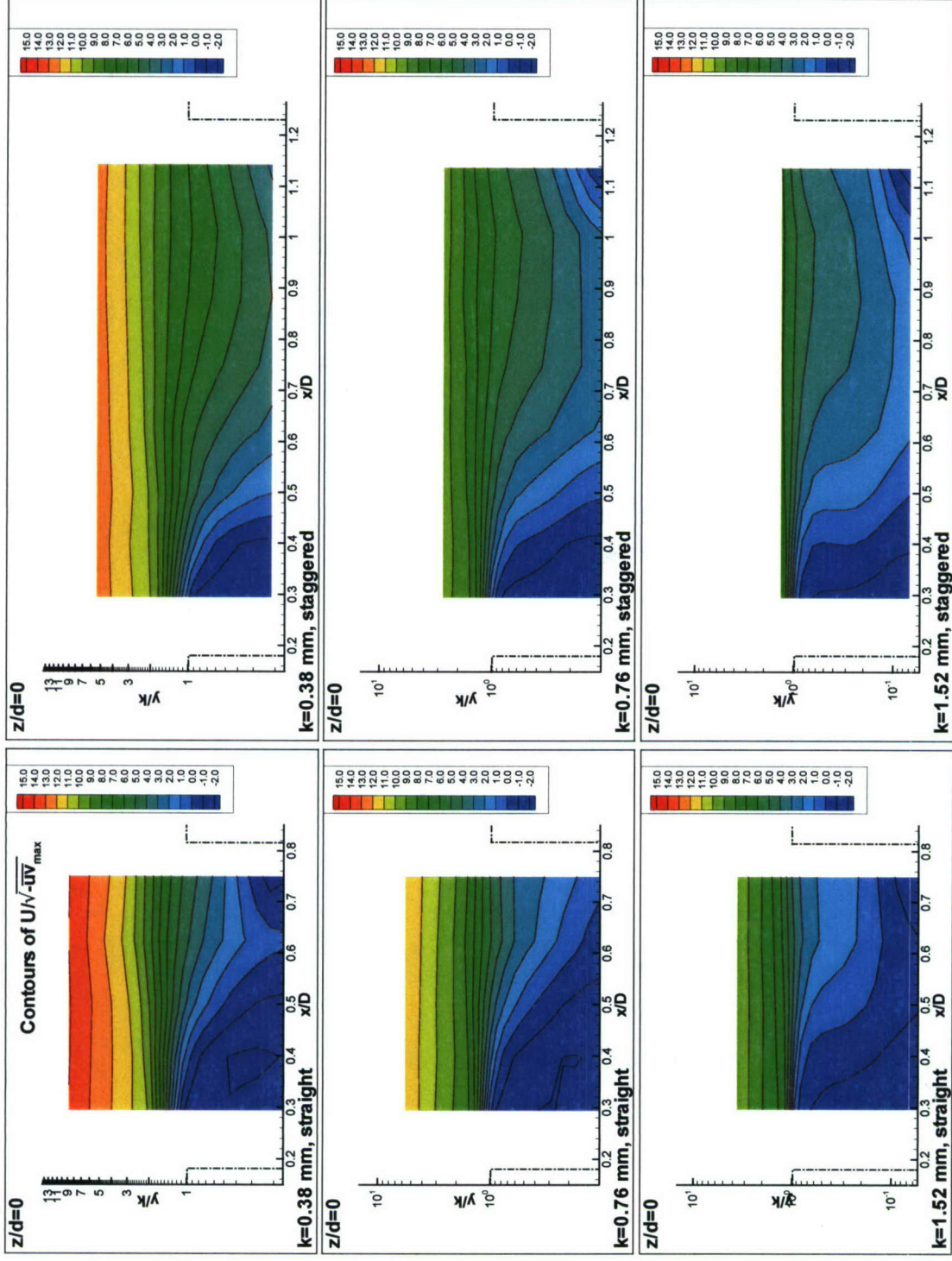


Figure 4.2. Semi-log contours of  $U/\sqrt{-uv_{\max}}$  in the  $y/k - x/D$  plane along center line ( $z/d = 0$ ) [ $k = 0.38 \text{ mm}$  (top row),  $k = 0.76 \text{ mm}$  (middle),  $k = 1.52 \text{ mm}$  (bottom)].

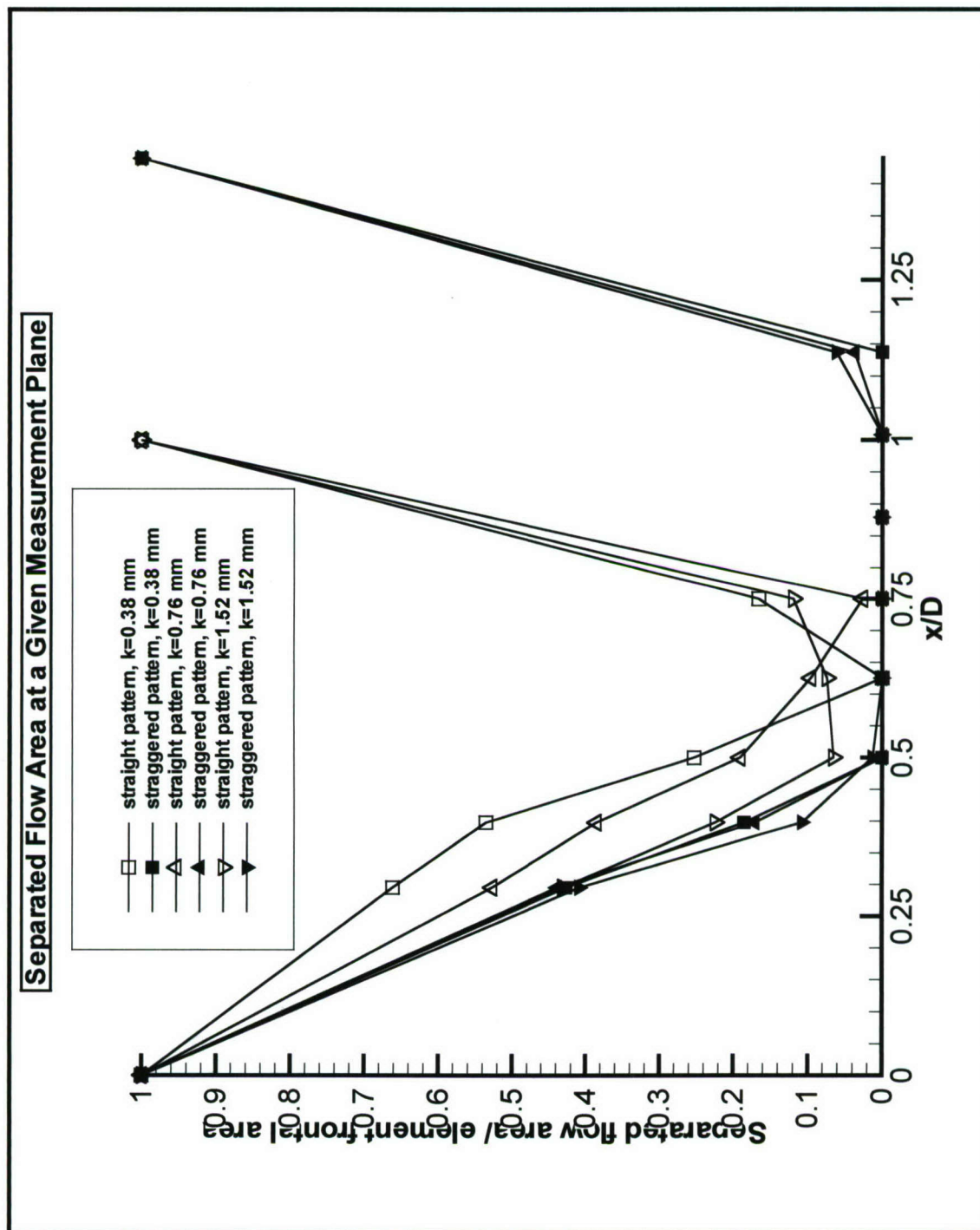


Figure 4.3. Variation of the ratio,  $A_{sep}/A$ , with streamwise distance,  $x/D$ . Values denoting 1 are due to the element itself by virtue of its location.



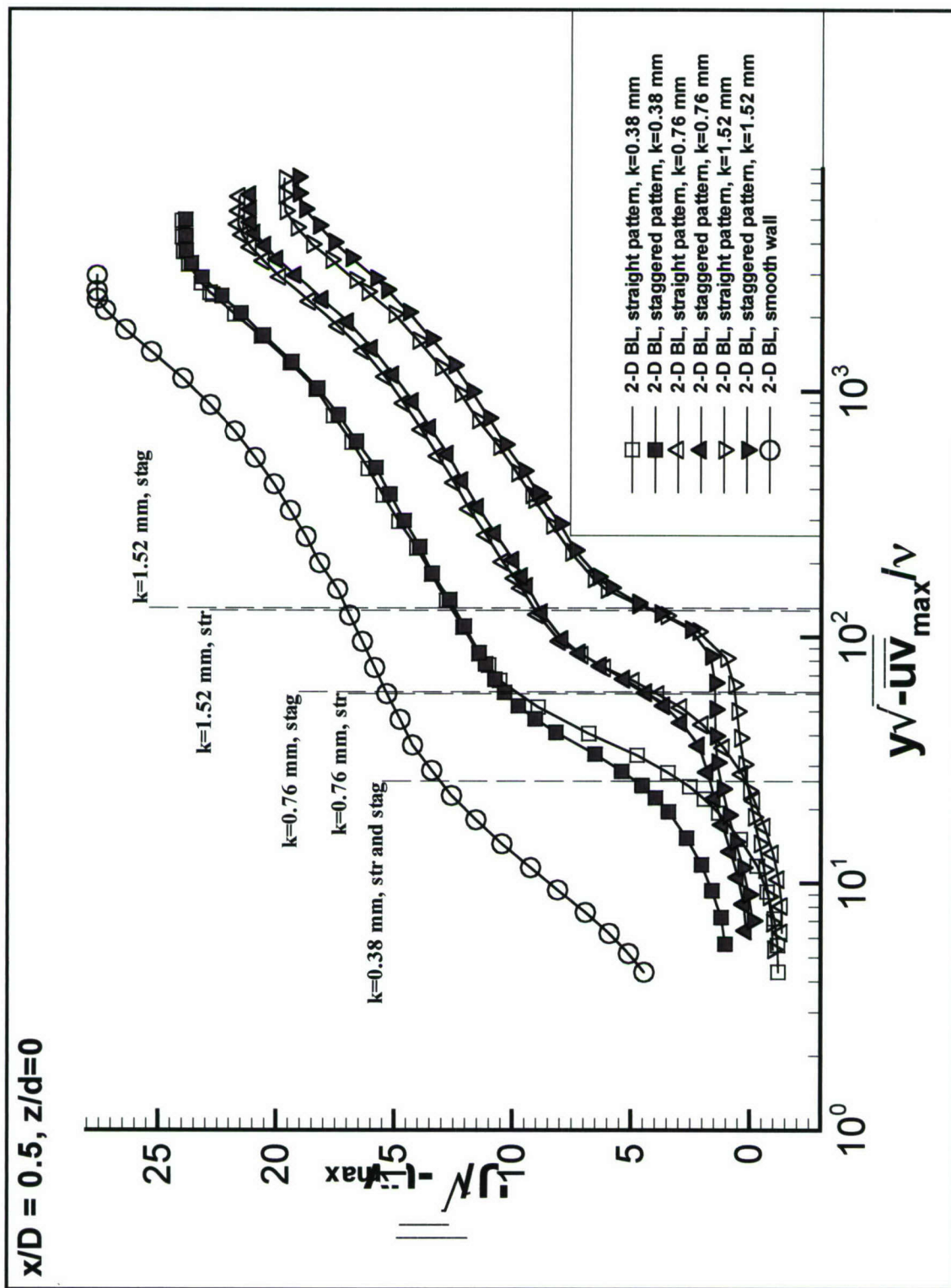


Figure 4.4.  $U/\sqrt{-u'u'}_{\max}/\nu$  versus  $y\sqrt{-u'u'}_{\max}/\nu$ , streamwise mean velocity profile at  $x/D=0.5, z/d=0$ .

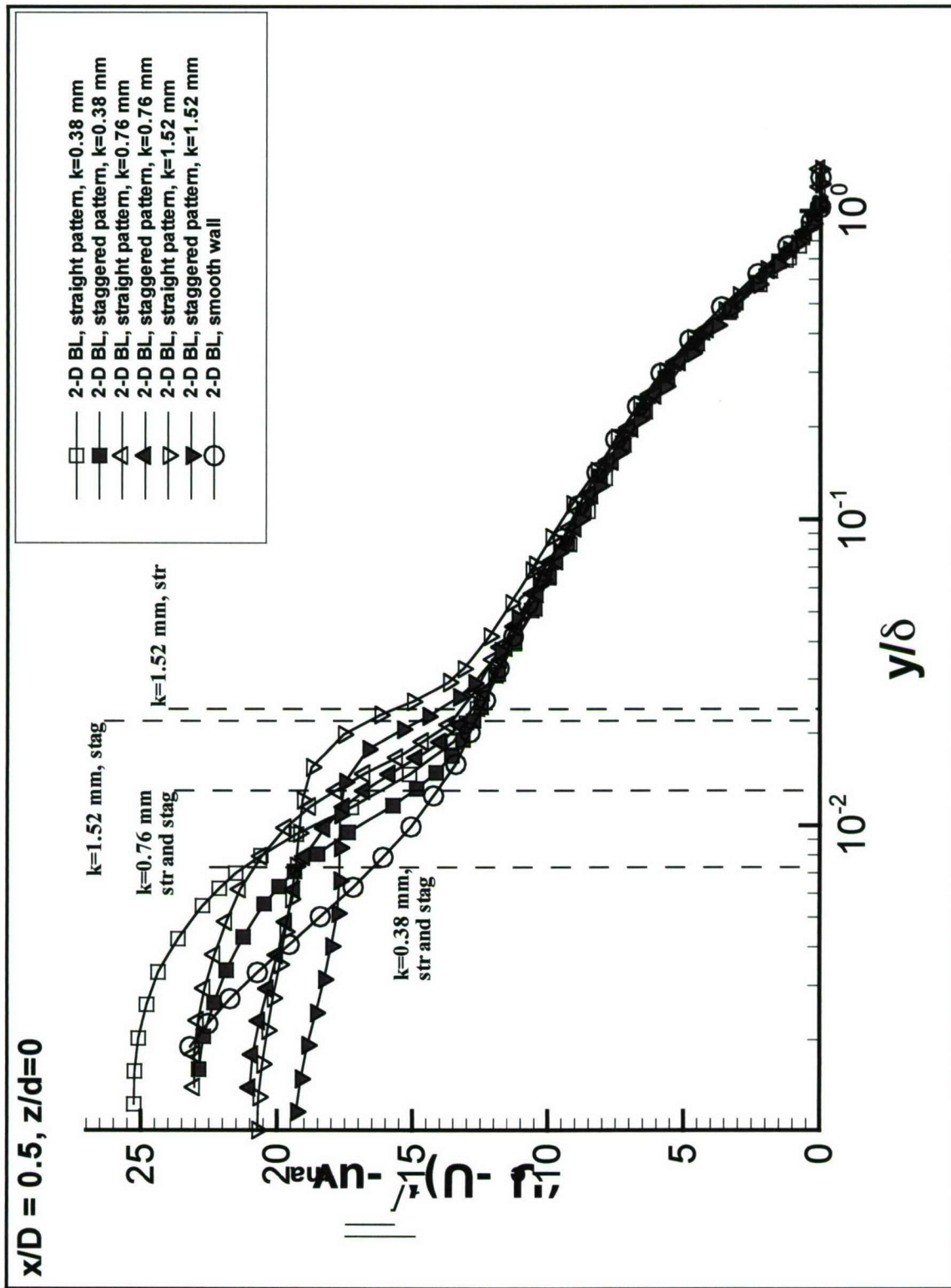


Figure 4.5. Velocity defect profiles,  $(U_e - U) / \sqrt{-u'_{\max}}$  versus  $y/d$ , at  $x/D=0.5, z/d=0$ .



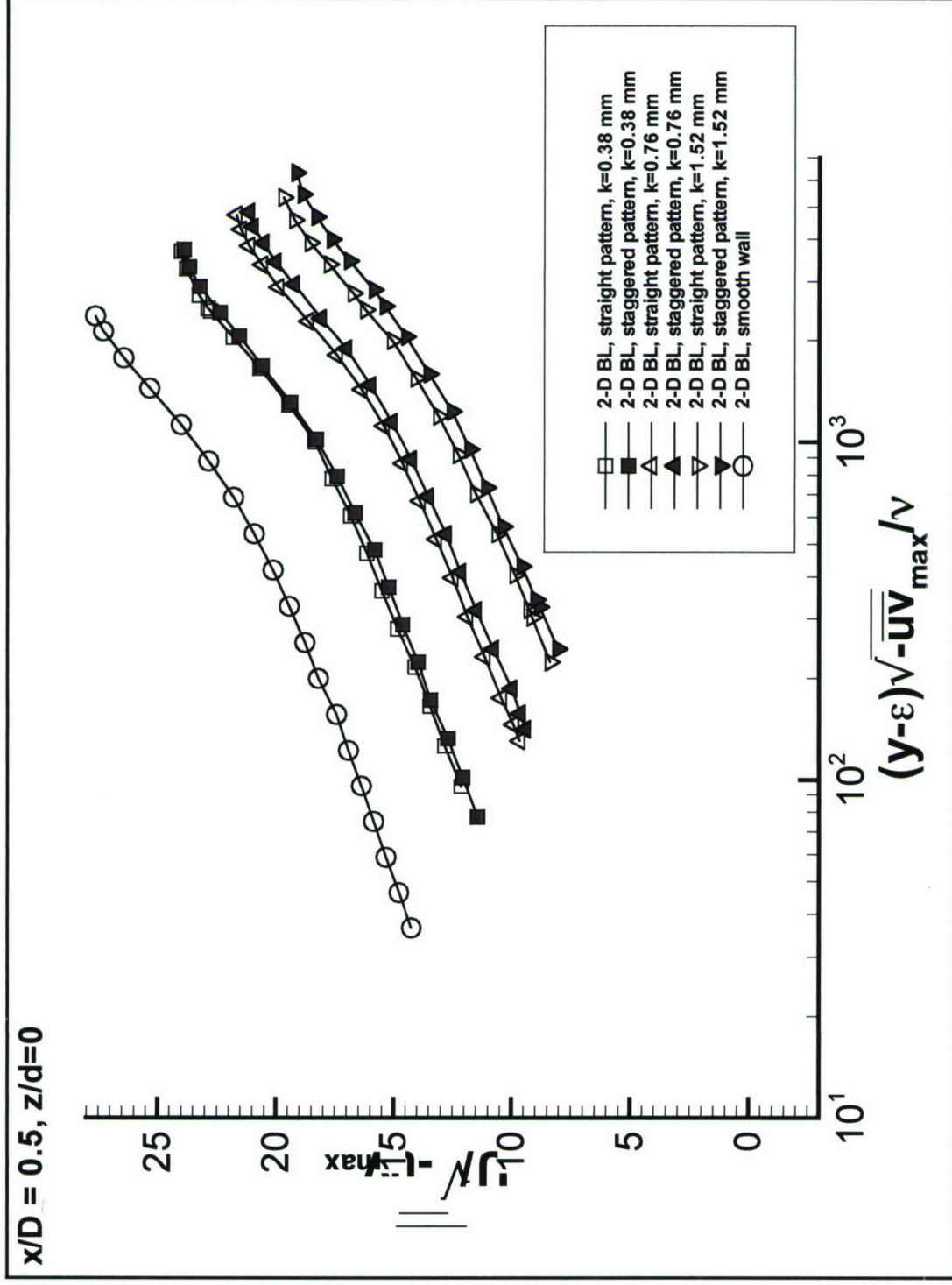


Figure 4.6.  $U/\sqrt{-uv_{\max}}$  versus  $(y-\epsilon)\sqrt{-u_{\max}v_{\max}}/\nu$ , streamwise mean velocity profile at  $x/D=0.5$ ,  $z/d=0$ . Corrected for displacement of origin and excludes locations in the viscous sublayer and buffer layer.

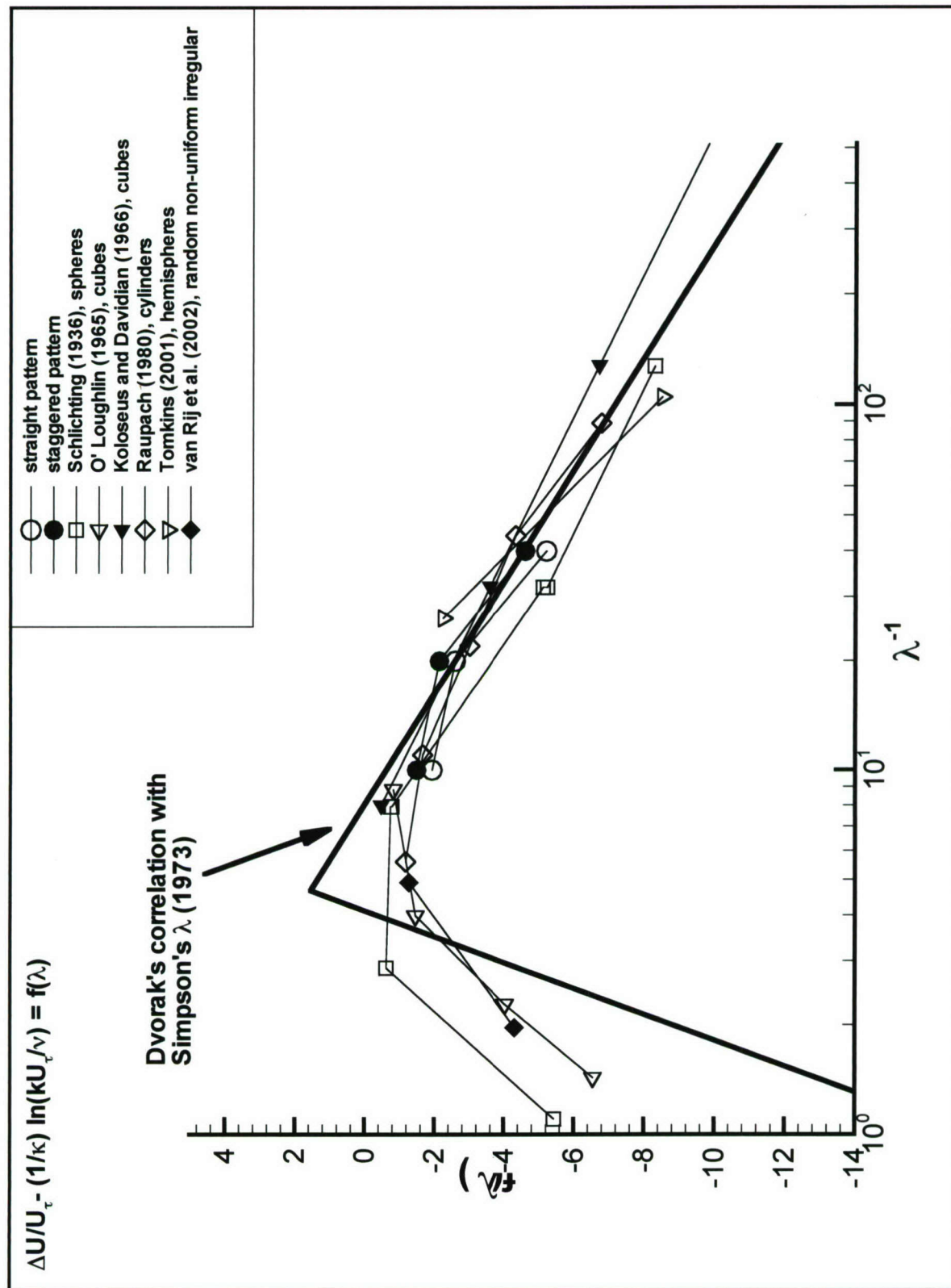


Figure 4.7 (a). Effects of roughness density,  $\lambda$ , on law of the wall intercept,  $f(\lambda)$ .



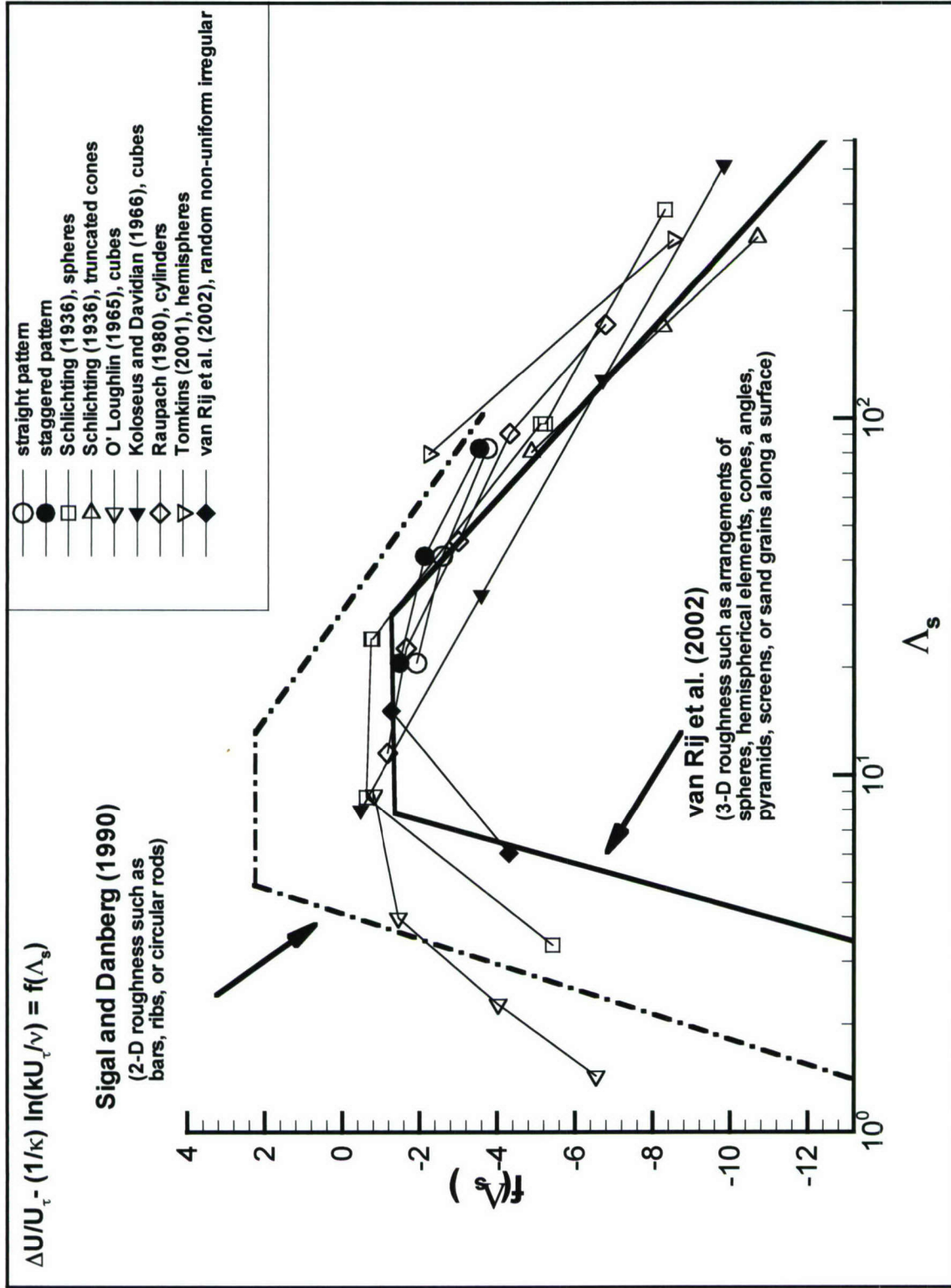


Figure 4.7 (b). Effects of roughness density,  $\Lambda_s$ , on law of the wall intercept,  $f(\Lambda_s)$ .

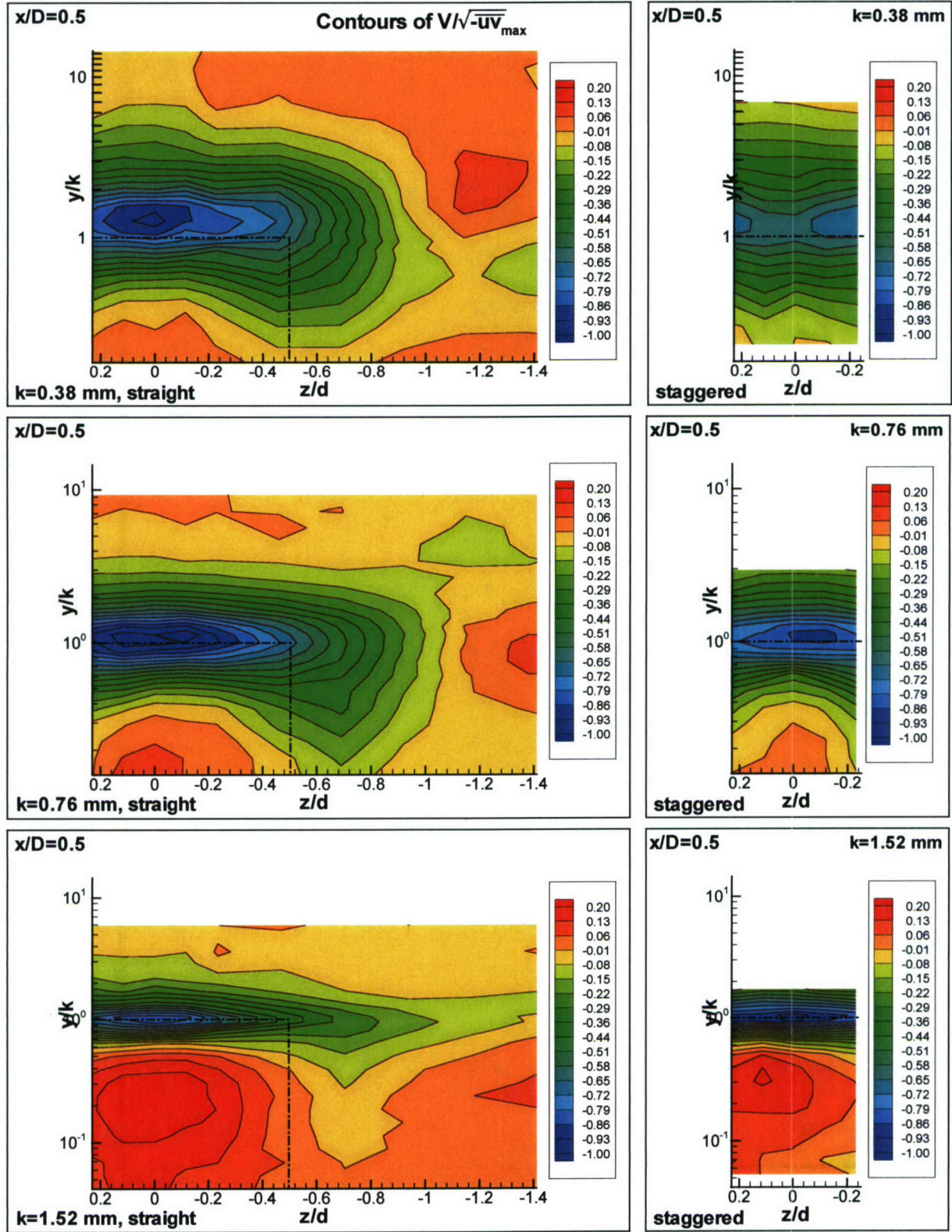


Figure 4.8 (a). Semi-log contours of  $V/\sqrt{-uv_{\max}}$  in the  $y/k - z/d$  plane at  $x/D = 0.5$  [ $k = 0.38$  mm (top row),  $k = 0.76$  mm (middle),  $k = 1.52$  mm (bottom)].



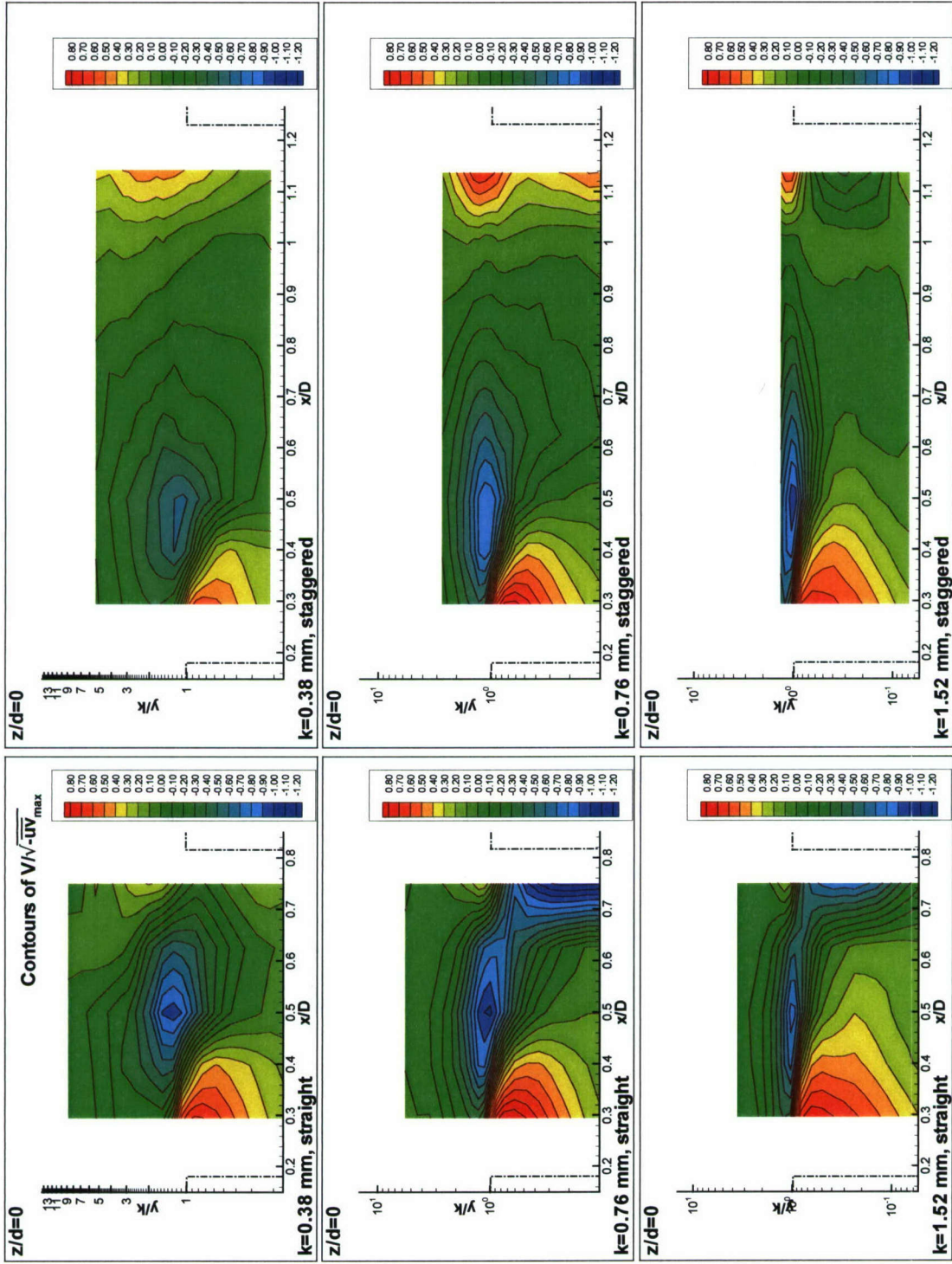


Figure 4.8 (b). Semi-log contours of  $V/\sqrt{-u'v'}_{\max}$  in the  $y/k - x/D$  plane along center line ( $z/d = 0$ ) [ $k = 0.38$  mm (top row),  $k = 0.76$  mm (middle),  $k = 1.52$  mm (bottom)].

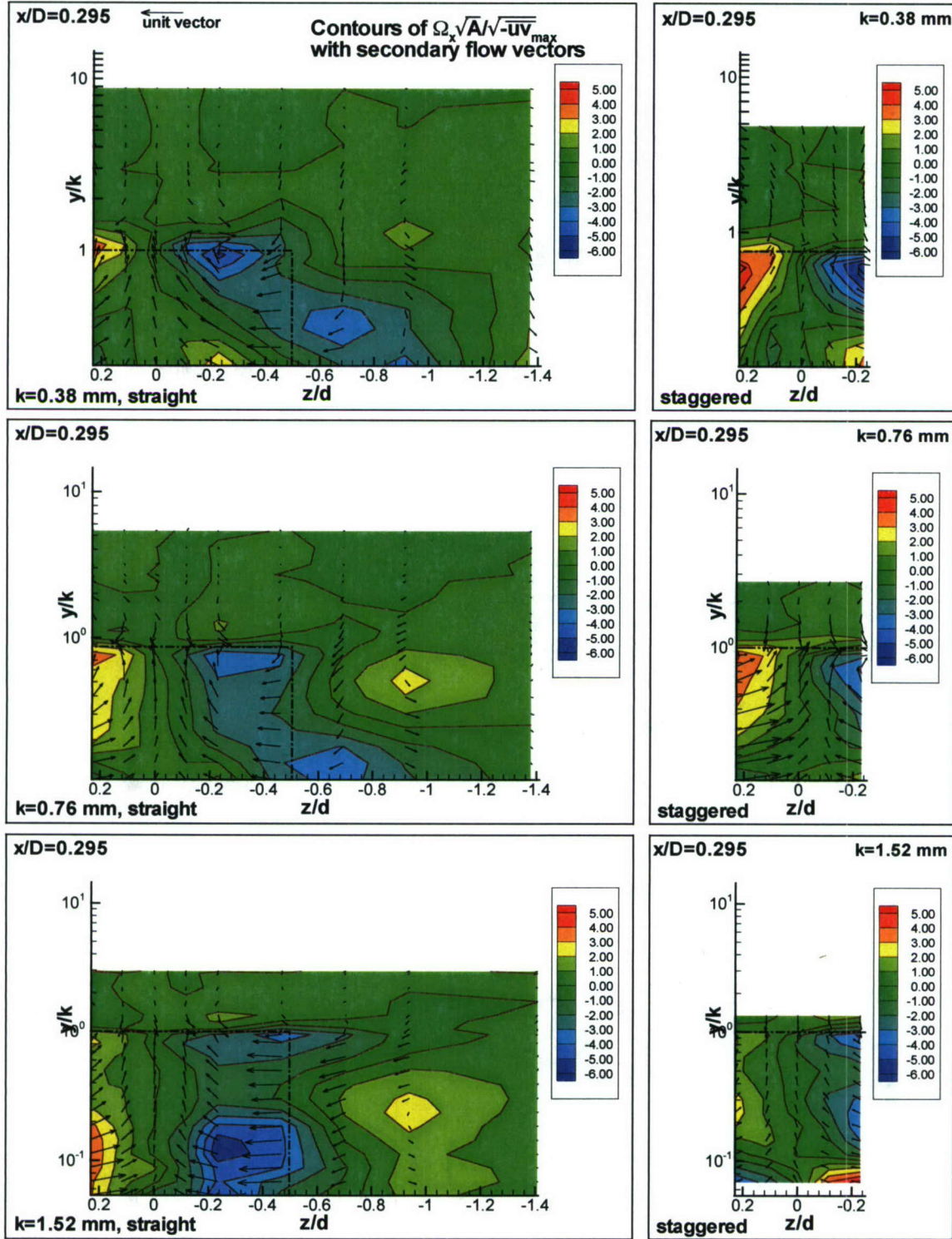


Figure 4.9 (a). Semi-log contours of streamwise vorticity,  $\Omega_x \sqrt{A} / \sqrt{-\overline{uv}_{\max}}$ , with secondary velocity vectors,  $V / \sqrt{-\overline{uv}_{\max}}$  and  $W / \sqrt{-\overline{uv}_{\max}}$  in the  $y/k - z/d$  plane at  $x/D = 0.295$  [ $k = 0.38$  mm (top row),  $k = 0.76$  mm (middle),  $k = 1.52$  mm (bottom)].



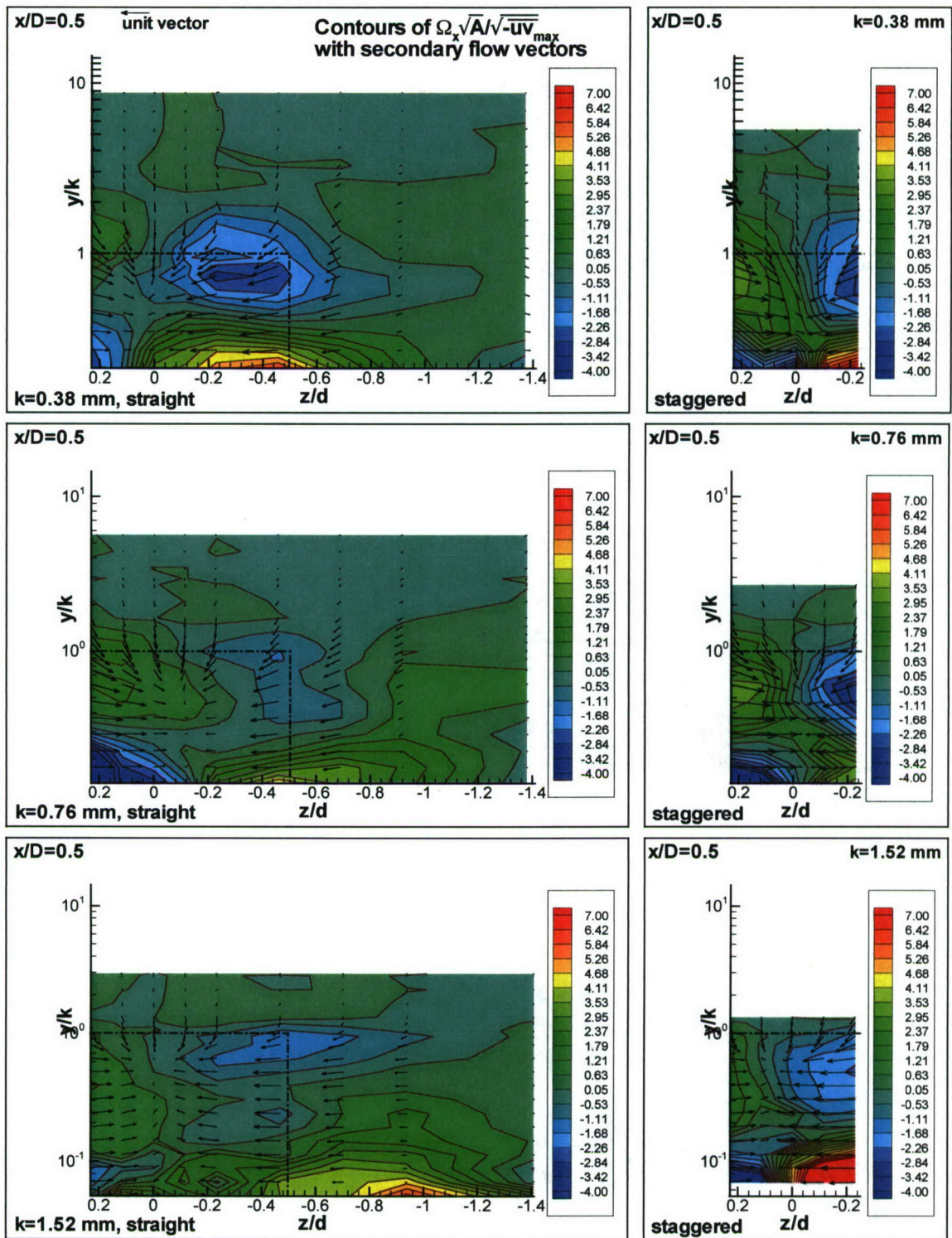


Figure 4.9 (b). Semi-log contours of streamwise vorticity,  $\Omega_x \sqrt{A} / \sqrt{-uv_{\max}}$ , with secondary velocity vectors,  $V / \sqrt{-uv_{\max}}$  and  $W / \sqrt{-uv_{\max}}$  in the  $y/k - z/d$  plane at  $x/D = 0.5$  [ $k = 0.38\text{mm}$  (top row),  $k = 0.76\text{mm}$  (middle),  $k = 1.52\text{mm}$  (bottom)].

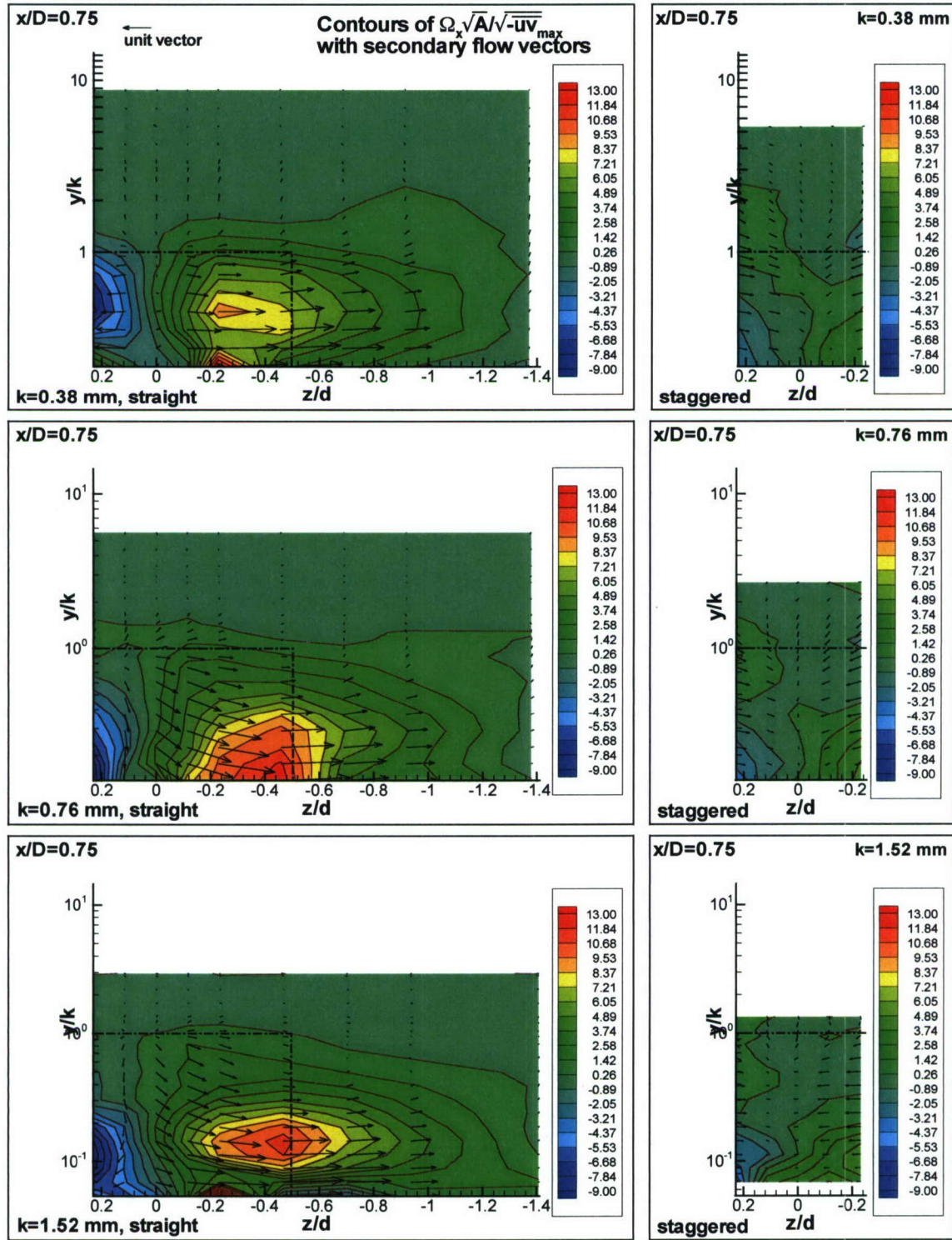


Figure 4.9 (c). Semi-log contours of streamwise vorticity,  $\Omega_x \sqrt{A} / \sqrt{-uv_{\max}}$ , with secondary velocity vectors,  $V / \sqrt{-uv_{\max}}$  and  $W / \sqrt{-uv_{\max}}$  in the  $y/k - z/d$  plane at  $x/D = 0.75$  [ $k = 0.38$  mm (top row),  $k = 0.76$  mm (middle),  $k = 1.52$  mm (bottom)].



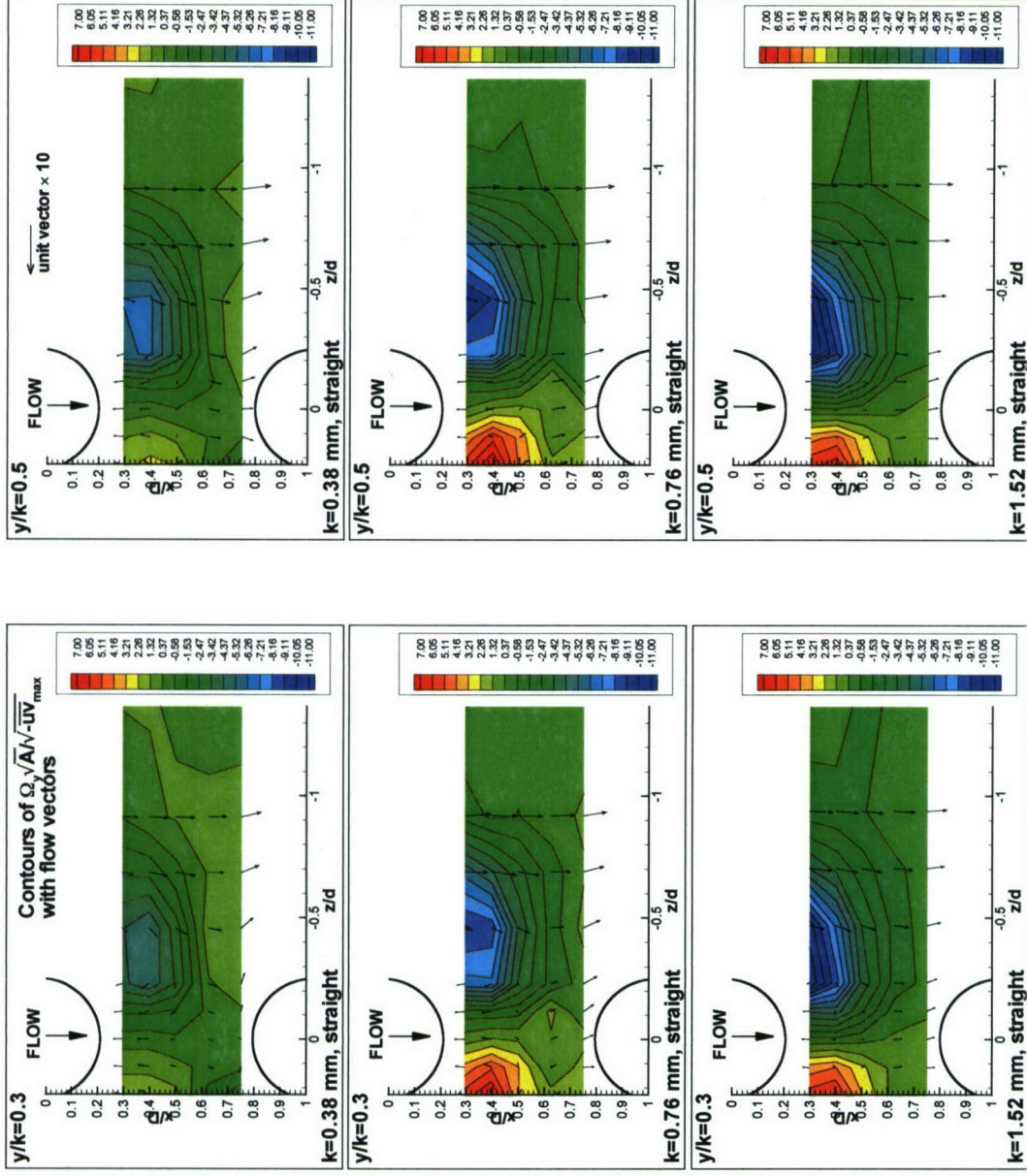


Figure 4.10 (a). Semi-log contours of wall-normal vorticity,  $\Omega_y \sqrt{A/\sqrt{uv}}_{\max}$ , with velocity vectors,  $U/\sqrt{-uv}_{\max}$  and  $W/\sqrt{-uv}_{\max}$  in the  $x/D - z/d$  plane at  $y/k = 0.3$  (left) and  $y/k = 0.5$  (right), [ $k = 0.38$  mm (top row),  $k = 0.76$  mm (middle),  $k = 1.52$  mm (bottom)], straight orientations only.

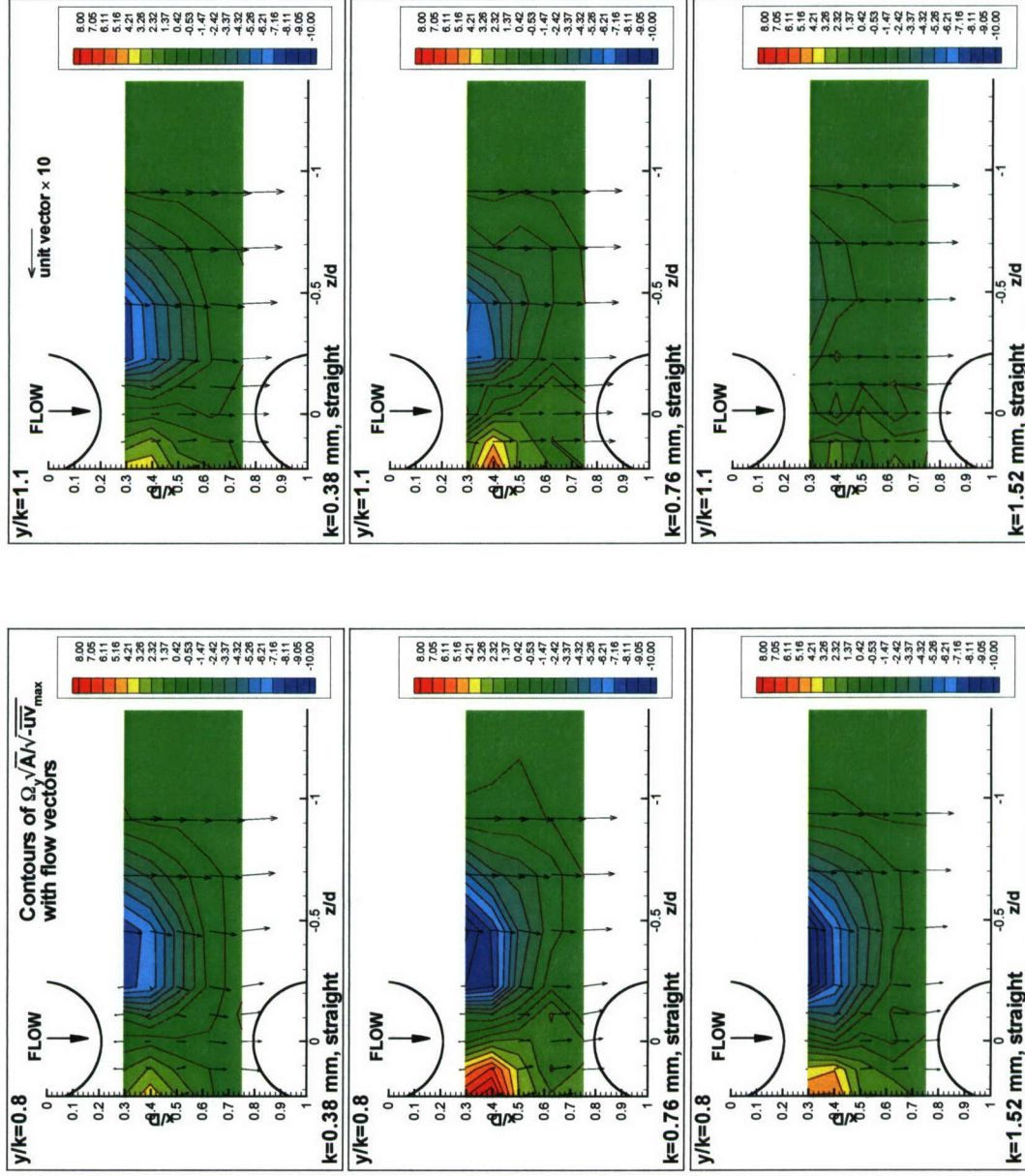


Figure 4.10 (b). Semi-log contours of wall-normal vorticity,  $\Omega_y \sqrt{A} / \sqrt{-\overline{uv}}$ , with velocity vectors,  $U/\sqrt{-\overline{uv}}_{\max}$  and  $W/\sqrt{-\overline{uv}}_{\max}$  in the  $x/D - z/d$  plane at  $y/k = 0.8$  (left) and  $y/k = 1.1$  (right), [ $k = 0.38$  mm (top row),  $k = 0.76$  mm (middle),  $k = 1.52$  mm (bottom)], straight orientations only.



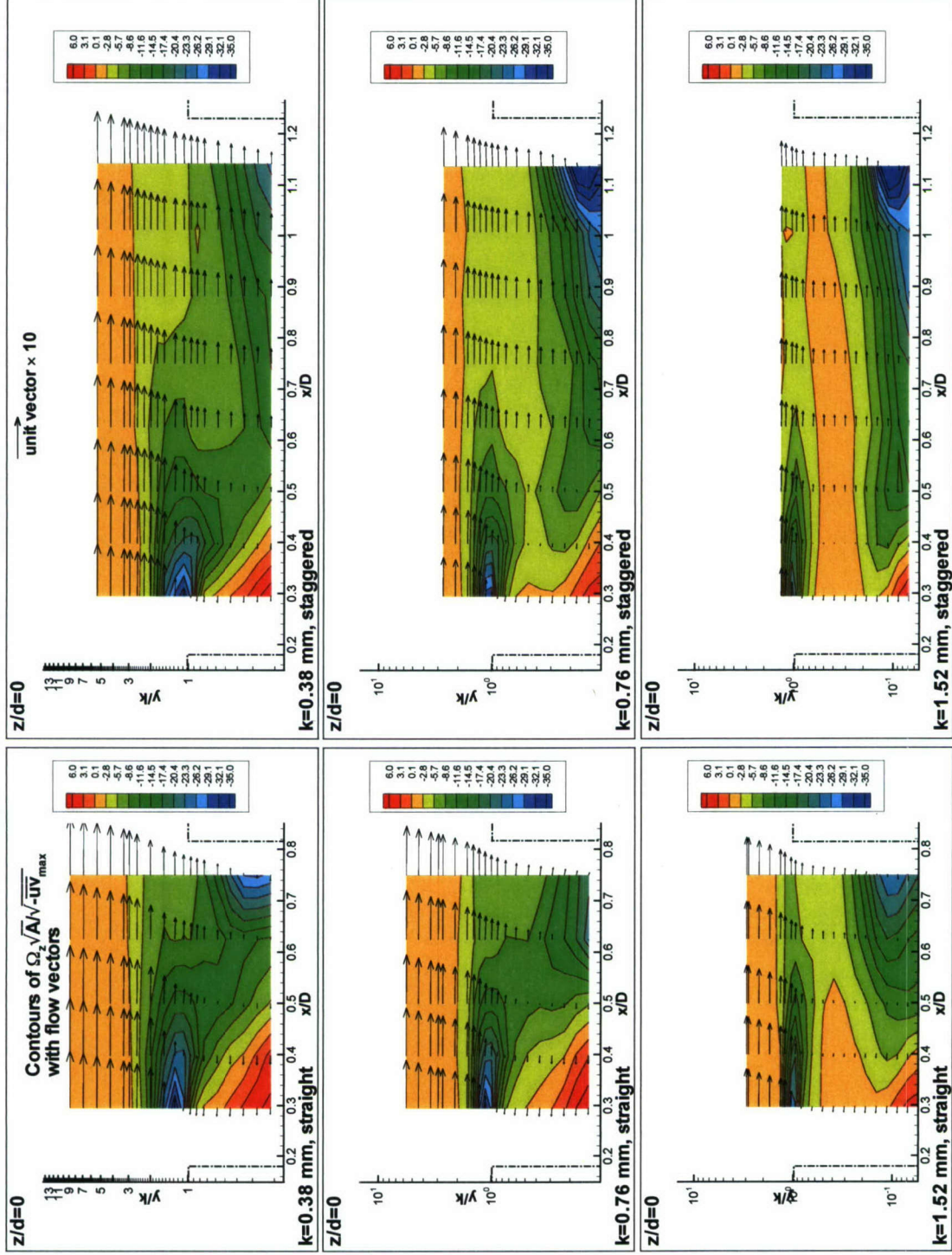


Figure 4.11. Semi-log contours of spanwise vorticity,  $\Omega_z \sqrt{A}/\sqrt{-uv_{\max}}$ , with velocity vectors,  $U/\sqrt{-uv_{\max}}$  and  $V/\sqrt{-uv_{\max}}$  in the  $y/k - x/D$  plane along center line ( $z/d = 0$ ) [ $k = 0.38\text{mm}$  (top row),  $k = 0.76\text{mm}$  (middle),  $k = 1.52\text{mm}$  (bottom)].

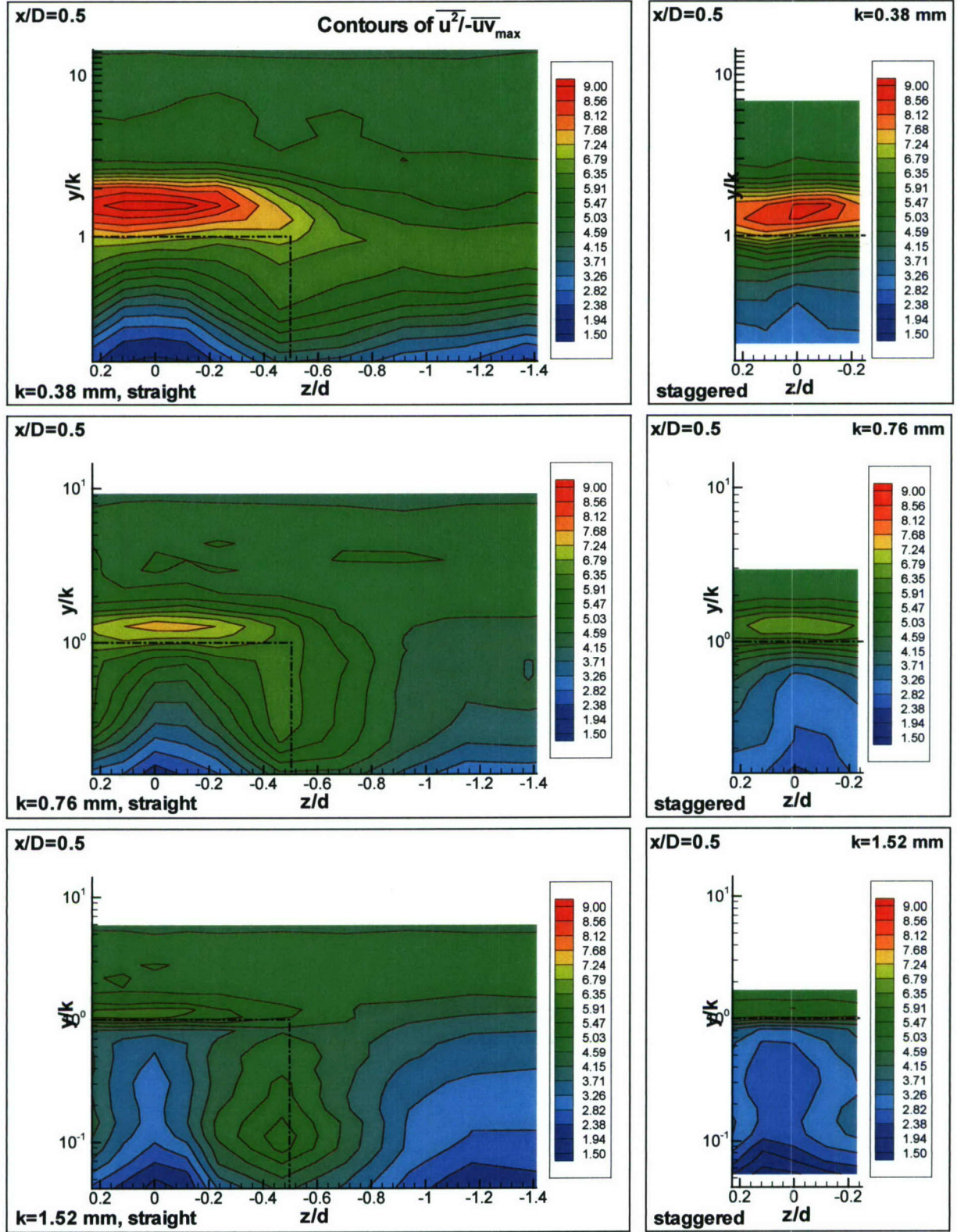


Figure 4.12 (a). Semi-log contours of  $\overline{u^2}/\overline{uv}_{\max}$  in the  $y/k - z/d$  plane at  $x/D = 0.5$



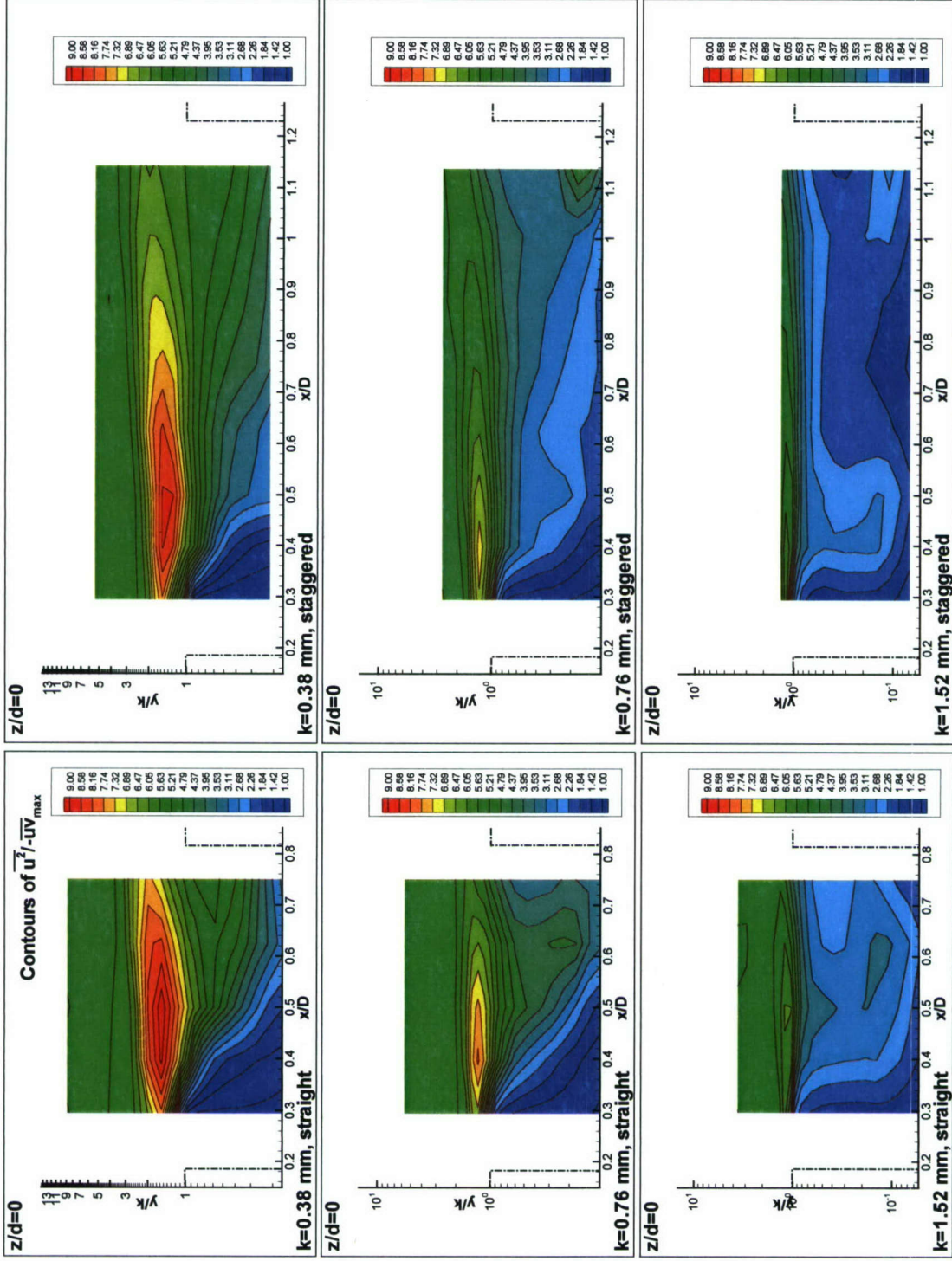


Figure 4.12 (b). Semi-log contours of  $\overline{u^2} / -\overline{u v}_{\max}$  in the  $y/k - x/D$  plane along the centerline.

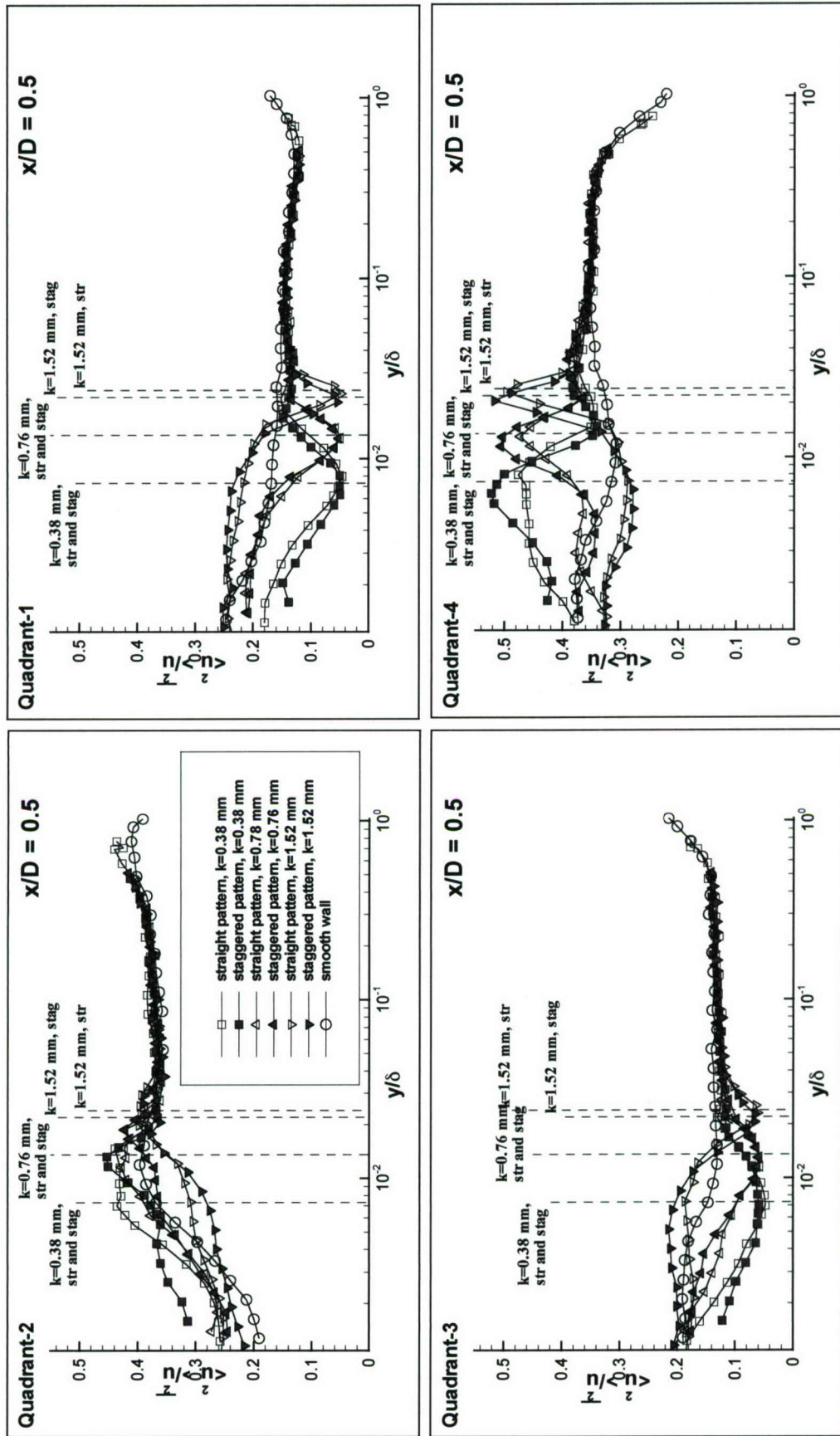


Figure 4.13 (a). Quadrant fraction to the Reynolds normal stress,  $\overline{u^2}$ , along the centerline, varying with  $y/\delta$ , at  $x/D=0.5$ .



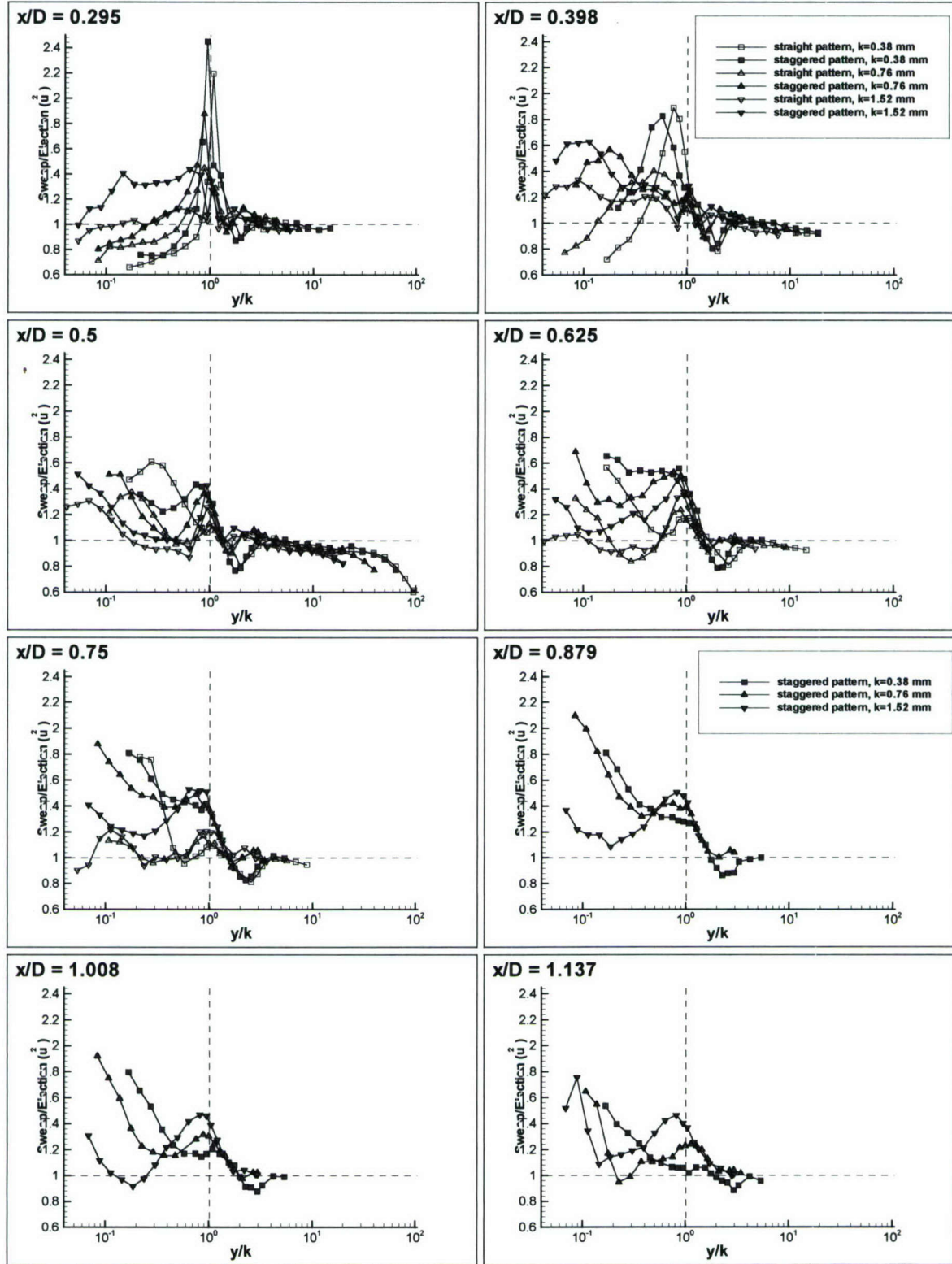


Figure 4.13 (b). Ratio of sweeps to ejections from quadrant contribution to the Reynolds normal stress,  $\overline{u^2}$ , along the centerline, varying with  $y/k$ , at various streamwise locations,  $x/D$ .

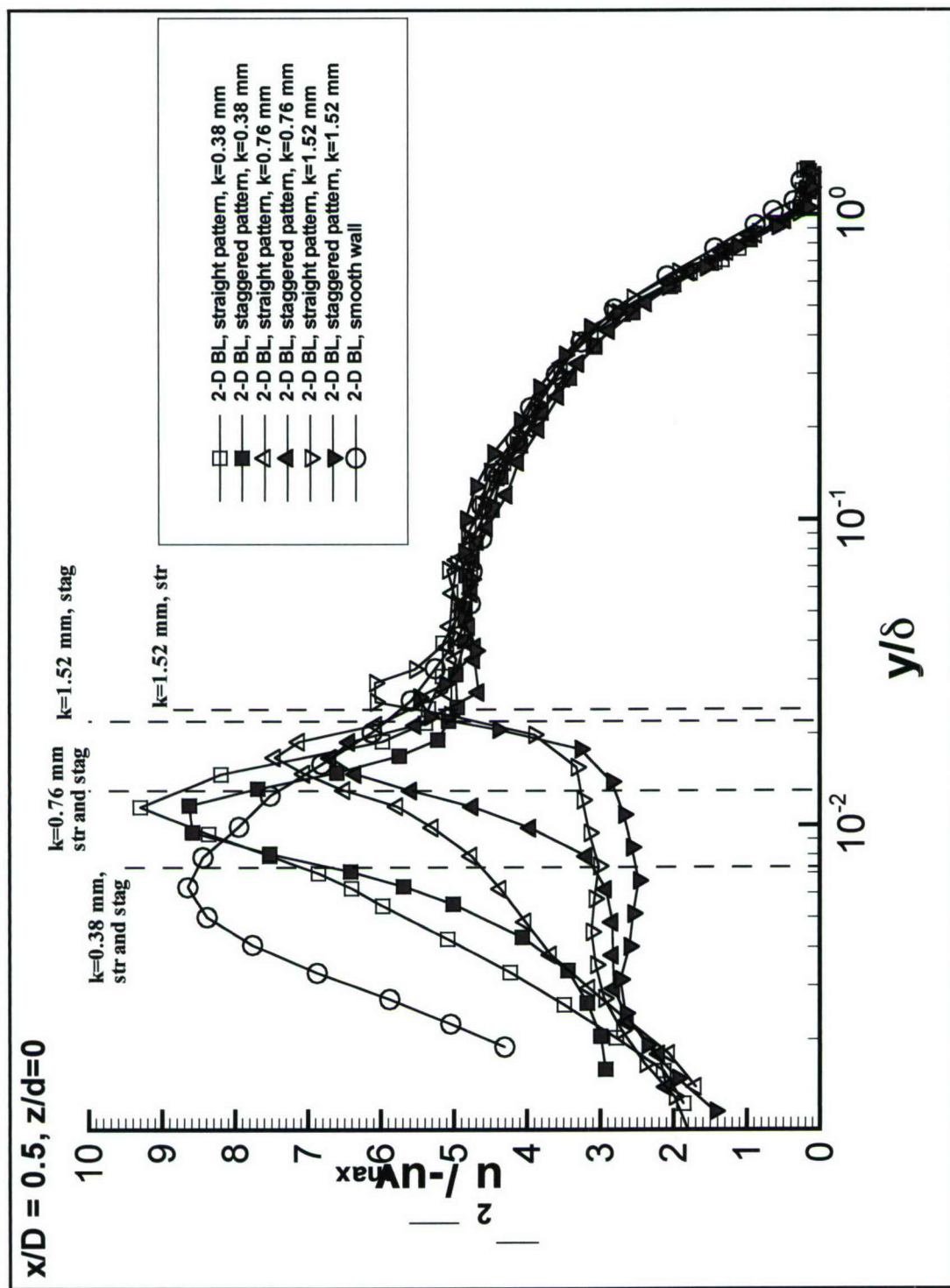


Figure 4.14. Variation of the streamwise Reynolds normal stresses,  $\overline{u^2} / \overline{-uv_{\max}}$ , with  $y/d$  at  $x/D = 0.5$ ,  $z = 0$ .



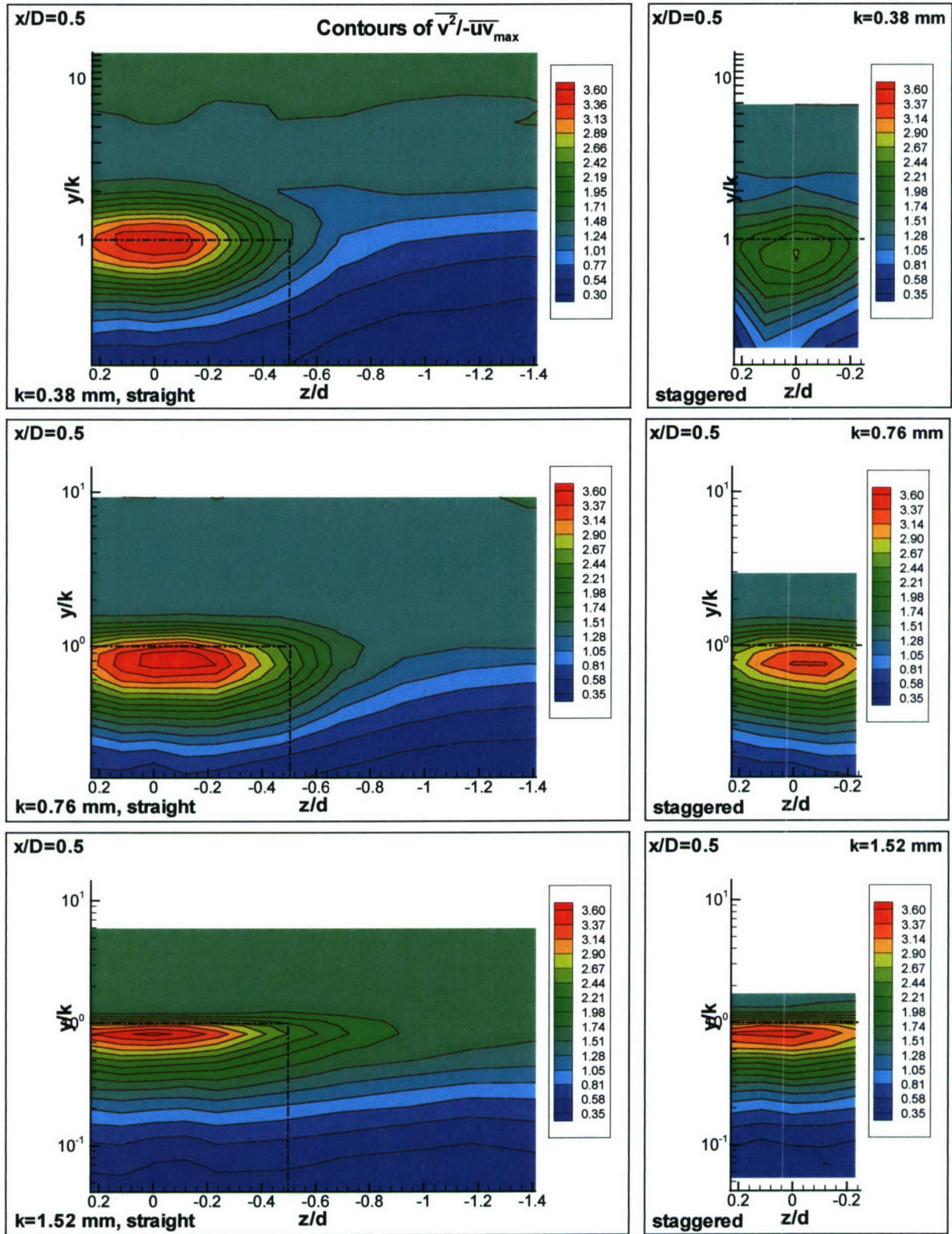


Figure 4.15 (a). Semi-log contours of  $\overline{v^2} / -\overline{u v}_{\max}$  in the  $y/k - z/d$  plane at  $x/D = 0.5$

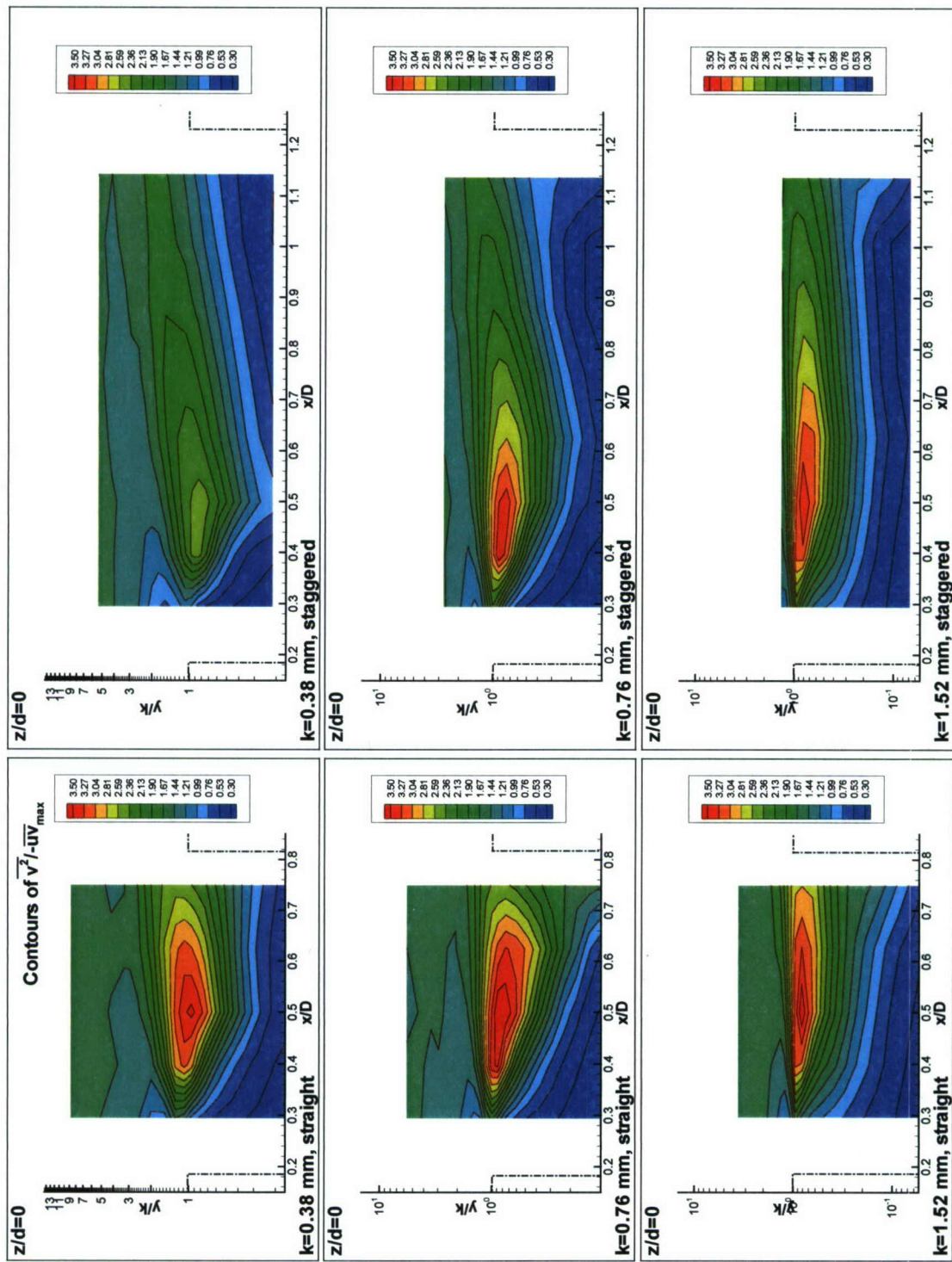


Figure 4.15 (b). Semi-log contours of  $\overline{v^2} / -\overline{uv}_{\max}$  in the  $y/k - x/D$  plane along the centerline.



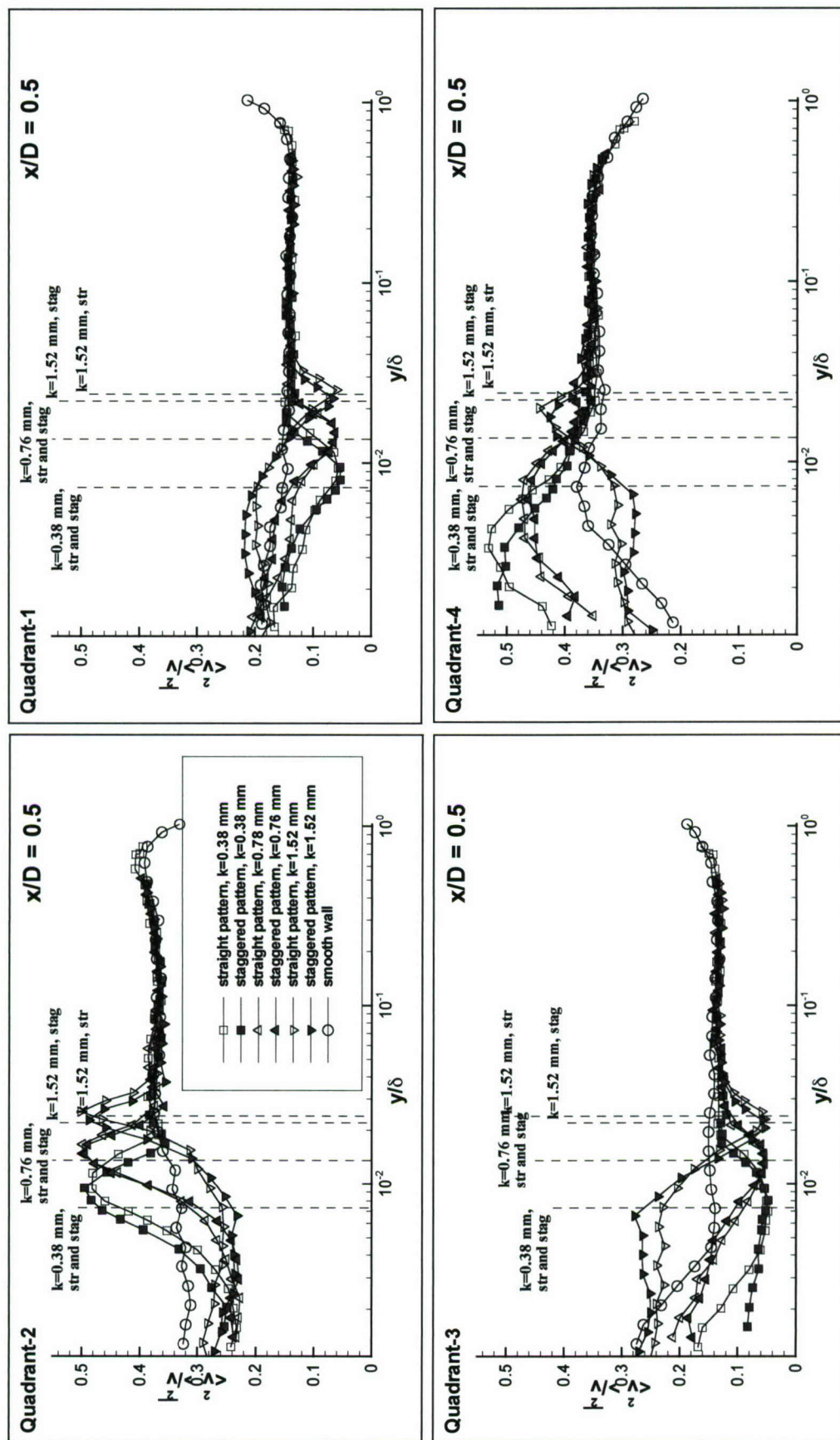


Figure 4.16 (a). Quadrant fraction to the Reynolds normal stress,  $\overline{v^2}$ , along the centerline, varying with  $y/\delta$ , at  $x/D=0.5$ .

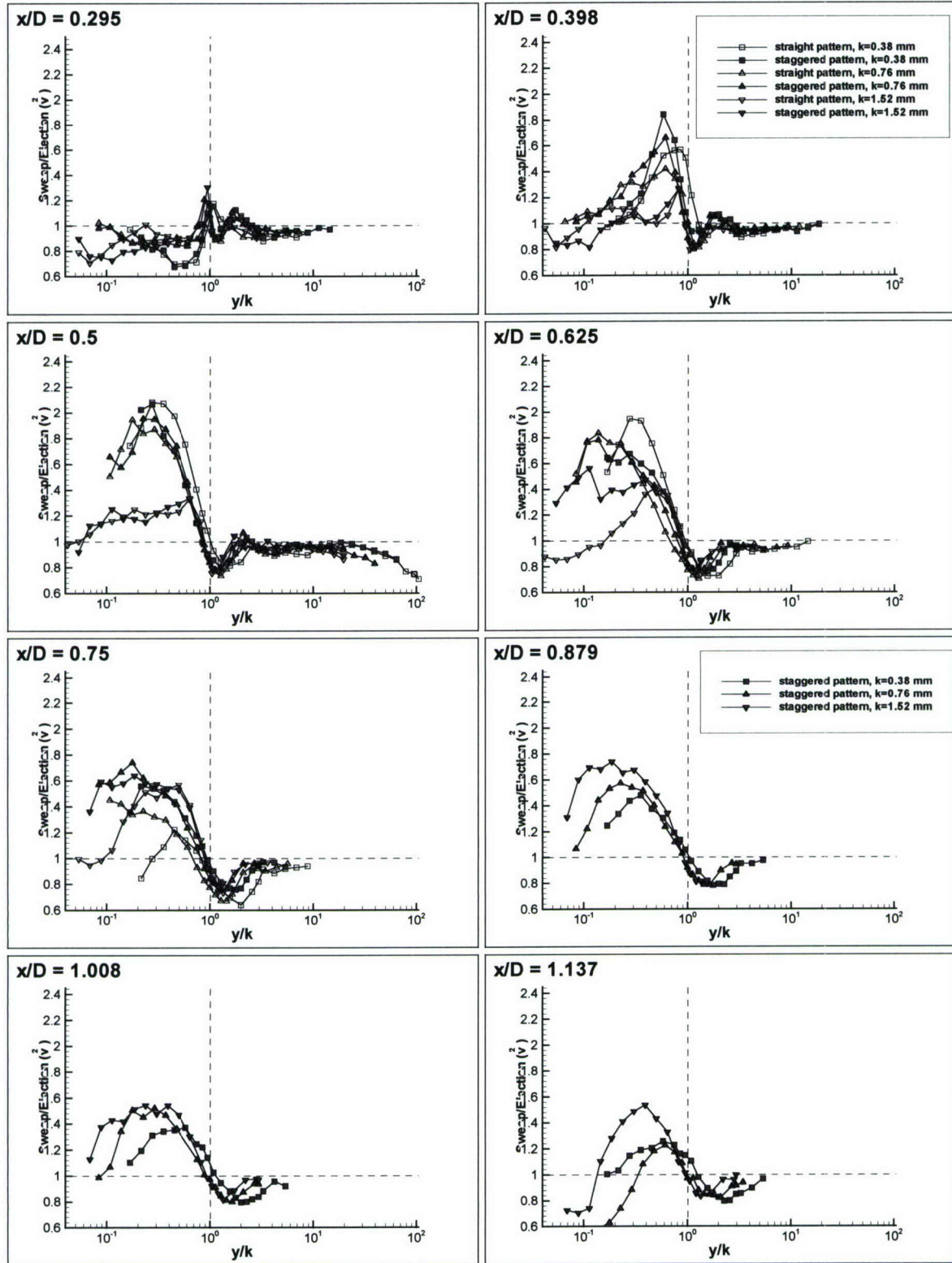


Figure 4.16 (b). Ratio of sweeps to ejections from quadrant contribution to the Reynolds normal stress,  $\overline{v^2}$ , along the centerline, varying with  $y/k$ , at various streamwise locations,  $x/D$ .



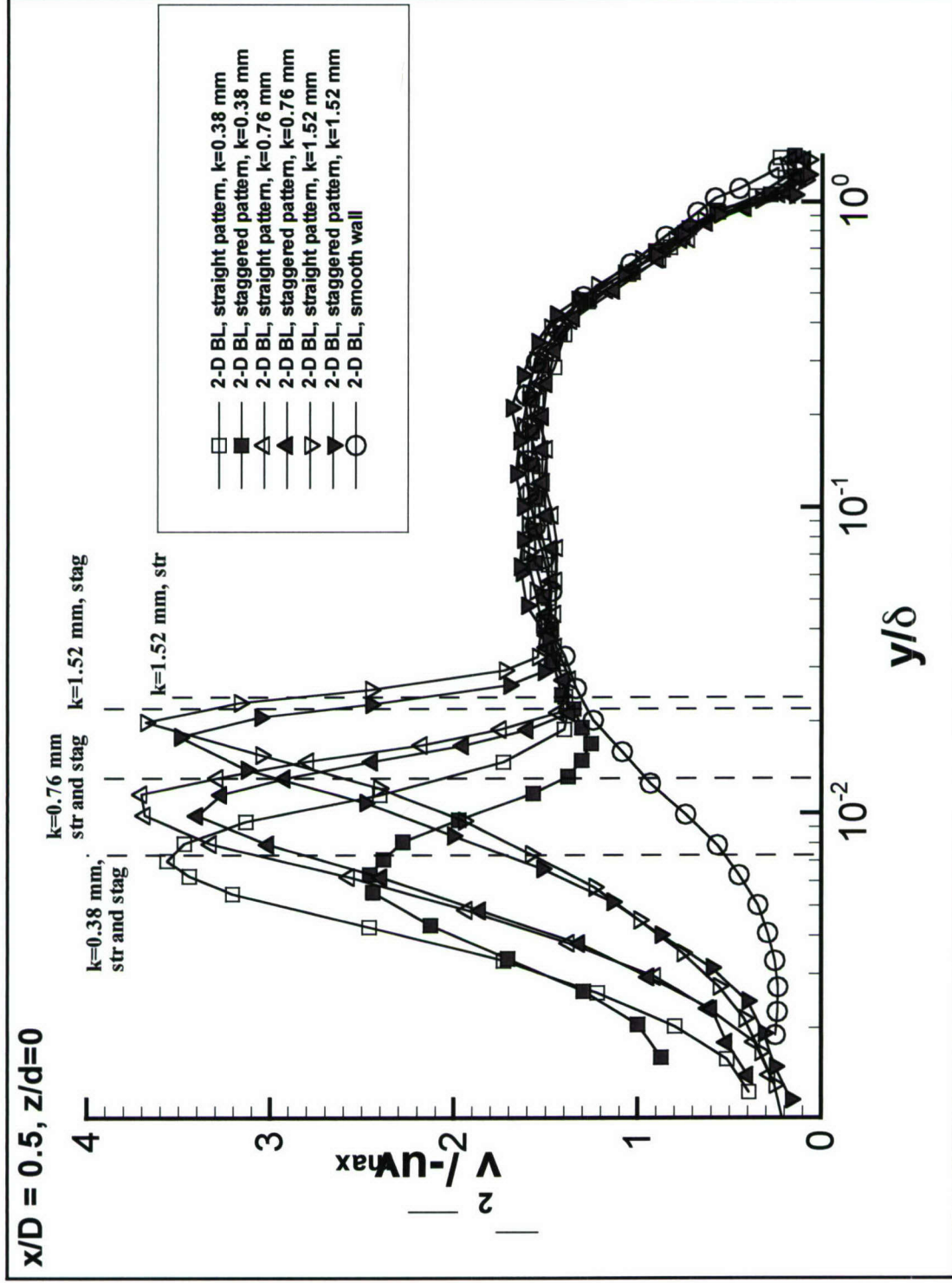


Figure 4.17. Variation of the wall-normal Reynolds normal stresses,  $\overline{v^2} / -\overline{u'v'_{\max}}$ , with  $y/\delta$  at  $x/D = 0.5, z = 0$ .

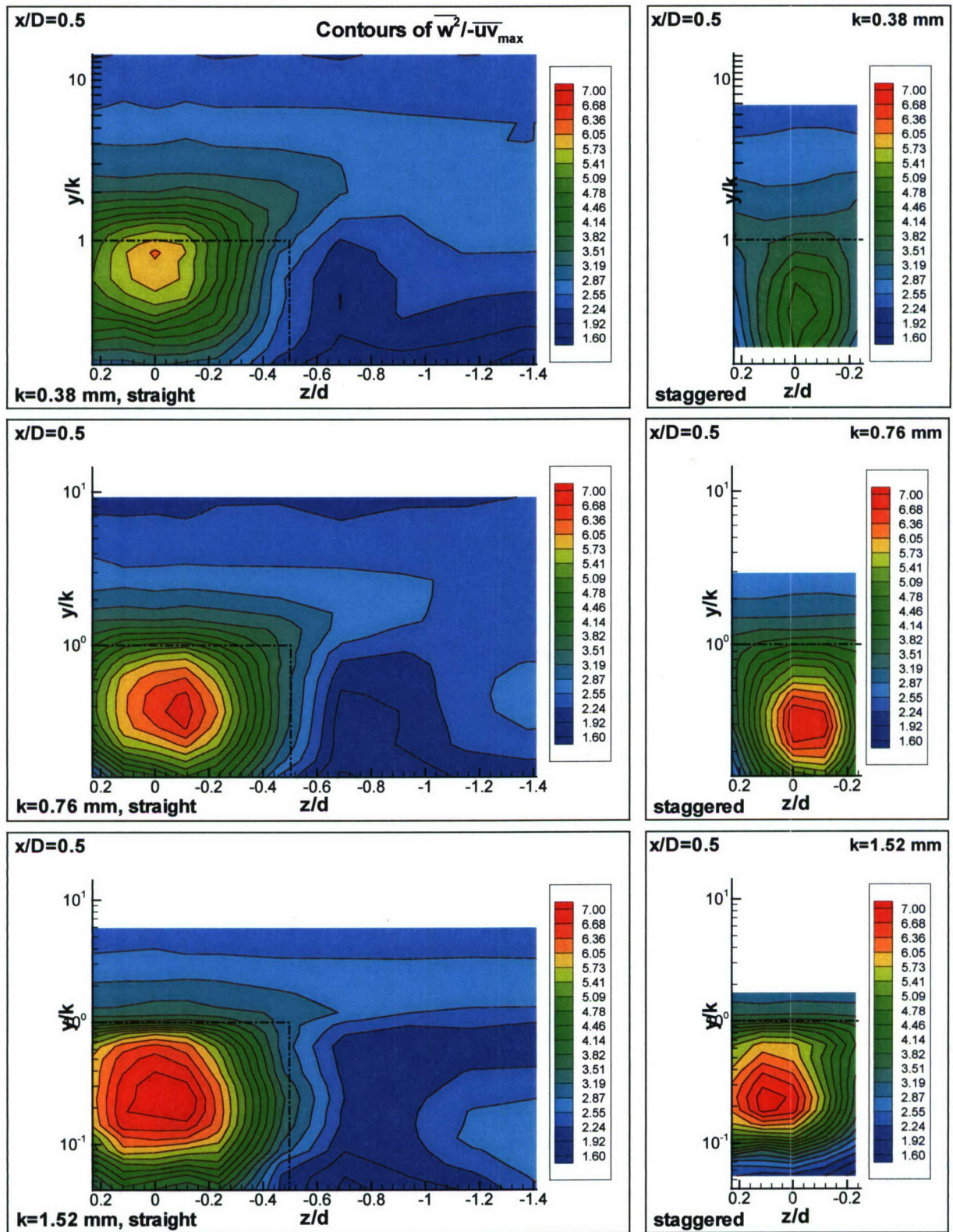


Figure 4.18 (a). Semi-log contours of  $\overline{w^2} / -\overline{uv}_{\max}$  in the  $y/k - z/d$  plane at  $x/D = 0.5$



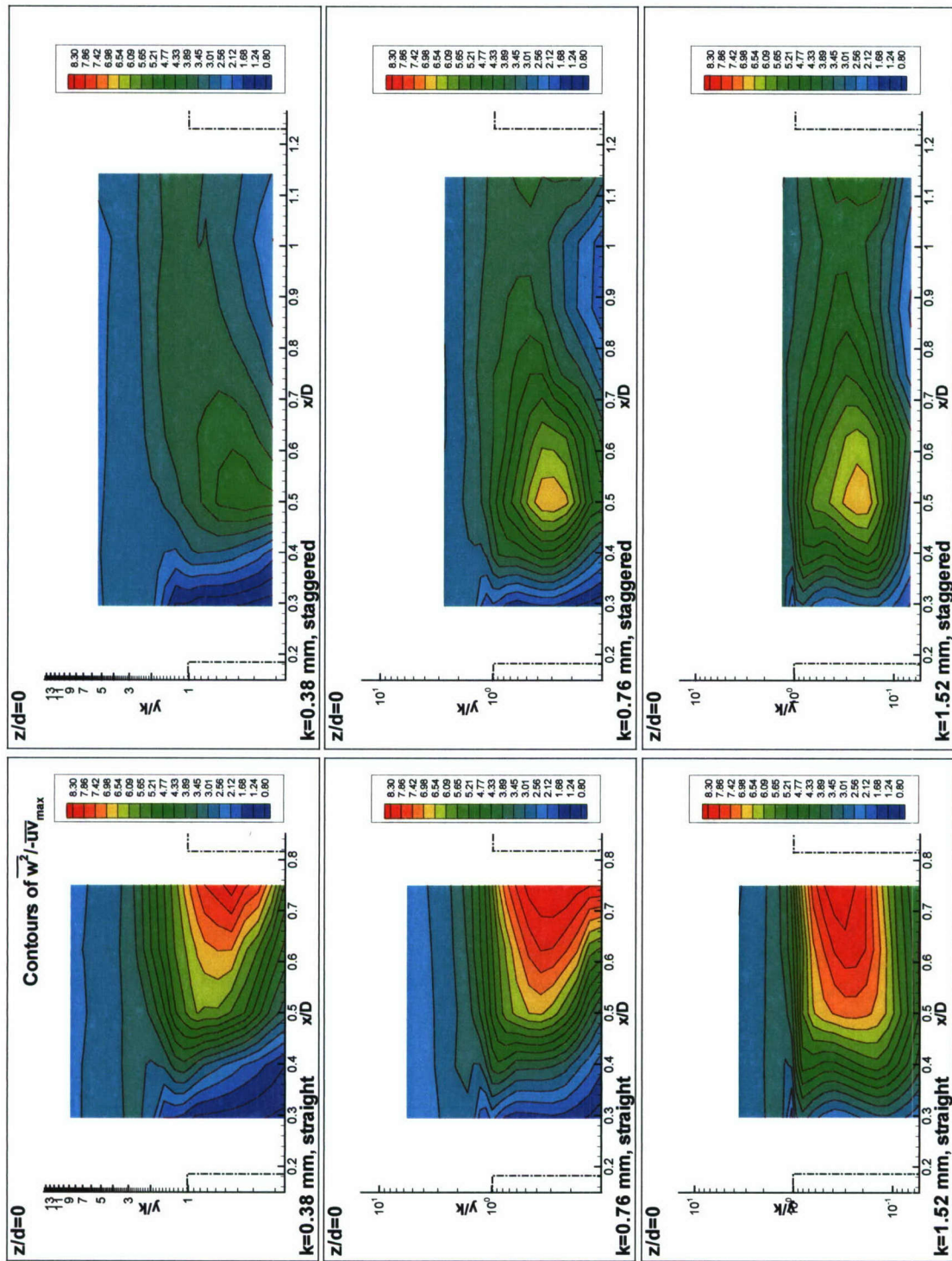


Figure 4.18 (b). Semi-log contours of  $\overline{w^2} / -\overline{uv}_{\max}$  in the  $y/k - x/D$  plane along the centerline.

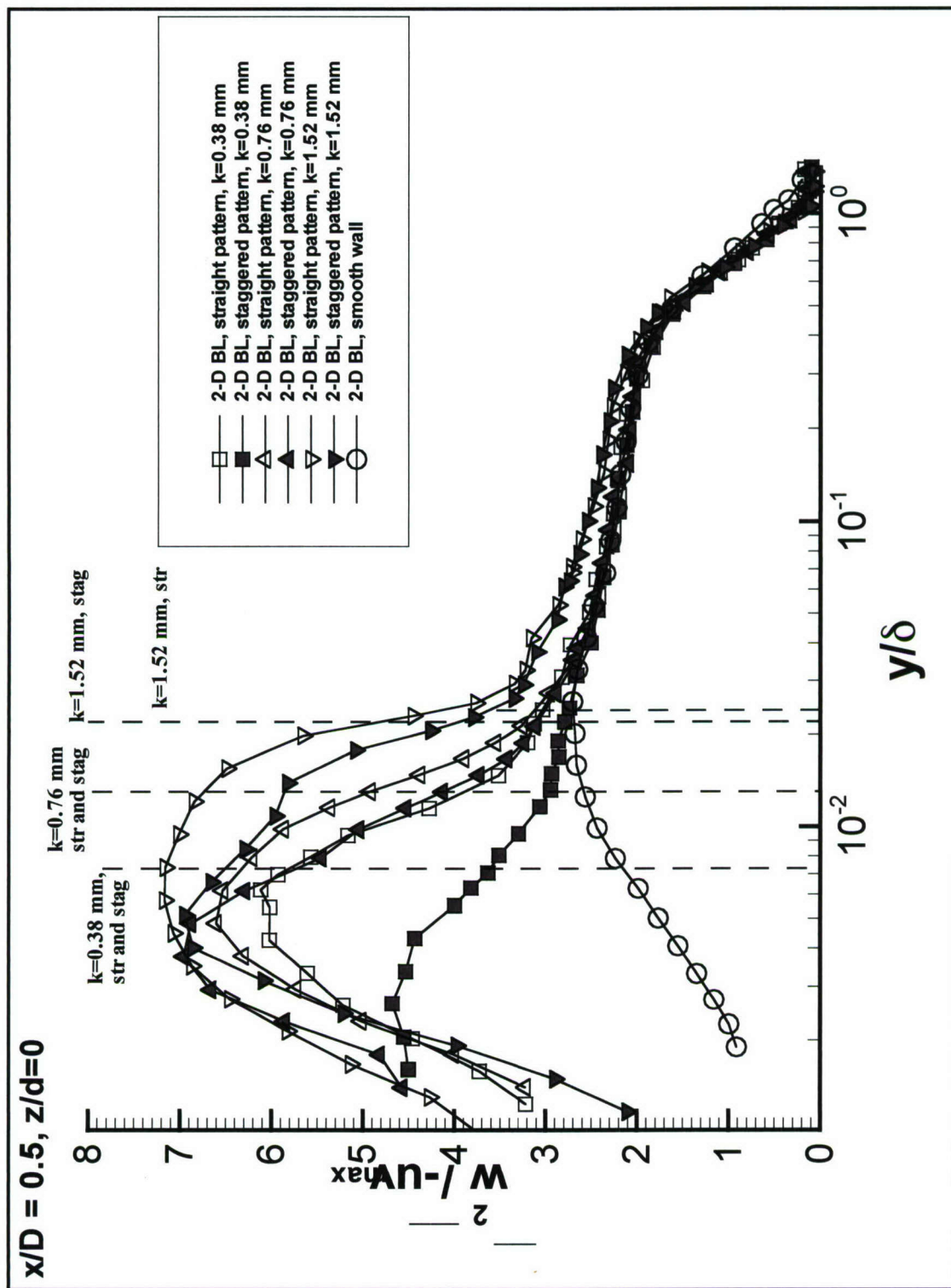


Figure 4.19. Variation of the spanwise Reynolds normal stresses,  $\overline{w^2} / -\overline{u v_{\max}}$ , with  $y/\delta$  at  $x/D = 0.5$ ,  $z = 0$ .



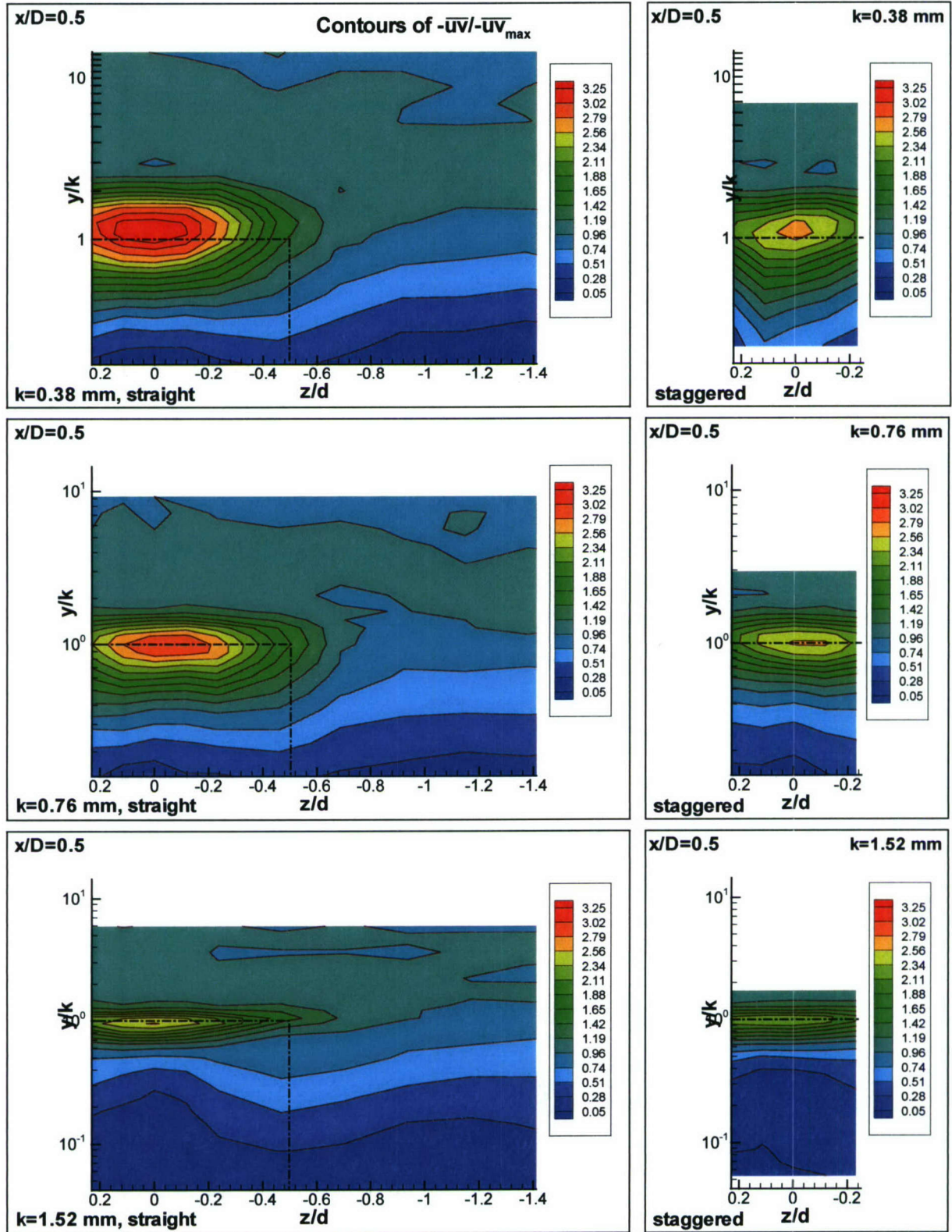


Figure 4.20 (a). Semi-log contours of  $-\overline{uv}/-\overline{uv}_{\max}$  in the  $y/k - z/d$  plane at  $x/D = 0.5$

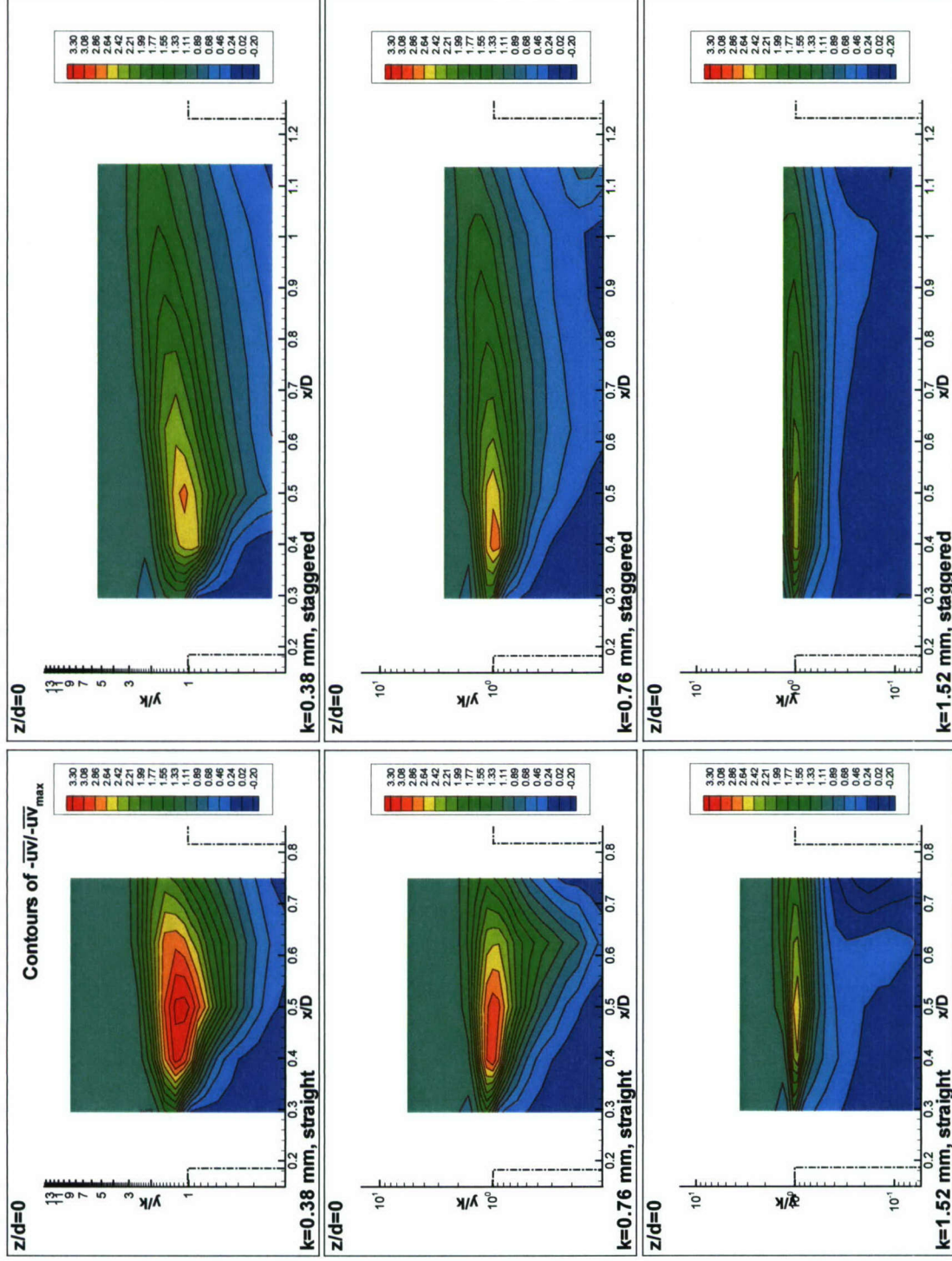


Figure 4.20 (b). Semi-log contours of  $-\overline{uv}/\overline{uv}_{\max}$  in the  $y/k - x/D$  plane along the centerline.



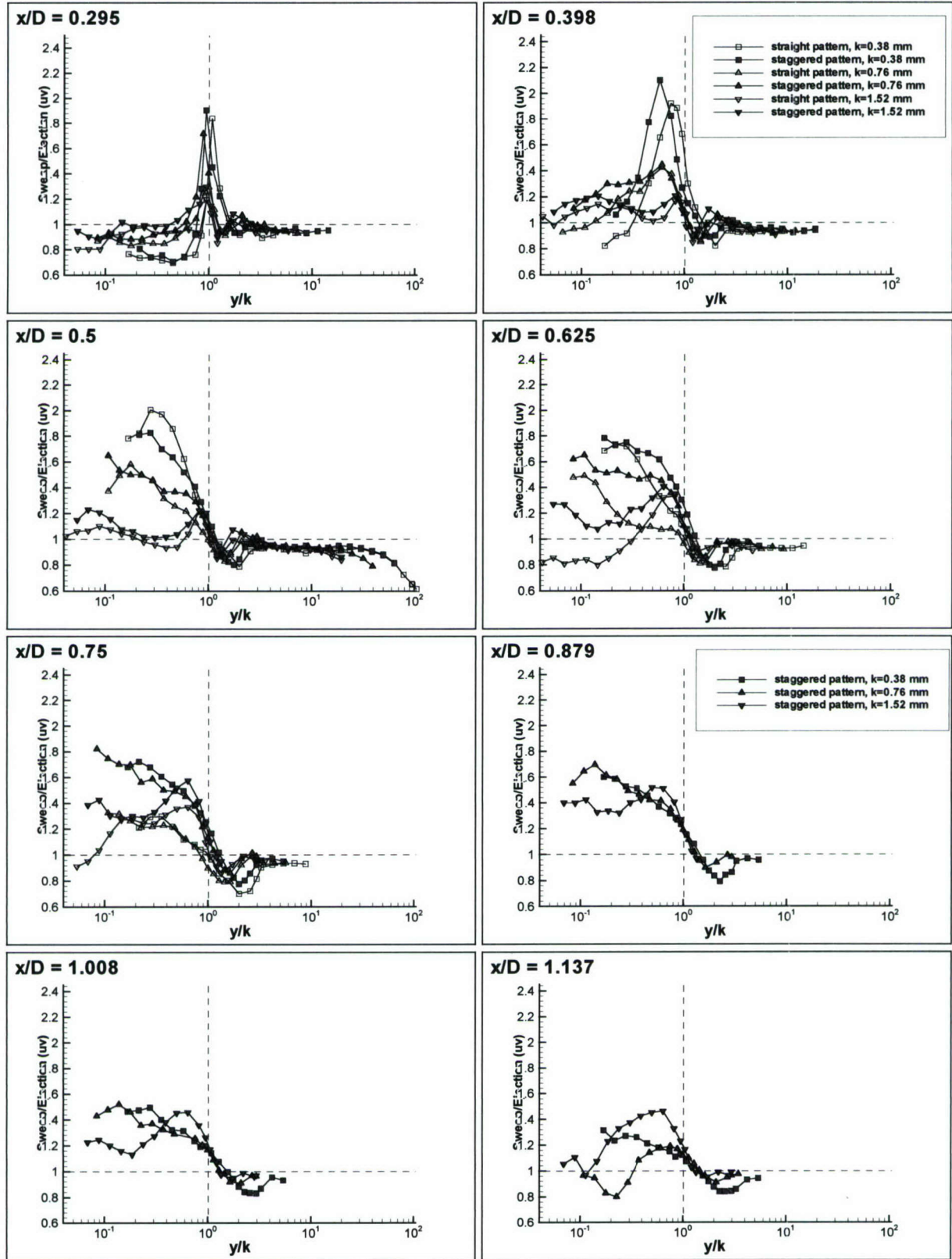


Figure 4.21. Ratio of sweeps to ejections from quadrant contribution to the Reynolds shear stress,  $-\overline{uv}$ , along the centerline, varying with  $y/k$ , at various streamwise locations,  $x/D$ .

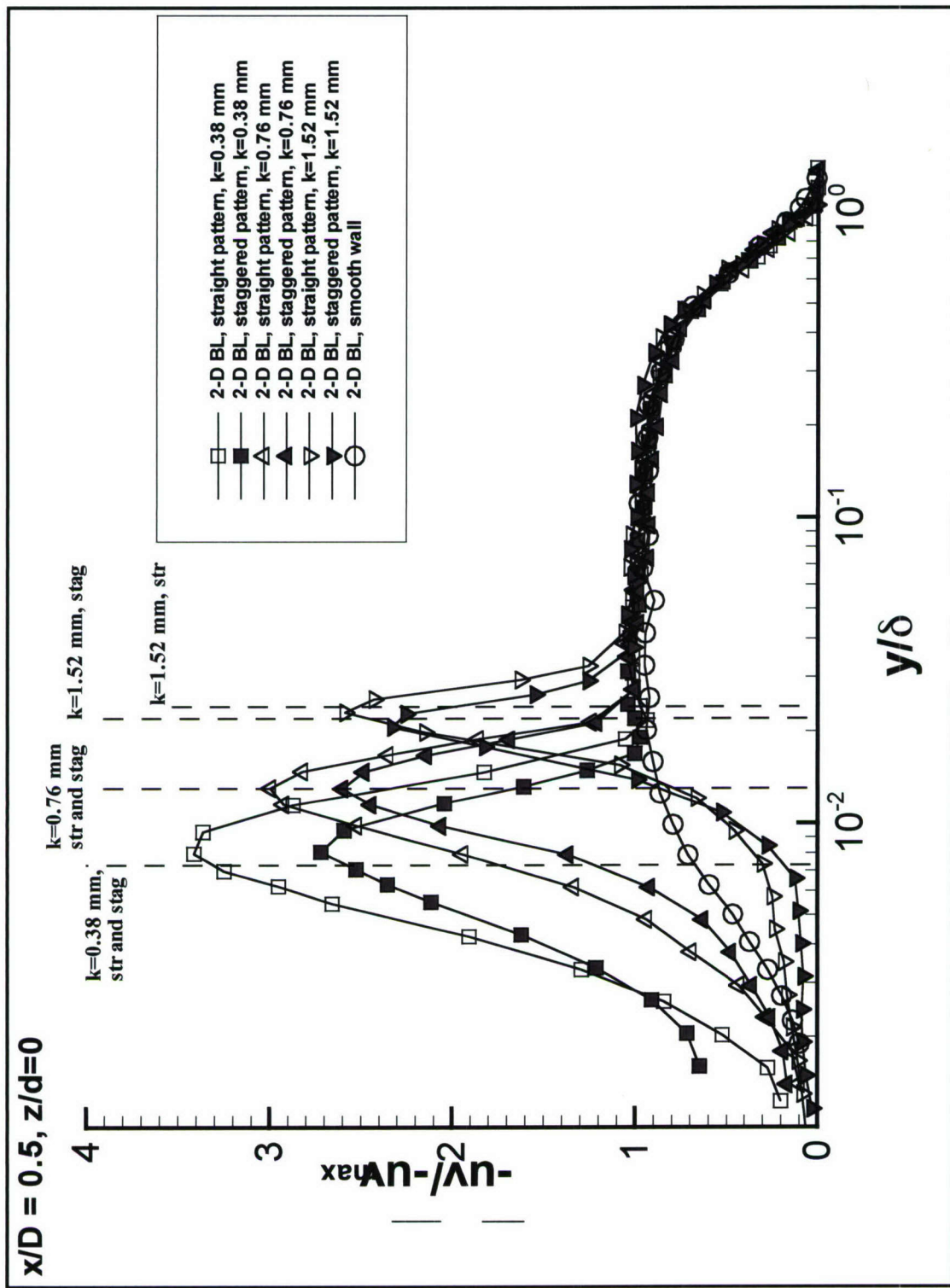


Figure 4.22. Variation of the streamwise Reynolds shear stresses,  $-\overline{uv}/-\overline{uv}_{max}$ , with  $y/\delta$  at  $x/D = 0.5$ ,  $z = 0$ .



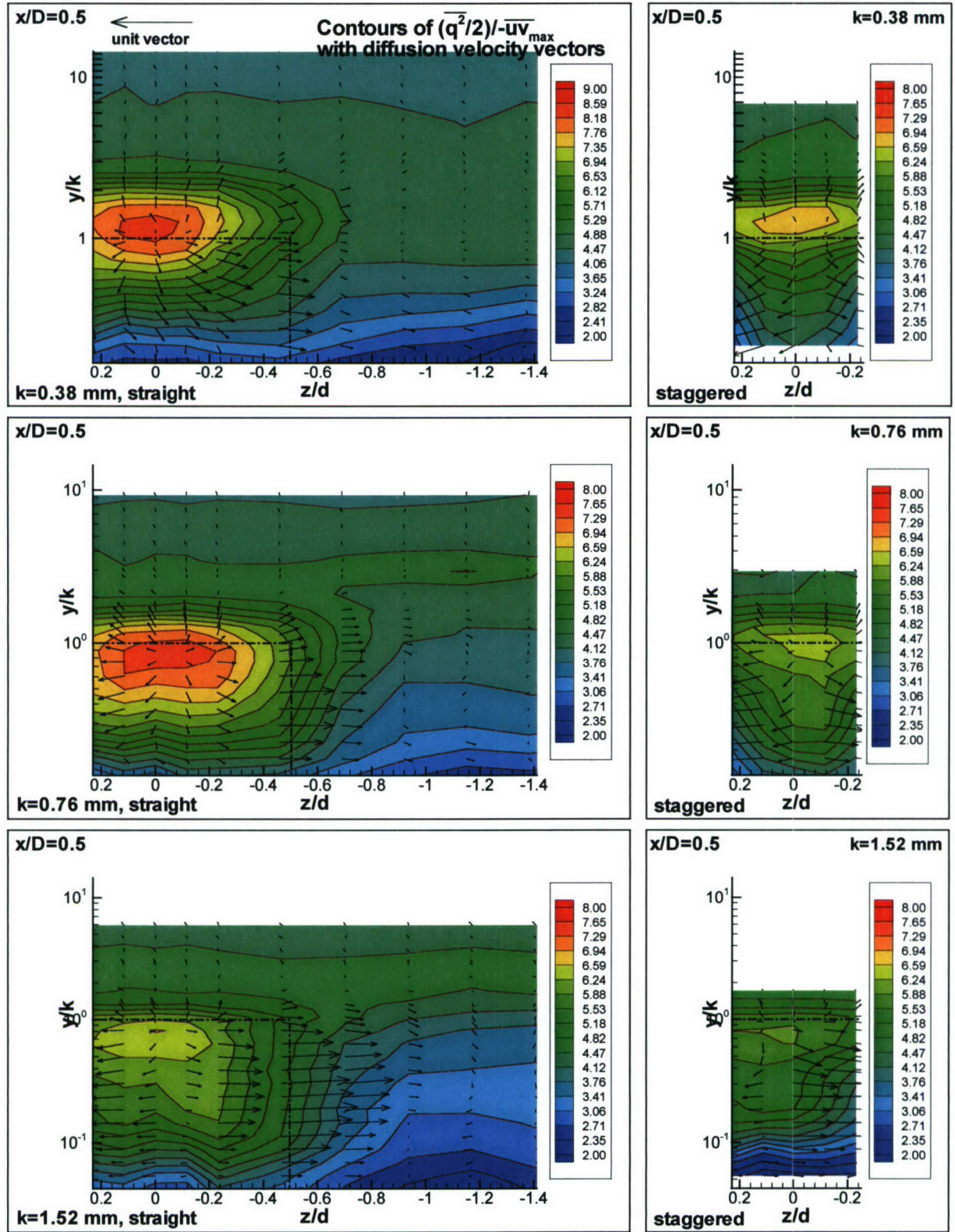


Figure 4.23 (a). Semi-log contours of turbulent kinetic energy (TKE),  $(\overline{q^2}/2) - \overline{uv}_{\max}$ , along with diffusion velocity vectors,  $V_q/\sqrt{-\overline{uv}_{\max}}$  and  $W_q/\sqrt{-\overline{uv}_{\max}}$ , in the  $y/k - z/d$  plane at  $x/D = 0.5$

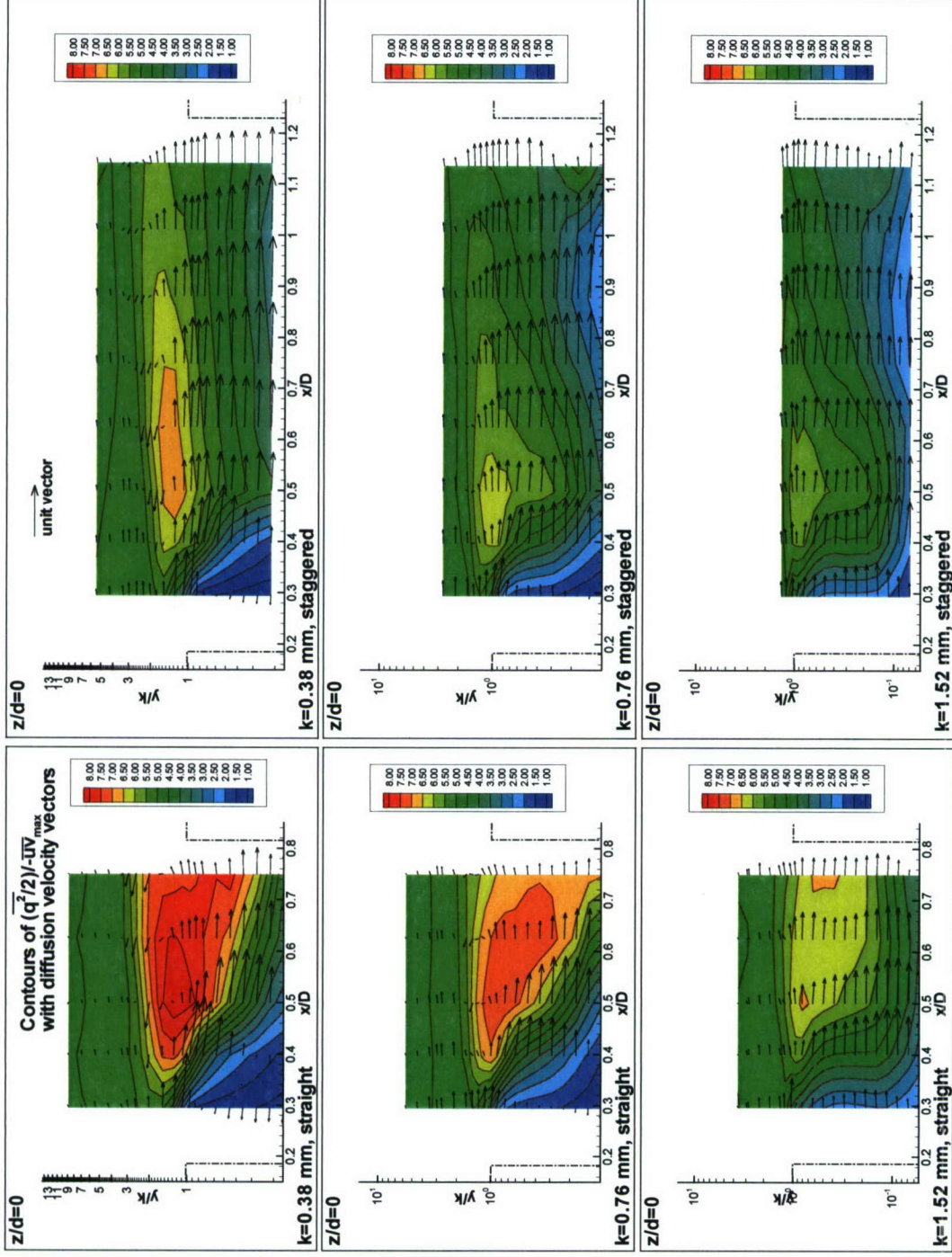


Figure 4.23 (b). Semi-log contours of turbulent kinetic energy (TKE),  $(\overline{q^2}/2) - \overline{uv}_{\max}$ , along with diffusion velocity vectors,  $U_q/\sqrt{-\overline{uv}_{\max}}$  and  $V_q/\sqrt{-\overline{uv}_{\max}}$ , in the  $y/k - x/D$  plane along the centerline.



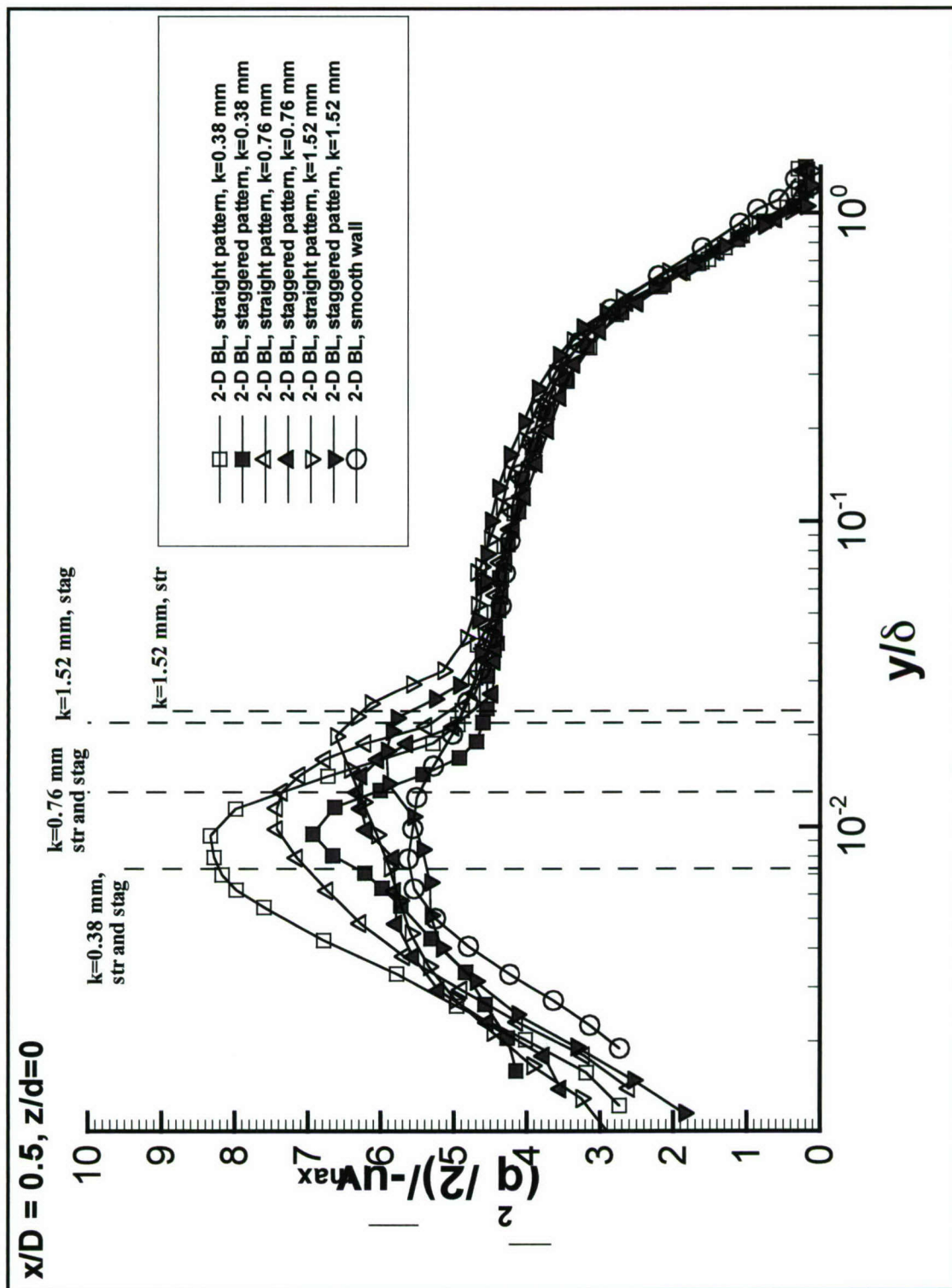


Figure 4.24. Variation of the turbulent kinetic energy,  $(\overline{q^2}/2)/(-\overline{u'v'_{\max}})$ , with  $y/\delta$  at  $x/D = 0.5, z = 0$ .

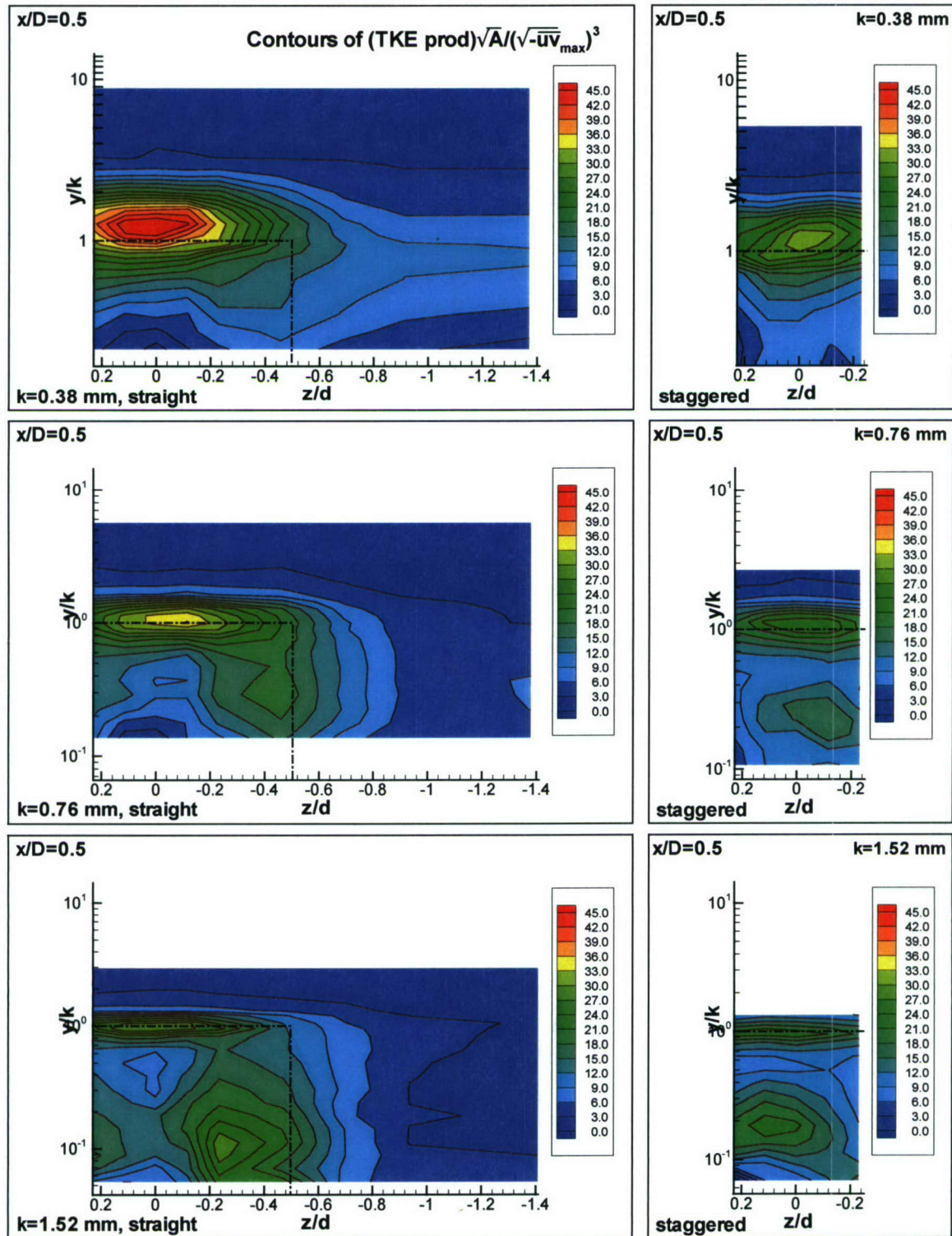


Figure 4.25 (a). Semi-log contours of production of TKE,  $(TKE \text{ Prod}) \sqrt{A} / (\sqrt{-\overline{uv}_{\max}})^3$ , in the  $y/k - z/d$  plane at  $x/D = 0.5$



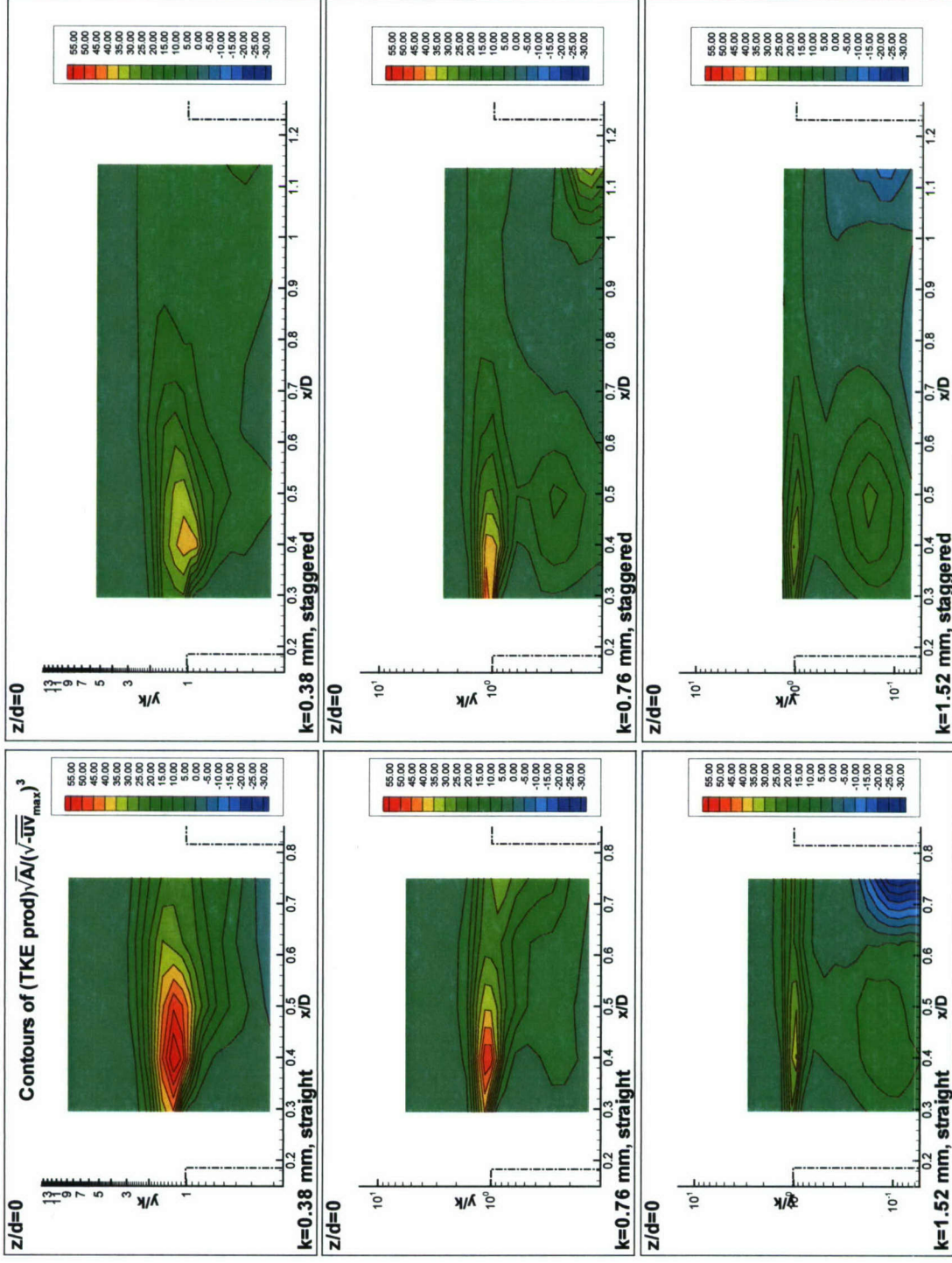


Figure 4.25 (b). Semi-log contours of production of TKE,  $(TKE \text{ Prod}) \sqrt{A} / (\sqrt{-u'v'_{\max}})^3$ , in the  $y/k - x/D$  plane along the centerline.

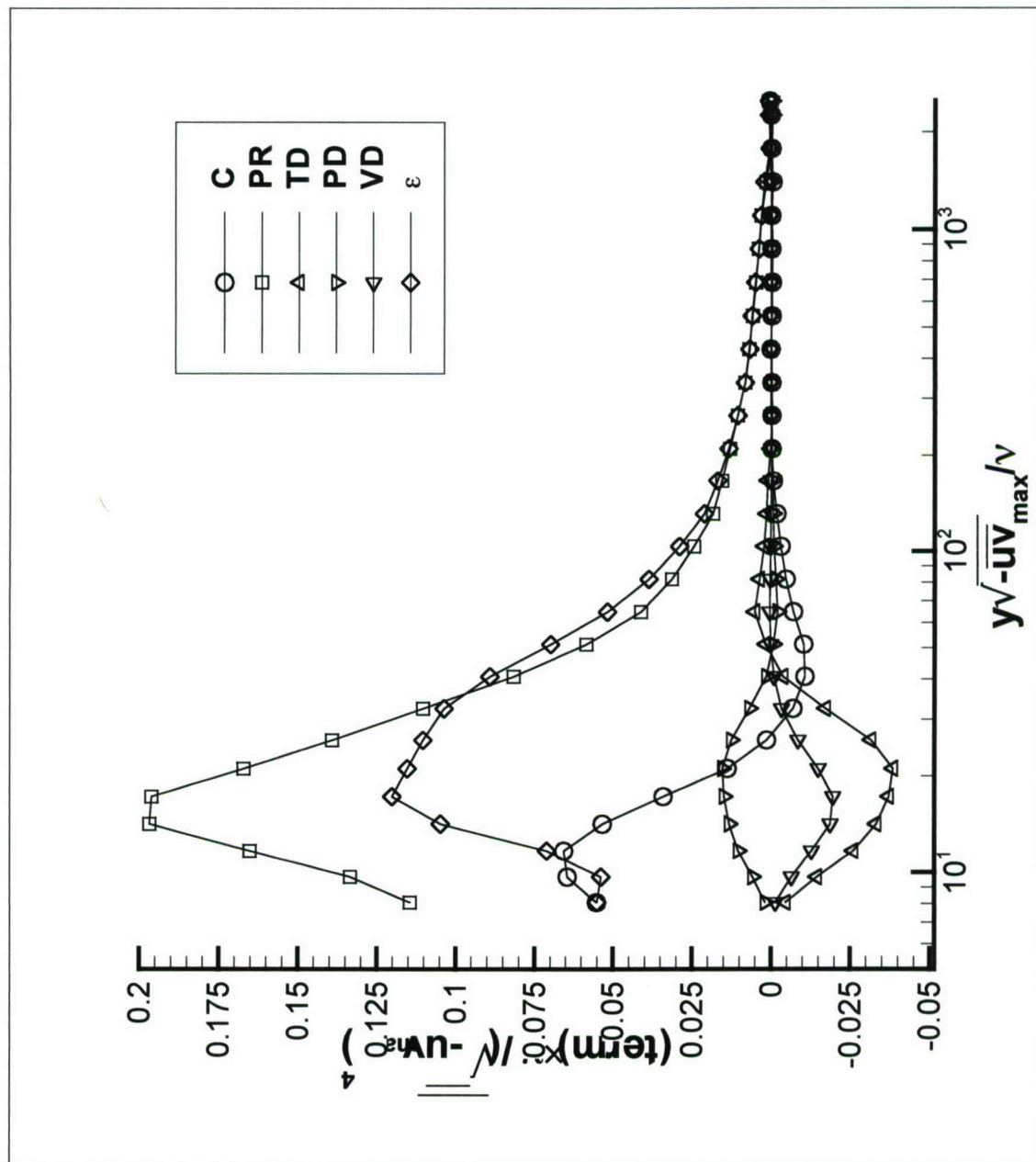


Figure 4.26. Variation of transport-rate budget of TKE,  $\overline{q^2}/2$ , normalized by  $(\sqrt{-u'v'_{\max}})^4/\nu$ , with  $y\sqrt{-u'v'_{\max}}/\nu$  (2-D smooth wall BL).



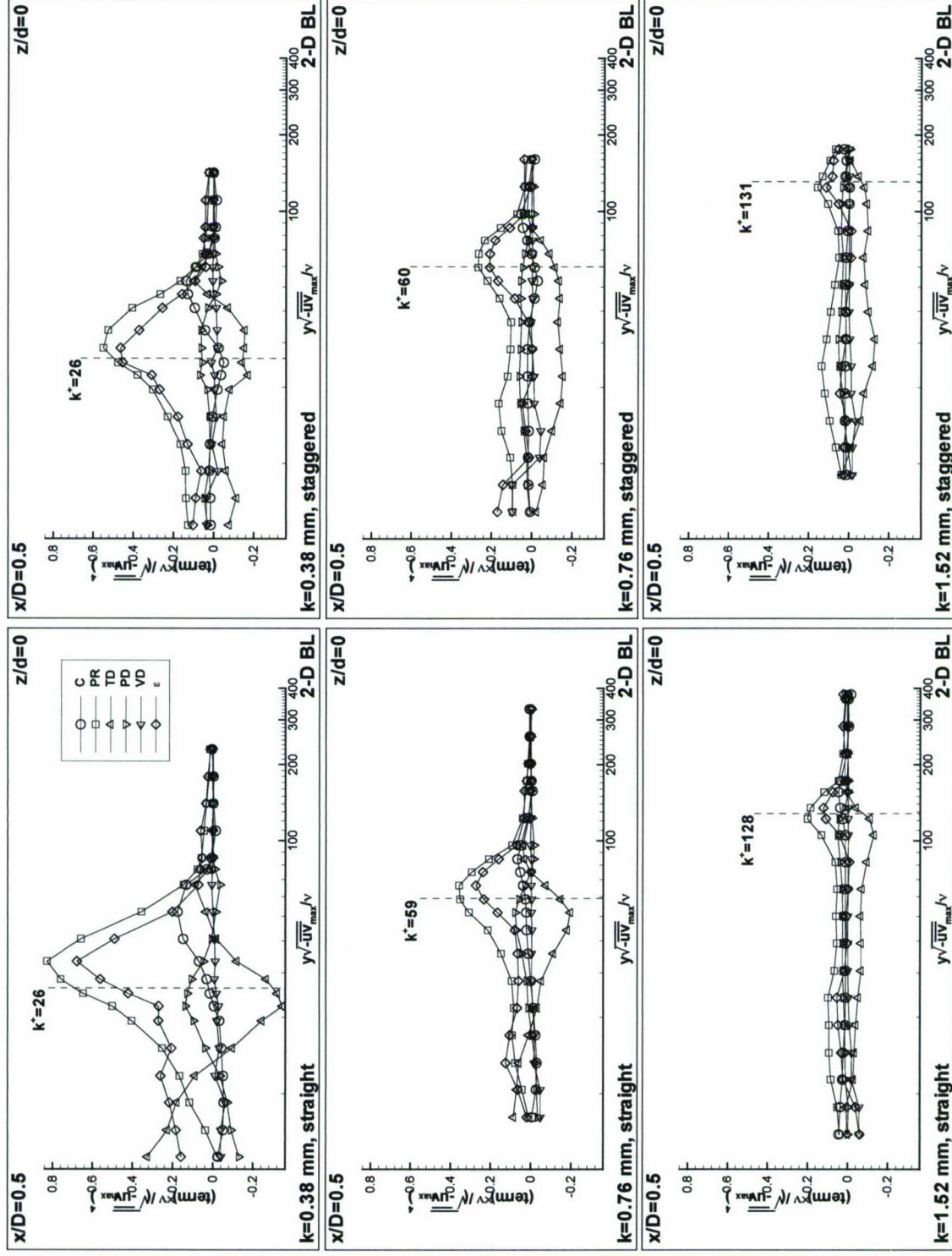


Figure 4.27. Variation of transport-rate budget of TKE,  $\overline{q^2}/2$ , normalized by  $(\sqrt{-u'v'_{\max}})^4/\nu$ , with  $y\sqrt{-u'v'_{\max}}/\nu$  at  $x/D = 0.5$  at the centerline.

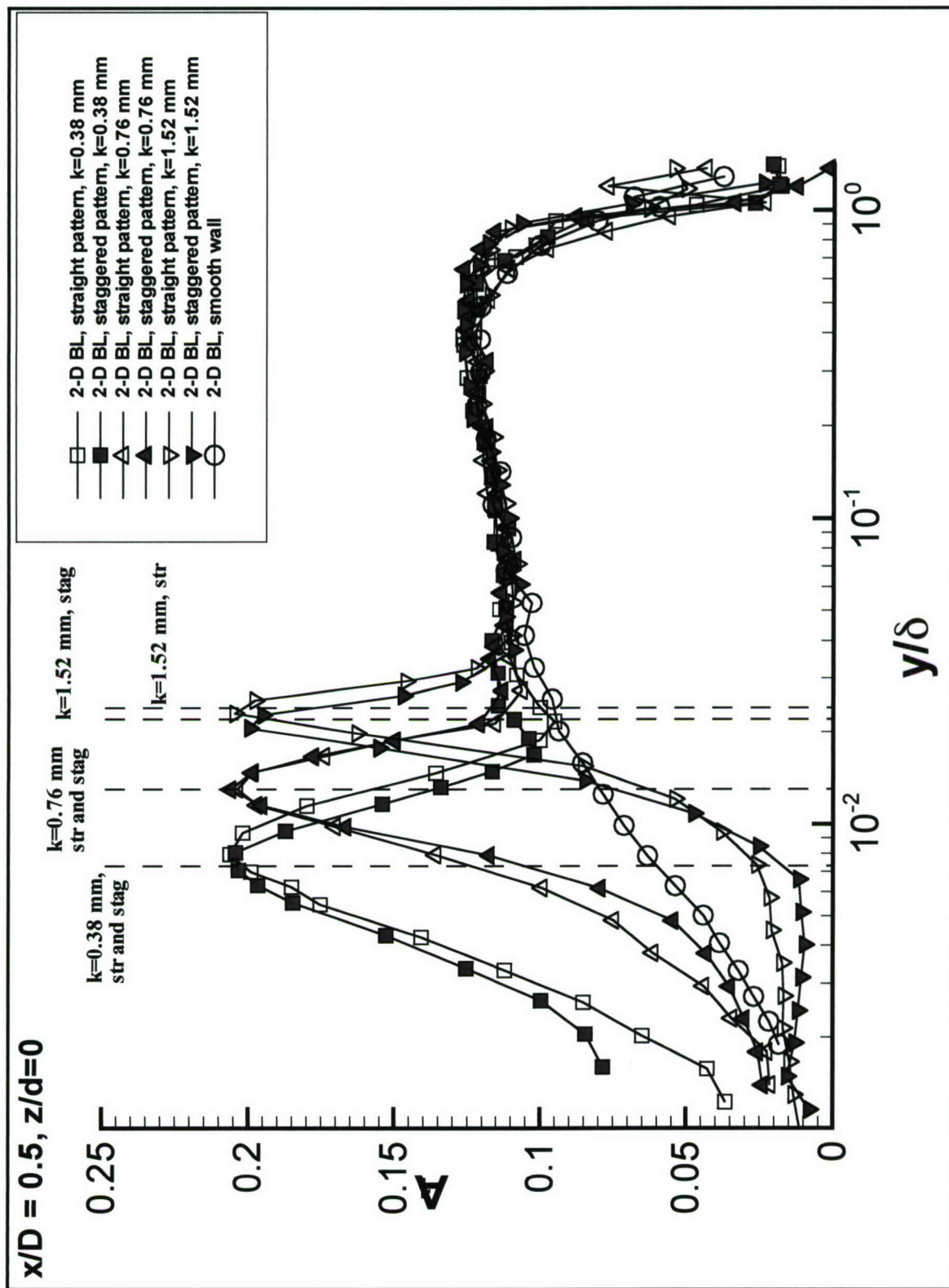


Figure 4.28 (a). Structural parameter,  $A_1$ , versus  $yU_\tau/\nu$ , profiles along the centerline.



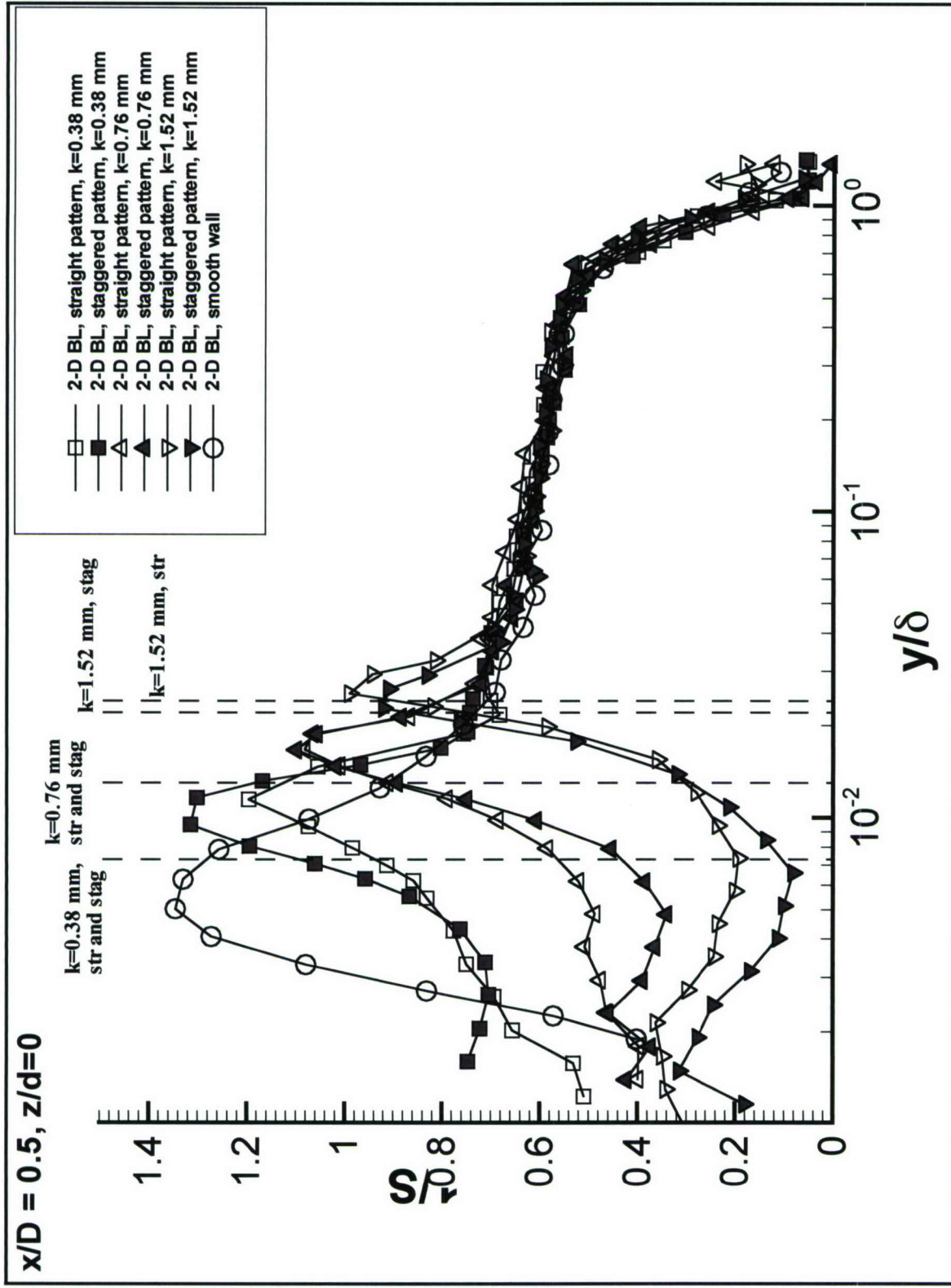


Figure 4.28 (b). Structural parameter,  $1/S$ , versus  $yU_\tau/\nu$ , profiles along the centerline.

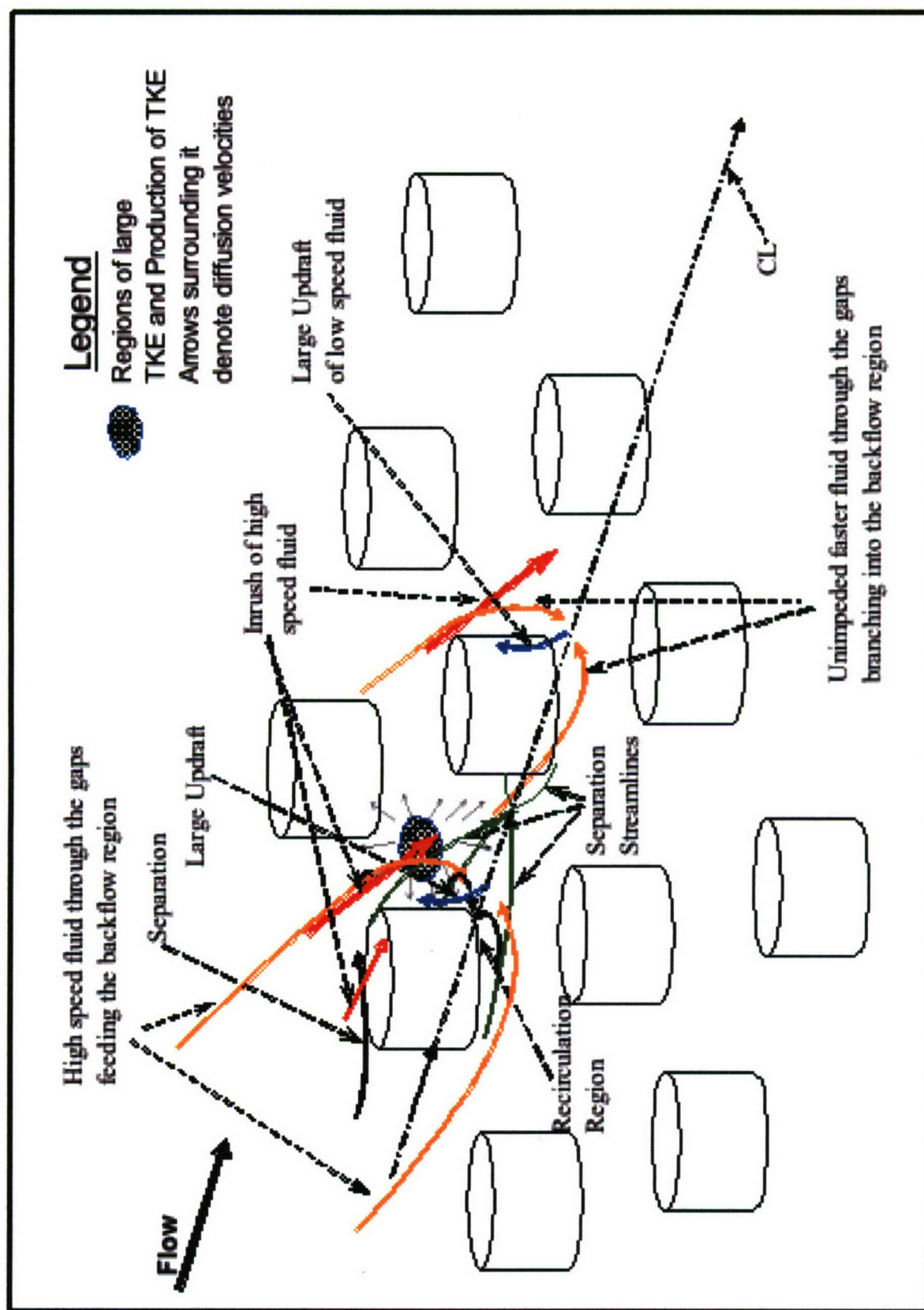


Figure 4.29. Schematic of the flow in a 2-D rough-wall (straight orientation). Similar structures are seen upstream and aft of each element.



## Chapter 5 Three-Dimensional Rough-Wall Turbulent Boundary Layers

This chapter presents measurements made at different stations in a rough-wall pressure-driven turbulent boundary layer that was created by a wing-body junction flow. Measurements are carried out at seven stations around the wing-body junction and a schematic of it is shown in Fig. 2.9 (a). The measurement locations (Table 2.1) are such that they are outside the strong horseshoe vortex system formed at the wing-body junction. At stations 1 to 3, strong streamwise pressure gradients are present and at subsequent stations significant spanwise gradients are present. At station 7, the flow shows signs of relaxation.

### 5.1 Results and Discussions

For the purpose of scaling the data-set in wall variables, the velocity scale ( $U_w$ ) is defined as  $\sqrt{\tau_{\max}/\rho}$ , where  $\tau_{\max}$  is the maximum value of the total shear stresses  $[\sqrt{(-\overline{uv})} + \sqrt{(-\overline{vw})}]$  at the overlap between the inner and outer regions of the boundary layers as indicated by the semi-logarithmic region in the streamwise  $U$  profiles. The corresponding length scale is then  $\nu/U_w$ , where  $\nu$  is the kinematic viscosity. Table 5.1 shows the velocity scale for the smooth wall and the six cases of rough-wall for each of the measurement stations. All the profiles in this chapter are in upstream or wind tunnel coordinates, normalized with the velocity scale ( $U_w$ ) and the length scale. The latter is the boundary layer thickness,  $\delta$ , where  $\delta$  is the distance from the wall where the streamwise velocity is  $0.995 U_e$ . The smooth wall 3-D boundary layers at the seven stations were also measured and are shown in all the plots, for the sake of comparison. Table 5.2 (a)-(g) presents the values of  $U_w$ ,  $U_e$ ,  $\delta$ , the streamwise displacement thickness ( $\delta^*$ ), the streamwise momentum thickness ( $\theta$ ), and Reynolds number ( $Re_\theta$ ), based on  $U_e$  and  $\theta$ , at all the seven stations for the six cases under consideration. The boundary layer parameters,  $\delta^*$  and  $\theta$  are defined as  $\delta^* = \int_0^\infty \left(1 - \frac{U}{U_e}\right) dy$  and  $\theta = \int_0^\infty \left(1 - \frac{U}{U_e}\right) \frac{U}{U_e} dy$ . Other parameters presented in the same table include  $k/\delta$  and the Roughness Reynolds number,  $k^+$ , based on  $U_w$  and  $\nu$ .

#### 5.1.1 Surface pressure gradients

The gradients of pressure in the streamwise and spanwise directions at the seven stations are shown in Figs. 5.1 (a) and (b) as  $dC_p/d(x/t)$  and  $dC_p/d(z/t)$  respectively, with the maximum thickness of wing ( $t$ ) used for non-dimensionalization the lengths. The plots reveal that the pressure gradients are unaffected by the roughness elements and the pressure imposed is mainly due to the presence of the wing-body junction. Further, the three-dimensionality, as indicated by the streamwise and spanwise pressure gradients, increases from station 1 through station 5 and then shows a relaxation at the subsequent stations. The bounds of uncertainty, with 20:1 odds, in the values of both  $dC_p/d(x/t)$  and  $dC_p/d(z/t)$  are same as  $\pm 0.08$ .



### 5.1.2 Mean velocities

Figure 5.2 shows the variation of streamwise velocity  $U/U_w$  with  $yU_w/\nu$  for all the seven stations. Above the element heights, the rough wall profiles show a curve decrement relative to the smooth wall with the decrements increasing with the height of the roughness element. All profiles show a semi-log region indicating that there is a distinct overlap between the inner layers and the outer region. At regions very close to the wall, most profiles, except the staggered  $k=0.38\text{ mm}$  and  $0.76\text{ mm}$  cases, show regions of reverse flow implying that flow has not re-attached behind the element: Conversely, the flow has reattached behind the elements for these two staggered cases. At 3 roughness heights and above, the profiles do not show any orientation effects, i.e, little differences in the  $U/U_w$  values between straight and staggered patterns.

The variation of the spanwise velocity  $W/U_e$  with  $y/\delta$  is shown in Fig. 5.3 for all the seven stations. For each case, the profiles show similar behavior as those for the smooth wall above 3 element heights with profiles collapsing into one another. The regions of dissimilarity among the  $W$  profiles are confined within the element heights at station 1 and these similarity regions propagate above the elements but within 3 element heights. Further, the regions of dissimilarity increase progressively from stations 1 through 7. Once again, no orientation effects are seen above 3 element heights in all the six cases. The fact that the profiles collapse above 3 element heights seem to indicate that the time-averaged streamwise vorticity at each station is the same; however, with different vorticity fluxes from the wall – the different local fluxes owing to the varying pressure gradients and contours of the roughness element. This behavior is mathematically expressed as:

$$\frac{4}{\text{Re}_L} \left( \frac{\partial (\bar{w}L/U_{ref})}{\partial (n/L)} \right) = (\vec{e}_n \times \vec{\nabla}) \cdot \vec{\omega}_p$$
, which is true for an incompressible flow over stationary surfaces with a unit vector normal to the surface,  $\vec{e}_n$ , where all vorticity ( $\vec{\omega}$ ) arises at the surface under the action of pressure gradients.

### 5.1.3 Reynolds stresses

The line plots presented in this section and the next one are for all the seven stations for the six cases of rough-wall geometry.

The variation of the streamwise turbulent normal stress  $\overline{u^2}/U_w^2$  with  $y/\delta$  is shown in Fig. 5.4. The profiles are seen to collapse with each other and the respective 3-D smooth wall boundary layers too in the outer regions except for the profiles at station 4 where only the rough-wall boundary layer data collapse. The normalized peak intensities are below those for the smooth wall.

The variations of the wall-normal turbulent normal stresses  $\overline{v^2}/U_w^2$  and the spanwise normal stresses,  $\overline{w^2}/U_w^2$ , with  $y/\delta$  are shown in Figs. 5.5 and 5.6. The effects of roughness are more pronounced in these quantities. All stations show increased levels throughout the boundary layer relative to the smooth wall with peak levels located below the element heights. The increases in stress levels in the outer region are qualitatively and quantitatively similar to 2-D rough wall boundary layers. The increases in  $\overline{v^2}$  and  $\overline{w^2}$  levels are mainly due to the sweeping motions induced by the inrush of faster moving fluid over and around the roughness elements. Also these quantities show a collapse in the outer regions of the BL.

Figure 5.7 shows the variations of the streamwise Reynolds shearing stress,  $-\overline{uv}/U_w^2$ , with  $y/\delta$ . Stations 1 through 3 show constant shear stress values in the log law region and the outer regions of the layers similar to those in the 2-D rough-wall boundary layers. At subsequent stations, as three-dimensionality becomes more pronounced, the constant levels are replaced by gentle “dip”



like regions. Large enhancements in the stresses are seen over those for the smooth wall BL, with peaks located close to the element heights and a behavior similar to that exhibited by the  $\overline{v^2}$  stresses.

Figure 5.8 shows the variation of the spanwise Reynolds shearing stress,  $-\overline{vw}/U_w^2$ , with  $y/\delta$ . Stations 1 through 3 display relatively low values of this shear stress when compared to those for the subsequent stations. Considerably high peak levels are seen at Stations 5, with values relaxing as Station 7 is approached. The levels of  $-\overline{vw}$  is an indicator of the flow three-dimensionality. The peak levels in  $-\overline{vw}$  are comparable to the peak levels in the streamwise shearing stress,  $-\overline{uv}$ . As evidenced by the  $-\overline{vw}$  profiles, the differences between the two orientations are confined within 3 roughness heights.

Figure 5.9 shows the variation of  $1/S$  with  $y/\delta$ , where  $1/S = \sqrt{(\overline{uv})^2 + (\overline{vw})^2} / \overline{v^2}$ . A fairly constant value of 0.6 is seen at the stations in the outer regions of the flow implying that three-dimensionality does not affect this parameter. This parameter remains a constant in 2-D rough wall boundary layers too, implying the effects of roughness on wall-normal stress and the total shear stress are similar.

To further investigate the effects of mean flow three-dimensionality on the flow structure, contours of different quantities are presented in tunnel coordinates. Values obtained in the corresponding 2-D rough wall case are presented in the LHS for the sake of comparison. Fig. 5.10 presents the contours of  $U/U_w$  in the  $y/k - z/d$  plane at  $x/D = 0.5$  with secondary flow vectors,  $V/U_w$  and  $W/U_w$ . The contours are seen to be skewed due to the presence of cross flow. The secondary flow vectors indicate a downwash away from the tunnel axis.

Contours of Reynolds stresses,  $\overline{u^2}/U_w^2$ ,  $\overline{v^2}/U_w^2$ ,  $\overline{w^2}/U_w^2$ ,  $-\overline{uv}/U_w^2$  and  $-\overline{vw}/U_w^2$  in the  $y/k - z/d$  plane at  $x/D = 0.5$  are presented in Figs. 5.11 (a)-(e). The contours presented are for the quantities obtained at station 5 for the straight orientation (all three roughness heights). Each of the stresses show skewness due to flow three-dimensionality with peak locations generally located in the direction of the velocity vector. Since most of the high magnitudes are seen in the vicinity of the element heights, it seems that the velocity vector hitting the top of the elements is the important factor as regards the magnitudes and also its direction.

## 5.1.4 Turbulent kinetic energy (TKE)

Figure 5.12 presents the contours of TKE,  $(\overline{q^2}/2)U_w^2$ , in the  $y/k - z/d$  plane at  $x/D = 0.5$  with diffusion velocity vectors,  $V_q/U_w$  and  $W_q/U_w$ . Much higher non-dimensional TKE levels are seen behind the elements in the 3-D case as compared to the 2-D rough-wall cases. Also, much larger diffusion is seen in the 3-D rough-wall cases. The largest diffusion is along the spanwise directions and is attributed to large  $\overline{w^3}$  which can also be considered as the transport of  $\overline{w^2}$  by the  $w$  fluctuations. Figure 5.13 shows the variations of the TKE,  $(\overline{q^2}/2)U_w^2$ , with  $y/\delta$ . A behavior similar to that of the normal stress profiles occurs with a collapse in the values at the outer regions of the TBL, implying that the motions in the outer regions are independent of the wall condition.

### 5.1.4.1 Transport-rate budget of turbulent kinetic energy (TKE)

For the transport rate budget of TKE in the case of the 3-D rough-wall TBL, only one case is presented here – that for Station 5 of the rough-wall with straight orientation containing the elements of the largest heights,  $k=1.52mm$  ( $k^+ = kU_w/\nu=141$ ). The profile at station 5 was taken at a distance of  $D/2$  from the center of the post (closest to station 5) at a direction given by the mean velocity vector at 3 element heights, i.e.,  $3k$  [Fig. 2.9 (b)].  $\alpha$  is the angle the velocity vector makes with the



tunnel axis at  $3k$  height. The task of TKE balance was made possible by the extensive measurements of mean velocities and fluctuating quantities (Reynolds stresses and the triple products) made on a fine grid ( $5 \times 25 \times 10$ ) of measurement points in a 3-D volume space, around the roughness elements, in the 3-D TBL at station 5 (Fig. 2.10 and Table 2.1). The results for the 3-D rough-wall TBL (straight orientation) at station 5 are compared with those obtained for the 2-D rough-wall TBL for the same orientation and height ( $k^+ = k\sqrt{-\overline{uv}_{\max}}/\nu = 128$ ). Further, the results for the rough-wall cases are compared with those obtained for the smooth-wall cases (2-D TBL and 3-D TBL at stations 5 in the wing/body junction flow). The transport-rate budget for the TKE in the 3-D case is carried out with the same scheme as outlined in the 2-D case (section 4.1.4.1).

Figure 5.14 presents the variation of the transport-rate budget of TKE,  $(\overline{q^2}/2)_p$ , normalized by  $U_{\tau o}^4/\nu$ , with  $yU_{\tau o}/\nu$ . Throughout the regions, from the near-wall to about 2 element heights, a large amount of TKE is produced in both 2-D and 3-D rough-wall layers. Since a large amount is produced and transported by velocity fluctuations, large values of turbulent diffusion occur that transport TKE from regions of high TKE regions to lower TKE regions. In the case of the 2-D rough-wall layers, considerable dissipation of TKE takes place, notably in the near-wall regions and in regions close to the element height. For 3-D rough-wall layers, however, high dissipation rates of TKE occur throughout these regions, up to 3 element heights, with values larger than those for the 2-D rough-wall. The same behavior holds true for the  $PR$  term. Further, the dissipation rates are comparable in magnitudes with that for the  $TD$  although with an opposite sign. Also, the distribution for dissipation rate is similar to that for the  $PR$ , indicating that the portion of TKE dissipated is proportional to that being generated. The pressure diffusion term,  $PD$ , is small in magnitude and is of significance only in regions slightly below the element height in the 2-D rough-wall layers. For the 3-D rough-wall layers, this term is relatively higher throughout the regions that are below the element height with an increase in levels as the element height is approached. However, these levels abruptly fall to zero close to the element height.

To permit a better understanding the flow physics in 2-D and 3-D rough-wall boundary layers, contour plots of TKE and its production rates are presented. As mentioned earlier, the planes chosen for presentation for the 2-D rough-wall layers are the  $y-z$  plane along  $x/D = 0.5$  and at  $x-y$  plane along  $z/D = 0$  which is also the axis of symmetry. For the 3-D rough-wall layers, the coordinate system chosen for the 2-D rough-wall layers is rotated by  $\alpha$  (counter clockwise about the  $y$  axis) to obtain a new coordinate system, as mentioned previously. In this case, at station 5,  $\alpha = 28^\circ$  which is the angle the velocity vector makes with the tunnel axis at 3 element heights [Fig. 2.9 (b)]. Quantities in the new coordinate system are indicated by a dash superscript.

The rationale behind this exercise was to find out if the 3-D rough-wall layers have an axis of symmetry similar to that in the 2-D case. This also permits a better comparison between the two cases of the rough-wall. Figure 5.15 (a) presents contours of TKE production rate normalized by  $U_{\tau o}^4/\nu$ : in the  $y-z$  plane along  $x/D = 0.5$  for the 2-D rough-wall, and in the  $y-z'$  plane along  $x'/D = 0.5$  for the 3-D rough-wall. In the case of the 2-D rough-wall, the plots reveal symmetric distribution about the  $z$  axis, with peak levels seen at the element height. The 3-D case shows a form of symmetry about  $z'/d = 0.2$ . Again, peak levels are seen close to element height in this case too. The peak levels and the extent of the TKE production rates are larger for the 3-D case when compared to those for the 2-D case. Similar observations hold true for the planes perpendicular to this plane too as is seen in the plots of the same quantity in the  $x-y$  plane along  $z/D = 0$  for the 2-D rough-wall, and in the  $x'-y$  plane along  $z'/D = 0$  for the 3-D rough-wall [Fig. 5.15 (b)].

For both cases of rough-wall layers, the major contributors to the production of TKE are  $-\overline{uv}\partial U/\partial y$ ,  $-\overline{u^2}\partial U/\partial x$ ,  $-\overline{v^2}\partial V/\partial y$ , and  $-\overline{w^2}\partial W/\partial z$ . This analysis is based on the plots of the individual terms and the plots are not presented here. For both 2-D and 3-D rough-wall cases, the



peak contributions of the latter three terms are at the regions below the element height and among these three terms, only the  $-\overline{u^2} \partial U / \partial x$  term and the  $-\overline{w^2} \partial W / \partial z$  have a relatively larger extent of influence. Among all the four terms, in general, only the  $-\overline{u^2} \partial U / \partial x$  term subtracts from the total net positive production rate, the exception being the net negative TKE production rate seen at the junction of downstream element. This negative production is attributed to the large negative  $-\overline{w^2} \partial W / \partial z$  term. On comparison between the two rough-wall cases, the TKE production rates for the 3-D case have higher peak values and a larger extent compared to those for the 2-D cases. This behavior is attributed to relatively larger values of  $-\overline{w^2} \partial W / \partial z$  and also due to the extra production term,  $-\overline{vw} \partial W / \partial y$ . In the 3-D rough-wall TBL, both these terms are comparable to each other in magnitudes.

In plots similar to Fig. 5.15 (a) and (b), the TKE levels and its diffusion (by means of diffusion velocity vectors) are presented in Figs. 5.16 (a) and (b). The plots of TKE presented along the  $x-y$  plane for the 2-D case and in the  $x'-y'$  plane for the 3-D rough-wall show high TKE levels aft of regions of high production rates. Clearly it is the transport of TKE by turbulent diffusion and pressure diffusion that is responsible for the “spreading” of TKE aft of the same regions. Considering these planes, the diffusion velocity vectors are comparable in magnitude when compared among the two rough-wall cases. However, when considering transverse planes,  $y-z$  plane for the 2-D case and along the  $y-z'$  plane for the 3-D case, slightly larger magnitudes of the diffusion velocity vectors are seen in the latter, when compared to those for the former. Considering the totality of the flow by considering the planar data, the diffusion terms of comparable magnitudes and the terms common to both cases are  $-\partial \overline{v^3} / \partial y$ ,  $-\partial \overline{vw^2} / \partial y$ , and  $-\partial \overline{w^3} / \partial z$ . There are no extra diffusion terms for the 3-D case and the very slightly elevated diffusion levels when compared to those for the 2-D case are not due to any extra contributing terms, but rather due to a combined effect of the different terms. The TKE contours for the 3-D rough-wall case seem to have a form of symmetry about  $z'/d=0.2$ .

### 5.1.5 Check of “flow symmetry” in 3-D rough-wall TBL

The previous section showed a measure of flow symmetry about  $z'/d=0.2$  when the TKE was presented in a coordinate system rotated by  $\alpha$  which is the angle the velocity vector makes with the tunnel axis at 3 element heights. In the case of 3-D rough-wall flow,  $k=1.52mm$ , straight pattern, station 5, this angle,  $\alpha$ , is  $28^\circ$ . The plots reveal that to achieve “flow symmetry” the coordinate system needs to be rotated by about  $19^\circ$  instead of  $28^\circ$ . Hence, results for the shear stress and TKE quantities are presented in a coordinate system rotated by  $\beta=19^\circ$  about the tunnel axis for this case of 3-D rough-wall TBL. Therefore,  $\beta$  can be defined as the angle through which the coordinate system needs to be rotated to obtain a “flow symmetry” in the quantities. Note that only the TKE is coordinate invariant. To check if a similar behavior of “flow symmetry” is seen in the cases of the other two heights, the same exercise is undertaken for the other two heights (straight pattern, Station 5) too. For these two cases of Station 5 and straight pattern,  $k=0.38mm$  and  $k=0.76mm$ , the coordinate system needed to be rotated by  $\beta$  of  $25^\circ$  and  $17^\circ$ , respectively. The quantities shown in the coordinate system have had a transformation matrix applied to it and are indicated by a double dash superscript.

Figure 5.17 presents the contours of TKE,  $(\overline{q^2}/2)U_w^2$  in a plane normal to the  $x''$ -axis, i.e., in  $y/k - z''/d$  plane at  $x''/D = 0.5$  with diffusion velocities,  $V_q''/U_w$  and  $W_q''/U_w$ . For the sake of comparison, the 2-D rough-wall cases are presented at the LHS of the figure, for the same heights and orientation. The plots reveal high TKE levels in the neighborhood of the element heights with peak levels located about  $z'' = 0$ . Also, large amounts of TKE are diffused from the regions of high TKE levels. Features similar to the distributions of TKE are seen in the distributions of the Reynolds shear stress levels (in the transformed coordinates),  $-\overline{uv''}/U_w^2$ , which is presented in Fig. 5.18. Though all



three cases of 3-D rough-wall show peak levels at  $z'' = 0$ , in the case of the smallest heights,  $k=0.38\text{mm}$ , a skewness in the distribution is seen while the other two cases show a form of symmetry about  $z'' = 0$ . These results seem to imply that the structures created aft of the elements are strongly dependant on the angle at which flow hits the top of the elements since the values of the angle,  $\beta$ , for these three cases are close to the angle the velocity vector makes at the element heights.

## 5.2 Conclusions

A series of experiments have been conducted in three-dimensional boundary layers fully developed over a fetch of roughness elements distributed sparsely around a wing-body junction. Very uniform circular cylindrical roughness elements of  $0.38\text{ mm}$ ,  $0.76\text{ mm}$  and  $1.52\text{ mm}$  height are used in square and diagonal patterns to yield six different cases of rough-wall. Based on the results, a schematic of a 3-D rough-wall TBL is presented in Fig. 5.19.

The data reveal that pressure gradient is not strongly influenced by the roughness elements. The effects of the spanwise pressure gradients imposed on the rough-wall boundary layers are seen in the significant mean flow skewing, close to the wall, within the elements and in the spanwise Reynolds shearing stresses, with peak levels being comparable to those for the streamwise shearing stresses. Considerable skewing is also seen in the profiles of Reynolds normal stresses and the TKE. The fact that  $W/U_e$  versus  $y/\delta$  profiles, for both smooth as well as rough-wall layers, are the same above 3 element heights seems to indicate that the time-averaged mean vorticity at each station is the same, albeit with different vorticity fluxes from the wall. The higher the roughness element height, the faster is the diffusion of turbulence from wall to the outer layers. The effect of roughness pattern orientation is seen in the mean flow and turbulence structure only up to 3 roughness heights from the wall. The effect of the flow three-dimensionality is seen in the much higher transport of the turbulent kinetic energy by the  $w$  fluctuations as compared to that by the  $v$  fluctuations. The collapse, in general, of the scaled (with  $U_{\tau_o}$ ) profiles of stresses and the TKE in the outer regions of the BL seem to indicate that the motions in these regions are independent of wall condition, a behavior similar to that seen in the case of the 2-D rough-wall TBL.

The term by term evaluation reveals that the major contributors to the transport rate of TKE are production and diffusion. The TKE balance also reveals that dissipation is an important term in rough-wall layers too. In general, high production rates occur behind the elements and the quantities produced are transported away from these regions by the velocity fluctuations. The regions of high TKE levels are located close to the element height. The velocity fluctuations and the pressure fluctuations, to a much lesser extent, transport TKE from these regions directed radially outward. Also, the general propagation of regions of high TKE production seems to occur in the direction of the local velocity vector at the element height. From these results, one can also conclude that it is the velocity hitting the top of the element which is responsible for all the structures seen behind. At distances downstream of the elements, this also reveals a possibility for the 3-D rough walls to display symmetric or anti-symmetric behavior (as the case maybe), as regards various quantities, about a coordinate system aligned with the velocity vector at the element height, as is seen behind the element about its axis of symmetry in the case of the 2-D rough-wall.



Table 5.1. Values of the velocity scale,  $U_w$ , (in  $m/s$ ) for the smooth wall and the six cases of 3-D rough-wall turbulent boundary layers at the seven stations.

Stations	Smooth wall	$k = 0.38mm$ straight	$k = 0.38mm$ staggered	$k = 0.76mm$ straight	$k = 0.76mm$ staggered	$k = 1.52mm$ straight	$k = 1.52mm$ staggered
1	0.995	1.145	1.143	1.274	1.263	1.439	1.436
2	0.997	1.160	1.143	1.315	1.284	1.472	1.452
3	1.011	1.166	1.151	1.349	1.306	1.509	1.491
4	1.006	1.234	1.223	1.337	1.344	1.560	1.500
5	1.063	1.204	1.197	1.329	1.344	1.535	1.496
6	1.048	1.149	1.182	1.288	1.299	1.433	1.440
7	1.022	1.130	1.119	1.255	1.234	1.539	1.458

Table 5.2 (a). Boundary layer parameters for the smooth wall.

Stations	$U_e$	$\delta$ , $mm$	$\delta^*$ , $mm$	$\theta$ , $mm$	$Re_\theta$
1	25.73	40.25	7.08	4.93	7666
2	25.46	39.96	7.14	4.93	7578
3	25.88	39.57	6.93	4.81	7523
4	28.13	39.82	6.12	4.48	7613
5	29.75	39.98	5.58	4.24	7615
6	31.06	40.16	5.10	3.99	7487
7	31.67	39.92	4.95	3.92	7504

Table 5.2 (b). Boundary layer parameters for  $k = 0.38mm$ , straight orientation.

Stations	$U_e$	$\delta$ , $mm$	$\delta^*$ , $mm$	$\theta$ , $mm$	$Re_\theta$	$k^+$	$k/\delta$
1	25.70	50.72	10.11	6.44	9999	26.3	0.0075
2	25.15	50.20	9.97	6.39	9706	26.6	0.0076
3	25.93	51.97	10.00	6.41	10041	26.8	0.0073
4	27.80	50.14	8.59	5.84	9813	28.3	0.0076
5	30.04	51.56	8.04	5.61	10179	27.6	0.0074
6	30.72	52.41	7.52	5.44	10098	26.4	0.0073
7	30.93	53.09	7.47	5.46	10201	25.9	0.0072

Table 5.2 (c). Boundary layer parameters for  $k = 0.38mm$ , staggered orientation.

Stations	$U_e$	$\delta$ , $mm$	$\delta^*$ , $mm$	$\theta$ , $mm$	$Re_\theta$	$k^+$	$k/\delta$
4	27.46	48.96	8.78	5.95	9867	26.2	0.0078
5	30.24	47.82	7.69	5.44	9926	26.2	0.0079
6	30.78	51.31	7.57	5.54	10290	26.4	0.0074

For stations 1, 2, 3, and 7 the measurements were made up to a distance of 30  $mm$  from the wall and not any further.

Table 5.2 (d). Boundary layer parameters for  $k = 0.76\text{ mm}$ , straight orientation.

Stations	$U_e$	$\delta$ , mm	$\delta^*$ , mm	$\theta$ , mm	$Re_\theta$	$k^+$	$k/\delta$
1	25.98	58.565	12.70	7.65	11997	58.5	0.0130
2	25.36	54.56	12.65	7.52	11518	60.4	0.0139
3	25.82	55.13	12.39	7.38	11503	61.9	0.0138
4	27.30	55.96	10.63	6.86	11310	61.4	0.0136
5	29.52	57.11	9.79	6.65	11859	61.0	0.0133
6	30.68	58.16	9.37	6.55	12132	59.1	0.0131
7	31.39	60.33	9.30	6.57	12452	57.6	0.0126

Table 5.2 (e). Boundary layer parameters for  $k = 0.76\text{ mm}$ , staggered orientation.

Stations	$U_e$	$\delta$ , mm	$\delta^*$ , mm	$\theta$ , mm	$Re_\theta$	$k^+$	$k/\delta$
1	26.22	56.36	12.77	7.77	12309	58.0	0.0135
2	25.47	54.93	12.60	7.63	11743	58.9	0.0138
3	25.79	54.19	12.19	7.36	11470	59.9	0.0140
4	27.5	56.06	10.96	7.07	11738	61.7	0.0136
5	29.75	58.38	10.10	6.86	12328	61.7	0.0130
6	30.87	59.74	9.59	6.82	12716	59.6	0.0127
7	31.09	61.01	9.47	6.72	12614	56.6	0.0125

Table 5.2 (f). Boundary layer parameters for  $k = 1.52\text{ mm}$ , straight orientation.

Stations	$U_e$	$\delta$ , mm	$\delta^*$ , mm	$\theta$ , mm	$Re_\theta$	$k^+$	$k/\delta$
1	26.04	61.48	15.47	8.51	13380	132.1	0.0247
2	25.76	61.57	15.44	8.46	13158	135.1	0.0247
3	25.82	60.25	14.73	8.12	12659	138.6	0.0252
4	27.84	61.11	13.58	7.96	13386	143.3	0.0249
5	29.25	64.25	12.87	8.09	14287	140.9	0.0237
6	30.94	69.69	12.37	8.11	15159	131.6	0.0218
7	31.11	70.1	12.14	8.08	15181	141.3	0.0217

Table 5.2 (g). Boundary layer parameters for  $k = 1.52\text{ mm}$ , staggered orientation.

Stations	$U_e$	$\delta$ , mm	$\delta^*$ , mm	$\theta$ , mm	$Re_\theta$	$k^+$	$k/\delta$
1	25.82	67.08	16.27	9.24	14405	131.8	0.0227
2	25.42	64.61	16.11	9.07	13922	133.3	0.0235
3	25.80	63.21	15.14	8.65	13484	136.9	0.0240
4	27.91	68.78	14.52	8.74	14731	137.7	0.0221
5	29.00	69.51	13.82	8.72	15267	137.3	0.0219
6	30.81	72.55	13.51	8.94	16642	132.2	0.0210
7	31.00	72.57	13.09	8.78	16446	133.9	0.0209



## Figures

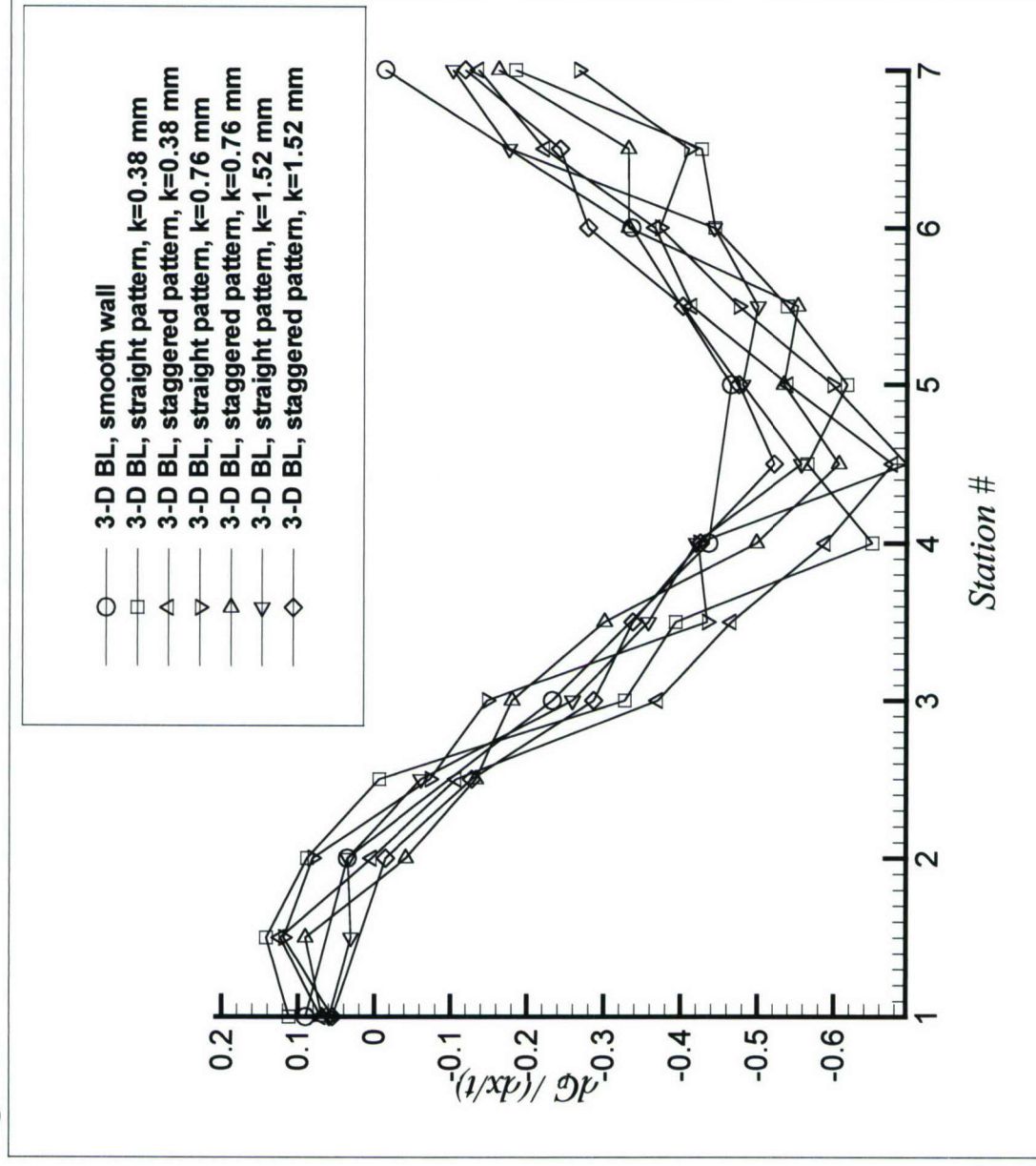


Fig. 5.1 (a). Pressure gradients in the  $x$ -direction as calculated at each station and in between adjacent stations. Also plotted are smooth wall data (From Ölçmen and Simpson, 1995).

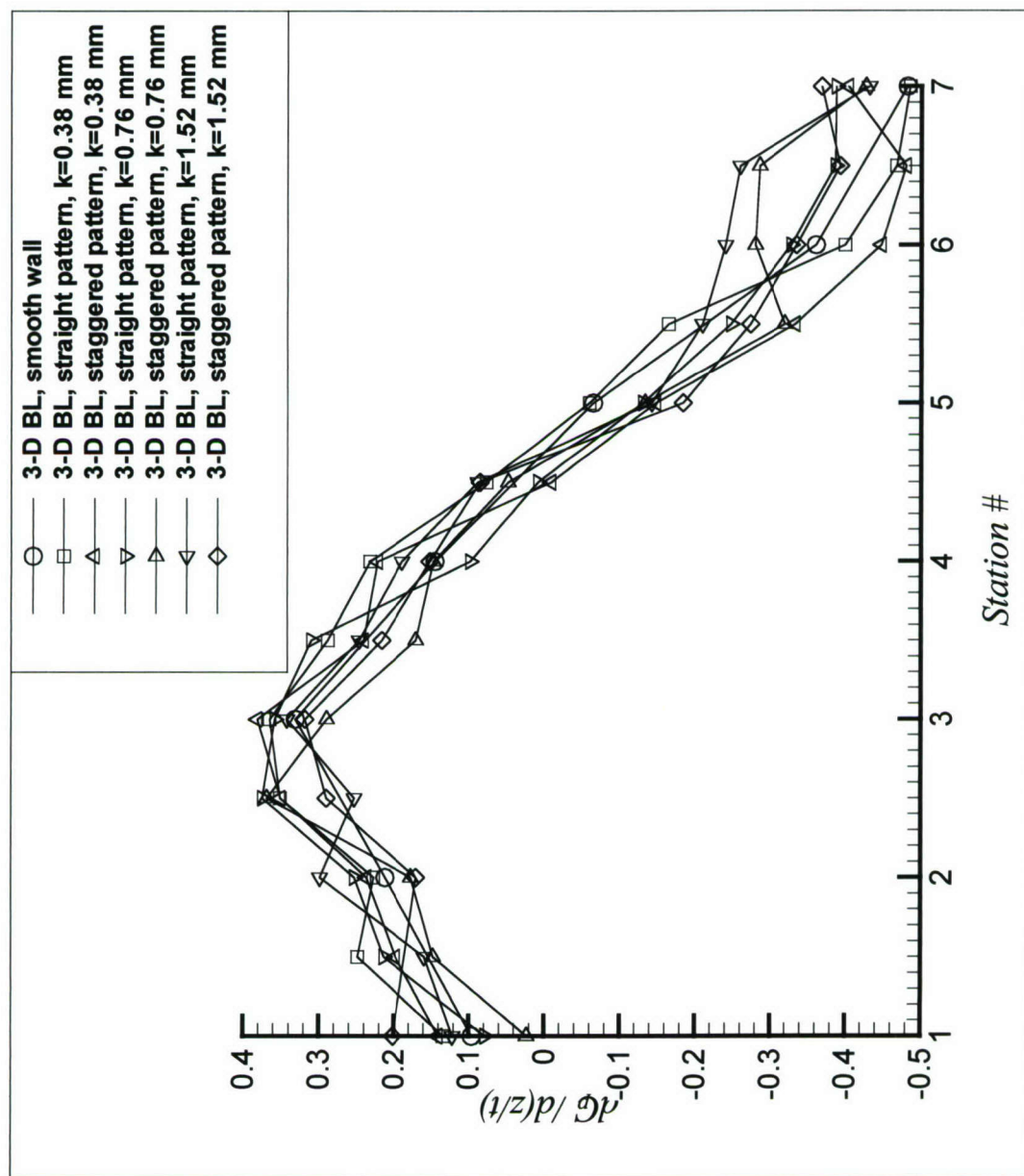


Figure 5.1 (b). Pressure gradients in the  $z$ -direction as calculated at each station and in between adjacent stations. Also plotted are smooth wall data (From Ölçmen and Simpson, 1995b).



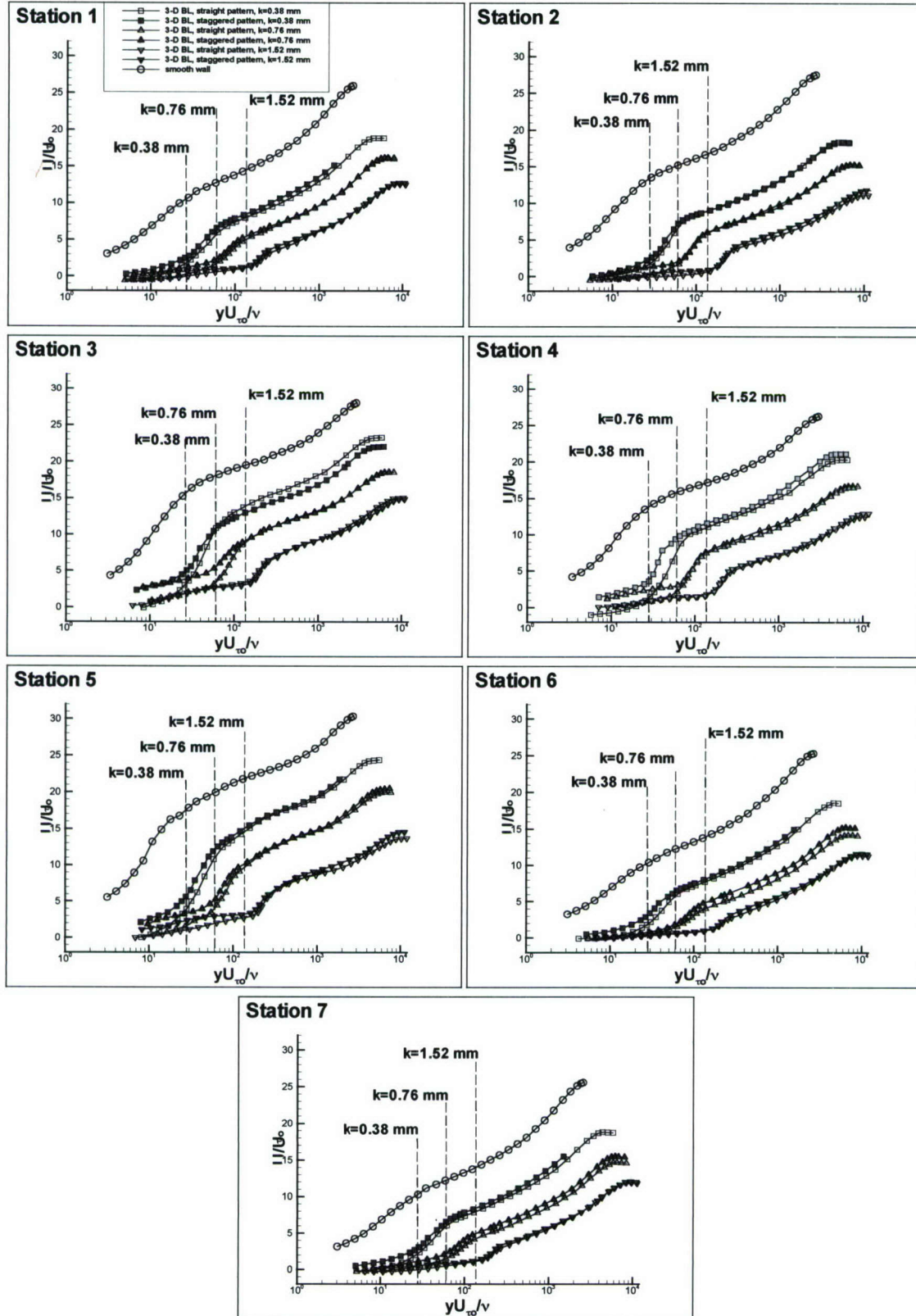


Figure 5.2.  $U/U_w$  versus  $yU_w/v$ , streamwise mean velocity profiles.

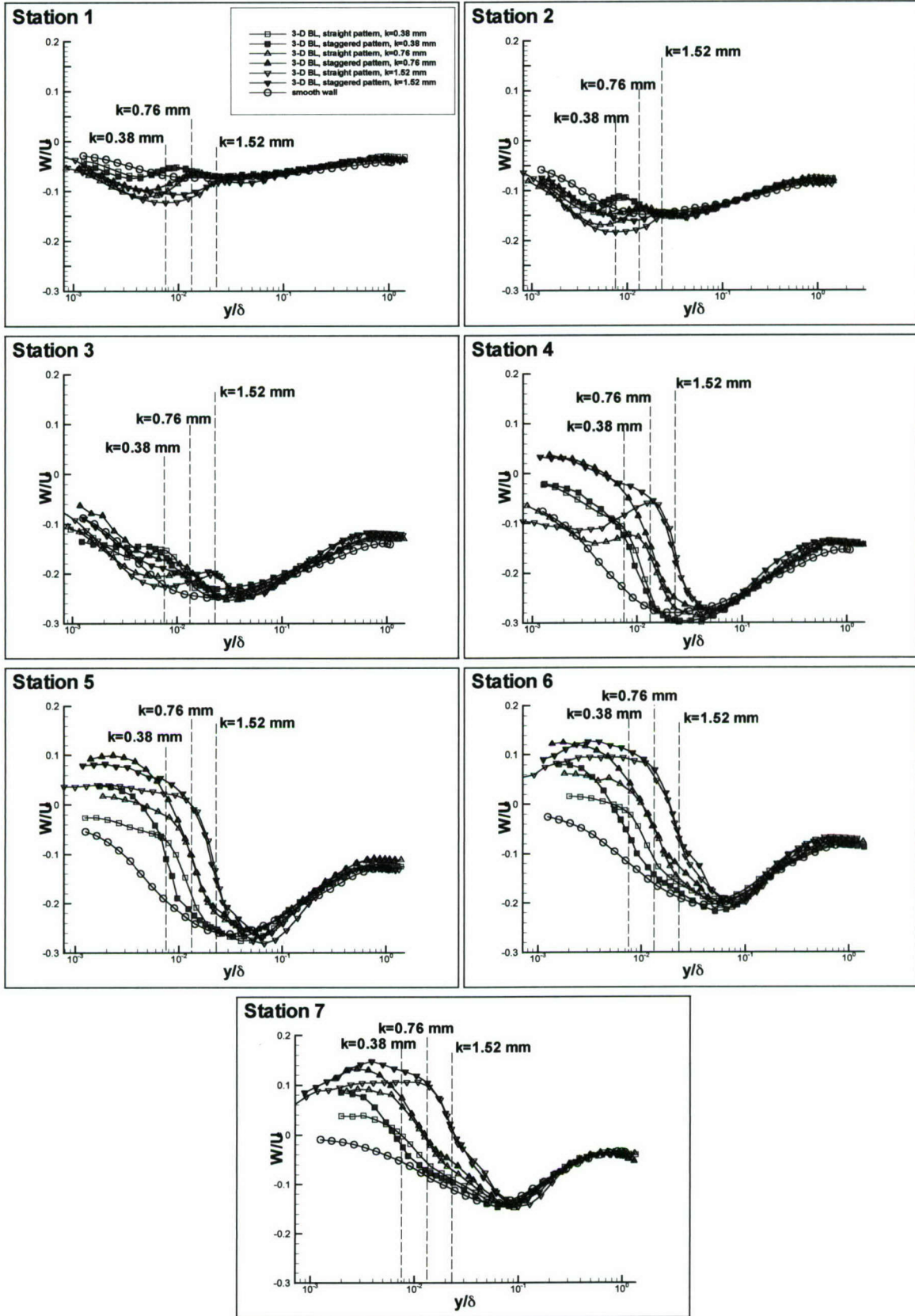


Figure 5.3.  $W/U_e$  versus  $y/\delta$ , spanwise mean velocity profiles



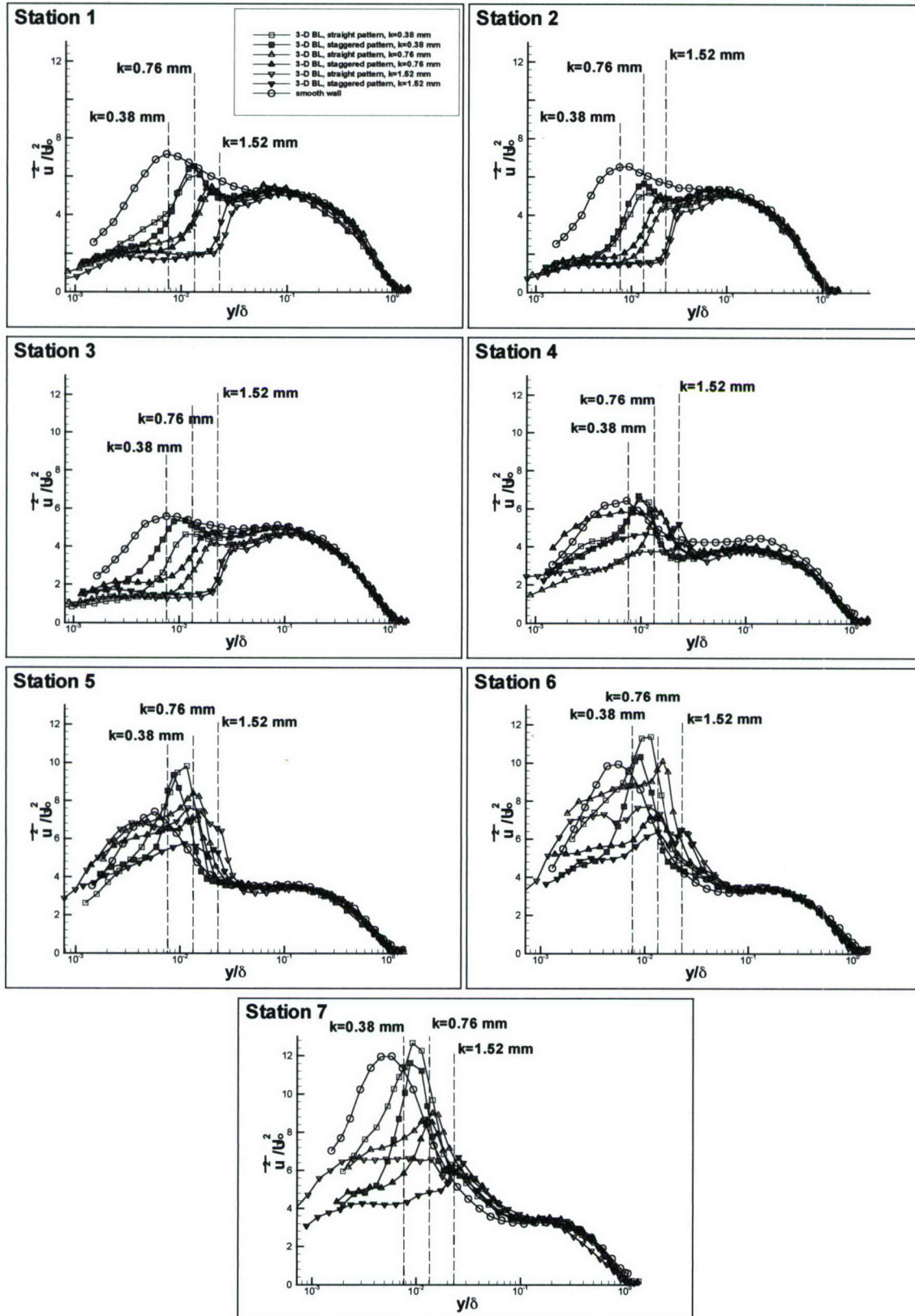


Figure 5.4.  $\overline{u^2}/U_w^2$  versus  $y/\delta$ , streamwise Reynolds normal stress profiles.

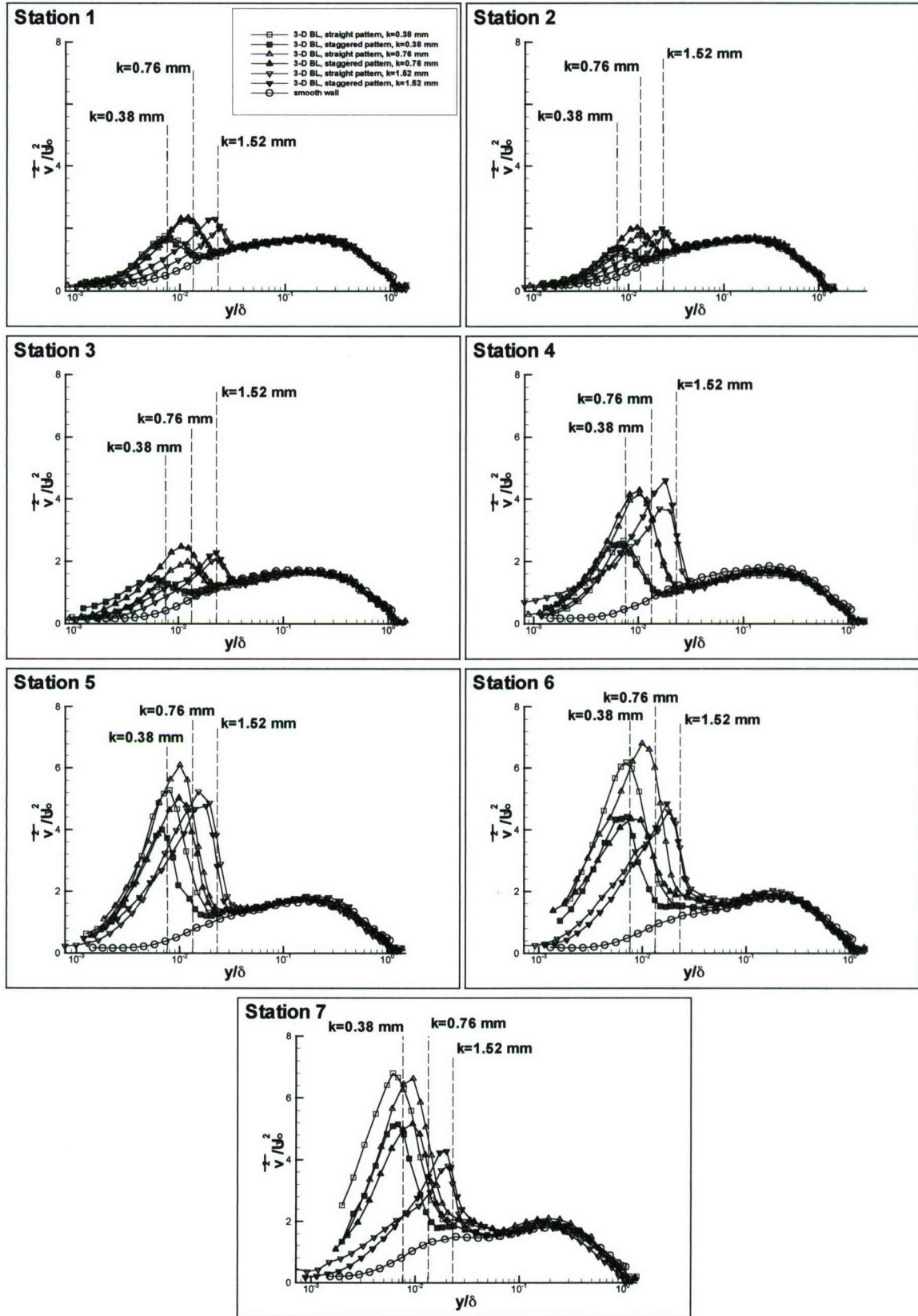


Figure 5.5.  $\overline{v^2}/U_\delta^2$  versus  $y/\delta$ , wall-normal Reynolds normal stress profiles.



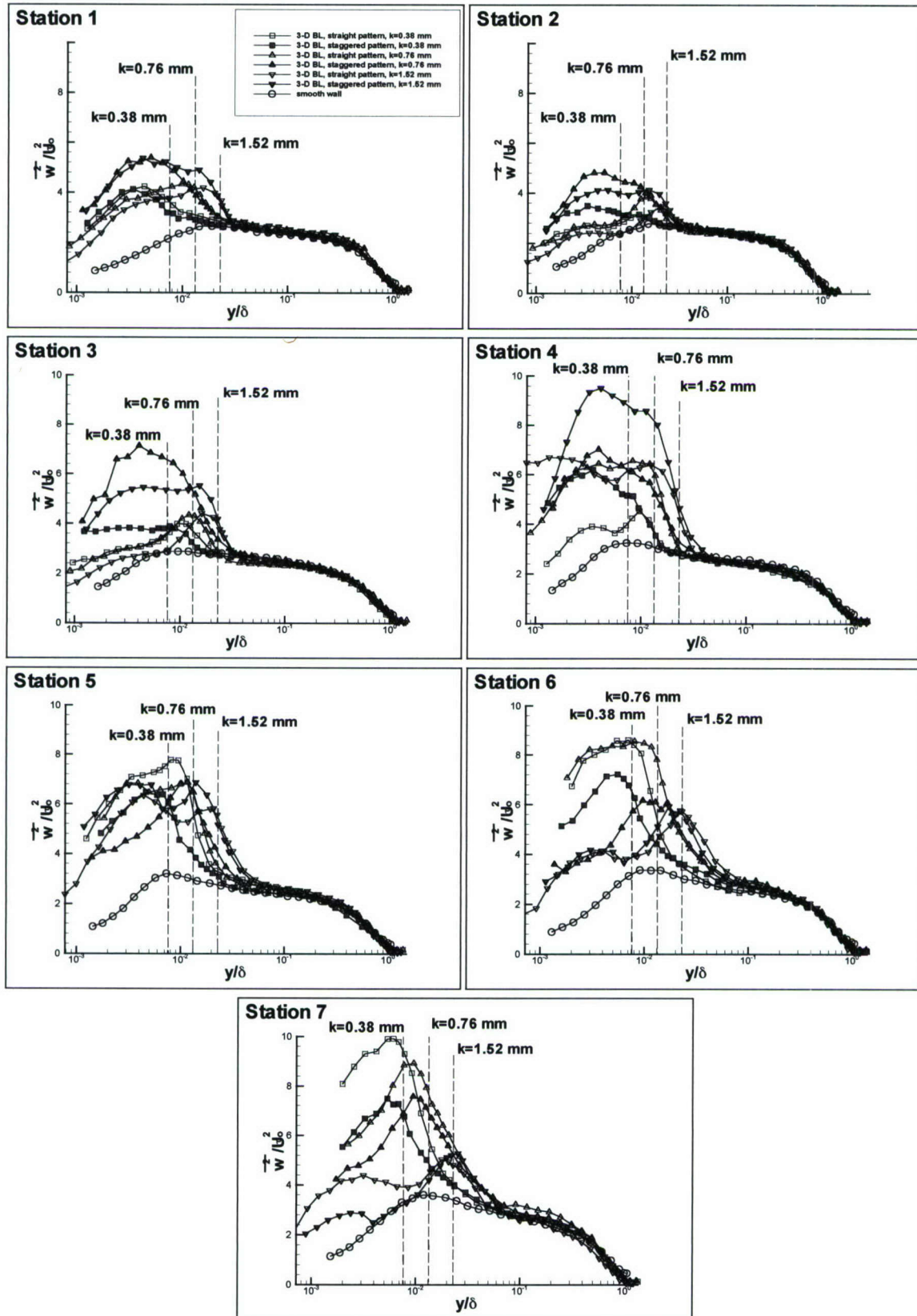


Figure 5.6.  $\overline{w^2}/U_w^2$  versus  $y/\delta$ , spanwise Reynolds normal stress profiles

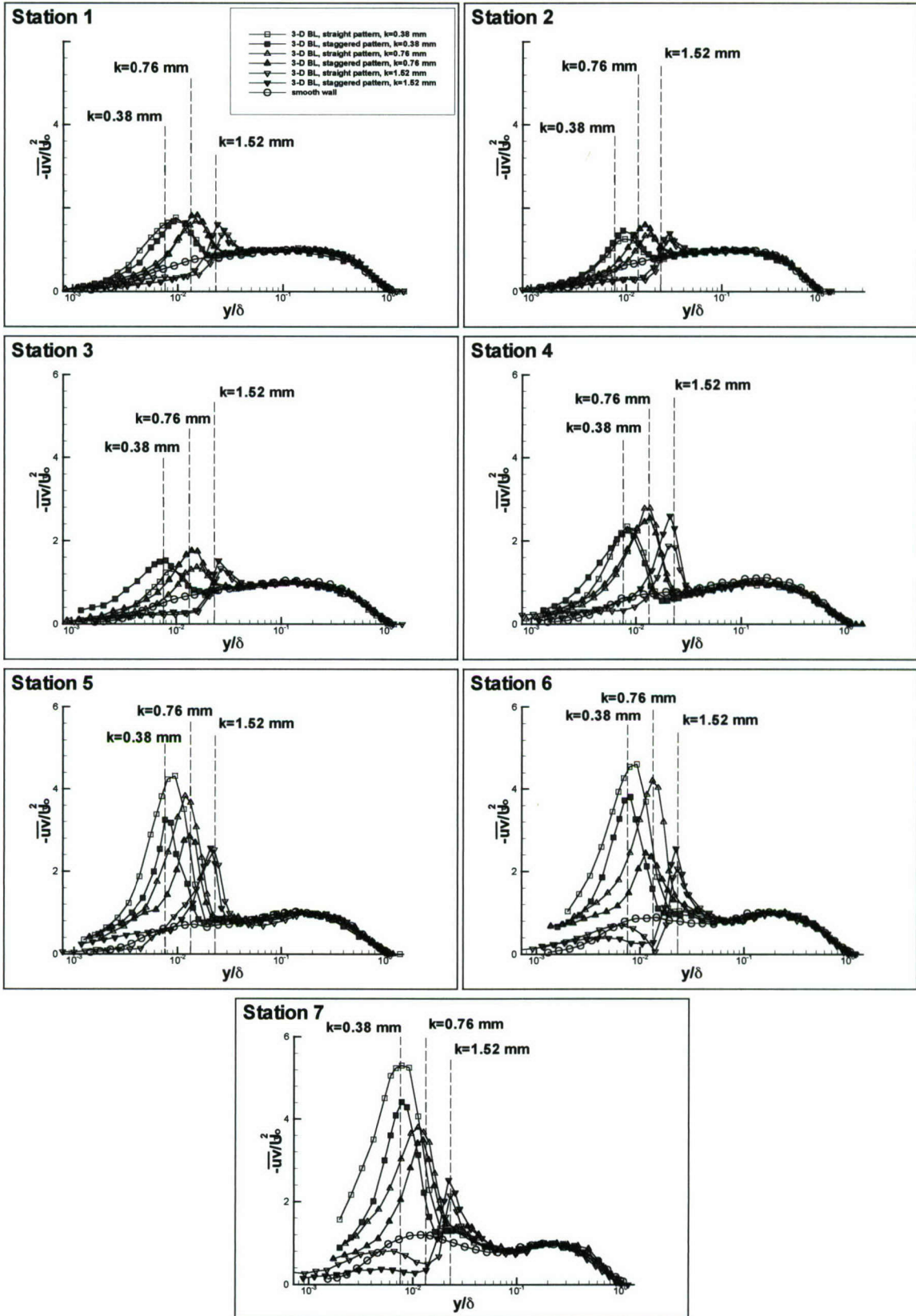


Figure 5.7.  $-\overline{uv}/U_w^2$  versus  $y/\delta$ , streamwise Reynolds shear stress profiles



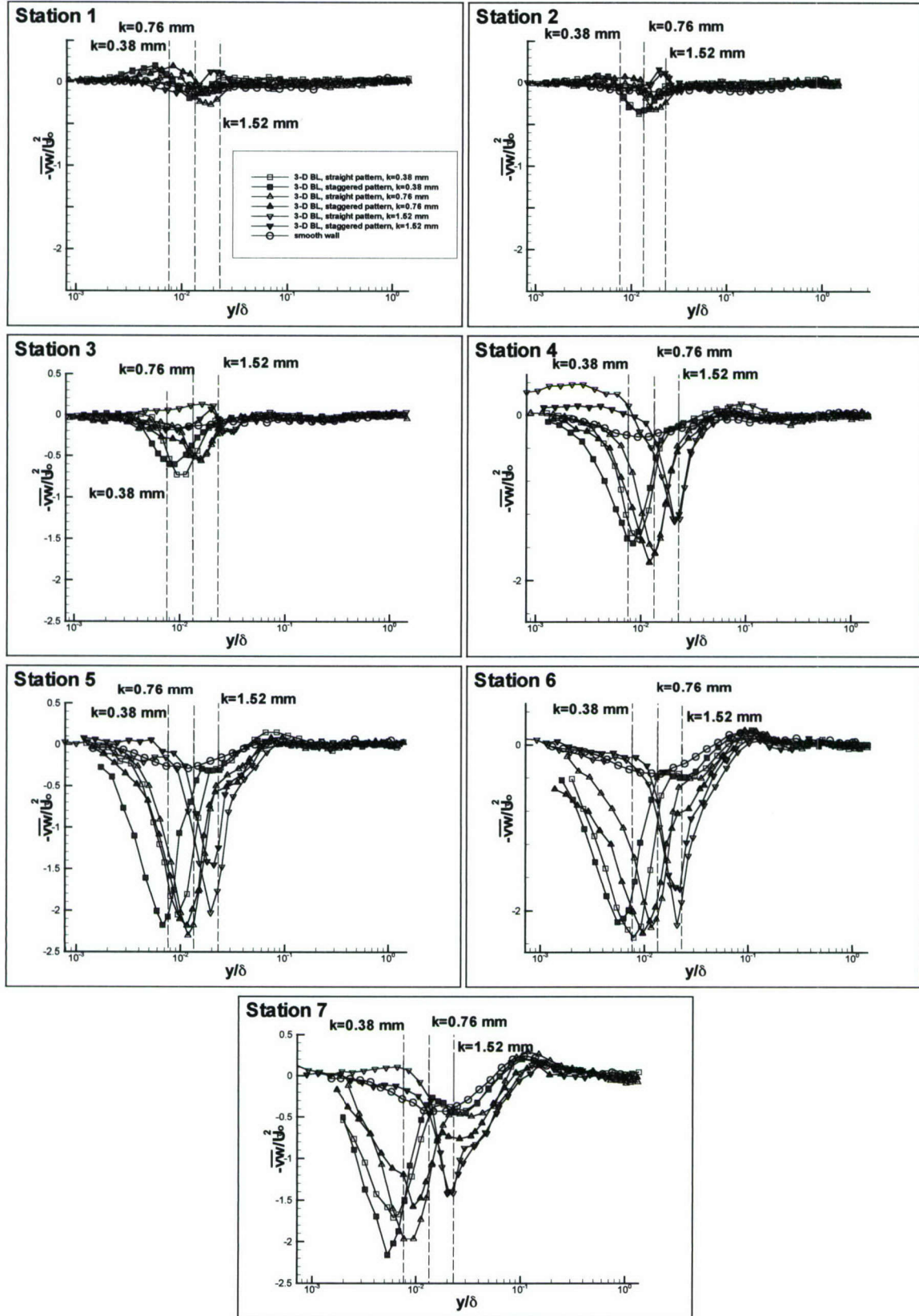


Figure 5.8.  $-\overline{vw}/U_\delta^2$  versus  $y/\delta$ , spanwise Reynolds shear stress profiles

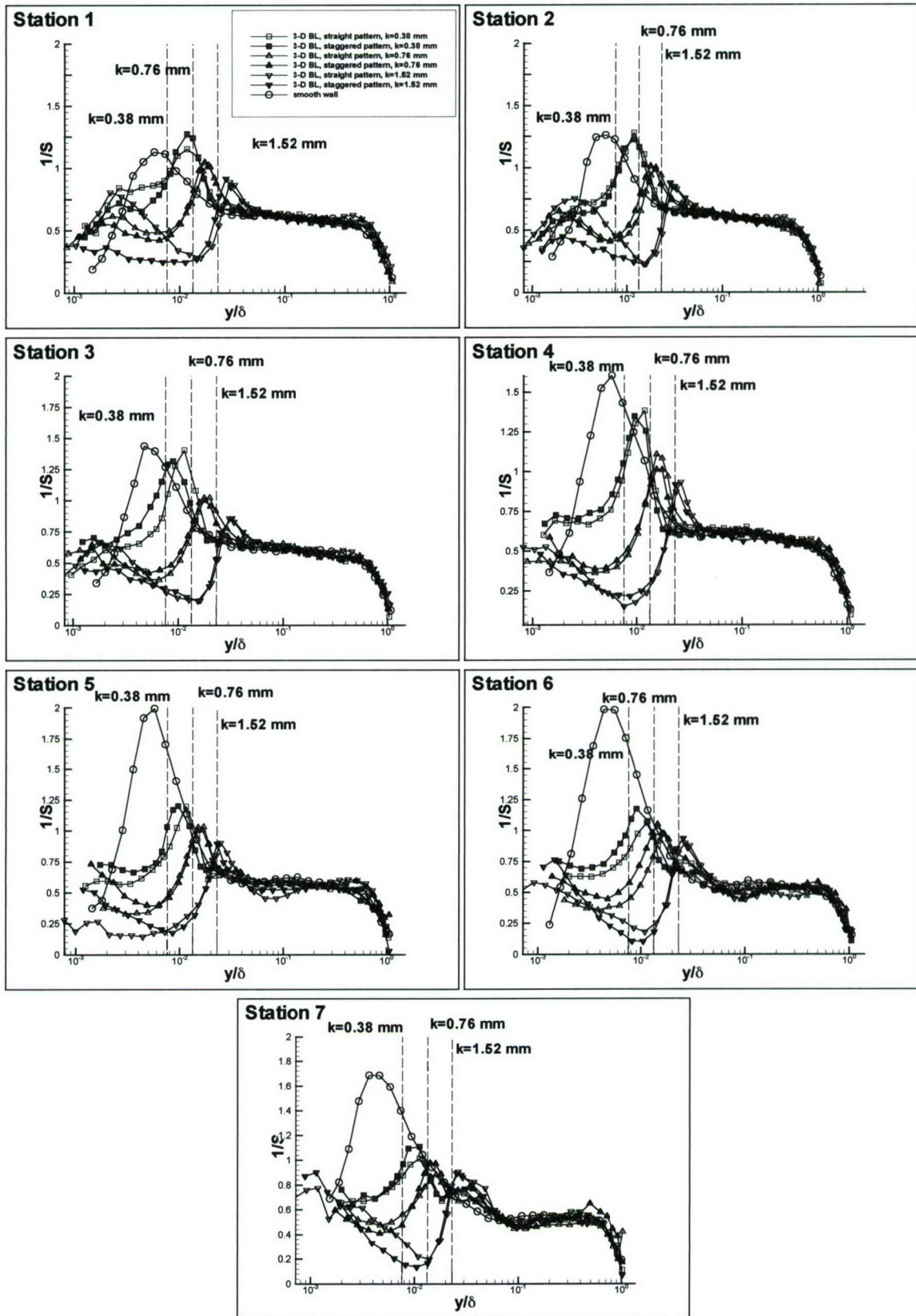


Figure 5.9. Structural parameter:  $1/S$  versus  $y/\delta$ .



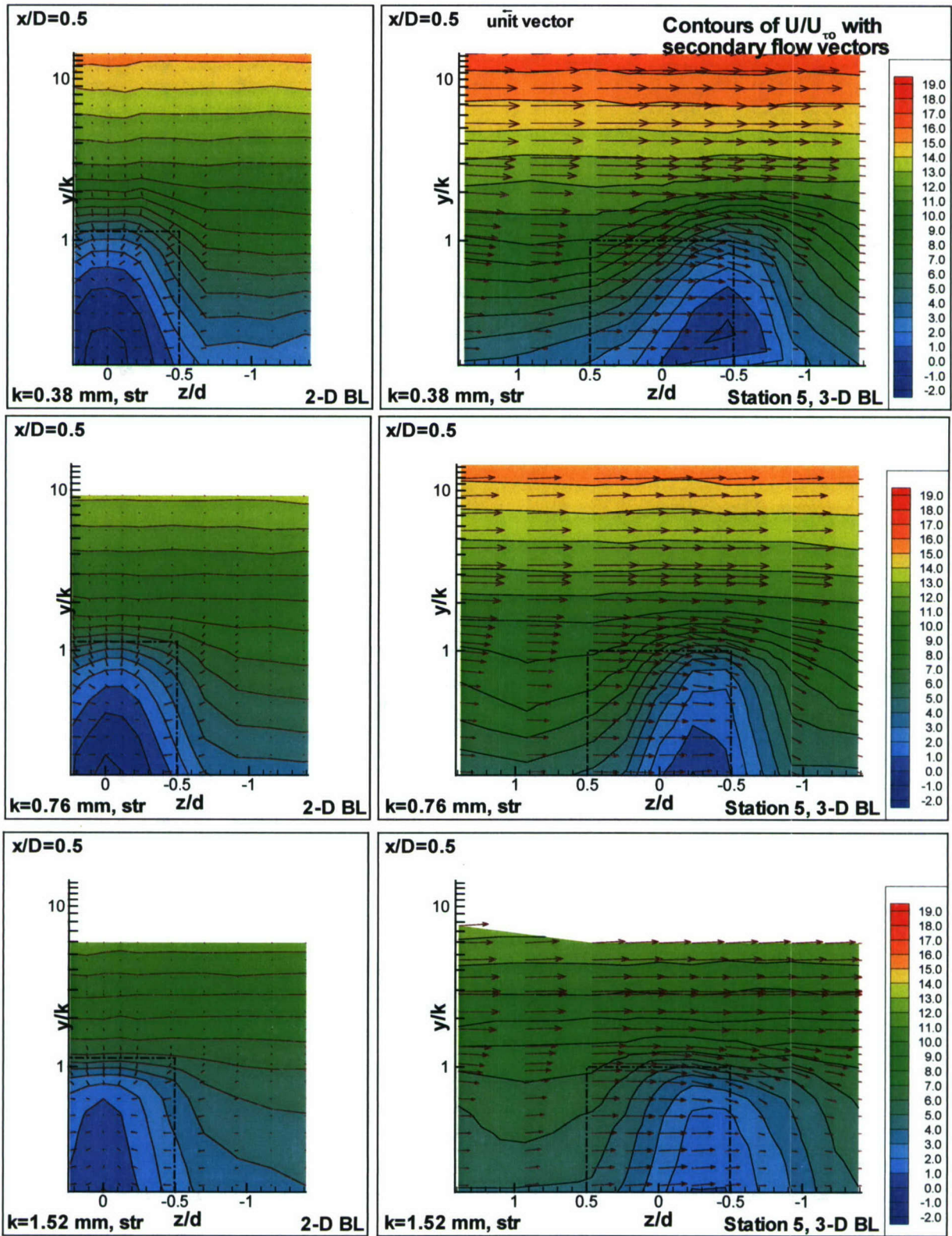


Figure 5.10. Semi-log contours of  $U/U_w$  in the  $y/k - z/d$  plane at  $x/D = 0.5$  with secondary flow vectors,  $V/U_w$  and  $W/U_w$  [ $k = 0.38 \text{ mm}$  (top row),  $k = 0.76 \text{ mm}$  (middle),  $k = 1.52 \text{ mm}$  (bottom)], (LHS: 2-D BL, RHS: Station 5, 3-D BL).

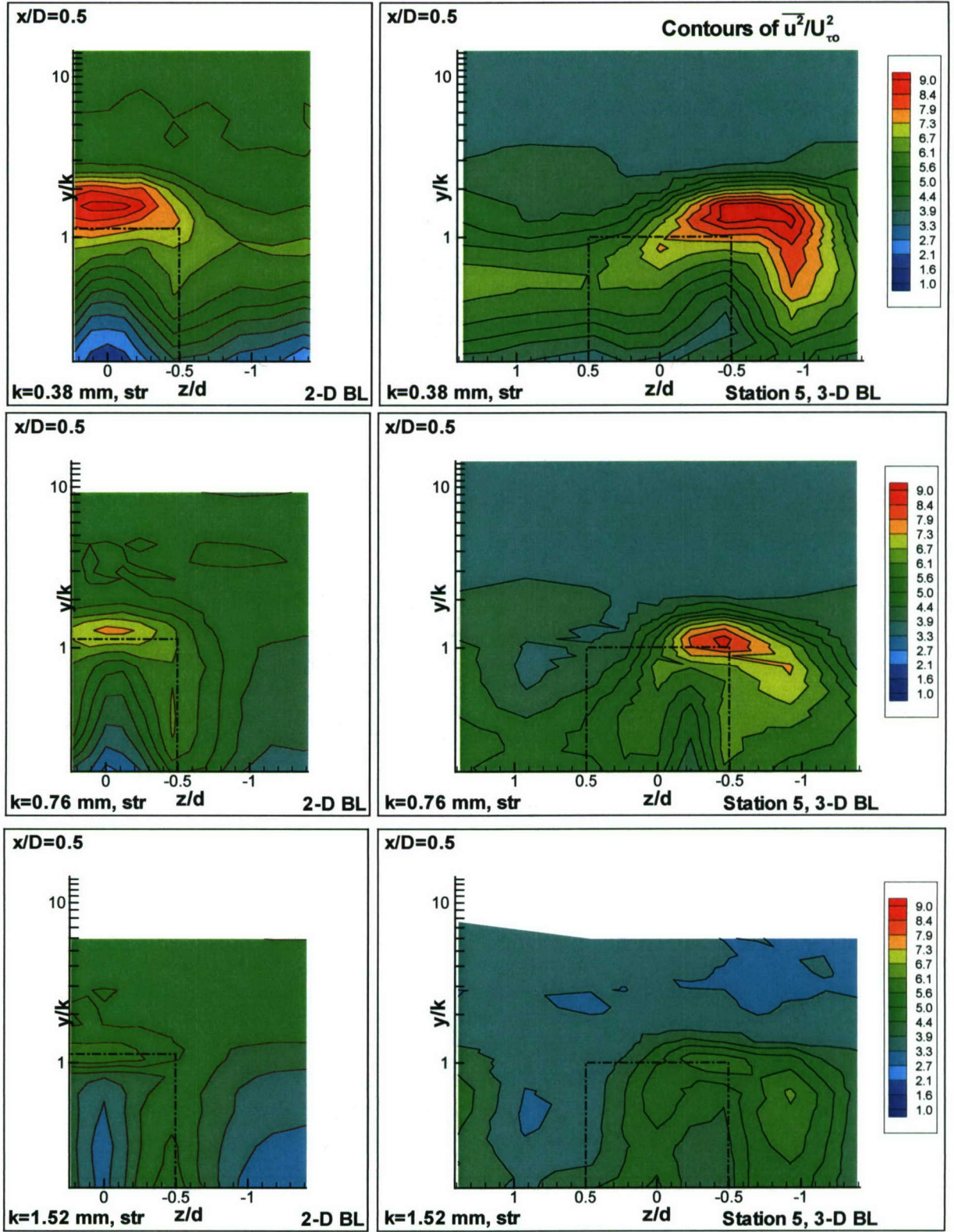


Figure 5.11 (a). Semi-log contours of  $\overline{u^2}/U_w^2$  in the  $y/k - z/d$  plane at  $x/D = 0.5$  [ $k = 0.38 \text{ mm}$  (top row),  $k = 0.76 \text{ mm}$  (middle),  $k = 1.52 \text{ mm}$  (bottom)], (LHS: 2-D BL, RHS: Station 5, 3-D BL).



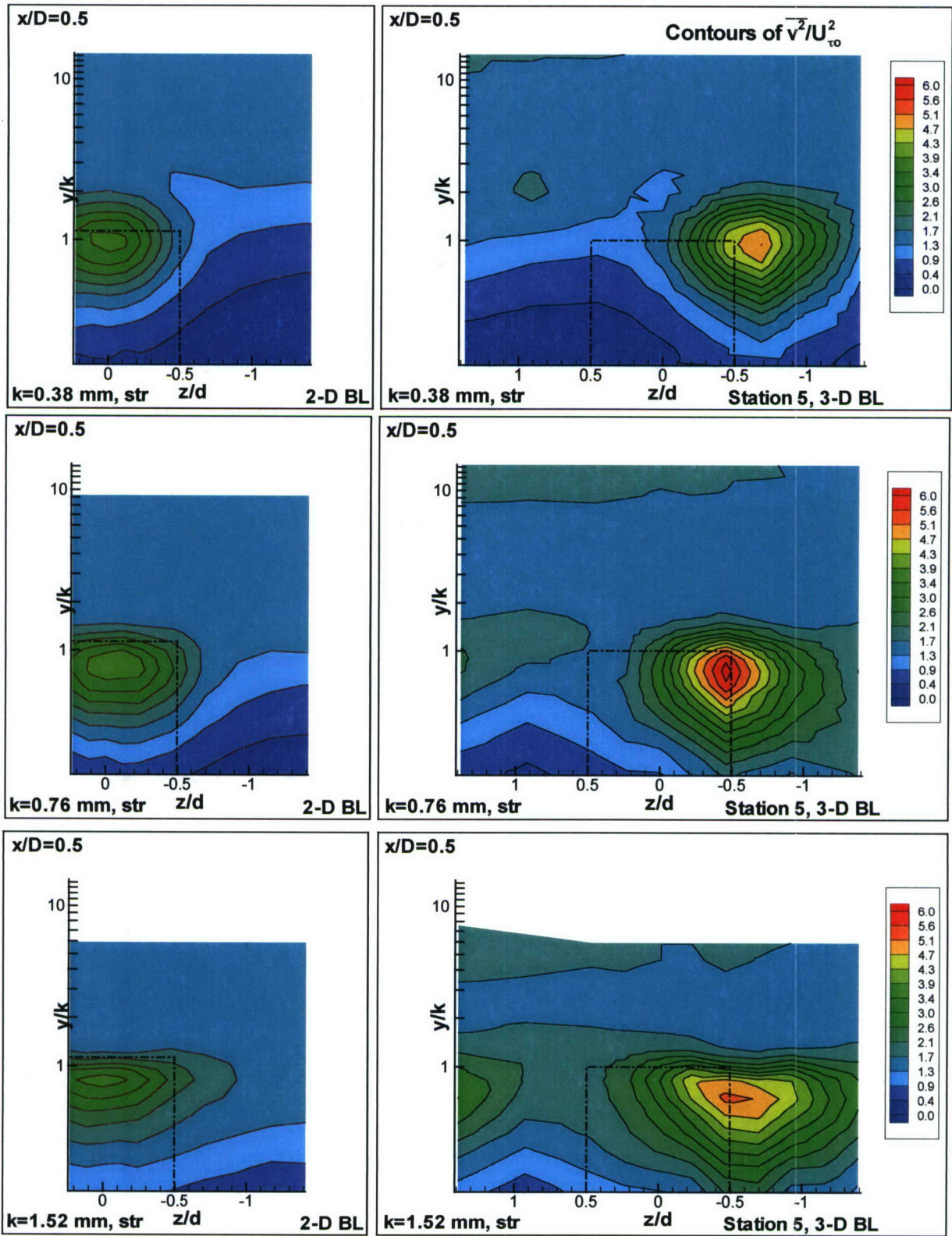


Figure 5.11 (b). Semi-log contours of  $\overline{v^2}/U_{\tau o}^2$  in the  $y/k - z/d$  plane at  $x/D = 0.5$  [ $k = 0.38\text{mm}$  (top row),  $k = 0.76\text{mm}$  (middle),  $k = 1.52\text{mm}$  (bottom)], (LHS: 2-D BL, RHS: Station 5, 3-D BL).

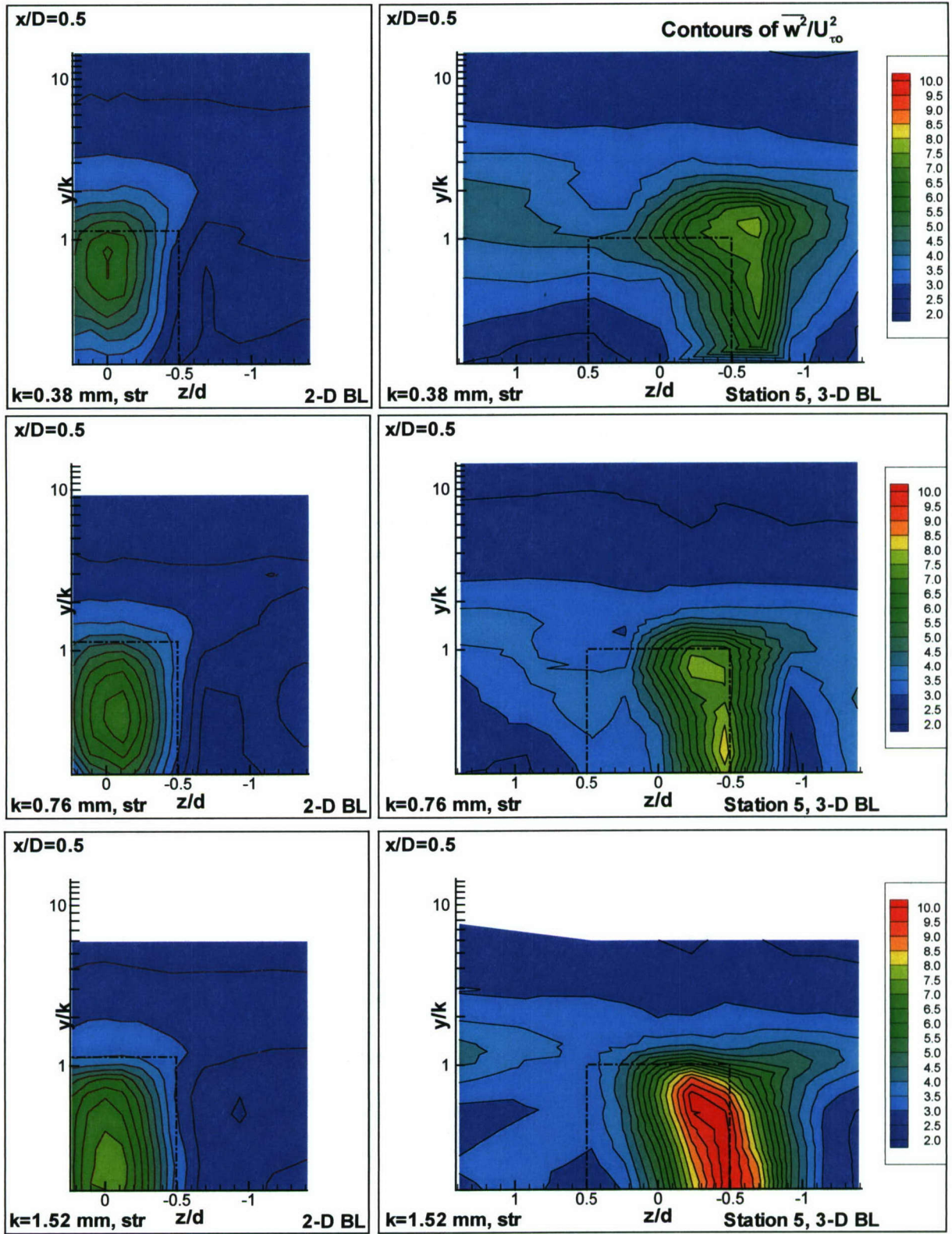


Figure 5.11 (c). Semi-log contours of  $\overline{w^2}/U_{\tau 0}^2$  in the  $y/k - z/d$  plane at  $x/D = 0.5$  [ $k = 0.38 \text{ mm}$  (top row),  $k = 0.76 \text{ mm}$  (middle),  $k = 1.52 \text{ mm}$  (bottom)], (LHS: 2-D BL, RHS: Station 5, 3-D BL).



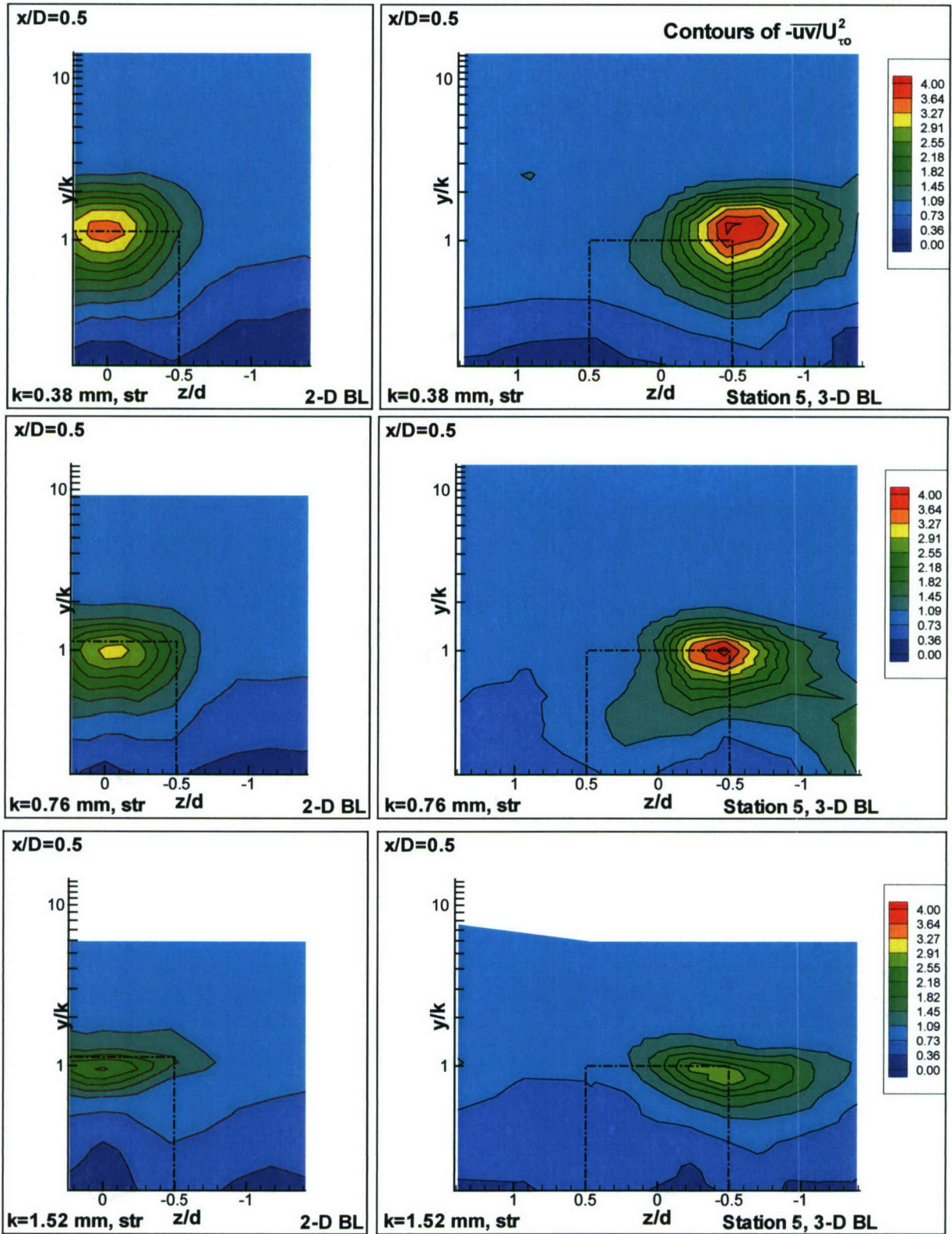


Figure 5.11 (d). Semi-log contours of  $-\overline{uv}/U_w^2$  in the  $y/k - z/d$  plane at  $x/D = 0.5$  [ $k = 0.38 \text{ mm}$  (top row),  $k = 0.76 \text{ mm}$  (middle),  $k = 1.52 \text{ mm}$  (bottom)], (LHS: 2-D BL, RHS: Station 5, 3-D BL).

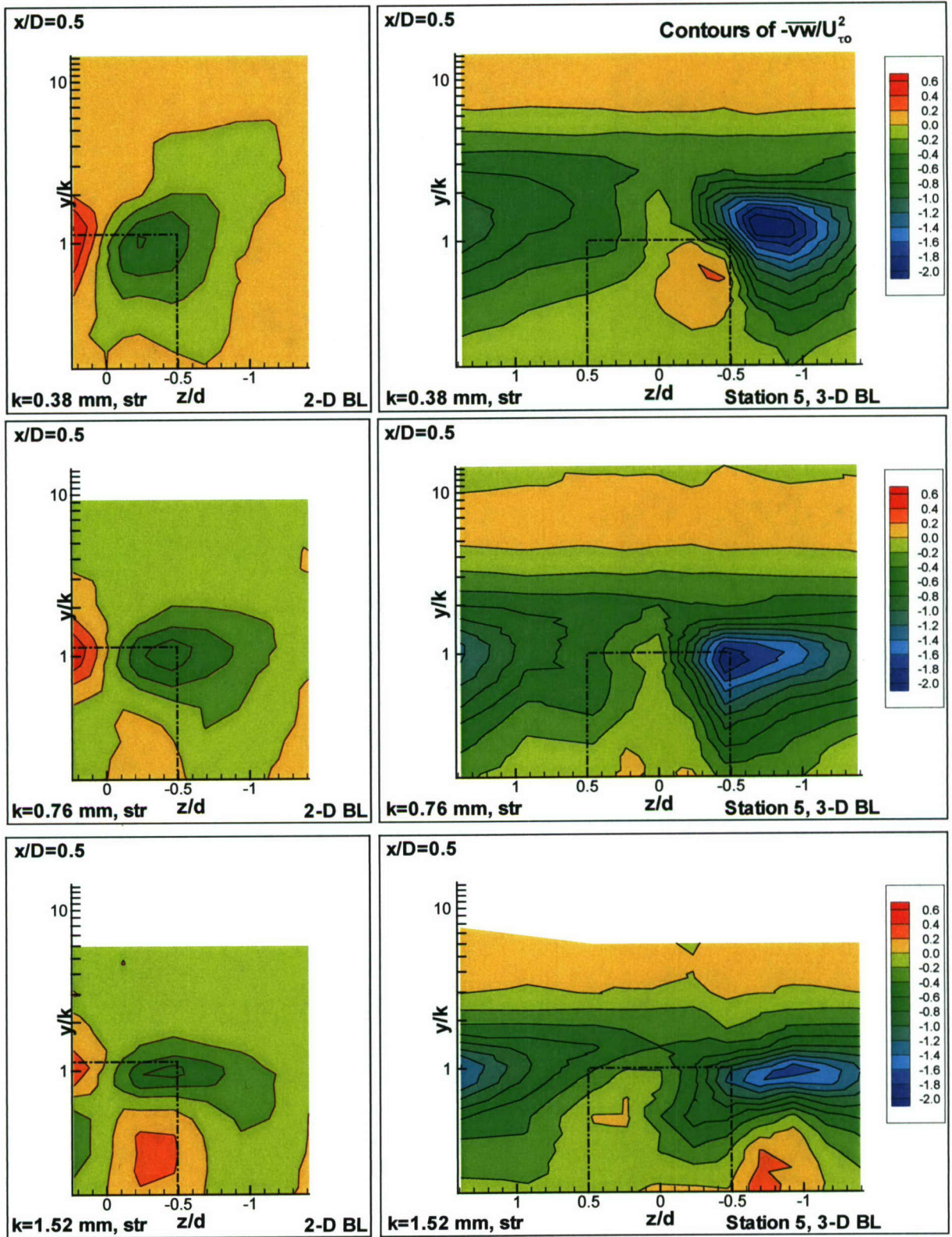


Figure 5.11 (e). Semi-log contours of  $-\overline{vw}/U_w^2$  in the  $y/k - z/d$  plane at  $x/D = 0.5$  [ $k = 0.38 \text{ mm}$  (top row),  $k = 0.76 \text{ mm}$  (middle),  $k = 1.52 \text{ mm}$  (bottom)], (LHS: 2-D BL, RHS: Station 5, 3-D BL).



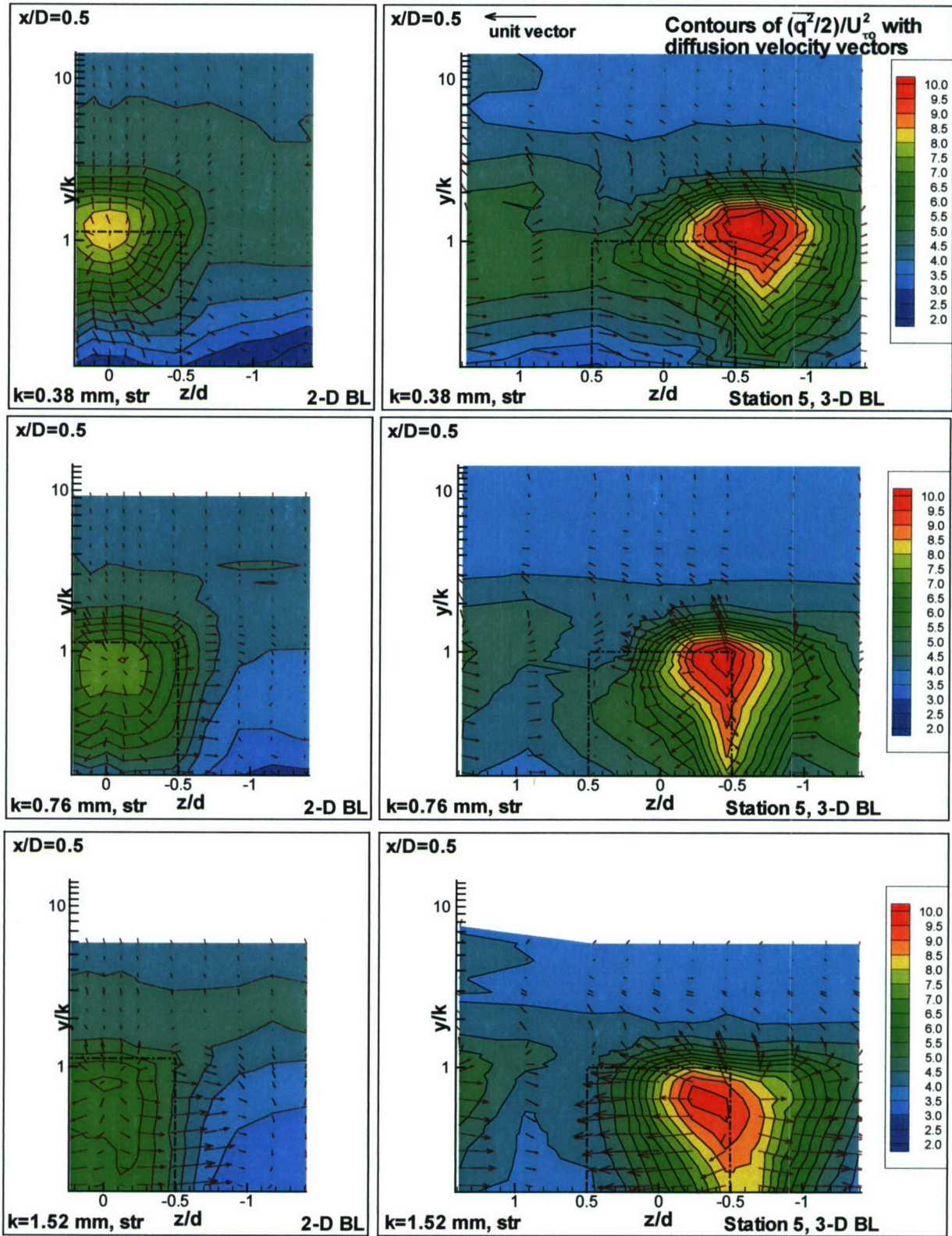


Figure 5.12. Semi-log contours of  $(\overline{q^2}/2)/U_w^2$  in the  $y/k - z/d$  plane at  $x/D = 0.5$  with diffusion velocities,  $V_q/U_w$  and  $W_q/U_w$  [ $k = 0.38 \text{ mm}$  (top row),  $k = 0.76 \text{ mm}$  (middle),  $k = 1.52 \text{ mm}$  (bottom)], (LHS: 2-D BL, RHS: Station 5, 3-D BL).

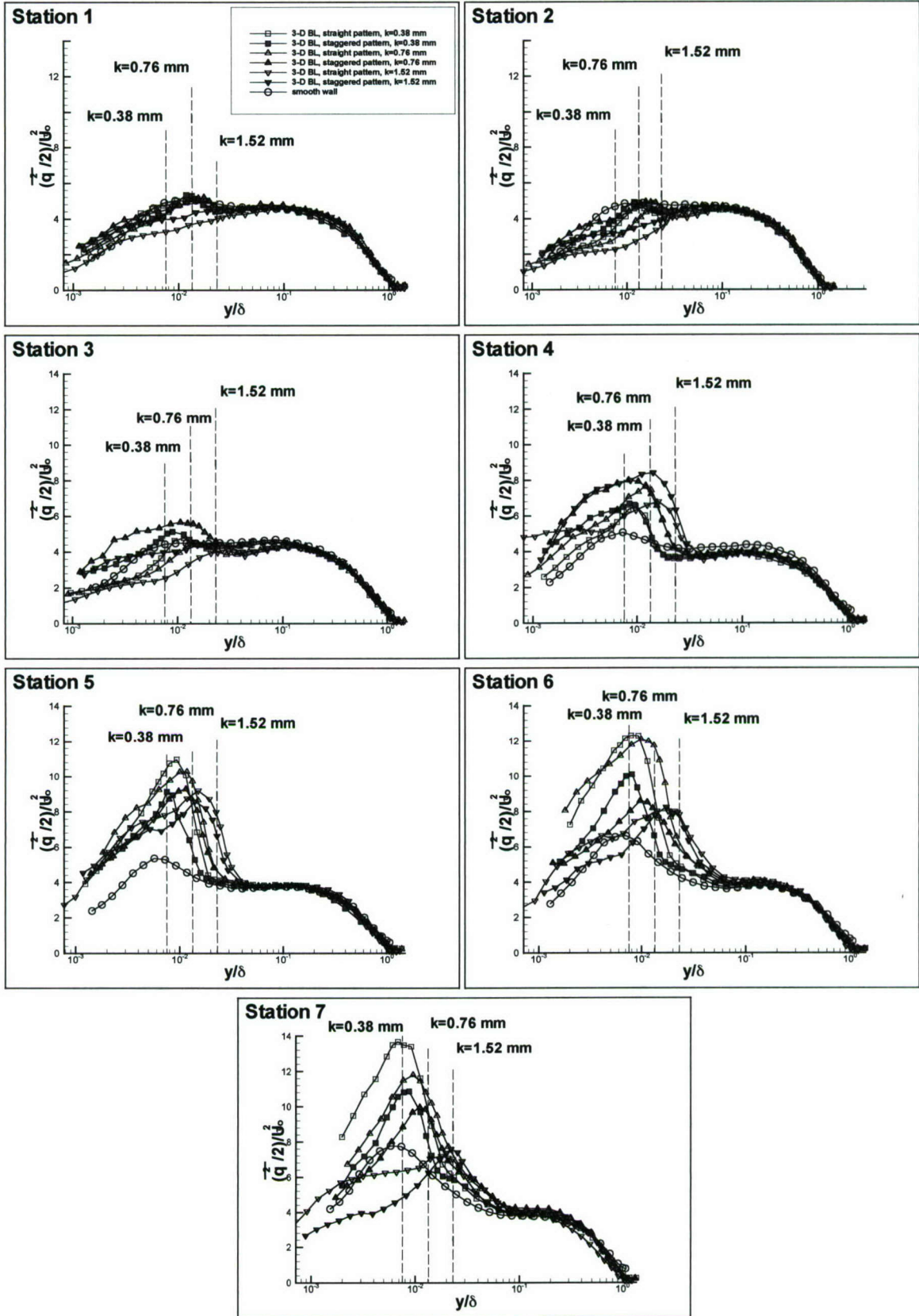


Figure 5.13.  $(\overline{q^2}/2)U_w^2$  versus  $y/\delta$ , TKE profiles



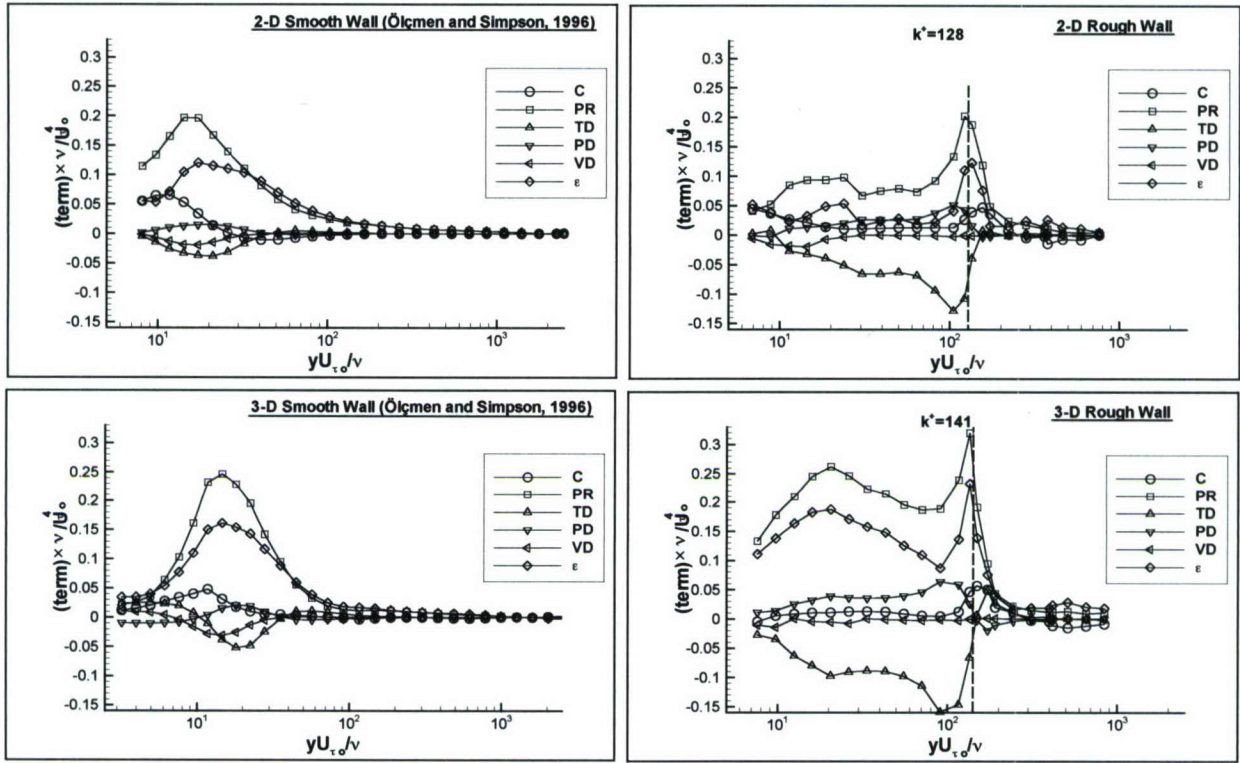


Figure 5.14. Variation of transport-rate budget of TKE,  $\overline{q^2}/2$ , normalized by  $U_{\tau o}^4/\nu$ , with  $yU_{\tau o}/\nu$ .

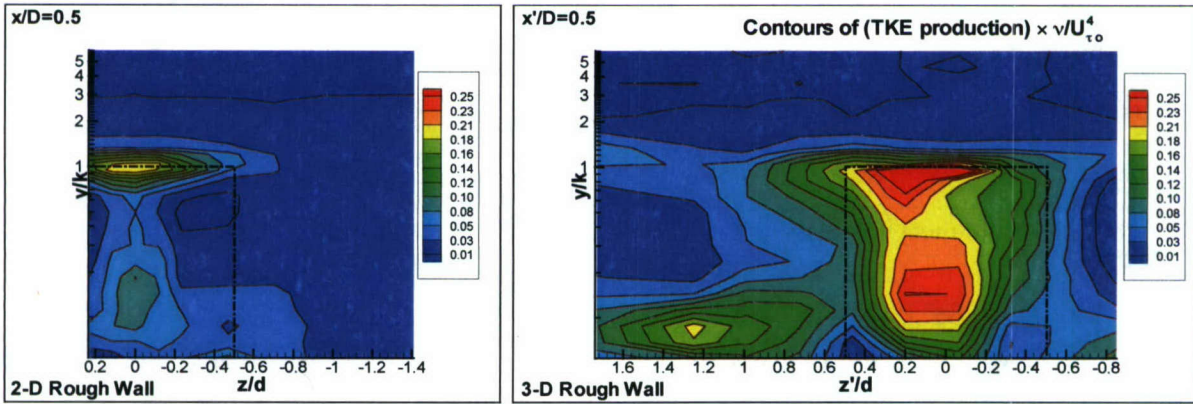


Figure 5.15 (a). Contours of TKE production rate normalized by  $U_{\tau o}^4/\nu$ : in the  $y-z$  plane along  $x/D=0.5$  for the 2-D rough-wall, and in the  $y-z'$  plane along  $x'/D=0.5$  for the 3-D rough-wall. Dashed lines show the outline of the cylinder.  $\alpha=28^\circ$ .

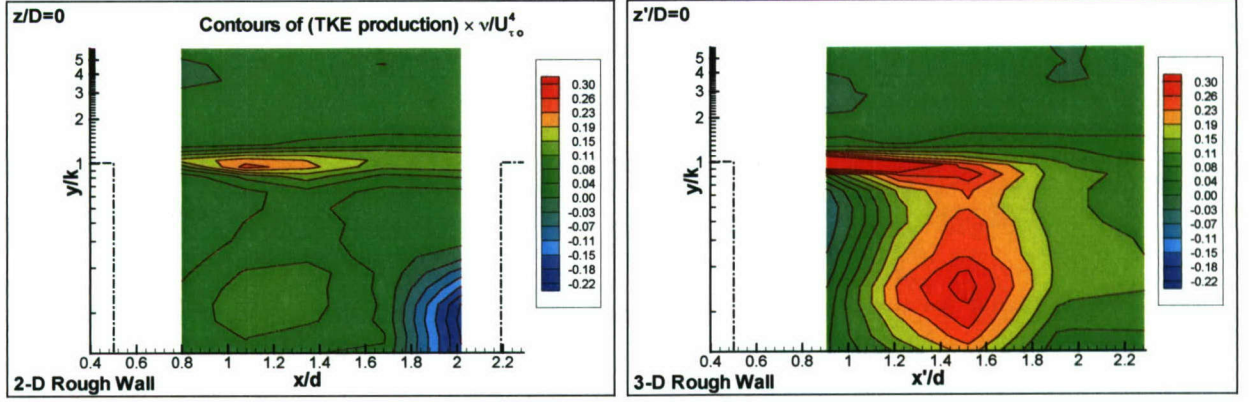


Figure 5.15 (b). Contours of TKE production rate normalized by  $U_{\tau_o}^4/\nu$  : in the  $x-y$  plane along  $z=0$  for the 2-D rough-wall, and in the  $x'-y$  plane along  $z'=0$  for the 3-D rough-wall.  $\alpha=28^\circ$ .

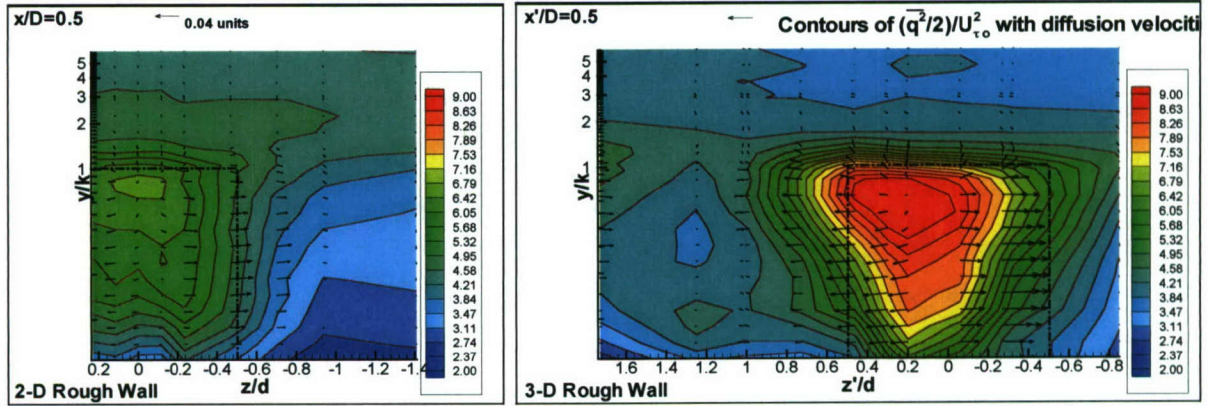


Figure 5.16 (a). Contours of TKE  $\left[\frac{(\overline{q^2})}{2}\right]/U_{\tau_o}^2$  with diffusion velocity vectors,  $V_q/U_{\tau_o} = \left[\frac{v\overline{q^2}}{\overline{q^2}}\right]/U_{\tau_o}$  and  $W_q/U_{\tau_o} = \left[\frac{w\overline{q^2}}{\overline{q^2}}\right]/U_{\tau_o}$  : in the  $y-z$  plane along  $x/D=0.5$  for the 2-D rough-wall, and in the  $y-z'$  plane along  $x'/D=0.5$  for the 3-D rough-wall.  $\alpha=28^\circ$ .

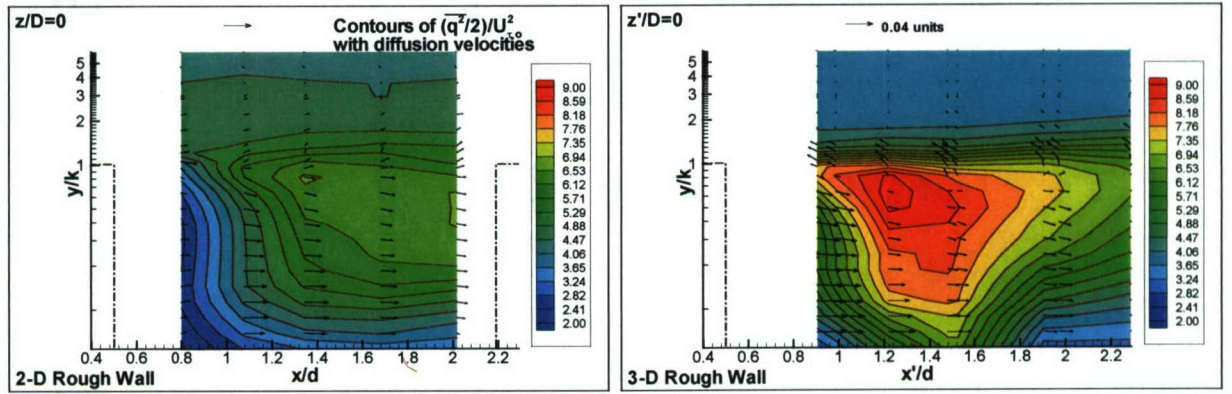


Figure 5.16 (b). Contours of TKE  $\left[\frac{(\overline{q^2})}{2}\right]/U_{\tau_o}^2$  with diffusion velocity vectors,  $U_q/U_{\tau_o} = \left[\frac{u\overline{q^2}}{\overline{q^2}}\right]/U_{\tau_o}$  and  $V_q/U_{\tau_o} = \left[\frac{v\overline{q^2}}{\overline{q^2}}\right]/U_{\tau_o}$  : in the  $x-y$  plane along  $z=0$  for the 2-D rough-wall, and in the  $x'-y$  plane along  $z'=0$  for the 3-D rough-wall.  $\alpha=28^\circ$ .



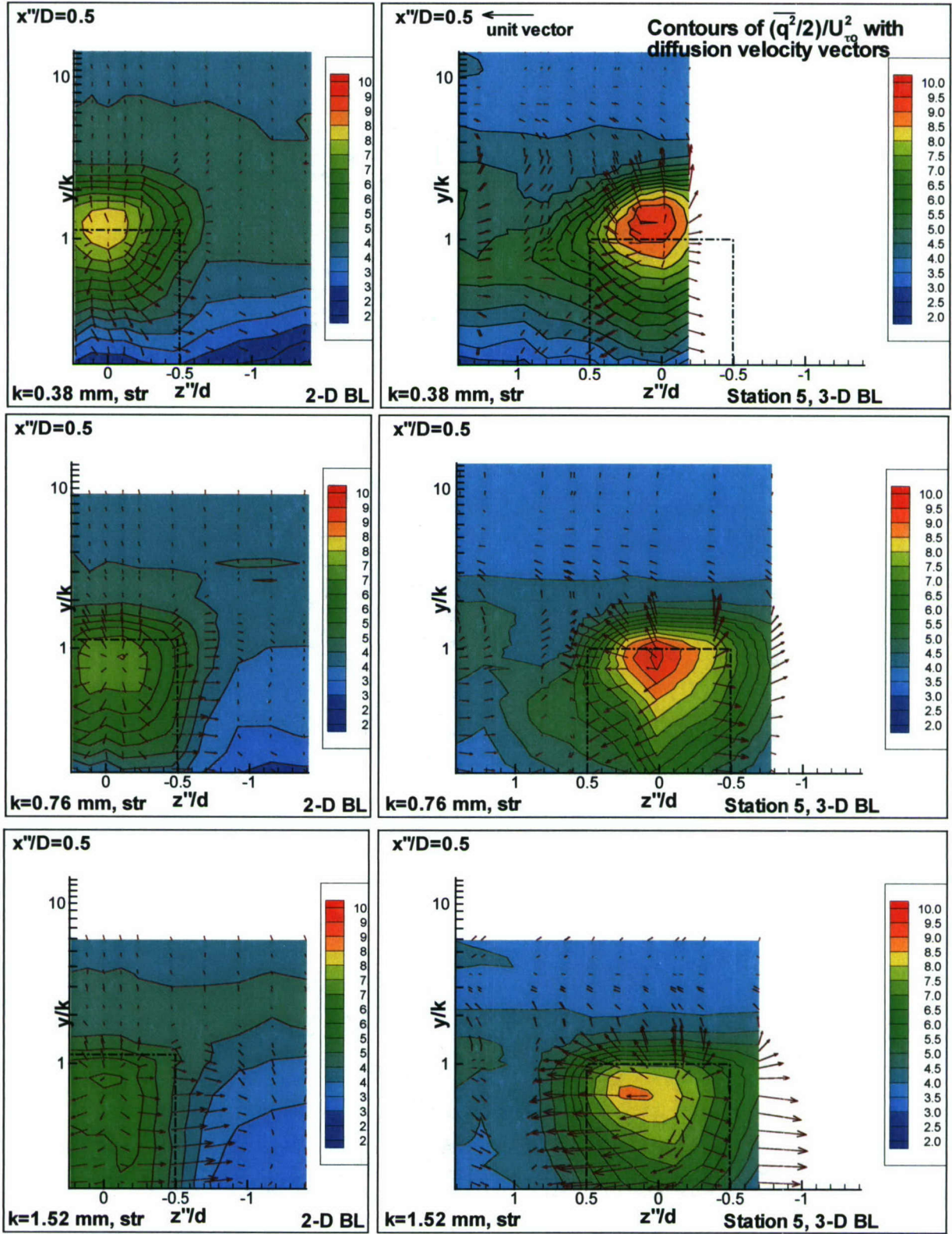


Figure 5.17. Semi-log contours of  $(\bar{q}^2/2)/U_w^2$  in the  $y/k - z''/d$  plane at  $x''/D = 0.5$  with diffusion velocities,  $V_q''/U_w$  and  $W_q''/U_w$  [ $k = 0.38 \text{ mm}$ ,  $\beta = 25^\circ$  (top row),  $k = 0.76 \text{ mm}$ ,  $\beta = 17^\circ$  (middle),  $k = 1.52 \text{ mm}$ ,  $\beta = 19^\circ$  (bottom)], (LHS: 2-D BL, RHS: Station 5, 3-D BL).

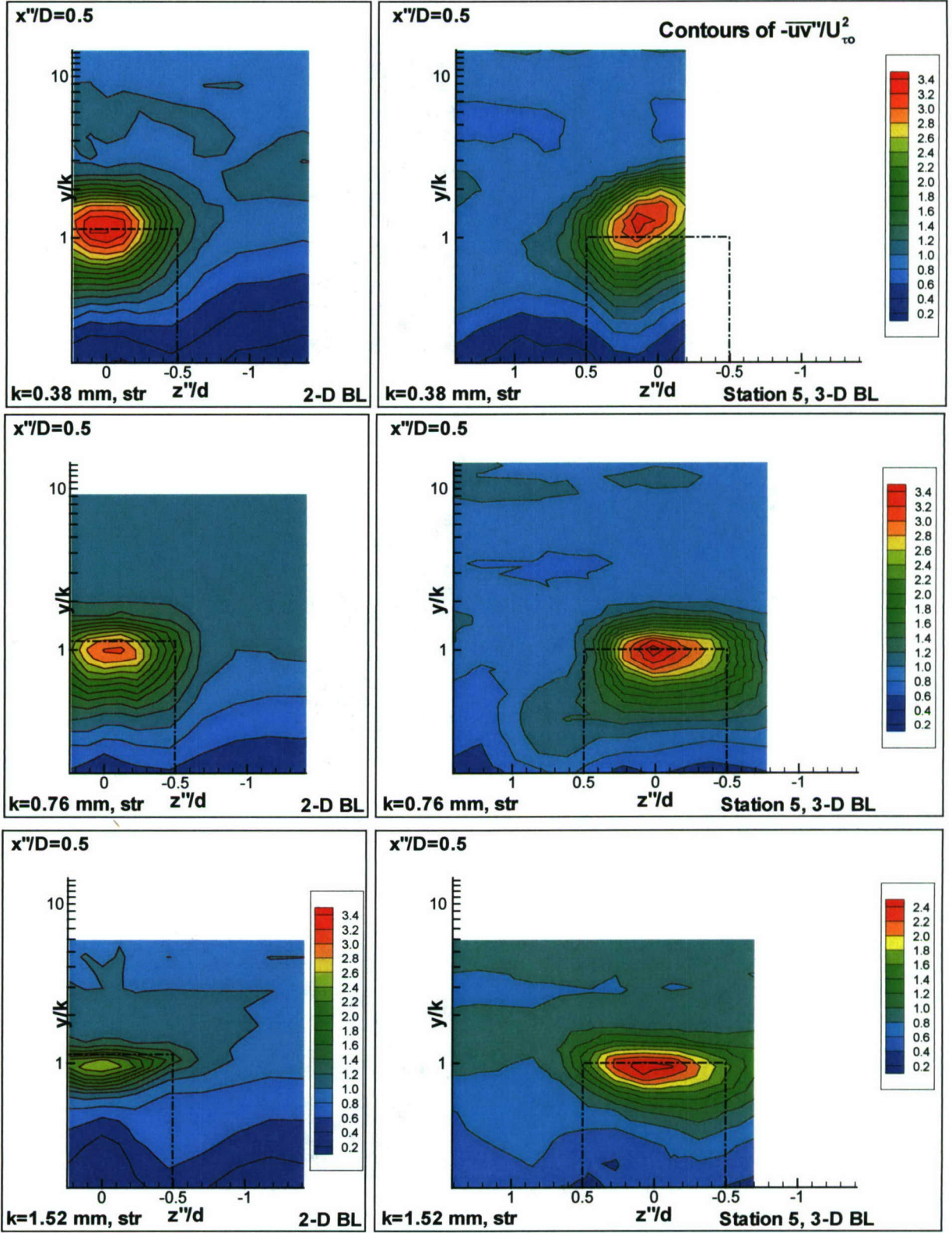


Figure 5.18. Semi-log contours of  $-\overline{uv''}/U_w^2$  in the  $y/k - z''/d$  plane at  $x''/D = 0.5$  [ $k = 0.38 \text{ mm}$ ,  $\beta = 25^\circ$  (top row),  $k = 0.76 \text{ mm}$ ,  $\beta = 17^\circ$  (middle),  $k = 1.52 \text{ mm}$ ,  $\beta = 19^\circ$  (bottom)], (LHS: 2-D BL, RHS: Station 5, 3-D BL).



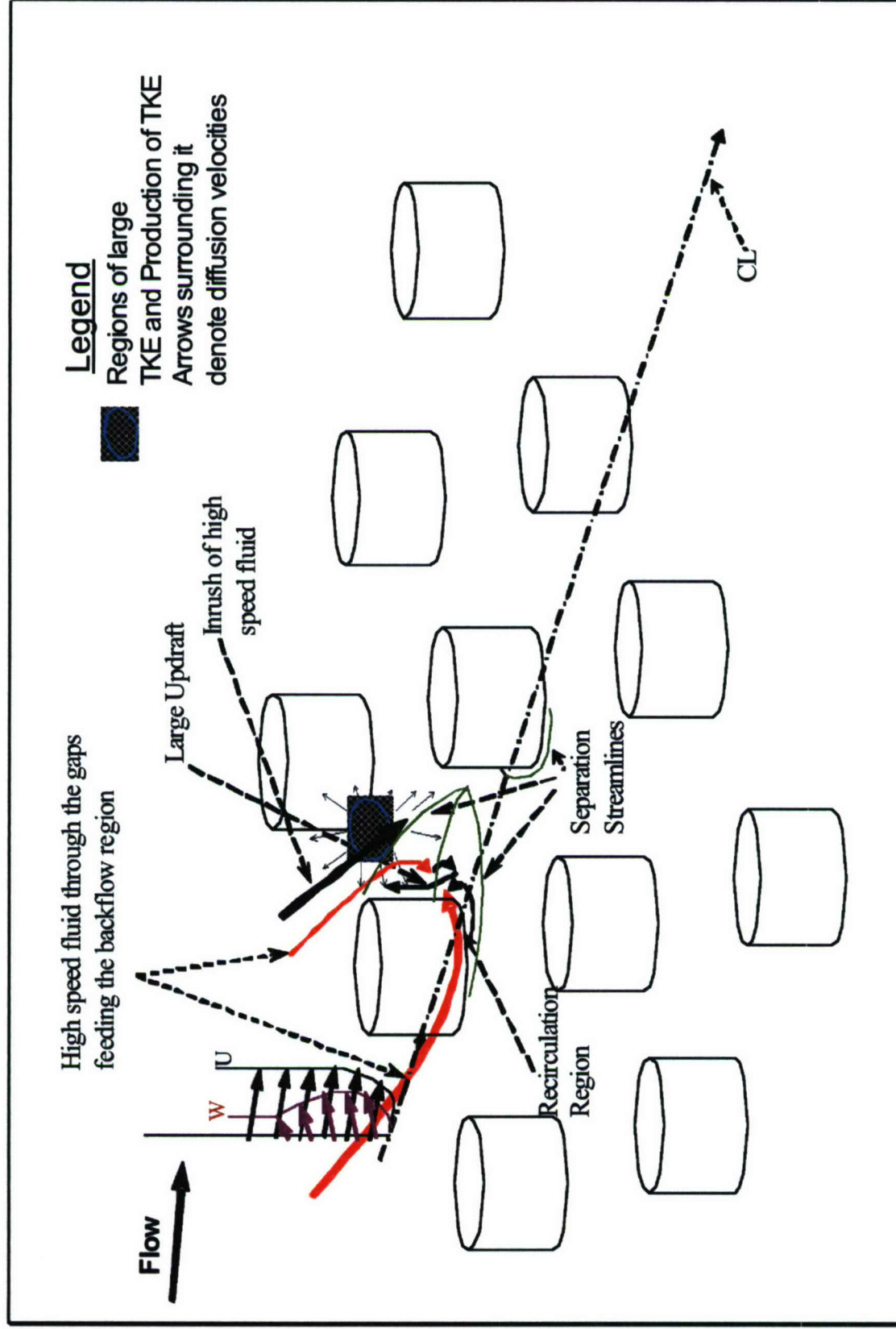


Figure 5.19. Schematic of the flow in a 3-D rough-wall turbulent boundary layer (straight orientation).

## Chapter 6    Comparison of the three flow cases: Single elements, 2-D TBL and 3-D TBL

While there are similarities in the flow structure as regards these three cases, there are a few notable differences too. This chapter deals with these aspects and aims to put them in the proper perspective. The discussions will draw from the figures and plots presented in the previous chapters.

As an upstream boundary layer approaches an individual roughness element, a roughness top vortex structure (RTVS) is formed at the top of roughness element and its trailing legs pass around the sides of the element, forming a pair of stream-wise vortices. The dimensions of the vortex trailing legs are of the order of the height and diameter of the roughness element, as also evidenced by the regions of distinctly large streamwise vorticity [Fig. 3.7 (a)]. The measurements on single roughness elements reveal that the RTVS causes an increased downwash behind the element, with greater momentum fluid being brought down closer to the wall behind the element. This greater momentum near the wall results in greater skin-friction drag. Large levels of stresses and TKE are produced in the neighborhood of the element height with peak levels located at the centerline, which is also the axis of flow symmetry. These high levels are generated at the confluence of the high speed shear layers emanating from the top and sides of the elements. The separated shear layers emanating from the top of the elements form a vortex pair which is responsible for the diffusion of the turbulence from the regions of high TKE production to rest of the boundary layers. The entire dynamics of the flow behind the single elements can be attributed to the roughness top vortex structure (RTVS) [Fig. 3.33].

While the flow structure in the case of the single elements can be explained by this vortex structure, the flow past a rough-wall is rather complex and different. Considerable streamwise vorticity behind the elements is produced just behind the elements where low speed ejecting fluid meets the fast moving sweeping fluid that is rushing over the elements (Fig. 4.9). This confluence occurs at the neighborhood of the element height and the streamwise vorticity produced in the trailing legs is of opposite sign to that generated by the single element RTVS. At locations closer to the mid-plane, considerably larger amounts of positive streamwise vorticity are generated as the high speed fluid is directed wallward and impinges on the subsequent element in the streamwise direction. The magnitudes of the streamwise vorticity in both the single elements and the 2-D rough-wall cases are comparable to each other. Unique to the distributed roughness elements (both 2-D and 3-D) is the generation of wall-normal mean vorticity which does not occur in the case of the single elements. The wall-normal vorticity also has magnitudes comparable to those for the streamwise mean vorticity (Fig. 4.10).

As regards the generation of the shear stresses and TKE, for both single elements and the 2-D rough-wall, large amounts are produced in the neighborhood of the element height with peak levels seen at the axis of flow symmetry which is the streamwise axis. For the 3-D rough-wall case, the peak levels are located at the axis where a “form of symmetry” is seen. While the locations for the large levels are the same for both the single elements and the rough-wall, the dynamics behind their generation are entirely different. In the case of the single elements, high levels are created at the element height at the confluence of the separated shear layers emanating from the top of the elements. This in combination with transport of turbulence towards the centerline by the convecting vortex pair is responsible for the production of Reynolds stresses and the TKE. Further, the same vortex pair is responsible for the diffusion of turbulence from the regions of high levels as it convects downstream.

As regards the rough-wall cases, the roughness elements create a large region of back flow behind them which is continuously fed by faster moving fluid flowing through the gaps in the rough-wall (Fig. 4.29). The fluid in the back flow region moves upward as low speed ejections where it collides with the intruding high speed flow, thus, leading to a strong mixing of shear layers. This is responsible for the generation of large levels of Reynolds stresses and turbulent kinetic energy (TKE) in the vicinity of the element height which is transported, primarily, by turbulent diffusion and to a



lesser extent by convection. Quadrant contributions to the Reynolds stresses reveal that the individual motions that contribute to their generations are similar as regards both single elements and 2-D rough-wall TBL. For both cases, the near-wall regions are dominated by sweeping motions while in the regions at the element height and beyond (into the outer layers), the ejection motions are predominant.

When the effect of flow three-dimensionality is imposed on the distribution of roughness elements, stark differences between the 2-D and 3-D cases are noted. There is a total absence of flow symmetry about the tunnel axis as is the case in the 2-D flows. The mean velocities, Reynolds stresses show obvious signs of skewing due to the imposition of spanwise pressure gradients and cross flow. Considerable levels of spanwise shear stresses are generated due to the significant gradients in the spanwise mean velocity profiles. The dynamics behind the generation and transport of Reynolds stresses and the TKE are the same in both cases. However, the direction of the propagation of regions of high production rates is different. In the case of the 2-D rough-wall, the direction is along the streamwise (tunnel) axis while in the case of the 3-D rough-wall, it is along the local mean velocity vector. This statement is especially true in the neighborhood of the element heights where large production rates are seen, with peak levels located along the direction of the velocity vector at the element height. The extent and magnitudes of the TKE generated aft of the elements is much more in the 3-D rough-wall TBL when compared to the 2-D case owing to the extra production term,  $-\overline{vw} \partial W / \partial y$ . A notable similarity in the behavior of the two rough-wall cases is the independence of the wall condition in the governance of the turbulence motions in the outer layers, as evidenced by the collapse of the profiles of Reynolds stresses and TKE in this region.



## Chapter 7 Conclusions

A thorough study of the mean flow and turbulence structure in two-dimensional and three-dimensional rough-wall turbulent boundary layers (TBL) has been carried out. The rough surface was generated using a uniform distribution of cylinders. This study was achieved in three parts: Part 1 dealt with the cylinders when placed individually in the turbulent boundary layers, Part 2 considered the effects when the same individual elements were placed in a sparse and regular distribution and in Part 3 the distributions were subjected to a 3-D turbulent boundary layer and the effects analyzed. In the first part, the individual elements were three cylinders of heights,  $k = 0.38 \text{ mm}$ ,  $0.76 \text{ mm}$  and  $1.52 \text{ mm}$ , each with a base diameter of  $1.98 \text{ mm}$ . In the second part on 2-D rough-wall turbulent boundary layers, the fetch for the rough-wall is generated by using these cylinders in *square* and *diagonal* patterns to yield six different roughness geometries, thus six cases of 2-D rough-wall boundary layers, with each distribution using cylinders of the same height. In the last part, the effect of mean flow three dimensionality on roughness is studied by subjecting the six cases of rough surfaces to a wing/body junction flow. Only some key conclusions are reviewed in this chapter as each of the chapters on the three-part study have a section detailing the individual conclusions.

The study on single elements revealed that the separated shear layers emanating from the top of the elements form a pair of counter rotating vortices that dominate the downstream flow structure. These vortices, termed as the roughness top vortex structure (RTVS), in conjunction with mean flow, forced over and around the elements, are responsible for the production of large Reynolds stresses in the neighborhood of the element height aft of the elements. The motions associated with the RTVS are responsible for the transport and diffusion of these large stress levels away from where it is produced. As measurements on single roughness elements have shown, this RTVS causes an increased downwash behind the element, with greater momentum fluid being brought down closer to the wall behind the element. This greater momentum near the wall results in greater skin-friction drag.

When the elements are placed in a distribution, the effects of RTVS are not apparent. The roughness elements create a region of separated back flow behind them which is continuously fed by faster moving fluid flowing over the elements. The fluid in the back flow region moves upward forming low speed ejections where it collides with the intruding high speed flow, leading to a strong mixing of shear layers. This is responsible for the generation of large levels of TKE in the vicinity of the element height. The sweeps of fluid are sources of large momentum and a quadrant analysis reveals that the sweeps penetrate all the way to the wall. This behavior is consistent with the prior studies on rough-wall TBL (Grass, 1971, Tomkins, 2001).

One of the key differences between the flow aft of the single elements and the distributed elements is the structure of the roughness top vortex. The flow separates at the top of the roughness elements with shear layers that convect as a vortical pair. However, in the case of the distributed elements, these vortical structures are overwhelmed by the intense mixing that occurs at the confluence of the high speed fluid over the top with the ejecting fluid from the back flow regions. Another difference is that the ejecting fluid is seen as an upwash of fluid as opposed to the strong downwash due to the RTVS as in the case of the single elements. Further, the upwash of fluid in the case of the distributed roughness is seen to generate regions of negative streamwise vorticity aft of the elements as opposed to the positive streamwise vorticity seen in the case of the single elements. Also, of significance is the ability of the distributed wall to generate large amounts of wall-normal vorticity.

Further, for the 2-D rough-wall TBL, the measurements of mean velocity  $U$  confirm the well-known fact that the velocity-defect law is similar for both smooth and rough surfaces, and the semi-logarithmic velocity-distribution curve is shifted by an amount  $\Delta U^+$  depending on the height of the roughness element showing that  $\Delta U^+$  is a function of  $k^+$  and roughness density parameter,  $\lambda$ . The magnitude of this intercept,  $\Delta U^+$ , also known as the roughness function, increases with the increase in the roughness height. Several correlations that relate the roughness function to height and roughness density were tested with the present data-set. The correlations of Simpson (1973) were found to fit the



experimental data better than the newer correlations. A novel modification was introduced to determine the law of the wall intercept for transitionally rough flows and this leads to a better comparison with the Simpson correlation.

As regards the 3-D rough-wall layers, the spanwise pressure gradients imposed by the flow lead to large skewing of the mean flow and turbulence stresses. The fact that  $W/U_e$  versus  $y/\delta$  profiles, for both smooth as well as rough-wall layers, are the same above 3 element heights seems to indicate that the time-averaged mean vorticity at each station is the same albeit with different vorticity fluxes from the wall. The higher the roughness elements' height the faster is the diffusion of turbulence from wall to the outer layers. The effect of roughness pattern orientation is seen in the mean flow and turbulence structure only up to 3 roughness heights from the wall in both 2-D as well as 3-D boundary layers. The transport rate budget of TKE brings out the relative importance of the various terms (that contribute to it) in the different regions of the TBL. The budgets for 2-D and 3-D TBL reveal that the dominant terms are production, diffusion and dissipation. Most of the TKE is produced in the neighborhood of the element height and is transported away from this region by the fluctuations. While the transport of TKE below the element height is primarily governed by sweep motions, that above the element height and beyond into the outer layers is governed by ejection motions.

From the results on the single elements and their distributions, it is possible to conceptualize an arbitrary rough-wall as a superposition of individual roughness elements, at least for sparse distributions. The elements forming this arbitrary rough-wall would generally be "peaky" in shapes as shown in Fig. 7.1. Since it is the larger elements in the rough-wall that dominate the flow structure, one can use a filtering technique to smooth out elements that are of the order of the Kolmogorov scales and only retain the remaining elements. One can then approximate the remaining elements as a discrete and sparse distribution and use the results obtained from the present study to analyze its effects *a priori*. The effects of the elements on the mean and turbulent structure, displayed in this figure, are based on the results garnered from the present study.

The issue of roughness has several parameters that govern the flow structure and several empirical correlations for determining the roughness functions are in vogue. A better correlation needs to be derived to correlate roughness functions with the various parameters with the help of the existing data-sets. The parameters must include the roughness height, shape, density and the manner of distribution of the roughness elements. While the present study has satisfied the dearth of a systematic study that examines the flow physics of rough-wall TBL with sparse distributions and low  $k/\delta$  values, there still remain vast areas where an improved understanding of the flow structure is needed. Future directions should invoke research on rough-wall layers with denser distributions and higher  $k/\delta$  values. There is a need for studies on rough-walls containing different shapes of 3-D objects distributed in different configurations thus providing various regimes of roughness density and  $k^+$ . Denser geometries would promote a greater flow interaction between the roughness elements and would lead to a different flow structure too. Sufficiently higher elements could even lead to an absence of a semi-logarithmic mean velocity region and this would imply a different flow aspect. As regards the individual element shape in a distribution, a 3-D roughness element with a Gaussian shape profile would be a good representative element to perform these suggested studies in the future.

## Figures

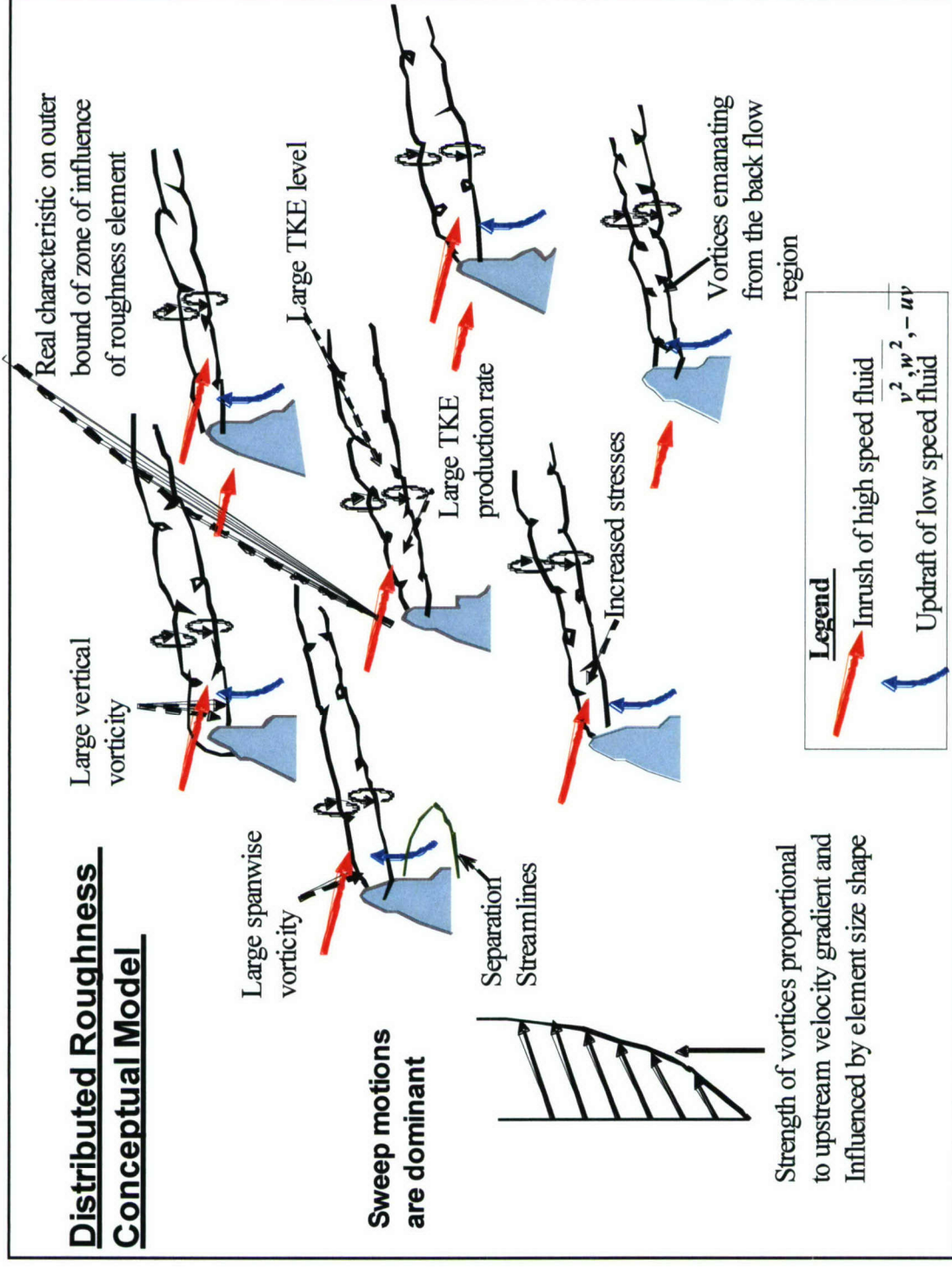


Figure 7.1. A conceptualized view of an arbitrary rough-wall.



## References

- Anderson, S. D., and Eaton, J. K., (1989), Reynolds stress development in pressure-driven three-dimensional turbulent boundary layers, *J. Fluid Mech.*, **202**, 263-294.
- Andreopoulos, J. and Bradshaw, P., (1981), Measurements of turbulence structure in the boundary layer on a rough surface. *Boundary-layer Meteorol.*, **20**, 201-213.
- Antonia, R. A., and Luxton, R. E., (1971), The response of a boundary layer to a step change in surface roughness. Part 1. Smooth to rough. *J. Fluid Mech.*, **48**, 721-761.
- Arie, M., Kiya, M., Tamura, H., and Kanayama, Y., (1975a), Flow over rectangular cylinders immersed in a turbulent boundary layer (Part 1, Correlation between pressure drag and boundary-layer characteristics). *Bull. JSME*, **18**, 1260-1268.
- Arie, M., Kiya, M., Tamura, H., Kosugi, M., and Takaoka, K., (1975b), Flow over rectangular cylinders immersed in a turbulent boundary layer (Part 2, Flow patterns and pressure distributions). *Bull. JSME*, **18**, 1269-1276.
- Ashill, P.R., Fulker, J.L., and Hackett, K.C., (2002), Studies of flows induced by Sub Boundary Layer Vortex Generators (SBVGs). *AIAA Paper 2002-0968*.
- Bandyopadhyay, P. R., and Watson, R. D., (1988), Structure of rough-wall turbulent boundary layers. *Phys. Fluids*, **31**, 1877-1883.
- Barrett, R.V., Rickards, J., Swales, C., and Brake, C.J., (1993), Enhanced performance of a cross-coupled three-dimensional laser doppler anemometer for small scale flow surveys using improved alignment and operational procedures, *Proc. ICIASF '93*, St. Louis, USA, Sep 1993.
- Bennington, J., (2004), Effects of various shaped roughness elements in two-dimensional high Reynolds number turbulent boundary layers, MS Thesis, Aug 2004, Department of Aerospace and Ocean Engineering, Virginia Polytechnic Institute and State University.
- Betterman, D., (1965), Contribution a l'etude de la couche limite turbulente de long de plaques rugueuses, *Rapport 65-6*, Centre National de la Recherche Scientifique, Paris, France
- Bradshaw, P., (1967), The turbulence structure of equilibrium boundary layers. *J. Fluid Mech.*, vol. 29, 625-645.
- Bradshaw, P, Ferris, D.H., and Atwell, N.P., (1967a), Calculation of boundary-layer development using the turbulent energy equation. *J. Fluid Mech.*, **28**, 593-616.
- Brown J. L., (1989), Geometric bias and time coincidence in 3D laser Doppler velocimeter systems. *Exp. in Fluids*, **7**, 25-32.
- Castro, I.P., and Robins, A.G., (1977), The flow around a surface-mounted cube in uniform and turbulent streams. *J. Fluid Mech.*, **79**, 307-335.
- Chen, C. K. and Roberson, J. A., (1974), Turbulence in wakes of roughness elements. *J. Hydraul. Div.*, Proc. ASCE, **100**, 53-67.
- Chen, C., Kim, P. J., and Walker, D. T., (1996), Angular bias errors in three-component laser velocimeter measurements. *J. Fluids Eng.*, **118**, 555-561.
- Chou, J.H., and Chao, S.Y., (2000), Branching of a horseshoe vortex around surface-mounted rectangular cylinders. *Exp Fluids*, **28**, 394-402.
- Coleman, H. W., Hodge K. B., and Taylor, R. P., (1984), A reevaluation of Schlichting's surface roughness experiment, *Trans. ASME, J. Fluids Engrg.*, **106**, 60-65.

- Coles, D. E., (1956), The law of the wake in the turbulent boundary layer''. *J. Fluid Mech.*, **1**, 191-226.
- Corino, C.R., and Brodkey, R.S., (1969), A visual investigation of the wall region in turbulent flow. *J. Fluid Mech.*, **37** (1), 1-30.
- Counihan, J., (1971), Wind tunnel determination of the roughness length as a function of the fetch and the roughness density of three-dimensional roughness elements, *Atmos. Environ.*, **5**, 637-642.
- Cutler, A.D., and Bradshaw, P., (1986), The interaction between a strong longitudinal vortex and a turbulent boundary layer. *AIAA Paper 86-1071*.
- Cutler, A.D., and Bradshaw, P., (1993a), Strong vortex/boundary layer interactions, Part I. Vortices high. *Exp Fluids*, **14**, 321-332.
- Cutler, A.D., and Bradshaw, P., (1993b), Strong vortex/boundary layer interactions, Part II. Vortices low. *Exp Fluids*, **14**, 393-401.
- Durst, F., Martinuzzi, R., Sender, J., and Thevenin, D., (1992), LDA-measurements of mean Velocity, rms-values and higher order moments of turbulence fluctuations in flow fields with strong velocity gradients, *International Symposium on Applications of Laser Techniques in Fluid Mechanics*, 1992, pp 232-240, Lisbon.
- Dvorak, F. A., (1969), Calculation of turbulent boundary layers on rough surfaces in pressure gradient, *AIAA J.*, **7**, 1752-1759.
- Esmaili, H., and Piomelli, U., (1992), Large-eddy simulation of turbulent boundary layers with embedded streamwise vortices. *AIAA Paper 92-0552*.
- Fontaine, A. A., and Deutsch, S., (1996), Structure of near wall turbulence downstream of a wall mounted protrusion: an interesting Reynolds stress suppression phenomena. *Exp Fluids*, **20**, 365-376.
- Gaudet, L. and Winter, K.G., (1973), Measurement of the drag of some characteristic aircraft excrescences immersed in turbulent boundary layers. *RAE Tech. Memo Aero. 1538*
- Gaudet, L., (1987), Measurement of the drag of various three-dimensional excrescences in turbulent boundary layers. *Aeronautical J.*, April 1987, 170-182.
- Grass, A. J., (1971), Structural features of turbulent flow over smooth and rough boundaries, *J Fluid Mech.*, **50**, 233-255.
- Gregory, N., and Walker, W.S., (1955), The effect of transition of isolated surface excrescences in the boundary layer. R. & M. 2779, Pt. I, 1955, Aeronautical Research Council, England.
- Hama, F. R., (1954), Boundary layer characteristics for smooth and rough surfaces. *Trans. Soc. Nav. Archit. Mar. Engrs.*, **62**, 333-358.
- Holman, J. P., (2001), Experimental methods for engineers, seventh ed., McGraw-Hill.
- Hunt, J.C.R., Abell, C.J., Peterka, J.A., and Woo, H., (1977), Kinematical studies of the flows around free or surface-mounted obstacles, applying topology to flow visualization. *J. Fluid Mech.* **86**, 179-200.
- Hussein, A. K. M. F., (1986), Coherent structures and turbulence. *J. Fluid Mech.*, **173**, 303-356.
- Hussein, H.J., and Martinuzzi, R.J., (1996), Energy balance for turbulent flow around a surface mounted cube placed in a channel. *Phys. Fluids*, **8** (3), 764-780.
- Ichimaya, M., (1999), The effect of a single roughness element on a flat plate boundary layer transition. *Engineering Turbulence Modeling and Experiments – 4*, W. Rodi and D. Laurence (Eds.), Elsevier Science Ltd., 1999.



- Jacobson, S.A., and Reynolds, W.C., (1998), Active control of streamwise vortices and streaks in boundary layers. *J. Fluid Mech.* **360**, 179-211.
- Jimenez, J., (2004), Turbulent flow over rough walls. *Annu. Rev. Fluid Mech.*, **36**, 173-196.
- Klebanoff, P. S., (1955), Characteristics of turbulence in a boundary layer with zero pressure gradient, NACA Rept. 1247.
- Klebanoff, P.S., Cleveland, W.G., and Tidstrom, K.D., (1992), On the evolution of a turbulent boundary layer induced by a three-dimensional roughness element. *J. Fluid Mech.* **237**, 101-187.
- Kline, S. J., and McClintock, F. A., (1953), Describing Uncertainties in Single-Sample Experiments. *Mech. Eng.*, **75**, 3-8.
- Kline S.J., Reynolds, W.C., Schraub, F.A., and Runstadler, P.W., (1967), The structure of turbulent boundary layers. *J. Fluid Mech.*, **30** (4), 741-773.
- Koloseus, H. J., and Davidian, J., (1966), Free-surface instability correlations, and roughness-concentration effects on flow over hydrodynamically-rough surfaces. *USGS Water Supply Paper 1592 C*.
- Krogstad, P.-Å., and Antonia, R. A., (1994), Structure of turbulent boundary layers on smooth and rough walls. *J. Fluid Mech.*, **277**, 1-21.
- Krogstad, P.-Å., and Antonia, R. A., (1999), Surface roughness effects in turbulent boundary layers. *Exp. Fluids.*, **27**, 450-460.
- Krogstad, P.-A., and Fannelop, T. K., (1983), Effect of roughness on three-dimensional turbulent boundary layers, *Proc. 2<sup>nd</sup> Symp. on Numerical and Physical Aspects of Aerodynamic Flows*, California State University, Long Beach, CA.
- Krogstad, P.-Å., Antonia, R. A., and Browne, L. W. B., (1992), Comparison between rough- and smooth-wall turbulent boundary layers. *J. Fluid Mech.*, **245**, 599-617.
- Ligrani, P. M., and Moffat, R. J., (1986), Structure of transitionally rough and fully rough turbulent boundary layers. *J. Fluid Mech.*, **162**, 69-98.
- Lee, B. E., and Soliman, B. F., (1977), An investigation of the forces on three dimensional bluff bodies in rough wall turbulent boundary layers, *Trans. ASME J. Fluids Engrg.*, **99**, 503-510.
- Logan, E., and Lin, S-H., (1982), Wakes from arrays of buildings. NASA CR-170666, 1982.
- Lumley, J.L., (1978), Computational modeling of turbulent flows, *Adv. Appl. Mech.*, vol. 18, 123-176.
- Marshall, J. K., (1971), Drag measurements in roughness arrays of varying density and distribution, *Agricultural metereol.*, **8**, 269-292.
- Martinuzzi, R., and Tropea, C., (1993), The flow around surface-mounted, prismatic obstacles placed in a fully developed channel flow. *Trans. ASME J. Fluids Eng.*, **115**, 85-92.
- McLaughlin, D. K., and Tiederman, W. G., (1973), Biasing correction for individual realization of laser anemometer measurements in turbulent flows. *Phys. Fluids*, **16** (12), 2082-2088.
- Mehta, R.D., Shabaka, I.M.M.A., Shibl, A., and Bradshaw, P., (1983), Longitudinal vortices imbedded in turbulent boundary layers. *AIAA Paper 83-0378*.
- Mulhearn, P. J., and Finnigan, J. J., (1978), Turbulent flow over a very rough random surface. *Boundary-layer Meteorol.*, **15**, 109-132.
- Nikuradse, J., (1933), Stromungsgesetze in rauhen rohren, *Forschungshefte*, **361**, VDI, also NACA TM 1292.

- O'Loughlin E. M., (1965), Resistance to flow over boundaries with small roughness concentrations, PhD Dissertation, Univ of Iowa.
- Ölçmen, M.S., and Simpson, R.L., (1995a), A five-velocity-component laser-Doppler velocimeter for measurements of a three-dimensional turbulent boundary layer, *Meas. Sci. and Tech.*, **6**, 702-716.
- Ölçmen, S. M., and Simpson, R. L., (1995b), An experimental study of a three-dimensional pressure-driven turbulent boundary layer, *J. Fluid Mech.*, **290**, 225-262.
- Ölçmen, S. M., and Simpson, R. L., (1996), Experimental transport-rate budgets in complex 3-D turbulent flow near a wing/body junction. *AIAA Paper 1996-2035*.
- Ölçmen, S. M., Simpson, R. L., and George, J., (2001), Some Reynolds number effects on two- and three-dimensional turbulent boundary layers. *Exp Fluids*, **31** (2), 219-228.
- Patel, V. C., (1998), Perspective Flow at High Reynolds Number and over Rough Surfaces - Achilles Heel of CFD. *ASME Journal of Fluids Engineering*, **120**, 434-444.
- Pauley, W. R., and Eaton, J. K., (1988), Experimental study of the development of longitudinal vortex pairs embedded in a turbulent boundary layer. *AIAA J.*, **26** (7), 816-823.
- Pauley, W. R., and Eaton, J. K., (1989), Boundary layer turbulence structure in the presence of embedded streamwise vortex pair. *Proc. Seventh Symposium on Turbulent Shear Flows*, , Stanford University, August 21-23, 1989.
- Perry, A. E., Schofield, W. H., and Joubert, P. N., (1969), Rough wall turbulent boundary layers, *J. Fluid Mech.*, **37**, 383-413.
- Perry, A. E., Lim, K. L., and Henbest, S. M., (1987), An experimental study of the turbulence structure in smooth- and rough-wall boundary layers, *J. Fluid Mech.*, **177**, 437-466.
- Raupach, M. R., Thom, A. S., and Edwards, I., (1980), A wind-tunnel study of turbulent flow close to regularly arrayed rough surfaces, *Boundary-layer Meteorol.*, **18**, 373-397.
- Raupach, M. R., (1981), Conditional statistics of Reynolds stress in rough-wall and smooth-wall turbulent boundary layers. *J Fluid Mech.*, **108**, 363-382.
- Raupach, M. R., Antonia, R. A., and Rajagopalan, S. (1991), Rough-wall turbulent boundary layers, *Appl Mech Rev.*, vol. 44, 1-25.
- Roberson, J. A., (1968), Surface resistance of plane boundaries roughened with discrete geometric shapes, *Bull. 308*, College of Engineering, Washington State University.
- Roberson, J. A., and Chen, C. K., (1970), Flow in conduits with low roughness concentration, *J. Hydraul. Div.*, Proc. ASCE, **96**, 941-957.
- Robinson, S.K., (1990), A perspective on coherent structures and conceptual models for turbulent boundary layer physics, *AIAA Paper 86-1071*.
- Rotta, J.C., (1962), Turbulent boundary layers in incompressible flow. *Prog. Aero Sci.*, vol. 2, Ferri, A., Kúchemann, D., Sterne, L.H.G., eds., Pergamon Press.
- Sakamoto, H., (1985), Aerodynamic forces acting on a rectangular prism placed vertically in a turbulent boundary layer. *J. Wind Eng. Ind. Aero.*, **18**, 131-151.
- Sakamoto, H., Moriya, M., Taniguchi, S., and Arie, M., (1982), The form drag of three-dimensional bluff bodies immersed in turbulent boundary layers. *Trans. ASME J. Fluids Eng.*, **104**, 326-334.
- Schlichting, H., (1936), Experimental investigation of the problem of surface roughness. *NACA TM 823*.



- Schofield, W. H., and Logan, E., (1990), Turbulent shear flow over surface mounted obstacles. *Trans. ASME J. Fluids Eng.*, **112**, 376-385.
- Sedney, R., (1973), A survey of the effects of small protuberances on boundary-layer flows. *AIAA J.*, June 1973, 782-792.
- Shabaka, I. M. M. A., Mehta, R. D., and Bradshaw, P., (1985), Longitudinal vortices imbedded in turbulent boundary layers. Part 1. Single vortex. *J. Fluid Mech.*, **155**, 37-57.
- Sigal, A., and Danberg, J. E., (1990), New correlation of roughness density effects on the turbulent boundary layer, *AIAA J.*, **28** (3), 554-556.
- Simpson, R. L., (1973), A generalized correlation of roughness density effects on the turbulent boundary layer, *AIAA J.*, **11**, 242-244.
- Simpson, R. L., (1996), Aspects of turbulent boundary-layer separation. *Prog. Aero. Sci.*, **32**, 5, 457-521.
- Simpson, R. L., (2001), Junction flows. *Annu. Rev. Fluid Mech.*, **33**, 415-443.
- Spalding D. B., (1961), A single formula for the law of the wall. *Trans ASME Series A, J Appl. Mech.*, **28** (3), 444-458.
- Schwarz, W.R., and Bradshaw, P., 1994, Turbulent structural changes in for a three-dimensional turbulent boundary layer in a 30° bend, *J. Fluid Mech.*, **272**, 183-209.
- Tani, I., (1961), Effect of two-dimensional and isolated roughness on laminar flow. Boundary Layer and Flow Control, its Principles and Applications. **2**, Lachmann, G. V. (Ed.), Pergamon Press, 1961, 637-656.
- Taniguchi, S., Sakamoto, H., and Arie, M., (1981), Flow around circular cylinders of finite height placed vertically in turbulent boundary layers. *Bull. JSME*, **24**, 37-44.
- Taylor, R. P., Coleman, H. W., and Hodge, B. K., (1984) A discrete element prediction approach for turbulent flow over rough surfaces, Rep. TFD-84-1, Mech. and Nucl. Eng. Dept., Mississippi State Univ.
- Taylor, R. P., Scaggs, W. F., and Coleman, H. W. (1988) Measurement and prediction of the effects of non-uniform surface roughness on turbulent flow friction coefficients, *Trans ASME J. Fluids Eng.*, **110**, 380-384.
- Tomkins, C. D., (2001), The structure of turbulence over smooth and rough walls. PhD Dissertation, University of Illinois at Urbana-Champaign.
- van Rij, J. A., Belnap, B. J., and Ligrani, P. M., (2002), Analysis and experiments on three-dimensional, irregular surface roughness. *Trans. ASME J. Fluids Eng.*, **124** (3), 671-677.
- Wendt, B.J., Greber, I., and Hingst, W.R., (1992), The structure and development of streamwise vortex arrays embedded in a turbulent boundary layer. *AIAA Paper 92-0551*.
- Westphal, R. V., Eaton, J. K., and Pauley, W. R., (1985), Interaction between a vortex and a turbulent boundary layer in a streamwise pressure gradient. *Turbulent Shear Flows 5*, F. Durst, B.E. Launder, J.L. Lumley, F.W. Schmidt, and J.H. Whitelaw (Eds.), Springer Verlag, New York, 266-277.
- Westphal, R. V., Pauley, W. R., and Eaton, J. K., (1987), Interaction between a vortex and a turbulent boundary layer, Part 1: Mean flow evolution and turbulence properties. *NASA TM-88361*.
- Whiffen, M. C., Lau, J. C., and Smith, D. M., (1979) Design of LV experiments for turbulence measurements. *Laser Velocimetry and Particle Sizing, Proceedings of the Third International Workshop on Laser Velocimetry*, H. D. Thompson, and W. H. Stevenson, Eds., Hemisphere, Washington, DC, 1979, 197-207.

- Wieghardt, K., (1946), Increase in turbulent skin friction caused by surface irregularities. MAP R & T No. 103, Translation of FB 1563, Zentrale Wissenschaftliche Berichte, 1942.
- Wooding, R. A., Bradley, E. F., and Marshall, J. K., (1973), Drag due to regular arrays of roughness elements of varying geometry, *Boundary-layer meteorol.*, **5**, 285-308.
- Yao, C. S., and Lin, J.C., (2002), Flow-field measurement of device-induced embedded streamwise vortex on a flat plate. *AIAA Paper 2002-3162*.
- Young, A. D., and Paterson J. H., (1981), Aircraft excrescence drag. *AGARDograph No. 264*.



## Appendix A      Method to approximate the vortex streamwise wavelength

- (i) Consider the secondary flow field in the  $y - z$  plane and find the location where  $V$  and  $W$  are zero. This is the center of rotation of the secondary flow where the radius of the vortex is zero and is denoted  $r_0$ . The subscript "0" denotes values at center of rotation.
- (ii) Therefore,  $r_0 = |z_0|$
- (iii) The circumferential velocity of the vortex,  $V_\theta$ , is  $V$  at  $y_0$  and  $z = 0$  (centerline).
- (iv) Then, the time of rotation for one revolution of the vortex,  $T_0$ , is equal to  $\frac{2\pi r_0}{V_\theta}$
- (v) If  $U_0$  is the streamwise velocity at  $y_0, z_0$  then the streamwise wavelength,  $\lambda$ , is given by

$$\lambda = \left( \frac{2\pi r_0}{V_\theta} \right) U_0$$

## Appendix B Computing the total drag due to the single element

The drag due to the single elements can be subdivided into a form pressure drag component and a skin friction component. The expression for the pressure drag is obtained through a rigorous analysis using a momentum balance involving the mean velocities and the Reynolds stresses. The skin friction component is obtained through a simplified approximation. Section B.1 contains the derivation for the form drag component and the section B.2 gives an approximation for the skin friction component. This component is due to the drastic change in the wall shear directly aft of the elements due to flow separation.

### B.1 Form drag

The expression for the form drag due to the element is derived in the following manner. First, the conservations laws are applied to a control volume (CV) enclosing one-half of the element and then they are applied to the same control volume without the half element (see Fig. B.1). The former case is indicated by a subscript 'E' and the latter case by a subscript 'NE'. The differences in the "form drag" terms between the two cases yield the form drag due to the element. The CV is chosen such that that the upstream conditions on Face 1 remain the same for both the cases and one of the faces (Face 4) of this rectangular CV is chosen such that it, simultaneously, divides the element and also coincides with the plane of flow symmetry. Therefore, the spanwise velocity component ( $W$ ) becomes zero on this face, thus yielding  $\vec{V} \cdot \vec{n} = 0$  everywhere on it, where,  $\vec{V}$ , the velocity vector is  $(U + u)\vec{i} + (V + v)\vec{j} + (W + w)\vec{k}$ . Face 2 is at 2.75 diameters ( $d$ ) downstream of the axis of the element where a full pressure recovery has taken place. Hence pressure is a constant everywhere on the sides of the CV. Face 3 is located at a spanwise distance of ' $z_u$ ' from the  $x$ -axis and is sufficiently away from the element such that both the mean and turbulent profiles do not exhibit the presence of the element but rather display undisturbed smooth wall features. The top face is located sufficiently away from the wall such that the  $U$  and  $V$  values remain the same for both the cases. Thus, the length, width and height of the rectangular CV are  $7.75d$ ,  $z_u$  and  $y_{top}$ , respectively.

Applying the conservation of mass to the control volume (CV) yields

$$\oint \rho (\vec{V} \cdot \vec{n}) dA = 0 \quad (B.1)$$

After time-averaging, the above equation becomes:

With element:

$$-\int_0^{y_{top}} \int_0^{-z_u} \rho U_1 dy dz \Big|_{E, Face 1} + \int_0^{y_{top}} \int_0^{-z_u} \rho U_2 dy dz \Big|_{E, Face 2} + \int_{-5d}^{2.75d} \int_0^{y_{top}} \rho W_3 dx dy \Big|_{E, Face 3} + \int_{-5d}^{2.75d} \int_0^{-z_u} \rho V_{top} dx dz \Big|_{E, Top Face} = 0 \quad (B.2)$$

Without the element:

$$-\int_0^{y_{top}} \int_0^{-z_u} \rho U_1 dy dz \Big|_{NE, Face 1} + \int_0^{y_{top}} \int_0^{-z_u} \rho U_2 dy dz \Big|_{NE, Face 2} + \int_{-5d}^{2.75d} \int_0^{y_{top}} \rho W_3 dx dy \Big|_{NE, Face 3} + \int_{-5d}^{2.75d} \int_0^{-z_u} \rho V_{top} dx dz \Big|_{NE, Top Face} = 0 \quad (B.3)$$

Applying the conservation of momentum to the control volume to get the  $x$ -component of forces acting on it yields

$$\oint \rho (\vec{V} \cdot \vec{i}) (\vec{V} \cdot \vec{n}) dA = - \oint \frac{dp}{dx} d\sigma - D_x \quad (B.4)$$



where,  $dA$  and  $d\sigma$  are the elemental area and volume, respectively; and,  $D_x$  is the  $x$ -component of the drag acting on the CV. This equation further leads to:  
with the element:

$$\begin{aligned} & - \int_0^{y_{top}} \int_0^{-z_u} \rho (U_1^2 + \overline{u_1^2}) dydz \Big|_{E, Face1} + \int_0^{y_{top}} \int_0^{-z_u} \rho (U_2^2 + \overline{u_2^2}) dydz \Big|_{E, Face2} + \int_{-5d}^{2.75d} \int_0^{y_{top}} [\rho U_3 W_3 + (\rho \overline{uw})_3] dx dy \Big|_{E, Face3} \\ & + \int_{-5d}^{2.75d} \int_0^{-z_u} [\rho U_{top} V_{top} + (\rho \overline{uv})_{top}] dx dz \Big|_{E, Top Face} = - \frac{dp}{dx} (Vol.) \Big|_E - D_{x,E} \end{aligned} \quad (B.5)$$

where,  $Vol.$  is the volume of the CV, and  
without the element:

$$\begin{aligned} & - \int_0^{y_{top}} \int_0^{-z_u} \rho (U_1^2 + \overline{u_1^2}) dydz \Big|_{NE, Face1} + \int_0^{y_{top}} \int_0^{-z_u} \rho (U_2^2 + \overline{u_2^2}) dydz \Big|_{NE, Face2} + \int_{-5d}^{2.75d} \int_0^{y_{top}} [\rho U_3 W_3 + (\rho \overline{uw})_3] dx dy \Big|_{NE, Face3} \\ & + \int_{-5d}^{2.75d} \int_0^{-z_u} [\rho U_{top} V_{top} + (\rho \overline{uv})_{top}] dx dz \Big|_{NE, Top Face} = - \frac{dp}{dx} (Vol.) \Big|_{NE} - D_{x,NE} \end{aligned} \quad (B.6)$$

Subtracting (6) from (5), gives

$$\begin{aligned} & - \int_0^{y_{top}} \int_0^{-z_u} \rho (U_2^2|_{NE} - U_2^2|_E) dydz - \int_0^{y_{top}} \int_0^{-z_u} \rho (\overline{u_2^2}|_{NE} - \overline{u_2^2}|_E) dydz - \int_{-5d}^{2.75d} \int_0^{y_{top}} \rho (U_3|_{NE} W_3|_{NE} - U_3|_E W_3|_E) dx dy \\ & - \int_{-5d}^{2.75d} \int_0^{y_{top}} [\rho \overline{uw}]_3|_{NE} - (\rho \overline{uw})_3|_E dx dy - \int_{-5d}^{2.75d} \int_0^{-z_u} \rho (U_{top}|_{NE} V_{top}|_{NE} - U_{top}|_E V_{top}|_E) dx dz \\ & = - \int_{-5d}^{2.75d} \int_0^{-z_u} [(-\rho \overline{uv})_{top}|_{NE} - (-\rho \overline{uv})_{top}|_E] dx dz - D_{x,E} + D_{x,NE} \end{aligned} \quad (B.7)$$

Please note that the streamwise mean velocity  $U$  profiles and streamwise normal stresses  $\overline{u^2}$  profiles on Face 1 are the same for the two cases. The streamwise pressure gradient is nominally zero and remains the same for both cases and hence these terms cancel each other.

Multiplying each of the terms in Eqs. B.2 and B.3 with their respective streamwise velocity at the top face,  $U_{top}$ , and then rearranging yields:

$$\begin{aligned} U_{top}|_E \int_{-5d}^{2.75d} \int_0^{-z_u} \rho V_{top} dx dz \Big|_{E, Top Face} &= U_{top}|_E \int_0^{y_{top}} \int_0^{-z_u} \rho U_1 dydz \Big|_{E, Face1} - U_{top}|_E \int_0^{y_{top}} \int_0^{-z_u} \rho U_2 dydz \Big|_{E, Face2} - U_{top}|_E \int_{-5d}^{2.75d} \int_0^{y_{top}} \rho W_3 dx dy \Big|_{E, Face3} \\ U_{top}|_{NE} \int_{-5d}^{2.75d} \int_0^{-z_u} \rho V_{top} dx dz \Big|_{NE, Top Face} &= U_{top}|_{NE} \int_0^{y_{top}} \int_0^{-z_u} \rho U_1 dydz \Big|_{NE, Face1} - U_{top}|_{NE} \int_0^{y_{top}} \int_0^{-z_u} \rho U_2 dydz \Big|_{NE, Face2} - U_{top}|_{NE} \int_{-5d}^{2.75d} \int_0^{y_{top}} \rho W_3 dx dy \Big|_{NE, Face3} \end{aligned}$$

Substituting the above two equations in the fifth term in the LHS of equation B.5 gives,

$$\begin{aligned}
& - \underbrace{\int_0^{y_{top}} \int_0^{-z_u} \rho (U_2^2|_{NE} - U_2^2|_E) dydz}_{1} - \underbrace{\int_0^{y_{top}} \int_0^{-z_u} (\rho \overline{u^2}|_{NE} - \rho \overline{u^2}|_E) dydz}_{2} \\
& - \underbrace{\int_{-5d}^{2.75d} \int_0^{y_{top}} \rho (U_3|_{NE} W_3|_{NE} - U_3|_E W_3|_E) dx dy}_{3} - \underbrace{\int_{-5d}^{2.75d} \int_0^{y_{top}} [\rho \overline{uw}]_3|_{NE} - (\rho \overline{uw})_3|_E dx dy}_{4} \\
& - \underbrace{\left[ U_{top}|_{NE} \int_0^{y_{top}} \int_0^{-z_u} \rho U_1|_{NE} dydz - U_{top}|_E \int_0^{y_{top}} \int_0^{-z_u} \rho U_1|_E dydz \right]_{Face1}}_5 + \underbrace{\left[ U_{top}|_{NE} \int_0^{y_{top}} \int_0^{-z_u} \rho U_2|_{NE} dydz - U_{top}|_E \int_0^{y_{top}} \int_0^{-z_u} \rho U_2|_E dydz \right]_{Face2}}_6 \\
& + \underbrace{\left[ U_{top}|_{NE} \int_{-5d}^{2.75d} \int_0^{y_{top}} \rho W_3|_{NE} dx dy - U_{top}|_E \int_{-5d}^{2.75d} \int_0^{y_{top}} \rho W_3|_E dx dy \right]_{Face3}}_7 \\
& = - \underbrace{\int_{-5d}^{2.75d} \int_0^{-z_u} (-\rho \overline{uv})_{top}|_{NE} - (-\rho \overline{uv})_{top}|_E dx dz}_{8} - \Delta D_{element}
\end{aligned} \tag{B.8}$$

For large spanwise distances away from the centerline ( $x$ -axis), on Face 3, terms 3, 4 and 7 reduce to zero. Term 5 too vanishes since the  $U_1$  profiles are the same for both cases of with and without the element. Term 6 can be further simplified since at the top edge of Face 2, the  $U$  values remain constant with  $z$ -direction and are the same for both cases, i.e.,  $U_{top}|_{NE} = U_{top}|_E$  on Face 2. These observations stem from the  $U$  data on the single elements at the top edges of Face 2 [see Fig. 3.4 (a)], edges that are also the top edges of the CV and are located, away from the wall. The top edges are at:  $7k$  for the smallest cylinder,  $4.5k$  for the intermediate cylinder and  $3k$  for the highest cylinder and the Gaussian spike, where  $k$  is the height of the single element. Face 3 of the CV for all the four single elements was located parallel to the  $x$ -axis at a spanwise distance of  $4d$  from it. If the normal distance from the wall is large enough, values of  $(-\rho \overline{uv})_{top}|_{NE}$  tend towards those of  $(-\rho \overline{uv})_{top}|_E$ , which is the case at the top faces of the CV [see Fig. 3.20 (a)], and hence term 8 reduces to zero too. Also,  $-\Delta D_{element} = -D_{x,E} + D_{x,NE}$ , where  $\Delta D_{element}$  is the form drag due to the element which can be expressed as

$$\Delta D_{element} = \rho \int_0^{y_{top}} \int_0^{-z_u} (U_2|_{NE} - U_2|_E) (U_2|_{NE} + U_2|_E - U_{top}|_{NE}) dydz + \rho \int_0^{y_{top}} \int_0^{-z_u} (\overline{u^2}|_{NE} - \overline{u^2}|_E) dydz \tag{B.9}$$

and is evaluated on Face 2 of the CV. This equation can be further simplified from the knowledge that at the furthest spanwise location on this face, i.e., at  $z = -z_u$ , the  $U$  and  $\overline{u^2}$  profiles considering the case with the element are same as those without the element. This leads to  $U_2|_{NE} = U_2|_{E, z=-z_u}$ ,

$U_{top}|_{NE} = U_{top}|_{E, z=-z_u}$ , and  $\overline{u^2}|_{NE} = \overline{u^2}|_{E, z=-z_u}$ . Hence this expression, evaluated on Face 2, becomes:

$$\Delta D_{element} = \rho \int_0^{y_{top}} \int_0^{-z_u} (U_2|_{E, z=-z_u} - U_2|_E) (U_2|_{E, z=-z_u} + U_2|_E - U_{top}|_{E, z=-z_u}) dydz + \rho \int_0^{y_{top}} \int_0^{-z_u} (\overline{u^2}|_{E, z=-z_u} - \overline{u^2}|_E) dydz \tag{B.10}$$

Please note that Face 2 is located at  $x/d = 2.75$  for all the four elements. In summary, to calculate the form drag due to the element all one needs to do is to measure the  $U$  and  $\overline{u^2}$  profiles on Face 2. As mentioned previously,  $y_{top} = 7k$  for the smallest cylinder,  $4.5k$  for the intermediate cylinder and  $3k$  for the highest cylinder and the Gaussian spike and  $z_u = 4d$  for all the four elements. Since only half



of the element or half of flow domain is considered in the above analysis, the total form drag due to the element would **twice** of that obtained from equation (8).

A form drag coefficient,  $C_{d,form}$ , expressed in terms of the free-stream dynamic pressure, can be given as,

$$C_{d,form} = \frac{2\Delta D_{element}}{\frac{1}{2}\rho U_e^2 A} = \frac{2\rho \int_0^{y_{top}} \int_0^{-z_u} \left\{ \left( U_2|_{E,z=-z_u} - U_2|_E \right) \left( U_2|_{E,z=-z_u} + U_2|_E - U_{top}|_{E,z=-z_u} \right) + \left( \overline{u_2^2}|_{E,z=-z_u} - \overline{u_2^2}|_E \right) \right\} dydz}{\frac{1}{2}\rho U_e^2 A} \quad (B.11)$$

where, the denominator is the free-stream dynamic pressure times the frontal projected area of the element ( $A$ ).

## B.2 Skin friction drag

This component of drag is due to the fact that the wall shear aft of the elements is not the same as the smooth wall values. The separated flow regions behind the elements have drastically different wall shear values and are much different from those away from the centerline and at the far spanwise locations. This aspect is taken into account using a simple approximation. The entire separated region from the elements to the downstream edge ( $x/d=2.75$ ) at the wall is approximated as a triangular section. Thus, the triangular section has the element diameter as the base with its apex at the downstream edge on the center line, i.e., at  $x/d=2.75$ ,  $z=0$ . The area of this triangular section where the wake influence is felt is denoted as  $A_{inner}$ . An average skin friction coefficient for this area is calculated and is denoted as  $C_{f,inner}$ . If no value is available, then the value of the skin friction coefficient at the apex is assigned to it. The rest of the floor area in the control volume (CV1) is denoted as  $A_{outer}$  and the smooth wall skin friction coefficient value is assigned to it and this is denoted as  $C_{f,outer}$ . Please note that the control volume (CV1) has width extending from  $-z_u$  to  $z_u$ . Hence, CV1 is twice as large as CV. The expression for the skin friction component of the drag,  $C_{d,skin}$ , is given by

$$C_{d,skin} = \frac{-[C_{f,outer} (\frac{1}{2}\rho U_e^2) A_{outer} + C_{f,inner} (\frac{1}{2}\rho U_e^2) A_{inner}]}{\frac{1}{2}\rho U_e^2 A} \quad (B.12)$$

Hence, the drag coefficient,  $C_d$ , is given by

$$C_d = C_{d,form} + C_{d,skin} \quad (B.13)$$

## Figures

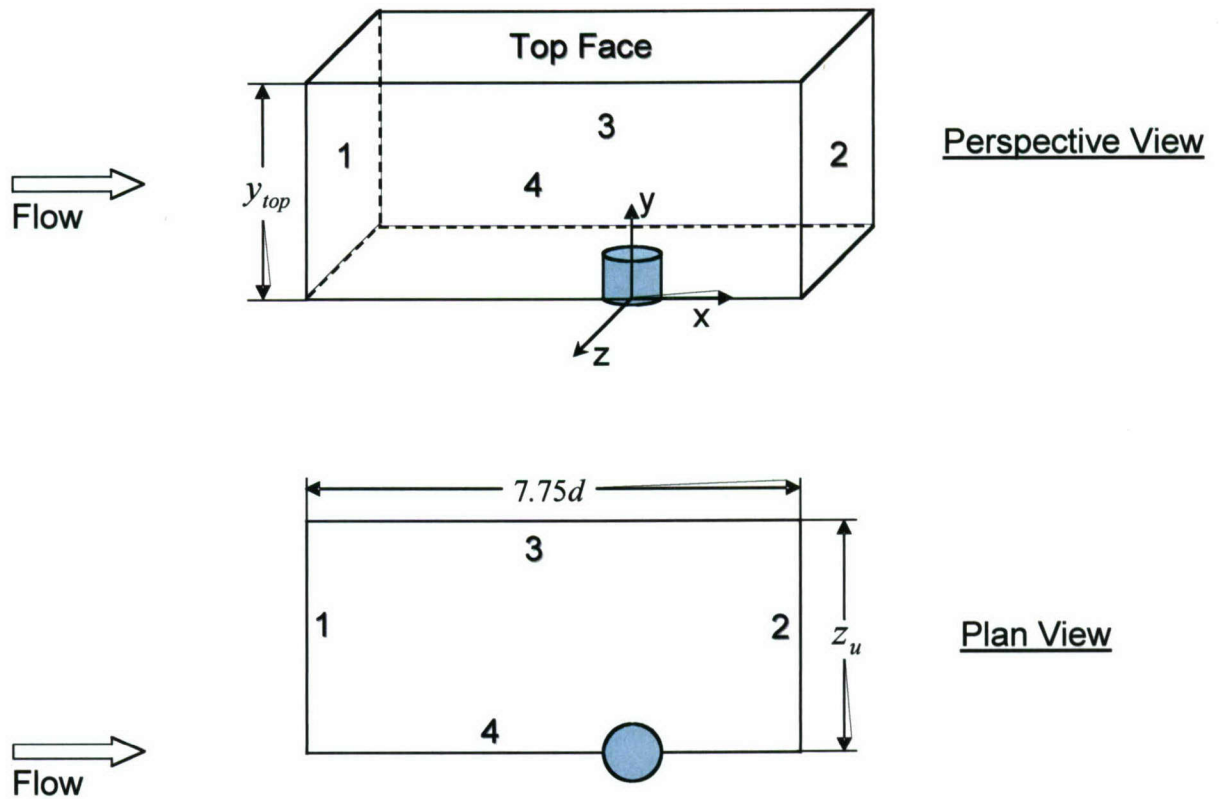


Figure B.1: Views of the element with the control volume enclosing one-half of the flow domain.



## Appendix C      Uncertainty analysis on the data

This section gives the bounds of uncertainties in the measured and inferred quantities. It also contains, in detail, several corrections that are applicable to the data acquired by the LDV system. The uncertainties in the quantities are discussed and presented in the following order:

- C.1. Corrections applicable to the acquired LDV data
- C.2. Friction/Scale velocity
- C.3. Wall location, mean velocities and turbulence quantities
- C.4. Drag due to single elements
- C.5. Circulation
- C.6. Mean Vorticity

### C.1 Corrections applicable to the acquired LDV data

There are several factors that introduce errors and distort the true value of the measurements and they are listed below. Each of them is discussed in detail and the corrections were made to the acquired data. Further, the effect of each correction is presented at the end of the sub-section.

1. Velocity bias effects
2. Angular bias effects
3. Fringe bias and geometric bias effects.
4. Broadening effects :
  - (a) Velocity gradient broadening
  - (b) Finite transit time broadening
  - (c) Instrument broadening

#### C.1.1 Velocity bias effects

McLaughlin and Tiedermann (1973) noticed that their mean velocity measurements of a turbulent boundary layer were consistently higher than the predicted theory. They reasoned that a uniformly seeded volume would yield a greater number of particle passages per unit time through the sample volume as the velocity increased. Since the number of measurements of the higher velocities would be greater than the number from lower velocities, the statistical velocity mean would be weighted towards the higher velocities leading to a “velocity bias” in the measurements. Applying a weighting function of inverse velocity to the statistical calculations would yield measurements much closer to the theory.

In order to determine if a velocity bias exists in the measurements, one needs to calculate a correlation coefficient ( $C$ ) between the data rate fluctuations and the fluctuations in the magnitudes of velocity which is defined as

$$C = \frac{\sum_{i=1}^n (V - |v_i|)(DR - dr_i)/n}{\sigma_v \sigma_{dr}}$$

where,  $V$  is the statistical mean velocity from the selected measurement ensemble and  $v_i$  is the  $i^{\text{th}}$  velocity during the shortest period of time considered to be independent from the other times.  $DR$  is defined as the statistical mean data rate of the data rate fluctuations,  $dr_i$ , during the  $i^{\text{th}}$  flow correlation time.  $\sigma_v$  and  $\sigma_{dr}$  denote the standard deviations in the velocity fluctuations and the data rate fluctuations, respectively.

For the present data set, the correlation coefficient was found to be the order of  $10^{-4}$  or less thus demonstrating the absence of any effects of “velocity bias.”

### C.1.2 Angular bias effects

For three-component laser velocimeter systems, the change in projected area of the coincident measurement volume for different flow directions will introduce an “angular” bias in naturally sampled data (Chen *et al.*, 1996). For the present orthogonal system and nearly spherical probe volume, there are only small variations in the projected areas of the measurement volume for the various flow directions and hence it is concluded that negligible bias effects are present.

### C.1.3 Fringe bias and geometric bias effects

Whiffen *et al.* (1979) have discussed this effect which is caused by the requirement that a particle cross sufficiently many fringes as it transits the measurement volume. In our case, this effect is not present since only particles passing through the coincident measurement volume are validated. The geometric bias as identified by Brown (1989) is eliminated as a valid sample also obeys true spatial coincidence in addition to the imposed temporal coincidence time window.

### C.1.4 Broadening effects

(a) *Velocity gradient broadening :*

Corrections to the measurements need to be applied when the probe volume encounters significant velocity gradients, e.g., at regions close to the wall. For the measurements made in a flow with a velocity gradient, successive particles passing through the measurement volume may have different velocities by virtue of its differing positions in the gradient. Hence, even if the flow is completely steady, the LDV will measure a velocity fluctuation. This error may be corrected simply by subtracting the extra variance from the measured value. For the mean velocity and turbulence quantities, following expressions (Durst *et al.*, 1992) are used to correct the measured data.

$$\begin{aligned}\overline{U}_{i \text{ true}} &= \overline{U}_{i \text{ meas}} - \frac{d^2}{32} \left( \frac{d^2 (\overline{U}_{i \text{ true}})}{dy^2} \right) \\ \overline{u_i^2} &= \overline{u_i^2} \text{ meas} - \frac{d^2}{16} \left( \frac{d (\overline{U}_{i \text{ true}})^2}{dy} \right) \\ \overline{u_i^3} &= \overline{u_i^3} \text{ meas} - \frac{3d^2}{16} \left( \frac{d \overline{u_i^2}}{dy} \right)_{\text{true}} \left( \frac{d \overline{U}_i}{dy} \right)_{\text{true}}\end{aligned}$$

For correcting the present data-set of nine double products and ten triple products in the regular Cartesian coordinates, the following extended derivations were used.

$$\begin{aligned}\overline{U}_{\text{true}} &= \overline{U}_{\text{meas}} - \frac{d^2}{32} \left( \frac{d^2 (\overline{U}_{\text{true}})}{dy^2} \right) \\ \overline{V}_{\text{true}} &= \overline{V}_{\text{meas}} - \frac{d^2}{32} \left( \frac{d^2 (\overline{V}_{\text{true}})}{dy^2} \right) \\ \overline{W}_{\text{true}} &= \overline{W}_{\text{meas}} - \frac{d^2}{32} \left( \frac{d^2 (\overline{W}_{\text{true}})}{dy^2} \right) \\ \overline{u^2}_{\text{true}} &= \overline{u^2}_{\text{meas}} - \frac{d^2}{16} \left( \frac{d (\overline{U}_{\text{true}})^2}{dy} \right)\end{aligned}$$



$$\begin{aligned}
\overline{v^2}_{true} &= \overline{v^2}_{meas} - \frac{d^2}{16} \left( \frac{d(\overline{V}_{true})}{dy} \right)^2 \\
\overline{w^2}_{true} &= \overline{w^2}_{meas} - \frac{d^2}{16} \left( \frac{d(\overline{W}_{true})}{dy} \right)^2 \\
\overline{uv}_{true} &= \overline{uv}_{meas} - \frac{d^2}{16} \left( \frac{d(\overline{U}_{true})}{dy} \right) \left( \frac{d(\overline{V}_{true})}{dy} \right) \\
\overline{uw}_{true} &= \overline{uw}_{meas} - \frac{d^2}{16} \left( \frac{d(\overline{U}_{true})}{dy} \right) \left( \frac{d(\overline{W}_{true})}{dy} \right) \\
\overline{vw}_{true} &= \overline{vw}_{meas} - \frac{d^2}{16} \left( \frac{d(\overline{V}_{true})}{dy} \right) \left( \frac{d(\overline{W}_{true})}{dy} \right) \\
\overline{u^2v}_{true} &= \overline{u^2v}_{meas} - \frac{d^2}{16} \left[ 2 \left( \frac{d(\overline{U}_{true})}{dy} \right) \left( \frac{d(\overline{uv}_{true})}{dy} \right) + \left( \frac{d(\overline{V}_{true})}{dy} \right) \left( \frac{d(\overline{u^2}_{true})}{dy} \right) \right] \\
\overline{u^2w}_{true} &= \overline{u^2w}_{meas} - \frac{d^2}{16} \left[ 2 \left( \frac{d(\overline{U}_{true})}{dy} \right) \left( \frac{d(\overline{uw}_{true})}{dy} \right) + \left( \frac{d(\overline{W}_{true})}{dy} \right) \left( \frac{d(\overline{u^2}_{true})}{dy} \right) \right] \\
\overline{v^2w}_{true} &= \overline{v^2w}_{meas} - \frac{d^2}{16} \left[ 2 \left( \frac{d(\overline{V}_{true})}{dy} \right) \left( \frac{d(\overline{vw}_{true})}{dy} \right) + \left( \frac{d(\overline{W}_{true})}{dy} \right) \left( \frac{d(\overline{v^2}_{true})}{dy} \right) \right] \\
\overline{v^2u}_{true} &= \overline{v^2u}_{meas} - \frac{d^2}{16} \left[ 2 \left( \frac{d(\overline{V}_{true})}{dy} \right) \left( \frac{d(\overline{vu}_{true})}{dy} \right) + \left( \frac{d(\overline{U}_{true})}{dy} \right) \left( \frac{d(\overline{v^2}_{true})}{dy} \right) \right] \\
\overline{w^2u}_{true} &= \overline{w^2u}_{meas} - \frac{d^2}{16} \left[ 2 \left( \frac{d(\overline{W}_{true})}{dy} \right) \left( \frac{d(\overline{wu}_{true})}{dy} \right) + \left( \frac{d(\overline{U}_{true})}{dy} \right) \left( \frac{d(\overline{w^2}_{true})}{dy} \right) \right] \\
\overline{w^2v}_{true} &= \overline{w^2v}_{meas} - \frac{d^2}{16} \left[ 2 \left( \frac{d(\overline{W}_{true})}{dy} \right) \left( \frac{d(\overline{wv}_{true})}{dy} \right) + \left( \frac{d(\overline{V}_{true})}{dy} \right) \left( \frac{d(\overline{w^2}_{true})}{dy} \right) \right] \\
\overline{uvw}_{true} &= \overline{uvw}_{meas} - \frac{d^2}{16} \left[ \left( \frac{d(\overline{U}_{true})}{dy} \right) \left( \frac{d(\overline{vw}_{true})}{dy} \right) + \left( \frac{d(\overline{V}_{true})}{dy} \right) \left( \frac{d(\overline{uw}_{true})}{dy} \right) + \left( \frac{d(\overline{W}_{true})}{dy} \right) \left( \frac{d(\overline{uv}_{true})}{dy} \right) \right] \\
\overline{u^3}_{true} &= \overline{u^3}_{meas} - \frac{d^2}{16} \left[ 3 \left( \frac{d(\overline{U}_{true})}{dy} \right) \left( \frac{d(\overline{u^2}_{true})}{dy} \right) \right] \\
\overline{v^3}_{true} &= \overline{v^3}_{meas} - \frac{d^2}{16} \left[ 3 \left( \frac{d(\overline{V}_{true})}{dy} \right) \left( \frac{d(\overline{v^2}_{true})}{dy} \right) \right] \\
\overline{w^3}_{true} &= \overline{w^3}_{meas} - \frac{d^2}{16} \left[ 3 \left( \frac{d(\overline{W}_{true})}{dy} \right) \left( \frac{d(\overline{w^2}_{true})}{dy} \right) \right]
\end{aligned}$$

Due to the small nearly spherical probe volume which was about 30 microns in the diameter (d), negligible changes occurred when the above corrections were applied.

(b) *Finite transit time broadening*

This error comes from the fact that, when processing a signal burst, one is trying to deduce a frequency from a limited number of cycles. The fewer the number of fringes, the lesser the number of

cycles and thus the larger is the potential error. Differing errors on successive bursts from particles traveling at the same speed give the impression of a velocity fluctuation when there is none. This error may be corrected simply by subtracting the extra variance from the measured value. This broadening relative to the mean frequency is expressed as

$$\frac{\sigma_F}{\omega_D} = \frac{1}{2\sqrt{2}N_\sigma}$$

where,  $N_\sigma$  fringes are found in a width  $\sigma_1$  of the volume. The effects of finite transit time broadening were found to be negligible.

### (c) Instrument broadening

Investigations by Ölçmen *et al.* (2001) on the instrument broadening effect on the measured frequency by the Macrodyne processors and found these effects to be negligible.

## C.2 Friction/scale velocity

Different scaling velocities were used for the three flow cases. For the case of the single elements, the velocity scale is the friction velocity ( $U_\tau$ ) of the undisturbed smooth wall TBL. Six independent profiles of the smooth wall TBL, taken during different days, are used to arrive at the uncertainty in this quantity with the aid of the student  $t$  distribution table. The uncertainty in the friction velocity,  $\delta(U_\tau)$ , is then given by:

$$\delta(U_\tau) = \frac{2.447\sigma}{\sqrt{n}},$$

where,  $\sigma$  is the standard deviation of the mean for each  $n$  number of independent smooth-wall 2-D TBL data-sets which in this case,  $n = 6$ . The number 2.447 is the value obtained from the student  $t$  distribution table for 6 independent observations. Using the above equation, the uncertainty in the friction velocity,  $\delta(U_\tau)$ , is  $\pm 3\%$ .

As regards the scaling velocities for the rough-wall cases,  $\sqrt{-uv_{\max}}$  for the 2-D TBL and  $U_{\tau o}$  for the 3-D TBL, the uncertainties are calculated with the aid of *Chauvenet's criterion*. This criterion is used to eliminate dubious data points where one first calculates the mean value and standard deviation for all data points. For the present case where 5 independent profiles were used, *Chauvenet's criterion* dictated that the limit of ratio of maximum acceptable deviation ( $d_{\max}$ ) to the standard deviation ( $\sigma$ ), i.e.,  $d_{\max}/\sigma$  be 1.65. Hence, all data points that lie beyond  $1.65\sigma$  were eliminated. After this process, the mean and standard deviation of the data sets were recalculated. Then the uncertainty in the quantities with 20:1 odds was given by  $\pm 1.96\sigma$ . With this approach, the uncertainties in  $\sqrt{-uv_{\max}}$  and  $U_{\tau o}$  with 20:1 odds were found to be  $\pm 4\%$  and  $\pm 5\%$ .

## C.3 Measurement location, mean velocities and turbulence quantities

The uncertainties in the measurement locations along the  $x$ ,  $y$  and  $z$  positions are  $\pm 25\mu$ ,  $\pm 10\mu$  and  $\pm 25\mu$ , respectively. Several corrections, as listed in section C.1, were applied to the data. However, each of these corrections to the values of mean velocities and turbulence quantities were less than an order of magnitude of the overall uncertainties and hence, these corrections were not applied to the entire data-sets. The overall uncertainties in the mean velocities and the turbulence quantities, acquired through the LDV, were determined using the same Chauvenet's criterion described in the previous section. In this case too, 5 independent profiles were used.

To obtain the overall uncertainties in the non-dimensionalized values of mean velocities and turbulence quantities, a scheme described by (Kline and McClintock, 1953, Holman, 2001) was used.



This scheme states that, if, result  $R$  can be expressed as a function of independent quantities,  $x_1, x_2, x_3, \dots, x_n$ , such that  $R = R(x_1, x_2, \dots, x_n)$ , and if  $w_1, w_2, w_3, \dots, w_n$  be the uncertainties in the independent quantities, then the uncertainty in the result,  $w_R$  is given by

$$w_R = \left[ \left( \frac{\partial R}{\partial x_1} w_1 \right)^2 + \left( \frac{\partial R}{\partial x_2} w_2 \right)^2 + \dots + \left( \frac{\partial R}{\partial x_n} w_n \right)^2 \right]^{1/2}$$

If the uncertainties in the independent quantities are all given with same odds, then the uncertainty in the results is given with the same odds as well. Using this scheme, the uncertainties in the non-dimensionalized values of the mean velocities and turbulence quantities, with 20:1 odds, is presented in Table C.1.

Table C.1. Uncertainty estimates of the measured quantities with odds 20:1 [Single Elements, 2-D Rough-wall TBL and 3-D Rough-wall TBL].

Single Elements		2-D Rough-wall TBL		3-D Rough-wall TBL	
Term	Uncertainty	Term	Uncertainty	Term	Uncertainty
$U/U_\tau$	$\pm 0.28$	$U/\sqrt{-\overline{uv}_{\max}}$	$\pm 0.28$	$U/U_{\tau o}$	$\pm 0.28$
$V/U_\tau$	$\pm 0.05$	$V/\sqrt{-\overline{uv}_{\max}}$	$\pm 0.05$	$V/U_{\tau o}$	$\pm 0.06$
$W/U_\tau$	$\pm 0.07$	$W/\sqrt{-\overline{uv}_{\max}}$	$\pm 0.07$	$W/U_{\tau o}$	$\pm 0.08$
$\overline{u^2}/U_\tau^2$	$\pm 0.20$	$\overline{u^2}/-\overline{uv}_{\max}$	$\pm 0.21$	$\overline{u^2}/U_{\tau o}^2$	$\pm 0.22$
$\overline{v^2}/U_\tau^2$	$\pm 0.08$	$\overline{v^2}/-\overline{uv}_{\max}$	$\pm 0.10$	$\overline{v^2}/U_{\tau o}^2$	$\pm 0.11$
$\overline{w^2}/U_\tau^2$	$\pm 0.09$	$\overline{w^2}/-\overline{uv}_{\max}$	$\pm 0.10$	$\overline{w^2}/U_{\tau o}^2$	$\pm 0.12$
$-\overline{uv}/U_\tau^2$	$\pm 0.07$	$-\overline{uv}/-\overline{uv}_{\max}$	$\pm 0.09$	$-\overline{uv}/U_{\tau o}^2$	$\pm 0.11$
$-\overline{uw}/U_\tau^2$	$\pm 0.07$	$-\overline{uw}/-\overline{uv}_{\max}$	$\pm 0.09$	$-\overline{uw}/U_{\tau o}^2$	$\pm 0.11$
$-\overline{vw}/U_\tau^2$	$\pm 0.08$	$-\overline{vw}/-\overline{uv}_{\max}$	$\pm 0.10$	$-\overline{vw}/U_{\tau o}^2$	$\pm 0.12$
$(\overline{q^2}/2)/U_\tau^2$	$\pm 0.24$	$(\overline{q^2}/2)/-\overline{uv}_{\max}$	$\pm 0.26$	$(\overline{q^2}/2)/U_{\tau o}^2$	$\pm 0.28$
$U_q/U_\tau$	$\pm 0.56$	$U_q/-\overline{uv}_{\max}$	$\pm 0.58$	$U_q/U_{\tau o}$	$\pm 0.61$
$V_q/U_\tau$	$\pm 0.30$	$V_q/-\overline{uv}_{\max}$	$\pm 0.35$	$V_q/U_{\tau o}$	$\pm 0.39$
$W_q/U_\tau$	$\pm 0.32$	$W_q/-\overline{uv}_{\max}$	$\pm 0.36$	$W_q/U_{\tau o}$	$\pm 0.40$

#### C.4 Drag due to single elements

Since the drag is obtained by the integration of the flow quantities in a plane, a perturbation (jitter) analysis was performed to arrive at the uncertainty in this quantity. This analysis is similar to the one presented by Bennington (2004). The expression for the drag reveals that its uncertainty is

primarily due to the individual uncertainties in the streamwise mean velocity,  $U$ , and the streamwise Reynolds normal stresses,  $\overline{u^2}$ . From the available uncertainties of these two quantities (Table C.1), the standard deviation ( $\sigma$ ) is calculated as  $\delta(\ )/1.96$ , where  $\delta(\ )$  is the uncertainty in the two quantities. This is because the uncertainty was arrived in the previous section using  $\pm 1.96\sigma$ . A set of random numbers was generated that had a normal distribution with a mean of 0 and a standard deviation of 1. This set of random numbers was multiplied by the standard deviations of the two quantities to obtain a 'perturbation' vector. The respective perturbations were added to the original quantities to yield the perturbed  $U$  and  $\overline{u^2}$ . Using these perturbed quantities the drag was recalculated. This process of perturbations is performed 10 times to obtain 10 values of drag and a standard deviation is obtained which when multiplied by 1.96 yields the uncertainty in this quantity. Since the measurement locations are relative to the centerline and the wall, the perturbations in the  $y$  and  $z$  positions were considered negligible and hence neglected. From this analysis, the uncertainty in drag coefficient,  $C_d$ , is found to be  $\pm 5\%$ .

### C.5 Circulation

The circulation ( $\Gamma$ ) aft of the single elements is obtained from a contour integral around a rectangular plane enclosing the region of interest. Of the two horizontal edges of this rectangular plane (normal to the streamwise axis) one is the wall and the other is a line parallel to the wall and also sufficiently far from it such that  $W=0$  on it. This implies that the uncertainty in circulation is primarily due to the uncertainty in the wall-normal velocity,  $V$ . Since circulation is an integrated value, a perturbation analysis was performed in this case too, similar to the scheme described in the previous section. In this case the  $V/U_\tau$  velocity profiles were perturbed and the perturbations in the  $y$  positions were considered negligible. Using the perturbation analysis, the uncertainty in  $\Gamma/(U_\tau \sqrt{A})$  is determined to be  $\pm 5\%$ .

### C.6 Mean vorticity

The normalized mean vorticity vector ( $\vec{\Omega}^+$ ) can be considered as a function of independent variables such as the velocity vector ( $\vec{V}$ ), position ( $\vec{s}$ ) and the friction/scale velocity ( $U_\tau$  or  $\sqrt{-uv_{\max}}$ ). Hence, following the scheme described by (Kline and McClintock, 1953, Holman, 2001), the uncertainty in  $\vec{\Omega}^+$  is given by

$$\left[ \left( \frac{\partial \vec{\Omega}^+}{\partial \vec{V}} \delta(\vec{V}) \right)^2 + \left( \frac{\partial \vec{\Omega}^+}{\partial \vec{s}} \delta(\vec{s}) \right)^2 + \left( \frac{\partial \vec{\Omega}^+}{\partial (U_\tau \text{ or } \sqrt{-uv_{\max}})} \delta(U_\tau \text{ or } \sqrt{-uv_{\max}}) \right)^2 \right]^{1/2}$$

From this analysis, the uncertainty in  $\Omega_x \sqrt{A}/\sqrt{-uv_{\max}}$  is  $\pm 0.15$  for the single elements and the uncertainties in  $\Omega_x \sqrt{A}/\sqrt{-uv_{\max}}$ ,  $\Omega_y \sqrt{A}/\sqrt{-uv_{\max}}$  and  $\Omega_z \sqrt{A}/\sqrt{-uv_{\max}}$  are  $\pm 0.15$ ,  $\pm 0.3$  and  $\pm 0.3$ , respectively, for the 2-D rough-wall TBL.



# Glossary

Roughness top vortex structure RTVS	Roughness top vortex structure emanating from the top of the individual protuberances or the single roughness element
BL	Boundary layer
Fetch	Uniform distribution of roughness elements (cylinders)
Roughness top vortex structure RTVS	Roughness top vortex structure emanating from the top of the individual protuberances or the single roughness element
Sweeps	Individual fluctuating motions that contribute to Reynolds stresses: belonging to quadrant 2 ( $u > 0, v < 0$ ) through quadrant analysis
Ejections	Individual fluctuating motions that contribute to Reynolds stresses: belonging to quadrant 4 ( $u < 0, v > 0$ ) through quadrant analysis
Inrush	Wallward flow of high speed fluid, especially that which occur over the top of the elements
Updraft	Upward draft of low speed fluid in the back flow regions located directly behind the elements
LDV	Laser Doppler Velocimeter
TBL	Turbulent Boundary Layer
TKE	Turbulent kinetic energy, TKE, ( $\overline{q^2}/2$ ), where, $\overline{q^2} = (\overline{u^2} + \overline{v^2} + \overline{w^2})$
VG	Vortex Generator

## Vita

Jacob George started his undergraduate education at the University of Kerala, Trivandrum, India where he obtained a Bachelor of Technology degree in Mechanical Engineering in November, 1990. In Fall 1994, he was awarded a Master of Science degree in Aerospace Engineering from the Indian Institute of Technology, Madras, India. For his Doctoral studies he entered the graduate program in the Aerospace and Ocean Engineering Department at Virginia Polytechnic Institute and State University in Blacksburg, Virginia, U.S.A. He completed the requirements for a Doctoral degree in Aerospace Engineering in the summer of 2005. During the graduate program, he also taught a few junior level courses in the Department of Aerospace Engineering at Virginia Tech. In April 2002, he was awarded the Paul E. Torgersen Research Excellence award, instituted by the College of Engineering at Virginia Tech, recognizing distinguished research by an engineering student in the PhD program. In January, 2003, he joined the Department of Aerospace Engineering at Virginia Tech as a Research Associate. In June, 2005, he will be employed as a Post Doctoral Researcher in the Department of Mechanical Engineering at Ohio State University, Columbus, Ohio, U.S.A., where he will be specializing in the area of aero-optics.